

Sheffield Hallam University

Control of texture and formability in ferritic stainless steels.

BOULTON, Catherine Dorothy.

Available from the Sheffield Hallam University Research Archive (SHURA) at:

<http://shura.shu.ac.uk/19374/>

A Sheffield Hallam University thesis

This thesis is protected by copyright which belongs to the author.

The content must not be changed in any way or sold commercially in any format or medium without the formal permission of the author.

When referring to this work, full bibliographic details including the author, title, awarding institution and date of the thesis must be given.

Please visit <http://shura.shu.ac.uk/19374/> and <http://shura.shu.ac.uk/information.html> for further details about copyright and re-use permissions.

SHEFFIELD CITY
POLYTECHNIC LIBRARY
POND STREET
SHEFFIELD S1 1WB

6834

100 908 401 1

TELEPEN



Sheffield City Polytechnic Library

REFERENCE ONLY

ProQuest Number: 10694255

All rights reserved

INFORMATION TO ALL USERS

The quality of this reproduction is dependent upon the quality of the copy submitted.

In the unlikely event that the author did not send a complete manuscript and there are missing pages, these will be noted. Also, if material had to be removed, a note will indicate the deletion.



ProQuest 10694255

Published by ProQuest LLC (2017). Copyright of the Dissertation is held by the Author.

All rights reserved.

This work is protected against unauthorized copying under Title 17, United States Code
Microform Edition © ProQuest LLC.

ProQuest LLC.
789 East Eisenhower Parkway
P.O. Box 1346
Ann Arbor, MI 48106 – 1346

CONTROL OF TEXTURE AND FORMABILITY
IN FERRITIC STAINLESS STEELS

by

CATHERINE DOROTHY BOULTON

A THESIS SUBMITTED TO THE COUNCIL
FOR NATIONAL ACADEMIC AWARDS IN
PARTIAL FULFILMENT OF THE REQUIREMENTS
FOR THE DEGREE OF

DOCTOR OF PHILOSOPHY

SEPTEMBER, 1986

SPONSORING ESTABLISHMENT :

DEPARTMENT OF METALS AND MATERIALS ENGINEERING,
SHEFFIELD CITY POLYTECHNIC,
SHEFFIELD,
ENGLAND.

COLLABORATING ESTABLISHMENT :

BRITISH STEEL CORPORATION (STAINLESS),
SHEPCOTE LANE,
SHEFFIELD,
ENGLAND.



PREFACE

The work described in this thesis was carried out at Sheffield City Polytechnic between 1st October 1982 and 30th September 1985, under the supervision of Dr. R.P. Stratton, Direction of Studies, and Dr. M.J. Dickson.

Mr. J. Wilkinson, of BSC Stainless, acted in an advisory capacity.

In accordance with the regulations for the PhD. in Industrial Metallurgy, the relevant parts of the MSc. in Metallurgical Process Management (Director of Studies Dr. A.J. Fletcher) were successfully completed. The candidate's performance during this course was assessed by means of written examinations and continuous assessment of specific assignments. The details of the course are given below :-

MODULE I

1. Process Metallurgy.
2. Mechanical Metallurgy.
3. Applied Thermodynamics.

MODULE II

1. Economics.
2. Accountancy
3. Finance
4. Operational Research
5. Numerical Methods
6. Computer Programming.

MODULE III

1. High Strength Steels
2. Stainless Steels
3. Secondary Steelmaking
4. Heat Treatment
5. Automatic and Computer-aided Control
6. Quality Assurance.

MODULE IV CASE STUDIES

1. Why have Stainless Maraging Steels never taken off?
2. The Japanese approach to Quality.
3. Properties, Applications and Processing of Ferritic Stainless Steels. *

* This case study, which is related to the current research, is presented with the thesis, as Appendix C.

ACKNOWLEDGEMENTS

The author is grateful to the Sponsoring Establishment, Sheffield City Polytechnic, and the Collaborating Establishment, BSC Stainless, for enabling this work to be carried out. I am particularly indebted to the supervisors, Dr. R.P. Stratton and Dr. M.J. Dickson, for all their help and advice. In addition, I would like to thank Mr. J. Wilkinson, the Industrial Supervisor, Dr. B. Harkness of BSC Stainless, and all SCP academic staff involved in the MSc. in Metallurgical Process Management. I am also grateful to the following technical staff for their assistance:- Dr. D.B. Lewis, Dr. J. Cawley, Mr. P. Haythorne, Mr. P. Slingsby, Mrs. R. Thomas, Mr. S. Leigh, and Mr. R. Day. Thanks are also due to my mother, Mrs. D. Ward, for typing this thesis. Finally, I must thank my husband, Brendan, for help with proof-reading but mostly for just being there and helping me to keep going.

ABSTRACT

The effects of processing variables on the microstructures, textures and press-formability of commercial 17 Cr, 0.05C (430) steel and low-interstitial Ti-stabilised 12 Cr (409) and 17 Cr (430 Ti) steels have been studied. The annealing textures have been correlated with tensile strain ratio measurements and from this correlation it has been possible to select combinations of cold rolling reduction and annealing treatments for texture control to improve deep drawability. Electron microscope examination has been used to identify possible nucleation mechanisms for the observed recrystallisation textures. Cold rolling texture development and tensile strain ratios have been discussed from theoretical considerations of slip in bcc metals.

Pronounced differences in microstructural features between high interstitial 430 and low-interstitial Ti-stabilised steels are reflected in differences in texture development at all stages. Hot band condition is an important variable, affecting texture development during subsequent cold rolling and annealing.

All three steels develop similar cold rolling textures, consisting mainly of $\sim\{100\} \langle 011 \rangle$, $\sim\{111\} \langle 112 \rangle$ and $\sim\{112\} \langle 110 \rangle$ components. The $\sim\{112\} \langle 110 \rangle$ orientation is more prominent in 430 Ti steel than in 430 steel, and it is suggested that this difference may be due to irregular flow in high interstitial 430 steel. Other differences in cold rolling textures are attributed to texture inheritance from the hot band.

Recrystallisation textures in 430 steel are mainly $\sim\{114\} \langle 841 \rangle$, with $\sim\{223\} \langle 962 \rangle$ present after high reductions, and \bar{r} -values are generally low.

Recrystallisation textures in 409 and 430 Ti steels are mainly $\sim\{110\} \langle 001 \rangle$ after low cold rolling reductions, $\sim\{554\} \langle 225 \rangle$ after moderate or high reductions and $\sim\{223\} \langle 962 \rangle$ after very high reductions. In most cases, $\sim\{100\} \langle 011 \rangle$ is only a minor component. Batch annealing of the hot rolled strip followed by cold rolling to 90% RA and rapid final annealing promotes maximum $\sim\{554\} \langle 225 \rangle$ intensity with low $\sim\{100\} \langle uvw \rangle$ intensity, and a correspondingly high \bar{r} -value.

The $\sim\{223\} \langle 962 \rangle$ and $\sim\{114\} \langle 841 \rangle$ orientations, attributed to grain boundary nucleation, have not been reported previously in 17 Cr ferritic stainless steels, although they have been reported occasionally in other low-carbon ferritic steels.

	<u>Page</u>
1. <u>INTRODUCTION</u>	1
2. <u>REVIEW OF LITERATURE</u>	2 - 74
2.1. Texture in Metals	2
2.2. Theories of Deformation Textures in BCC Metals	9
2.3. Theories of Recrystallisation Textures in BCC Metals	16
2.4. Press Formability of Metals	33
2.5. Physical Metallurgy of Ferritic Stainless Steels	47
2.6. Previous work on Texture and Formability of Ferritic Steels	57
3. <u>EXPERIMENTAL METHODS</u>	75 - 93
3.1. Heat Treatment	75
3.2. Cold Rolling	75
3.3. Specimen Preparation	75
3.4. Grain Size Measurement	77
3.5. Scanning Electron Metallography ...	78
3.6. Transmission Electron Metallography	78
3.7. Hardness Measurement	81
3.8. Tensile Testing	81
3.9. Simulative Formability Testing	84
3.10. Assessment of Roping Severity	85
3.11. Pole Figure Determination	86
3.12. Texture Parameter Evaluation	91

4.	<u>EXPERIMENTAL RESULTS</u>	94 - 135
	4.1. Microstructural Features	96
	4.2. Hot Rolling Textures	106
	4.3. Cold Rolling Textures	110
	4.4. Primary Recrystallisation Textures.	116
	4.5. Uniaxial Tensile Data	127
	4.6. Roping Tests	132
	4.7. Simulative Formability Tests	133
5.	<u>DISCUSSION</u>	136 - 169
	5.1. Textures of hot rolled or hot rolled and pre-annealed strip ...	136
	5.2. Cold Rolling Textures	139
	5.3. Recrystallisation Textures	149
	5.4. Press Formability	160
	5.5. Processing Schedules for Optimum Texture and Formability	167
6.	<u>CONCLUSIONS</u>	170 - 171
7.	<u>SUGGESTIONS FOR FURTHER WORK</u>	172 - 173
8.	<u>REFERENCES</u>	174 - 184
9.	<u>TABLES</u>	185 - 222
10.	<u>FIGURES</u>	223 - 428
	<u>APPENDICES</u>	I - LXII
	<u>APPENDIX A</u> Crystal Rotations due to Slip in Plane Strain Rolling	I
	<u>APPENDIX B</u> Calculation of Theoretical r-values and earing profiles using the method of Vieth and Whiteley	VII
	<u>APPENDIX C</u> Properties , Applications and Processing of Ferritic Stainless Steels - A Case Study	XIX

Since the advent of the AOD process, commercial production of low interstitial grades of ferritic stainless steels has become viable. Coupled with the possibility of stabilising with niobium or titanium, or of alloying with molybdenum, this has led to a new generation of ferritic alloys which are weldable and have enhanced corrosion resistance. Although ferritic stainless steels still cannot rival austenitic grades in terms of general corrosion resistance and stretch formability, they are readily cold worked and have adequate corrosion resistance for many applications. New markets are emerging for these alloys, especially as cheaper replacement materials for more costly grades of steel, and/or as improved replacement materials for lower grades of steel with inferior corrosion resistance.

Recent interest has been shown in the crystallographic textures of ferritic stainless steels and their effect on formability, but there are still areas of dispute that require further study. Little attention has been devoted to commercial steels, most of the previous studies having been performed on vacuum melted laboratory casts. The present investigation is concerned with the effects of processing variables (in particular, annealing treatments before and/or after cold rolling, and cold rolling reduction) on the microstructures, textures and press-forming characteristics of 17% Cr, 0.05%C (430) steel, low-interstitial titanium-stabilised 12% Cr (409) steel, and low-interstitial titanium stabilised 17% Cr (430 Ti) steel, supplied in the as-hot-rolled condition.

2.1. TEXTURE IN METALS

2.1.1. Origins of Texture

(a) Solidification

A texture can arise as a result of directional solidification, and columnar grains in an ingot usually exhibit preferred orientation. For example, the growth direction in bcc metals is invariably $\langle 100 \rangle$, i.e., $\langle 100 \rangle$ directions are normal to the mould wall and parallel with the direction of heat flow and hence the axis of columnar grains. (1) The central equiaxed zone of an ingot does not show preferred orientation.

(b) Deformation

A deformation texture is developed due to rotation of crystals by slip under the action of imposed stress/strain. The re-orientation is gradual, proceeding until a texture is reached that is stable against indefinitely continued flow of the same type. (1) The nature of the stable texture is influenced by the imposed stress system and the slip systems operative in the material. Under tension the stress axis moves towards the operative slip direction whilst in compression it moves towards the pole of the operative slip plane. (2)

Uniaxial stressing causes alignment of specific directions parallel with the axis of stressing. This type of preferred orientation is known as a "wire" or "fibre" texture. In general there are no special radial orientations, although in wire drawing radial compressive stresses may cause certain planes to lie parallel with the surface of the wire to produce a "cylindrical"

texture. A simple fibre texture is usually described in terms of a direction $\langle uvw \rangle$ parallel with the stress axis.

Rolling of sheet or strip under plane strain conditions causes alignment of specific crystallographic directions with the rolling direction and specific planes with the rolling plane. Hence rolling textures are often described in terms of one or more ideal orientations expressed as $\{hkl\} \langle uvw \rangle$ where $\{hkl\}$ is the rolling plane and $\langle uvw \rangle$ the rolling direction.

Deformation textures can be influenced by temperature, particularly if it is high enough to permit recrystallisation, e.g., hot rolling produces a much less pronounced texture than cold rolling due to dynamic recrystallisation. The occurrence of a phase transformation may further randomise the crystal orientations. (1)

Second phases may also have an effect, e.g., high carbon steels form less pronounced textures than low carbon steels due to Fe_3C being harder than ferrite and forcing it to flow in irregular directions. (4)

(c) Recrystallisation

When a cold worked metal containing a strong preferred orientation is annealed there are a number of possibilities. The final annealing texture could be :

- (i) the same as the deformation texture, particularly if recovery alone occurs,
- (ii) a different texture due to recrystallisation into new grains with orientations different from but crystallographically related to those of the

deformation texture, or

- (iii) a randomised texture, especially if a phase transformation occurs during annealing.

Recrystallisation textures are affected by composition, time and temperature of annealing, and prior processing. In particular, important factors include the deformation texture, microstructure and presence or absence of a phase transformation.

2.1.2. Representation of Texture

Although a texture can be labelled by a single ideal orientation, $\langle uvw \rangle$ or $\{hkl\} \langle uvw \rangle$, this type of description is often inadequate in practice. More usually, descriptions are in terms of more than one ideal orientation or the spread between ideal orientations.

A more complete description of a texture is given by a pole figure, determined by X-ray texture goniometry. (5) A pole figure is a stereographic projection which shows the variation in pole density with orientation for a selected set of crystal planes. (5) Intensities are plotted as multiples of the intensity expected from a randomly oriented specimen and the pole figure is contoured. Ideal orientations may be plotted on the pole figure for reference. For cubic crystals, a particular orientation on a pole figure can be described by any of the following (6) :-

Three	$\{100\}$	poles
Four	$\{111\}$	poles
Six	$\{110\}$	poles
Twelve	$\{hk0\}$	poles
Twenty-four	$\{hkl\}$	poles

For simplicity, practical selection of poles is normally limited to $\{100\}$, $\{111\}$ or $\{110\}$. However, since there is no Bragg reflection from the $\{100\}$ planes of bcc or fcc metals, the second order $\{200\}$ reflection must be measured, and it is usual to refer to the pole figure in terms of the $\{200\}$ reflection used in its determination. A similar situation arises with the $\{222\}$ reflection in bcc metals and the $\{220\}$ reflection in fcc metals. Bcc textures are therefore described by $\{110\}$, $\{200\}$ or $\{222\}$ pole figures and fcc textures by $\{111\}$, $\{200\}$ or $\{220\}$ pole figures.

Conventional pole figures are the most common method of presenting textural data for processes requiring specification of two perpendicular directions. For deformation processes of higher symmetry that require only one axis to be specified, an inverse pole figure or axis distribution chart can be useful. This figure uses a stereographic unit triangle as a reference frame and contour lines to show the frequency at which various directions in the crystal coincide with the specimen axis under consideration. (7)

An alternative description of texture is provided by the orientation distribution function (odf), which specifies volume densities of crystallites having

a given orientation. (8) Methods of calculating the orientation distribution function from conventional pole figure data are now available (9) and have been used for quantification of relationships between texture and mechanical properties. (8,10) Three-dimensional odf's are computed from data obtained from several pole figures of different reflecting planes. Preferred orientations can be described by density functions within the three-dimensional figure, using contour surfaces to separate volumes of higher and lower orientation density. In order to present the results it is usual to take a series of sections through the figure, showing the contour surfaces as a series of contour lines. (8) Odf's have not been applied as widely as conventional pole figures and axis distribution charts, due to their greater complexity and the large amount of data needed.

2.1.3. General Observations in BCC Metals

(a) Tension and Compression Textures

Body centred cubic metals invariably have a simple $\langle 110 \rangle$ fibre texture after cold drawing. (1,3) Compression textures consist of a major $\langle 111 \rangle$ fibre texture component plus a weaker $\langle 100 \rangle$ component. (1,3)

(b) Rolling Textures

The cold rolling textures of all bcc metals are essentially the same and are largely unaffected by alloy additions, except possibly those causing precipitation. (3) The textures develop gradually with increasing deformation and comprise a continuous spread of orientations from

$\{100\} \langle 011 \rangle$ through $\{111\} \langle 011 \rangle$ to $\{111\} \langle 112 \rangle$. (7)

The spread has also been described in terms of partial fibre textures.

Barrett and Levenson, (11) investigating rotations of single crystals of iron, recorded two continuous sets of orientations :-

- (i) $\langle 110 \rangle$ parallel with RD and $\{001\}$ between 0° and $45-55^\circ$ from the rolling plane,
- (ii) $\{111\}$ parallel with the rolling plane and a spread about the sheet plane normal (ND);
(i.e. a partial tension axis along RD and a partial compression axis along ND ($RD // \langle 110 \rangle$, $ND // \langle 111 \rangle$)).

Richards and Ormay (12) preferred to depict the cold rolling textures of low carbon steels in terms of two partial $\langle 110 \rangle$ fibre textures A and B :-

- (A) $\langle 110 \rangle$ parallel to RD, with orientations in the spread from $(21\bar{1}) [011]$ - $(100) [011]$ - $(2\bar{1}1) [011]$;
- (B) $\langle 110 \rangle$ 60° away from RD (30° from ND) in the plane containing RD and ND, and comprising the spread from $(21\bar{1}) [110]$ - $(55\bar{4}) [225]$ - $(12\bar{1}) [101]$.

In general, it is found that the strongest component is $\{100\} \langle 011 \rangle$ and that $\{112\} \langle 110 \rangle$ is always present. The $\{111\} \langle 110 \rangle$ orientation has been reported less frequently and $\{111\} \langle 112 \rangle$ has been reported as a strong component in some instances but not in others. (3)

(c) Recrystallisation Textures

Reported recrystallisation textures of cold-rolled

and annealed bcc metals have included the following components :- $\{111\} \langle 110 \rangle$, $\{110\} \langle 001 \rangle$, $\{100\} \langle 011 \rangle$ and $\{111\} \langle 112 \rangle$ (or more precisely $\{554\} \langle 225 \rangle$ which is within $\sim 6^\circ$ of $\{111\} \langle 112 \rangle$). (3,7,13) Development of recrystallisation textures is markedly affected by material and processing variables, to the extent that quite different annealing textures can be obtained from two specimens exhibiting essentially similar cold rolling textures. The primary recrystallisation textures of low carbon steels, in particular ferritic stainless steels, are considered in detail in a later section.

2.2.1. Slip Systems

Development of a deformation texture is brought about mainly by crystal rotations due to slip. In bcc crystals the slip direction is invariably $\langle 111 \rangle$, but the slip plane is not well defined. For many years there has been a dispute (14-20) as to whether bcc metals deform by :-

- (i) $\langle 111 \rangle$ pencil glide (non-crystallographic slip in closest packed directions on planes of maximum shear stress),
- (ii) a combination of $\{110\} \langle 111 \rangle$, $\{112\} \langle 111 \rangle$ and $\{123\} \langle 111 \rangle$ slip, or
- (iii) elementary slip on $\{110\}$ and/or $\{112\}$ planes giving the appearance of (i) or (ii).

It is often assumed that, when all three slip planes ($\{110\}$, $\{112\}$ and $\{123\}$) operate, the critical resolved shear stress for slip (τ_c) on each plane is equal. However, Smoluschowski and Opinsky (21) suggested that the magnitudes of the critical resolved shear stresses for slip on $\{110\}$, $\{112\}$ and $\{123\}$ planes are in the ratio 1:1.03:1.05 respectively.

2.2.2. Deformation Models

Theories of texture development tend to fall into two categories depending on the deformation model chosen, i.e., either the imposed stress model (Sachs) or the imposed strain model (Taylor).

According to the Taylor model, (22) all crystals undergo the macroscopic shape change. At least five independent slip systems are required and the choice of

operative slip systems is governed by the principle of minimum internal work, i.e., the combination which will operate is that giving the lowest algebraic sum of shears. An indication of the work necessary to carry out the deformation of a grain in a particular orientation is given by the Taylor "M-Factor" or stress factor, which is the ratio of the applied stress to the shear stress developed on the operative slip plane(s). (22,23)

Grains of low M-value deform easily, but high M-value grains are crystallographically hard. (22,23)

Although Taylor failed to recognise the necessity of ensuring that the yield criterion was not violated, it was later shown (24,25) that Taylor's minimum shear sum was in fact equivalent to fulfilment of the yield criterion. The equivalence of Taylor's theory with a later analysis, developed by Bishop and Hill (26) and based on maximum external work, was also demonstrated. (24,25)

Whereas the Taylor model ignores stress equilibrium requirements and concentrates on grain continuity, the reverse is true of the Sachs constant stress model (27) which, for a uniaxial tensile test, leads to results that would be obtained assuming a series of parallel but free single crystals. (25) The component of strain in the tensile direction would be the same for every grain, although all other strain components would vary from grain to grain; the tensile stress would differ from grain to grain but all other stress components would be zero. This situation would fulfil stress equilibrium and yield criteria, but would violate compatibility requirements. (25)

The Sachs model is considered a lower bound theory and the Taylor model an upper bound theory. The Taylor analysis generally leads to superior predictions of the flow curve, strain ratios and deformation textures. (10,28) Recently Wierzbanski and Jasienski (29) concluded from numerical predictions that the essential difference between the two models is the occurrence of latent slip in Taylor-type deformation, i.e., principal slip systems account for the macroscopic shape change but differences in shape between individual grains are accounted for by latent slip.

2.2.3. Rolling Textures

Taylor (22) considered only fcc metals in his analysis, and for a long time this mathematical solution was considered too unwieldy to apply to bcc metals, in which the large number of slip systems available results in there being over a million ways of choosing five. (4) However, more recently a number of authors have applied computer simulation studies to the deformation of bcc metals, using the generalised Taylor model to predict the combination of slip systems which would operate for any given initial orientation and hence to calculate lattice rotations. (20,23,30,31) Earlier theories of bcc texture development required additional assumptions to make the data manageable.

Calnan and Clews (2) were responsible for one of the earliest theories of rolling textures in bcc metals. They reasoned that, due to the symmetrical disposition of slip planes, no grain rotation would occur during multiple

slip. For the high degree of preferred orientation observed after severe plastic deformation, there must, therefore, be a considerable amount of single and duplex slip to effect the necessary grain rotations, with some multiple slip to maintain grain boundary cohesion. Once the effective tensile stress reaches a direction sufficiently symmetrical for multiple slip to take place, no further rotation would occur and a stable end orientation would be achieved. In order to predict rolling textures, it was assumed that orientations would persist which satisfied both tension and compression end points simultaneously. The bcc rolling textures predicted for slip on various systems were listed as follows. (2)

Slip System	Textures in order of decreasing magnitude
$\{110\} \langle 111 \rangle$	$\{211\} \langle 110 \leftarrow 311 \rangle$, $\{111\} \langle 110 \rangle$, $\{100\} \langle 011 \rangle$
$\{112\} \langle 111 \rangle$	$\{111\} \langle 110 \leftarrow 211 \rangle$, $\{100\} \langle 011 \rangle$
$\{123\} \langle 111 \rangle$	$\{311\} \langle 110 \leftarrow 311 \rangle$, $\{111\} \langle 110 \rangle$, $\{100\} \langle 011 \rangle$
3 systems	$\{411\} \langle 110 \leftarrow \sim 511 \rangle$, $\{111\} \langle 110 \rangle$, $\{100\} \langle 011 \rangle$

Dillamore and Roberts (32) developed a theory of rolling textures based on primary and conjugate slip followed by cross-slip, assuming a bi-axial state of stress. For bcc metals, assuming operative slip systems of type $\{110\} \langle 111 \rangle$, they concluded that most material would rotate under the action of primary and conjugate slip to orientations of type $\{112\} \langle 110 \rangle$ and that, after cross slip, the rolling texture should be adequately described by the spread from $\{100\} \langle 011 \rangle$ towards

$\{211\} \langle 011 \rangle$.

Neither Calnan and Clews ⁽²⁾ nor Dillamore and Roberts ⁽³²⁾ accounted for the strong $\{111\} \langle 112 \rangle$ component observed in some, but not all, rolling textures. However, Dillamore, Butler and Green ⁽³³⁾ later predicted, from the results of a total strain analysis of slip rotations during rolling, that the stable end orientations for bcc metals were $\{112\} \langle 110 \rangle$, $\{001\} \langle 110 \rangle$ and $\{11, 11, 8\} \langle 4, 4, 11 \rangle$. They concluded that $\{111\} \langle 112 \rangle$ was not a stable end orientation.

Kamijo ⁽³⁴⁾ used a method similar to that of Dillamore and Roberts ⁽³²⁾ , considering slip on $\{110\}$, $\{112\}$ and $\{123\}$ planes and assuming $\tau_c \{123\} = \tau_c \{112\} = 1.05 \tau_c \{110\}$, to study slip rotations towards stable end positions on a stereographic projection. He proposed that the operation of slip systems of types $\{011\} \langle 111 \rangle$ and $\{112\} \langle 111 \rangle$ would account for development of texture components $\{111\} \langle 112 \rangle$, $\{112\} \langle 110 \rangle$ and $\{100\} \langle 011 \rangle$, although only the latter two components would remain as stable end orientations. The gradual displacement of $\{111\} \langle 112 \rangle$ towards $\{112\} \langle 110 \rangle$ was attributed to conjugate slip on $\{110\} \langle 111 \rangle$ systems. Kamijo ⁽³⁴⁾ also concluded that the $\{110\} \langle 001 \rangle$ orientation (when present), although not developed by slip rotations, is stable provided that the rolling direction does not deviate even slightly towards $\langle 111 \rangle$. If this deviation does occur, slip rotations lead to development of the $\{111\} \langle 112 \rangle$ orientation (inevitably via $\{554\} \langle 225 \rangle$).

Dillamore and Katoh (28) compared theoretical pole figures and odf maps, derived using both Sachs and Taylor theories and assuming $\langle 111 \rangle$ pencil glide, with experimental results for iron cold rolled to 70% RA. Discrepancies between predicted and observed data were attributed to non-homogeneous deformation. It was pointed out that, if favourably oriented grains (low Taylor M-value) are to undergo exactly the same strain as harder, less favourably oriented grains (high Taylor M-value), the stress continuity condition is violated. In reality the softer grains will yield first and it will require stress concentrations within these grains to cause the harder grains to deform. Hence the softer grains will incur more lattice curvature, since they will be forced to accommodate any harder grains which fail to conform to the imposed shape change. Dillamore and Katoh (28) suggested that it would be more favourable for the harder grains to deform heterogeneously, with a strain different from the mean strain, if this resulted in a reduction of the total energy of deformation. The softer grains must then accommodate these heterogeneities.

In view of the complexity of deformation of real polycrystals in which equilibrium, yield and compatibility requirements must be met simultaneously and there is the additional complication of non-homogeneous flow and deformation bands, discrepancies between observations and predictions of deformation texture, based on either constant stress or constant strain, are inevitable. However, most workers are in agreement that the framework of the Taylor model allows the most

2.3. THEORIES OF RECRYSTALLISATION TEXTURES IN BCC METALS

2.3.1. Oriented Growth versus Oriented Nucleation

Historically, two principal mechanisms have been proposed to account for annealing textures ⁽¹⁰⁾ :-

- (i) The Oriented Growth theory assumes that all possible orientations are present at the start of recrystallisation and that selection of favoured ones occurs during growth.
- (ii) The Oriented Nucleation theory assumes that the growth rate is independent of the orientation of newly formed grains, and that this orientation depends on the availability of nuclei in the deformation substructure.

More recently, compromise theories have been proposed in which both nucleation and growth conditions have to be satisfied. There has been much experimentation and discussion in trying to decide which approach best describes the observed behaviour. ^(13,35-38)

It is found that recrystallisation textures often bear crystallographic relationships to the original deformation texture. For bcc metals, the relationship is described as a 25° - 35° rotation about a $\langle 110 \rangle$ axis which is common to both the cold working and recrystallisation textures. ^(3,7,19,36) Such relationships were supposed to correspond to high rates of growth associated with high boundary mobility, ⁽¹⁹⁾ and experimental evidence does show that mobilities of

low angle ($< 15^\circ$ misorientation) and possibly of very high angle ($> 45^\circ$) boundaries are restricted compared with the intermediate range. (10,38)

Dillamore (13) used a purely geometric method, based on oriented growth, to predict major components of annealing textures. Under conditions of high growth rate, the major components were predicted as $\{hhl\} \langle 110 \rangle$ with $\{111\} \langle 110 \rangle$ predominating, whereas for low growth rate, the major components were predicted as $\{554\} \langle 225 \rangle$ and $\{10,8,7\} \langle 1,3,5 \rangle$. (It should be pointed out that the latter is not actually a true orientation and was possibly meant to be $\{11,8,7\} \langle 1,3,5 \rangle$).

Dillamore, Smith and Watson (37) later compared growth and nucleation theories on the basis of results obtained from electron microscope examination of pure iron and low carbon steels. Having evaluated the driving force for recrystallisation as a function of orientation, they concluded that, although both theories forecast broadly similar textures, oriented nucleation predicts a component near $\{001\} \langle 110 \rangle$ (arising from grain-boundary nucleation), which is in fact observed experimentally but is not accounted for by oriented growth.

It is now generally agreed that experimental evidence is more in favour of oriented nucleation, at least as far as bcc metals are concerned. (7,10,39,40) Dillamore (40) has criticised his earlier geometric approach, deciding that, although simple formal transformations may be found to convert one texture into another, this should not be taken to imply a mechanism.

The "special growth relationship" concept of pure oriented growth theory was refuted on the basis of electron microscope observations which showed that all probable nucleation sites occur in regions of high lattice curvature where, by definition, a special growth relationship cannot be sustained. (40)

Although oriented nucleation is more widely accepted, it is still recognised that growth processes can be important, e.g., in situations where precipitation and recrystallisation interact. (40) During recrystallisation, precipitates forming preferentially on new grain boundaries inhibit growth of the first formed grains, forcing further nucleation to occur in unrecrystallised regions from less favourable nuclei. In such cases, the resultant annealing texture tends to be similar to the deformation texture. Also, alloying elements in dilute solid solution have the effect of increasing the ratio of nucleation rate to growth rate, thereby reducing the sharpness of the annealing texture and causing it to resemble the deformation texture more closely. The effect of decreasing solute content is seen in steels with very low manganese and/or interstitial contents, where the $\{111\}$ sheet plane texture component is markedly strengthened during recrystallisation. (41)

2.3.2. Nucleation

Modern theories of recrystallisation tend to nullify the classical argument between oriented growth and oriented nucleation. Recrystallisation is now

envisaged as a continuous process of growth, in which the embryo is stable with respect to its surroundings at all stages. However, the velocity of growth is not constant: there is an initial slow growth or incubation period corresponding with the nucleation stage, followed by a sharp increase in growth rate coinciding with the start of the classical growth stage.

Most workers (42-45) now agree that no new orientations are developed during recrystallisation, so that a nucleus must either pre-exist in the deformed state or be evolved in the recovery process. A nucleus comprises a nearly perfect lattice region, of the order of $1\mu\text{m}$ diameter, which is separated from the deformed matrix by a newly formed high angle boundary and is capable of growth into the matrix in at least one direction. (45,46) The nucleation process consists of development of such a region, usually by growth of subgrains in the deformed matrix, (46) and electron microscope observations have shown a number of configurations in which such nuclei are likely to occur. (10) Nucleation sites available at low strains ($< 40\%$ RA) differ from those at higher strains. (43)

In general, nucleation occurs in regions of high lattice curvature, although continuous recrystallisation by subgrain growth without high angle boundary movement is possible in regions of very low lattice curvature under certain circumstances. For normal, discontinuous recrystallisation, nucleation is associated with grain interiors (in-situ), grain boundaries, transition bands, shear bands or second phase particles.

(a) In-situ Nucleation

For a subgrain to act as a nucleus it must be capable of growing into the deformed matrix and quickly achieving a high angle boundary. (47) High local stored energy (associated with small subgrain size but large variation in size) and sharp lattice curvature (which allows the growing embryo to develop a high angle grain boundary quickly) are necessary for rapid subgrain growth. (46-49) Consequently, nuclei develop preferentially in those regions where there are high local misorientations, e.g., grain boundaries and transition bands. However, after moderate to high cold reductions, individual subgrains in the grain interiors may be sufficiently misoriented to achieve these conditions. (44)

The distribution of stored energy within a deformed structure can vary with orientation of individual grains, but conflicting results exist as to the ranking of various orientations. According to Smith and Dillamore, (49) the stored energy of cold working (V) in bcc metals increases in the following order :-

$$V \{100\} \langle 011 \rangle < V \{211\} \langle 011 \rangle < V \{111\} \langle uvw \rangle < V \{011\} \langle 100 \rangle .$$

In-situ nucleation should, therefore, normally occur in the reverse order, i.e., $\{011\}$, $\{111\}$, $\{211\}$, $\{100\}$. However, Takechi, Kado and Nagashima (50) found that, in low carbon steel rolled to very high reductions ($\sim 90\%$ RA), the order of stored energy of the main components changed to :-

$$V \{311\} \approx V \{411\} > V \{211\} > V \{111\} > V \{100\} ,$$

whereas, in low carbon, niobium-stabilised steels cold rolled to 72% RA, Willis and Hatherly ⁽⁵¹⁾ recorded :-

$$V \{211\} > V \{100\} > V \{111\} .$$

In the absence of restrictions to growth, nuclei formed earliest should constitute the largest grains in the recrystallised material and should, therefore, dominate the recrystallisation texture, provided that there are sufficient numbers of viable nuclei of that component. In heavily cold worked bcc metals, the fact that in-situ nucleated $\{110\}$ grains do not constitute a major component of the recrystallisation texture is attributed to limited availability of $\{110\}$ nuclei in the deformed structure. ⁽⁴⁷⁾

(b) Grain Boundary Nucleation

According to Hutchinson ⁽⁴⁷⁾ there are two possible mechanisms for grain boundary nucleation :-

- (i) an existing high angle boundary may bow out into the grain which has the higher stored energy at the interface (termed strain induced boundary migration), or
- (ii) a nucleus may develop from a subgrain close to the grain boundary.

Strain induced boundary migration (SIBM) is accepted by many authors as an important origin of new grains at low to moderate (10%-50% RA) deformations, ^(42,43,46,47) although Doherty and Cahn ⁽⁴⁶⁾ suggested that preferential subgrain growth close to the boundary might be a necessary precursor to this mechanism.

Doherty and Cahn ⁽⁴⁶⁾ proposed that nucleation should occur preferentially at grain edges in deformed

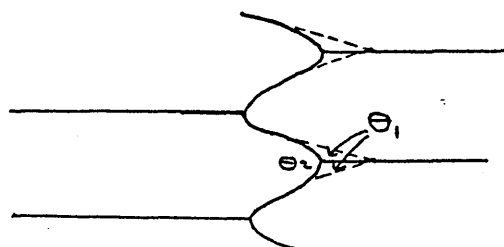
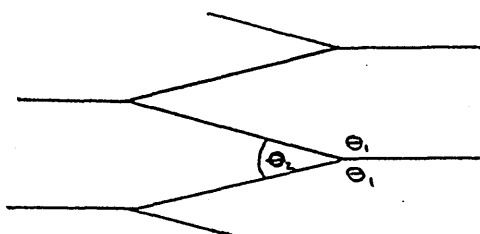
metals, according to the following diagrams :-

After Cold Deformation

During Annealing

Rolling direction \longrightarrow

$$\theta_1 > 120^\circ > \theta_2$$



The shape change produced by deformation causes the triple point to deviate from 120° . During annealing, as the boundaries attempt to re-establish the equilibrium angle, subgrains in the θ_1 region may become enlarged and more favourable as nuclei.

Grain boundary nucleation favours orientations close to, although often rotated slightly away from, the stable deformation texture. (42,47) Dillamore and Katoch (42) considered that material at the extremities of the deformation texture spread would probably be associated with grain boundary regions. Bcc recrystallisation texture components believed to originate from grain boundary nuclei include $\{100\} \langle 011 \rangle$, $\{554\} \langle 225 \rangle$, $\{111\} \langle 110 \rangle$ and $\{114\} \langle 841 \rangle$. (42,46,47)

(c) Transition Band Nucleation and Shear Band Nucleation

(i) Transition Bands

During constrained deformation of polycrystals, individual grains are often observed to deform inhomogeneously, leading to mutually misoriented blocks

known as deformation bands. These are separated by fairly narrow microbands, known as transition bands, accommodating the misorientation but containing a small volume of the original orientation. Within a transition band, the high local stored energy and rapid change in orientation create a suitable source of potential recrystallisation nuclei. (46,48) Deformation bands and transition bands may arise in several ways :- (52)

- (i) local differences in stress may cause different parts of a crystal to undergo different strains, inducing relative rotation within the grain,
- (ii) different combinations of slip systems may separately accommodate the imposed strain in different parts of the crystal, giving different slip rotations,
- (iii) orientations which are metastable during deformation may split into two twin-related orientations during rolling.

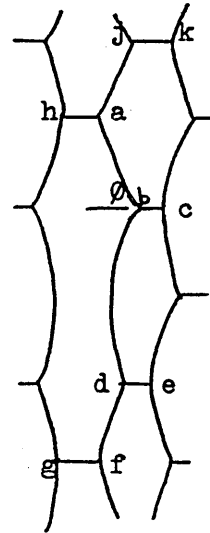
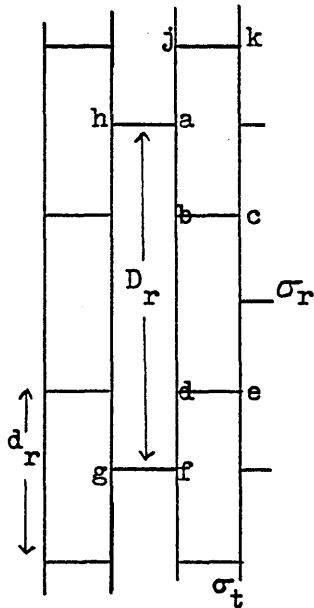
A $\{110\} \langle 001 \rangle$ texture component in bcc metals can, with increasing deformation, split into two twin-related $\{111\} \langle 112 \rangle$ components, (52) and transition band nucleation is responsible for reproduction of the original $\{110\} \langle 001 \rangle$ component on annealing. (39) Hu (53) reported that microbands separating neighbouring deformation bands in silicon iron, cold rolled to 80% RA, were sources of $\{113\} \langle uvw \rangle$ recrystallisation nuclei.

Dillamore et al (52) analysed the conditions under which transition bands develop and proposed a model for nucleation by subgrain growth in a transition band.

They envisaged the structure of a transition band to be of the form shown in the following diagrams :-

After Cold Rolling

During Annealing



σ_t = energy of vertical sub-boundaries

σ_r = energy of horizontal sub-boundaries

d_r = length of average subgrain

D_r = length of large subgrain ahgfdb

d_t = width of average subgrain.

The vertical sub-boundaries of energy σ_t are parallel with the transition band and would have a relatively large misorientation; the horizontal boundaries of energy σ_r may have smaller misorientations. During annealing, the triple point angles should relax to an equilibrium configuration, as shown, with the angle ϕ given by :-

$$\cos \phi = \frac{\sigma_r}{2 \sigma_t} \dots \dots \dots \text{Equation (1)}$$

In order that the large subgrain ahgfdb may continue to

grow, points b and c must come into contact before this equilibrium angle is achieved. This will only occur if the particular subgrain has a sufficient size advantage compared with the average subgrain such that :-

$$D_r > \frac{4}{3} (d_r + d_t \left[\left(\frac{4 \sigma_t^2}{\sigma_r^2} \right) - 1 \right]^{\frac{1}{2}}) \dots \text{Equation (2)}$$

Under these conditions, it will be able to grow both normal to the transition band and along it. Growth perpendicular to the transition band would increase the misorientation of the subgrain boundaries and hence their mobility. From their analysis, the authors (52) concluded that intermediate lattice curvatures were necessary for transition band nucleation. At high strains the critical value of D_r increases such that transition bands may cease to be viable nucleation sites, whereas at low strains transition bands are not sufficiently well developed for equation (2) to be satisfied.

(ii) Shear Bands

After heavy cold rolling reductions ($\epsilon > 1.0$), instabilities may develop during deformation and "shear bands" of elongated subgrains may form, inclined at an angle of $\sim \pm 35^\circ$ to the rolling direction (as viewed perpendicular to the transverse direction). These macroscopic shear bands cross grain boundaries without deviation, and the planes of the shear bands are related to specimen geometry rather than crystallography. (54)

Unlike transition bands, changes in orientation across shear bands are not systematic. (54,55) In bcc metals, only one set of shear bands forms in a particular volume

of material, and neighbouring volumes develop bands of opposing image. (54)

Shear band development is preceded by formation of microbands of elongated subgrains, which form initially on the slip planes and become aligned with the rolling plane at strain levels of $\epsilon \approx 1.0$ ($\sim 60\%$ RA). (54,55) These microbands are separated by low-angle boundaries. They do not cross grain boundaries.

Shear bands are reputed to provide favoured sites for nucleation. However, in ferritic materials, macroscopic shear bands do not appear to develop at strains below $\epsilon \approx 1.6$ (80% RA) and they are not abundant at strains $\leq \epsilon \approx 4$ (98% RA). (54) Osterle, Wever and Bunge (55) observed shear bands optically in alpha-iron cold-rolled to 85% RA, but were unable to detect shear bands in the same material using the electron microscope

(d) Effect of Dispersed Second-phase Particles

A dispersion of second-phase particles may affect recrystallisation in the following ways :-

(i) Precipitation after cold work

Precipitation after cold work but before recrystallisation influences the mobility of dislocations during recovery, inhibiting subgrain growth except for a few "breakaway" subgrains. The resultant structure tends to be coarse grained with a relatively sharp recrystallisation texture. (39)

Precipitation during recrystallisation occurs predominantly on moving grain boundaries, impeding their motion and allowing time for less favoured nucleation sites to operate before growth of the first formed grains

CAMERA 7

WHITE CARD

NEEDED BEHIND SOME

OF THE PAGES

consumes the deformed matrix. In this instance, the annealing texture is likely to be similar to the deformation texture, but reduced in intensity. (39)

(ii) Particles present before cold work

The effect of second phase dispersion present before cold deformation depends to a large extent on particle size and distribution: a coarse dispersion accelerates recrystallisation whereas very fine precipitates inhibit recrystallisation. (41,56-59)

Coarse particles stimulate nucleation at or near their surfaces, generally promoting a relatively fine grained structure with a texture similar to the deformation texture. (56,57) Chan and Humphreys (60) have recently studied particle-stimulated nucleation in situ using the High Voltage Electron Microscope (HVEM). In an aluminium-nickel alloy containing a coarse dispersion of Al_3Ni particles, the majority of such nuclei were misoriented by $15^\circ-45^\circ$ to the matrix. It was also noted that some particle-nucleated grains stopped growing at an early stage. The authors concluded that particle stimulated nucleation causes a randomisation of texture in the early stages of recrystallisation, and that sharper textures observed after completion of recrystallisation could be associated with more rapid growth of selected orientations. (60)

Fine particles interact with dislocations, retarding recovery and hindering subgrain boundary motion. Only the largest subgrains can act as nuclei, leading to a coarse grained structure showing marked texture selectivity. (56,57,59) Dillamore and Hutchinson (57)

actually utilised this effect to enhance the $\{111\} \langle uvw \rangle$ component of aluminium-killed, low-carbon steel, at the expense of the $\{100\} \langle uvw \rangle$ component.

Nes (61) found that co-existence of fine and coarse dispersions reduces the effectiveness of the coarse particles in stimulating nucleation. He argued that this reduced performance is inevitable, given that the fine dispersion introduces subgrain growth selectivity in the manner outlined.

In a study of the effect of carbide and nitride particles on the recrystallisation of ferrite, Gladman, McIvor and Pickering (56) reported that particles $\sim 0.5 - 20 \mu\text{m}$ ($5 \times 10^3 - 200 \times 10^3 \text{ \AA}$) diameter accelerated nucleation whereas fine particles $\sim 5 \text{ nm}$ (50 \AA) diameter retarded nucleation. It was also found that small volume fractions of intermediate sized particles $\sim 20 \text{ nm}$ (200 \AA) diameter had little effect on recrystallisation, although they could be effective in inhibiting subsequent grain growth. Other studies (62) indicated a marked retardation of recrystallisation at interparticle spacings equivalent to the deformation cell diameter.

Model for particle-retarded nucleation

Nes (63) developed a quantitative model for the effect of finely dispersed second phase particles on nucleation within a transition band. In addition to the critical condition for nucleation predicted by Dillamore (equation 2), the following criterion must also be satisfied if nucleation is to occur in the presence of a fine dispersion :-

$$D_r \geq \frac{2 d_r}{1 - \left(\frac{3}{4} \alpha \frac{\sigma_r}{\sigma_t} \frac{f}{r} d_r \right)} \dots\dots\dots \text{Equation (3)}$$

where

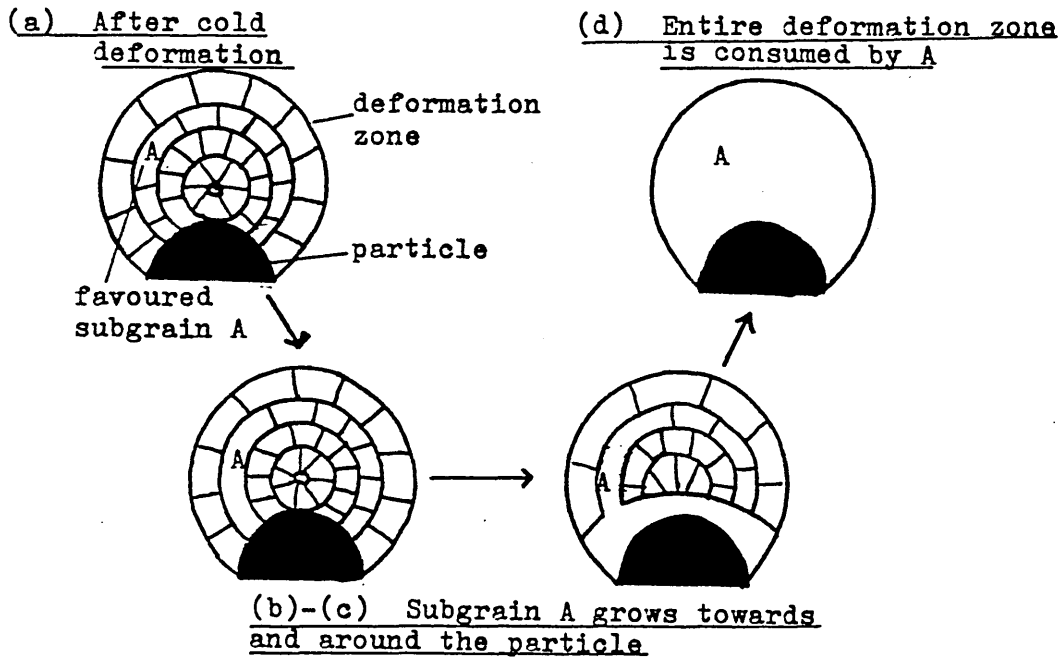
- D_r = length of favoured subgrain parallel with transition band
- d_r = length of average subgrain parallel with transition band
- d_t = width of average subgrain
- σ_t = energy of vertical sub-boundaries
- σ_r = energy of horizontal sub-boundaries
- α = a constant of the order of unity
- f = volume fraction of precipitate
- r = mean particle radius.

This model implies that it is the relationship between cell size and interparticle spacing which is important. For a constant volume fraction of precipitate, smaller particle sizes can be tolerated without risk of inhibiting nucleation as the average subgrain size decreases.

Models for particle-stimulated nucleation

Particle stimulated nucleation in deformed aluminium was studied extensively by Humphreys, (58) who noted that the cell structure in the matrix remote from coarse particles showed well-developed plate shaped subgrains elongated parallel with the rolling direction, whereas subgrains in a narrow region around each particle were much smaller and more equiaxed. Misorientations of up to 35° were observed between these regions, termed deformation zones, and the matrix. It was suggested that the size of these deformation zones was of the same order of magnitude as the particles

themselves. Humphryes (58) proposed a model for nucleation within such zones from pre-existing subgrains. The nucleus is envisaged as growing towards and around the particle to consume the entire deformation zone, as illustrated in the following sequence of diagrams :-



At this stage growth may continue into the matrix, or it may cease and eventually the nucleus will be consumed by more favourable growing grains. The critical particle diameter for effective particle stimulated nucleation is given by the following equation :-

$$r > \frac{2 \gamma}{E} \dots\dots\dots \text{Equation (4)}$$

where :

- r = radius of nucleus (assumed = particle diameter)
- γ = grained boundary energy
- E = stored energy.

In a subsequent analysis, Nes (59) suggested a resemblance between the type of deformation zone

substructure envisaged by Humphreys (58) and Dillamore's (42) representation of a transition band, such that the Dillamore analysis could be used to determine the critical dimensions for nucleation from a favoured over-size subgrain. Nes (59) re-expressed the critical condition for continued growth of a nucleus beyond the deformation zone as follows :-

$$\delta = \frac{1}{K} \bar{\rho}_m \frac{\gamma}{\gamma'} \quad \dots\dots\dots \text{Equation (5)}$$

where :

δ = mean diameter of new grain (\equiv particle diameter)

$\bar{\rho}_m$ = mean matrix sub-boundary spacing

γ = specific energy of new grain boundary towards matrix

γ' = mean matrix sub-boundary specific energy

K = dimensionless constant ~ 1 .

Since γ is $\geq \gamma'$ (for small misorientations, $\gamma > \gamma'$; for misorientations $\geq 15^\circ$, $\gamma = \gamma'$), the value of δ must be greater than the average subgrain size, or at least equal to it at high strains.

2.3.3. Grain Growth

Grain growth occurs after completion of primary recrystallisation, with larger than average grains growing at the expense of subcritical grains. The driving force for grain growth is a reduction in grain boundary energy. (45,47)

In general, if the grain size distribution for a particular component is biased towards the larger grains,

this component should be enhanced by grain growth. The dominant components of a primary recrystallisation texture will often have this size advantage and so grain growth normally makes the primary recrystallisation texture sharper and more well-defined. (47,64)

Fine second phase particles may present a restriction to the movement of grain boundaries, causing a transition from normal to abnormal grain growth. Only the most favoured grains may be able to grow, rendering the process even more orientation selective. (47,64)

There is no single index which will enable the press formability of a specific material to be reliably predicted for all products or production conditions. (65) However, for a given tool configuration and lubrication conditions, the forming limit (which relates primarily to the exhaustion of ductility (66,67) is governed by the inherent formability of the metal itself. The most influential characteristics are plastic anisotropy, work hardening ability and grain size.

Anisotropy caused by mechanical fibering may have a profound effect on both stretching and drawing characteristics. However, mechanical fibering is not a significant source of anisotropy in low carbon, clean steels and will not be considered further.

Preferred orientation is the other source of plastic anisotropy, which affects mainly deep drawability. The orientation of grains affects the ease of deformation in a particular mode and determines whether the material is resistant to thinning, (68) e.g., in bcc metals texture components with $\{111\}$ planes parallel to the sheet surface are effective in improving deep drawability whilst $\{100\}$ $\langle uvw \rangle$ components are most detrimental. (69)

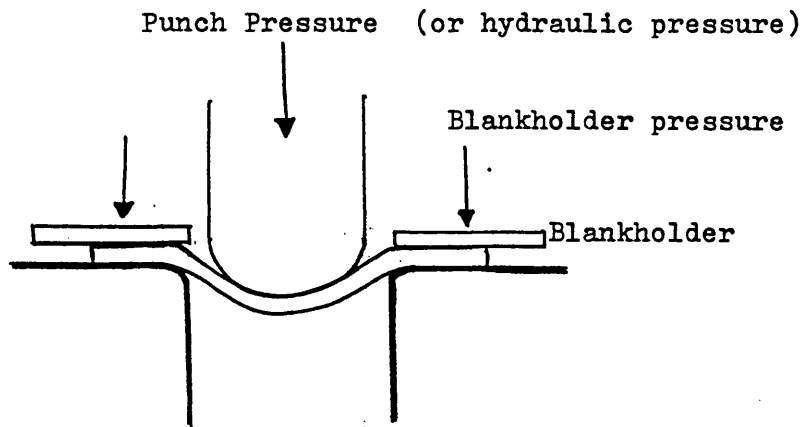
Stretch formability is controlled by the work hardening rate, which is largely unaffected by orientation. Increasing grain size is beneficial, although grain sizes coarser than ASTM 6 (average grain diameter $\sim 45\mu\text{m}$) promote orange peel defects during press forming.

2.4.1. Principles of Press Forming Operations

Most press forming operations are a complex interaction of stretching and deep drawing. Usually one of these processes will predominate, but both will be taking place simultaneously. However, in order to analyse the factors which influence pressing behaviour it is necessary to consider their effect on simple stretch forming and deep drawing operations.

(a) Simple Bi-axial Stretching

The tool configuration for simple bi-axial stretching is shown in the following diagram :-



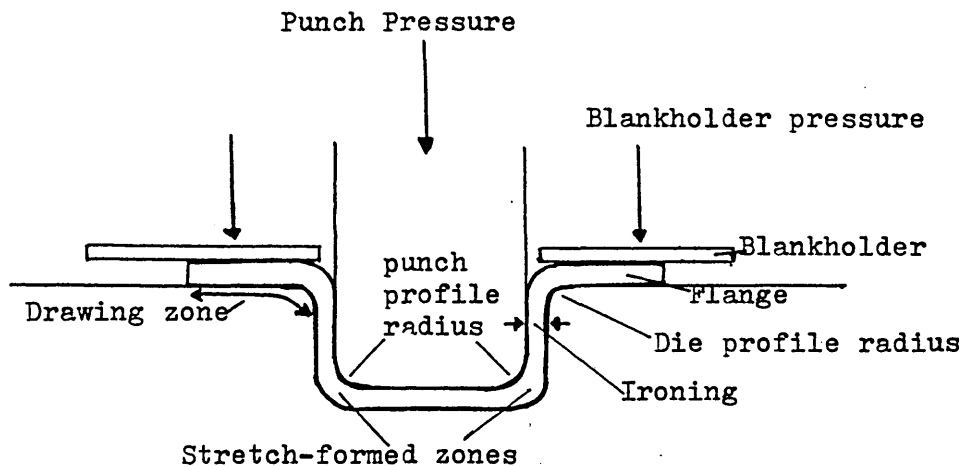
The blankholder pressure is sufficient to prevent the inward movement of material in the flange. When pressure is applied, either hydraulically or via a round nosed punch, the material over the die becomes stretched biaxially to form a dome-shaped cup. The operation is completed when the maximum or required depth of cup is obtained.

Using hydraulic pressure the stress system is pure biaxial tension, with the principal stresses in the

plane of the sheet (σ_1 and σ_2) being of equal magnitude and the normal stress $\sigma_3 = 0$. Also, since $d\epsilon_1 = d\epsilon_2 = \frac{-d\epsilon_3}{2}$, deformation and failure can occur only by sheet thinning. When a punch is used, the material which is in contact with the punch is restrained and the stress system is not pure biaxial tension.

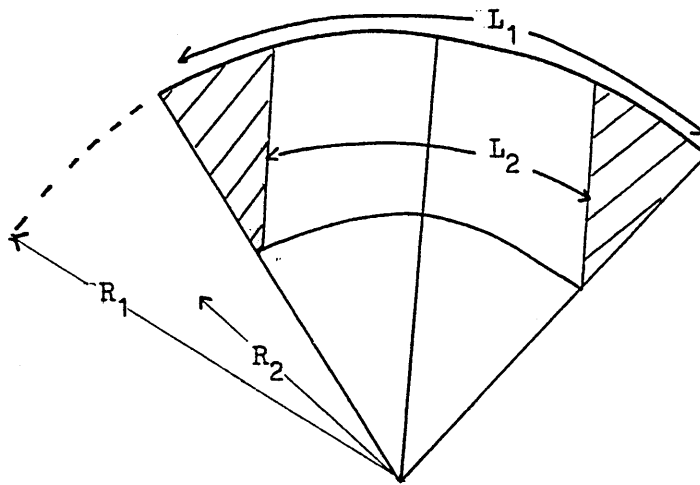
(b) Flat-bottomed Cup Drawing

The tool configuration during simple flat-bottomed cup drawing, starting with a circular blank, is shown in the following diagram :-



The pressure on the blankholder is insufficient to prevent inward movement of material in the flange, so that as the punch descends it causes material to flow inwards over the die profile radius to form the walls of the cup. The operation is complete when the periphery of the blank is reduced to the circumference of the cup wall. Since there occurs a zone of material which is stretched over the punch profile radius the operation is not, strictly speaking, pure drawing. The extent of this zone depends on the tool geometry.

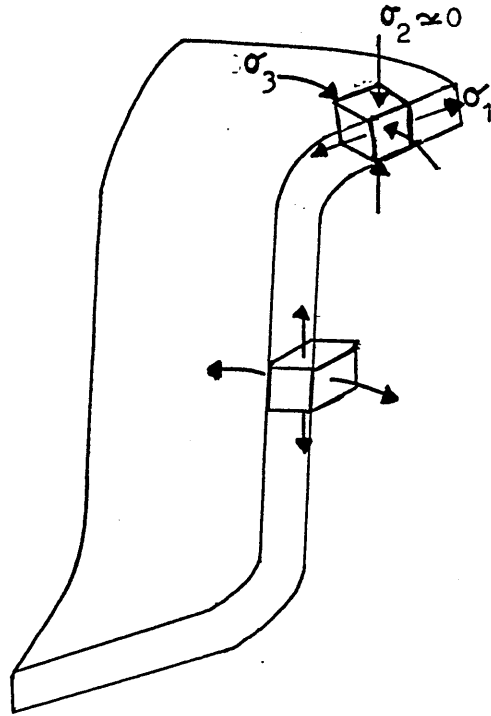
The requirement of blank holder pressure becomes apparent from the following argument. The following diagram shows a sector from a circular blank prior to drawing :-



During movement into the die mouth, arc L_1 and radius R_1 have to reduce to L_2 and R_2 causing a displacement of material in the shaded areas. This condition prevails throughout the circular blank, setting up a hoop compressive stress around the annular rim outside the die aperture. Without some blankholder pressure this stress would cause buckling or wrinkling.

The blankholder also restricts the tendency of the metal to thicken uniformly around the annular rim and progressively between the die mouth and outside edge, and so produces an elongation outwards. A differential speed of movement is thus set up, with material near to the die mouth moving over the die face at a greater speed than the metal at the outer edge of the blank.

The following diagram shows the directions of the principal stresses in the flange and the wall of a partly-drawn cup :-



In the flange, the effect of blankholder pressure is relatively small and can be ignored ($\sigma_2 \approx 0$). The important stresses are therefore, σ_1 (radial tension) and σ_3 (circumferential compression). Also, since little thickening occurs, $d\epsilon_2 = 0$, and a condition of plane strain is imposed.

2.4.2. Earing

Earing is the waviness of the rim of cylindrical cups deep drawn from circular blanks ⁽⁷⁰⁾; it is not observed in articles produced by pure stretch forming. The waviness appears in the extremities of the wall and in the cross-section of the cup wall. ⁽⁷⁰⁾ Material beneath

a trough is significantly thicker than material beneath an ear, the variation in thickness being most pronounced at a level corresponding with the bottom of the troughs. For quantitative comparisons, the extent of earing is usually calculated from the following formula :- (70)

$$\% \text{ Earing} = \left(\frac{\text{Peak height} - \text{trough height}}{\text{Mean cup height}} \right) \times 100$$

..... Equation (6)

2.4.3. The Erichsen Test

The Erichsen test is a widely used simulative test for stretch formability. (65,71,72) In this test a spherical ball punch is used to bulge sheet metal at a specified rate until either necking or fracture occurs, punch movement to drop-in-load, necking or fracture being recorded. (72) The test is covered by an ASTM standard (72) and a British standard (73) describes a modified version, although the only difference is the specification of a range of blankholder force. (73)

Test results can vary with blankholder force, type of lubrication and choice of end point criterion. (72) Use of polythene sheet over the punch as a lubricant seems to give the most reproducible conditions. (71)

2.4.4. The Swift Cupping Test

The usual simulative test for deep drawability is the Swift Cupping test. (65,71,74) It is not covered by a British or ASTM standard but the ASM handbook does refer to proposals for its standardisation, as reported by

Kemmis. (74) In this test, a standard sized punch (32 mm. diameter or 50 mm. diameter) is used and drawability is measured as the maximum blank diameter (D_c) which can be drawn without failure. Blank sizes are increased by increments of 2.5 mm. and sheet metal is rated in terms of the limiting drawing ratio (LDR) defined as :- (65,66)

$$\text{LDR} = \frac{D_c}{d_p} \quad \text{..... Equation (7)}$$

where

D_c = critical blank diameter

d_p = punch diameter

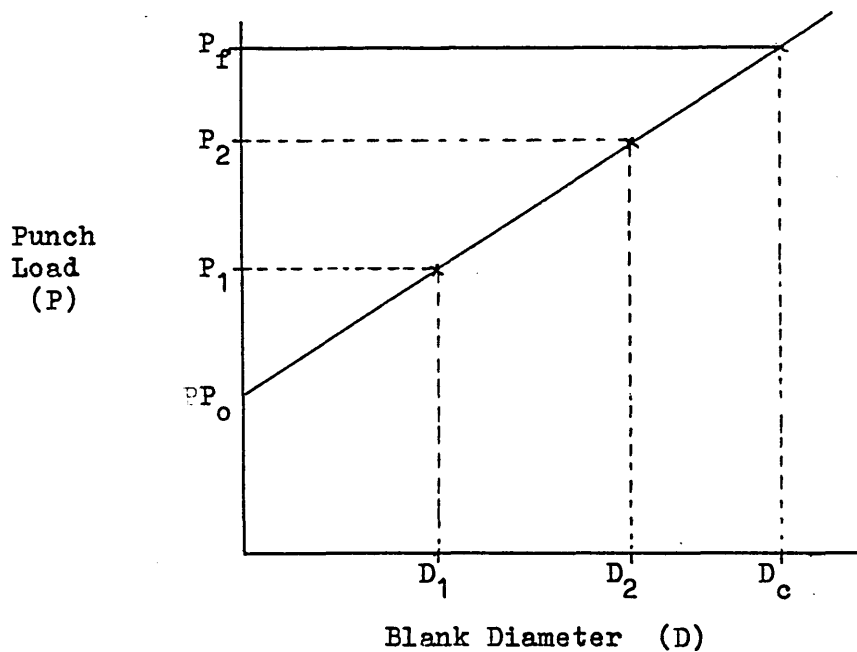
The test results can vary with deformation rate, type of lubrication and die clearance/design. Kemmis (74) recommends die sizes appropriate to various sheet thicknesses in the range of 0.3 mm. to 1.86 mm., and a drawing speed which is constant but below 35 mm. sec.⁻¹. Use of polythene sheet lubricant applied only to the die side of the blank seems to give the most reproducible conditions. (71)

The Swift test is essentially a trial and error method of determining the LDR. As such, it is time consuming and requires relatively large amounts of material. Modified tests (75-77) have been developed which make use of the fact that for many materials, including ferritic stainless steels and other low carbon steels, there is a linear relationship between maximum drawing load and blank diameter. The slope (K) and

intercept (P_0) of this relationship can be obtained by testing two subcritical blanks.

In one approach Thorpe (75) used a relationship between D_c and a parameter N , which is related to K , P_0 and the UTS, to determine D_c from two subcritical blanks and a tensile test.

Wilson, Sunter and Martin (77) used the principle that, if the flange of the blank is clamped after the maximum drawing load is achieved (secondary clamping), then both the drawing load (P_d) and the fracture load (P_f) can be measured using one blank of subcritical size. If the value of P_d for a second subcritical blank size is determined then the relationship between punch load and blank size is established, and the value of D_c at the fracture load can be predicted, according to the following diagram :-



(a) Maximum Uniform strain (ϵ_u)

The maximum uniform strain (ϵ_u) in uniaxial tension is an indication of stretch formability and is, in principle, simple to determine from the maximum point on the load/extension curve. However, this is often flat and extended, making direct determination of ϵ_u difficult and inaccurate.

(b) Work hardening coefficient (n)

For many engineering materials, (including ferritic stainless steels), whose flow curves are of the familiar form $\sigma_y = Y + K \epsilon^n$, the work hardening coefficient (n) is equal in value to ϵ_u and is more easily determined, being the gradient of a $\ln \sigma / \ln \epsilon$ graph. (78)

The n-value effectively controls the increase in yield stress or strength of the material during deformation. The higher the n-value, the steeper is the stress/strain curve and the larger the uniform elongation. (66)

Low carbon steels and ferritic stainless steels have n-values in the range 0.2 - 0.3 whereas austenitic stainless steels have n-values of the order of 0.45-0.5, reflecting their superior stretch formability. (67,79)

The method of determining strain hardening exponents is covered by an ASTM standard. (80)

(c) Plastic strain ratio (r)

A useful index of plastic anisotropy, which also reflects deep drawability, is the plastic strain ratio (r). This is defined as the ratio of the width true strain (ϵ_w) to the thickness true strain (ϵ_t) in the testing of a

$$r = \frac{\ln \left(\frac{w_o}{w_f} \right)}{\ln \left(\frac{t_o}{t_f} \right)} \dots\dots \text{Equation (8)}$$

or, since there is less inaccuracy involved in measuring length (L) than thickness (t), (66,81) by

$$r = \frac{\ln \left(\frac{w_o}{w_f} \right)}{\ln \left(\frac{L_f w_f}{L_o w_o} \right)} \dots\dots \text{Equation (9)}$$

where

- w_o = width before straining
- w_f = width after straining
- L_o = length before straining
- L_f = length after straining

Dripke and Worner (81) give a detailed procedure for measurement of r-values, which is also covered by an ASTM standard. (82) Only r-values measured at equivalent strains are comparable, and it is normal practice to use a specified elongation of either 15% or 20%.

For anisotropic materials, r can vary with the direction of testing, and it is usual to measure plastic strain ratios at three orientations within the sheet, i.e., with the tensile axis inclined at 0°, 45°, and 90° to the

rolling direction. (66) The index of mean normal anisotropy (\bar{r}) is given by :- (66)

$$\bar{r} = \frac{(r_0 + 2r_{45} + r_{90})}{4} \dots\dots\dots \text{Equation (10)}$$

If \bar{r} is greater than unity the material has high resistance to thinning and should, therefore, possess good drawability. (66) In low carbon ferritic steels, it has been found that preferred orientations of the "cube-on-corner" type, in which $\{111\}$ planes lie parallel with the sheet surface, produce the highest \bar{r} values. (83)

The variation of r within the plane of the sheet is known as planar anisotropy (Δr) and is given by :- (66,81)

$$\Delta r = \frac{(r_0 + r_{90} - 2r_{45})}{2} \dots\dots \text{Equation (11)}$$

The degree of planar anisotropy affects the earing tendency of the sheet. (66,70,81) The maximum ears form in positions around the circumference of a blank where a tensile test piece taken from the blank at that point would show a maximum r_e -value. The height of the ears is close to being proportional to $|\Delta r|$; the higher $|\Delta r|$ the greater the earing tendency. (66,70) If Δr is positive ($r_0, r_{90} > r_{45}$), earing occurs at $\sim 0^\circ$ and $\sim 90^\circ$ to the rolling direction, whereas a negative Δr -value ($r_{45} > r_0, r_{90}$) leads to $\sim 45^\circ$ earing. (66,70) An exception to this is

sometimes observed in ferritic stainless steels exhibiting a strong $\{111\}$ $\langle 112 \rangle$ recrystallisation texture, whose six-fold symmetry favours the formation of ears at 0° and 60° to the rolling direction. (84,85)

For optimum drawability, a high value of \bar{r} and a low value of $|\Delta r|$ are required. However, it is usually found that as \bar{r} increases, so also does $|\Delta r|$. (66)

2.4.6. Comparison of Mechanical and Simulative Tests

There is no universal agreement as to whether mechanical or simulative tests give the more reliable information about sheet metal press formability, and both are of limited value for predicting performance in complex operations. (71,77) Sometimes the only way of determining what is actually happening is by use of visible strain patterns, assessed from distortion of regular patterns applied to the sheet before forming. (86,87) The main uses of formability testing are for ranking materials and for acceptance purposes.

2.4.7. Theoretical Predictions of r-values and Earing Characteristics

A number of authors have studied the relationship between crystal orientation and plastic anisotropy theoretically. (88-90) Vieth and Whiteley⁽⁸⁹⁾ were the first to devise a model for calculation of r-values and earing profiles for bcc single crystal orientations, assuming deformation occurred by slip on system(s) of highest resolved shear stress. The authors considered crystallographic slip on $\{110\}$, $\{112\}$ and $\{123\}$

planes (with equal τ_c on each plane), and also pencil glide. For prediction of r-values, they considered situations in which either no rotation or a large rotation of the tensile axis occurred. The latter assumption of a large rotation gave more realistic predictions of r-values for single crystals. Vieth and Whiteley (89) also reported that troughs and ears predicted according to their calculations corresponded with positions of minimum and maximum r-values, but that no quantitative relationship between r-values and radial strain could be established.

More recently, Lee and Oh (90) used a similar method to predict r-values for ideal orientations, although they assumed that slip occurred only on

$\{110\} \langle 111 \rangle$ systems in bcc metals, and that all slip systems contributed to the deformation in proportion to their Schmid factors.

$$(\text{Schmid factor} = \cos \lambda \cos \phi = \frac{\tau}{\sigma} \dots \text{Equation (12)})$$

where λ = angle between stress axis and slip direction

ϕ = angle between stress axis and slip plane normal

τ = resolved shear stress on slip system

σ = applied stress)

Lee and Oh (90) used the results of their calculations to estimate r-values of sheet metals, whose textures could be described by one or more ideal orientations, as follows :-

$$r = \sum r_i V_i \dots \dots \dots \text{Equation (13)}$$

where r_i = r-value of texture component i

V_i = volume fraction of texture component i.

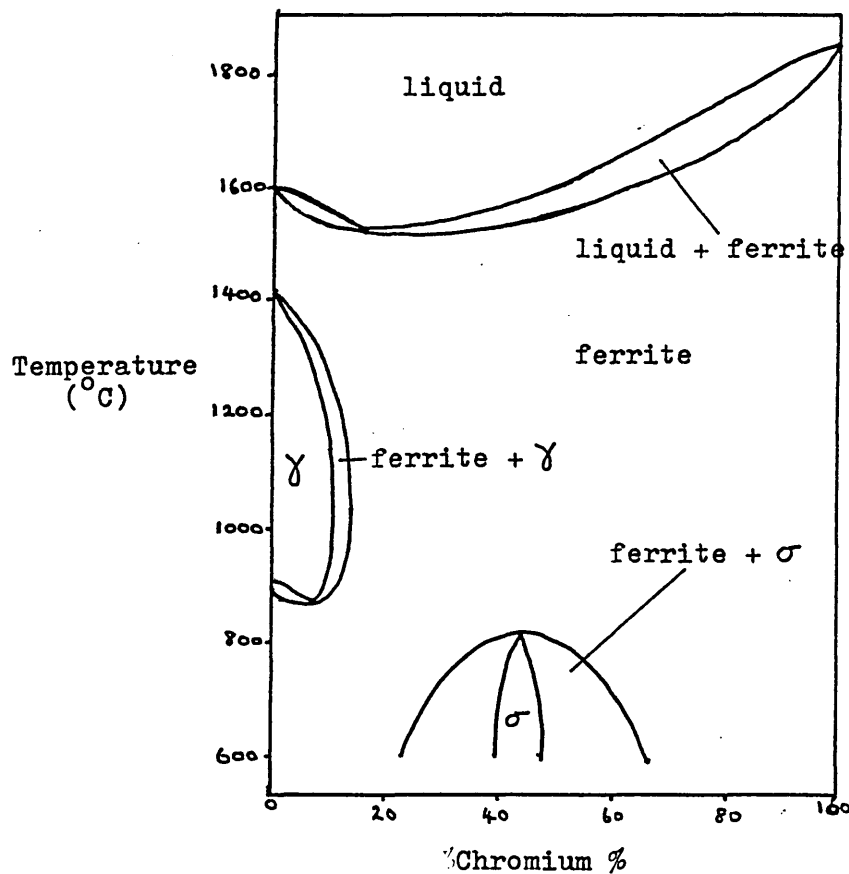
The authors claimed reasonable agreement between observed and predicted r-values.

2.5.1. Compositions

Ferritic stainless steels occur over a wide range of chromium contents, from ~11% to ~25%. These steels are generally nickel-free but may contain other additions such as aluminium, molybdenum, niobium or titanium.

The following iron-chromium equilibrium diagram indicates that a simple Fe - 16% Cr alloy would be ferritic at all temperatures up to the solidus :-

Iron-Chromium Equilibrium Diagram



however, the presence of carbon and residual elements extends the gamma loop and broadens the ($\alpha + \gamma$) region. (91) Lower chromium varieties, such as AISI 410 (12% Cr, 0.1%C) are austenitic at temperatures around 1000°C and transform to martensite on cooling. (92) By comparison, a 17% Cr steel has a duplex ($\alpha + \gamma$) structure at high temperatures and transforms to a mixture of ferrite and martensite on cooling to room temperature. A 20% Cr steel should be ferritic at all temperatures up to the solidus. (92) Ferrite promoting elements such as niobium, titanium, molybdenum and silicon extend the fully ferritic range to lower chromium contents. (91,93)

2.5.2. Transformations

Castro and Tricot (94-96) made extensive investigations into isothermal transformations in 17% Cr steels. They reported that steels containing 15-17% Cr and 0.05-0.1%C consist of carbides and ferrite at room temperature in the equilibrium state. Heating to 850°-900°C results in partial transformation to austenite, the temperature at which γ first appears being designated the A_1 temperature. At this stage there is little dissolution of carbides. As the temperature increases above A_1 , the amount of austenite in the structure increases progressively to a maximum at the Θ_m temperature (temperature of maximum γ content), which coincides roughly with completion of carbide dissolution ($\sim 1050-1100^\circ\text{C}$). Thereafter the proportion of austenite decreases until it disappears altogether at the A_5 temperature $\sim 1250-1300^\circ\text{C}$. (94) Delta ferrite

is then stable up to the solidus $\sim 1450^{\circ}\text{C}$.

Quenching from above A_5 produces first a mixture of ferrite with intergranular and intragranular austenite, the latter in a Widmanstätten pattern. (94) This is unavoidable even by energetic quenching of small samples. On further cooling, the austenite transforms to martensite, the M_s temperature being $\sim 150-260^{\circ}\text{C}$. Untempered martensite may thus be a source of brittleness in steels not tempered after high temperature treatments. (94) Precipitation of intergranular and intragranular $M_{23}C_6$ carbides and intragranular Cr_2N nitrides also occurs on cooling, even during water quenching. (95,97)

Further investigations (96) led to the following regression equations for approximate determination of the A_1 temperature and the maximum amount of γ at the θ_m temperature as functions of composition :-

$$A_1 (^{\circ}\text{C}) = 30(\%Cr) + 73(\%Si) - 250(\%C) - 280(\%N) - 66(\%Mn) - 115(\%Ni) + 405 \quad \dots \text{Equation (14)}$$

$$\gamma_{\text{max}} (\%) = 470(\%N) + 420(\%C) + 30(\%Ni) + 7(\%Mn) - 11.5(\%Cr) - 11.5(\%Si) + 186 \quad \dots \text{Equation (15)}$$

Castro and Tricot (96) also found that nitrogen restricts grain growth by promoting austenite formation and by formation of Cr_2N nitrides. Nitrogen has no apparent effect on the solidus temperature, whereas carbon was found to lower it by $\sim 7^{\circ}\text{C}$ for an increase of 0.010%C.

Later studies (98-100) concentrated on 17% Cr steels containing titanium and niobium, used to improve

weldability and corrosion resistance, and vanadium which was sometimes added to reduce the incidence of roping. For the range 15-19% Cr, they proposed the following formulae for estimating the A_1 temperature and the maximum austenite content at the θ_m temperature :-

$$\begin{aligned}
 A_1 \text{ (}^\circ\text{C)} &= 35(\%Cr) + 60(\%Mo) + 73(\%Si) + 170(\%Nb) \\
 &+ 290(\%V) + 620(\%Ti) + 750(Al) + 1400(\%B) \\
 &- 250(\%C) - 280(\%N) - 115(\%Ni) - 66(\%Mn) \\
 &- 18(\%Cu) + 310 \qquad \dots\text{Equation (16)}
 \end{aligned}$$

$$\begin{aligned}
 \gamma_{\max} (\%) &= 420(\%C) + 470(\%N) + 23(\%Ni) + 9(\%Cu) \\
 &+ 7(\%Mn) - 11.5(\%Cr) - 11.5(\%Si) - 12(\%Mo) \\
 &- 23(\%V) - 47(\%Nb) - 49(\%Ti) - 52(\%Al) \\
 &+ 189 \qquad \dots\text{Equation (17)}
 \end{aligned}$$

These empirical formulae do not allow for possible interactions between elements because they were determined using experimental melts of 17%Cr steels containing single alloying additions. In the presence of carbon and nitrogen, the ferrite forming effect of titanium is higher than would appear from its coefficient, due to its effect in removing these austenite stabilisers from solid solution (which outweighs the effect of simultaneous titanium removal). It is, therefore, necessary to eliminate titanium, carbon and nitrogen locked inside Ti(CN) particles from the calculation and consider only titanium remaining in solid solution, (98) i.e.,

$$[Ti]_{ss} = Ti - 4C - 3.4N \qquad \dots\text{Equation (18)}$$

Similar considerations apply to niobium and aluminium. (98)

Although dissolution of chromium carbides and nitrides is complete at $\sim \theta_m$ temperature, the solubility of complex carbides and nitrides of niobium, zirconium and titanium is restricted and remains partial even near the solidus. (92,98)

Kaltenhauser (91) derived a formula for a "ferrite factor" $F(a)$ which he used to describe the ability of steels to remain fully ferritic at all temperatures :-

$$F(a) = -40 (C+N) - 2Mn - 4Ni + Cr + 6 Si \\ + 8 Ti + Mo + 2 Al \quad \dots \text{Equation (19)}$$

Austenite is formed on heating if $F(a)$ is less than an experimentally determined level, which Kaltenhauser found to be $F(a) = 17$ for 17% Cr steels and $F(a) \approx 13.5$ for 12% Cr steels.

2.5.3. 475°C Embrittlement

Ferritic stainless steels containing more than 13% Cr are susceptible to 475°C embrittlement. (92,101,102) Holding in, or slow cooling through, the range 320-550°C results in a continuous increase in hardness accompanied by a decrease in impact strength (92) and is, therefore, to be avoided. This phenomenon has been attributed to precipitation of fine particles ($\sim 20\text{nm}$ diameter) of the chromium rich bcc phase α' . (97,101) The effect is reversible, e.g., by annealing at 815°C. (102)

The corrosion resistance of ferritic stainless steels is very much superior to that of mild steel, although it cannot rival that of most austenitic stainless steels. Ferritic stainless steels are virtually immune to stress corrosion cracking in chloride environments, but are susceptible to intergranular attack in the heat affected zone of a weld or after incorrect heat treatment. (92) This sensitisation is caused by precipitation of chromium rich carbides in the grain boundaries during heating above $\sim 900^{\circ}\text{C}$, resulting in a chromium-depleted region adjacent to the grain boundaries. (103) It can be rectified by annealing in the range $650\text{-}850^{\circ}\text{C}$, which permits diffusion of chromium to the denuded areas. Additions of titanium or niobium reduce susceptibility by removal of carbon from solid solution as titanium or niobium carbides. (92,97) However, Devine and Ritter (104) found that heating above $\sim 1000^{\circ}\text{C}$ may cause some decomposition of titanium carbides and nitrides, releasing carbon and nitrogen into solid solution. If the steel is quenched and subsequently aged $\leq 600^{\circ}\text{C}$, chromium carbides are precipitated at grain boundaries and the material becomes sensitised. Aging above $\sim 600^{\circ}\text{C}$ prevents such sensitisation by preferential precipitation of $\text{Ti}(\text{CN})$. This has important implications for post-welding heat treatment, especially for service conditions above room temperature. Devine and Ritter (104) found that sensitisation could be avoided altogether in 12% Cr steels by a very high Ti/C ratio (≥ 57.5), nitrogen

apparently having little effect on susceptibility.

Titanium additions are to be avoided for nitric acid service since HNO_3 attacks $\text{Ti}(\text{CN})$. (102)

2.5.5. Low Interstitial and Stabilised Steels

Since the advent of modern techniques, such as AOD and VIM, it has been possible to produce low interstitial ferritic stainless steels with improved toughness, corrosion resistance and weldability, coupled with reduced tendency to form austenite on heating and hence martensite on cooling. Low interstitial steels are usually annealed in the range $750-900^\circ\text{C}$. It is generally found that rapid cooling promotes superior toughness, by suppressing precipitation of carbides and nitrides and delaying the onset of 475°C embrittlement. (102)

Stabilising additions of titanium and/or niobium combine with carbon and nitrogen to form carbonitrides, the stability of which enables low interstitial steels containing as little as 12%Cr to retain a fully ferritic structure at all temperatures, avoiding martensite formation. (92,93,102) However, the lower carbide content and lack of transformation does allow easier grain coarsening of these steels during heat treatment. Also, excessive stabilising additions can cause problems with heat treatment because lower temperatures do not allow completion of recrystallisation whereas higher temperatures lead to grain coarsening. Titanium additions also increase the impact transition temperature. (102)

for effective stabilisation, there is a minimum alloy content which, in the case of titanium, is somewhat higher than predicted from stoichiometric considerations. Hooper (93) found that titanium additions of at least $10 \times (C+N)$ were required to avoid sensitisation in a 12%Cr, low interstitial steel. Steigerwald et al (102) suggested that titanium may also combine with other elements such as sulphur, and that this might explain the need for higher levels than stoichiometry requires. SEM analysis of cuboid Ti(CN) particles by Ball and Hoffman (105) indicated that they are frequently associated with aggregates of sulphides.

The optimum niobium content is reported as $\sim 8 \times (C+N)$, which approximates to stoichiometry. (106)

2.5.6. Roping

Roping is a surface phenomenon occurring to varying degrees in ferritic stainless steel sheet. It becomes evident after tensile straining above $\sim 10\%$ elongation and appears as corrugations which are always parallel with the sheet rolling direction, irrespective of the direction of testing. (107) It also occurs during press forming operations, impairing the surface appearance of a product. Sometimes a batch of steel may be totally unsuitable, particularly for applications requiring a good surface finish.

Most authors agree that roping is a manifestation of anisotropic plasticity of bands of contrasting textures, but there are several theories of the actual mechanism. (108-113) Although roping is thought to be

associated with texture, the difference between severely affected sheet and good sheet is not revealed by pole figure texture representations because these show only the existence of components, not their distribution within the microstructure. Etch pitting techniques have, therefore, been used to demonstrate texture banding in sheets showing high roping tendency. (108)

More recent studies (114,115) have associated roping not with texture but with segregation of carbon and chromium in the two-phase ($\alpha + \gamma$) region of non-stabilised steels during hot rolling. Such segregation is retained after cold rolling and annealing, (114,115) and Suzuki and Asami (114) reported good correlation between the height of roping corrugations and the undulating segregation pattern observed in transverse sections. No explanation was given for formation of the undulating pattern and its retention in the final product. (114)

The tendency for roping to occur increases with increasing carbon content but decreases with increasing nitrogen content, the effect of nitrogen being ~ 3 times that of carbon. Decreasing the chromium content reduces roping, although there is some loss of corrosion resistance. (107) Stabilisation of 17%Cr steel is also known to be beneficial, but Ti-stabilised sheet is not immune to surface wrinkling during pressing because of the tendency towards easy grain coarsening. (116) Niobium and aluminium additions reduce roping but, in common with titanium, reduce the polishability of the steel. (107)

Various processing variables also affect the severity of roping. The phenomenon is not normally observed in cross rolled sheet, (107) but cross rolling is not applicable to a production route involving continuous coils. Reducing the hot rolling finishing temperature is reputedly one of the most effective means of reducing roping, (107) whereas omission of the annealing treatment prior to cold rolling has been found to accentuate the phenomenon. (117) Valloire, Penelle and Bavay (118) related roping in Titanium-stabilised 17%Cr steel to bands of coarse $\{100\}$ $\langle 011 \rangle$ grains in the centre of the hot rolled strip. Increasing the overall grain size of the hot band, by raising the annealing temperature to 950°C, was reported to reduce roping without impairing the grain size of the final product. (118) High cold rolling reductions with intermediate treatments have been found to improve the surface quality of 17%Cr steel sheet appreciably, the beneficial effect increasing with increasing cold reduction before a given intermediate heat treatment. (107)

2.6.1. Hot Rolling Textures

Ordinary low carbon steels show substantially random textures after hot rolling in the austenite region. (119). By contrast, ferritic stainless steels, in which the ferrite-austenite transformation is lacking or only partial, exhibit quite pronounced hot rolling textures even when processing commences from temperatures as high as 1100-1200°C. The major components reported are those in which $\{100\}$ planes are parallel with the sheet surface. (120-122) Dickson and Cooke (122) also detected $\{112\}$ $\langle 110 \rangle$ and $\{111\}$ $\langle 112 \rangle$ as minor components in Ti-stabilised, 12%Cr steel. These orientations are normally observed in the cold rolling textures of bcc metals, implying that the material had received some deformation below the dynamic recrystallisation temperature.

Dickson and Cooke (122) also reported a strong $\{110\}$ $\langle 001 \rangle$ surface texture. This is a common recrystallisation component in bcc metals subjected to low or moderate cold reductions, and suggests that the surface had undergone recrystallisation in the later stages of rolling.

Similar hot rolling textures have been observed in other low carbon steels (including silicon steels) which have been rolled in the α or $(\alpha + \gamma)$ phase fields, below $\sim 900^\circ\text{C}$. (12,50,51,119,123,124) The main component is generally $\{100\}$ $\langle uvw \rangle$, except in steels stabilised with niobium or titanium in which a strong

$\{112\} \langle 110 \rangle$ component has been detected. (51,124)

Through-thickness texture variations, with strong

$\{110\} \langle 001 \rangle$ surface textures decreasing in intensity with depth below the surface, are also a feature of ordinary low carbon steels rolled between 800°C and 900°C. (12,50,119,123)

2.6.2. Cold Rolling Textures

The cold rolling textures of ferritic stainless steels and other low carbon steels are most commonly described in terms of the ideal orientations $\{100\} \langle 011 \rangle$,

$\{112\} \langle 110 \rangle$, $\{111\} \langle 112 \rangle$ and sometimes $\{111\} \langle 110 \rangle$. Variations in the rates of development of these textures and the prominence of each component within the spread at a particular rolling reduction have been reported by different authors. (84,106,122,125-129)

Most workers report that, as cold rolling reduction increases, the $\{111\} \langle 112 \rangle$ component (which is usually a constituent at low or moderate reductions) is progressively replaced by $\{112\} \langle 110 \rangle$ and that there is a simultaneous increase in the intensity of the

$\{100\} \langle 011 \rangle$ orientation. (84,119,122) However, it has been noted that, as the hot rolling temperature or temperature of annealing prior to cold rolling is raised, the proportion of $\{111\} \langle 112 \rangle$ at any given cold reduction increases but the fraction of $\{100\} \langle 011 \rangle$ decreases. (119,122)

Stabilisation with niobium or titanium has been claimed to enhance the $\{111\} \langle 112 \rangle$ and/or $\{112\} \langle 110 \rangle$ cold rolling texture components in both ferritic

stainless steels (125,126) and ordinary low carbon steels. (124,130-132) Miyaji and Watanabe found a similar effect in 17%Cr steels containing fine dispersions of either Cr_2N or ϵ -Cu. (120,127)

It seems likely that some of the differences observed might arise as a result of variations in the condition of hot rolled material prior to cold rolling, which is often not discussed. A strong hot rolling texture would be expected to have some effect on the development of the cold rolling texture. Stabilisation with niobium or titanium reputedly enhances the

$\{112\} \langle 110 \rangle$ orientation in the hot rolling texture, (51,124) and since this is a stable end orientation it would be expected to become more prominent during subsequent cold rolling. (131) The presence of a significant $\{110\} \langle 001 \rangle$ texture prior to cold rolling has been found to enhance the $\{111\} \langle 112 \rangle$ component at high cold rolling reductions. (122) Again, this is not surprising since, during cold rolling, the metastable $\{110\} \langle 001 \rangle$ orientation is believed to split gradually into two twin related $\{111\} \langle 112 \rangle$ orientations, separated by a transition band. (133)

2.6.3. Recrystallisation Textures

The major recrystallisation texture components observed in ferritic stainless steels have generally been described in terms of the ideal orientations

$\{111\} \langle 112 \rangle$, $\{554\} \langle 225 \rangle$ (which is very close to $\{111\} \langle 112 \rangle$), $\{111\} \langle 110 \rangle$, $\{110\} \langle 001 \rangle$ and $\{100\} \langle 011 \rangle$. All these components have been

reported in other bcc metals, ⁽³⁾ and particularly in low carbon steels. (124,128,129,134) Although relatively few ideal orientations have been used to describe the observed textures, the prominence of a particular component is markedly affected by composition and processing. These variables have a much more pronounced effect on recrystallisation textures than on deformation textures. (84)

Most workers have sought improved drawability, associated with a high volume fraction of grains having $\{111\}$ planes parallel to the rolling plane and a low volume fraction of $\{100\}$ $\langle uvw \rangle$ components. (69) However, Miyaji and Watanabe ⁽¹²¹⁾ purposely developed a strong $\{100\}$ $\langle 011 \rangle$ texture for optimum magnetic characteristics in 17%Cr, low interstitial steel to be used in cover sheets for encased motors.

(a) Effects of Composition and Cold Rolling Reduction

The recrystallisation textures of steels containing 12%-28%Cr have been examined by various workers. Within this range, variations in chromium content appear to make little difference to recrystallisation textures, ⁽⁸⁴⁾ although its presence in solid solution may be expected to alter the recrystallisation temperature to varying degrees. The most important compositional variables seem to be the interstitial content, presence of stabilising additions such as niobium or titanium, or presence of other additions which cause precipitation within the matrix. However, Hutchinson and Ushioda, ⁽¹³⁵⁾ investigating low-carbon deep drawing steels, suggested that carbon

in solid solution only affects the recrystallisation texture adversely in the presence of manganese in solid solution, and they proposed an optimum manganese level of $\sim (\frac{55}{32} \%S + \frac{55}{16} \%O)$ for $\{111\} \langle uvw \rangle$ textures.

(i) Low Interstitial Steels (≤ 0.05 (C+N))

In lightly cold rolled, low interstitial, ferritic stainless steels the recrystallisation texture components observed are mainly $\{110\} \langle 001 \rangle$ plus a minor $\{100\} \langle 011 \rangle$. (84,121)

The strength of $\{110\} \langle 001 \rangle$ decreases with increasing cold reduction so that eventually $\{100\} \langle 011 \rangle$ becomes the major component. Lewis (84) found that the intensity of $\{111\}$ type orientations also increased with increasing prior cold work, but was still relatively weak after 75% reduction.

Miyaji and Watanabe (121) found a strong $\{110\} \langle 001 \rangle$ final texture even after 70% reduction in a 17%Cr steel which had been annealed at 1100°C before cold rolling. However, in the same steel cold rolled without prior annealing, the recrystallisation texture was completely dominated by $\{100\} \langle 011 \rangle$ (121) This difference may have been due to an initially coarser hot-band grain size in the pre-annealed material. A similar effect was recorded by Matsuo, Hayami and Nagashima (136) for high-purity, vacuum melted iron having a coarse initial grain size.

Lewis (84) interpreted the observed textures in terms of nucleation potential. At low reductions, in the absence of second-phase particles, transition bands and grain boundaries compete as nucleation sites. The

grain boundary area of an initially coarse-grained structure is relatively small and deformation band nucleation, favouring $\{110\} \langle 001 \rangle$ recrystallised grains, predominates. ⁽⁸⁴⁾ At higher cold reductions (or at low reductions in a structure having a fine or elongated prior grain structure, as in non-annealed hot-band studied by Miyaji and Watanabe ⁽¹²¹⁾), the increased grain boundary area encourages $\{100\} \langle 011 \rangle$ nucleation close to the grain boundaries. ⁽⁸⁴⁾

Lewis ⁽⁸⁴⁾ attributed the increase in the $\{111\}$ recrystallisation texture component with increasing prior cold work to in situ nucleation by growth of the higher energy $\{111\}$ subgrains within the grains interiors. Grain boundary nucleation is considered another possible origin of $\{111\} \langle 110 \rangle$ and $\{111\} \langle 112 \rangle$ grains, since these are "hard" ($M \sim 3.5$) orientations lying close to the stable deformation texture. ⁽⁴²⁾

(ii) High Interstitial Steels

Texture development in high interstitial stainless steels has not been widely studied. Lewis ⁽⁸⁴⁾ looked at high (C+N), 17%Cr steel and found a major $\{100\} \langle 011 \rangle$ recrystallisation texture but only a weak $\{110\} \langle 001 \rangle$ component even after prior reductions as low as 35%RA. He attributed this to the microstructure of the steel in which a highly "pancaked" grain structure persists throughout processing, due to the pinning action of austenite at the hot rolling temperature and martensite at lower temperatures. Consequently, a large grain boundary area is available even after low cold rolling reductions, promoting grain

boundary nucleation of $\{100\} \langle 011 \rangle$ grains.

(iii) Steels Stabilised with Niobium or Titanium

It is generally agreed that additions of titanium, niobium, or even zirconium promote the development of $\{111\} \langle 112 \rangle / \{554\} \langle 225 \rangle$ recrystallisation textures in 17%Cr stainless steels, especially after high cold reductions. (84,85,125,126,137,138) Niobium additions favour textures which have an appreciable degree of rotation about the $\{111\}$ sheet plane normal, whereas titanium and zirconium additions reputedly produce more sharply defined $\{111\} \langle 112 \rangle / \{554\} \langle 225 \rangle$ textures with less rotational freedom. (84,85,138) It has also been noted that, although both niobium and titanium retard recrystallisation, the latter has a greater effect. The grain size of Nb-stabilised steel is usually finer than that of Ti-stabilised steel. (84,85,125)

Most authors report that $\{110\} \langle 001 \rangle$ is present at low reductions (35-50% RA), but that its strength rapidly decreases with increasing prior cold work, so that it is not observed in samples cold-rolled to 75% RA before annealing. (84,85,125,139) After higher cold reductions, annealing textures in which the sheet plane is near $\{111\}$ are considerably enhanced. At prior reductions greater than 70% RA, all workers report a major $\{111\} \langle 112 \rangle$ or $\{554\} \langle 225 \rangle$ texture, sometimes with spread towards $\{111\} \langle 110 \rangle$, and only a minor $\{100\} \langle 011 \rangle$ component. The intensity of the $\{111\} \langle 112 \rangle$ type orientation increases progressively with prior cold reduction up to 90% RA. (84,85,125,126,137,139)

Sawatani et al (125) and Dickson and Cooke (122) also considered prior reductions over 90% RA in titanium stabilised, 17%Cr and 12%Cr steels respectively. The former (125) recorded a major $\{112\} \langle 110 \rangle$ recrystallisation texture after 95% prior reduction. Dickson and Cooke (122) reported an exclusive $\{223\} \langle 10,7,2 \rangle$ texture in 12%Cr steel which had been hot rolled, cold rolled (without pre-annealing) to 95% RA and subsequently heat treated at 900°C. This orientation is virtually identical with $\{223\} \langle 962 \rangle$, which has been identified in ordinary niobium-stabilised, low carbon steel cold rolled to 80% RA before annealing. (124)

The beneficial effect of titanium and niobium in enhancing $\{111\}$ textures in ferritic stainless steels has been widely attributed to the presence of Ti(CN) or Nb (CN) particles. However, there is disagreement as to the mechanism by which the precipitates act. Sawatani et al (125) and Kado et al (137) attribute the effect to a fine dispersion of particles, which restricts nucleation in grain interiors to the most favoured subgrains. This particle-pinning mechanism has also been proposed to account for the effects of titanium and niobium in other low carbon steels. (130,140) By contrast, Lewis (84) found evidence of particle-stimulated nucleation by coarse carbonitrides, and he reported that, after short annealing times, the majority of nuclei at particle/matrix interfaces had $\{111\}$ planes parallel with the rolling plane. This is contrary to the conclusions of other authors, (106,141) that particle-stimulated nucleation is

essentially random in low carbon steels.

There is an alternative view, expressed by Hutchinson, ⁽¹⁰⁶⁾ that the beneficial effect of titanium and niobium is due to purification of the matrix, for which coarse particles are more effective. This is supposed to aid in-situ nucleation of $\{111\} \langle uvw \rangle$ grains and is in agreement with work by Takahashi and Okamoto ⁽¹⁴²⁾ which suggests that nitrogen in solid solution interferes with recovery by stabilising dislocations. The process of recovery obviously favours in situ nucleation, whereas migration of existing high angle boundaries (SIBM) is more likely to occur in the early stages of recrystallisation when recovery is inhibited.

Sawatani et al ⁽¹²⁵⁾ recommended a titanium content of 0.2% for optimum $\{111\} \langle uvw \rangle$ texture enhancement in 17%Cr, low interstitial steel. This corresponds with a level of titanium $\sim 10 \times (C+N)\%$ for the steel studied. Kado et al ⁽¹³⁷⁾ made a more systematic study of the effects of varying titanium and carbon contents. They concluded that the $\{554\} \langle 225 \rangle$ texture was most prominent when the amount of titanium in solid solution, expressed as equation (18), had a value between 0% and 0.07%. At lower titanium contents, $\{110\} \langle 001 \rangle$ persisted as the major recrystallisation texture component even after prior cold reduction as high as 82% RA. Excessive titanium caused a decrease in the $\{111\} \langle uvw \rangle$ intensity which Kado et al ⁽¹³⁷⁾ assigned to excessive precipitation or coarsening of the precipitate. However, solute drag seems a more likely

éxplanation for the reduced texture selectivity since the maximum precipitation must coincide with removal of all carbon and nitrogen from solid solution, although in practice a slight excess of titanium is needed to account for combination with sulphur and oxygen.

In the case of niobium the optimum level, recommended for full stabilisation and for $\{111\}$ $\langle uvw \rangle$ texture control, is usually considered to be $\sim 8 \times (C+N)\%$, (106,140) which approximates to the stoichiometric ratio. Excessive niobium restricts post-recrystallisation grain growth, reducing the $\{111\}$ $\langle uvw \rangle$ texture intensity. This orientation is normally augmented by grain growth when present as the major recrystallisation component.

(iv) Steels containing other precipitates

A dispersion of ϵ -Cu (120,126,143) or Cr_2N (127) particles has been found to encourage $\sim \{111\}$ $\langle 112 \rangle$ textures, the effect becoming more pronounced with increasing prior cold reduction over 60% RA. Miyaji and Watanabe (120) found that excessive precipitation resulted in retention of the cold rolling texture after annealing.

(b) Effects of other processing variables

(i) Hot rolled condition

There does not appear to have been any systematic investigation of the influence of annealing treatment prior to cold rolling on final recrystallisation textures in ferritic stainless steel sheet. However, Dickson and Cooke (122) demonstrated the importance of this variable in Ti-stabilised, 12%Cr steel. They found that pre-

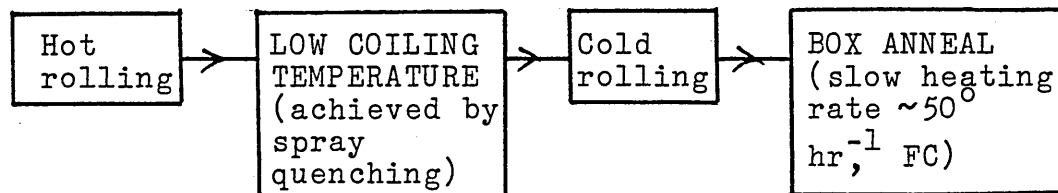
annealing at 1050°C promoted a $\{110\}$ $\langle 001 \rangle$ recrystallisation texture after cold rolling reductions up to 75% RA whereas after 95% reduction the annealing texture was mainly $\{554\}$ $\langle 225 \rangle$. Omission of the hot-band annealing treatment prior to cold rolling led to development of different recrystallisation textures : a strong $\{554\}$ $\langle 225 \rangle$ after only 75% RA and a new component, $\{223\}$ $\langle 10,7,2 \rangle$, after 95% RA.

The grain size of the steel prior to cold rolling is likely to be an important factor and might explain the differences in behaviour observed by Dickson and Cooke, ⁽¹²²⁾ since 1050°C is high enough to cause substantial grain coarsening in Ti-stabilised steels. A similar effect of coarse initial grain size in displacing $\{111\}$ $\langle uvw \rangle$ recrystallisation textures to higher cold reductions has been observed in pure iron. ⁽¹³⁶⁾ Matsuo et al ⁽¹³⁶⁾ attributed the effect of initial grain size to discrepancies in the development of local inhomogeneities during cold working, leading to differences in subsequent nucleation behaviour.

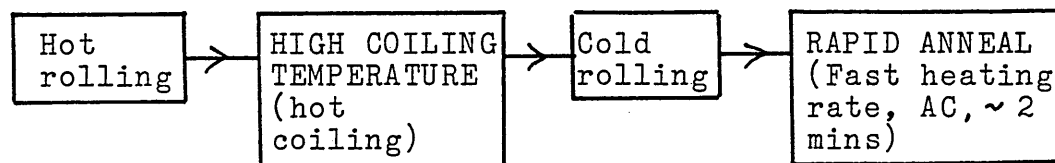
Horta, Wilson and Roberts ⁽¹⁴⁴⁾ suggested that control of the hot-band condition is more critical for "rapid" final annealing (fast heating rate, AC or WQ, treatment time \sim 2 mins) than for "box" type final annealing (slow heating rate, FC - total treatment time \sim 24 hrs). For initially coarse-grained material, they noted a large increase in $\{110\}$ $\langle uvw \rangle$ intensity (compared with initially fine-grained material) after rapid annealing, but not after box annealing.

For ordinary low carbon steels cold rolled without

pre-annealing, the hot-strip coiling temperature is an important variable. The coiling temperature is optimised in conjunction with the final annealing treatment after cold rolling, according to the following schedules :- (106)



or,



According to Hutchinson and Ushioda, (135) hot coiling of low-carbon deep drawing steels (before cold rolling and continuous (rapid) annealing) ensures wide interparticle spacings of cementite and hence a relatively pure matrix remote from the particles, favouring $\{111\} \langle uvw \rangle$ textures for short-time, high temperature annealing. For niobium and titanium stabilised steels, hot coiling ensures re-precipitation of any titanium/niobium carbonitrides dissolved during soaking for hot-rolling. (135) Hot coiling has the disadvantage that the ends of the coil tend to cool more quickly than the centre, resulting in some inconsistency of properties.

(ii) Annealing temperature of cold rolled sheet

Raising the final annealing temperature above that required to just complete recrystallisation has been

reported to enhance the $\sim \{111\} \langle 112 \rangle$ texture component in Ti-stabilised ferritic stainless steels. (125)

However, rapid grain coarsening occurs above $\sim 950^\circ\text{C}$, so that utilisation of this effect is restricted.

(iii) Heating rate for annealing of cold rolled sheet

The heating rate for final annealing has been found to have an effect on the relative intensities of components in the recrystallisation textures of both ferritic stainless steels and ordinary low carbon steels, especially after reductions $< 60\%$ RA. (106,126,144,145)

Slow heating, as in box annealing, generally strengthens $\{111\} \langle uvw \rangle$ components. (126,144,145) However, the condition of the steel prior to cold rolling also affects the response to final annealing. With continuous (rapid) annealing of low carbon steels, the combination of highest intensity of $\{111\} \langle uvw \rangle$ recrystallisation texture components with minimum $\{100\} \langle uvw \rangle$ intensity is achieved after higher cold reductions than with box annealing, where 60-70% RA is usually considered optimum (106)

(iv) Two-stage cold rolling

Some workers have claimed further strengthening of the $\{111\} \langle 112 \rangle$ recrystallisation texture, in stabilised ferritic stainless steels, by two-stage cold rolling incorporating an intermediate annealing treatment. (85,137)

The best results were achieved with a high second cold reduction, $\sim 80-85\%$ RA. Kado et al (137) found that the $\{100\} \langle 011 \rangle$ orientation persisted in the recrystallisation texture even after high single-stage

reductions, whereas with two-stage cold rolling it was practically eliminated from the annealing texture when the second reduction exceeded 80% RA. However, Sawatani et al (125) detected no significant differences between annealing textures developed after single and two-stage rolling.

2.6.4 Formability

(a) Effects of Texture

Deep drawability is improved by a texture that gives high through-thickness strength, i.e., high \bar{r} -values. High \bar{r} -values are also associated with dent resistance and low tendency towards edge splitting. (106)

It is generally acknowledged that, in low carbon steel sheet, texture components with $\{111\}$ planes parallel to the rolling plane are effective in increasing \bar{r} -values whereas $\{100\}$ $\langle uvw \rangle$ components are most harmful. (131,139,140,144,146) Studies of strain ratios and recrystallisation textures have shown that this is also true for ferritic stainless steels. (84,85,125,147) Various authors have correlated r -values with parameters based upon the volume fraction of material with specific $\{hkl\}$ planes parallel to the sheet surface.

Lewis and Pickering (84) derived the following relationships for ferritic stainless steels, from regression analysis :-

$$\bar{r} = 0.77 + 0.36 \log \frac{I \{111\}}{I \{100\}} \quad \dots \text{Equation (20)}$$

$$\text{LDR} = 2.17 + 0.13 \log \frac{I \{111\}}{I \{100\}} \quad \dots \text{Equation (21)}$$

The average strain ratio has also been found to depend on the ratio $I_{\{113\}}/I_{\{100\}}$ in ordinary low carbon steels. (131,139,144)

Hutchinson, et al, (134) found that \bar{r} could not be correlated solely with $\{111\}$, $\{110\}$ and $\{100\}$ intensities, attributing a reduction in \bar{r} in heavily cold rolled ($> 85\%$ RA) and annealed electrolytic iron to the development of a $\{114\} \langle 841 \rangle$ recrystallisation texture.

Messien and Greday (146) found no simple relationship between \bar{r} and texture, but determined the following empirical formulae, relating texture components to r_0 , r_{45} and r_{90} in Ti-stabilised, low carbon steels.

$$r_0 = 0.045 \left(\frac{I_{\{113\}}}{I_{\{100\}}} \right) + 0.89 \quad \dots \text{Equation (22)}$$

$$r_{90} = 0.058 \left(\frac{I_{\{113\}}}{I_{\{100\}}} \right) + 1.16 \quad \dots \text{Equation (23)}$$

$$r_{45} = 2.86 - 0.62 \left(\frac{I_{\{332\}}}{I_{\{112\}}} \right) \quad \dots \text{Equation (24)}$$

Planar anisotropy must also be considered, since this results in earing. Ears occur in the directions where $\{100\}$ pole densities are highest. (148) High planar anisotropy can also have other effects on deep drawing performance. Thomson (149) quotes an example of an automotive body component that could only be successfully formed when the blank was placed transversely, so that its high r_{90} direction lay along the

direction of maximum depth of draw.

Yantac, Roberts and Wilson (147) correlated Δr -values in a 12% Cr steel with $f_{\{211\}}$, the volume of material having $\{211\}$ planes parallel to the rolling plane. Δr decreased as $f_{\{211\}}$ increased, the optimum value of $f_{\{211\}}$ being $\sim 25\%$, since above this level Δr becomes negative. Horta, Wilson and Roberts (144) associated low Δr in ordinary low carbon steels with a low value of the ratio $I_{\{110\}}/I_{\{112\}}$. The effect of the $\{112\}$ sheet plane component is to increase r_{45} , which leads to lower (eventually negative) values of Δr . (146,149)

The work hardening coefficient is largely independent of texture. Brickner and Berger (150) noted that, in general, as \bar{r} increases in ferritic stainless steels, \bar{n} also tends to show a slight increase.

(b) Effects of Composition

Brickner and Berger (150) found that, in general, increasing carbon, manganese and chromium all tended to reduce \bar{r} whereas increasing silicon and niobium contents improved \bar{r} . Molybdenum appeared to have very little effect. All the elements studied altered r_0 and r_{90} , but not r_{45} . The authors (150) therefore, concluded that raising \bar{r} by compositional control inevitably raised Δr .

Other authors have found that $\{111\} \langle uvw \rangle$ texture components are favoured by very low manganese contents, (135,137) that molybdenum has no significant effect on texture, (84) and that increasing carbon promotes $\{100\} \langle uvw \rangle$ texture components. The observations of Brickner and Berger (150) can thus be

explained by the effects of compositional changes on texture.

Niobium and titanium are widely recognised as effective additions for increasing deep drawability, (84,85,116,125,137) and are known to promote $\sim \{111\} \langle 112 \rangle$ recrystallisation textures at the expense of $\{100\} \langle uvw \rangle$ and $\{110\} \langle uvw \rangle$ components. The LDR and \bar{r} -values of Ti-stabilised steels are higher than those of Nb-stabilised steels. However $|\Delta r|$, and hence the earing tendency of Nb-stabilised steels is also lower, due to the greater rotational freedom of the $\{111\} \langle uvw \rangle$ texture components. (84,85)

The effects of composition on work hardening coefficients have been studied by Miyakusu, Uematsu and Hoshino, (151) who found that alloying elements in solid solution decrease n-values. Multiple regression analysis yielded the following relationship between n-value and composition for ferritic stainless steels, and the authors (151) reported a correlation coefficient of 0.91:-

$$n = 0.3274 - \left\{ 0.015 \text{ Si} + 0.003 \text{ Mn} + 0.560 \text{ P} \right. \\ \left. + 0.050 [\text{Al}]_{\text{ss}} + 0.069 [\text{Ti}]_{\text{ss}} \right. \\ \left. + 0.094 [\text{C+N}]_{\text{ss}}^{\frac{1}{2}} \right\} \dots \text{Equation (25)}$$

(c) Effects of Processing Variables

Most workers have found that increasing the cold rolling reduction prior to final annealing increases the value of \bar{r} and hence the LDR in stabilised ferritic stainless steels, the highest \bar{r} values being realised

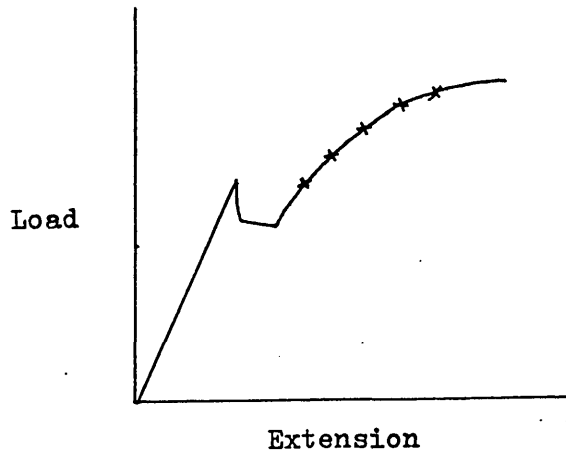
after reductions $> 80\%$ RA. (116,125,137,147) In ordinary Ti-stabilised steels, the optimum cold reduction is $\sim 90\%$ RA, at which level \bar{r} is high and $|\Delta r|$ goes through a minimum. (116) Above 90% RA, \bar{r} decreases as a consequence of an increase in $\{100\} \langle uvw \rangle$ components in the recrystallisation texture, even though $\{111\} \langle uvw \rangle$ components also continue to increase.

There is some dispute as to whether maximum \bar{r} values are promoted by a single-stage cold rolling reduction (116,125) or by a two-stage process incorporating an intermediate anneal. (102,137) In either case, the important factor is the proportion of $\{100\} \langle uvw \rangle$ oriented material in the recrystallisation texture, which must be as low as possible for good drawability. (147) Although two-stage rolling has been claimed to enhance \bar{r} in some cases, it is also reputed to increase planar anisotropy in both ordinary and stainless Ti-stabilised steels. (137,139)

Nakagawa et al (117) and Kado et al (137) reported that omission of the annealing treatment prior to cold rolling in 17-18% Cr, Ti-stabilised steels resulted in high \bar{r} values with low planar anisotropy. However, Nakagawa et al (117) found that this omission led to an increase in the severity of roping. Lowering the hot rolling finishing temperature is known to reduce the incidence of roping, and is also supposed to promote higher \bar{r} values. (117,125, 147)

3.8.2. Strain Hardening Exponents (n-values)

Strain-hardening exponents were determined in accordance with ASTM E646-78 (which applies to sheet 0.13-6.4mm thick), using load-extension curves produced during straining to 15% elongation. The load and corresponding extension were determined for five different points between the end of the discontinuous yielding (Lüders band) section and the maximum load region, as shown in the following diagram.



The strain hardening exponent was determined from the logarithmic form of power curve representation of true stress versus true strain within the plastic range :-

$$\ln \sigma = \ln k + n \cdot \ln \epsilon$$

where

$$\sigma = S (1 + e)$$

$$\epsilon = \ln (1 + e)$$

$$S = \text{engineering stress} = \text{load/original area}$$

$$e = \text{engineering strain} = \text{extension/original length}$$

The value of the slope (n), intercept (ln k) and standard deviation, (s), for the linear relationship between

$\ln \sigma$ and $\ln \epsilon$ were determined by linear regression.

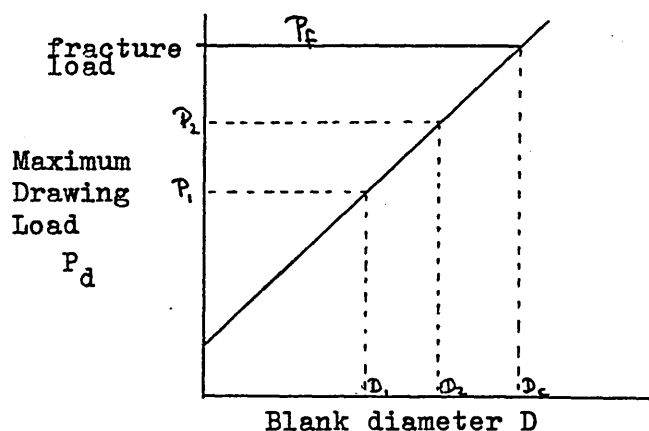
3.9. SIMULATIVE FORMABILITY TESTING

3.9.1. Swift Cupping Test

Swift cupping tests were carried out on a Hille machine, which is equipped with a calibrated load cell, using a standard 50mm diameter punch travelling at a constant speed of 160mm min^{-1} . Polythene sheet was used as a lubricant, placed between the die face and the blank.

The two-blank 'Secondary Swift Test' suggested by Wilson, Sunter and Martin (77) was used for prediction of limiting Drawing Ratios (LDR) using two subcritical blanks of diameters 80mm and 100mm. The 80mm diameter blanks were drawn using only primary blankholder restraint of 1000kgf, whereas an additional secondary clamping force of 1000kgf was applied to the 100mm diameter blanks once the maximum drawing load had been achieved.

The fracture load was determined from the 100mm blank by failure under secondary clamping. Critical blank diameters were predicted, from graphs of maximum drawing load versus blank diameter, according to the following diagram.



Depending on the availability of material, a second 100mm diameter blank was fully drawn without secondary clamping, for measurement of earing profile.

Preliminary tests on commercially cold rolled and laboratory annealed sheet, using a larger variety of blank sizes, confirmed a linear relationship between blank diameter and drawing load for ferritic stainless steels, and indicated good agreement (within ~ 5%) between values of D_c and LDR obtained via the two-blank test and via the conventional, multiblank Swift test.

3.9.2. Erichsen Tests

Erichsen stretch-formability tests were carried out in accordance with BS3855:1965, using the Hille machine. Sheet specimens were clamped with a blank-holder force of 1000kgf, and stretched under the action of a spherical ball punch of diameter 20mm, travelling at a constant speed of 30mm min^{-1} . Polythene sheet was used as lubricant between the punch and the blank. The test was halted when a crack appeared through the full thickness of the sheet. The test result is the depth of penetration of the punch.

3.10 ASSESSMENT OF ROPING SEVERITY

Roping severity can be assessed qualitatively by visual examination and comparison with arbitrary standards. However, profile measurement using a Talysurf was used in the present work to give more quantitative results. Roping assessment was performed on the same tensile test pieces (strained to 15%

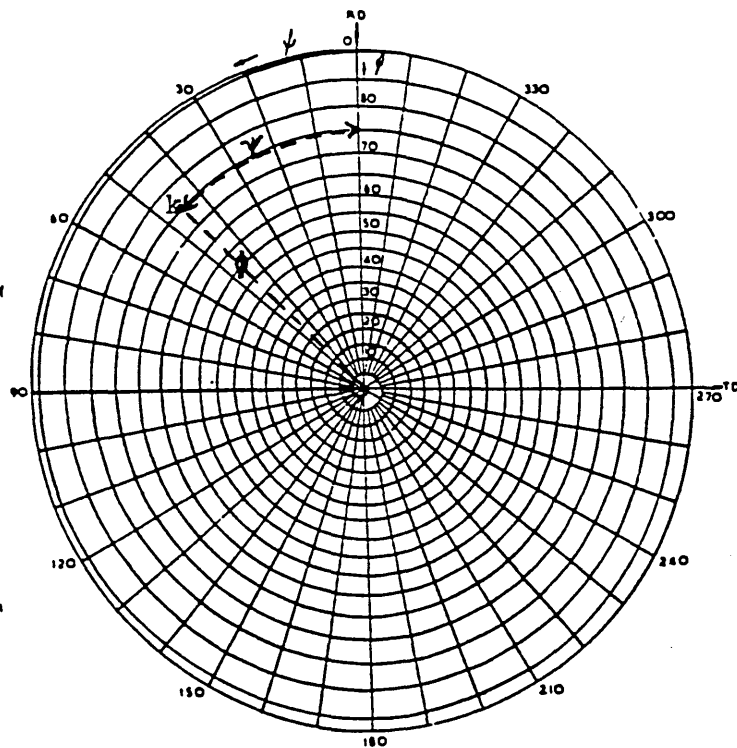
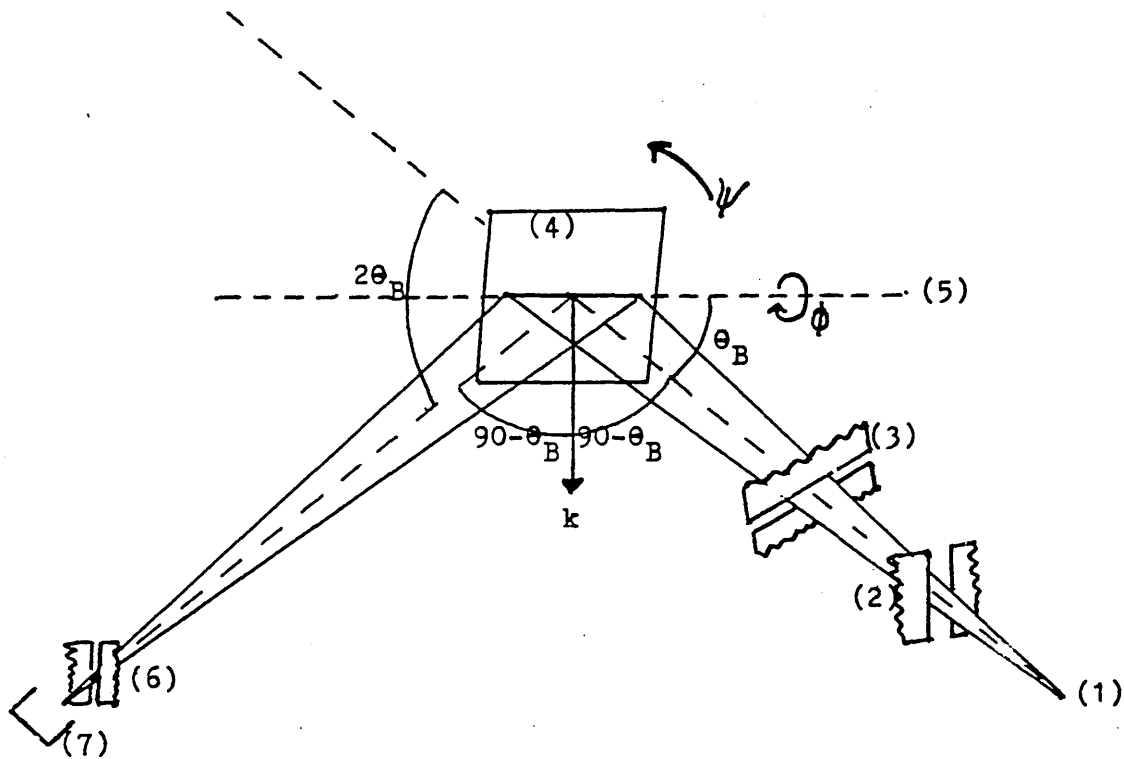
elongation) used for r_o evaluation.

The Talysurf stylus traces the contours of the surface, perpendicular to the rolling direction, recording both surface roughness and waviness. Opposite surfaces were scanned along exactly the same line, to demonstrate the corrugations associated with roping. Optimum horizontal and vertical magnifications of X20 and X500 respectively were chosen for the test. The equipment is capable of filtering out any slope associated with setting up error or bowing of the sample, but over a limited scanning distance only. However, in order to scan the full width of the specimens used, a direct (unfiltered) profile measurement was preferred, and the resultant trace does include any distortion of the test piece.

3.11 POLE FIGURE DETERMINATION

Quantitative pole figures were determined by the Schulz X-ray reflection method using a Siemens texture goniometer.

The geometric arrangement of the goniometer and corresponding stereographic projection are illustrated schematically by the following diagram.



Geometric Arrangement of Texture Goniometer and Corresponding Stereographic Projection.

A monochromatic X-ray beam from the source (1) is restricted by divergence slits (2) and subsequently passes through a narrow horizontal slit (3) to the specimen (4). The major circle of the goniometer is set so that its axis makes the Bragg angle θ_B , for a particular set of $\{hkl\}$ planes, with the central ray of the incident beam. The arm holding the receiving slits and the counter is set at the angle $2\theta_B$ so that the $\{hkl\}$ diffraction plane normal remains fixed in space. Under these conditions, for any position of the specimen, only those grains oriented such that an $\{hkl\}$ plane normal coincides with the fixed normal will contribute to the measured intensity of the reflected beam received at the counter. The reflected intensity is thus proportional to the $\{hkl\}$ pole density on the pole figure for the position under investigation.

In practice the angle θ_B is not critical to within $\sim \frac{1}{2}^\circ$ and is simply set to the calculated value. The angle $2\theta_B$ requires fine adjustment with the specimen positioned in the holder in order to maximise the measured intensity of the diffracted beam.

When mounted on the goniometer the specimen is subjected to three types of movement :-

- (i) simple translation to and fro, which improves the statistical averaging of the texture measurement by increasing the number of grains that are sampled.
- (ii) Rotation about an axis perpendicular to the specimen surface (azimuth angle ψ). The sample is initially aligned such that $\psi = 0$

corresponds with the rolling direction.

- (iii) Rotation about an orthogonal axis (radial or inclination angle ϕ).

By providing simultaneously a fast rotation of the angle ψ with a slow rotation through the angle ϕ , the diffracted intensity along a spiral trace is determined, as indicated in the diagram.

The radial angle ϕ was changed by 5° during a complete revolution around the ψ axis, which took 6 minutes. Hence, the total time required to scan from $\phi = 90^\circ$ (specimen horizontal) to $\phi = 0^\circ$ (specimen vertical) was 108 minutes. The curve representing the reflected intensity in relation to the azimuth (ψ) and inclination (ϕ) angles was recorded by a Siemens chart recorder as counts/sec v. seconds. A digital readout of the total integrated intensity (i.e. total counts) was also obtained.

The main problem with the Schulz reflection method is the defocussing effect which causes a drop in measured intensity at high values of the angle ϕ . There is a slight loss in intensity when ϕ is between 50° and 70° , but this is so small that it can be neglected. However, serious defocussing occurs above $\phi = 70^\circ$, but, by allowing for the theoretical decrease in intensity, reasonable accuracy can be obtained in the range $\phi = 70^\circ - 85^\circ$. Provided that the measurements in this region are not used for quantitative comparison they are useful for completing the definition of the texture.

Both "zero" (background) and "random" (no preferred orientation) intensity must be determined in order to find the interval between these which corresponds to $1x$ random intensity.

Zero intensity was assessed as the average intensity of diffracted radiation measured when the counter was moved to either side of the $2\theta_B$ position. In certain highly textured samples, this corresponded with the minimum intensity observed in the range $\phi = 0^\circ - 50^\circ$.

The random level was obtained by total integration of the diffracted intensity (i.e. total counts) over the whole angular range, assuming the decrease after $\phi = 70^\circ$ to be linear.

A series of reference lines was drawn on the chart, representing multiples and sub-multiples of the "random" diffracted intensity. When plotting a contour on the pole figure, marks were made on the spiral path (illustrated in the diagram) at each point corresponding to the values of ϕ and γ where the measured intensity trace cuts the reference line concerned. These marks were then joined to give a contour line which separates areas above the reference level from those below it.

Having plotted the pole figure, the intensity levels of ideal orientations describing the main texture components can be obtained from the chart, to give semi-quantitative information about the texture. Care is required in the interpretation of such data since the intensity recorded at a discrete point says little about

the distribution of poles around that orientation. Also, when evaluating the intensity of ideal orientations, account must be taken of the fact that textures such as $\{100\} \langle 011 \rangle$ are described by a single set of poles, whereas components such as $\{211\} \langle 011 \rangle$ consist of two complementary orientations $(211) [01\bar{1}]$ and $(211) [0\bar{1}1]$, whose intensities, if not equal, must be averaged to give the true intensity of $\{211\} \langle 011 \rangle$ in terms of \times random units. Other textures, for example $\{223\} \langle 962 \rangle$, consist of four, symmetrically disposed, equivalent sets of poles.

In the present study, $\{200\}$ pole figures were determined using $\text{MoK}\alpha$ radiation monitored by a scintillation counter. Table 1 indicates the positions at which the intensities of the main texture components were measured. Selected $\{222\}$ pole figures were also determined, mainly to distinguish components with poles at the periphery of $\{200\}$ pole figures, especially $\{100\} \langle 001 \rangle$ and $\{110\} \langle 001 \rangle$ where the peripheral poles in $\{200\}$ pole figures coincide.

3.12 TEXTURE PARAMETER EVALUATION

Texture parameters (P-values), which indicate the volume fraction of material having $\{hkl\}$ planes parallel with the sheet surface, were measured using a Philips diffractometer and $\text{MoK}\alpha$ radiation monitored by a scintillation counter. The specimen and detector were rotated such that a series of Bragg reflections, for which the diffracting plane normals were all perpendicular to the plane of the sheet, were scanned.

The following nine reflections were recorded using a Philips Chart recorder :-

{110} , {200} , {211} , {310} , {222} ,
 {321} , {411 + 330} , {420} , {332} .

The relative integrated line intensities ($I_{\{hkl\}}$) were determined by area evaluation using an Optomax image analyser. The errors involved in measurement of relative peak areas were usually within $\pm 5\%$, although for very small areas this could rise to $\pm 12\%$.

Texture parameters were calculated as follows :-

$$P_{\{hkl\}} = \frac{\frac{I_{\{hkl\}}}{R_{\{hkl\}}}}{\frac{1}{N} \sum \frac{I_{\{hkl\}}}{R_{\{hkl\}}}}$$

where

- $P_{\{hkl\}}$ = texture parameter
- $I_{\{hkl\}}$ = relative integrated line intensity of the textured sample, determined experimentally.
- $R_{\{hkl\}}$ = relative integrated line intensity of a random sample, as calculated in Table 2.
- N = number of reflections used (= 9 in this case).

P-values defined thus are automatically self-corrected for non-textural factors governing line intensity.

Since the {411} and {330} reflections coincide, the {411} line intensity must be obtained by peak separation. This involves subtraction of the area of

the {330} peak, calculated from its known relationship with the {110} peak, from the total peak area.

Texture parameters are useful for the purpose of correlating textural data with measured properties.

v

Commercial, high-interstitial 17% Cr (430) steel and low interstitial, Ti-stabilised ~17% Cr (430Ti) and 12% Cr (409) steels, whose compositions are listed in Table 3(A), have been studied using material in the following starting conditions :-

- (i) as hot rolled;
- (ii) hot rolled and "rapid" pre-annealed (heating rate $\sim 5000^{\circ}\text{C hr}^{-1}$, AC);
- (iii) hot rolled and "batch" pre-annealed (heating rate = $50^{\circ}\text{C hr}^{-1}$, FC at $50^{\circ}\text{C hr}^{-1}$).

(Hot rolling temperatures are recorded in Table 3(B))
The sequence of texture development and variation in microstructure as a result of subsequent cold rolling and annealing have been investigated. Selected samples have also been examined using uniaxial tensile measurements (r_e , \bar{r} , Δr , n , roping severity), Swift and Erichsen tests and electron microscopy.

In Tables 8-25, texture data taken from pole figures is presented in terms of the main ideal orientations observed. By implication, such descriptions are simplified and limited, but they do serve a useful purpose in summarising major differences. Selected {200} pole figures, with the positions of relevant ideal orientations superimposed, are also included in the results. Intensities of ideal orientations, derived from pole figures have been plotted against various parameters, e.g., cold rolling strain, to highlight any variation. Carbide particle sizes have

been evaluated using SEM and also TEM of carbon extraction replicas. Thin foil electron microscopy has been used to identify possible nucleation sites and orientations of possible nuclei in partially recrystallised sheet samples. Strain ratio (r-value) measurements have been correlated with texture parameters (obtained from X-ray diffractometry) and also with Limiting Drawing Ratios (Swift Test results).

4.1.1. General Microstructural Features in High Interstitial 430 (17 Cr, 0.077 (C+N)) Steel

Table 4 summarises the main microstructural features and Fig.1 shows the variation in hardness with increasing annealing temperature for both hot rolled strip and cold rolled sheet. A selection of photomicrographs (Figs.2-7) illustrates the main microstructural observations.

The hardness-annealing curves (Fig.1), indicate that a $\frac{1}{2}$ hr. treatment at 750°C was sufficient to promote full recrystallisation. Annealing above 900°C , followed by air cooling, caused an increase in hardness which coincided with the appearance of martensite in the microstructure at grain boundary triple points (Fig.3b) indicating that annealing had been carried out in the two-phase ($\alpha + \gamma$) field. The structure was two-phase up to $\geq 1200^{\circ}\text{C}$, the A_5 temperature being between 1200°C and 1250°C . Grain growth was slow in the ($\alpha + \gamma$) region (Fig. 3b & 3c), but extremely rapid above the A_5 temperature (Fig.3d). Cooling from above A_5 through the ($\alpha + \gamma$) field, caused partial transformation of ferrite to austenite, which formed in Widmanstätten patterns and which transformed to martensite on further cooling to room temperature (Fig.3d). The steel was characterised by a "pancaked" grain structure after annealing below the A_5 temperature (Fig.4).

Microexamination of as-hot-rolled strip revealed a difference between surface and centre (Fig.2).

Grains at the centre (Fig.2b) were heavily deformed, indicating working below the dynamic recrystallisation temperature in the later stages of hot rolling. By contrast, surface grains (Fig.2a) were smaller and more equiaxed, implying that recrystallisation of the surface had occurred during the later stages of hot rolling, although probably not after completion of hot rolling since there was no appreciable difference in hardness between surface and centre. Microstructural changes occurring during annealing of the hot rolled strip between 850°C and 1250°C are illustrated by Fig.3. Although recrystallisation was largely complete after ½ hr. at 750°C, unrecrystallised grains persisted at the centre of the section after annealing at 850°C (Fig.3a).

Grain sizes were small after cold rolling and annealing and there was little difference in final grain size between material cold rolled without prior annealing (Fig.4a) and material which received a "rapid" anneal at 1000°C before cold rolling (Fig.4b). "Batch" annealing at 1000°C prior to cold rolling tended to promote a more equiaxed grain structure in the finished product (Fig.4c). Annealing at 1000°C after cold rolling (Fig.4d) produced a coarser grain size than final annealing at 900°C.

Carbide size and morphology in hot rolled strip was markedly affected by annealing (Figs.5-7). The as-hot-rolled strip was heavily banded, with the majority of carbides located at the original deformed boundaries (Fig.5a). Rapid annealing between ~ 750°C-850°C (Fig.5b) caused some spherodisation and slight coarsening of the

carbides, the mean particle size (average of length and width) being $\sim 1\mu\text{m}$ with some fine intragranular particles $\leq 0.5\mu\text{m}$. Batch annealing $\sim 850^\circ\text{C}$ (Fig.5c) caused pronounced spherodisation and coarsening of carbides, giving rise to a more uniform distribution of particles $\sim 1-2\mu\text{m}$ diameter, with some fine particles $\leq 0.5\mu\text{m}$ diameter still present. Annealing in the $(\alpha + \gamma)$ phase field resulted in grain boundary carbide films and colonies of irregular shaped carbides corresponding with the austenite regions of the high-temperature microstructure (Fig.6). Batch annealing at 1000°C (Fig.6a,7a) gave rise to a semi-continuous grain boundary carbide film, with colonies of rather coarse lamellar carbides and some near-spheroidal intragranular carbides $\sim 1-2\mu\text{m}$ diameter. Rapid annealing at 1200°C , followed by water quenching and tempering (Fig.6b), resulted in a fine, discontinuous grain boundary precipitate, colonies of tempered martensite containing carbide precipitates (Fig.6b) and also some fine, intragranular precipitates $\sim 0.1\mu\text{m}$ diameter (Fig.6b and 7b).

4.1.2. General Microstructural Features in Low Interstitial 430 Ti Steel
(a) $\sim 17\text{ Cr, } 0.5\text{ Ti, } 0.029\text{ (C+N) Steel}$

Table 5 summarises the main microstructural features and Fig.8 shows the variation in hardness with increasing annealing temperature, for both hot rolled strip and cold rolled sheet. Figures 9-20 illustrate microstructural observations.

The hardness-annealing curves (Fig.8) indicate

that a $\frac{1}{4}$ hr. treatment at 800°C was sufficient to promote full recrystallisation. The microstructure of the steel, at all temperatures, consisted of ferrite containing a dispersion of Ti (CN) particles, i.e., there was no ($\alpha + \gamma$) phase field and hence no risk of introducing martensite into the structure. Annealing promoted an equiaxed grain structure, and grain growth was rapid above 900°C (Figs.11,14 and 15).

Microexamination of hot rolled strip (Fig.10) revealed a finer structure at the surface than at the centre of the section, although no such difference was observed after annealing above 800°C. The changes occurring during annealing of hot rolled strip between 750°C and 1000°C are shown in Fig.11. Differences in hot band structure were reflected in the cold rolled microstructures after reductions of 70% RA (Fig.12), but were less obvious after very high cold rolling reductions (Fig.13).

Grain sizes of samples subjected to the same cold rolling and annealing schedule tended to be similar (Figs.9,14 and 15), despite differences in hot-band condition and cold rolled microstructure. Batch annealing after cold rolling resulted in a slightly coarser grain size than rapid annealing at the same temperature (Table 5).

Carbide distributions in hot band material (Figs.16-18) consisted of two dispersions; one of large angular, pinkish carbides $\sim 2-5\mu\text{m}$ diameter (typically referred to as Ti (CN)), which was unaffected by annealing, the other of finer ($\leq 1\mu\text{m}$ diameter)

carbides (Figs.16-18) whose size and frequency varied with annealing treatment as follows :-

(i) As hot rolled

Only occasional particles 0.1-0.5 μ m diameter were present (Fig.16a).

(ii) Hot rolled and annealed at 850°C

Rapid annealing at 850°C caused precipitation of many small particles 0.02-0.3 μ m diameter (Fig.16b,18a,18c). Batch annealing resulted in a somewhat lower frequency of carbides 0.05-0.3 μ m diameter (Figs.16c,18b).

(iii) Hot rolled and annealed at 1000°C

With rapid annealing at 1000°C (AC or WQ) only occasional fine particles 0.05-0.3 μ m diameter were observed, (Figs.17a,17b,18d). By contrast, slow heating (50°C hr⁻¹) or furnace cooling (50°C hr⁻¹) resulted in a high frequency of fine precipitates \leq 0.3 μ m diameter (Figs.17c,17d), similar to the dispersions obtained by annealing at 850°C.

Analysis of the larger (\geq 2 μ m) diameter carbides using the EDAX facility or the SEM confirmed that they were titanium-rich, and X-ray mapping indicated that sulphur was also associated with titanium at the peripheries of some particles (Fig.19). Diffraction patterns obtained from particles \geq 1 μ m diameter during TEM examination of thin foils were compatible with the reciprocal lattice of titanium carbonitride. (Fig.20).

(b) ~17 Cr, 0.3-0.4 % Ti Steels

Microstructural features for 0.3% Ti and 0.4% Ti steels are summarised in Table 6. The lower titanium content of these steels reduced the $\frac{1}{2}$ hr recrystallisation

temperature of heavily cold worked sheet from $\sim 800^{\circ}\text{C}$ for 0.5% Ti steel to $\sim 750^{\circ}\text{C}$ for 0.3% Ti steel (Fig.21). Grain sizes and microstructures of 0.4% Ti and 0.5% Ti steels were very similar (Table 6), but grain coarsening occurred above $\sim 850^{\circ}\text{C}$ in the 0.3% Ti steel, so that average grain diameters after cold rolling and annealing were $\sim 65\mu\text{m}$ compared with $\sim 25\mu\text{m}$ for 0.4/0.5% Ti steels. In the 0.3% Ti steel, pronounced stringers of large Ti (CN) particles were present throughout the structure, but especially at the surface (Fig.22). Such segregation was not observed in the 0.4/0.5% Ti steels.

4.1.3. General Microstructural Features in Low Interstitial 409 (12 Cr, 0.5 Ti, 0.039 (C+N)) Steel

Table 7 summarises the main microstructural features and Fig.23 shows the variation in hardness with increasing annealing temperature for both hot rolled strip and cold rolled sheet. Figures 24 and 25 illustrate microstructural observations.

Microstructures observed in 409 steel were essentially similar to those reported for 430 Ti (17% Cr, 0.5 Ti) steel, with some slight differences in response to heat treatment. The $\frac{1}{4}$ hr recrystallisation temperature for heavily cold rolled 409 sheet was $\sim 750^{\circ}\text{C}$, compared with $\sim 800^{\circ}\text{C}$ for 430 Ti (0.5 Ti) sheet. Complete recrystallisation of hot-rolled 409 strip proved more difficult, requiring a minimum temperature of 850°C (Fig.23).

Average grain sizes in hot rolled and annealed 409 strip were slightly coarser than in 430 Ti (0.5% Ti)

strip (for equivalent annealing treatments), whereas grain sizes of cold rolled and annealed 409 sheet (Table 7) were slightly finer than 430 Ti sheet. Rapid grain coarsening of 409 steel occurred above $\sim 900^{\circ}\text{C}$ (Fig.24), as in 430 Ti steel. Carbide sizes and distributions in hot rolled and annealed 409 steel (Fig.25) also resembled those observed in 430 Ti strip.

4.1.4 Examination of Partially Recrystallised Samples

Selected samples of 430 and 430 Ti steels were examined optically and by TEM, after cold rolling 60-90% RA and annealing for 5 minutes at $650-700^{\circ}\text{C}$, in order to identify possible sites and orientations of recrystallisation nuclei. Thin foils were obtained parallel to the rolling plane, and therefore contained the rolling direction and transverse direction in the plane of the foil. Although several thin foils ($\sim 8-10$) were examined from each sample, it is recognised that the total area subjected to TEM analysis was still very small, so that the information yielded by the results must necessarily be limited as an identification of possible sites and orientations of recrystallisation nuclei.

(a) High Interstitial 17% Cr, (430) Steel. Optical Examination

Optical resolution of possible nucleation sites was difficult due to the highly elongated nature of the deformed grains and the large number of carbides present. Deformed grain boundaries appeared to be the main source of possible nuclei (Fig.26). With batch annealing at

1000°C before cold rolling, occasional nuclei associated with large carbide particles were also observed (Fig.26c), although the particles themselves were often located at the original deformed boundaries.

TEM Examination

Most of the potential nuclei (oversized subgrains $> \sim 2 \mu\text{m}$ diameter and having a significant size advantage over their neighbours) observed in 430 steel were associated with, or close to, grain boundaries (Fig.27). Occasionally, large subgrains were found in grain interiors (Fig.28), apparently remote from features such as grain boundaries and large particles. No examples of particle-stimulated nucleation were observed. The following orientations were determined for possible grain boundary nuclei :-

- (i) Material annealed $\leq 850^\circ\text{C}$ before cold rolling
 $\sim \{137\} \langle 851 \rangle$; $\sim \{113\} \langle 521 \rangle$; $\sim \{111\} \langle 011 \rangle$.
- (ii) Material annealed $\geq 1000^\circ\text{C}$ before cold rolling
 $\sim \{113\} \langle 521 \rangle$; $\sim \{111\} \langle 123 \rangle$; $\sim \{111\} \langle 121 \rangle$;
 $\sim \{112\} \langle uvw \rangle$.

- (b) Low Interstitial, Ti-stabilised, 17% Cr
(430 Ti) steel
Optical Examination

For cold rolling reductions up to $\sim 80\%$ RA, possible nuclei associated with carbide particles and nuclei in grain interiors (apparently remote from grain boundaries and particles) were observed (Fig.29). Possible nuclei were also occasionally associated with grain boundaries. For higher cold rolling reductions, optical resolution of embryo recrystallised grains in the heavily cold-worked structure was very difficult.

TEM Examination

Figs. 30-36 are TEM photomicrographs illustrating the main observations. It was found that annealing for 5 minutes at 650-750°C caused precipitation of fine particles in material which had been either (i) cold rolled without pre-annealing (Fig.30) or (ii) rapid annealed at 1000°C before cold rolling (Figs.31b and 35b). (These pre-treatments had resulted in a much lower frequency of fine carbides in the strip and hence in the cold-rolled sheet than pre-annealing at 750-850°C).

Potential recrystallisation nuclei in 430 Ti steel were associated with the following features :-

- (i) Grain interiors.
- (ii) Large carbide particles.
- (iii) Microbands.
- (iv) Grain boundaries.

(i) Grain interiors

Nucleation within grain interiors, apparently remote from large particles and grain boundaries (although it might be associated with particles or grain boundaries above or below the plane of the foil) was observed frequently with cold rolling reductions $\geq \sim 80\%$ RA, and especially with rapid pre-annealing at 1000°C (Fig.31). The majority of such nuclei observed had $\sim\{111\}$ $\langle uvw \rangle$ orientations.

(ii) Carbide particles

Nucleation within the deformation zones of coarse Ti (CN) particles ($\geq \sim 2\mu\text{m}$ diameter) was observed frequently in 430 Ti steel for cold reductions up to

80-90% RA (Fig.32). Particle stimulated nuclei almost invariably displayed $\sim \{111\} \langle uvw \rangle$ orientations. However, it appeared that not all particles were active in stimulating nucleation, and deformation zone subgrains with lower stored energy orientations (e.g., $\sim \{100\} \langle uvw \rangle$) remained comparatively small (Fig.33).

(iii) Microbands

Microbands of subgrains elongated in the rolling direction (on the section examined), and often located adjacent to or close to grain boundaries, were observed (Figs. 34 & 35). Such microbands were sources of oversized subgrains, especially at high cold rolling reductions (Figs. 34b and 35), and most of the potential nuclei originating in microbands had $\sim \{113\} \langle uvw \rangle$ orientations, in particular $\sim \{113\} \langle 741 \rangle$ and $\sim \{113\} \langle 521 \rangle$.

(iv) Grain boundaries

Recrystallisation associated with prior grain boundaries (Fig.36) was observed occasionally in samples cold rolled to 70-80% RA, and more frequently in samples cold rolled to 90% RA. Orientations of oversized grain boundary subgrains included $\sim \{111\} \langle 123 \rangle$, $\sim \{112\} \langle 241 \rangle$, $\{001\} \langle 340 \rangle$, $\sim \{113\} \langle uvw \rangle$ and $\sim \{012\} \langle 121 \rangle$.

4.2.1. High Interstitial 430 ($\sim 17\text{Cr}$, $0.077 (\text{C+N})$) Steel

Table 8 summarises the observed textures in terms of the main ideal orientations and Figs.37-43 represent a selection of $\{200\}$ pole figures illustrating these observations. Fig.44 shows the through-thickness variation in intensity of texture components, and Figs.45-46 show the effects of annealing on the intensities of the same components.

The texture of 5mm. thick hot rolled strip consisted of a surface texture (Fig.37), mainly $\sim \{110\} \langle 001 \rangle$, and a centre texture (Figs. 39 & 42) mainly $\sim \{100\} \langle 011 \rangle$ + minor $\sim \{554\} \langle 225 \rangle$ and $\sim \{112\} \langle 110 \rangle$ components. Fig. 44 shows that $\sim \{110\} \langle 001 \rangle$ persisted as the major component to a depth of $\sim 0.75\text{mm.}$, but below this it was gradually replaced by $\sim \{100\} \langle 011 \rangle$, whose intensity increased as the "quarterplane" (midway between surface and centre) was approached (Fig.39).

The surface texture was unaffected by annealing of the hot rolled strip (Fig.38). Fig.45 shows the effect of increasing annealing temperature on the intensities of the main ideal orientations at the quarterplane. Annealing $\geq 650^\circ\text{C}$ resulted in an increase in intensity of the $\sim \{110\} \langle 001 \rangle$ component (Figs.40 & 41) accompanied by a progressive decrease in the intensities of $\sim \{100\} \langle 011 \rangle$ and $\sim \{554\} \langle 225 \rangle$ with increasing annealing temperature (Figs.40 & 41). The $\sim \{112\} \langle 110 \rangle$ component was absent from the

quarterplane of samples annealed $\geq 650^\circ\text{C}$. Fig.46 shows the variation in texture intensity with increasing annealing temperature for the midplane. Again, annealing $\geq 650^\circ\text{C}$ caused a reduction in $\sim\{554\} \langle 225 \rangle$ intensity. Annealing $\geq \sim 1000^\circ\text{C}$ (Fig.43) also caused a reduction in $\sim\{100\} \langle 011 \rangle$ and $\sim\{112\} \langle 110 \rangle$ intensity, although $\sim\{100\} \langle 011 \rangle$ remained the major component at the midplane for all annealing treatments explored. Batch annealing at 1000°C (Fig.43) resulted in a higher $\sim\{110\} \langle 001 \rangle$ intensity (1.6x random) at the midplane than rapid annealing at the same temperature (0.8 x random).

4.2.2. Low Interstitial 430 Ti Steel
(a) 17% Cr, 0.5 Ti, 0.029 (C+N) Steel

Table 9 summarises the observed textures in terms of the main ideal orientations and Figs.47-53 represent a selection of $\{200\}$ pole figures illustrating the observations. Fig.54 shows through-thickness variation in intensity of texture components, and Figs.55-56 show the effect of annealing on the intensities of the same components. Figs.47-49 and Fig.54 show that, in 4mm thick hot rolled strip, a strong $\sim\{110\} \langle 001 \rangle$ surface texture persisted to a depth of $\sim 0.75\text{mm}$, but below this depth the texture changed progressively to $\sim\{100\} \langle 011 \rangle$ plus minor $\sim\{112\} \langle 110 \rangle$ and $\sim\{554\} \langle 225 \rangle$ components.

The surface texture was unaffected by annealing at temperatures up to 1000°C , still consisting mainly of a strong $\sim\{110\} \langle 001 \rangle$ component (Fig.50). Fig.55 shows the effect of increasing annealing temperature on intensities of the main ideal orientations at the

quarterplane (1mm below the surface of the strip). The main feature was the sharp decrease in intensity of $\sim \{112\} \langle 110 \rangle$ intensity when annealing was carried out above $\sim 800^\circ\text{C}$ (Fig.51). The intensity of $\sim \{554\} \langle 225 \rangle$ was a minimum when annealing was carried out between 800°C and 900°C . Fig.52 is a typical pole figure for the quarterplane of a sample batch annealed at 850°C (for comparison with Fig.48), showing that the minor $\sim \{110\} \langle 001 \rangle$ component became more prominent as a result of batch annealing.

Fig.56 shows the variation in intensity of the main ideal orientations with increasing annealing temperature, for the midplane. Annealing above 750°C caused a decrease in $\sim \{100\} \langle 011 \rangle$ and $\sim \{112\} \langle 110 \rangle$ intensities, accompanied by a simultaneous increase in $\sim \{554\} \langle 225 \rangle$ intensity, although $\sim \{100\} \langle 011 \rangle$ remained the most prominent component (Fig.53).

(b) 17% Cr, 0.3-0.4% Ti steels

There were no appreciable differences between hot rolling textures observed in 430 Ti steel containing 0.5% Ti and 430 Ti steels containing 0.4% Ti and 0.3% Ti (Figs.57 & 58).

4.2.3. Low Interstitial 409 (12 Cr, 0.5 Ti, 0.039 (C+N)) Steel

Textures of hot rolled and of hot-rolled and annealed 4mm thick strip are summarised in Table 10 and Figs.59-62. A strong $\sim \{110\} \langle 001 \rangle$ surface texture persisted to the quarterplane, at a depth of 1mm (Figs.59 & 62). Below this depth, it was replaced

progressively by constituents of the centre texture, mainly $\sim\{100\} \langle 011 \rangle$, $\sim\{112\} \langle 110 \rangle$ and minor $\sim\{554\} \langle 225 \rangle$ (Fig.60). Fig.61 shows that, for the midplane, annealing at 850°C caused a reduction in intensity of the $\sim\{100\} \langle 011 \rangle$ component and promoted a minor $\sim\{110\} \langle 001 \rangle$ component, but had little effect on the intensity of the $\sim\{112\} \langle 110 \rangle$ component.

4.2.4. Comparison between High Interstitial 430 and Low Interstitial 430 Ti and 409 Steels

Tables 8-10 show that the hot rolling textures of all three steels were similar, consisting of a centre texture, mainly $\sim\{100\} \langle 011 \rangle$ + minor $\sim\{112\} \langle 110 \rangle$ and $\sim\{554\} \langle 225 \rangle$ components, and a surface texture, mainly $\sim\{110\} \langle 001 \rangle$. The main differences were the considerably higher intensity of $\sim\{112\} \langle 110 \rangle$ and lower intensity of $\sim\{100\} \langle 011 \rangle$ in the centre textures of low-interstitial, Ti stabilised 17% Cr (430 Ti) and 12% Cr (409) steels compared with high interstitial 17% Cr (430) steel. High temperature annealing $\geq 1000^\circ\text{C}$ was necessary to reduce the intensity of the $\sim\{100\} \langle 011 \rangle$ component in 430 strip to the same order as its intensity in 430 Ti and 409 strip. Comparison of the two low-interstitial, Ti-stabilised steels shows that the $\sim\{110\} \langle 001 \rangle$ surface texture persisted to a greater depth in the 12% Cr steel (Figs.48,54,59,62) and that the $\sim\{112\} \langle 110 \rangle$ component of the centre texture was not so readily removed by annealing in the 12% Cr steel as it was in the 17% Cr steel (Figs.53,61).

4.3.1. High Interstitial 430 (~ 17 Cr, 0.077 (C+N))
Steel

The cold rolling textures observed in high interstitial 430 steel are summarised in Table 11, in terms of the main ideal orientations, and selected $\{200\}$ pole figures are presented in Figs.63-69. Variations in intensities of the main texture components have been plotted as functions of processing variables (Figs.70-74).

After low cold rolling reductions (50-60% RA), the texture was mainly $\sim\{110\} \langle 001 \rangle$ with a minor $\sim\{100\} \langle 011 \rangle$ component (Fig.63). With increasing cold reduction, the $\sim\{110\} \langle 001 \rangle$ orientation was replaced gradually by $\sim\{554\} \langle 225 \rangle / \sim\{111\} \langle 112 \rangle$, and there was an increase in the intensity of the $\sim\{100\} \langle 011 \rangle$ component (Figs.64-67). At 80% RA (Figs.65 & 66), $\sim\{110\} \langle 001 \rangle$ was only a minor component, and it was not detected at higher reductions (Figs.67-69). After very high cold rolling reductions (~ 95% RA), the texture consisted of a spread between three orientations : $\sim\{100\} \langle 011 \rangle$, $\sim\{111\} \langle 112 \rangle$ and $\sim\{112\} \langle 110 \rangle$, although $\{100\} \langle 011 \rangle$ was always the most prominent component (Figs.68 & 69).

Fig.70 shows the effect of increasing cold rolling strain (ϵ_1) on the intensities of the $\sim\{100\} \langle 011 \rangle$, $\sim\{111\} \langle 112 \rangle$ and $\sim\{112\} \langle 110 \rangle$ orientations. The intensity of $\sim\{100\} \langle 011 \rangle$ increased progressively with increasing cold reduction, and the intensity of $\sim\{111\} \langle 112 \rangle$ also increased

with cold rolling reduction, especially, of the $\sim \{112\} \langle 110 \rangle$ orientation became a significant component of the cold rolling texture only above 80% RA ($\epsilon_1 = 1.6$).

Figs.71-73 show the effects of increasing rapid pre-annealing temperature on the main components of the cold rolling texture. For cold reductions in the range 70-95% RA, the intensity of $\sim \{100\} \langle 011 \rangle$ was maximised by pre-annealing at 750-850°C (Fig.71), which minimised the intensity of $\sim \{111\} \langle 112 \rangle$ (Fig.72). The $\sim \{112\} \langle 110 \rangle$ component became important only at high cold rolling reductions, when it was maximised by pre-annealing between 750°C and 850-1000°C (Fig.73).

Batch annealing prior to cold rolling caused a slight reduction in $\sim \{100\} \langle 011 \rangle$ intensity compared with rapid pre-annealing at the same temperature (Fig.74), but otherwise had little effect on development of cold rolling textures (Figs.68 & 69).

4.3.2. Low Interstitial 430 Ti Steel

Cold rolling textures observed in 430 Ti steel are summarised, in terms of the main ideal orientations, in Tables 12-14, and Figs.75-86 are selected $\{200\}$ pole figures illustrating the observations. Variations in intensity of the main texture components are shown in Figs.87-91, as functions of cold rolling strain and pre-annealing temperature.

(a) $\sim 17\%$ Cr, 0.5 Ti, 0.029 (C+N) Steel

The cold rolling textures are summarised in Table 12. After low cold rolling reductions (50-60% RA),

the texture was mainly $\sim \{110\} \langle 001 \rangle$, with a minor $\sim \{100\} \langle 011 \rangle$ component and spread towards $\sim \{111\} \langle 112 \rangle$ (Fig.75). With increasing cold rolling reduction (Figs.76-80), $\{110\} \langle 001 \rangle$ was replaced by $\sim \{554\} \langle 225 \rangle / \sim \{111\} \langle 112 \rangle$, which became a major component at $\sim 80\%$ RA (Figs.78-80). After very high cold rolling reductions (90-95% RA) (Figs.81-84), the texture consisted of a spread between three orientations: $\sim \{100\} \langle 011 \rangle$, $\sim \{112\} \langle 110 \rangle$ and $\sim \{111\} \langle 112 \rangle$. Of these, $\sim \{100\} \langle 011 \rangle$ and $\sim \{112\} \langle 110 \rangle$ were approximately equal in intensity and stronger than $\sim \{111\} \langle 112 \rangle$ (Figs.82-84).

Fig.87 shows the effect of increasing cold rolling strain on the intensities of the main texture components. The intensities of both $\sim \{100\} \langle 011 \rangle$ and $\sim \{112\} \langle 110 \rangle$ increased with cold rolling reduction, although without pre-annealing $\sim \{100\} \langle 011 \rangle$ exhibited a slight drop in intensity above 90% RA ($\epsilon_1 = 2.3$), coinciding with a sharp rise in intensity of $\sim \{112\} \langle 110 \rangle$. A peak in $\sim \{111\} \langle 112 \rangle$ intensity occurred at $\sim 80\%$ RA ($\epsilon_1 = 1.6$), the effect being most pronounced with a high pre-annealing temperature (1000°C). The $\sim \{110\} \langle 001 \rangle$ intensity decreased rapidly with increasing cold rolling reduction above 60% RA ($\epsilon_1 = 0.9$).

The effects of increasing rapid annealing temperature prior to cold rolling are shown in Figs.88-90. For cold rolling reductions of 70-90% RA, the intensity of $\sim \{100\} \langle 011 \rangle$ decreased with increasing prior annealing temperature above the recrystallisation

temperature ($\sim 800^\circ\text{C}$). For very high reductions ($\sim 95\%$ RA), pre-annealing appeared to make little difference (Fig.88). A similar trend was observed for the $\sim \{112\} \langle 110 \rangle$ orientation (Fig.89), although in this instance the decrease in intensity with prior annealing $> 800^\circ\text{C}$ was most marked after cold rolling to 95% RA. By contrast the $\sim \{111\} \langle 112 \rangle$ intensity increased with prior annealing temperatures above $\sim 800^\circ\text{C}$, the sharpest rise occurring after cold rolling to 70-80% RA (Fig.90).

Fig.91 compares intensities of the main ideal orientations for samples batch annealed at 850°C and rapid annealed at 850°C prior to cold rolling. For reductions between 70% RA and 90% RA, batch pre-annealing resulted in a lower $\sim \{100\} \langle 011 \rangle$ intensity and delayed the development of the $\sim \{112\} \langle 110 \rangle$ component. Also the $\sim \{110\} \langle 001 \rangle$ component was more persistent (Fig.77). The intensity of $\sim \{111\} \langle 112 \rangle$ was higher at reductions of 80-90% RA ($\epsilon_1 = 1.6-2.3$) with batch pre-annealing.

(b) $\sim 17\%$ Cr, 0.3-0.4% Ti Steels

Cold rolling textures of low interstitial 430 Ti steels containing 0.3% and 0.4% Ti were similar to those of 0.5% Ti steel, with some subtle differences (Tables 13 & 14). The $\sim \{554\} \langle 225 \rangle / \sim \{111\} \langle 112 \rangle$ component developed at lower cold rolling reductions (60-70% RA) at the expense of the $\sim \{110\} \langle 001 \rangle$ texture (Fig.85). The $\sim \{112\} \langle 110 \rangle$ component was less prominent after high cold rolling reductions

($\sim 95\%$ RA) with lower titanium content steel
(Figs.84 & 86).

4.3.3. Low Interstitial 409 ($\sim 12\%$ Cr, 0.5 Ti, 0.039 (C+N)) Steel

Development of cold rolling textures in low interstitial 409 (12% Cr, 0.5 Ti) steel is summarised in Table 15 and Figs.92-95. These results show the same sequence of texture development as in low interstitial 430 Ti (17% Cr, 0.5 Ti) steel (see Table 12 & Fig.87). The main differences were greater persistence of the $\sim \{110\} \langle 001 \rangle$ texture, and delayed development of $\sim \{111\} \langle 112 \rangle$ and $\sim \{112\} \langle 110 \rangle$ components in the 12% Cr steel (Figs.92 & 93). However, after very high cold rolling reductions ($\sim 95\%$ RA), especially without pre-annealing (Fig.94), the texture of 409 ($\sim 12\%$ Cr, 0.5 Ti) steel was similar to that of low interstitial 430 Ti steel.

4.3.4. Comparison between High Interstitial (430) and Low Interstitial Ti-stabilised (430 Ti and 409) Steels

At low to moderate reductions (50-60% RA), the $\sim \{110\} \langle 001 \rangle$ texture component was present in all steels. With increasing cold reduction, $\sim \{110\} \langle 001 \rangle$ was replaced by $\sim \{554\} \langle 225 \rangle / \sim \{111\} \langle 112 \rangle$, and there was also an increase in intensity of the $\sim \{100\} \langle 011 \rangle$ component.

At high cold reductions ($\geq 90\%$ RA), $\sim \{112\} \langle 110 \rangle$ became a definite component of the texture. However, it was more prominent in 430 Ti and

409 steels than in 430 steel, for which the intensity of $\sim \{111\} \langle 112 \rangle$ continued to increase up to 95% RA, even without pre-annealing.

After very high cold rolling reductions (95% RA) the steels exhibited similar textures, consisting of a spread between three orientations: $\sim \{100\} \langle 011 \rangle$, $\sim \{112\} \langle 110 \rangle$ and $\sim \{111\} \langle 112 \rangle$. However, the most prominent orientations in the low-interstitial Ti-stabilised (430 Ti and 409) steels were $\sim \{100\} \langle 011 \rangle$ and $\sim \{112\} \langle 110 \rangle$, whereas $\sim \{100\} \langle 011 \rangle$ and $\sim \{111\} \langle 112 \rangle$ predominated in high interstitial 430 steel.

For high interstitial steel and for low-interstitial Ti-stabilised steel, a lower intensity of $\sim \{100\} \langle 011 \rangle$ in the hot rolled and annealed strip resulted in a correspondingly reduced intensity of this orientation in the cold rolling texture. Similarly, a higher intensity of the $\sim \{110\} \langle 001 \rangle$ component in the hot band made this orientation more persistent in the cold rolling texture, with a corresponding delay in development of the $\sim \{111\} \langle 112 \rangle$ and subsequently the $\sim \{112\} \langle 110 \rangle$ orientations.

4.4.1. High Interstitial 430 (~ 17 Cr, 0.077(C+N)) Steel

Primary recrystallisation textures are summarised in Tables 16-18, and Figs.96-115 are selected pole figures. Figs.116-120 show variations in intensities of the main texture components, as functions of processing variables.

The recrystallisation textures were complex. For reductions of ~ 50-80% RA (Figs.96-104), the most prominent components were generally $\sim \{114\} \langle uvw \rangle$ (especially $\sim \{114\} \langle 841 \rangle$) or $\sim \{100\} \langle uvw \rangle$ (especially $\sim \{100\} \langle 001 \rangle$) and also $\sim \{110\} \langle 001 \rangle$. Figs.100 and 101 show respectively $\{200\}$ and $\{222\}$ pole figures for 430 steel, to illustrate the presence of a $\sim \{100\} \langle 001 \rangle$ component. After high cold rolling reductions (90-95% RA), a spread between $\sim \{114\} \langle 841 \rangle$ and $\{223\} \langle 962 \rangle$ was usually developed (Figs.105-108). Certain combinations of high temperature ($\geq 1000^\circ\text{C}$) pre-annealing (especially batch pre-annealing at 1000°C), followed by cold rolling to high reductions (90-95% RA), promoted the development of a $\sim \{111\} \langle 110 \rangle$ component, on a spread between $\sim \{554\} \langle 225 \rangle$ and $\sim \{111\} \langle 110 \rangle$, but $\sim \{114\} \langle 841 \rangle$ was always present (Figs.109-112).

Effect of final annealing temperature

If annealing was carried out below $\sim 750^\circ\text{C}$, the texture was similar to the original cold rolling texture (Fig.113). For a common prior processing schedule, recrystallisation textures of specimens annealed in the range $\sim 800 - \sim 1000^\circ\text{C}$ were similar (Table 16), but

showed slight sharpening of the texture with increasing annealing temperature, especially between $\sim 800^{\circ}\text{C}$ and $\sim 900^{\circ}\text{C}$. This effect was most pronounced after high cold rolling reductions (Figs.106 & 114).

Effect of temperature of annealing prior to cold rolling

The effects of increasing (rapid) annealing temperature prior to cold rolling on the recrystallisation textures developed by both rapid and batch final annealing at 900°C are shown in Figs.116-120. For prior cold rolling reductions $\leq 80\%$ RA, textures developed by batch annealing at 900°C or by rapid annealing at 900°C were indistinguishable, although differences in behaviour were observed after very high reductions $\sim 90-95\%$ RA. The main features of Figs.116-120 are summarised as follows :-

(i) $\sim \{110\} \langle 001 \rangle$ (Fig.116)

For 50% RA, $\sim \{110\} \langle 001 \rangle$ was maximised when the annealing temperature prior to cold rolling was $\sim 850^{\circ}\text{C}$. For cold reductions between 60-80% RA, $\sim \{110\} \langle 001 \rangle$ was enhanced by annealing $\geq 1000^{\circ}\text{C}$ before cold rolling.

(ii) $\sim \{100\} \langle uvw \rangle$ (Fig.117)

Annealing before cold rolling had little effect on the strength of the $\sim \{100\} \langle uvw \rangle$ recrystallisation texture component for cold rolling reductions $\leq 80\%$ RA. After very high cold reductions ($\sim 95\%$ RA), $\sim \{100\} \langle uvw \rangle$ was maximised by annealing $\sim 850^{\circ}\text{C}$ before cold rolling, and by batch annealing after cold rolling.

(iii) $\sim \{114\} \langle 841 \rangle$ (Fig.118)

The intensity of $\sim \{114\} \langle 841 \rangle$ generally increased

with increasing cold rolling reduction above $\sim 70\%$ RA, except with batch annealing after cold rolling to 95% RA, when the intensity was very much lower than for rapid final annealing. Annealing before cold rolling had little effect on the $\sim \{114\} \langle 841 \rangle$ component unless the pre-annealing temperature was $> 1000^\circ\text{C}$, or after 95% cold reduction, when pre-annealing caused a decrease in its intensity.

(iv) $\sim \{223\} \langle 962 \rangle$ (Fig.119)

The $\sim \{223\} \langle 962 \rangle$ orientation became a significant component of the recrystallisation texture only after cold rolling reductions $\geq 90\%$ RA.

(v) $\sim \{111\} \langle 110 \rangle$ (Fig.120)

With rapid annealing after cold rolling, the $\sim \{111\} \langle 110 \rangle$ component was developed after high cold rolling reductions ($\sim 90\%$ RA), but only if the annealing temperature prior to cold rolling was $\geq 1000^\circ\text{C}$. Batch annealing after cold rolling allowed its development with lower pre-annealing temperatures ($\geq 850^\circ\text{C}$) (Fig.115)

4.4.2. Low Interstitial 430 Ti Steel

The primary recrystallisation textures are summarised in Tables 19-24, and Figs.121-152 are selected pole figures. Variations in intensities of the main texture components are shown in Figs.153-165, as functions of processing variables.

(a) $\sim 17\text{Cr}, 0.5 \text{Ti}, 0.029 (\text{C+N})$ Steel

After low cold rolling reductions (50-60% RA), the texture was mainly $\sim \{110\} \langle 001 \rangle$ (Figs.121 & 122).

Moderate to high cold reductions ($\sim 70-90\%$ RA) promoted mainly $\sim \{554\} \langle 225 \rangle$ textures (Figs.123-131 and Figs.133-136), and very high cold rolling reductions (95% RA or 90% RA if pre-annealing was omitted (Fig.132)) promoted mainly $\sim \{223\} \langle 962 \rangle$ (Figs.132,137-139). Prior processing had a pronounced effect on the recrystallisation textures, and the hot band condition was one of the most influential variables (Figs.127-131 and 132-136). The type of final annealing treatment, whether rapid or batch, was also important (Figs.139 & 140).

Effect of final annealing temperature

If annealing was carried out below $\sim 750^\circ\text{C}$, the texture (Fig.141) was similar to the original cold rolling texture. For cold rolling reductions $\leq 90\%$ RA, recrystallisation textures of samples annealed at 800°C were similar to those promoted by annealing at 900°C but reduced in intensity (compare Figs.142-144 with Figs.124, 128 & 134). However, with very high reductions (95% RA), provided that the hot rolled strip was pre-annealed before cold rolling, final annealing at 800°C (Fig.145) promoted a texture centred on $\sim \{554\} \langle 225 \rangle$ with a minor $\sim \{100\} \langle 011 \rangle$ component, instead of the sharp $\sim \{223\} \langle 962 \rangle$ texture developed by final annealing at 900°C (Fig.146).

Raising the final annealing temperature from 900°C to 950°C caused pronounced grain growth (Table 5) and enhanced the dominant texture component developed after a given processing schedule; i.e., $\sim \{554\} \langle 225 \rangle$ was enhanced for cold rolling reductions $\leq 80/90\%$ RA, whereas $\sim \{223\} \langle 962 \rangle$ was enhanced for very high cold.

rolling reductions ($\sim 95\%$ RA) (Figs.146 & 147).

Effect of cold rolling strain

Figs.153-156 show the effects of cold rolling strain on the intensities of the main recrystallisation texture orientations, for three different conditions prior to cold rolling and for rapid and batch final annealing at 900°C :-

(i) $\sim \{110\} \langle 001 \rangle$ (Fig.153)

The intensity of the $\sim \{110\} \langle 001 \rangle$ component decreased with increasing prior cold rolling reduction above $\sim 60\%$ RA ($\epsilon_1 = 0.9$). It was not present as a true component for reductions $> 70\%$ RA unless pre-annealing was carried out at $\sim 1000^{\circ}\text{C}$, when it persisted for reductions up to $\sim 80\%$ RA ($\epsilon_1 = 1.6$).

(ii) $\sim \{554\} \langle 225 \rangle$ (Fig.154)

The intensity of the $\{554\} \langle 225 \rangle$ component increased with prior cold reduction, to a maximum at $\sim 80-90\%$ RA ($\epsilon_1 = 1.6-2.3$). The maximum $\sim \{554\} \langle 225 \rangle$ intensity was slightly lower after batch final annealing than after rapid final annealing, unless the pre-annealing treatment before cold rolling was omitted.

(iii) $\sim \{223\} \langle 962 \rangle$ (Fig.155)

The $\{223\} \langle 962 \rangle$ component was significant after cold rolling reductions $\geq 80\%$ RA ($\epsilon_1 = 1.6$) and, in general, the intensity of this component increased with increasing cold rolling strain. The highest intensity was given by rapid final annealing, either without pre-annealing or with rapid pre-annealing $\leq 850^{\circ}\text{C}$. The maximum

$\sim \{223\} \langle 962 \rangle$ intensity was generally lower after batch final annealing than after rapid final annealing,

unless pre-annealing before cold rolling was at 1000°C.

(iv) $\sim \{100\} \langle uvw \rangle$ (Fig.156)

The $\sim \{100\} \langle uvw \rangle$ orientation was a minor component of the recrystallisation textures, and did not generally show much variation with cold rolling strain. It was most prominent when pre-annealing was omitted.

Effect of Pre-annealing Temperature

Figs.157 & 158 show the effect of increasing rapid pre-annealing temperature on the intensities of the $\sim \{554\} \langle 225 \rangle$ and $\sim \{100\} \langle uvw \rangle$ components developed by both batch and rapid final annealing at 900°C. For cold rolling reductions $\geq 80\%$ RA, the intensity of $\sim \{554\} \langle 225 \rangle$ (Fig.157) generally increased with increasing pre-annealing temperature above $\sim 750^\circ\text{C}$. Rapid final annealing promoted maximum intensity after pre-annealing at $\sim 850^\circ\text{C}$ and cold-rolling to 80-90% RA. Fig.158 shows that the intensity of $\sim \{100\} \langle uvw \rangle$ decreased with increasing pre-annealing temperature.

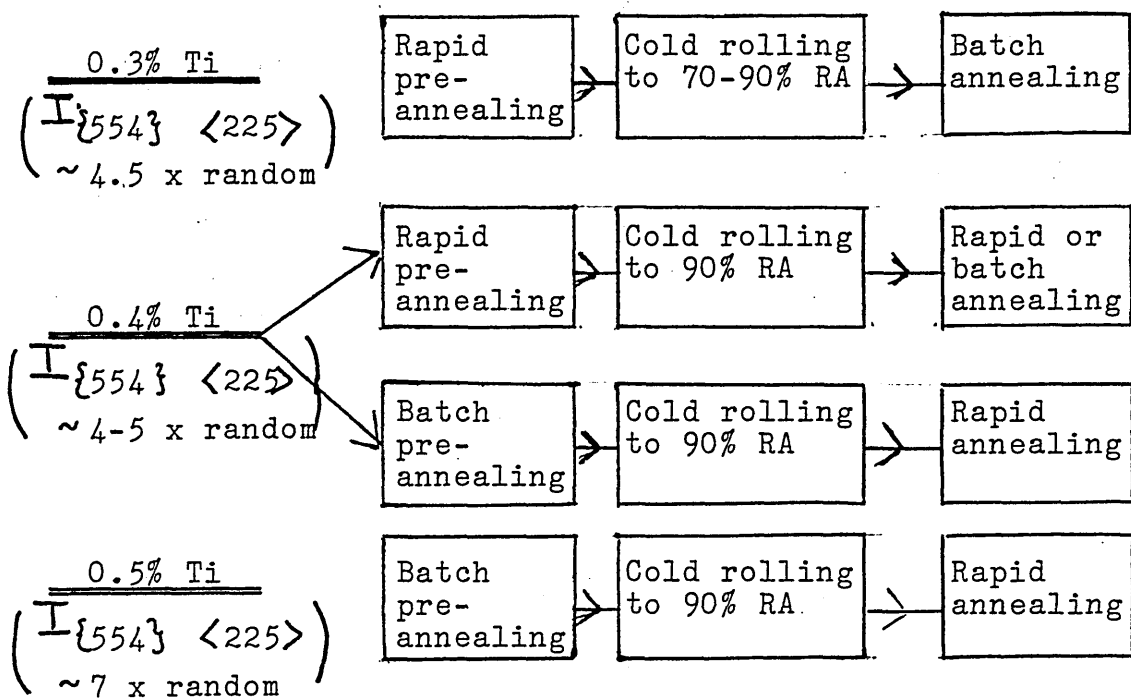
Fig.159 compares intensities of the main orientations in the recrystallisation textures of samples which had been batch pre-annealed at 850°C and rapid pre-annealed at 850°C, as a function of cold rolling strain. Both rapid and batch final annealing treatments at 900°C are considered. The main differences are in the $\sim \{110\} \langle 001 \rangle$ and $\sim \{554\} \langle 225 \rangle$ components. With low cold rolling reductions (50-60% RA), $\sim \{110\} \langle 001 \rangle$ was stronger with batch pre-annealing and $\sim \{554\} \langle 225 \rangle$ was correspondingly less prominent. At high reductions (80-90% RA), the $\sim \{554\} \langle 225 \rangle$

orientation had a higher maximum intensity with batch pre-annealing. For both pre-annealing treatments, higher $\sim \{554\} \langle 225 \rangle$ intensities were developed by rapid final annealing than by batch final annealing.

(b) $\sim 17\%$ Cr, 0.3-0.4% Ti Steels

Recrystallisation textures observed in 430 Ti steels containing 0.3 and 0.4% Ti are summarised in Tables 21-24, Figs.148-152 and Figs.160-165. Comparison of these results with those for $\sim 17\%$ Cr, 0.5% Ti steel demonstrates the effect of titanium content in the range 0.3-0.5%.

The sequence of texture development following increasing cold reduction corresponded with that observed in 0.5% Ti steel; i.e., $\sim \{110\} \langle 001 \rangle \Rightarrow \sim \{554\} \langle 225 \rangle \Rightarrow \sim \{223\} \langle 962 \rangle$ (Figs.148-152). Figs.159,160 and 161 show respectively the variations in intensity of the main texture components with prior cold rolling reduction for 0.5% Ti, 0.4% Ti and 0.3% Ti steels. These graphs show that the maximum intensity of the $\sim \{554\} \langle 225 \rangle$ orientation decreased with decreasing titanium content, and that the following conditions maximised $\sim \{554\} \langle 225 \rangle$ intensity :-



Figs.162-165 show the variation in intensity of $\sim \{100\} \langle uvw \rangle$ and $\sim \{554\} \langle 225 \rangle$ orientations as a function of calculated percentage of titanium in solid solution ($[Ti]_{ss}$), for different processing schedules. The $\sim \{100\} \langle uvw \rangle$ component varied only slightly. For cold rolling reductions $\leq 70\%$ RA, low $[Ti]_{ss}$ and batch final annealing promoted highest $\sim \{554\} \langle 225 \rangle$ intensities (Figs.164 & 165). For 80-90% RA, higher $[Ti]_{ss}$ contents maximised $\sim \{554\} \langle 225 \rangle$ intensity (Figs.164 & 165), especially with rapid final annealing (Fig.164). For cold rolling reductions $> 90\%$ RA, the intensity of the $\sim \{554\} \langle 225 \rangle$ orientation decreased in favour of the $\sim \{223\} \langle 962 \rangle$ orientation (Fig.152).

4.4.3. Low Interstitial 409 (~12 Cr, 0.46Ti, 0.039 (C+N)) Steel

Primary recrystallisation textures developed in 409 steel (for rapid final annealing at 900°C) are summarised in Table 25, and Figs.166-174 are selected {200} pole figures. Fig.175 shows variations in intensities of the main texture components as functions of prior cold rolling strain.

Fig.166 shows that, for specimens annealed below ~ 800°C, the texture was similar to the original cold rolling texture. For rapid final annealing at 900°C, the sequence of texture development with increasing prior cold reduction was the same as for ~17% Cr, titanium stabilised (430 Ti) steel; i.e., $\sim\{110\} \langle 001 \rangle \Rightarrow \sim\{554\} \langle 225 \rangle \Rightarrow \sim\{223\} \langle 962 \rangle$ (Figs.167-174). However, with high cold rolling reductions ($\geq 90\%$ RA), the $\sim\{223\} \langle 962 \rangle$ texture was less developed in 409 steel than in 430 Ti steel (compare Figs.172 & 137, 173 & 146, 174 & 139).

Batch pre-annealing of 409 steel at 850°C promoted higher $\sim\{554\} \langle 225 \rangle$ intensities than rapid pre-annealing at 850°C (Figs.169,170 & 175). Rapid pre-annealing at 1000°C, cold rolling to 90-95% RA and rapid final annealing at 900°C promoted a $\sim\{111\} \langle uvw \rangle$ texture (Figs.171 & 174), with intensity peaks near $\sim\{554\} \langle 225 \rangle$.

Fig. 175 shows the variation in intensity of the main orientations with prior cold rolling strain, for different hot band conditions and rapid final annealing at 900°C. The main features are summarised as follows :-

(i) $\sim \{100\} \langle uvw \rangle$

Omission of the pre-annealing treatment resulted in a higher $\sim \{100\} \langle uvw \rangle$ intensity in the recrystallisation texture. Otherwise variations in $\sim \{100\} \langle uvw \rangle$ intensity were small.

(ii) $\sim \{110\} \langle 001 \rangle$

The intensity of $\sim \{110\} \langle 001 \rangle$ decreased with increasing cold reduction, although it became more persistent as the temperature of pre-annealing was increased.

(iii) $\sim \{554\} \langle 225 \rangle$

Without pre-annealing, the maximum intensity of the $\sim \{554\} \langle 225 \rangle$ orientation was ~ 2 x random. This was achieved with reductions of $\sim 80-90\%$ RA ($\epsilon_1 = 1.6-2.3$) and corresponded with maximum $\sim \{100\} \langle 011 \rangle$ intensity (2.5 x random).

The general effect of pre-annealing was to increase its intensity. Maximum $\sim \{554\} \langle 225 \rangle$ intensity (~ 6 x random) was achieved by batch pre-annealing at 850°C and cold rolling reductions $\sim 90\%$ RA ($\epsilon_1 = 2.3$).

(iv) $\sim \{223\} \langle 962 \rangle$

This component developed only after cold rolling reductions $> 80\%$ RA ($\epsilon_1 = 1.6$), generally increasing with increasing cold reduction. It was most prominent when pre-annealing was omitted (Figs.172-174).

4.4.4. Comparison between High Interstitial ~17% Cr, Steel (430) and Low Interstitial, Titanium Stabilised, 17% Cr, Steel (430 Ti)

The primary recrystallisation textures of high interstitial 430 and low interstitial, 430 Ti steels were very different. A major $\sim \{111\} \langle uvw \rangle$ texture did not occur in high interstitial 430 steel, whereas a strong $\sim \{554\} \langle 225 \rangle$ (near $\sim \{111\} \langle 112 \rangle$) recrystallisation texture occurred in 430 Ti steel. Textures developed in high interstitial 430 steel were more complex, and not as strong as textures developed in 430 Ti steel. Processing variables, especially hot band condition, had a more pronounced effect on 430 Ti than on 430 steel.

4.5. UNIAXIAL TENSILE DATA

4.5.1. High Interstitial 17% Cr, (430) Steel

Strain ratios (r-values) and work-hardening coefficients (n-values) for selected cold rolled and annealed samples are listed in Tables 26 and 27.

r-values (Table 26)

The r_0 -values were low (always < 1.0) but generally increased with increasing pre-annealing temperature.

The effects of cold rolling reduction and pre-annealing temperature on the relative magnitudes of r_{45} and r_{90} -values are summarised as follows :-

70% RA; All pre-annealing treatments :- $r_{90} > r_{45}$
(Δr positive)

80% RA; (i) Without pre-annealing or
with pre-annealing 850°C :- $r_{45} > r_{90}$
(Δr negative)

(ii) Pre-annealing $\geq 1000^\circ\text{C}$:- $r_{90} > r_{45}$
(Δr positive)

90% RA; (i) Without pre-annealing or
with pre-annealing
 $\leq 1000^\circ\text{C}$:- $r_{45} > r_{90}$
(Δr negative)

(ii) Pre-annealing 1200°C :- $r_{90} > r_{45}$
(Δr positive)

Values of \bar{r} were generally low, the highest values being given by pre-annealing at 1000°C + cold rolling to 80-90%RA + rapid final annealing at 900°C .

n-values (Table 27)

Values of \bar{n} were all in the range 0.22-0.26. No systematic effects of processing variables were observed.

4.5.2. Low Interstitial 17% Cr, Ti-stabilised (430 Ti) Steel

Observed r -values and n -values, for selected cold rolled and annealed samples, are listed in Table 28. Shortage of material restricted the amount of 100mm wide strip that could be produced, and so Tables 29 & 30 show additional results, as r_0 only, for specimens from 25mm wide cold rolled and annealed 430 Ti strip of varying titanium contents (0.3-0.5% Ti).

(a) \bar{r} and \bar{n} values for 0.5% Ti Steel (Table 28)

Values of r_0 , r_{45} , r_{90} and \bar{r} were generally much higher than for 430 steel. Average strain ratio (\bar{r}) measurements ranged from 1.98-2.42, and a combination of high \bar{r} and relatively low $|\Delta r|$ was achieved by annealing (rapid or batch) at 850°C + cold rolling to 80-90%RA + rapid final annealing at 900°C.

Values of \bar{n} ranged from 0.23-0.25, similar to 430 steel.

(b) r_0 -values for 0.3-0.5% Ti Steels

(i) Rapid final anneal at 900°C (heating rate $\sim 5000^\circ\text{C hr}^{-1}$, AC) (Table 29)

With moderate (60-70% RA) cold rolling reductions, lower titanium-content steels showed higher r_0 -values after rapid final annealing, whereas, with reductions of 80-90% RA, highest r_0 -values were realised for 0.5% Ti steel. Batch pre-annealing generally resulted in higher

r_0 -values than rapid pre-annealing, except for the 0.3% Ti steel where the effect was reversed. For all cold rolling reductions, omission of the pre-annealing treatment resulted in the lowest r_0 -values.

(ii) Batch final anneal at 900°C (heating rate = 50°C hr⁻¹, FC) (Table 30)

Values of r_0 were generally lower than with rapid final annealing, especially with high cold rolling reductions. Highest r_0 -values were given for 0.3% Ti steel with rapid pre-annealing + cold rolling to ~80% RA. The r_0 -values were lowest when pre-annealing was omitted.

4.5.3. Low Interstitial, ~ 12% Cr, Ti-stabilised (409) Steel

Observed r_0 -values and n-values for cold rolled and annealed 409 steel are presented in Table 31. The r_0 , r_{45} , r_{90} and \bar{r} -values were generally higher than for 430 steel, but lower than 430 Ti steel. The \bar{r} -values increased with increasing cold rolling reduction. Batch pre-annealing promoted higher r_0 and r_{90} values, whereas rapid pre-annealing maximised r_{45} -values. Consequently, similar \bar{r} -values were observed with rapid and batch pre-annealing followed by cold rolling to a common reduction.

Average work hardening coefficients were similar to those measured for 430 and 430 Ti steels, varying between 0.24 and 0.26.

4.5.4. Relationships between r-values and Texture Parameters

The r_o and \bar{r} values for 430, 430 Ti, and 409 steels were plotted against various combinations of texture parameters ($P_{\{hkl\}}$) determined by X-ray diffractometry. These relationships were quantified by linear regression analysis, which shows the highest correlation for the following :-

r_o (Fig.176)

$$(i) \quad r_o = 0.114 \left[P_{\{111\}} / P_{\{100\}} \right] + 0.711$$

(Correlation coefficient = 0.761)

$$(ii) \quad r_o = 0.265 \left[P_{\{111\}} + P_{\{332\}} \right] + 0.372$$

(Correlation coefficient = 0.749)

r_{45} (Fig.177)

$$r_{45} = 0.013 \left[P_{\{211\}} / (P_{\{321\}} + P_{\{110\}}) \right] + 1.078$$

(Correlation coefficient = 0.730)

r_{90} (Fig.178)

$$(i) \quad r_{90} = 0.294 \left[P_{\{111\}} + P_{\{332\}} \right] + 0.615$$

(Correlation coefficient = 0.818)

$$(ii) \quad r_{90} = 0.123 \left[P_{\{111\}} / P_{\{100\}} \right] + 1.008$$

(Correlation coefficient = 0.804)

\bar{r} (Fig.179)

$$(i) \quad \bar{r} = 0.334 P_{\{111\}} + 0.620$$

(Correlation coefficient = 0.787)

$$(ii) \quad \bar{r} = 0.243 \left[P_{\{111\}} + P_{\{332\}} \right] + 0.658$$

(Correlation coefficient = 0.785)

Δr

No simple relationship was found between Δr and combinations of texture parameters.

4.6. ROPING TESTS

Roping tests, comprising visual examination and Talysurf measurements, were conducted on tensile specimens used for measurement of r_o -values. For comparison, samples of cold-rolled and annealed 430 sheet, representing typical and severe roping in commercial supply, were also examined. The visual appearance of severe roping is illustrated by Fig.180, and a typical example of roping in a ferritic stainless steel sink is shown in Fig.181.

Talysurf measurements of samples representing severe roping (Fig.182) and typical roping (Fig.183) indicated maximum peak-to-valley heights of $\sim 40 \mu\text{m}$ and $\sim 12 \mu\text{m}$ respectively. By contrast, for the samples of laboratory cold-rolled and annealed 430, 430 Ti or 409 steels under investigation, the maximum peak-to-valley height was $\sim 8 \mu\text{m}$, and roping was not apparent visually.

4.7.1. Swift Cupping Test

(a) Limiting Drawing Ratios

The modified, two-blank Swift Test was used to assess critical blank diameters (D_c) and limiting drawing ratios (LDR) of selected samples (Table 32). In general, low interstitial Ti-stabilised 430 Ti (~ 17 Cr) and 409 (~ 12 Cr) steels showed higher LDRs than high interstitial 430 (~ 17 Cr, steel, especially with cold rolling reductions $\sim 80\%$ RA.

(b) Earing Profiles

For those samples with sufficient material available, additional 100mm diameter blanks were drawn to completion without secondary clamping, for comparison of earing profiles. Positions of ears with respect to the rolling direction were noted, and percentage earing was calculated (Table 33). Typical earing profiles are shown on drawn cups in Figs.184 and 185, and graphically in Fig.186.

Because of the very limited availability of material, it was not possible to check these tests. For this reason, and the practical difficulty of varying specimen thickness, the results must be regarded as indicative of trends in earing behaviour only.

High interstitial ~ 17 Cr (430) steel cups developed ears close to (or within $\sim 15^\circ$ of) 0° and 90° . By contrast, earing in the 430 Ti and 409 samples occurred mainly at $\sim 0^\circ$ and $\sim 60-80^\circ$. The earing profiles of cups

drawn from blanks <~lmm thick were sometimes non-uniform (probably due to slight inaccuracies in **positioning** of the blank or uneven die clearance), so that the calculated earing percentages are of limited value. Minimum cup wall heights (which indicate the useful cup height for a given blank diameter), were also recorded, and these results showed only small variations (Table 33).

4.7.2. Erichsen Stretch-Forming Tests

Results of Erichsen tests are recorded in Table 34. The results indicate a general increase of punch penetration to fracture with increasing sheet thickness. Samples of the same thickness exhibited similar stretch-forming properties, irrespective of composition and pre-annealing treatment. This is in agreement with the previous observation that composition and processing schedule had no systematic effect on \bar{n} -values, which are also used to indicate stretch-formability.

4.7.3. Relationship between Limiting Drawing Ratio and Strain Ratios

Limiting Drawing Ratios were plotted against tensile strain ratio measurements for 430, 430 Ti and 409 steels. LDRs tended to increase with \bar{r} -value (Fig.187), and the following relationship was determined by linear regression analysis :-

$$\text{LDR} = 0.166 \bar{r} + 1.994.$$

$$(\text{Correlation coefficient} = 0.50)$$

The low correlation coefficient may be due to the use of non-constant blank thicknesses in the Swift tests (different final thicknesses from different cold-rolling reductions and different starting thicknesses).

5.1. TEXTURES OF HOT-ROLLED OR HOT-ROLLED AND PRE-ANNEALED STRIP

5.1.1. Hot-rolling Textures

The centre textures of hot rolled 430, 430 Ti and 409 steels are typical of cold-rolled bcc metals, and the deformed microstructure observed at the centre of the hot-rolled strip indicates that there had been some deformation below the dynamic recrystallisation temperature in the later stages of hot rolling. However, the relatively low hardness and difficulty of effecting complete recrystallisation of the centre, especially in 409 steel which had been finished at a slightly higher temperature (Table 3B), suggest that substantial recovery had occurred.

By contrast, the $\sim\{110\} \langle 001 \rangle$ surface texture observed in all the steels is a bcc recrystallisation texture. (3,7) Its presence suggests that recrystallisation of the surface had occurred at a late stage during hot rolling, and this is supported by metallographic evidence of smaller, more equiaxed grains at the surfaces of hot-rolled strip. Roll surface friction (causing a temperature rise at the surface of the strip during hot rolling) and/or heavier effective deformation in the surface layers (resulting in an increase in the driving force for recrystallisation, i.e. lowering of the dynamic recrystallisation temperature at the surface) are possible reasons for the observed

differences between surface and centre. Similar effects, i.e. $\sim \{110\} \langle 001 \rangle$ surface textures and a recrystallised surface microstructure with a deformed centre, have been reported for other low carbon steels rolled between $\sim 800^\circ\text{C}$ and 900°C , although rolling below $\sim 800^\circ\text{C}$ resulted in 'cold rolled' structures throughout. (119,123) Dickson and Cooke (122) also reported a strong $\sim \{110\} \langle 001 \rangle$ surface texture and a similar through-thickness variation in texture in hot-rolled, 12% Cr, Ti-stabilised ferritic stainless steel.

Texture components observed at the centre of hot rolled strip were mainly $\sim \{100\} \langle 011 \rangle$ plus minor $\sim \{112\} \langle 110 \rangle$ and $\sim \{554\} \langle 225 \rangle$ components, with $\sim \{112\} \langle 110 \rangle$ much more prominent in the Ti-stabilised steel. Other authors (12,50,119,123) have recorded mainly $\sim \{100\} \langle uvw \rangle$ hot rolling textures in ordinary low carbon steels and in ferritic stainless steels. The occurrence of a $\sim \{112\} \langle 110 \rangle$ hot rolling texture in Nb-stabilised and Ti-stabilised steels has also been reported previously. (51,122,124) Gillanders, Dasarathay and Hudd (124) suggested that the $\sim \{112\} \langle 110 \rangle$ texture, observed in Nb-stabilised, low carbon steel, originated from an fcc rolling texture developing in unrecrystallised austenite at the hot rolling temperature, and transforming to $\sim \{112\} \langle 110 \rangle$ with the transformation from austenite to ferrite. However, the present work shows that the $\sim \{112\} \langle 110 \rangle$ texture is developed in Ti-stabilised 17% Cr steel, which is fully ferritic at all temperatures. It is suggested that, during hot rolling of Ti-stabilised steel, unconstrained.

deformation below the dynamic recrystallisation

temperature promotes relatively rapid development of

$\sim \{112\} \langle 110 \rangle$, which is a stable bcc cold rolling texture, (3,12,32,34) whereas in the high interstitial 430 steel (without titanium), irregular flow, resulting from the presence of austenite or a high volume fraction of carbides, might suppress development of a strong

$\sim \{112\} \langle 110 \rangle$ texture component.

5.1.2. Effect of Pre-Annealing

The pre-annealing of hot rolled strip enhances the $\sim \{110\} \langle 001 \rangle$ component slightly, whereas components typical of cold rolling textures, especially $\sim \{112\} \langle 110 \rangle$ decrease in intensity. Batch pre-annealing promotes higher $\sim \{110\} \langle 001 \rangle$ intensities near the centre than rapid annealing at the same temperature. This is attributed to subgrain growth during slow heating for batch annealing, which should favour $\sim \{110\} \langle 001 \rangle$ nucleation. (47,49)

The $\sim \{110\} \langle 001 \rangle$ surface texture persists to a greater depth in 409 (12 Cr, 0.5 Ti) steel than in 430 and 430 Ti steels, and the $\sim \{112\} \langle 110 \rangle$ component of the centre texture is less readily removed by annealing. This may be due to its slightly higher hot-rolling finishing temperature (Table 3B), which would allow more recrystallisation near the surface during the final stages of rolling, but would also reduce the driving force for subsequent recrystallisation of the centre by allowing more recovery. Hardness-recrystallisation measurements for 409 hot-rolled strip (Fig.23) confirm that full recrystallisation during

annealing requires temperatures $\geq 850^\circ\text{C}$.

5.2. COLD ROLLING TEXTURES

After high cold rolling reductions, similar cold rolling textures are developed in high interstitial 430 steel and low interstitial 430 Ti and 409 steels, comprising a spread between three orientations:

$$\sim \{100\} \langle 011 \rangle, \sim \{111\} \langle 112 \rangle \text{ and } \sim \{112\} \langle 110 \rangle.$$

Figures 188 and 189 show that Richards and Ormay's ⁽¹²⁾ description of bcc rolling textures (two partial $\langle 110 \rangle$ fibre textures, one parallel with RD and one inclined at 60° to RD) fits the observed spread better than Barrett and Levenson's ⁽¹¹⁾ description (partial $\langle 110 \rangle // \text{RD}$ and partial $\langle 111 \rangle // \text{ND}$), although neither description fits the observed spread exactly.

5.2.1. Slip rotations during cold rolling

Most workers analysing cold rolling texture development have considered a random starting texture. However, strong hot-rolling textures were present in the commercial materials examined, and similar hot rolling textures have been reported previously in a ferritic stainless steel, ⁽¹²²⁾ and also in other low-carbon steels which had been rolled $\leq 900^\circ\text{C}$. ^(12,50,51,120,123-125)

A limited analysis of slip rotations has, therefore, been carried out, assuming a starting texture containing

$$\sim \{110\} \langle 001 \rangle, \sim \{111\} \langle 112 \rangle, \sim \{112\} \langle 110 \rangle$$

and $\sim \{100\} \langle 011 \rangle$ components. Slip is considered to occur when the critical resolved shear stress (τ_c) is reached on one or more systems, assuming either :-

- (i) $\tau_c \{110\} = \tau_c \{112\} = \tau_c \{123\}$ (EQUAL τ_c), or
(ii) $\tau_c \{110\} : \tau_c \{112\} : \tau_c \{123\} = 1:1.03:1.05$ (UNEQUAL τ_c)

Details of equations used for predicting the operative slip systems (which were programmed for the Apple IIe microcomputer using Applesoft Basic language) are given in Appendix A. Table 35 gives operative slip systems predicted for selected orientations.

This method of predicting slip rotations is similar to the one used by Dillamore and Roberts,⁽³²⁾ who considered $\{110\} \langle 111 \rangle$ slip only, and later by Kamijo⁽³⁴⁾ who assumed that the values of τ_c on $\{110\}$, $\{112\}$ and $\{123\}$ planes respectively were in the ratio 1:1.05:1.05.

The criterion of stability of an "end" orientation depends not only on symmetry, but also on whether slip rotations will tend to return the material to this orientation if fluctuations of the stress axes cause it to be displaced.⁽³²⁾ Dillamore and Roberts⁽³²⁾ suggested that the most likely displacements of the stress axes during rolling are as follows :-

(A) Both compression axis and tensile axis are displaced along the great circle joining them.

(B) The tensile axis is displaced around the great circle 90° away from the compression axis.

These criteria have been used to test the stability of various orientations. The behaviour of the various starting texture components during cold rolling is predicted as follows :-

(i) (011) [$\bar{1}00$]

Due to the symmetrical disposition of slip systems (Table 35) the (011) [$\bar{1}00$] orientation is stable (assuming either equal τ_c or unequal τ_c) provided that no fluctuations of the stress axes occur.

Displacement (A) Slip on the (211) [$\bar{1}11$] system would cause rotation to (111) [$\bar{2}11$] along the [$0\bar{1}1$] great circle, i.e. via (144) [$\bar{8}11$], (122) [$\bar{4}11$] and (455) [$\bar{5}22$] (Fig.190), which was also predicted by Kamijo (34). Fig.191 shows that the texture spread, after moderate ($\sim 70\%$ RA) cold rolling reductions from a strong $\sim \{110\} \langle 001 \rangle$ starting texture, is in agreement with this analysis.

Displacement (B) Conjugate slip on (211) [$\bar{1}11$] + ($\bar{2}11$) [$\bar{1}\bar{1}\bar{1}$] systems, or (321) [$\bar{1}11$] + ($\bar{3}12$) [$\bar{1}\bar{1}\bar{1}$] systems, or (110) [$\bar{1}11$] + ($\bar{1}01$) [$\bar{1}\bar{1}\bar{1}$] systems is predicted, depending upon the instantaneous position of the tensile axis and the assumed ratio of τ_c . (Table 35) The ND would remain at [011], due to the symmetrical disposition of slip planes, and slip rotations would return the RD to [$\bar{1}00$]. The $\{011\} \langle 100 \rangle$ component should, therefore, be stable with respect to displacement (B).

(ii) (111) [$\bar{1}\bar{1}2$]

The (111) [$\bar{1}\bar{1}2$] orientation is not stable, (33) but this analysis suggests that it would be removed only with difficulty. For both equal and unequal τ_c , (112) [$\bar{1}\bar{1}1$] slip is predicted, causing a rotation towards the (112) [$\bar{1}\bar{1}1$] orientation, along the [$\bar{1}10$] great circle (Fig.192). However, for displacements of

$\sim 8^\circ$ - 14° , (i.e. between $\sim (334) [\bar{2}\bar{2}3]$ and $(335) [\bar{5}\bar{5}6]$), slip on $(110) [\bar{1}11] + (110) [1\bar{1}1]$ systems would tend to return the material towards $(111) [\bar{1}\bar{1}2]$ (Table 35 and Fig.192). An oscillating spread of orientations between $\sim (111) [\bar{1}\bar{1}2]$ and $\sim (334) [\bar{2}\bar{2}3]$ would, therefore, be expected to remain, in the absence of fluctuations of the stress axes.

Displacement (A) A large (A)-type displacement of the stress axes, would however, remove the $(111) [\bar{1}\bar{1}2]$ orientation. If the ND was displaced to $[112]$ and the RD to $[\bar{1}\bar{1}1]$ (i.e. a $\sim 19\frac{1}{2}^\circ$ displacement), slip on the $(\bar{1}\bar{1}2) [\bar{1}\bar{1}\bar{1}]$ system would cause rotation towards the $(001) [\bar{1}\bar{1}0]$ orientation. (Table 35 & Fig.192)

Displacement (B) Assuming unequal τ_c , conjugate slip on $(110) [\bar{1}11] + (011) [\bar{1}\bar{1}1]$ systems would cause rotation of the lattice to $(121) [\bar{1}01]$, for displacements of the tensile axis $\geq \sim 10^\circ$ (Table 35 & Fig.192).

Kamijo ⁽³⁴⁾ suggested that since the resolved shear stresses on the $(101) [\bar{1}\bar{1}1]$, $(011) [\bar{1}\bar{1}1]$, $(011) [1\bar{1}1]$ and $(110) [\bar{1}11]$ systems are equal for the $(111) [\bar{1}\bar{1}2]$ orientation (although lower than the shear stress on $(112) [\bar{1}\bar{1}1]$), co-operative slip on either $(101) [\bar{1}\bar{1}1] + (110) [1\bar{1}1]$ systems or $(011) [\bar{1}\bar{1}1] + (110) [\bar{1}11]$ systems would be expected, causing rotation of a $(111) [\bar{1}\bar{1}2]$ crystal to either $(211) [0\bar{1}1]$ or $(121) [\bar{1}01]$. Kamijo ⁽³⁴⁾ described this re-orientation in terms of a rotation about a $\langle 110 \rangle$ axis $\sim 60^\circ$ from RD, as used by Richards and Ormay ⁽¹²⁾ in their description of bcc rolling textures. Fig.193 is a $\{110\}$ pole figure showing that

the $\{111\}$ $\langle 112 \rangle$ (or more precisely $\{554\}$ $\langle 225 \rangle$), $\{223\}$ $\langle 962 \rangle$ and $\{112\}$ $\langle 110 \rangle$ ideal orientations share a common $\langle 110 \rangle$ axis $\sim 30^\circ$ from ND (i.e. $\sim 60^\circ$ from the RD).

(iii) (001) $[\bar{1}\bar{1}0]$

For both equal and unequal γ_c , the operative slip systems are predicted as (112) $[\bar{1}\bar{1}1]$ and $(\bar{1}\bar{1}2)$ $[\bar{1}\bar{1}\bar{1}]$, whose symmetrical disposition indicates that (001) $[\bar{1}\bar{1}0]$ is a stable orientation (Table 35 and Fig.194). Very large A-type displacements ($> 35^\circ$) of the stress axes are required to prevent slip rotations returning the material to the (001) $[\bar{1}\bar{1}0]$ orientation, which is also stable against B-type displacements of the tensile axis (Table 35 and Fig.194).

However, should the compressive axis be displaced along the $[\bar{1}\bar{1}0]$ great circle, towards $[\bar{1}\bar{1}1]$, by $> 8^\circ$ for equal γ_c or $> 20^\circ$ for unequal γ_c , slip rotations would promote $(1\bar{1}6)$ $[\bar{1}\bar{1}0]$ or $(1\bar{1}2)$ $[\bar{1}\bar{1}0]$ orientations respectively (Table 35 and Fig.194).

(iv) (112) $[\bar{1}\bar{1}0]$

If equal γ_c is assumed, (112) $[\bar{1}\bar{1}0]$ is not predicted as a stable end orientation, and slip on $(\bar{1}23)$ $[\bar{1}\bar{1}1]$ + $(2\bar{1}3)$ $[\bar{1}\bar{1}\bar{1}]$ would cause the ND to rotate to $[\bar{1}\bar{1}6]$, resulting in development of a (116) $[\bar{1}\bar{1}0]$ orientation (Table 35 and Fig.195).

For unequal γ_c , the operative slip systems are (011) $[\bar{1}\bar{1}1]$ + (101) $[\bar{1}\bar{1}\bar{1}]$, and (112) $[\bar{1}\bar{1}0]$ is predicted as an end orientation. Slip rotations return the material to (112) $[\bar{1}\bar{1}0]$ after an 'A'-type

displacement of the tensile and compressive axes (Table 35 and Fig.195). The ND would also return to $[112]$ after a displacement along the $[\bar{1}\bar{1}0]$ great circle towards $[111]$, but after a displacement of more than $\sim 10^\circ$ towards $[001]$ (i.e. beyond $[113]$), slip rotations would promote development of the $(001) [\bar{1}\bar{1}0]$ orientation (Table 35 and Fig.195).

Comparison of observed and predicted cold rolling textures

This limited analysis of crystal rotations accounts for the following general observations :-

- (i) Persistence of the $\sim\{011\} \langle 100 \rangle$ hot-rolling texture component (stable in the absence of stress fluctuations) and its gradual rotation to $\sim\{111\} \langle 112 \rangle$ via $\sim\{554\} \langle 225 \rangle$ (A-type displacement of stress axes).
- (ii) Persistence of the $\sim\{111\} \langle 112 \rangle$ component, although not a stable end orientation, up to high cold rolling reductions (difficult to remove in the absence of stress fluctuations).
- (iii) Persistence of, and spread between, $\sim\{001\} \langle 110 \rangle$ and $\sim\{112\} \langle 110 \rangle$, assuming "unequal τ_c ". (If equal τ_c is assumed, $\sim\{112\} \langle 110 \rangle$ is not predicted as a stable end orientation. This is the only important difference between predictions made assuming equal and unequal τ_c).
- (iv) Reinforcement of $\sim\{001\} \langle 110 \rangle$ and $\sim\{112\} \langle 110 \rangle$ at high cold rolling reductions, corresponding with a decrease in $\sim\{111\} \langle 112 \rangle$ intensity (accounted for, respectively, by A-type and B-type displacements of the stress axes).

5.2.2. Effects of processing and material variables on development of cold rolling textures

Hot band condition, especially the presence of a strong texture in the hot-rolled or hot-rolled + annealed strip, can have a marked effect on development of cold rolling textures. The $\sim\{110\} \langle 001 \rangle$ component, observed after low cold rolling reductions (50-60% RA), is not a normal cold rolling texture orientation and is inherited from the hot band. Also, for a given cold rolling schedule, the intensities of $\sim\{100\} \langle 011 \rangle$ and $\sim\{112\} \langle 110 \rangle$ components of the cold rolling texture are related to their intensities in the hot-band texture (e.g. the intensities of $\sim\{112\} \langle 110 \rangle$ and $\sim\{100\} \langle 011 \rangle$ were much higher in both the hot band and cold rolling textures of 430 Ti strip when pre-annealing was omitted than with pre-annealing at 1000°C). This is not surprising since $\sim\{112\} \langle 110 \rangle$ and $\sim\{100\} \langle 011 \rangle$ are predicted as stable end orientations, which would be expected to persist, and also to increase in intensity at the expense of the $\sim\{111\} \langle 112 \rangle$ component after high cold rolling reductions.

The behaviour of the $\sim\{111\} \langle 112 \rangle$ component (as a cold rolling texture and also as a recrystallisation texture) is more complex. Most workers report that, for low carbon steels including ferritic stainless steels, the $\sim\{111\} \langle 112 \rangle$ component is present after low or moderate cold reductions, but that it is progressively replaced by $\sim\{112\} \langle 110 \rangle$ and that there is a simultaneous increase in $\sim\{100\} \langle 011 \rangle$ intensity. (84,119,122) The present results for 430 Ti

steel indicate that maximum $\sim\{111\} \langle 112 \rangle$ intensity is achieved by cold rolling reductions $\sim 80\%$ RA, whereas, for high interstitial 430 steel, there is a progressive increase in $\sim\{111\} \langle 112 \rangle$ intensity up to 95% RA. Comparison of Fig.71 with Fig.72, and of Fig.88 with Fig.90 indicates that, for a given cold rolling reduction, maximum $\sim\{111\} \langle 112 \rangle$ intensity corresponds with minimum $\sim\{100\} \langle 011 \rangle$ intensity. Again, this indicates probable texture inheritance from the hot band. Pre-annealing treatments which minimise $\sim\{100\} \langle 011 \rangle$ in the hot rolled + pre-annealed strip also maximise either $\sim\{110\} \langle 001 \rangle$ or $\sim\{111\} \langle 112 \rangle$ in the pre-annealed strip (Figs.45 & 56). This would be expected to enhance the $\sim\{111\} \langle 112 \rangle$ component in cold rolled material, since the $\sim\{110\} \langle 001 \rangle$ orientation rotates to $\sim\{111\} \langle 112 \rangle$ if fluctuations of the stress axes occur. Goodman and Hu ⁽¹¹⁹⁾ also observed that maximum $\{200\}$ reflection intensity coincided with minimum $\{222\}$ reflection intensity for cold rolled low carbon steel and an iron-carbon alloy, and that a high $\{222\} / \{200\}$ intensity ratio in hot rolling textures corresponded with a high ratio in subsequent cold rolling textures.

Although a similar spread of orientations is developed, in the same sequence, during cold rolling of both high interstitial 430 steel and low interstitial 430 Ti and 409 steels, the following differences are apparent from the results :-

- (i) $\sim\{110\} \langle 001 \rangle$ generally persists to higher reductions in 430 and 409 steels than in 430 Ti steel.

- (ii) $\sim \{111\} \langle 112 \rangle$ is developed after higher cold rolling reductions in 430 and 409 steels than in 430 Ti steel.
- (iii) $\sim \{100\} \langle 011 \rangle$ is generally stronger in 430 steel than in 430 Ti and 409 steels.
- (iv) $\sim \{112\} \langle 110 \rangle$ is not well developed in 430 steel but is readily developed in 430 Ti and 409 steels, with high cold rolling reductions.

Texture inheritance from the hot band explains the behaviour of $\sim \{110\} \langle 001 \rangle$ and $\sim \{111\} \langle 112 \rangle$, and of the $\sim \{100\} \langle 011 \rangle$ component, which is generally stronger in hot rolled or hot rolled + pre-annealed 430 strip than in 430 Ti or 409 hot band. However, texture inheritance alone may not account for the behaviour of the $\sim \{112\} \langle 110 \rangle$ component. Although $\sim \{112\} \langle 110 \rangle$ is a much stronger component of the hot rolling texture of 430 Ti steel than of 430 steel, its intensity is reduced rapidly by pre-annealing $\geq \sim 750^\circ\text{C}$ (Figs.55 & 56). Nonetheless, the $\sim \{112\} \langle 110 \rangle$ component is more developed in 430 Ti steel than in 430 steel, even when a higher pre-annealing temperature is used (Figs.68,69 & 83). This might be due in part, to the greater persistence of the $\sim \{110\} \langle 001 \rangle$ texture (and corresponding delay in development of the $\sim \{111\} \langle 112 \rangle$ and $\sim \{112\} \langle 110 \rangle$ orientations) in 430 steel compared with 430 Ti steel. However, a well developed $\sim \{112\} \langle 110 \rangle$ texture would not be expected in 409 steel if that was the only cause, since the $\sim \{110\} \langle 001 \rangle$ texture is equally persistent in this steel. The large proportion of coarse carbides in high interstitial 430 steel may inhibit texture

development by causing irregular flow of ferrite. (4)

Other workers have also reported that stabilisation with niobium or titanium enhances $\sim \{112\} \langle 110 \rangle$ cold rolling textures in ferritic stainless steels, (125,126) and in other low carbon steels. (124,130-132) Miyaji and Watanabe (120,127) recorded a similar effect in ferritic stainless steels containing fine dispersions of Cr_2N and $\epsilon\text{-Cu}$, which they attributed to changes in slip rotations due to the many fine precipitates. From the results of the present work it is difficult to isolate the effects of fine precipitates from the effects of texture inheritance due to the strong hot rolling textures. For example :- samples of 430 Ti steel pre-annealed at 850°C contain many fine particles and exhibit prominent $\sim \{112\} \langle 110 \rangle$ components at high cold rolling reductions. However, samples cold rolled without pre-annealing contain a low frequency of fine precipitates and exhibit a strong $\sim \{112\} \langle 110 \rangle$ component in both the hot-rolling texture and subsequent cold rolling texture. By contrast, samples pre-annealed at 1000°C (AC) exhibit less well-developed $\sim \{112\} \langle 110 \rangle$ components after high reductions. This might be due to the low frequency of fine particles, or to delayed development of the $\sim \{111\} \langle 112 \rangle$ and $\sim \{112\} \langle 110 \rangle$ components because of greater persistence of the $\sim \{110\} \langle 001 \rangle$ orientation, or even a combination of these factors.

5.3.1. High Interstitial 17% Cr (430) Steel

Strong $\sim\{111\}$ $\langle uvw \rangle$ textures have not been developed in high interstitial 430 sheet, and recrystallisation textures are mainly $\sim\{114\}$ $\langle uvw \rangle$, especially $\sim\{114\}$ $\langle 841 \rangle$. A $\sim\{110\}$ $\langle 001 \rangle$ component is present after low or moderate cold rolling reductions (50-80% RA) and a $\sim\{223\}$ $\langle 962 \rangle$ component is present at high reductions ($\geq 90\%$ RA).

Transition band nucleation is an acknowledged source of $\sim\{110\}$ $\langle 001 \rangle$ recrystallisation textures, ^(39,52) whereas the $\sim\{114\}$ $\langle 841 \rangle$ component (which has been reported previously in high purity iron and ordinary low carbon steels, ⁽⁴²⁾ but not in ferritic stainless steels), is thought to originate at boundaries of deformed $\sim\{100\}$ $\langle 011 \rangle$ grains. ⁽⁴²⁾ Lewis and Pickering ⁽⁸⁴⁾ found that grain boundary nucleation predominated in high interstitial 17% Cr steel, even after very low cold rolling reductions ($\sim 35\%$ RA), due to the large grain boundary area associated with the small grain size and 'pancaked' grain structure. They ⁽⁸⁴⁾ reported a major grain boundary nucleated $\sim\{100\}$ $\langle 011 \rangle$ component.

The present results also indicate that grain boundary regions are the main sources of recrystallisation nuclei in commercial, high interstitial 430 steel. Orientations of grain boundary recrystallisation nuclei (determined by analysis of TEM electron diffraction patterns) include $\sim\{137\}$ $\langle 851 \rangle$ and $\sim\{113\}$ $\langle 521 \rangle$, .

which are close to $\sim\{114\} \langle 841 \rangle$ (Fig.196), and $\sim\{111\} \langle 123 \rangle$ which is near $\sim\{223\} \langle 962 \rangle$ (Fig.197). The $\sim\{223\} \langle 962 \rangle$ texture component is present only with high cold rolling reductions, when $\sim\{112\} \langle 110 \rangle$ is a component of the cold rolling texture. It is thought to originate in the grain boundary regions of deformed $\sim\{112\} \langle 110 \rangle$ grains which have developed as a result of slip rotations from material having an initial $\sim\{111\} \langle 211 \rangle$ orientation, as described in the previous analysis. (The $(223) [\bar{9}62]$ orientation is related to the $(112) [\bar{1}10]$ and $(455) [\bar{5}22]$ orientations by, respectively, a $\sim 17^\circ$ clockwise rotation and an $\sim 18^\circ$ anticlockwise rotation about a $\langle 110 \rangle$ axis common to all three orientations (Fig.198).

TEM examination of partially recrystallised samples also showed occasional $\sim\{100\} \langle 001 \rangle$ nuclei, apparently evolving remote from grain boundaries (Fig.28b). A $\sim\{100\} \langle 001 \rangle$ texture component has been detected by X-ray texture goniometry (Figs.100 & 101).

Attempting to produce more favourable recrystallisation textures in high interstitial 430 steel, by control of hot band condition and subsequent processing, has proved difficult. Minor $\sim\{111\} \langle uvw \rangle$ texture components are promoted by combinations of high pre-annealing temperatures ($\geq 1000^\circ\text{C}$) and high cold rolling reductions ($\geq 90\%$ RA), but $\sim\{114\} \langle 841 \rangle$ is always present. Occasional $\sim\{111\} \langle 110 \rangle$ and $\sim\{111\} \langle 121 \rangle$ grain-boundary nuclei have been observed by TEM, and other authors have also attributed these components to grain boundary nucleation. (42,46,47)

High pre-annealing temperatures ($\geq 1000^{\circ}\text{C}$) coarsen the carbides or promote colonies of martensite (on cooling from the $(\alpha + \gamma)$ region) at grain boundary triple points, thereby increasing carbide interparticle spacings. This is reputed to enhance $\sim \{111\} \langle uvw \rangle$ textures by effectively providing a "purer" ferrite matrix (with respect to carbon and nitrogen) remote from such particles. (106)

Hutchinson and Ushioda (135) have recently reported that, for a manganese-free, iron-carbon alloy containing 0.023%C, dissolution of carbides (which occurred during slow-heating for final annealing) did not affect the texture adversely. They concluded that degradation of the annealing texture was associated with the simultaneous presence of carbon and manganese in the ferrite matrix, and recommended an optimum manganese content as follows :-

$$\text{Mn}\% \text{ (optimum)} = \left(\frac{55}{32} \right) \text{S}\% + \left(\frac{55}{16} \right) \text{O}\%$$

(i.e. just sufficient to combine with all the sulphur and oxygen in the steel).

5.3.2. Low Interstitial, Titanium-Stabilised (430 Ti and 409) Steels

Recrystallisation textures developed in low interstitial 430 Ti and 409 steels are much stronger (and more favourable from a formability viewpoint) than those developed in high interstitial 430 steel, and are markedly influenced by processing variables. Texture components observed are mainly $\sim \{110\} \langle 001 \rangle$ after low.

to moderate cold rolling reductions, $\sim\{554\} \langle 225 \rangle$ after moderate to high reductions and $\sim\{223\} \langle 962 \rangle$ after very high reductions, with $\sim\{100\} \langle 011 \rangle$ usually only a minor component of texture. Recrystallisation textures of 409 (12 Cr, 0.5 Ti) steel are similar to those observed in 430 Ti (17 Cr, 0.5 Ti) steel, although slightly reduced in intensity. Lewis and Pickering (84) also reported that variations in chromium content in the range 17-25% Cr had little effect on texture development.

(i) $\sim\{100\} \langle 011 \rangle$ and related components

Although only a subsidiary component, it is important to consider $\sim\{100\} \langle 011 \rangle$ because of its extremely detrimental effect on drawability. This component (which is considered a grain-boundary nucleated orientation (42,46,47,84) is prominent only after high cold rolling reductions, even though it constitutes a major component of the cold rolling texture spread. The intensity of $\sim\{100\} \langle 011 \rangle$ is greatest when pre-annealing before cold rolling is omitted, so that the total grain boundary area is large, and least with initially coarse-grained material (e.g. annealed 1000°C before cold rolling), which has a correspondingly smaller grain boundary area. Occasional $\sim\{001\} \langle 340 \rangle$ (near $\sim\{001\} \langle 110 \rangle$ grain boundary nuclei have been observed during TEM examination of partially recrystallised samples.

Microbands of elongated subgrains, often close to grain boundaries, are sources of $\sim\{113\} \langle uvw \rangle$ recrystallisation nuclei, especially $\sim\{113\} \langle 741 \rangle$ and $\sim\{113\} \langle 521 \rangle$ which are near $\sim\{114\} \langle 841 \rangle$ (Fig.196),

although this is not an important component of the recrystallisation textures. Hu (53) also reported that microbands of elongated subgrains were sources of $\sim\{113\} \langle uvw \rangle$ nuclei in rolled, $\{001\} \langle uvw \rangle$ oriented, crystals of silicon-iron.

(ii) $\sim\{110\} \langle 001 \rangle$

The $\sim\{110\} \langle 001 \rangle$ recrystallisation texture component is present usually only with cold rolling reductions $\leq 70\%$ RA, except with coarse initial grain size (e.g. annealed 1000°C before cold rolling), when it persists to higher reductions (to the detriment of the more desirable $\sim\{554\} \langle 225 \rangle$ component) with rapid final annealing, though not with batch final annealing (Fig.153). Horta, Wilson and Roberts (144) also found that the $\sim\{110\} \langle 001 \rangle$ component was enhanced, at the expense of $\sim\{111\} \langle uvw \rangle$ orientations, during rapid final annealing of initially coarse-grained low carbon steel, but not during final batch annealing. They suggested that a coarse initial grain size would favour deformation band nucleation of $\sim\{110\} \langle 001 \rangle$ grains, which would grow quickly during rapid annealing (before nucleation occurred in other components). Recovery during slow heating for batch annealing would allow nucleation of other orientations to occur before growth of $\sim\{110\} \langle 001 \rangle$, resulting in reduced $\sim\{110\} \langle 001 \rangle$ texture selectivity. (144)

Batch pre-annealing before cold rolling promotes stronger $\sim\{110\} \langle 001 \rangle$ recrystallisation textures with cold rolling reductions of $\sim 50-60\%$ RA than rapid pre-annealing. This is attributed to the increased

intensity of the $\sim\{110\} \langle 001 \rangle$ texture in the hot-rolled + annealed strip (Fig.52), possibly generating a higher frequency of potential in situ and/or transition band $\sim\{110\} \langle 001 \rangle$ nuclei during final annealing.

(iii) $\sim\{554\} \langle 225 \rangle$ (near $\sim\{111\} \langle 112 \rangle$)

The intensity of the $\sim\{554\} \langle 225 \rangle$ component is markedly affected by processing variables. For 0.5% Ti steels (409 and 430 Ti), it is maximised after cold rolling reductions of 80-90% RA, and by rapid final annealing. Lower $\sim\{554\} \langle 225 \rangle$ intensities developed by batch final annealing probably result from reduced texture selectivity, due to prolonged recovery during slow heating. With coarse initial grain sizes, development of a strong $\sim\{554\} \langle 225 \rangle$ texture by rapid final annealing requires higher cold rolling reductions than for finer initial grain sizes, and the $\sim\{110\} \langle 001 \rangle$ component is more persistent. A similar effect of coarse initial grain size was reported by Matsuo, Hayami and Nagashima, ⁽¹³⁶⁾ for high purity iron. They attributed the effect to discrepancies in development of local inhomogeneities during cold rolling, leading to differences in subsequent nucleation behaviour.

Batch pre-annealing before cold rolling generally has a beneficial effect on $\sim\{554\} \langle 225 \rangle$ texture development (Fig.159), especially with high cold rolling reductions and rapid final annealing. Hutchinson ⁽¹⁰⁶⁾ suggested that prolonged annealing before cold rolling of titanium and niobium stabilised low-carbon steels ensures that all carbon and nitrogen are properly combined and do

not inhibit in situ nucleation of $\sim\{111\}$ $\langle uvw \rangle$ grains. Retardation of $\sim\{111\}$ $\langle uvw \rangle$ nucleation would be more detrimental with rapid final annealing than with batch final annealing, due to the shorter times involved. (144)

Other authors have suggested that the beneficial effect of titanium and niobium in promoting $\sim\{554\}$ $\langle 225 \rangle$ textures is due to the particles themselves, either as a fine distribution which inhibits nucleation in all but the most favoured subgrains, (125,126) or as coarse particles which stimulate nucleation. (84)

Both particle stimulated nucleation and (apparent) in situ nucleation have been observed in partially recrystallised samples of 430 Ti (0.5 Ti) steel examined by TEM. In situ nuclei have been observed most frequently in samples which had been pre-annealed at 1000°C before cold rolling to reductions $\geq 80\%$ RA. The majority of these nuclei have $\sim\{111\}$ $\langle uvw \rangle$ orientations.

Most particle-stimulated nuclei also have $\sim\{111\}$ $\langle uvw \rangle$ orientations, but not all particles appear to be effective in stimulating nucleation. Subgrains with low stored energy orientations (e.g. $\sim\{100\}$ $\langle uvw \rangle$) in particle deformation zones tend to remain small. These observations are in agreement with work by Lewis and Pickering (84) but at variance with other authors, (60,106,141) who have generally concluded that particle-stimulated nucleation is essentially random in low carbon steels. Chan and Humphreys (60) noted that some grains which nucleated at particles stopped growing at an early stage, and concluded that subsequent

sharpening of textures could be associated with more rapid growth of selected orientations.

Nes⁽⁶¹⁾ proposed that the effectiveness of coarse particles in stimulating nucleation would be reduced in the presence of a fine dispersion, and the process would hence become more orientation-selective. In the samples of 430 Ti examined in the present work, fine particles ($< 0.01-0.3 \mu\text{m}$ diameter) were either present before cold rolling (for samples pre-annealed $\sim 850^\circ\text{C}$), or were precipitated in the very early stages of annealing (for samples cold-rolled without pre-annealing or with pre-annealing at 1000°C). Some, though not all, of these particles would be small enough to restrict nucleation of less favourable orientations. (56,106) However, with batch pre-annealing, (which promotes highest $\sim \{554\} \langle 225 \rangle$ intensity, especially at high cold rolling reductions), there is not a high frequency of particles small enough to restrict nucleation (finest particles $\geq 0.05 \mu\text{m}$). It seems likely, therefore, that purification of the matrix with respect to interstitial elements is more important for selective nucleation of $\sim \{554\} \langle 225 \rangle$ grains, either in situ or in particle deformation zones.

Variations in titanium content of 430 Ti steel have a significant effect on the intensity of the $\sim \{554\} \langle 225 \rangle$ component. All three steels examined have titanium contents in excess of the levels required for stabilisation, and so the effects observed are attributed to the percentage of titanium in solid solution, $[\text{Ti}]_{\text{ss}}$.

Maximum $\sim\{554\} \langle 225 \rangle$ intensity is achieved for 0.5% Ti ($\sim 0.4\%[\text{Ti}]_{\text{ss}}$), with high cold rolling reductions ($\sim 80-90\%$ RA) and rapid final annealing. However, with moderate reductions (60-70% RA), highest $\sim\{554\} \langle 225 \rangle$ intensities are developed by 0.3 Ti ($\sim 0.2\%[\text{Ti}]_{\text{ss}}$) steel (Figs.164,165), especially with batch final annealing. No distinction between optimum titanium contents for different cold rolling reductions has been reported previously for ferritic stainless steels, and other workers have reported optimum titanium contents which were just sufficient to remove all carbon and nitrogen from solid solution. (125,137)

Alloying elements in dilute solid solution are known to retard recrystallisation by a solute-drag effect, which impedes movement of grain boundaries. (106) Recovery is thought to be inhibited to a lesser extent, so that the overall effect is to increase the ratio of nucleation rate to growth rate, although both are retarded. Consequently, the resultant texture is generally less sharp and resembles the deformation texture more closely. (41) This could explain why sharper $\sim\{554\} \langle 225 \rangle$ textures have been observed for the lower $[\text{Ti}]_{\text{ss}}$ steels at moderate cold rolling reductions. However, in situations where grain boundaries may be important sources of recrystallisation nuclei, solute drag effects may inhibit S.I.B.M., and so eliminate unfavourable texture components originating from this source. (106) This could explain why the higher $[\text{Ti}]_{\text{ss}}$ steels exhibit sharper $\sim\{554\} \langle 225 \rangle$

textures at high cold rolling reductions than lower

$[Ti]_{ss}$ steels.

(iv) $\sim \{223\} \langle 962 \rangle$

This component is prominent only after high cold rolling reductions, when the grain boundary area is large and $\sim \{112\} \langle 110 \rangle$ is a major component of the cold rolling texture. As discussed previously (Section 5.3.1), it is thought to originate at the boundaries of $\sim \{112\} \langle 110 \rangle$ grains. Grain boundary nuclei observed during TEM examination of heavily cold rolled and partially recrystallised 430 Ti steel include $\sim \{112\} \langle 241 \rangle$ and $\sim \{111\} \langle 123 \rangle$, which are close to $\sim \{223\} \langle 962 \rangle$ (Fig.197).

A coarse initial grain size delays development of the $\sim \{223\} \langle 962 \rangle$ recrystallisation texture to higher cold rolling reductions. This could be a consequence of the reduced grain boundary area and/or the delay in development of the $\sim \{112\} \langle 110 \rangle$ cold rolling texture. Batch annealing after cold rolling generally leads to a lower $\sim \{223\} \langle 962 \rangle$ intensity than rapid final annealing (Fig.155), presumably due to reduced texture selectivity resulting from slow heating.

The titanium content of 430 Ti steel influences the intensity of the $\sim \{223\} \langle 962 \rangle$ component, which is strongest in the lowest $[Ti]_{ss}$ steel. This is compatible with the suggestion that high $[Ti]_{ss}$ might inhibit S.I.B.M. The annealing temperature may also affect grain boundary nucleated components, and S.I.B.M. might be inhibited to a greater extent at lower annealing

temperatures . For 0.5% Ti steel cold rolled to 95% RA, provided that the material is pre-annealed before cold rolling, final annealing at 800°C promotes a texture centred on $\sim\{554\} \langle 225 \rangle$, whereas annealing at 900°C promotes a sharp $\sim\{223\} \langle 962 \rangle$ texture.

A $\sim\{223\} \langle 962 \rangle$ component has previously been reported by Gillanders, Dasarathay and Hudd (124) in Nb-stabilised low carbon steel, and a practically identical orientation, $\sim\{223\} \langle 10,7,2 \rangle$, was reported by Dickson and Cooke (122) for Ti-stabilised 12% Cr steel after high cold rolling reductions.

5.4.1. Effects of Processing and Resultant Texture(i) Deep drawability

The deep-drawability of the 12-17% Cr steels examined was assessed by uniaxial tensile determination of strain ratios and by Swift cupping tests. The amount of material available for cupping tests was limited, but the results indicate a direct relationship between the average strain ratio (\bar{r}) and the LDR. Lewis and Pickering ⁽⁸⁴⁾ also reported a similar relationship for 17-25% Cr steels.

Variations in r -values, resulting from differences in composition and processing, reflect the effects of texture. Processing schedules which maximise r_0 and \bar{r} -values are essentially those which promote strong $\sim \{554\} \langle 225 \rangle$ textures with only weak $\sim \{100\} \langle uvw \rangle$ components. For high interstitial 430 steel, r_0 and \bar{r} -values are generally low, reflecting the difficulty in developing $\sim \{111\} \langle uvw \rangle$ textures. By contrast, much higher r_0 and \bar{r} -values are achieved for 409 and 430 Ti steels, in which strong $\sim \{554\} \langle 225 \rangle$ textures are developed. The highest \bar{r} -values ($\sim 2.3-2.4$) are obtained for 430 Ti (0.5% Ti) steel with pre-annealing at 850°C, + cold rolling to 80-90% RA + rapid final annealing. Samples with high r_0 -values generally exhibit correspondingly high \bar{r} -values. Although limited material availability prevented \bar{r} -values of 430 Ti steels containing 0.3% Ti and 0.4% Ti from being determined, it may be inferred (from the r_0 -values) that the best

\bar{r} -values for low to moderate cold rolling reductions (~ 60 - 70% RA) would probably be obtained with the 0.3% Ti steel.

Direct relationships between the texture parameter ratio $P \{111\} / P \{100\}$ and r_0 and \bar{r} -values have been determined by linear regression analysis. (Since $\{554\}$ is very close to $\{111\}$, grains with $\sim\{554\}$ $\langle uvw \rangle$ orientations are accounted for by the $P \{111\}$ texture parameter. (49) Other workers (84,146) also related r_0 , r_{90} and/or \bar{r} to the ratio of the volume fractions of $\{111\} \langle uvw \rangle : \{100\} \langle uvw \rangle$ components. In the present work, other relationships between r_0 , r_{90} , \bar{r} and $(P \{111\} + P \{332\})$ have also been obtained. However, it is thought that these relationships, which do not include $P \{100\}$, seem reasonable only because high $P \{111\}$ almost invariably corresponds with low $P \{100\}$, for the samples examined.

High r_{45} values correlate with high values of the ratio $P \{211\} / (P \{321\} + P \{110\})$. Other authors (144,147) have also reported that r_{45} -values are maximised with a high volume fraction of $\sim\{211\} \langle uvw \rangle$ oriented material. Samples with strong $\sim\{223\} \langle 962 \rangle$ textures (e.g. 430 Ti steel after cold rolling to 90% RA without pre-annealing + rapid final annealing) exhibit low r_0 -values but higher r_{90} -values and very high r_{45} -values (Table 28).

(ii) Stretch formability

There are no systematic effects of composition or processing variables on stretch-formability, as assessed

by uniaxial tensile determination of work hardening coefficients and Erichsen tests. Mean strain hardening exponents are within the range 0.22-0.26 for all samples examined. These low values reflect the poor inherent stretch-formability of ferritic stainless steels, compared with austenitic stainless steels.

5.4.2. Theoretical Prediction of r-values and Earing Profiles

Theoretical r-values and radial strains in drawing of circular blanks have been calculated, for the main recrystallisation texture ideal orientations, using the method of Vieth and Whiteley ⁽⁸⁹⁾ (programmed for the Apple IIe microcomputer using Applesoft Basic language). Computer program listings are included in Appendix B. Possible rotation of the lattice during straining is ignored, and crystallographic slip on $\{110\}$, $\{112\}$ and $\{123\}$ planes (i.e. 48 systems) is considered, assuming either :-

- (i) EQUAL γ_c ($\gamma_c \{110\} = \gamma_c \{112\} = \gamma_c \{123\}$),
as used by Vieth and Whiteley. ⁽⁸⁹⁾
- (ii) UNEQUAL γ_c ($\gamma_c \{110\} : \gamma_c \{112\} : \gamma_c \{123\}$
 $= 1:1.03:1.05$).

The results of the computations are shown in Table 36 and Figs.199-206. (Some of these orientations were considered by Vieth and Whiteley ⁽⁸⁹⁾ in their original work, (assuming equal γ_c), but have been re-considered here for comparison with predictions assuming unequal γ_c).

There are, in some cases, large differences between r-values predicted assuming equal and unequal γ_c on the various slip planes: the latter assumption leads.

to predictions of infinite r -values for more orientations (Figs.200-202). Fig.201 indicates that, although the $\{554\} \langle 225 \rangle$ orientation is close to $\{111\} \langle 112 \rangle$, widely differing r_0 -values are predicted for these two orientations. This illustrates the limitations of this type of approach. Table 36 and Fig.200 show that the r_0 -value for the $\{110\} \langle 001 \rangle$ orientation is predicted as $r_0 = 1.0$, but an infinite r_0 -value is indicated for $\theta = 2.5^\circ$ (where θ is the angle between the test direction and the rolling direction). This might explain discrepancies in r_0 -values predicted for the $\{110\} \langle 001 \rangle$ orientation by Evans, Bitcon and Hughes (129) ($r_0 = 1.0$), and Mishra and Darman (131) ($r_0 = \infty$), using a similar approach.

Earing profiles calculated for a specific orientation are very similar for either equal or unequal γ_c (Figs.203-206). Peaks and troughs generally coincide with maximum and minimum r -values respectively, and also with azimuth angle positions of $\{200\}$ poles on the pole figures for the ideal orientations.

5.4.3. Comparison between observed and predicted results

(i) Strain ratios

Theoretical r -values have been calculated for samples containing a mixture of texture components, assuming that :-

$$r = \sum r_i V_i \dots\dots\dots (\text{Eq. 13}) \quad (90)$$

where r_i and V_i are respectively the r -values and volume fractions of individual texture components. All

equivalent (hkl) [uvw] orientations which constitute a texture component $\{hkl\} \langle uvw \rangle$ were taken into consideration in determining the r-value for that component. (e.g. $r_{\theta} \{223\} \langle 962 \rangle = \frac{1}{4} r_{\theta} (223) [\bar{9}62] + \frac{1}{4} r_{\theta} (223) [6\bar{9}2] + \frac{1}{4} r_{\theta} (223) [9\bar{6}\bar{2}] + \frac{1}{4} r_{\theta} (223) \bar{6}9\bar{2}$).

Volume fractions of individual components were approximated by their relative peak intensities on the pole figures, and also by the relative magnitudes of texture parameters determined from X-ray diffractometry. For the latter, it was assumed that the $\{223\}$ reflection represented the $\sim \{554\} \langle 225 \rangle / \sim \{111\} \langle 112 \rangle$ orientation only, and that the $\{114\}$ reflection represented the $\sim \{114\} \langle 841 \rangle$ orientation. No $\{223\}$ reflection is obtained ($h+k+l =$ odd number, therefore $\{223\}$ is a missing reflection), but the $\{112\}$ reflection was assumed to represent the $\sim \{112\} \langle 531 \rangle$ orientation, which is close to $\sim \{223\} \langle 962 \rangle$.

Observed and calculated r-values for heavily cold-rolled (90% RA) and annealed samples are compared in Tables 37 and 38 and Fig.207. (Due to the disproportionately high r_{θ} -values predicted for the $\sim \{554\} \langle 225 \rangle$ orientation, r_{θ} -values are based on $\sim \{111\} \langle 112 \rangle$). Limitations of this approach include :-

- (i) It is only applicable to very well developed textures, hence only samples cold rolled to 90% RA before annealing have been considered.
- (ii) Orientations with infinite r-values are

predicted, so that realistic predictions cannot always be made.

- (iii) Restraints imposed by neighbouring grains cannot be taken into consideration.

The best correlation between observed and calculated r -values is obtained using texture data from pole figures and theoretical r -values calculated assuming equal τ_c on the various slip planes (Table 37 & Fig.207). Predicted r -values are generally higher than observed r -values. (Calculated r_{45} -values for $\sim\{223\} \langle 962 \rangle$ textures, and r_{90} -values for $\{114\} \langle 841 \rangle$ textures are lower than observed values by ~ 0.2 . Otherwise calculated r -values are higher than observed values by $\sim 0.2-0.8$.) The ideal relationship between observed and calculated values is $r_{obs} = r_{calc}$, whereas the relationship determined by linear regression is :-

$$r_{calc} = 1.06 r_{obs} + 0.17$$

(correlation co-efficient = 0.86)

Discrepancies are inevitable due to the limitations inherent in the methods of calculating r -values and volume fractions of texture components. The correlation between observed and predicted r -values is, therefore, surprisingly good.

(ii) Earing profiles

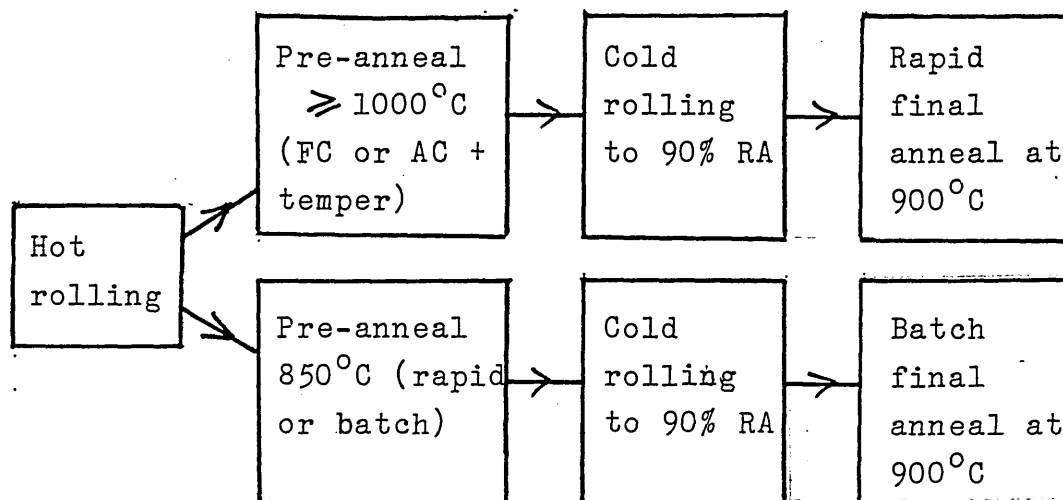
There were insufficient experimental results at high cold rolling reductions to make a detailed comparison of observed and predicted earing profiles - However, predicted ears for individual orientations correspond with

azimuth angle positions of $\{200\}$ poles on their pole figures, and earing generally occurs in directions of highest $\{100\}$ pole density. (148) For the $\sim\{554\} \langle 225 \rangle$ orientation, earing is predicted at $\sim 10^\circ$ and $\sim 50-80^\circ$, and samples with strong $\sim\{554\} \langle 225 \rangle$ textures actually exhibit ears near 0° and $\sim 60-80^\circ$. Unfortunately, no earing profiles were obtained for samples with strong $\sim\{223\} \langle 962 \rangle$ textures, for which low earing is predicted (Fig.206).

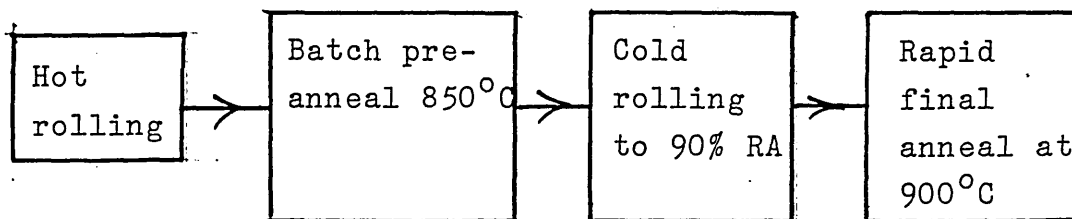
5.5. PROCESSING SCHEDULES FOR OPTIMUM TEXTURES AND FORMABILITY

Strong $\sim\{554\}$ $\langle 225 \rangle$ textures which promote high \bar{r} -values ($\sim 1.6-2.4$) are developed in titanium stabilised low-interstitial (430 Ti and 409) steels. Only minor $\sim\{111\}$ $\langle uvw \rangle$ components are developed in high interstitial 430 steel, and unfavourable $\sim\{114\}$ $\langle 841 \rangle$ or $\sim\{100\}$ $\langle uvw \rangle$ components are always present, so that \bar{r} -values are generally low. For the hot-rolled, commercial steels examined, the following processing schedules maximise $\sim\{111\}$ $\langle uvw \rangle$ textures :-

430 Steel (~ 17 Cr, 0.077 (C+N))

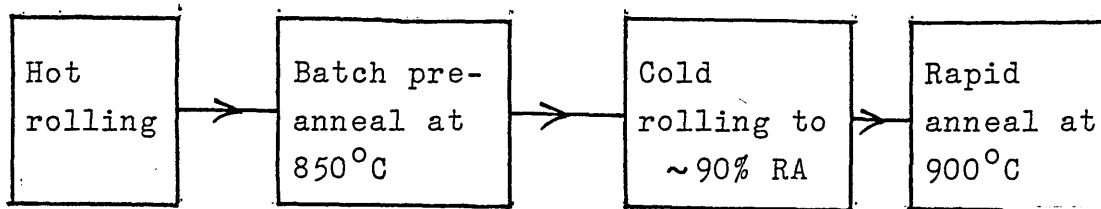


409 Steel (~ 12 Cr, 0.5 Ti, 0.039 (C+N))

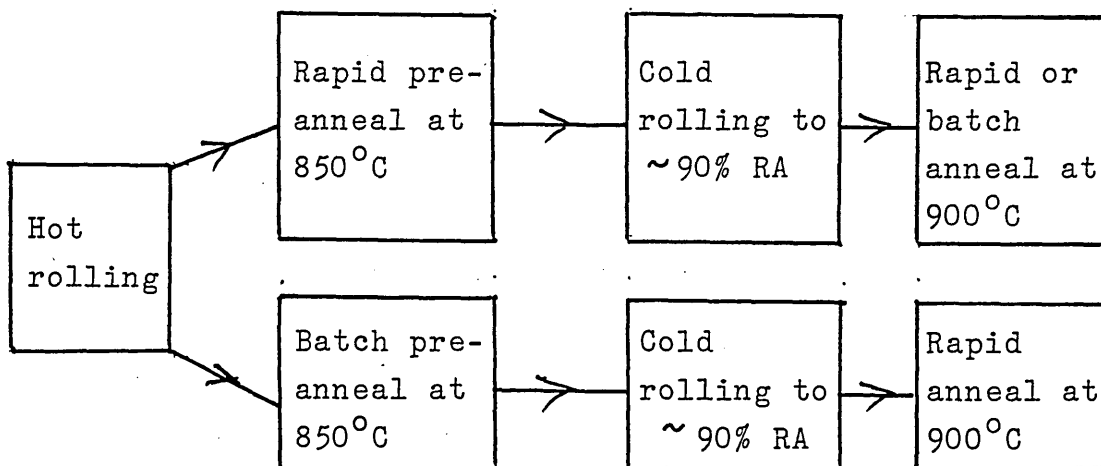


430 Ti Steel (~ 17 Cr, 0.03 (C+N) + Ti)

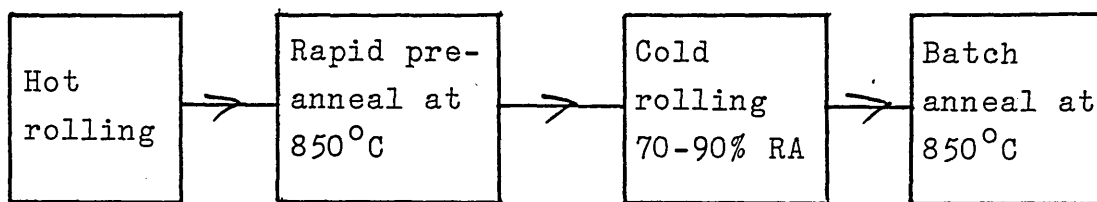
(i) 0.5% Ti Steel ($0.4 [Ti]_{ss}$)



(ii) 0.4% Ti Steel ($0.3 [Ti]_{ss}$)



(iii) 0.3% Ti Steel ($0.2 [Ti]_{ss}$)



Maximum $\sim\{554\} \langle 225 \rangle$ intensity is achieved for the 0.5% Ti steel.

Hot-band condition is an important variable, and it must be remembered that the commercial materials studied had strong hot-rolling textures, which were modified but not removed by pre-annealing. Differences in starting .

condition, which are often ignored, might explain the conflicting differences between results of other authors.

Commercial limitations which might affect the viability of the suggested processing schedules have been considered in a case study (Appendix C). However, it should be pointed out that, in practice, the final annealing temperature for 430 steel would normally be limited to $\leq \sim 850^{\circ}\text{C}$, because of the risk of partial transformation to austenite at higher temperatures, which would introduce martensite into the structure on cooling. High temperature ($> \sim 900^{\circ}\text{C}$) pre-annealing treatments would sensitise 430 steel, although slow cooling or tempering should rectify this, provided that sufficient time is given in the $650\text{-}850^{\circ}\text{C}$ temperature range to permit re-diffusion of chromium to denuded regions. The titanium stabilised steels do not suffer sensitisation even at temperatures $\sim 1000^{\circ}\text{C}$.

- (i) In general, hot band condition is an important variable, and may influence texture development during subsequent cold rolling and annealing.
- (ii) Deformation of ferrite below the dynamic recrystallisation temperature is responsible for development of the centre $\sim \{100\} \langle 011 \rangle$, $\sim \{111\} \langle 112 \rangle$ and $\sim \{112\} \langle 110 \rangle$ components of the hot rolling texture. By contrast, the $\sim \{110\} \langle 001 \rangle$ surface texture is due to recrystallisation at the surface.
- (iii) The cold rolling texture of ferritic stainless steels consists of a spread between the $\sim \{100\} \langle 011 \rangle$, $\sim \{111\} \langle 112 \rangle$ and $\sim \{112\} \langle 110 \rangle$ orientations after high cold reductions.
- (iv) At moderate ($\leq 60\%$ RA) reductions, texture inheritance from the hot band accounts for the presence of a $\sim \{110\} \langle 001 \rangle$ component in cold rolled sheet, and also affects the relative intensities of the true cold rolling texture components.
- (v) The $\sim \{112\} \langle 110 \rangle$ component of the cold rolling texture develops more readily in the low interstitial, titanium stabilised, 409 (12 Cr, 0.5 Ti, 0.03C) and 430 Ti (17 Cr, 0.5 Ti, 0.03C) steels than in standard 430 (17 Cr, 0.05C) steel.
- (vi) In 409 and 430 Ti steels, strong $\sim \{554\} \langle 225 \rangle$ textures, with correspondingly high \bar{r} -values, are developed as a result of suitable cold rolling and annealing treatments. This type of recrystallisation texture is not developed in standard 430 steel.

(vii) Recrystallisation textures in 430 steel are complex, consisting mainly of $\sim\{114\} \langle 841 \rangle$ and $\sim\{100\} \langle uvw \rangle$ components, with $\sim\{223\} \langle 962 \rangle$ present after high cold rolling reductions ($\geq 90\%$ RA).

(viii) With very high cold rolling reductions ($\sim 95\%$ RA), $\sim\{223\} \langle 962 \rangle$ replaces $\sim\{554\} \langle 225 \rangle$ as the main recrystallisation texture component in 409 and 430 Ti steels.

(ix) Strong $\sim\{554\} \langle 225 \rangle$ (near $\sim\{111\} \langle 112 \rangle$) textures correspond with high r_0 and \bar{r} -values, whereas strong $\sim\{223\} \langle 962 \rangle$ (near $\sim\{112\} \langle 531 \rangle$) textures give high r_{45} -values.

(x) Linear relationships between \bar{r} -value and the LDR, and between r -values and various texture parameters, have been determined for the commercial steels under consideration.

(xi) In general, processing schedules which promote maximum $\sim\{111\} \langle uvw \rangle$ texture intensities, (and hence highest \bar{r} -values), involve batch-annealing before cold rolling to high reductions (80-90% RA) and rapid final annealing.

(i) Control of the texture of standard 430 steel (17 Cr, 0.05C) for improved deep drawability is not practicable within commercial processing limitations. Modifications to the composition are more effective, and good texture control can be achieved with low-interstitial, Ti-stabilised steels. However, titanium is an expensive alloying addition. Hutchinson and Ushioda (135) reported that carbon was only detrimental to the texture of low carbon Fe-C alloys in the presence of manganese and that low manganese contents (just sufficient to combine with sulphur and oxygen) lead to improved textures. The effect of manganese on textures of 430 steel could be investigated.

(ii) Titanium stabilisation promotes high \bar{r} -values, and also imparts resistance to hot-cracking during welding. Niobium stabilisation is reputed to promote low planar anisotropy (Δr), but is less effective in promoting high \bar{r} -values, and does not impart resistance to hot-cracking. Mixed stabilisation, say (Nb + Ti) might combine the benefits of individual additions.

(iii) Previous workers have disagreed on the usefulness of double-cycle rolling, and/or on the optimum reductions for each cycle. The effect of two stage cold rolling needs to be re-examined, taking into account the starting condition, which has often been overlooked. However, it

must be remembered that double-cycle cold rolling is expensive, and significant improvements in properties and pressing performance would be required to justify its use.

(iv) Studies of recrystallisation behaviour in ferritic stainless steels have generally been restricted to examination of samples which have been cold rolled and heat-treated for short times, usually at temperatures between 650-750°C. This does not show the effect of a slow heating rate (as in batch annealing), and may not reflect structural changes after very short times at higher temperatures. Instantaneous observation of the recrystallisation process is, therefore, desirable.

- 1 BARRETT & MASSALSKI: "Structure of Metals", McGraw Hill.
- 2 E.A. CALNAN & C.J.B. CLEWS: Phil. Mag., June 1951, 42, (329), 616-635.
- 3 I.L. DILLAMORE & W.T. ROBERTS: Metallurgical Reviews, 1965, (10), 271-380.
- 4 BARRETT: "Structure of Metals", McGraw Hill.
- 5 G.J. DAVIES: J. Sheff. Univ. Met. Soc., 1975, 17-26.
- 6 B.D. CULLITY: "Elements of X-ray Diffraction", Addison Wesley, 1978.
- 7 M. HATHERLY & W.B. HUTCHINSON : Institute of Metallurgists, Monograph No. 5.
- 8 W.B. HUTCHINSON: Trans. Indian Inst. Metals, Oct. 1981, 34, (5), 355-363.
- 9 H.J. BUNGE: "Texture Analysis in Materials Science", Butterworths, 1982.
- 10 I.L. DILLAMORE & R.E. SMALLMAN: Metal Science Journal, 1972, (6), 184-188.
- 11 C.S. BARRETT & L.H. LEVENSON: Trans. Amer. Inst. Min. Met. Eng., 1941, (145), 281-288.
- 12 P.N. RICHARDS & M.K. ORMAY: Trans. Met. Soc. AIME, April, 1969, (245), 715-723.
- 13 I.L. DILLAMORE: Trans. Met. Soc. AIME, 1965, (233), 702-707.
- 14 R. MADDIN & N.K. CHEN: Progress in Metal Physics, 1954, (5), 53.

- 15 C.M. VAN DER VALT: Acta Met., Apr. 1969, (17)
393-395.
- 16 T. KAMIJO: Trans. Jap. Inst. Metals, 1969,
(10), 242-246.
- 17 J. BLAHOVEC: Physica Status Solidi; (b), 1971,
(45), K5-K8.
- 18 G.Y. CHIN: Met. Trans. Aug. 1972, (3), 2213-2216.
- 19 H. HU: Texture, 1974, (1), 233-258.
- 20 K. WIERZBANOWSKI: Scripta Met. 1979, (13),
1121-1123.
- 21 R. SMOLUSCHOWSKI & A.J. OPINSKY: Carnegie Inst.
of Technology, Conference on Plastic Deformation
of Crystalline Solids, 1950.
- 22 G.I. TAYLOR: J. Inst. Metals, 1938, (62), 307-324.
- 23 P. VAN HOUTTE & E. AERNOUDT: Z. Metallkunde,
1975, 66, (H4), 202-209 & (H5), 303-306.
- 24 G.Y. CHIN & W.L. MAMMEL: Trans. Met. Soc. AIME,
June, 1969, (245), 1211-1214.
- 25 U.F. KOCKS: Met. Trans., May 1970, (1), 1121-1143.
- 26 BISHOP & HILL: Phil. Mag., 1951, (42), 1298-1309.
- 27 G. SACHS: Z. Ver. Deut. Eng., 1928, (72), 734.
- 28 I.L. DILLAMORE & H. KATOH: Metal Science, 1974,
(8), 21-27.
- 29 K. WIERZBANOWSKI & Z. JASIENSKI: Scripta Met.,
1981, (15), 585-589.
- 30 P. VAN HOUTTE & E. AERNOUDT: Mat. Sci. Eng.,
1976, (23), 11-22.
- 31 P. ÖSTRÖM: Scandinavian. J. Metallurgy, 1979,
(8), 277-283.

- 32 I.L. DILLAMORE & W.T. ROBERTS: Acta. Met., 1964,
(12), 281-293.
- 33 I.L. DILLAMORE, E. BUTLER & D. GREEN: Metal
Science J., 1968, (2), 161-167.
- 34 T. KAMIJO: Trans. Japan Inst. Metals, 1969,
(10), 242-246.
- 35 P.A. BECK: Acta Met., 1953, (1), 230-234.
- 36 H. HU: Trans. AIME, Oct. 1957, 1164-1168.
- 37 I.L. DILLAMORE, C.J.E. SMITH & T.W. WATSON:
Metal Science J., 1967, (1), 49-54.
- 38 D.B. TITOROV: Phys. Met. Metallogr., 1973,
36, (1), 82-87.
- 39 M. HATHERLY & I.L. DILLAMORE: J. Aust. Inst.
Metals, June 1975, 20, (2), 71-84.
- 40 I.L. DILLAMORE: Metals Forum, Sept. 1978,
1, (3), 136-145.
- 41 W.B. HUTCHINSON & I.L. DILLAMORE: Metalurgia I.
Odlawnictwo, 1979, 5, (2), 257-272.
- 42 I.L. DILLAMORE & H. KATOH: Metal Sci., 1974,
(8), 73-83.
- 43 J. GREWEN, J. HUBER & M. HATHERLY: Metals Forum,
Sept. 1978, 1, (3), 115-122.
- 44 R.D. DOHERTY: Metal Sci., 1974, (8), 132-142.
- 45 F. HAESSNER: "Recrystallisation of Metallic
Materials", Dr. Riederer Verlag GmbH; Stuttgart,
1978.
- 46 R.D. DOHERTY & R.W. CAHN: J. Less Common Metals,
1972, (28), 279-296.
- 47 W.B. HUTCHINSON: Metal Science, 1974, (8),
185-196.

- 48 Y. INOKUTI & R.D. DOHERTY: Acta Met., 1978,
(26), 61-80.
- 49 C.J.E. SMITH & I.L. DILLAMORE: Metal Sci. J.,
1970, (4), 161-167.
- 50 H. TAKECHI, H. KATO & S. NAGASHIMA: Trans. Met.
Soc. AIME, Jan. 1968, (242), 56-65.
- 51 D.J. WILLIS & M. HATHERLY: 4th Intl. Conf. on
Textures, Cambridge, July 1975. (Metals Soc.)
p.48-53.
- 52 I.L. DILLAMORE, P.L. MORRIS, C.J.E. SMITH &
W.B. HUTCHINSON: Proc. Royal Soc. (London),
1972, (A 329), 405-420.
- 53 H. HU: Acta Met., 1962, (10), 1112-1116.
- 54 M. HATHERLY & A.S. MALIN: Scripta Met., 1984,
(18), 449-454.
- 55 W. ÖSTERLE, H. WEVER & A.J. BUNGE: Metal
Science J., July 1983, (17), 330-340.
- 56 T. GLADMAN, I.D. McIVOR & F.B. PICKERING:
J.I.S.I., May 1971, 380-390.
- 57 I.L. DILLAMORE & W.B. HUTCHINSON: Trans. I.S.I.
Japan, Supplement, 1971, (11), 877-883.
- 58 F.J. HUMPHREYS: Acta Met., 1977, (25), 1323-1344.
- 59 E. NES: Metal. I. Odlew, 1979, 5, (2), 209-224.
- 60 H.M. CHAN & F.J. HUMPHREYS: Metal Sci., Nov.
1984, (18), 527-529.
- 61 E. NES: Acta Met., 1976, (24), 391-398.
- 62 U. KÖSTER: Metal Sci., 1974, (8), 151-160.
- 63 E. NES: Scripta Met., 1976, (10), 1025-1028.
- 64 J. HANSEN & H. MECKING: 4th Intl. Conf. on
Texture, Cambridge, July 1975, (Metals Soc.)

- 65 S.P. KEELER: Sheet Metal Ind., May 1971, 357-364.
- 66 S.P. KEELER: Machinery, Apr. 1968, 94-103.
- 67 P.N. RICHARDS: Sheet Metal Ind., Oct. 1981,
784-790.
- 68 G.L. MONTGOMERY: Metals Progress, Sept. 1968,
121-138.
- 69 I.L. DILLAMORE, W.T. ROBERTS & D.V. WILSON:
"Stainless Steels", ISI, 1969, 37-50.
- 70 J.C. WRIGHT: Sheet Metal Ind., Nov. 1965,
814-831.
- 71 A.F. TURNER: Sheet Metal Ind., Jan. 1976, 16-20.
- 72 AMERICAN SOCIETY FOR TESTING METALS: ASTM
E643-78.
- 73 BRITISH STANDARDS INSITUTE: BS 3855-1965.
- 74 O.H. KEMMIS: Sheet Metal Ind., Mar. 1957,
203-208.
- 75 J.M. THORP: Sheet Metal Ind., Feb. 1973, 99-104.
- 76 P.E. THOMAS & J.M. THORP: Sheet Metal Ind.,
June 1974, 338-340.
- 77 D.V. WILSON, B.J. SUNTER & D.F. MARTIN:
Sheet Metal Ind., June 1966, 465-476.
- 78 K.J. BLOM: Sheet Metal Ind., Jan. 1980,
25-29 & 80.
- 79 PECKNER & BERNSTEIN: "Handbook of Stainless
Steels", McGraw Hill.
- 80 AMERICAN SOCIETY FOR TESTING METALS: ASTM
E646-78.
- 81 M. DRIPKE & H.P. WÖRNER; Sheet Metal Ind.,
Feb. 1981, 131-137.

- '82 AMERICAN SOCIETY FOR TESTING METALS:
ASTM E517-74.
- 83 R.L. WHITELEY, D.E. WISE & D.J. BLICKWEDE:
Sheet Metal Ind., May 1961, 349-358.
- 84 D.B. LEWIS & F.B. PICKERING: "Advances in the
Phys. Met. & Application of Steels" - Proc. Intl.
Conf., Liverpool, Sept. 1981, (Metals Soc.).
- 85 R.M. DAVISON: Met. Trans., (6A), Dec. 1975, 2243.
- 86 P.N. RICHARDS: Sheet Metal Ind., Nov. 1981,
913-917.
- 87 S.P. KEELER: Sheet Metal Ind., June 1971,
440-449.
- 88 G.E.G. TUCKER: Acta Met., April 1961, (9), 275.
- 89 R.W. VIETH & R.L. WHITELEY: IDDRG Colloq.,
London, 3rd June 1964, (Inst. Sheet Metal Eng.)
- 90 D.N. LEE & K.H. OH: J. Materials Science, 1985,
(20), 3111-3118.
- 91 R.H. KALTENHAUSER: Metals. Eng. Quarterly,
May 1971, 41-47.
- 92 R.A.E. HOOPER, D.T. LLEWELLYN & V.T. McNEALY:
Sheet Metal Ind., Jan. 1972, 26.
- 93 R.A.E. HOOPER: Sheet Metal Ind., Jan. 1978,
15-22.
- 94 R. CASTRO & R. TRICOT: Metal Treatment and Drop
Forging (M.T.D.F.), Oct. 1964, 401-410.
- 95 R. CASTRO & R. TRICOT: M.T.D.F., Nov. 1964,
436-440.
- 96 R. CASTRO & R. TRICOT: M.T.D.F. Dec. 1964,
469-478 & 491.

- 97 S.R. MEDIRATTA & V. RAMASWAMY: Tool Alloy
Steel, Dec. 1976, 10, (12), 451-461.
- 98 R. TRICOT & R. CASTRO: Metal Treatment, Aug.
1966, 299-310.
- 99 R. TRICOT & R. CASTRO: Metal Treatment,
Sept. 1966, 355-367.
- 100 R. TRICOT & R. CASTRO: Metal Treatment,
Oct. 1966, 401-405.
- 101 T.J. NICHOL, A. DATTA & G. AGGEN: Met. Trans.
Apr. 1980, (11A), 573-585.
- 102 R.F. STEIGERWALD, J.H. DUNDAS, D. REDMOND &
R.M. DAVISON: The Metallurgist & Materials
Technologist, Apr. 1978, 181-189.
- 103 M. TAKEDA, et al: Tetsu-to-Hagane 1977,
63, (5), 622-630 (Translation BISI 17032).
- 104 T. DEVINE & A.M. RITTER: Met. Trans., Aug. 1983,
(14A), 1721-1728.
- 105 A. BALL & J.P. HOFFMAN: Metals Technology,
Dec. 1981, 329-338.
- 106 W.B. HUTCHINSON: Swedish Inst. Metals Research,
Report No. 1M-1727, Jan. 1983.
- 107 K. WETZLAR & M. MOZEK: DEW Technische Berichte,
1970, 10, (2), 188-196.
- 108 H. CHAO: Trans. ASM, 1967, (60), 37-50.
- 109 H. TAKECHI, H. KATO, T. SUNAMI, T. NAKAYAMA:
Trans. Japan Inst. Metals, 1967, (8), 233-239.
- 110 R.N. WRIGHT: Met. Trans. 1972, 3, (1), 83-91.
- 111 H. CHAO: Met. Trans., Apr. 1973, 1183-1186.
- 112 R.N. WRIGHT: Met. Trans., Sept. 1976, (7A),
1385-1388.

- 113 H. CHAO & R.N. WRIGHT: Met. Trans., June 1977,
(8A), 1009-1010.
- 114 K. SUZUKI & S. ASAMI: Trans. Iron & Steel Inst.,
Japan, 1984, (24), 359-364.
- 115 K. SUZUKI, S. ASAMI, K. SUZUKI: Trans. ISIJ,
1984, (24), 1-6.
- 116 T. SAWATANI, K. SHIMIZU, T. NAKAYAMA & T. HIRAI:
Trans. ISIJ, 1978, 18, (11), 686-695.
- 117 Y. NAKAGAWA, T. SAKAMOTO, I. YAMAUCHI, T. YAMAZAKI
& M. UENO: Tetsu-to-Hagane, 1980, (6), 657-666.
- 118 F.R. VALLOIRE, R. PENELLE, J.C. BAVAY: Bull.
Cercle. Étude Metaux, Sept. 1984, 15, (7),
5.5-5.12.
- 119 S.R. GOODMAN & H. HU: Met. Trans., June, 1970,
(1), 1629-1640.
- 120 H. MIYAJI & S. WATANABE: Trans. Nat. Res. Inst.
Metals (Japan), 1980, 22, (1), 1-10.
- 121 H. MIYAJI, S. WATANABE & R. KANEKO: Trans. Nat.
Res. Inst. Metals (Japan), 1979, 21, (4), 155-164.
- 122 M.J. DICKSON & M.J. COOKE: To be published.
- 123 P.N. RICHARDS: J.I.S.I., Oct. 1969, 1333-1339.
- 124 R. GILLANDERS, C. DASARATHY, R.C. HUDD: 4th Intl.
Conf. on Texture, Cambridge, July 1975, 245-254.
- 125 T. SAWATANI, K. SHIMIZU, T. NAKAYAMA & M. MIYOSHI:
Trans. I.S.I. Japan, 1978, 18, (11), 676-685.
- 126 H. MIYAJI & S. WATANABE: Trans. Nat. Res. Inst.
Metals (Japan), 1980, 22, (3), 131-143.
- 127 H. MIYAJI & S. WATANABE: Trans. Nat. Res. Inst.
Metals (Japan), 1981, 23, (1), 1-10.

- 128 J.T. MICHALAK & R.D. SCHOONE: Trans. Met. Soc.
AIME, June 1968, (242), 1149-1160.
- 129 P.R.V. EVANS, J.C. BITCON, & I.F. HUGHES:
J.I.S.I., March, 1969, 331-339.
- 130 R.H. GOODENOW & J.F. HELD: Met. Trans., Sept. 1970
(1), 2507-2515.
- 131 S. MISHRA & C. DÄRMANN: Intl. Metals Reviews,
1982, 27, (6), 307-320.
- 132 A.P. DAVIDSON & D.R.F. WEST: Metal Sci.,
Mar-Apr. 1979, 170-178.
- 133 H. HU: "Recovery & Recrystallisation of Metals"
1963, (London), Gordon & Breech.
- 134 W.B. HUTCHINSON, T.W. WATSON & I.L. DILLAMORE:
J.I.S.I., Nov. 1969, 1479-1483.
- 135 W.B. HUTCHINSON & K. USHIODA: Scand. J.
Metallurgy, 1984, (13), 269-275.
- 136 M.MATSUO, S. HAYAMI & S. NAGASHIMA: Advances in
X-ray Analysis, 1970, (14), 214-230.
- 137 S. KADO, T. YAMAZAKI, T. SAKAMOTO, Y. NAKAGAWA,
S. INOUE, S. IZUMI, T. ASHIURA, & S. UCHIDA:
Trans. I.S.I. Japan, 1979, (19), 315-323.
- 138 J.M. HAUSER, B. BAROUX, H. GIRAUD, Ph. MAITREPIERRE:
Bull. Cercle Étud. Metaux, Sept. 1984, 15,
(7), 7.6-7.14.
- 139 R.M. DAVISON: Met. Trans., Nov. 1974, (5)
2287-2294.
- 140 P.R. MOULD & J.M. GRAY: Met. Trans., Dec. 1972,
(3), 3121-2132.
- 141 I.L. DILLAMORE, H. KATOH & K. HASLAM: Texture,
1974, (1), 151-156.

- 142 M. TAKAHASHI & A. OKAMOTO: Trans. I.S.I. Japan,
1979, (19), 391-400.
- 143 Z. YONG-XIN et al: Acta Metallurgica Sinica,
1978, (3), 292-297 (Translation BISI 18699).
- 144 R.M.S.B. HORTA, D.V. WILSON & W.T. ROBERTS:
J.I.S.I., Jan. 1972, 42-51.
- 145 M.K. ORMAY & P.N. RICHARDS: Trans. Met. Soc. AIME,
Sept. 1969, (245), 2081-2087.
- 146 P. MESSIEN & T. GREDAY: 4th Intl. Conf. on
Texture, Cambridge, 1975, 266-274.
- 147 M. YANTAC, W.T. ROBERTS & D.V. WILSON: Texture,
1972, 1, (1), 71-86.
- 148 D.J. BLICKWEDE: Trans. ASM, 1968, (61), 653-679.
- 149 T.R. THOMSON: 4th Intl. Conf. on Texture,
Cambridge, 1975, 287.
- 150 K.G. BRICKNER & J.A. BERGER: Sheet Metal Ind.,
Jan. 1976, 26-32 & 40.
- 151 K. MIYAKUSU, Y. UEMATSU, K. HOSHINO: IDDRG 13th
Biennial Congress, Melbourne, Australia,
20-24th Feb. 1984.
- 152 D.G. BRANDON: "Modern Techniques in
Metallography", Butterworths, 1966.
- 153 I.S. BRAMMAR & M.A.P. DEWEY: "Specimen
Preparation for Electron Metallography",
(Blackwell Scientific, 1966).
- 154 R.E. SMALLMAN & K.H.G. ASHBEE: "Modern
Metallography", Pergamon, 1969.
- 155 K.W. ANDREWS, D.J. DYSON, & S.R. KEOWN:
"Interpretation of Electron Diffraction Patterns"
(Hilger, 1967).

156

B.J. DUGGAN & R.L. SEGALL: Acta Met.,

April, 1971, (19), 317-320.

TABLE 1MEASUREMENT OF THE INTENSITIES OF IDEAL ORIENTATIONS
FROM {200} POLE FIGURES

$$(I \{hkl\} \langle uvw \rangle = I (\phi + \psi))$$

where $I (\phi + \psi)$ = intensity at inclination ϕ ,
azimuth ψ .

$$I \{100\} \langle 011 \rangle = I (0^\circ)$$

$$I \{110\} \langle 001 \rangle = I (45^\circ + 90^\circ)$$

$$I \{112\} \langle 110 \rangle = I [(35^\circ + 90^\circ) + (40^\circ + 270^\circ)] / 2$$

$$I \{111\} \langle 112 \rangle = I [(55^\circ) + (55^\circ + 180^\circ)] / 2$$

$$I \{111\} \langle 110 \rangle = I [(55^\circ + 90^\circ) + (60^\circ + 270^\circ)] / 2$$

$$I \{554\} \langle 225 \rangle = I [(60^\circ) + (60^\circ + 180^\circ)] / 2$$

$$I \{223\} \langle 962 \rangle = I [(65^\circ + \sim 160^\circ) + (65^\circ + \sim 200^\circ) + \\ (65^\circ + \sim 340^\circ) + (60^\circ + \sim 20^\circ)] / 4$$

$$I \{114\} \langle 841 \rangle = I [(25^\circ + \sim 250^\circ) + (25^\circ + \sim 290^\circ) + \\ (20^\circ + \sim 70^\circ) + (20^\circ + \sim 110^\circ)] / 4$$

TABLE 2

CALCULATION OF THEORETICAL LINE INTENSITIES FOR 17 Cr. STEELS (6)
 (DATA OBTAINED FROM CULLITY (6) AND PEARSONS TABLES FOR X-RAY CRYSTALLOGRAPHY)

{hkl}	$N = h^2 + k^2 + l^2$	$\sin^2 \theta = \frac{\lambda^2}{4a^2}$	$\sin \theta$	θ	$\frac{\sin \theta}{\lambda} (\text{\AA}^{-1})$	Atomic scattering factor f_{Fe}	Structure factor $ F ^2 = 4f^2$	Temp. factor e^{-2M}	Multi-licity factor P	Lorenz Polarisation factor $\left(\frac{1 + \cos^2 2\theta}{\sin^2 \theta \cos \theta} \right)$	Relative Integrated Intensity
(110)	2	0.0306	0.1751	10.081	0.2463	18.4	1354	0.9590	12	62.3614	971705
(200)	4	0.0613	0.2476	14.333	0.3483	15.2	924	0.9196	6	29.8076	151967
(211)	6	0.0919	0.3032	17.649	0.4266	13.1	686	0.8819	24	19.0207	276173
(310)	10	0.1532	0.3914	23.043	0.5508	10.4	433	0.8109	24	10.5049	88523
(222)	12	0.1839	0.4288	25.390	0.6033	9.7	376	0.7777	8	8.4279	19716
(321)	14	0.2145	0.4631	27.589	0.6517	9.1	331	0.7457	48	6.9758	82647
(330)	18	0.2758	0.5251	31.678	0.7389	8.2	269	0.6858	12	5.1178	11330
(411)									24		22659
(420)	20	0.3064	0.5536	33.611	0.7789	7.8	243	0.6576	24	4.5060	17281
(332)	22	0.3371	0.5806	35.490	0.8169	7.5	225	0.6307	24	4.0309	13728

$$I = |F|^2 P \left(\frac{1 + \cos^2 2\theta}{\sin^2 \theta \cos \theta} \right) e^{-2M}, \text{ where } M = \frac{1.15 \times 10^4 \pi}{A \Theta^2} \left[\phi(x) + \frac{x}{4} \right] \left(\frac{\sin \theta}{\lambda} \right)^2$$

A = atomic weight; $x = \frac{\Theta}{T}$ where Θ = Debye temp. (430°K for Fe)

Lattice parameter (a) for Fe, 17Cr = 2.8709Å; λ (Mo K) = 0.7107Å

TABLE 3

(A) CHEMICAL COMPOSITIONS OF STEELS USED IN THE PRESENT WORK

Element (wt. %)	430 (17 Cr)	430 Ti (~17 Cr, 0.5 Ti)	430 Ti (~17 Cr, 0.4 Ti)	430 Ti (~17 Cr, 0.3 Ti)	409 Ti (~12 Cr, 0.5 Ti)
Carbon	0.050	0.019	0.016	0.012	0.030
Silicon	0.23	0.33	0.43	0.43	0.54
Manganese	0.34	0.39	0.42	0.40	0.39
Phosphorus	0.023	0.016	0.017	0.014	0.027
Sulphur	0.002	0.002	0.003	0.003	0.003
Chromium	16.36	15.40	15.55	16.50	11.30
Molybdenum	0.02	0.02	0.08	0.02	0.43
Nickel	0.12	0.14	0.17	0.12	0.27
Copper	0.050	0.03	0.10	0.04	0.050
Aluminium	0.006	0.048	0.031	0.034	0.047
Titanium	0.010	0.52	0.41	0.31	0.46
Niobium	0.010	<0.01	0.01	<0.01	0.010
Nitrogen	0.027	0.010	0.015	0.017	0.009
Boron	0.001	<0.0005	0.0005	<0.0005	0.001
Cobalt	0.02	-	-	0.025	-

(B) HOT ROLLING TEMPERATURES

Steel	Initial (Slab) Rolling Temperature (°C)	Finishing Temperature (°C)
430	~ 1200° C	~900° C
430 Ti	~ 1100° C	~ 900° C
409	~ 1150° C	~930° C

TABLE 4

SUMMARY OF MICROSTRUCTURAL FEATURES IN 430 (17 Cr,
0.077 (C+N)) STEEL

Feature	Observation
Minimum recrystallisation treatment for heavily cold worked sheet.	$\frac{1}{2}$ hr. at 750°C
Minimum recrystallisation treatment for hot rolled strip.	$\frac{1}{2}$ hr. at 800°C (except for a few persistent grains at centre).
Grain growth	Slow above 900°C Rapid above 1200°C
Temperature range of ($\alpha + \gamma$) phase field.	$\geq 900^{\circ}\text{C}$ but $< 1250^{\circ}\text{C}$
Grain size after hot rolling and annealing. (a) Heating rate $\sim 5000^{\circ}\text{C hr}^{-1}$ (i) $800-900^{\circ}\text{C}$, AC (ii) 1000°C , AC + temper (iii) 1200°C , WQ + temper (iv) 1250°C , WQ + temper (b) Heating rate = $50^{\circ}\text{C hr}^{-1}$ (v) 850°C , FC (vi) 1000°C , FC	 $\sim 18\mu\text{m}$ (ASTM 8.5) $\sim 25\mu\text{m}$ (ASTM 7.5) $\sim 54\mu\text{m}$ (ASTM 5) $1000\mu\text{m}$ (1mm) - coarser than ASTM 00 $\sim 20\mu\text{m}$ (ASTM 8) $\sim 38\mu\text{m}$ (ASTM 6)
Grain size after cold rolling and annealing for $\frac{1}{2}$ hr. at 900°C , AC (Heating rate $\sim 5000^{\circ}\text{C hr}^{-1}$)	$11 - 14 \mu\text{m}$ (ASTM 9.5-9) Grains not equiaxed
Grain size after cold rolling and annealing for $\frac{1}{2}$ hr. at 1000°C AC and temper (Heating rate $\sim 5000^{\circ}\text{C hr}^{-1}$)	$17 - 23 \mu\text{m}$ (ASTM 8.5-7.5)

TABLE 5

SUMMARY OF MICROSTRUCTURAL FEATURES IN 430 Ti
(17 Cr, 0.5 Ti, 0.029 (C+N)) STEEL

Feature	Observations
Minimum recrystallisation treatment for heavily cold worked sheet	$\frac{1}{2}$ hr. at 800°C
Minimum recrystallisation treatment for hot rolled strip	$\frac{1}{2}$ hr. at 800°C
Grain growth	Rapid above 900°C
Temperature range of ($\alpha + \delta$) phase field	No gamma present at any temperature
Grain size after hot rolling and annealing. (a) (Heating rate $\sim 5000^{\circ}\text{C hr}^{-1}$) (i) 800-900°C, AC (ii) 1000°C, AC or FC (b) (Heating rate = 50°C hr ⁻¹) (iii) 850°C, FC (iv) 1000°C, AC	 $\sim 40\mu\text{m}$ (ASTM 6) $\sim 125\mu\text{m}$ (ASTM 2.5) $\sim 45\mu\text{m}$ (ASTM 5.5) $\sim 156\mu\text{m}$ (ASTM 2.0)
Grain size after cold rolling and annealing. (a) <u>Rapid annealing</u> (Heating rate $\sim 5000^{\circ}\text{C hr}^{-1}$, AC) (i) 800°C (ii) 900°C (iii) 950°C (b) <u>Batch annealing</u> (Heating rate = 50°C hr ⁻¹ , AC) (iv) 900°C	Grains equiaxed 15-25 μm (ASTM 8.5-7.5) 15-28 μm , (ASTM 8.5-7) 45-95 μm (ASTM 5.5-3.5) 26-31 μm (ASTM 7.25-6.5)

TABLE 6

SUMMARY OF MICROSTRUCTURAL FEATURES IN 430 Ti
(17 Cr, 0.3 Ti and ~17 Cr, 0.4 Ti) STEELS

Feature	Observations	
	0.3% Ti Steel	0.4% Ti Steel
Minimum re-crystallisation treatment for heavily cold worked sheet	$\frac{1}{2}$ hr. at ~ 750°C	$\frac{1}{2}$ hr at ~ 800°C
Grain growth	Rapid above ~ 850°C	Rapid above ~ 900°C
Temperature range of ($\alpha + \gamma$) phase field	No gamma present at any temperature	No gamma present at any temperature
Grain size after hot rolling and annealing at 850°C	40 - 50 μm (ASTM 6-5)	40 - 50 μm (ASTM 6-5)
Grain size after cold rolling and annealing at 900°C	63 - 71 μm (ASTM 4.5)	23 - 28 μm (ASTM 7.5-7)

TABLE 7

MICROSTRUCTURAL FEATURES IN 409
(12% Cr, 0.5 Ti, 0.039 (C+N)) STEEL

Feature	Observation
Minimum recrystallisation treatment for heavily cold worked sheet.	$\frac{1}{4}$ hr at 750°C
Minimum recrystallisation treatment for hot rolled strip	$\frac{1}{4}$ hr. at 850°C
Grain growth	Rapid above 900°C
Temperature of range of ($\alpha + \gamma$) phase field	No gamma present at any temperature
Grain size after hot rolling and annealing (Heating rate $\sim 5000^{\circ}\text{C hr}^{-1}$, AC) (i) 800-900°C (ii) 1000°C	$\sim 55\mu\text{m}$ (ASTM 5) $\sim 140\mu\text{m}$ (ASTM 2.5)
Grain size after cold rolling and annealing (Heating rate $\sim 5000^{\circ}\text{C hr}^{-1}$, AC) (i) 900°C (ii) 950°C	Grains equiaxed 15-20 μm (ASTM 8.5-8) 40-55 μm (ASTM 6-5)

TABLE 8

SUMMARY OF TEXTURES OF 5mm THICK HOT ROLLED AND
HOT-ROLLED + ANNEALED 430 (17 Cr, 0.077 (C+N)) STRIP

Position	Textures
Surface	<p><u>As hot-rolled</u> :- Mainly $\sim\{110\}$ $\langle 001 \rangle$ <u>After annealing $\geq 650^\circ\text{C}$</u> :- Mainly $\sim\{110\}$ $\langle 001 \rangle$</p>
Quarter plane (1.25mm below surface)	<p><u>As hot-rolled</u> :- Mainly $\sim\{100\}$ $\langle 011 \rangle$ + minor $\sim\{112\}$ $\langle 110 \rangle$, $\sim\{554\}$ $\langle 225 \rangle$ and $\sim\{110\}$ $\langle 001 \rangle$ <u>After annealing $\geq 650^\circ\text{C}$</u> :- Mainly $\sim\{100\}$ $\langle 011 \rangle$ + minor $\sim\{110\}$ $\langle 001 \rangle$</p>
Midplane (2.5mm below surface)	<p><u>As hot-rolled</u> :- Mainly $\sim\{100\}$ $\langle 011 \rangle$ + minor $\sim\{112\}$ $\langle 110 \rangle$ and $\sim\{554\}$ $\langle 225 \rangle$ <u>After annealing $\leq 850^\circ\text{C}$</u> :- Mainly $\sim\{100\}$ $\langle 011 \rangle$ + minor $\sim\{112\}$ $\langle 110 \rangle$ and $\sim\{554\}$ $\langle 225 \rangle$ <u>After annealing $\geq 1000^\circ\text{C}$</u> :- Mainly $\sim\{100\}$ $\langle uvw \rangle$ + minor $\sim\{112\}$ $\langle 110 \rangle$.</p>

TABLE 9

SUMMARY OF TEXTURES OF 4mm THICK HOT ROLLED AND
HOT-ROLLED + ANNEALED 430 Ti (17 Cr, 0.5 Ti, 0.029 (C+N))
STRIP

Position	Textures
Surface	<p><u>As hot-rolled</u> :- Mainly $\sim \{110\} \langle 001 \rangle$ <u>After annealing</u> :- Mainly $\sim \{110\} \langle 001 \rangle$</p>
Quarter plane (1mm below surface)	<p><u>As hot-rolled</u> :- Mainly $\sim \{100\} \langle 011 \rangle$ + minor $\sim \{554\} \langle 225 \rangle$, $\sim \{112\} \langle 110 \rangle$.</p> <p><u>After annealing < 800°C</u> :- Mainly $\sim \{100\} \langle 011 \rangle$ + minor $\{554\} \langle 225 \rangle$, $\sim \{112\} \langle 110 \rangle$.</p> <p><u>After annealing 850-1000°C</u> :- Mainly $\{100\} \langle uvw \rangle$ + a minor $\{110\} \langle 001 \rangle$.</p>
Midplane (2mm below surface)	<p><u>As hot-rolled</u> :- Mainly $\sim \{100\} \langle 011 \rangle$, $\sim \{112\} \langle 110 \rangle$ + a minor $\sim \{554\} \langle 225 \rangle$ + spread between.</p> <p><u>After annealing < 800°C</u> :- Mainly $\sim \{100\} \langle 011 \rangle$ + minor $\sim \{112\} \langle 110 \rangle$ and $\sim \{554\} \langle 225 \rangle$ + spread between.</p> <p><u>After annealing 850-1000°C</u> :- Mainly $\sim \{100\} \langle uvw \rangle$ + minor $\sim \{554\} \langle 225 \rangle$ + spread which includes $\sim \{110\} \langle 001 \rangle$.</p>

TABLE 10

SUMMARY OF TEXTURES OF 4mm THICK HOT ROLLED AND HOT-ROLLED + ANNEALED 409 (12 Cr, 0.5 Ti, 0.039 (C+N)) STRIP

Position	Textures
Surface	<p><u>As hot-rolled</u> :- Mainly $\sim\{110\}$ $\langle 001 \rangle$</p> <p><u>After annealing at 850-1000°C</u> :-</p> <p>Mainly $\sim\{110\}$ $\langle 001 \rangle$</p>
Quarter plane (1mm below surface)	<p><u>As hot-rolled</u> :- Mainly $\sim\{110\}$ $\langle 001 \rangle$</p> <p><u>After annealing 850-1000°C</u> :-</p> <p>Mainly $\sim\{110\}$ $\langle 001 \rangle$</p>
Midplane (2mm below surface)	<p><u>As hot-rolled</u> :- Mainly $\sim\{100\}$ $\langle 011 \rangle$ and $\sim\{112\}$ $\langle 110 \rangle$ + a minor $\sim\{554\}$ $\langle 225 \rangle$</p> <p><u>After annealing 850-1000°C</u> :-</p> <p>Mainly $\sim\{100\}$ $\langle 011 \rangle$ and $\{112\}$ $\langle 110 \rangle$ + minor $\sim\{554\}$ $\langle 225 \rangle$ and $\sim\{110\}$ $\langle 001 \rangle$.</p>

TABLE 11

SUMMARY OF COLD ROLLING TEXTURES OF 430 (17 Cr, 0.077 (C+N)) STEEL

Cold Rolling Reduction	Annealing treatment prior to cold rolling	Cold rolling textures
50-60% RA	As hot rolled or annealed 650-1200°C	Mainly $\sim\{110\}\langle 001\rangle$ + minor $\sim\{100\}\langle 011\rangle$
70% RA	As hot rolled or annealed 650-850°C	Mainly $\sim\{110\}\langle 001\rangle$ and $\sim\{100\}\langle 011\rangle$ + spread
	Annealed 1000°C - 1200°C	Mainly $\sim\{100\}\langle 011\rangle$ + minor $\sim\{554\}\langle 225\rangle$ and $\sim\{110\}\langle 001\rangle$
80% RA	As hot rolled or annealed 650°C	Mainly $\sim\{100\}\langle 011\rangle$ + minor $\sim\{110\}\langle 001\rangle$ and $\sim\{112\}\langle 110\rangle$
	Annealed 750-850°C	Mainly $\sim\{100\}\langle 011\rangle$ + minor $\sim\{110\}\langle 001\rangle$ + spread towards $\sim\{112\}\langle 110\rangle$
	Annealed 1000°C - 1200°C	Mainly $\sim\{100\}\langle 011\rangle$ + minor $\sim\{554\}\langle 225\rangle$ and $\sim\{110\}\langle 001\rangle$
90-95% RA	As hot rolled or annealed 650-1200°C	Spread between $\sim\{100\}\langle 011\rangle$, $\sim\{111\}\langle 112\rangle$ and $\sim\{112\}\langle 110\rangle$

TABLE 12

SUMMARY OF COLD ROLLING TEXTURES OF 430 Ti
(17 Cr, 0.5 Ti, 0.029 (C+N)) STEEL

Cold rolling reduction	Annealing treatment prior to cold rolling	Cold rolling textures
50% RA	As hot rolled or annealed 750-1000°C	Mainly $\sim \{110\} \langle 001 \rangle$ + minor $\sim \{100\} \langle 011 \rangle$
60% RA	As hot rolled or annealed 750-1000°C	Mainly $\sim \{110\} \langle 001 \rangle$ + minor $\sim \{100\} \langle 011 \rangle$ and $\sim \{554\} \langle 225 \rangle$
70% RA	As hot rolled	Mainly $\sim \{100\} \langle 011 \rangle$ + minor $\sim \{554\} \langle 225 \rangle$ + spread.
	Annealed 750-850°C, AC (Heating rate $\sim 5000^\circ\text{C hr}^{-1}$)	Mainly $\sim \{100\} \langle 011 \rangle$ + minor $\sim \{554\} \langle 225 \rangle$ and $\sim \{110\} \langle 001 \rangle$
	Annealed 1000°C, AC (Heating rate $\sim 5000^\circ\text{C hr}^{-1}$)	Mainly $\sim \{111\} \langle 112 \rangle$ + minor $\sim \{100\} \langle 011 \rangle$ + spread
	Annealed 850°C, FC (Heating rate = 50°C hr^{-1})	Mainly $\sim \{110\} \langle 001 \rangle$ + minor $\sim \{100\} \langle 011 \rangle$ and $\sim \{554\} \langle 225 \rangle$
80% RA	As hot rolled or annealed 750-850°C, AC (Heating rate $\sim 5000^\circ\text{C hr}^{-1}$)	Mainly $\sim \{100\} \langle 011 \rangle$ and $\sim \{554\} \langle 225 \rangle$ + minor $\sim \{112\} \langle 110 \rangle$
	Annealed 1000°C, AC (Heating rate $\sim 5000^\circ\text{C hr}^{-1}$)	Mainly $\sim \{111\} \langle 112 \rangle$ + minor $\sim \{100\} \langle 011 \rangle$
	Annealed 850°C, FC (Heating rate = 50°C hr^{-1})	Mainly $\sim \{554\} \langle 225 \rangle$ + minor $\sim \{100\} \langle 011 \rangle$ and $\sim \{110\} \langle 001 \rangle$
90% RA	As hot rolled or annealed 750-1000°C	Spread between $\sim \{100\} \langle 011 \rangle$, and $\sim \{112\} \langle 110 \rangle$, and $\sim \{111\} \langle 112 \rangle$
95% RA	As hot rolled	Spread between $\sim \{100\} \langle 011 \rangle$ and $\sim \{112\} \langle 110 \rangle$
	Annealed 750-1000°C	Spread between $\sim \{100\} \langle 011 \rangle$, and $\sim \{112\} \langle 110 \rangle$, and $\sim \{111\} \langle 112 \rangle$

TABLE 13

SUMMARY OF COLD ROLLING TEXTURES OF 430 Ti
(17% Cr, 0.4 Ti, 0.031 (C+N)) STEEL

Cold rolling reduction	Commercial Annealing treatment prior to cold rolling	Cold rolling textures
60% .RA	Rapid 900°C anneal or Batch 780°C anneal	Mainly $\sim\{110\} \langle 011 \rangle$ + minor $\sim\{100\} \langle 011 \rangle$ and $\sim\{554\} \langle 225 \rangle$
70% RA	Rapid 900°C anneal or Batch 780°C anneal	Mainly $\sim\{100\} \langle 011 \rangle$ + minor $\sim\{554\} \langle 225 \rangle$ + spread
80% RA	Rapid 900°C anneal or Batch 780°C anneal	Mainly $\sim\{100\} \langle 011 \rangle$ + $\sim\{554\} \langle 225 \rangle$ + spread.
90% - 95% RA	Rapid 900°C anneal or Batch 780°C anneal	Spread between $\sim\{100\} \langle 011 \rangle$, $\sim\{112\} \langle 110 \rangle$ and $\sim\{111\} \langle 112 \rangle$

TABLE 14

SUMMARY OF COLD ROLLING TEXTURES OF 430 Ti
(17 Cr, 0.3 Ti, 0.029 (C+N)) STEEL

Cold rolling reduction	Annealing treatment prior to cold rolling	Cold rolling textures
60% RA	Rapid 850°C anneal or Batch 850°C anneal	Mainly $\sim \{110\} \langle 001 \rangle$ + minor $\sim \{100\} \langle 011 \rangle$ and $\sim \{554\} \langle 225 \rangle$
70% RA	Rapid 850°C anneal or Batch 850°C anneal	Mainly $\sim \{554\} \langle 225 \rangle$ + minor $\sim \{110\} \langle 001 \rangle$ and $\sim \{100\} \langle 011 \rangle$
80% RA	Rapid 850°C anneal or Batch 850°C anneal	Mainly $\{100\} \langle 011 \rangle$ + $\{554\} \langle 225 \rangle$ + spread.
90% - 95% RA	Rapid 850°C anneal or Batch 850°C anneal	Spread between $\{100\} \langle 011 \rangle$, $\{112\} \langle 110 \rangle$, and $\{111\} \langle 112 \rangle$

TABLE 15

SUMMARY OF COLD ROLLING TEXTURES OF 409
 (~ 12 Cr, 0.5 Ti, 0.039 (C+N)) STEEL

Cold rolling reduction	Annealing treatment prior to cold rolling	Cold rolling textures
70% RA	As hot rolled or annealed 750-1000°C, AC (Heating rate ~5000°C hr ⁻¹ , AC)	Mainly $\sim\{110\} \langle 001 \rangle$ + minor $\sim\{554\} \langle 225 \rangle$ + spread between.
80% RA	As hot rolled or annealed 750-850°C, AC (Heating rate ~5000°C hr ⁻¹).	Mainly $\sim\{554\} \langle 225 \rangle$ and $\sim\{100\} \langle 011 \rangle$ + minor $\sim\{110\} \langle 001 \rangle$.
	Annealed 1000°C, AC (Heating rate ~5000°C hr ⁻¹)	Mainly $\sim\{554\} \langle 225 \rangle$ + minor $\sim\{100\} \langle 011 \rangle$ and $\sim\{110\} \langle 001 \rangle$.
90% RA	As hot rolled or annealed 750-850°C, AC (Heating rate ~5000°C hr ⁻¹)	Mainly $\sim\{100\} \langle 011 \rangle$ and $\{111\} \langle 112 \rangle$ + minor $\{112\} \langle 110 \rangle$ + spread between.
	Annealed 1000°C, AC (Heating rate ~5000°C hr ⁻¹)	Mainly $\sim\{111\} \langle 112 \rangle$ + minor $\sim\{100\} \langle 011 \rangle$
95% RA	As hot rolled	Spread between $\sim\{100\} \langle 011 \rangle$ and $\sim\{112\} \langle 110 \rangle$
	Annealed 750-1000°C, AC (Heating rate ~5000°C hr ⁻¹)	Spread between $\sim\{100\} \langle 011 \rangle$, $\sim\{111\} \langle 112 \rangle$ and $\sim\{112\} \langle 110 \rangle$

SUMMARY OF PRIMARY RECRYSTALLISATION TEXTURES OF
430 (17 Cr, 0.077 (C+N)) STEEL

(Hot band condition = as hot rolled, or hot rolled and
'rapid' annealed 650-850°C)

Cold rolling reduction	Temperature of rapid final annealing treatment	Recrystallisation textures
70% RA	800°C	Mainly $\sim\{110\}$ $\langle 001 \rangle$ and $\sim\{100\}$ $\langle uvw \rangle$ (especially $\sim\{100\}$ $\langle 001 \rangle$).
	900°C	Mainly $\sim\{114\}$ $\langle uvw \rangle$ + minor $\sim\{110\}$ $\langle 001 \rangle$
	1000°C	Mainly $\sim\{114\}$ $\langle 841 \rangle$ + minor $\sim\{110\}$ $\langle 001 \rangle$
80% RA	800°C	Mainly $\sim\{110\}$ $\langle 001 \rangle$ + $\sim\{114\}$ $\langle uvw \rangle$ + spread.
	900°C	Mainly $\{114\}$ $\langle 841 \rangle$ + minor $\{110\}$ $\langle 001 \rangle$
	1000°C	Mainly $\sim\{114\}$ $\langle 841 \rangle$ + minor $\sim\{110\}$ $\langle 001 \rangle$ and $\sim\{100\}$ $\langle uvw \rangle$
90% RA	800°C	Spread between $\sim\{114\}$ $\langle uvw \rangle$ and $\sim\{100\}$ $\langle uvw \rangle$
	900°C	Mainly $\sim\{114\}$ $\langle 841 \rangle$ + $\sim\{223\}$ $\langle 962 \rangle$ in a spread
	1000°C	Mainly spread between $\sim\{114\}$ $\langle 841 \rangle$ and $\sim\{223\}$ $\langle 962 \rangle$
95% RA	800°C	Spread between $\sim\{114\}$ $\langle 841 \rangle$ and $\sim\{223\}$ $\langle 962 \rangle$ + $\{100\}$ $\langle uvw \rangle$
	900°C	Spread between $\sim\{114\}$ $\langle 841 \rangle$ and $\sim\{223\}$ $\langle 962 \rangle$ + $\sim\{100\}$ $\langle uvw \rangle$
	1000°C	Spread between $\sim\{114\}$ $\langle 841 \rangle$ and $\sim\{223\}$ $\langle 962 \rangle$ + $\sim\{100\}$ $\langle uvw \rangle$

TABLE 17

SUMMARY OF PRIMARY RECRYSTALLISATION TEXTURES OF
430 (17 Cr, 0.077 (C+N)) STEEL

(Final annealing treatment $\frac{1}{2}$ hr at 900°C, AC.
 Heating rate $\sim 5000^\circ\text{C hr}^{-1}$)

Cold rolling reduction	Annealing treatment prior to cold rolling	Recrystallisation textures
50-60% RA	As hot rolled or annealed 650-1000°C, AC (Heating rate $\sim 5000^\circ\text{C hr}^{-1}$)	Weak textures $\sim \{110\} \langle 001 \rangle +$ $\sim \{114\} \langle uvw \rangle +$ spread
	Annealed 1200°C, WQ + temper (Heating rate $\sim 5000^\circ\text{C hr}^{-1}$), or annealed 850-1000°C, FC (Heating rate = 50°C hr ⁻¹)	Weak textures $\sim \{110\} \langle 001 \rangle +$ $\sim \{100\} \langle uvw \rangle +$ spread between
70-80% RA	As hot rolled or annealed 650-850°C, AC (Heating rate $\sim 5000^\circ\text{C hr}^{-1}$)	Mainly $\sim \{114\} \langle 841 \rangle$ in a $\sim \{114\} \langle uvw \rangle$ spread
	Annealed 1000-1200°C, AC or WQ + temper (Heating rate $\sim 5000^\circ\text{C hr}^{-1}$)	Mainly $\sim \{114\} \langle 841 \rangle$, + $\sim \{110\} \langle 001 \rangle +$ spread.
	Annealed 850-1000°C, FC (Heating rate = 50°C hr ⁻¹)	Mainly $\sim \{100\} \langle uvw \rangle$ + $\sim \{110\} \langle 001 \rangle +$ spread
90% RA	As hot rolled or annealed 650-1000°C, AC (Heating rate $\sim 5000^\circ\text{C hr}^{-1}$)	Mainly $\sim \{114\} \langle 841 \rangle$ and $\sim \{223\} \langle 962 \rangle$ in a spread
	Annealed 850-1000°C, FC (Heating rate = 50°C hr ⁻¹)	Mainly $\sim \{114\} \langle 841 \rangle$ + spread between $\sim \{111\} \langle 110 \rangle$ and $\sim \{554\} \langle 225 \rangle$, which includes $\sim \{223\} \langle 962 \rangle$
	Annealed 1200°C, WQ + temper (Heating rate $\sim 5000^\circ\text{C hr}^{-1}$)	Mainly $\sim \{114\} \langle uvw \rangle$ and $\sim \{111\} \langle 110 \rangle +$ minor $\sim \{110\} \langle 001 \rangle$ + spread.
95% RA	As hot rolled or annealed 650-1000°C	Spread between $\sim \{114\} \langle 841 \rangle$ and $\sim \{223\} \langle 962 \rangle +$ $\sim \{100\} \langle uvw \rangle$.
	Annealed 1200°C, WQ + temper (Heating rate $\sim 5000^\circ\text{C hr}^{-1}$)	Spread between $\sim \{114\} \langle 841 \rangle$, $\sim \{223\} \langle 962 \rangle$ and $\sim \{111\} \langle 110 \rangle$.

TABLE 18

SUMMARY OF PRIMARY RECRYSTALLISATION TEXTURES OF 430 (17 Cr, 0.077 (C+N)) STEEL (Final annealing treatment 1 hr at 900°C, FC., Heating rate = 50°C hr⁻¹)

Cold rolling reduction	Annealing treatment prior to cold rolling	Recrystallisation textures
50-60% RA	As hot rolled or annealed 650-1000°C, AC (Heating rate ~ 5000°C hr ⁻¹)	Weak textures. ~{110} <001> + ~{114} <uvw> + spread.
	Annealed 1200°C, WQ + temper (Heating rate ~ 5000°C hr ⁻¹) or annealed 850-1000°C, FC (Heating rate = 50°C hr ⁻¹)	Weak textures. ~{110} <001> + ~{100} <uvw> + spread between
70-80% RA	As hot rolled or annealed 650-850°C, AC (Heating rate ~ 5000°C hr ⁻¹)	Mainly ~{114} <841> in a ~{114} <uvw> spread.
	Annealed 1000-1200°C, AC or WQ + temper (Heating rate ~ 5000°C hr ⁻¹)	Mainly ~{114} <841> + ~{110} <001> + spread
	Annealed 850-1000°C, FC (Heating rate = 50°C hr ⁻¹)	Mainly ~{100} <uvw> + ~{110} <001> + spread.
90% RA	As hot rolled	Mainly ~{114} <841> and ~{223} <962> in a spread.
	Annealed 850-1200°C, AC or WQ + temper (Heating rate ~ 5000°C hr ⁻¹)	Mainly ~{114} <uvw> and ~{111} <110> + minor ~{110} <001> + spread.
	Annealed 850-1000°C, FC (Heating rate = 50°C hr ⁻¹)	Mainly ~{114} <841> + spread between ~{111} <110> and ~{554} <225>, which includes ~{223} <962>
95% RA	As hot rolled	~{100} <uvw> + spread between ~{114} <841> and ~{223} <962> .
	Annealed 850°C	Mainly ~{100} <uvw> + spread between ~{114} <841> , ~{223} <962> and ~{554} <225> .
	Annealed 1000°C	Spread between ~{111} <110> and ~{554} <225> , + ~{100} <uvw> spread towards ~{114} <841>

TABLE 19

SUMMARY OF PRIMARY RECRYSTALLISATION TEXTURES OF 430 Ti (17 Cr, 0.5 Ti, 0.029 (C+N)) STEEL. (Final annealing treatment 1 hr. at 900°C, AC. Heating rate ~ 5000°C hr⁻¹)

Cold rolling reduction	Annealing treatment prior to cold rolling	Recrystallisation textures
50-60% RA	As hot rolled, or annealed 750-850°C, AC. (Heating rate ~ 5000°C hr ⁻¹)	Mainly ~{110} <00> + minor ~{554} <225> and ~{100} <01> .
	Annealed 1000°C, AC (Heating rate ~ 5000°C hr ⁻¹)	Mainly ~{110} <00> + minor ~{554} <225> .
	Annealed 850°C, FC (Heating rate = 50°C hr ⁻¹)	Mainly ~{110} <00> + spread towards ~{554} <225> .
70% RA	As hot rolled, or annealed 750°C, AC (Heating rate ~ 5000°C hr ⁻¹)	Mainly ~{554} <225> and ~{100} <01> + minor ~{110} <00> .
	Annealed 850-1000°C, AC or FC, (Heating rate = 50°C hr ⁻¹ or ~ 5000°C hr ⁻¹)	Mainly ~{110} <00> and ~{554} <225> + minor ~{100} <01> .
80% RA	As hot rolled or annealed 750°C, AC (Heating rate ~ 5000°C hr ⁻¹)	Mainly ~{554} <225> and ~{100} <01> + minor ~{223} <962> .
	Annealed 850°C, AC (Heating rate ~ 5000°C hr ⁻¹)	Mainly ~{554} <225> + minor ~{100} <01> .
	Annealed 850-1000°C, FC (Heating rate = 50°C hr ⁻¹ or ~ 5000°C hr ⁻¹)	Mainly ~{554} <225>
	Annealed 1000°C, AC (Heating rate ~ 5000°C hr ⁻¹ or ~ 50°C hr ⁻¹)	Mainly ~{110} <00> and ~{554} <225>
90% RA	As hot rolled or annealed 750°C, AC (Heating rate ~ 5000°C hr ⁻¹)	Mainly ~{223} <962> + minor ~{100} <01> and ~{554} <225>
	Annealed 850-1000°C, AC or FC, (Heating rate = 50°C hr ⁻¹ or ~ 5000°C hr ⁻¹)	Mainly ~{554} <225> spread towards ~{223} <962> + minor ~{100} <01>
95% RA	As hot rolled or annealed 750-850°C	Mainly ~{223} <962>
	Annealed 1000°C	Mainly ~{223} <962> and ~{554} <225> .

TABLE 20

SUMMARY OF PRIMARY RECRYSTALLISATION TEXTURES OF 430 Ti
(17 Cr, 0.5 Ti, 0.029 (C+N)) STEEL. (Final annealing
treatment 1 hr. at 900°C, FC. Heating rate = 50°C hr⁻¹)

Cold rolling reduction	Annealing treatment prior to cold rolling	Recrystallisation textures
50-60% RA	As hot rolled or annealed 750-850°C, AC (Heating rate ~ 5000°C hr ⁻¹)	Mainly ~ {110} <00> + minor ~ {554} <225> and ~ {100} <011>
	Annealed 1000°C, AC (Heating rate ~ 5000°C hr ⁻¹)	Mainly ~ {110} <001> + minor ~ {554} <225>
	Annealed 850°C, FC (Heating rate = 50°C hr ⁻¹)	Mainly ~ {110} <001> + spread towards ~ {554} <225>
70% RA	As hot rolled	Mainly ~ {554} <225>
	Annealed 850-1000°C AC (Heating rate ~ 5000°C hr ⁻¹) or, annealed 850°C, FC (Heating rate = 50°C hr ⁻¹)	Mainly ~ {110} <001> and ~ {554} <225>
80% RA	As hot rolled or annealed 850°C, AC (Heating rate ~ 5000°C hr ⁻¹) or annealed 850°C, FC (Heating rate = 50°C hr ⁻¹)	Mainly ~ {554} <225> + minor ~ {100} <011>
	Annealed 1000°C, AC (Heating rate ~ 5000°C hr ⁻¹)	Mainly ~ {554} <225> + minor ~ {110} <001>
90% RA	As hot rolled	Mainly ~ {223} <962> and ~ {554} <225> + minor ~ {100} <011>
	Annealed 850°C, AC (Heating rate ~ 5000°C hr ⁻¹) or, annealed 850°C, FC (Heating rate = 50°C hr ⁻¹)	Mainly ~ {554} <225> and ~ {223} <962> + minor ~ {100} <011>
	Annealed 1000°C, AC (Heating rate ~ 5000°C hr ⁻¹)	Mainly ~ {554} <225> spread towards ~ {223} <962>
95% RA	As hot rolled or annealed 850°C	Mainly ~ {223} <962> + minor ~ {100} <011>
	Annealed 1000°C, AC (Heating rate ~ 5000°C hr ⁻¹)	Mainly ~ {223} <962> + minor ~ {554} <225>

TABLE 21

SUMMARY OF PRIMARY RECRYSTALLISATION TEXTURES OF 430 Ti
 (~17Cr, 0.4 Ti, 0.031 (C+N)) STEEL. (Final annealing
 treatment = $\frac{1}{2}$ hr. at 900°C, AC. Heating rate $\sim 5000^\circ\text{C hr}^{-1}$)

Cold rolling reduction	Annealing treatment prior to cold rolling	Recrystallisation textures
60% RA	Commercial line anneal (nominally 2 mins. $\sim 900^\circ\text{C}$)	Mainly $\sim\{110\} \langle 001 \rangle$ + minor $\sim\{554\} \langle 225 \rangle$ and weak $\sim\{100\} \langle uvw \rangle$
	Commercial batch anneal at $\sim 780^\circ\text{C}$	Mainly $\sim\{554\} \langle 225 \rangle$, + minor $\sim\{110\} \langle 001 \rangle$ and $\sim\{100\} \langle uvw \rangle$
70% RA	Line) or Batch)	Mainly $\sim\{554\} \langle 225 \rangle$ + minor $\sim\{110\} \langle 001 \rangle$ and $\sim\{100\} \langle uvw \rangle$ + spread between
80% RA	Line) or Batch)	Mainly $\sim\{554\} \langle 225 \rangle$ + spread + minor $\sim\{100\} \langle uvw \rangle$
90% RA	Line) Batch)	Mainly $\sim\{554\} \langle 225 \rangle$ + minor $\sim\{223\} \langle 962 \rangle$
95% RA	Line) Batch)	Mainly $\sim\{223\} \langle 962 \rangle$

TABLE 22

SUMMARY OF PRIMARY RECRYSTALLISATION TEXTURES OF 430 Ti
 (~17 Cr, 0.4 Ti, 0.031 (C+N)) STEEL. (Final annealing-1)
 treatment 1 hr. at 900°C, FC,. Heating rate = 50° hr⁻¹)

Cold rolling reduction	Annealing treatment prior to cold rolling	Recrystallisation textures
60% RA	Commercial 'Line' anneal at ~900°C) or Commercial batch anneal at ~780°C)	Mainly ~{110} <001> spread towards ~{554} <225>
70% RA	Line or Batch)	Mainly ~{554} <225> + minor ~{100} <uvw> + spread
80% RA	Line Batch)	Mainly ~{554} <225> + minor ~{100} <uvw> + spread
90% RA	Line	Mainly ~{554} <225> + minor ~{100} <uvw> + spread towards ~{223} <962>
	Batch	Mainly ~{554} <225> + minor ~{223} <962> and ~{100} <uvw>
95% RA	Line	Mainly ~{223} <962>
	Batch	Mainly ~{223} <962> + minor ~{100} <uvw>

TABLE 23

SUMMARY OF PRIMARY RECRYSTALLISATION TEXTURES OF 430 Ti
 (~17 Cr, 0.3 Ti, 0.029 (C+N)) STEEL. (Final annealing
 treatment = $\frac{1}{2}$ hr at 900°C, AC. Heating rate ~5000°C hr⁻¹).

Cold rolling reduction	Annealing treatment prior to cold rolling	Recrystallisation textures
60% RA	Rapid 850°C	Mainly $\sim\{110\}$ $\langle 001 \rangle$ + minor $\sim\{554\}$ $\langle 225 \rangle$ and weak $\sim\{100\}$ $\langle uvw \rangle$
	Batch 850°C	Mainly $\sim\{554\}$ $\langle 225 \rangle$ + minor $\sim\{110\}$ $\langle 001 \rangle$ and $\sim\{100\}$ $\langle 011 \rangle$
70% RA	Rapid 850°C	Mainly $\{554\}$ $\langle 225 \rangle$ + minor $\sim\{110\}$ $\langle 001 \rangle$ and $\sim\{100\}$ $\langle uvw \rangle$ + spread.
	Batch 850°C	Mainly $\sim\{554\}$ $\langle 225 \rangle$ + minor $\sim\{110\}$ $\langle 001 \rangle$ + spread
80% RA	Rapid 850°C)	Mainly $\sim\{554\}$ $\langle 225 \rangle$ + spread + minor $\sim\{100\}$ $\langle uvw \rangle$
	Batch 850°C)	
90% RA	Rapid 850°C)	Mainly $\sim\{223\}$ $\langle 962 \rangle$ + minor $\sim\{554\}$ $\langle 225 \rangle$
	Batch 850°C)	
95% RA	Rapid 850°C	Mainly $\sim\{223\}$ $\langle 962 \rangle$
	Batch 850°C	

TABLE 24

SUMMARY OF PRIMARY RECRYSTALLISATION TEXTURES OF 430 Ti
 (~17 Cr, 0.3 Ti, 0.029 (C+N)) STEEL. (Final annealing
 treatment = 1 hr. at 900°C, FC. Heating rate = 50°C hr⁻¹)

Cold rolling reduction	Annealing treatment prior to cold rolling	Recrystallisation textures
60% RA	Rapid 850°C	Mainly $\sim\{110\}$ $\langle 001 \rangle$ + spread towards $\sim\{554\}$ $\langle 225 \rangle$ + weak $\sim\{100\}$ $\langle uvw \rangle$
	Batch 850°C	Mainly $\sim\{554\}$ $\langle 225 \rangle$ + minor $\sim\{110\}$ $\langle 001 \rangle$ and $\sim\{100\}$ $\langle uvw \rangle$
70% RA	Rapid 850°C	Mainly $\sim\{554\}$ $\langle 225 \rangle$ + spread
	Batch 850°C	Mainly $\sim\{554\}$ $\langle 225 \rangle$ + minor $\{110\}$ $\langle 001 \rangle$ and $\sim\{100\}$ $\langle uvw \rangle$
80% RA	Rapid 850°C) Batch 850°C)	Mainly $\sim\{554\}$ $\langle 225 \rangle$ + spread
90% RA	Rapid 850°C	Mainly $\sim\{554\}$ $\langle 225 \rangle$ + minor $\sim\{223\}$ $\langle 962 \rangle$
	Batch 850°C	Mainly $\sim\{223\}$ $\langle 962 \rangle$ + minor $\sim\{554\}$ $\langle 225 \rangle$
95% RA	Rapid 850°C) Batch 850°C)	Mainly $\sim\{223\}$ $\langle 962 \rangle$

TABLE 25

SUMMARY OF PRIMARY RECRYSTALLISATION TEXTURES OF 409 (12 Cr, 0.46 Ti, 0.039 (C+N)) STEEL (Final annealing treatment = $\frac{1}{2}$ hr at 900°C, AC. Heating rate $\sim 5000^{\circ}\text{C hr}^{-1}$)

Cold rolling reduction	Annealing treatment prior to cold rolling	Recrystallisation textures
70% RA	As hot-rolled or annealed 750°C, AC (Heating rate $\sim 5000^{\circ}\text{C hr}^{-1}$)	Mainly $\sim\{554\} \langle 225 \rangle$ + minor $\sim\{110\} \langle 001 \rangle$ and $\sim\{100\} \langle uvw \rangle$
	Annealed 850°C, AC (Heating rate $\sim 5000^{\circ}\text{C hr}^{-1}$)	Mainly $\sim\{554\} \langle 225 \rangle$ and $\sim\{110\} \langle 001 \rangle$ + minor $\sim\{100\} \langle uvw \rangle$
	Annealed 850°C, FC (heating rate = 50°C hr ⁻¹)	Mainly $\sim\{554\} \langle 225 \rangle$ + minor $\sim\{110\} \langle 001 \rangle$
	Annealed 1000°C, AC (Heating rate $\sim 5000^{\circ}\text{C hr}^{-1}$)	Mainly $\sim\{110\} \langle 001 \rangle$ + $\sim\{554\} \langle 225 \rangle$ + spread between
80% RA	As hot rolled	Mainly $\sim\{554\} \langle 225 \rangle$ + $\sim\{100\} \langle 011 \rangle$ + spread
	Annealed 750-850°C, AC (Heating rate $\sim 5000^{\circ}\text{C hr}^{-1}$)	Mainly $\sim\{554\} \langle 225 \rangle$ + minor $\sim\{110\} \langle 001 \rangle$ and $\sim\{100\} \langle uvw \rangle$
	Annealed 850°C, FC (Heating rate = 50°C hr ⁻¹)	Mainly $\sim\{554\} \langle 225 \rangle$
	Annealed 1000°C, AC (Heating rate $\sim 5000^{\circ}\text{C hr}^{-1}$)	Mainly $\sim\{110\} \langle 001 \rangle$ + spread between $\sim\{554\} \langle 225 \rangle$ and $\sim\{111\} \langle 110 \rangle$
90% RA	As hot rolled or annealed 750°C, AC (Heating rate $\sim 5000^{\circ}\text{C hr}^{-1}$)	Mainly $\sim\{554\} \langle 225 \rangle$ + $\sim\{223\} \langle 962 \rangle$ + minor $\sim\{100\} \langle uvw \rangle$
	Annealed 850°C, AC or FC. (Heating rate $\sim 5000^{\circ}\text{C}$ or = 50°C hr ⁻¹)	Mainly $\sim\{554\} \langle 225 \rangle$
	Annealed 1000°C, AC (Heating rate $\sim 5000^{\circ}\text{C hr}^{-1}$)	Mainly $\sim\{554\} \langle 225 \rangle$ + $\sim\{111\} \langle uvw \rangle$ fibre texture
95% RA	As hot rolled or annealed 750°C, AC (Heating rate $\sim 5000^{\circ}\text{C hr}^{-1}$)	Mainly $\sim\{223\} \langle 962 \rangle$
	Annealed 850°C, AC (Heating rate $\sim 5000^{\circ}\text{C hr}^{-1}$)	Mainly $\sim\{223\} \langle 962 \rangle$ + $\sim\{554\} \langle 225 \rangle$
	Annealed 1000°C, AC (Heating rate $\sim 5000^{\circ}\text{C hr}^{-1}$)	Mainly $\sim\{554\} \langle 225 \rangle$ + $\sim\{111\} \langle uvw \rangle$ fibre texture.

TABLE 26

r-VALUES OF 430 (17% Cr, 0.77 (C+N)) STEEL

(Final annealing treatment = $\frac{1}{2}$ hr at 900°C, AC. Heating rate $\sim 5000^{\circ}\text{C hr}^{-1}$)

Cold rolling reduction	Annealing treatment before cold rolling	r_0	r_{45}	r_{90}	\bar{r}	Δr
70% RA	As hot rolled	0.55	0.72	0.80	0.70	-0.05
	"Rapid" 850°C	0.52	0.72	1.72	0.92	+0.40
	Rapid 1000°C + temper	0.59	0.56	1.87	0.90	+0.67
	Rapid 1200°C + temper	0.97	0.47	2.03	0.99	+1.03
80% RA	As hot rolled	0.48	1.34	0.93	1.02	-0.64
	Rapid 850°C	0.86	1.07	0.97	0.99	-0.16
	Rapid 1000°C + temper	0.98	1.10	1.84	1.26	+0.31
	Rapid 1200°C + temper	0.97	0.51	1.23	0.81	+0.59
90% RA	As hot rolled	0.59	0.70	0.44	0.61	-0.19
	Rapid 850°C	0.68	1.11	0.85	0.94	-0.35
	Rapid 1000°C + temper	0.69	1.83	0.99	1.34	-0.99
	Rapid 1200°C + temper	0.79	0.55	0.74	0.66	+0.22

TABLE 27

n-VALUES OF 430 (~ 17 Cr, 0.077 (C+N)) STEEL

(Final annealing treatment = $\frac{1}{2}$ hr. at 900°C, AC. Heating rate $\sim 5000^{\circ}\text{C hr}^{-1}$)

Cold rolling reduction	Annealing treatment before cold rolling	n_0	n_{45}	n_{90}	\bar{n}
70% RA	As hot rolled	0.242	0.233	0.160	0.22
	Rapid 850°C	0.220	0.258	0.243	0.24
	Rapid 1000°C + temper	0.230	0.255	0.244	0.25
	Rapid 1200°C + temper	0.282	0.232	0.220	0.24
80% RA	As hot rolled	0.256	0.222	0.254	0.24
	Rapid 850°C	0.253	0.190	0.256	0.22
	Rapid 1000°C + temper	0.250	0.234	0.247	0.24
	Rapid 1200°C + temper	0.249	0.256	0.242	0.25
90% RA	As hot rolled	0.262	0.250	0.227	0.25
	Rapid 850°C	0.251	0.252	0.249	0.25
	Rapid 1000°C + temper	0.230	0.280	0.256	0.26
	Rapid 1200°C + temper	0.230	0.260	0.260	0.25

TABLE 28

r-VALUES AND n-VALUES OF 430Ti (17Cr, 0.029(C+N), 0.5Ti) STEEL.

(Final annealing treatment = $\frac{1}{2}$ hr. at 900°C, AC. Heating rate ~5000°C hr⁻¹)

(A) r-VALUES

Cold rolling reduction	Annealing treatment before cold rolling	r ₀	r ₄₅	r ₉₀	\bar{r}	Δr
80% RA	As hot rolled	1.22	2.64	1.40	1.98	-1.33
	Rapid 1000°C	1.95	1.45	2.20	1.76	+0.63
	Batch 850°C	2.35	2.11	2.58	2.29	+0.36
90% RA	As hot rolled	0.88	2.82	1.78	2.08	-1.49
	Rapid 850°C	2.07	2.56	2.47	2.42	-0.29
	Batch 850°C	2.10	1.93	2.49	2.11	+0.37

(B) n-VALUES

Cold rolling reduction	Annealing treatment before cold rolling	n ₀	n ₄₅	n ₉₀	\bar{n}
80% RA	As hot rolled	0.265	0.240	0.246	0.25
	Rapid 1000°C	0.218	0.263	0.244	0.25
	Batch 850°C	0.210	0.232	0.237	0.23
90% RA	As hot rolled	0.261	0.245	0.245	0.25
	Rapid 850°C	0.263	0.226	0.211	0.23
	Batch 850°C	0.259	0.212	0.238	0.23

TABLE 29

 r_o -VALUES FOR 430 Ti (~ 17 Cr, Ti -stabilised) STEEL

(Samples extracted from 25mm wide cold-rolled and annealed strip unless marked with asterisk *)

(Final annealing treatment = $\frac{1}{2}$ hr at 900°C, AC, heating rate ~ 5000°C hr⁻¹)

[Ti] _{ss} %	Cold rolling reduction	Annealing treatment before cold rolling	r_o
~ 0.4 (0.5% Ti steel)	60% RA	As hot rolled	0.49
		Rapid 850°C	0.95
		Rapid 1000°C	0.71
		Batch 850°C	1.10
	70% RA	As hot rolled	0.54
Rapid 850°C		1.23	
Rapid 1000°C		0.72	
Batch 850°C		1.25	
80% RA	As hot rolled *	1.22	
	Rapid 1000°C *	1.95	
	Batch 850°C *	2.35	
90% RA	As hot rolled *	2.08	
	Rapid 850°C *	2.42	
	Batch 850°C *	2.10	
95% RA	Rapid 850°C	0.69	
	Rapid 1000°C	1.01	
	Batch 850°C	1.41	
~ 0.3 (0.4% Ti steel)	60% RA	Rapid (commercial) 900°C	1.27
		Batch (commercial) 780°C	1.16
	70% RA	Rapid 900°C	1.21
		Batch 780°C	1.33
	80% RA	Rapid 900°C	1.75
90% RA	Rapid 900°C	1.47	
	Batch 780°C	1.52	
95% RA	Rapid 900°C	1.68	
	Batch 780°C	1.14	
~ 0.2 (0.3% Ti steel)	60% RA	Batch 850°C	2.26
	70% RA	Batch 850°C	1.52
	80% RA	Rapid 850°C	2.22
		Batch 850°C	1.52
	90% RA	Rapid 850°C	1.52
Batch 850°C		1.42	
95% RA	Rapid 850°C	1.15	
	Batch 850°C	1.24	

TABLE 30

 r_c -VALUES FOR 430 Ti (~ 17 Cr, Ti-stabilised) STEEL

(Samples extracted from 25mm wide, cold rolled and annealed strip. Final annealing treatment = 1 hr at 900°C, FC, heating rate = 50°C hr⁻¹)

[Ti] _{ss} %	Cold rolling reduction	Annealing treatment before cold rolling	r_c
~ 0.4 (0.5% Ti steel)	70% RA	Rapid 850°C	0.78
		Rapid 1000°C	0.98
		Batch 850°C	1.24
	80% RA	As hot rolled	0.54
		Rapid 850°C	1.43
		Rapid 1000°C	1.23
		Batch 850°C	1.33
	90% RA	As hot rolled	0.57
		Rapid 850°C	0.87
		Rapid 1000°C	1.37
	95% RA	Batch 850°C	1.41
		As hot rolled	0.41
Rapid 850°C		0.70	
~ 0.3 (0.4% Ti steel)	80% RA	(Commercial) rapid 900°C	1.81
		(Commercial) batch 780°C	1.23
	90% RA	Rapid 900°C	1.62
		Batch 780°C	1.12
	95% RA	Rapid 900°C	1.30
		Batch 780°C	0.84
~ 0.2 (0.3% Ti steel)	80% RA	Rapid 850°C	2.42
		Batch 850°C	1.70
	90% RA	Rapid 850°C	1.48
		Batch 850°C	1.25
	95% RA	Rapid 850°C	0.72
		Batch 850°C	0.93

TABLE 31

r-VALUES AND n-VALUES OF 409 (~ 12 Cr, 0.5 Ti, 0.039 (C+N)) STEEL. (Final annealing treatment = $\frac{1}{2}$ hr at 900°C, AC, heating rate ~ 5000°C hr⁻¹)

(A) r-VALUES

Cold rolling reduction	Annealing treatment before cold rolling	r ₀	r ₄₅	r ₉₀	\bar{r}	Δr
70% RA	Rapid 850°C	1.12	1.10	1.70	1.26	+0.31
	Batch 850°C	1.45	0.93	2.39	1.43	+0.99
80% RA	Rapid 850°C	1.09	1.43	1.78	1.43	+0.005
	Batch 850°C	1.34	1.17	1.79	1.37	+0.40
90% RA	Rapid 850°C	0.94	1.87	1.67	1.59	-0.57
	Batch 850°C	1.34	1.54	1.87	1.57	+0.07

(B) n-VALUES

Cold rolling reduction	Annealing treatment before cold rolling	n ₀	n ₄₅	n ₉₀	\bar{n}
70% RA	Rapid 850°C	0.270	0.246	0.247	0.25
	Batch 850°C	0.248	0.258	0.255	0.25
80% RA	Rapid 850°C	0.278	0.235	0.267	0.25
	Batch 850°C	0.263	0.255	0.228	0.25
90% RA	Rapid 850°C	0.278	0.256	0.265	0.26
	Batch 850°C	0.262	0.214	0.259	0.24

TABLE 32

SWIFT CUPPING TESTS (50mm dia. punch)

(Final annealing treatment = $\frac{1}{2}$ hr at 900°C AC, heating rate
 $\sim 5000^{\circ}\text{C hr}^{-1}$)

(i) 430 (~17 Cr, 0.077 (C+N)) STEEL

Cold rolling reduction	Sheet thickness (mm)	Annealing treatment before cold rolling	Critical Blank Dia. (Dc)mm	LDR
70% RA	1.5	Batch 850°C	114	2.28
80% RA	1.0	As hot-rolled Rapid 850°C Batch 850°C Rapid 1200°C + temper	105 105 106 102	2.10 2.10 2.12 2.04
90% RA	0.5	Rapid 850°C Rapid 1200°C + temper	104 105	2.08 2.10

(ii) 430 Ti (~17 Cr, 0.029 (C+N), 0.5 Ti) STEEL

Cold rolling reduction	Sheet thickness (mm)	Annealing treatment before cold rolling	Dc (mm)	LDR
80% RA	0.8	As hot rolled Rapid 1000°C	126 111	2.52 2.22
90% RA	0.4	As hot rolled Batch 850°C	117 105	2.34 2.10

(iii) 409 (~12 Cr, 0.039 (C+N), 0.5 Ti) STEEL

Cold rolling reduction	Sheet thickness (mm)	Annealing treatment before cold rolling	Dc (mm)	LDR
70% RA	1.0	Rapid 850°C Batch 850°C	112 114	2.24 2.28
80% RA	0.8	Rapid 850°C Batch 850°C	121 122	2.42 2.44
90% RA	0.4	Rapid 850°C Batch 850°C	111 112	2.22 2.24

TABLE 33

EARING PROFILES OF CUPS DRAWN FROM 100mm DIAMETER BLANKS

(Punch diameter = 50mm)

(Final annealing treatment = $\frac{1}{2}$ hr at 900°C, AC,heating rate $\sim 5000^{\circ}\text{C hr}^{-1}$)(i) 430 (~ 17 Cr, 0.077 (C+N)) STEEL

Cold rolling reduction	Annealing treatment before cold rolling	Min. cup wall height mm	% Ear-ing	Positions of ears with respect to RD
80% RA	As hot rolled	34.5	20.3	$\sim 0^{\circ}$; $\sim 90^{\circ}$
	Rapid 850°C	35	21.5	$\sim 0^{\circ}$; $\sim 90^{\circ}$
	Batch 850°C	36	18.6	$\sim 15^{\circ}$; $\sim 105^{\circ}$ (near 0° ; 90°)
	Rapid 1200°C + temper	33	25.5	$\sim 0^{\circ}$; $\sim 90^{\circ}$

(ii) 430 Ti (~ 17 Cr, 0.029 (C+N), 0.5 Ti) STEEL

Cold rolling reduction	Annealing treatment before cold rolling	Min. cup wall height mm	% Ear-ing	Positions of ears with respect to RD
80% RA	As hot rolled	34	17.1	$\sim 0^{\circ}$; $\sim 60^{\circ}$
	Rapid 1000°C	35	17.1	$\sim 0^{\circ}$; $\sim 60-80^{\circ}$
90% RA	Batch 850°C	33	44.8	$\sim 0^{\circ}$; $\sim 60-80^{\circ}$

(iii) 409 (~ 12 Cr, 0.039 (C+N) 0.5 Ti) STEEL

Cold rolling reduction	Annealing treatment before cold rolling	Min. cup wall height mm	% Ear-ing	Positions of ears with respect to RD
80% RA	Rapid 850°C	34	20.1	$\sim 0^{\circ}$; $\sim 60^{\circ}$
	Batch 850°C	34	37.3	$\sim 0^{\circ}$; $\sim 60-80^{\circ}$

TABLE 34

ERICHSEN STRETCH FORMING TESTS

(Final annealing treatment = $\frac{1}{2}$ hr at 900°C, AC
heating rate $\sim 5000^{\circ}\text{C hr}^{-1}$)

(i) 430 (17 Cr, 0.077 (C+N)) STEEL

Cold rolling reduction	Sheet thickness (mm)	Annealing treatment before cold rolling	Punch penetration (mm)
70% RA	1.5	As hot rolled	11.0
		Rapid 850°C	11.1
		Batch 850°C	11.3
		Rapid 1200°C + temper	11.4
80% RA	1.0	As hot rolled	9.7
		Rapid 850°C	10.7
		Batch 850°C	9.7
		Rapid 1200°C + temper	9.9
90% RA	0.5	Rapid 850°C	8.9
		Batch 850°C	9.1

(ii) 430 Ti (~17 Cr, 0.029 (C+N), 0.5 Ti) STEEL

Cold rolling reduction	Sheet thickness (mm)	Annealing treatment before cold rolling	Punch penetration (mm)
80% RA	0.8	As hot rolled	10.3
		Rapid 1000°C	9.2
		Batch 850°C	9.6
90% RA	0.4	Rapid 850°C	10.1

(iii) 409 (~12 Cr, 0.039 (C+N), 0.5 Ti) STEEL

Cold rolling reduction	Sheet thickness (mm)	Annealing treatment before cold rolling	Punch penetration (mm)
70% RA	1.2	Rapid 850°C	10.8
		Batch 850°C	10.9
90% RA	0.4	Rapid 850°C	10.4

TABLE 35

OPERATIVE SLIP SYSTEMS PREDICTED DURING ROLLING,
FOR SELECTED ORIENTATIONS

Orientation	Operative Slip System(s) (i.e. those on which τ_c is reached first)	
	EQUAL τ_c ($\tau_c \{110\} = \tau_c \{112\} = \tau_c \{123\}$)	UNEQUAL τ_c ($\tau_c \{110\} : \tau_c \{112\} : \tau_c \{123\} = 1:1.03:1.05$)
(011) [$\bar{1}00$]	(211) [$\bar{1}11$] + ($\bar{2}11$)[$\bar{1}\bar{1}\bar{1}$]	(211) [$\bar{1}11$] + ($\bar{2}11$) [$\bar{1}\bar{1}\bar{1}$]
(144) [$\bar{8}11$]	(211) [$\bar{1}11$]	(211) [$\bar{1}11$]
(122) [$\bar{4}11$]	(211) [$\bar{1}11$]	(211) [$\bar{1}11$]
(455) [$\bar{5}22$]	(211) [$\bar{1}11$]	(211) [$\bar{1}11$]
(111) [$\bar{2}11$]	(211) [$\bar{1}11$]	(211) [$\bar{1}11$]
(011) [$\bar{6}11$]	(321) [$\bar{1}11$] + ($\bar{3}12$)[$\bar{1}\bar{1}\bar{1}$]	(321) [$\bar{1}11$] + ($\bar{3}12$) [$\bar{1}\bar{1}\bar{1}$]
(011) [$\bar{5}11$]	(321) [$\bar{1}11$] + ($\bar{3}12$)[$\bar{1}\bar{1}\bar{1}$]	(211) [$\bar{1}11$] + ($\bar{2}11$) [$\bar{1}\bar{1}\bar{1}$]
(011) [$\bar{4}11$]	(321) [$\bar{1}11$] + ($\bar{3}12$)[$\bar{1}\bar{1}\bar{1}$]	(321) [$\bar{1}11$] + ($\bar{3}12$) [$\bar{1}\bar{1}\bar{1}$]
(011) [$\bar{5}22$]	(321) [$\bar{1}11$] + ($\bar{3}12$)[$\bar{1}\bar{1}\bar{1}$]	(110) [$\bar{1}11$] + ($\bar{1}01$) [$\bar{1}\bar{1}\bar{1}$]
(011) [$\bar{1}\bar{1}\bar{1}$]	(110) [$\bar{1}11$] + ($\bar{1}01$)[$\bar{1}\bar{1}\bar{1}$]	(110) [$\bar{1}11$] + ($\bar{1}01$) [$\bar{1}\bar{1}\bar{1}$]
(111) [$\bar{1}\bar{1}2$]	(112) [$\bar{1}\bar{1}\bar{1}$]	(112) [$\bar{1}\bar{1}\bar{1}$]
(334) [$\bar{2}23$]	(110) [$\bar{1}11$] + (110)[$\bar{1}\bar{1}\bar{1}$]	(110) [$\bar{1}11$] + (110) [$\bar{1}\bar{1}\bar{1}$]
(335) [$\bar{5}56$]	(110) [$\bar{1}11$] + (110)[$\bar{1}\bar{1}\bar{1}$]	(110) [$\bar{1}11$] + (110) [$\bar{1}\bar{1}\bar{1}$]
(112) [$\bar{1}\bar{1}\bar{1}$]	($\bar{1}\bar{1}2$) [$\bar{1}\bar{1}\bar{1}$]	($\bar{1}\bar{1}2$) [$\bar{1}\bar{1}\bar{1}$]
(111) [$\bar{3}25$]	(123) [$\bar{1}\bar{1}\bar{1}$]	(112) [$\bar{1}\bar{1}\bar{1}$]
(111) [$\bar{3}\bar{1}4$]	($\bar{2}31$) [$\bar{1}11$]	(110) [$\bar{1}11$] + (011) [$\bar{1}\bar{1}\bar{1}$]
(111) [$\bar{1}01$]	(110) [$\bar{1}11$] + (011)[$\bar{1}\bar{1}\bar{1}$]	(110) [$\bar{1}11$] + (011) [$\bar{1}\bar{1}\bar{1}$]
(001) [$\bar{1}\bar{1}0$]	(112) [$\bar{1}\bar{1}\bar{1}$] + ($\bar{1}\bar{1}2$)[$\bar{1}\bar{1}\bar{1}$]	(112) [$\bar{1}\bar{1}\bar{1}$] + ($\bar{1}\bar{1}2$) [$\bar{1}\bar{1}\bar{1}$]
(001) [$\bar{5}10$]	(101) [$\bar{1}\bar{1}\bar{1}$] + ($\bar{1}01$)[$\bar{1}\bar{1}\bar{1}$]	(101) [$\bar{1}\bar{1}\bar{1}$] + ($\bar{1}01$) [$\bar{1}\bar{1}\bar{1}$]
(114) [$\bar{2}21$]	($\bar{1}\bar{1}2$) [$\bar{1}\bar{1}\bar{1}$]	($\bar{1}\bar{1}2$) [$\bar{1}\bar{1}\bar{1}$]
(1 $\bar{1}$ 8) [$\bar{1}\bar{1}0$]	(213) [$\bar{1}\bar{1}\bar{1}$] + ($\bar{1}\bar{2}3$)[$\bar{1}\bar{1}\bar{1}$]	(112) [$\bar{1}\bar{1}\bar{1}$] + ($\bar{1}\bar{1}2$) [$\bar{1}\bar{1}\bar{1}$]
(1 $\bar{1}$ 3) [$\bar{1}\bar{1}0$]	(213) [$\bar{1}\bar{1}\bar{1}$] + ($\bar{1}\bar{2}3$)[$\bar{1}\bar{1}\bar{1}$]	(101) [$\bar{1}\bar{1}\bar{1}$] + (0 $\bar{1}$ 1) [$\bar{1}\bar{1}\bar{1}$]
(112) [$\bar{1}\bar{1}0$]	($\bar{1}\bar{2}3$) [$\bar{1}\bar{1}\bar{1}$] + (2 $\bar{1}$ 3)[$\bar{1}\bar{1}\bar{1}$]	(011) [$\bar{1}\bar{1}\bar{1}$] + (101) [$\bar{1}\bar{1}\bar{1}$]
(123) [$\bar{5}41$]	(101) [$\bar{1}\bar{1}\bar{1}$]	(101) [$\bar{1}\bar{1}\bar{1}$]
(111) [$\bar{1}\bar{1}0$]	(011) [$\bar{1}\bar{1}\bar{1}$] + (101)[$\bar{1}\bar{1}\bar{1}$]	(011) [$\bar{1}\bar{1}\bar{1}$] + (101) [$\bar{1}\bar{1}\bar{1}$]
(113) [$\bar{1}\bar{1}0$]	($\bar{1}\bar{2}3$) [$\bar{1}\bar{1}\bar{1}$] + (2 $\bar{1}$ 3)[$\bar{1}\bar{1}\bar{1}$]	(011) [$\bar{1}\bar{1}\bar{1}$] + (101) [$\bar{1}\bar{1}\bar{1}$]
(114) [$\bar{1}\bar{1}0$]	($\bar{1}\bar{2}3$) [$\bar{1}\bar{1}\bar{1}$] + (2 $\bar{1}$ 3)[$\bar{1}\bar{1}\bar{1}$]	($\bar{1}\bar{2}3$) [$\bar{1}\bar{1}\bar{1}$] + (2 $\bar{1}$ 3) [$\bar{1}\bar{1}\bar{1}$]

TABLE 36

THEORETICAL r-VALUES FOR IDEAL ORIENTATIONS ASSUMING
CRYSTALLOGRAPHIC SLIP, 48 SYSTEMS, NO ROTATION

Orientation	Assumptions	r_0	r_{45}	r_{90}	\bar{r}	Δr
(100) [011]	EQUAL τ_c	0	1.0	0	0.5	-1.0
	UNEQUAL τ_c	0	1.0	0	0.5	-1.0
(100) [001]	EQUAL τ_c	1.0	~ 0	1.0	0.5	+1
	UNEQUAL τ_c	1.0	~ 0	1.0	0.5	+1
(110) [001]*	EQUAL τ_c	1.0*	0.21	∞	∞	∞
	UNEQUAL τ_c	1.0*	0.56	∞	∞	∞
(111) [$\bar{1}10$] (111) [$1\bar{1}0$]	EQUAL τ_c	2	3.83	3	3.17	-1.33
	UNEQUAL τ_c	2	3.83	∞	∞	∞
(111) [$\bar{2}11$] (111) [$1\bar{2}1$]	EQUAL τ_c	3	3.83	2	3.17	-1.33
	UNEQUAL τ_c	∞	3.83	2	∞	∞
(455) [$\bar{5}22$] (545) [$2\bar{5}2$]	EQUAL τ_c	16.5	2.89	3.13	6.35	+6.92
	UNEQUAL τ_c	16.5	1.53	3.13	5.67	+8.28
(223) [$\bar{9}62$] (223) [$9\bar{6}2$]	EQUAL τ_c	1.61	1.60	2.84	1.91	+0.63
	UNEQUAL τ_c	5.70	0.64	2.84	2.46	+3.63
(223) [$\bar{6}92$] (223) [$6\bar{9}2$]	EQUAL τ_c	1.61	5.09	2.84	3.66	-2.87
	UNEQUAL τ_c	5.70	5.09	2.84	4.68	-0.82
(114) [$\bar{8}41$] (114) [$8\bar{4}1$]	EQUAL τ_c	0.83	1.46	0.11	0.97	-0.99
	UNEQUAL τ_c	0.83	1.46	0.11	0.97	-0.99
(114) [$\bar{8}71$] (114) [$8\bar{7}1$]	EQUAL τ_c	0.83	0.82	0.11	0.65	-0.35
	UNEQUAL τ_c	0.83	0.82	0.11	0.65	-0.35
(112) [$\bar{5}31$] (112) [$5\bar{3}1$]	EQUAL τ_c	0.92	2.20	2.0	1.83	-0.74
	UNEQUAL τ_c	0.56	3.55	2.76	2.61	-1.89
(112) [$\bar{3}51$] (112) [$3\bar{5}1$]	EQUAL τ_c	0.92	2.42	2.0	1.94	-0.96
	UNEQUAL τ_c	0.56	1.77	2.76	1.72	-0.11

"UNEQUAL τ_c " :- $\tau_c \{110\} : \tau_c \{112\} : \tau_c \{123\} =$
1:1.03:1.05

* r_0 for $\{110\} \langle 001 \rangle = 1.0$, but $r_{2.5} = \infty$.

TABLE 37

COMPARISON BETWEEN OBSERVED AND PREDICTED r-VALUES (TEXTURE DATA TAKEN FROM POLE FIGURES)
 (Samples cold rolled to 90% RA and annealed ½ hr at 900°C, AC (heating rate ~ 5000°C hr⁻¹)

STEEL	Annealing treatment before cold rolling	Texture (from Pole Figures)	r-values			
			Assumptions	r ₀	r ₄₅	r ₉₀
430 (17 Cr, 0.077 (C+N))	As hot rolled	0.1 {100} <011> + 0.1 {100} <001> + 0.8 {114} <841>	Observed Equal ∇^c Unequal ∇^c	0.59 0.76 0.76	0.70 1.01 1.01	0.44 0.19 0.19
	½ hr at 850°C, AC (heating rate ~ 5000°C hr ⁻¹)	0.1 {100} <011> + 0.1 {100} <001> + 0.6 {114} <841> + 0.2 {223} <962>	Observed Equal ∇^c Unequal ∇^c	1.11 0.92 0.92	0.85 1.45 1.36	0.85 0.73 0.73
430 Ti (17 Cr, 0.5 Ti, 0.029 (C+N))	As hot rolled	0.9 {223} <962> + 0.05 {100} <001> + 0.05 {100} <011>	Observed Equal ∇^c Unequal ∇^c	0.88 1.5 1.5	2.82 3.07 2.63	1.78 2.61 2.61
	½ hr at 850°C, AC (heating rate ~ 5000°C hr ⁻¹)	0.4 {554} <225> + 0.4 {223} <962> + 0.1 {100} <011> + 0.1 {100} <001>	Observed Equal ∇^c Unequal ∇^c	2.07 7.34/1.94* 14.85/∞*	2.56 2.60 1.86	2.47 2.49 2.49
430 Ti (17 Cr, 0.5 Ti, 0.029 (C+N))	1 hr at 850°C, FC (heating rate = 50°C hr ⁻¹)	0.9 {554} <225> + 0.05 {100} <011> + 0.05 {100} <001>	Observed Equal ∇^c Unequal ∇^c	2.10 14.85/2.75* 14.85/∞*	1.93 2.65 1.43	2.49 2.87 2.87

NOTES * Calculated r-values using {111} <112> in place of {554} <225>

TABLE 38

COMPARISON BETWEEN OBSERVED AND PREDICTED r-VALUES (TEXTURE DATA FROM TEXTURE PARAMETERS)
 (Samples cold rolled to 90% RA and annealed ½ hr at 900°C, AC (heating rate ~ 5000°C hr⁻¹)

STEEL	Annealing treatment before cold rolling	Texture Parameters (from Texture Parameters)	r-values			
			Assumptions	r ₀	r ₄₅	r ₉₀
430 Ti (17 Cr, 0.077 (C+N))	As hot rolled	0.3 {114} <uvw> + 0.2 {100} <uvw> + 0.2 {112} <uvw> + 0.3 (random)	Observed	0.59	0.7	0.74
			Equal γ_c	0.78	1.15	0.78
			Unequal γ_c	0.72	1.22	0.94
430 Ti (17 Cr, 0.077 (C+N))	½ hr at 850°C, AC (heating rate ~ 5000°C hr ⁻¹)	0.4 {100} <uvw> + 0.3 {114} <uvw> + 0.2 {112} <uvw> + 0.1 (random)	Observed	1.11	0.85	0.85
			Equal γ_c	0.73	1.10	0.73
			Unequal γ_c	0.66	1.17	0.89
430 Ti (17 Cr, 0.5 Ti, 0.029 (C+N))	As hot rolled	0.4 {111} <uvw> + 0.3 {112} <uvw> + 0.1 {114} <uvw> + 0.2 {100} <uvw>	Observed	0.88	2.82	1.78
			Equal γ_c	6.95/1.65*	2.06	1.96
			Unequal γ_c	6.89/∞*	1.62	2.17
430 Ti (17 Cr, 0.5 Ti, 0.029 (C+N))	½ hr at 850°C, AC (heating rate ~ 5000°C hr ⁻¹)	0.6 {111} <uvw> + 0.3 {112} <uvw> + 0.1 {100} <uvw>	Observed	2.07	2.56	2.47
			Equal γ_c	10.43/2.13*	3.04	1.85
			Unequal γ_c	10.11/∞*	1.77	2.76
430 Ti (17 Cr, 0.5 Ti, 0.029 (C+N))	1 hr at 850°C, FC (heating rate = 50°C hr ⁻¹)	0.6 {111} <uvw> + 0.3 {112} <uvw> + 0.1 {100} <uvw>	Observed	2.1	1.93	2.49
			Equal γ_c	10.43/2.13*	3.04	1.85
			Unequal γ_c	10.11/∞*	1.77	2.76

NOTES

- (i) {100} <uvw> assumed
 - (ii) {114} <uvw> assumed
 - (iii) {111} <uvw> assumed
 - (iv) {112} <uvw> assumed
- {100} <001> + ½ {100} <011>
 {114} <841>
 ~ {554} <225> unless otherwise indicated (* = {111} <112>)
 {112} <531>

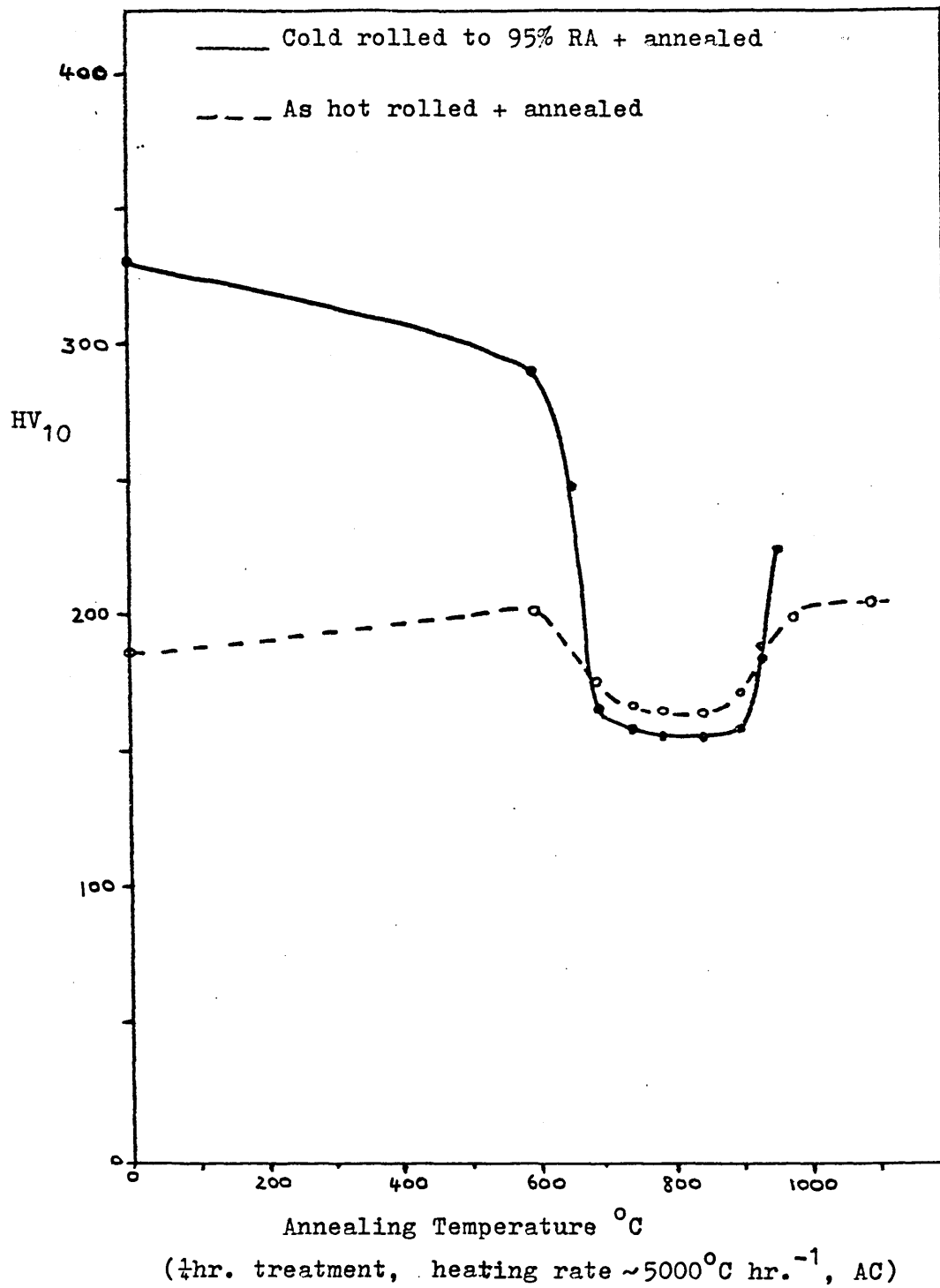


FIGURE 1 Variation of Hardness with Annealing Temperature
for 430 Steel



2 (a) Surface X200



2 (b) Centre X200

FIG. 2 MICROSTRUCTURES OF HOT ROLLED 430 (17 Cr, 0.077 (C+N)) STRIP (HOT ROLLING FINISHING TEMPERATURE ~ 900°C)

(61)



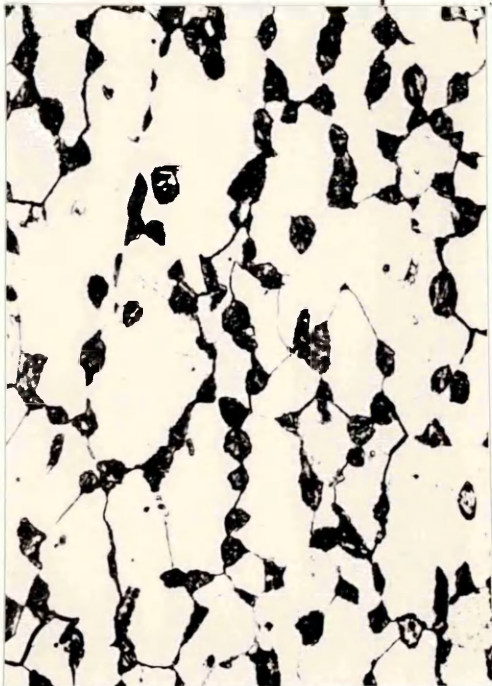
3 (a) Annealed 850°C
X200

(62)



3 (b) Annealed 1000°C
X200

(158)



3 (c) Annealed 1200°C
X200

(129)



3 (d) Annealed 1250°C
X200

FIG.3 MICROSTRUCTURES OF HOT ROLLED AND ANNEALED
430 (17 Cr, 0.077 (C+N)) STRIP (Centre)



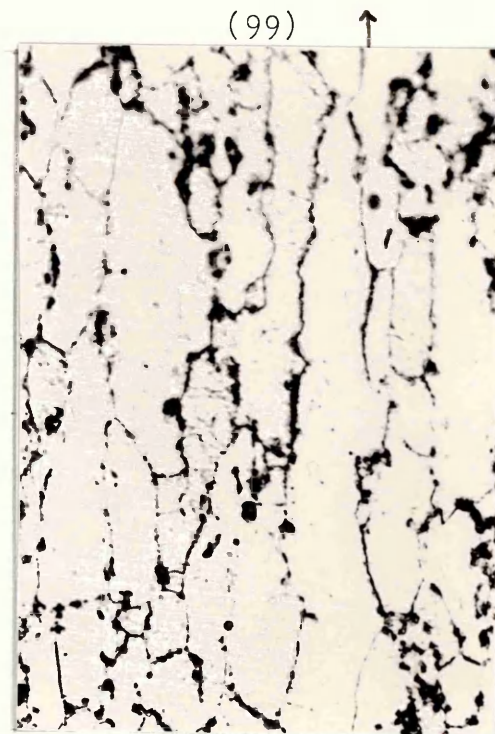
4 (a) Cold rolled without prior annealing to 90% RA: "Rapid" anneal, 900°C
X400



4 (b) "Rapid anneal 1000°C + temper, cold rolled to 90% RA, Rapid anneal 900°C
X400



4 (c) "Batch" anneal 1000°C cold rolled to 90% RA: "Rapid" anneal 900°C.
X400



4 (d) Cold rolled without prior anneal to 90% RA, "Rapid" anneal 1000°C and temper
X400

FIG. 4 MICROSTRUCTURES OF COLD ROLLED AND ANNEALED 430 (17 Cr, 0.077 (C+N))

(646)



5 (a) As hot-rolled (1600 x 1.4)

(728)



5 (b) Rapid anneal at 850°C
(1600 x 1.2)

(719)



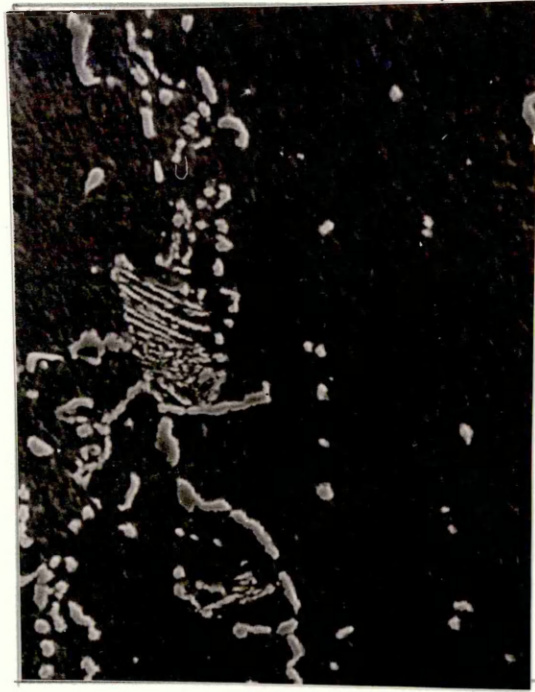
5 (c) Batch anneal at 850°C
(1600 x 1.4)

FIG. 5 SEM PHOTOGRAPHS OF 5mm THICK 430 (17 Cr, 0.077 (C+N)) STEEL STRIP

(722)



6 (a) Batch anneal at
1000°C
(1600 x 1.2)



(295)



6 (b) Rapid anneal at
1200°C WQ + temper
(1600 x 1.2)

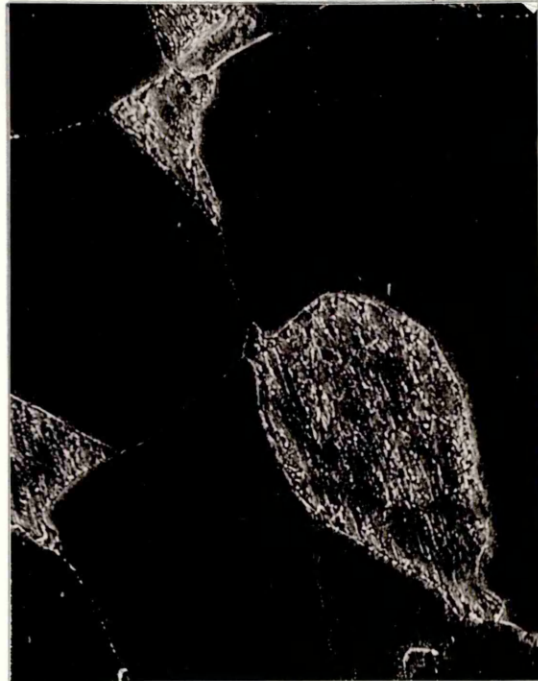
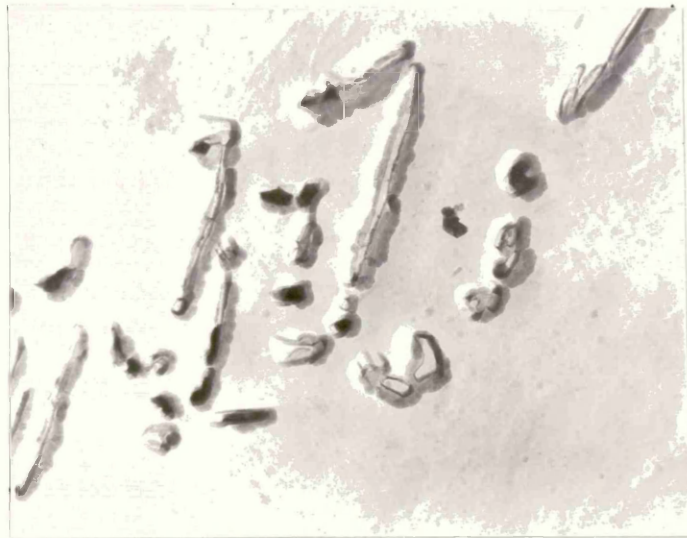


FIG.6 SEM PHOTOGRAPHS OF 5mm THICK 430 (17 Cr, 0.077 (C+N)) STEEL STRIP

(6548)

7 (a) X10k
Batch anneal at
1000°C



(6553)

7 (b) X20k
Rapid anneal at
1200°C, WQ +
temper



FIG.7 TEM PHOTOMICROGRAPHS OF EXTRACTION REPLICAS FOR
HOT ROLLED AND ANNEALED 430 (17 Cr, 0.077 (C+N))
STEEL STRIP

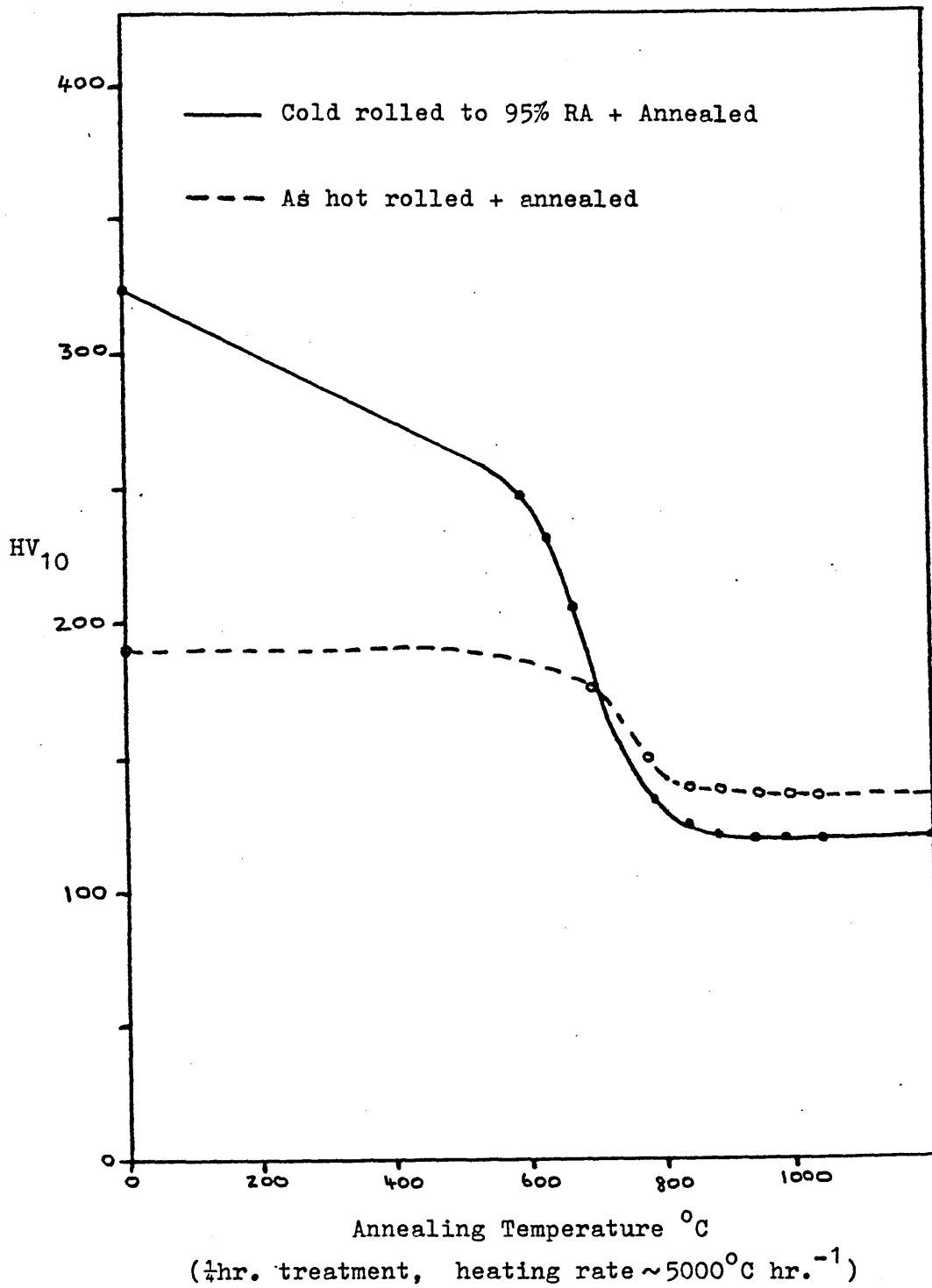
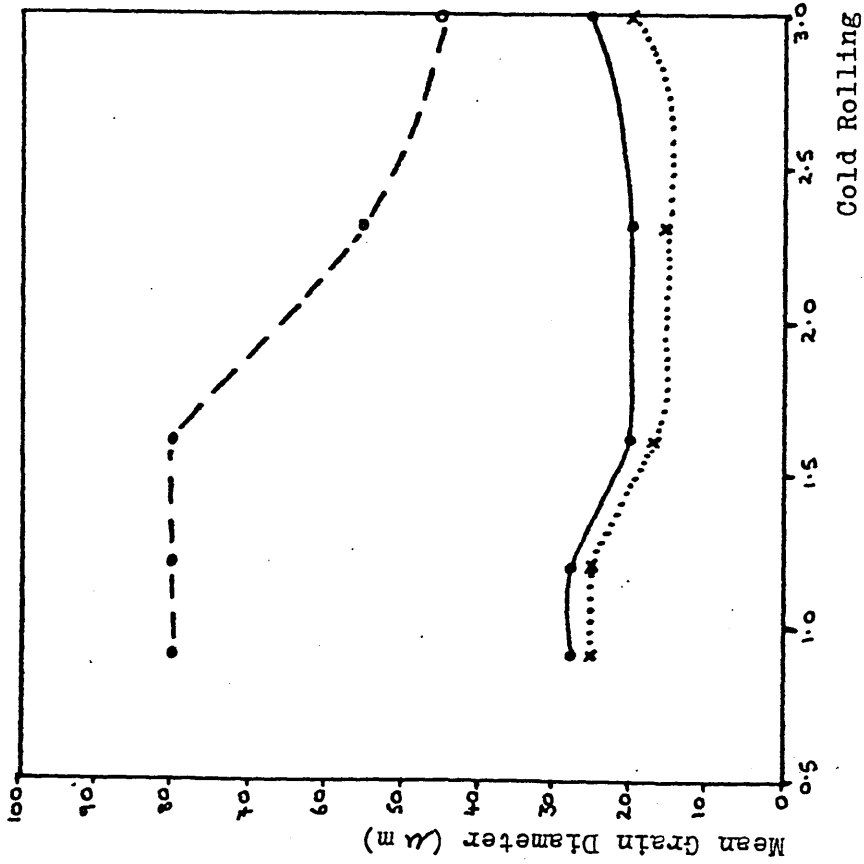


FIGURE 8 Variation of Hardness with Annealing Temperature
for 430Ti (0.5%Ti) Steel.

Without annealing or with annealing
at 750-850° C before cold rolling.



Annealed at 1000° C before cold
rolling

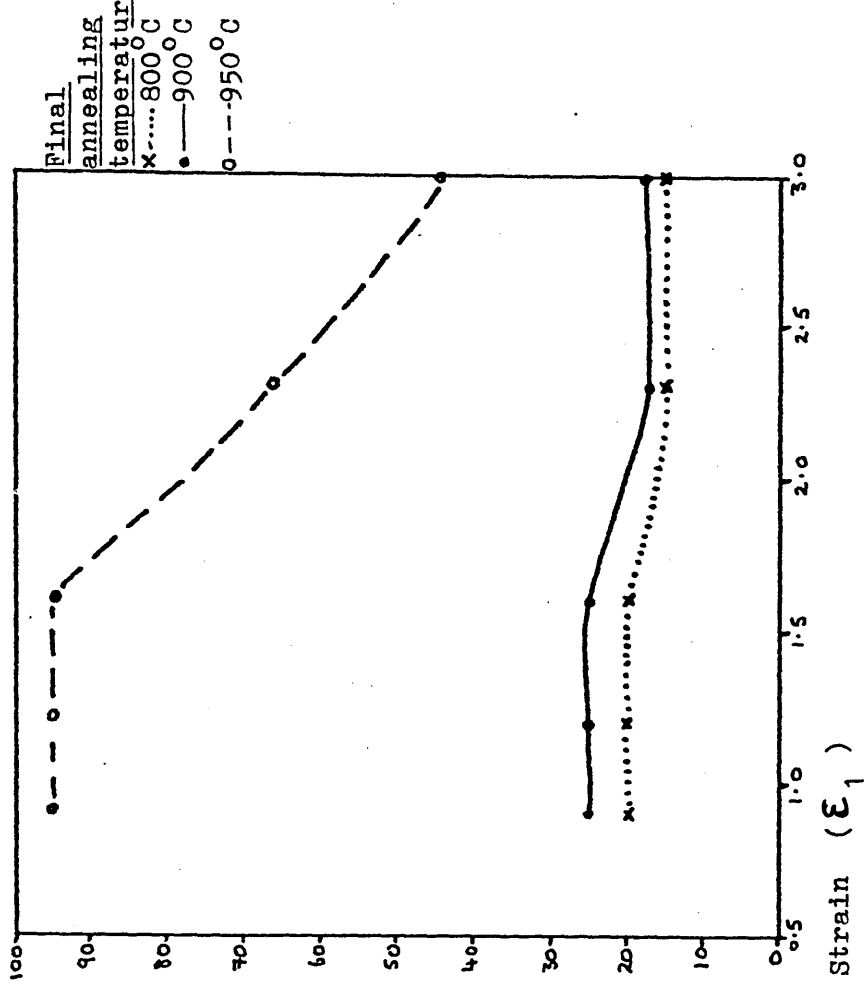
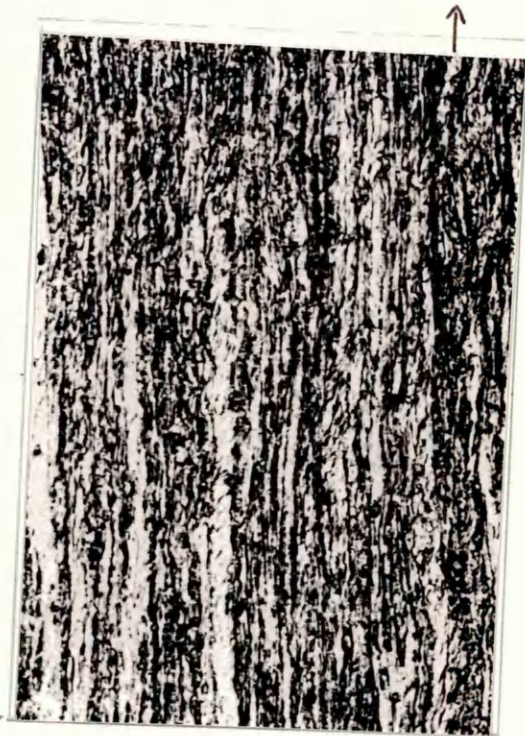


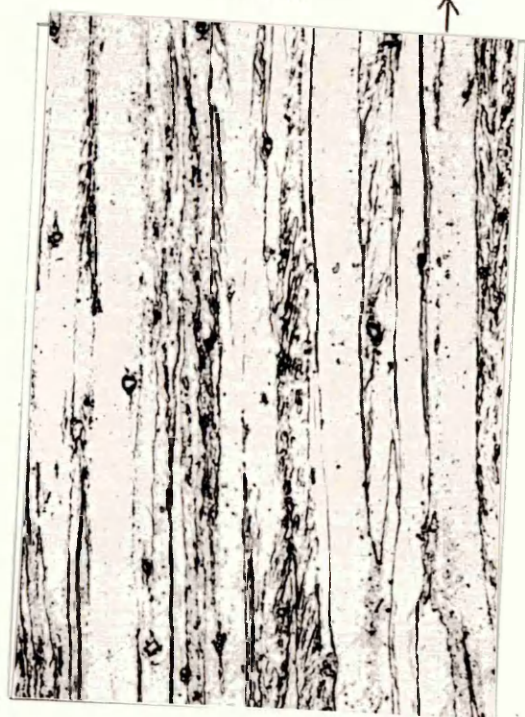
FIGURE 9 Variation of Grain Size with Cold Rolling Reduction for Cold Rolled + Annealed
430T1 (0.5% Ti) Steel

(53)



10 (a) Surface X200

(54)

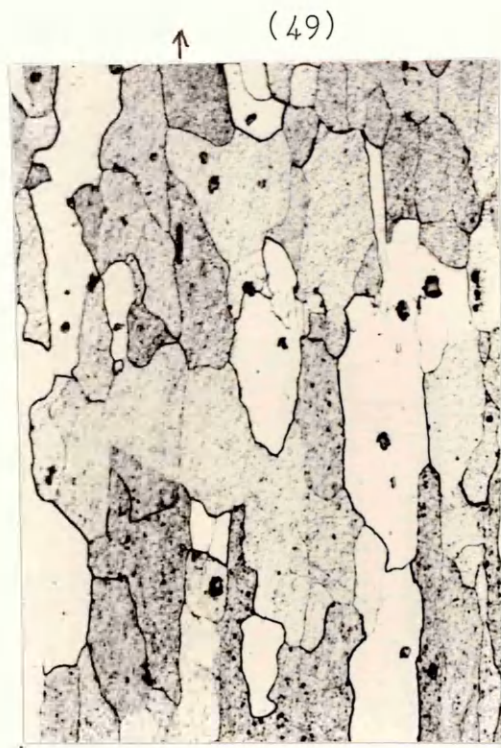


10 (b) Centre X200

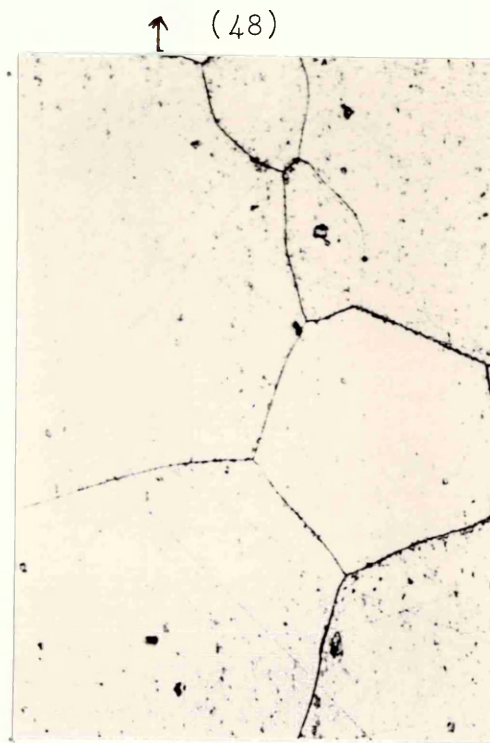
FIG.10 MICROSTRUCTURE OF HOT ROLLED 430 Ti (17 Cr, 0.5 Ti
0.029 (C+N))
(Hot rolling finishing temperature $\sim 900^{\circ}\text{C}$)



11 (a) Annealed 750°C , AC
X200



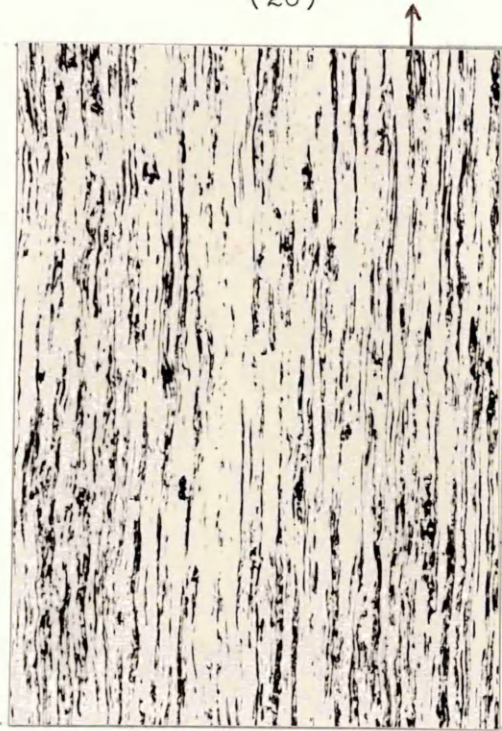
11 (b) Annealed 850°C , AC
X200



11 (c) Annealed 1000°C , AC
X200

FIG.11 MICROSTRUCTURES OF HOT ROLLED AND ANNEALED
430 Ti (17 Cr, 0.5 Ti, 0.029 (C+N))

(20)



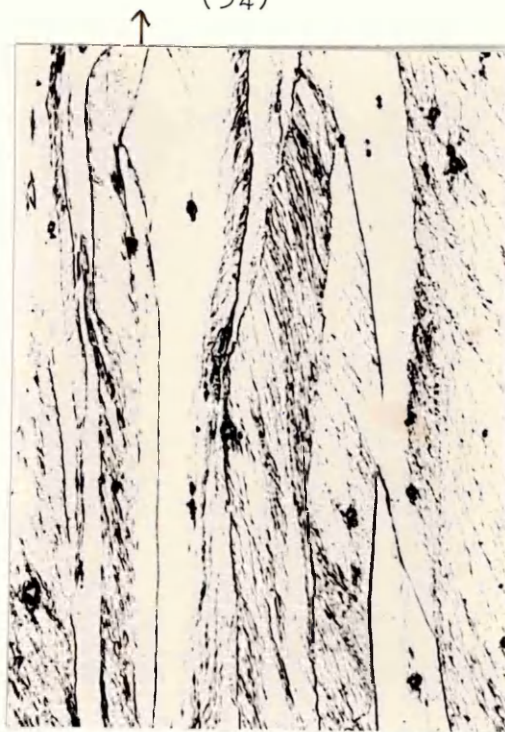
12 (a) As hot rolled + cold rolled
to 70% RA X200

(66)



12 (b) Annealed 850°C, AC +
cold rolled to 70% RA X200

(34)



12 (c) Annealed 1000°C, AC
+ cold rolled to 70% RA
X200

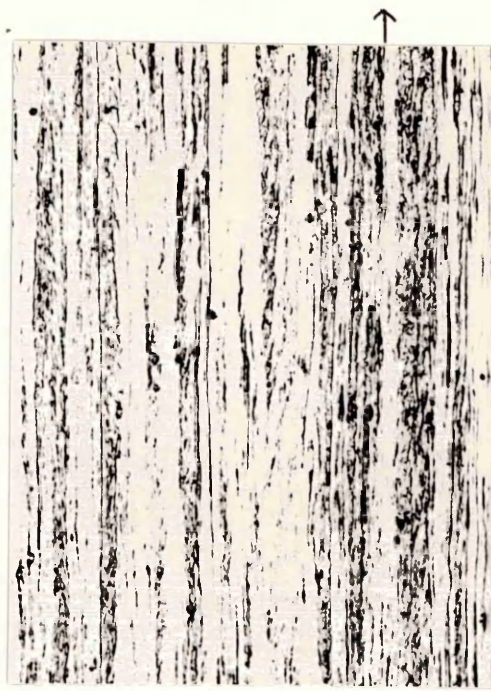
FIG.12 MICROSTRUCTURES OF COLD ROLLED 430 Ti (17 Cr,
0.5 Ti, 0.029 (C+N))

(28)



13 (a) As hot rolled + cold
rolled to 90% RA X200

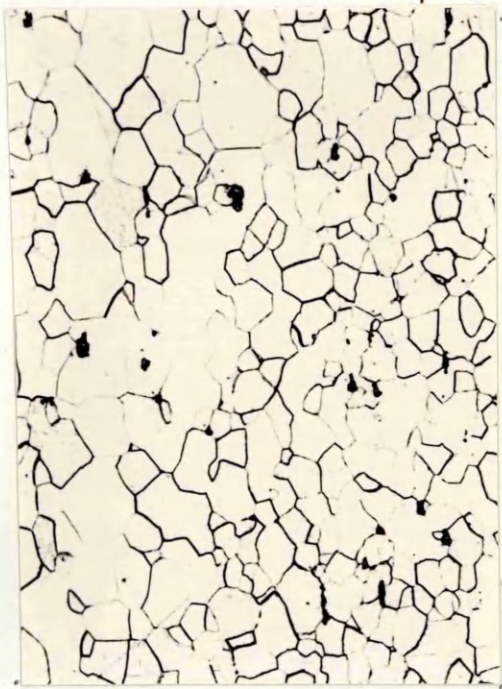
(42)



13 (b) Annealed 1000°C, AC
+ cold rolled to 90% RA X200

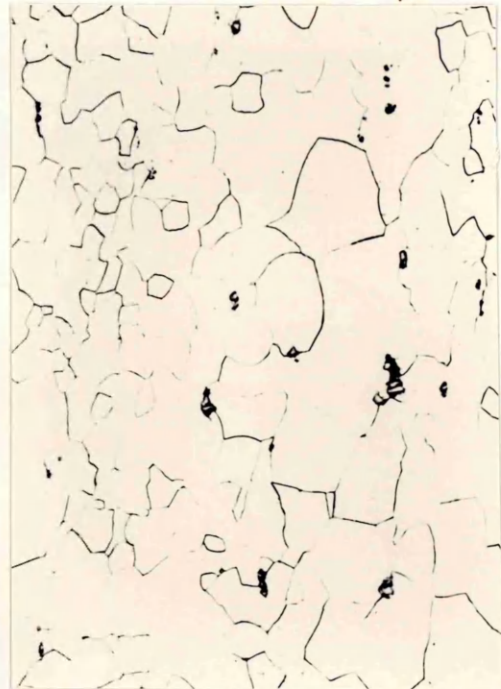
FIG.13 MICROSTRUCTURES OF COLD ROLLED 430 Ti (17 Cr,
0.5 Ti, 0.029 (C+N))

(22)



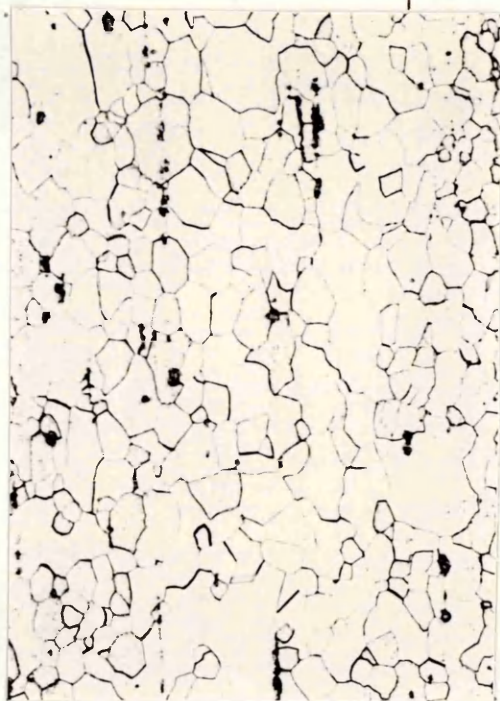
14 (a) As hot rolled + cold rolled to 70% RA + 'rapid' anneal 900°C X200

(36)



14 (b) Annealed 1000°C, AC + cold rolled to 70% RA + 'rapid' anneal 900°C X200

(30)



14 (c) As hot rolled + cold rolled to 90% RA + 'rapid' anneal 900°C X200

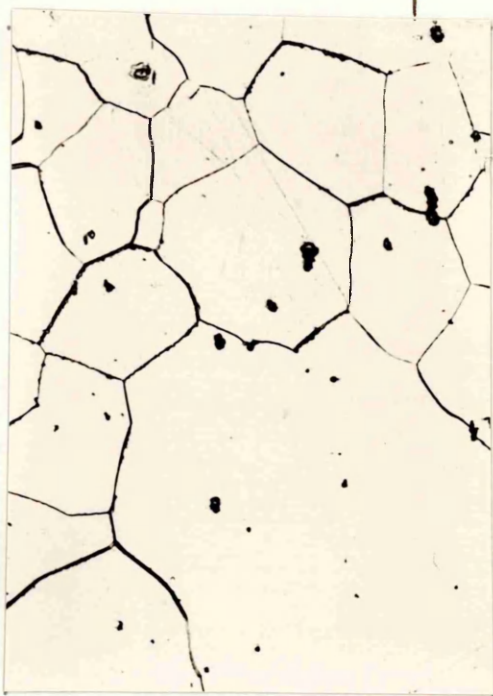
(44)



14 (d) Annealed 1000°C, AC + cold rolled to 90% RA + 'rapid' anneal 900°C X200

FIG.14 MICROSTRUCTURES OF COLD ROLLED AND ANNEALED
430 Ti (17 Cr, 0.5 Ti, 0.029 (C+N))

(23)



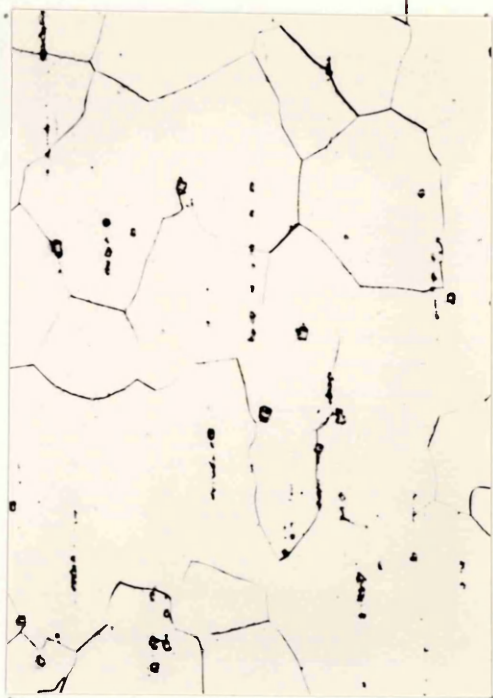
15 (a) As hot rolled + cold rolled to 70% RA + 'rapid' anneal 950°C X200

(37)



15 (b) Annealed 1000°C, AC + cold rolled to 70% RA + 'rapid' anneal 950°C X200

(31)



15 (c) As hot rolled + cold rolled to 90% RA + 'rapid' anneal 950°C X200

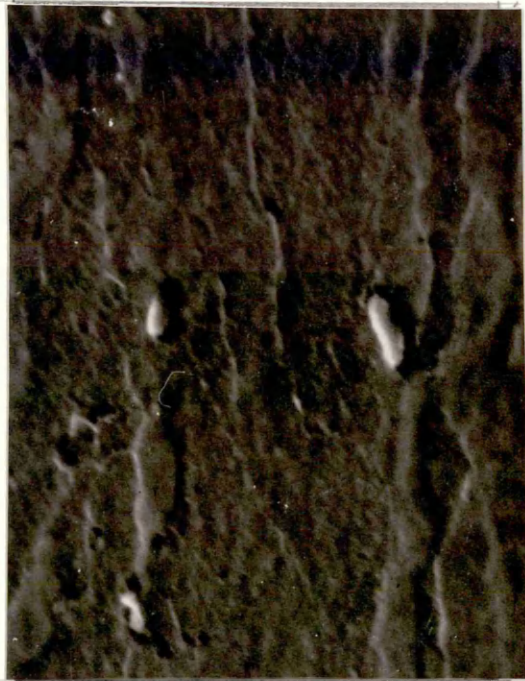
(45)



15 (d) Annealed 1000°C + cold rolled to 90% RA + 'rapid' anneal 950°C X200

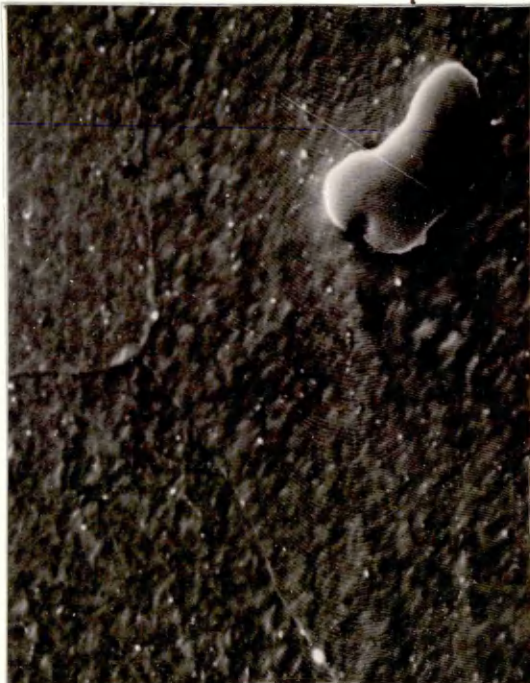
FIG.15 MICROSTRUCTURES OF COLD ROLLED AND ANNEALED 430 Ti (17 Cr, 0.5 Ti, 0.029 (C+N))

(555)



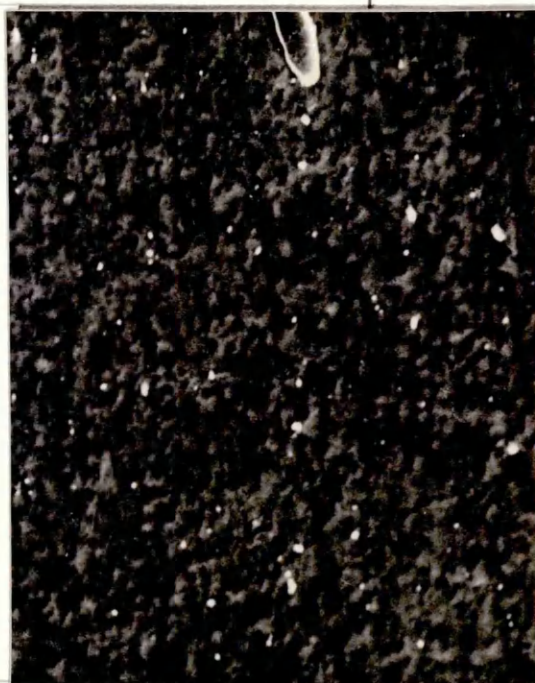
16 (a) As hot-rolled X3200

(650)



16 (b) "Rapid" anneal at 850°C
X3200

(730)



16 (c) Batch anneal at 850°C
X3200

FIG.16 SEM PHOTOMICROGRAPHS OF HOT ROLLED AND ANNEALED
430 Ti (0.5% Ti) STEEL

(1620)



17(a) Rapid anneal at 1000°C, AC X3200



(1622)



17(b) Rapid anneal at 1000°C, WQ X3200

(1019)



17(c) Annealed 1000°C, AC (Heating rate = 50°C hr⁻¹) X3200



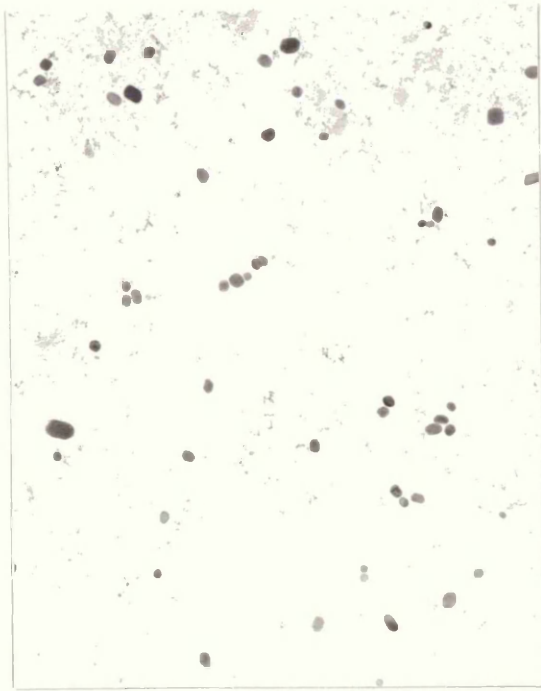
(1029)



17(d) Annealed 1000°C, FC (Heating rate ~ 5000°C hr⁻¹) X3200

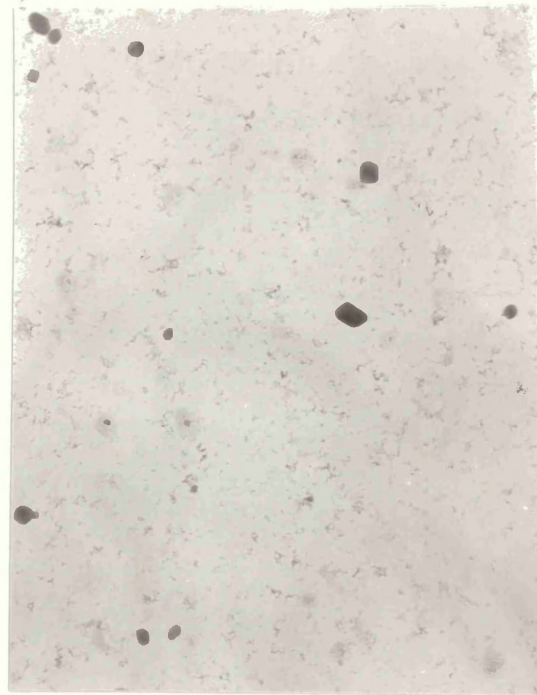
FIG.17 SEM PHOTOMICROGRAPHS OF HOT ROLLED AND ANNEALED 430 Ti (0.5% Ti) STEEL

(6396)



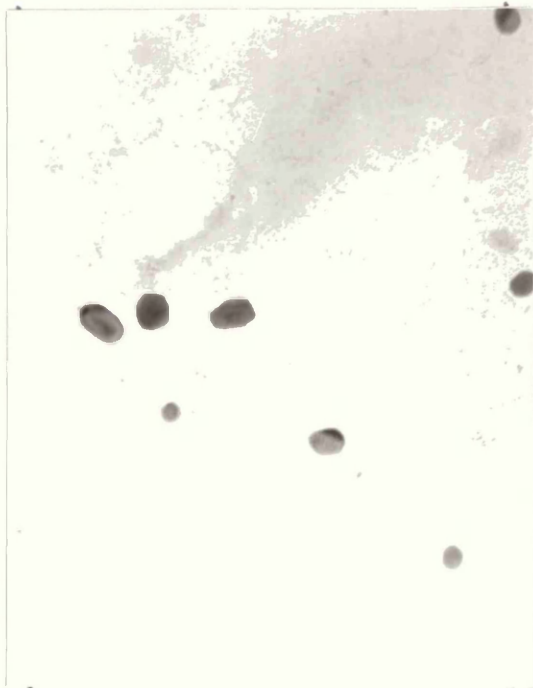
18(a) Rapid anneal at 850°C
X20k

(6382)



18(b) Batch anneal at 850°C
X20k

(6399)



18(c) Rapid anneal at 850°C
X50k

(6379)



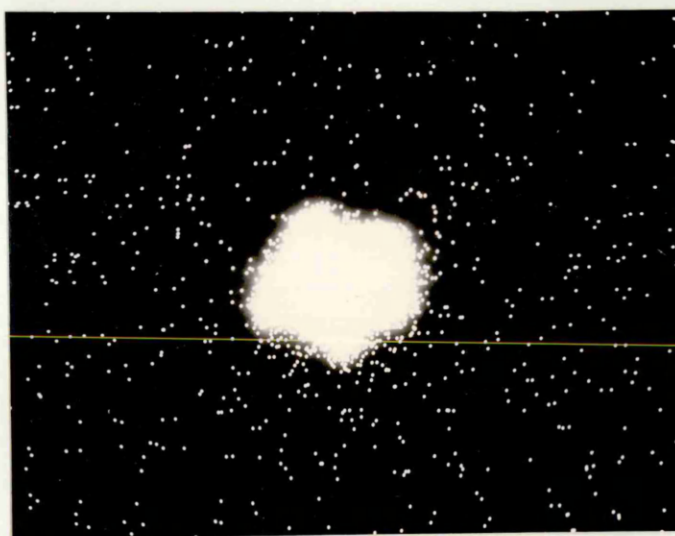
18(d) Rapid anneal at 1000°C
X50k

FIG.18 TEM PHOTOMICROGRAPHS OF EXTRACTION REPLICAS OF
HOT ROLLED AND ANNEALED 430 Ti (0.5% Ti) STEEL

(5268)
Large particle
X3200



(5270)
Titanium $K\alpha$
Map



(5269)
Sulphur $K\alpha$
Map

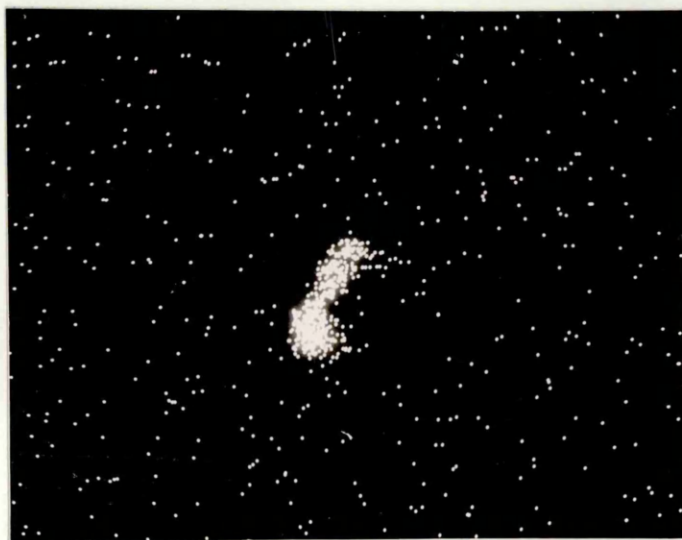


FIG.19 SEM PHOTOGRAPHS OF LARGE TITANIUM-RICH CARBIDE IN 430 Ti (0.5 Ti) STEEL



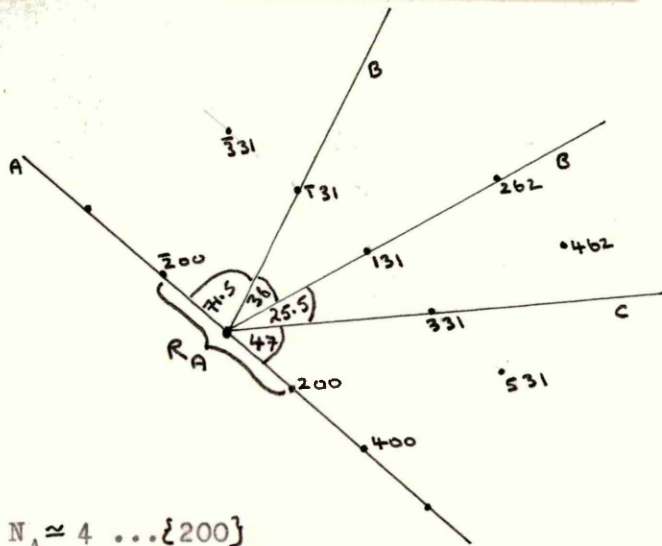
$$2\lambda L = 51.8 \text{ mm} \cdot \text{\AA}$$

$$d = \frac{2\lambda L}{R}$$

$$d = \frac{a}{\sqrt{N}}$$

$$a(\text{TiC}) = 4.36 \text{ \AA}$$

(cubic)



- $R_A \approx 24 \text{ mm}$
- $R_B \approx 40 \text{ mm}$
- $R_C \approx 52 \text{ mm}$

- $d_A \approx 2.61 \text{ \AA}; N_A \approx 4 \dots \{200\}$
- $d_B \approx 1.30 \text{ \AA}; N_B \approx 11 \dots \{311\}$
- $d_C \approx 1.00 \text{ \AA}; N_C \approx 19 \dots \{133\}$

Check angles

- $[\bar{2}00] \wedge [331] \approx 46.5^\circ$ (observed $\approx 47^\circ$)
- $[\bar{2}00] \wedge [131] \approx 72.5^\circ$ (observed $\approx 71.5^\circ$)
- $[131] \wedge [131] \approx 35^\circ$ (observed $\approx 36^\circ$)
- $[131] \wedge [331] \approx 26^\circ$ (observed $\approx 25.5^\circ$)

FIG. 20 ELECTRON DIFFRACTION PATTERN FOR A LARGE TiC CARBIDE PARTICLE IN 430Ti STEEL

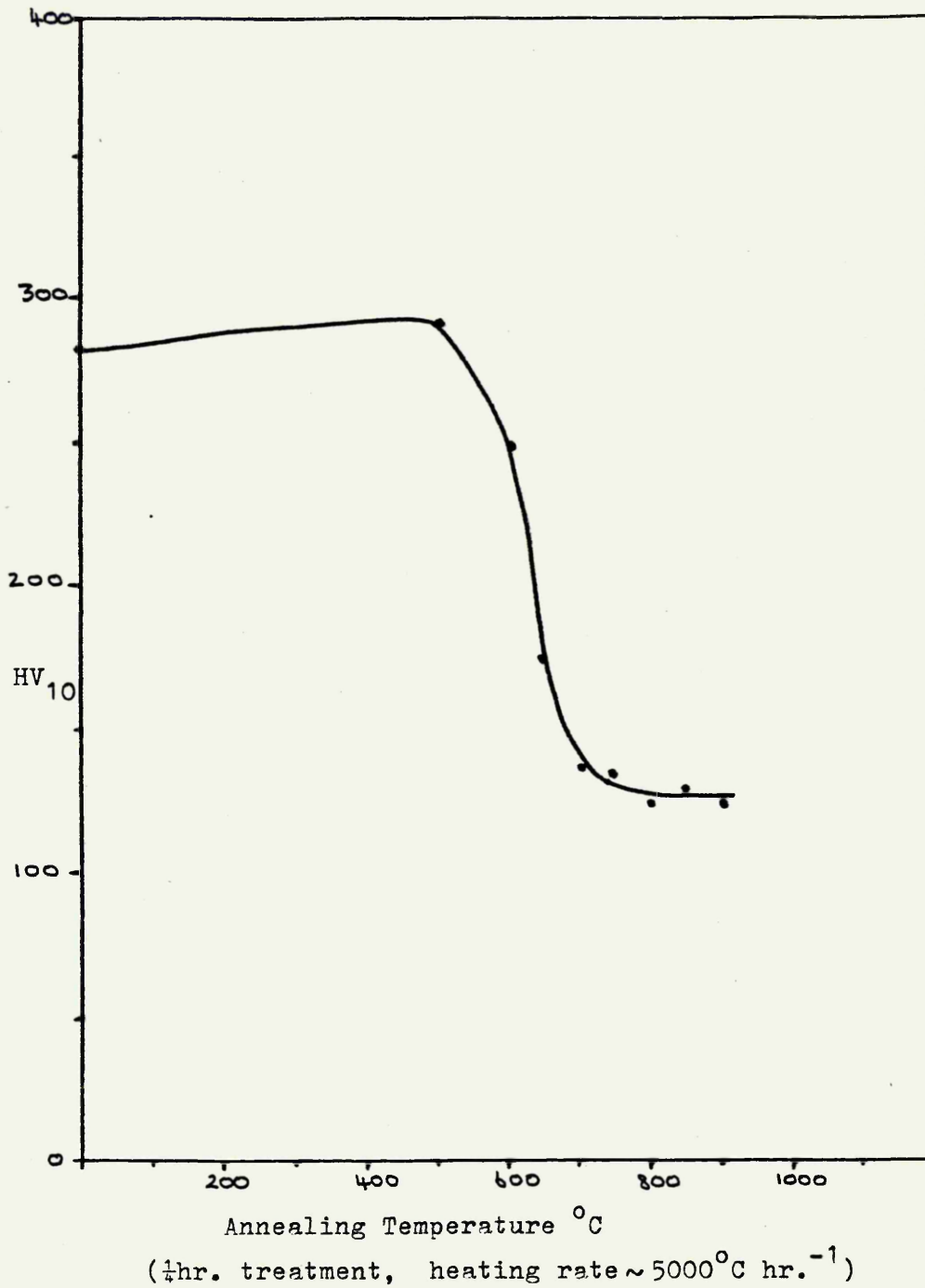
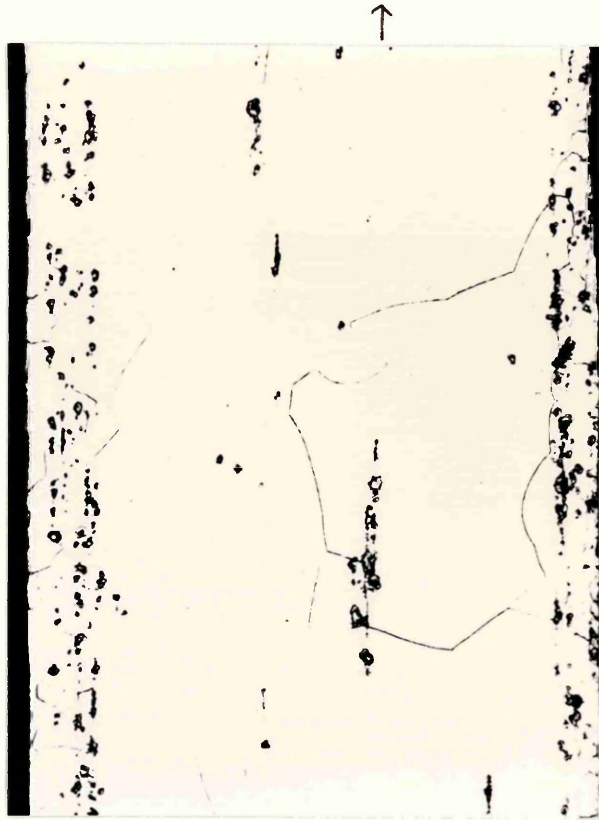


FIGURE 21 Variation of Hardness with Annealing Temperature
for 430Ti (0.3% Ti) Steel after Cold Rolling
to 95% RA and Annealing.



Batch anneal at 850°C , cold
rolled to 90% RA, and rapid
anneal at 900°C X200

FIG.22 Ti (CN) STRINGERS IN 430 Ti (0.3 Ti) STEEL

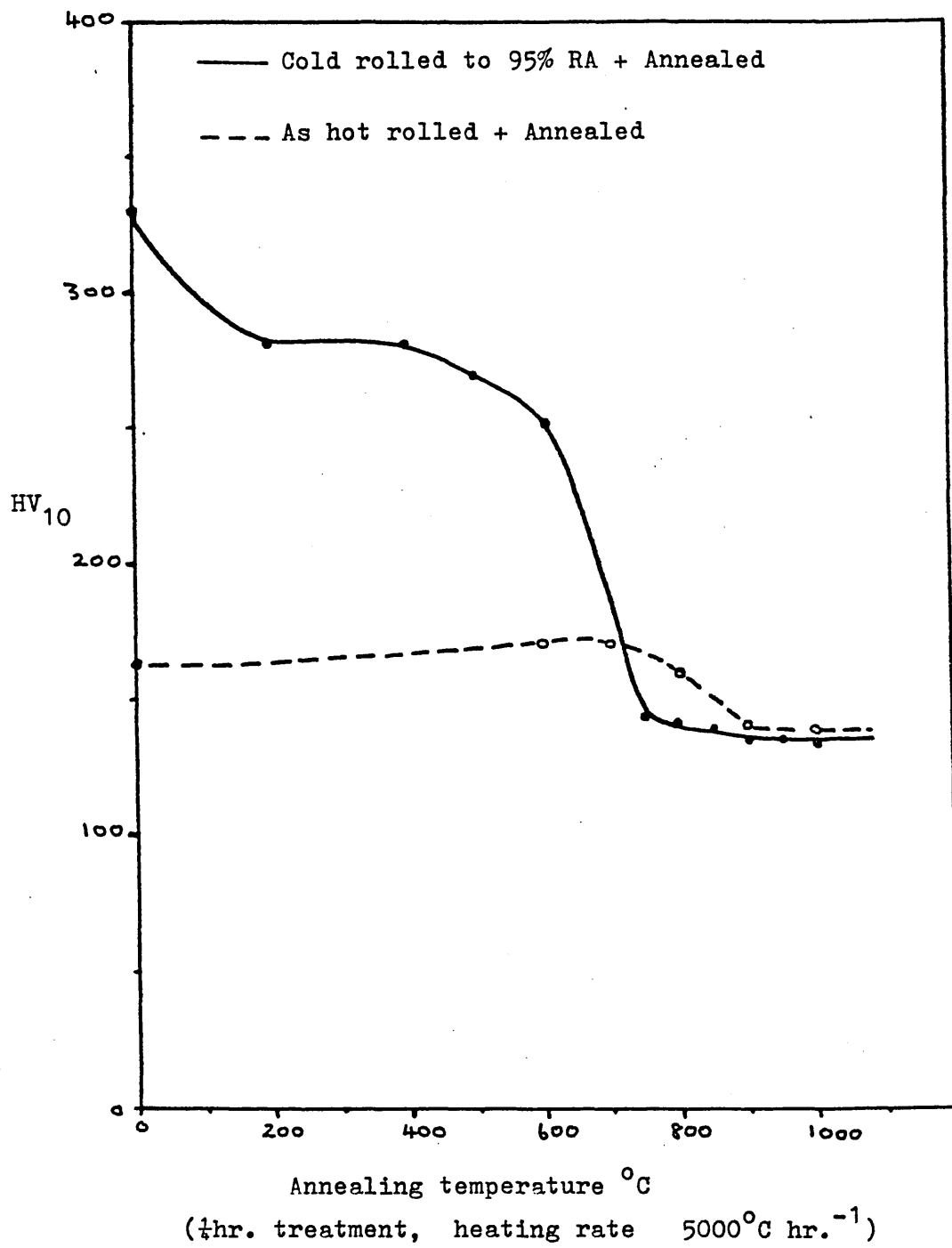
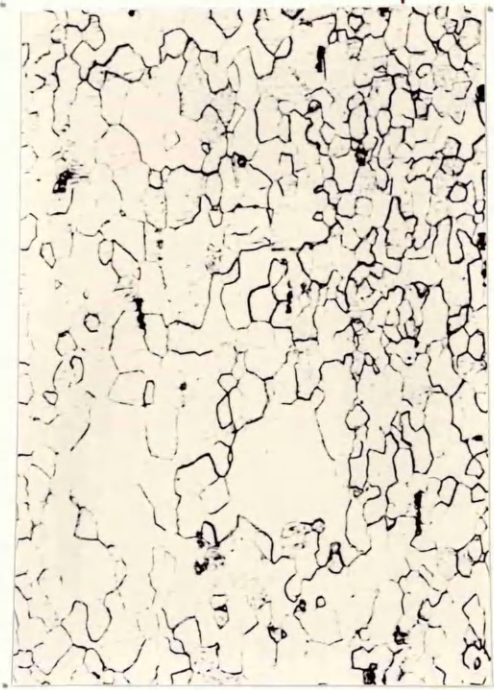


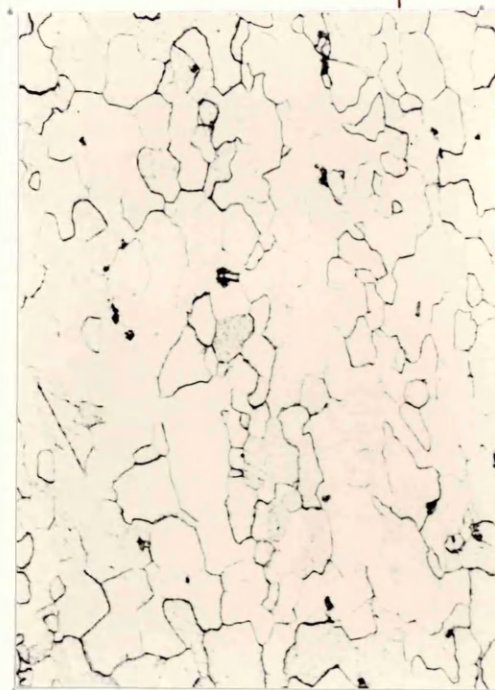
FIGURE 23 Variation of Hardness with Annealing Temperature
for 409 Steel.

(86)



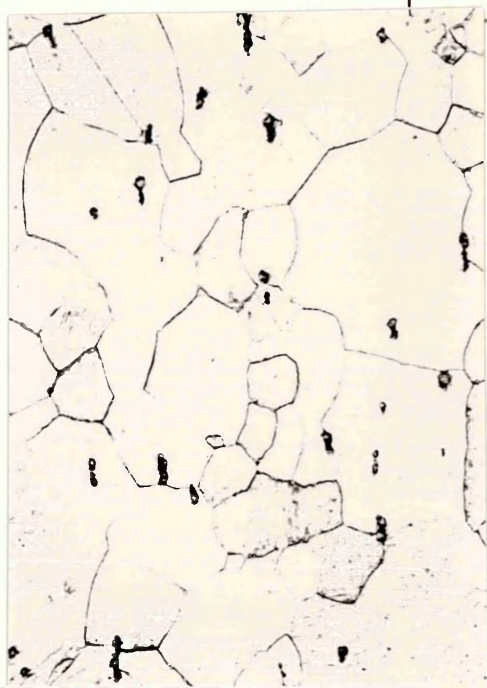
24(a) Hot rolled, cold rolled to 70% RA and 'rapid' annealed at 900°C X200

(89)



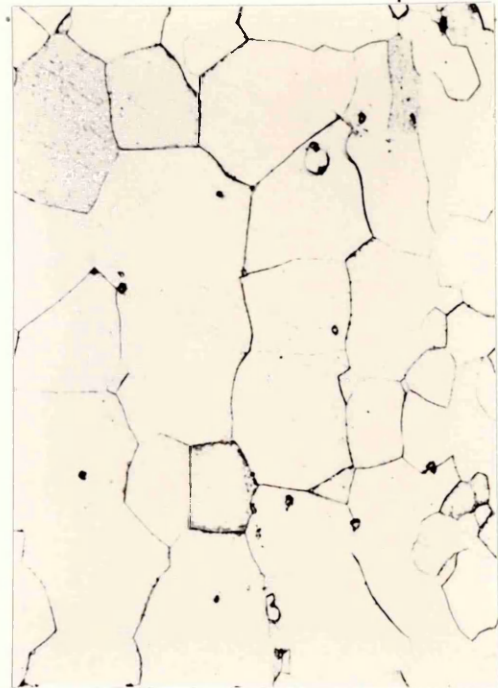
24(b) Hot rolled and rapid annealed at 1000°C, cold rolled to 70% RA and rapid annealed at 900°C X200

(87)



24(c) As hot rolled, cold rolled to 70% RA, rapid anneal 950°C X200

(90)



24(d) Hot rolled, rapid anneal 1000°C, cold rolled to 70% RA, rapid anneal 950°C X200

FIG.24 MICROSTRUCTURES OF COLD ROLLED AND ANNEALED 409 (12 Cr, 0.5 Ti) STEEL

(1615)



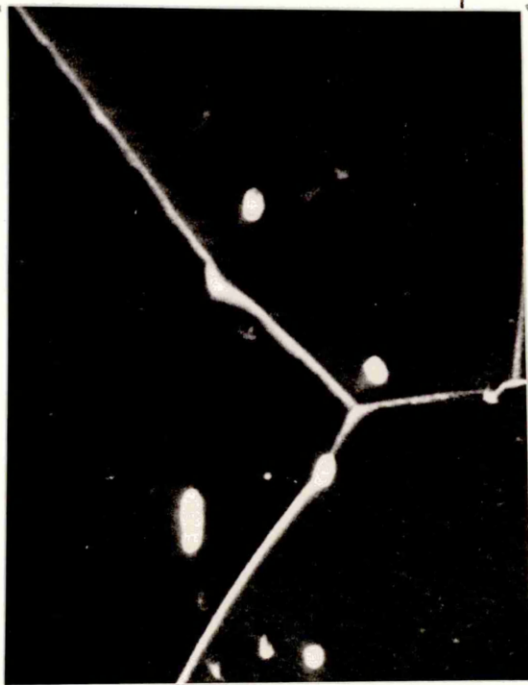
25 (a)

Rapid anneal at

850°C

X3200

(1617)



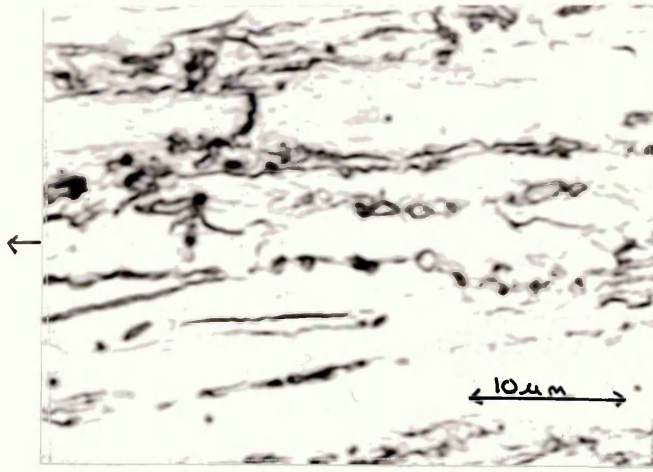
25 (b)

Rapid anneal at

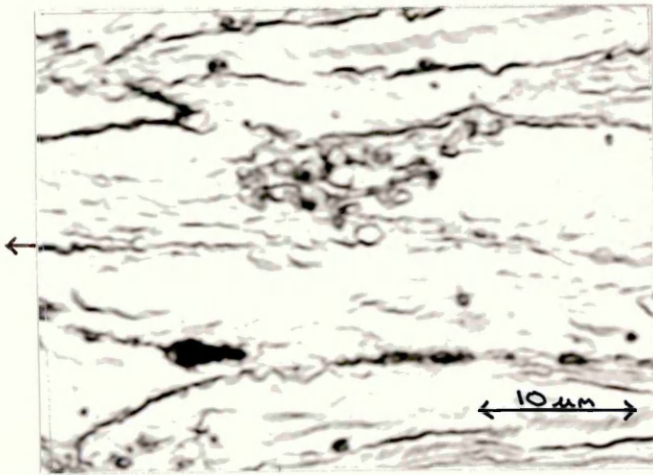
1000°C

X3200

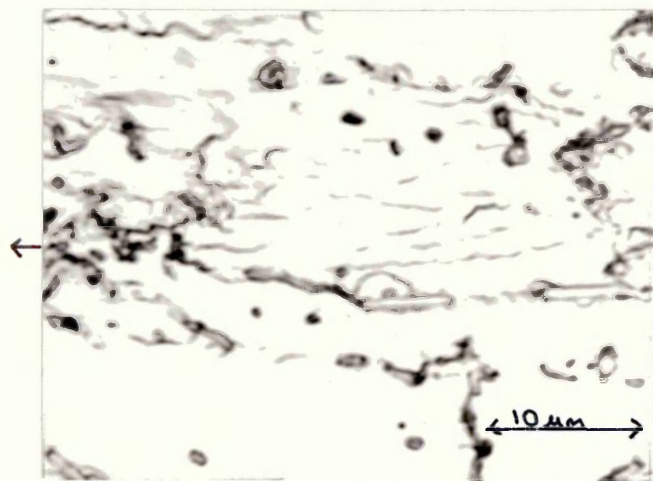
FIG. 25 SEM MICROGRAPHS OF HOT ROLLED AND ANNEALED
409 (12 Cr, 0.5% Ti) STEEL



(a) Batch anneal
at 1000°C + cold
rolled to 80% RA +
5 mins at 650°C , AC



(b) Batch anneal
at 850°C + cold
rolled to 80% RA +
5 mins at 650°C , AC



(c) Batch anneal
at 1000°C + cold
rolled to 70% RA +
5 mins at 650°C , AC

FIG. 26 TYPICAL MICROSTRUCTURES OF 430 STEEL AFTER
COLD ROLLING AND ANNEALING FOR 5 mins at 650°C



(5125)

(a) Batch anneal at 1000°C + cold rolled to 90% RA + 5 mins at 650°C



(6021)

(b) Batch anneal at 1000°C + cold rolled to 80% RA + 5 mins at 650°C

FIG.27 TEM MICROGRAPHS OF OVERSIZED SUBGRAINS AT GRAIN BOUNDARIES IN 430 STEEL AFTER COLD ROLLING AND ANNEALING FOR 5 mins at 650°C



(6008)

(a) (Cold rolled to 80% RA)
Large (012) [142] subgrain

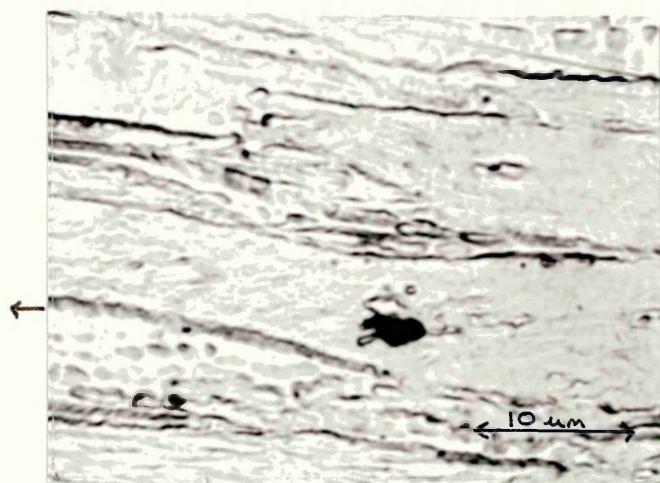


(5781)

(b) (Cold rolled to 70% RA)
Large (001) [010] subgrain

FIG. 28 TEM MICROGRAPHS OF LARGE SUBGRAINS IN 430 STEEL
AFTER COLD ROLLING AND ANNEALING FOR 5 mins at 650°C

(a) Rapid anneal at
850°C + cold rolled
to 80% RA + 5 mins
at 650°C.



(b) Rapid anneal at
850°C, + cold
rolled to 80% RA +
5 mins at 650°C

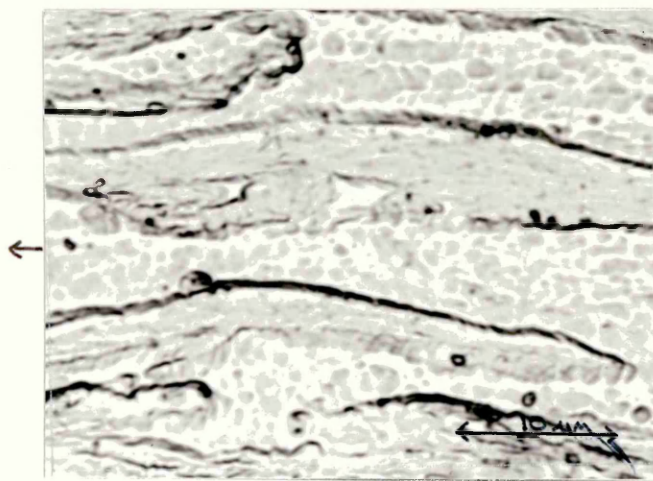
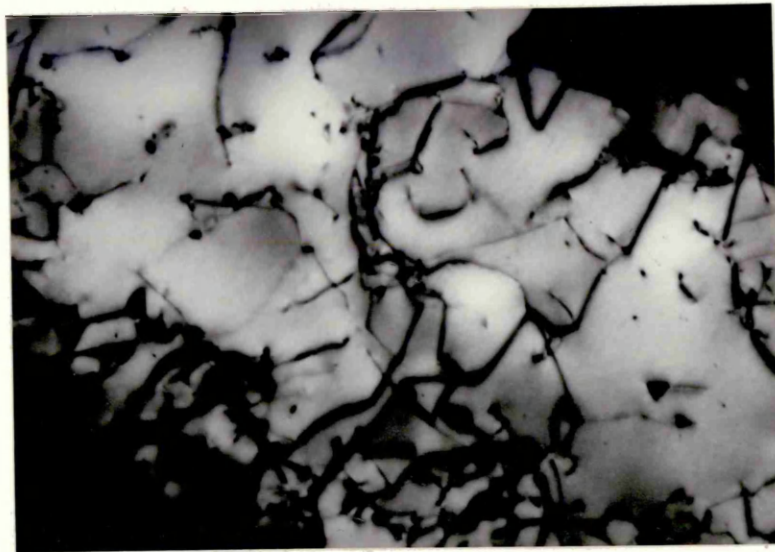


FIG.29 TYPICAL MICROSTRUCTURES OF 430 Ti STEEL AFTER
COLD ROLLING AND ANNEALING FOR 5 mins at 650°C



(5772)

(a)

← 0.1 μm →



(5774)

(b)

← 0.2 μm →

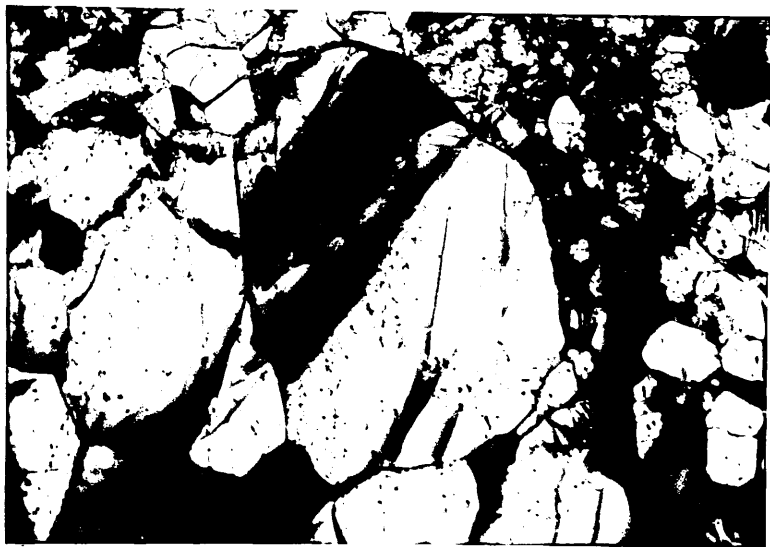
FIG. 30 TEM MICROGRAPHS SHOWING SUBSTRUCTURE CONTAINING
VERY FINE PARTICLES IN 430Ti STEEL (HOT ROLLED,
COLD ROLLED TO 60% RA. ANNEALED 5 mins at 650°C)



(4642)

(a)

← 1.0 μm →

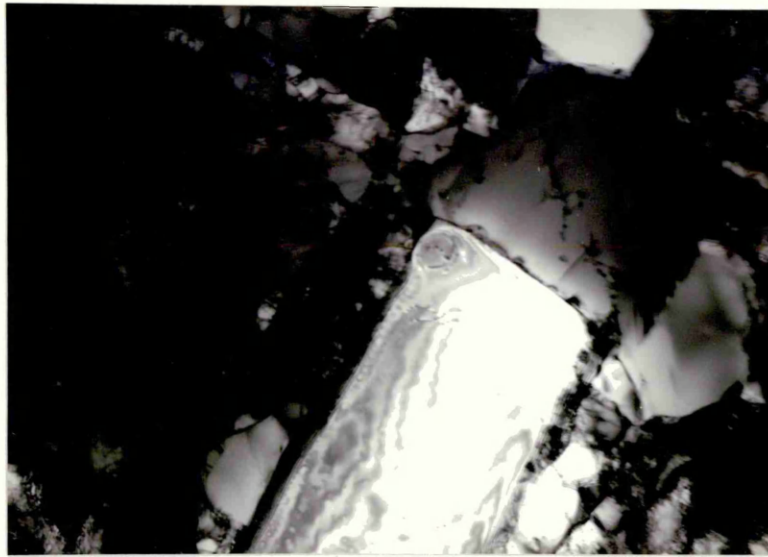


(5225)

(b)

← 2 μm →

FIG. 31 TEM MICROGRAPHS SHOWING OVERSIZED SUBGRAINS, APPARENTLY IN GRAIN INTERIORS OF 430 Ti STEEL (RAPID ANNEAL AT 1000°C, AC, COLD ROLLED TO 90% RA AND ANNEALED 5 mins at 700°C)



(4645)

← 1.0 μm →

(a) Rapid anneal at 1000°C + cold
rolled to 90% RA + 5 mins at 650°C

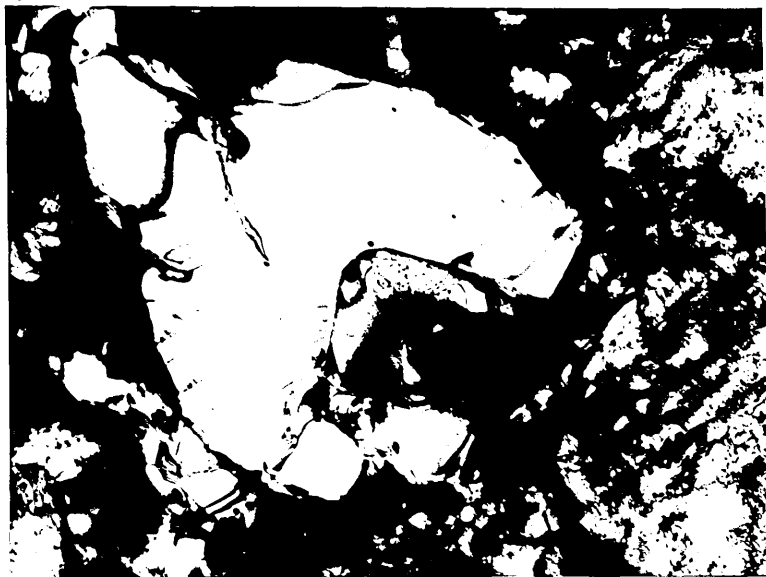


(5268)

← 1.0 μm →

(b) Rapid anneal 850°C + cold
rolled to 80% RA + 5 mins at 650°C

FIG. 32 TEM MICROGRAPHS OF LARGE Ti (CN) PARTICLES
AND THEIR DEFORMATION ZONES IN PARTIALLY
RECRYSTALLISED 430 Ti STEEL

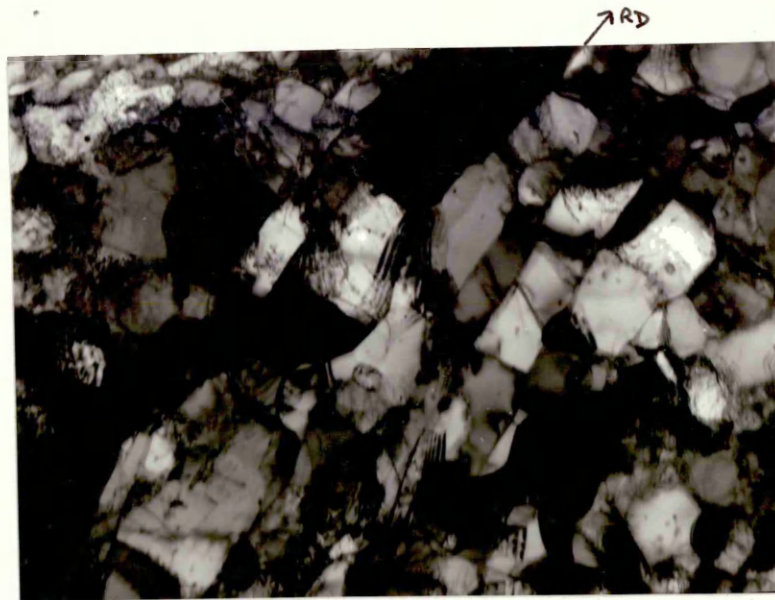


(5261)

← 1.0 μm →

Rapid anneal 850°C + cold rolled to
80% RA + 5 mins at 650°C

FIG. 33 TEM MICROGRAPH OF LARGE Ti (CN) PARTICLE
WITH SMALL SUBGRAINS IN THE DEFORMATION ZONE



(5632)

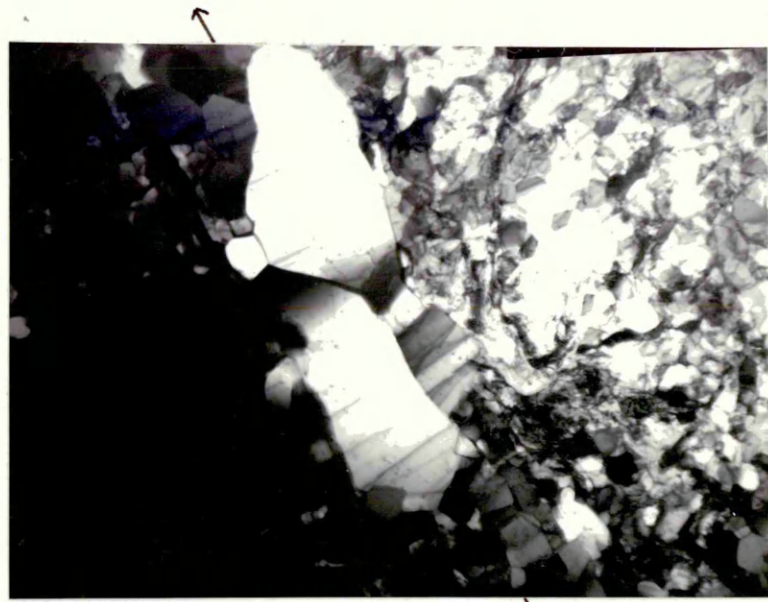
↙ ↔ 0.5 μm ↔
 (a) Batch anneal at 850°C + cold rolled
 to 70% RA + 5 mins at 600°C



(5496)

↙ ↔ 1.0 μm ↔
 (b) Annealed 750°C + cold rolled to
 90% RA + 5 mins at 650°C

FIG.34 TEM MICROGRAPHS SHOWING MICROBANDS OF ELONGATED SUBGRAINS IN 430 Ti STEEL



(5201)

(a)



(5204)

(b)

FIG. 35 TEM MICROGRAPHS OF LARGE SUBGRAINS IN A MICROBAND
ADJACENT TO A GRAIN BOUNDARY IN 430 Ti STEEL.
(RAPID ANNEAL AT 1000°C; COLD ROLLED TO 80% RA,
5 mins at 700°C)

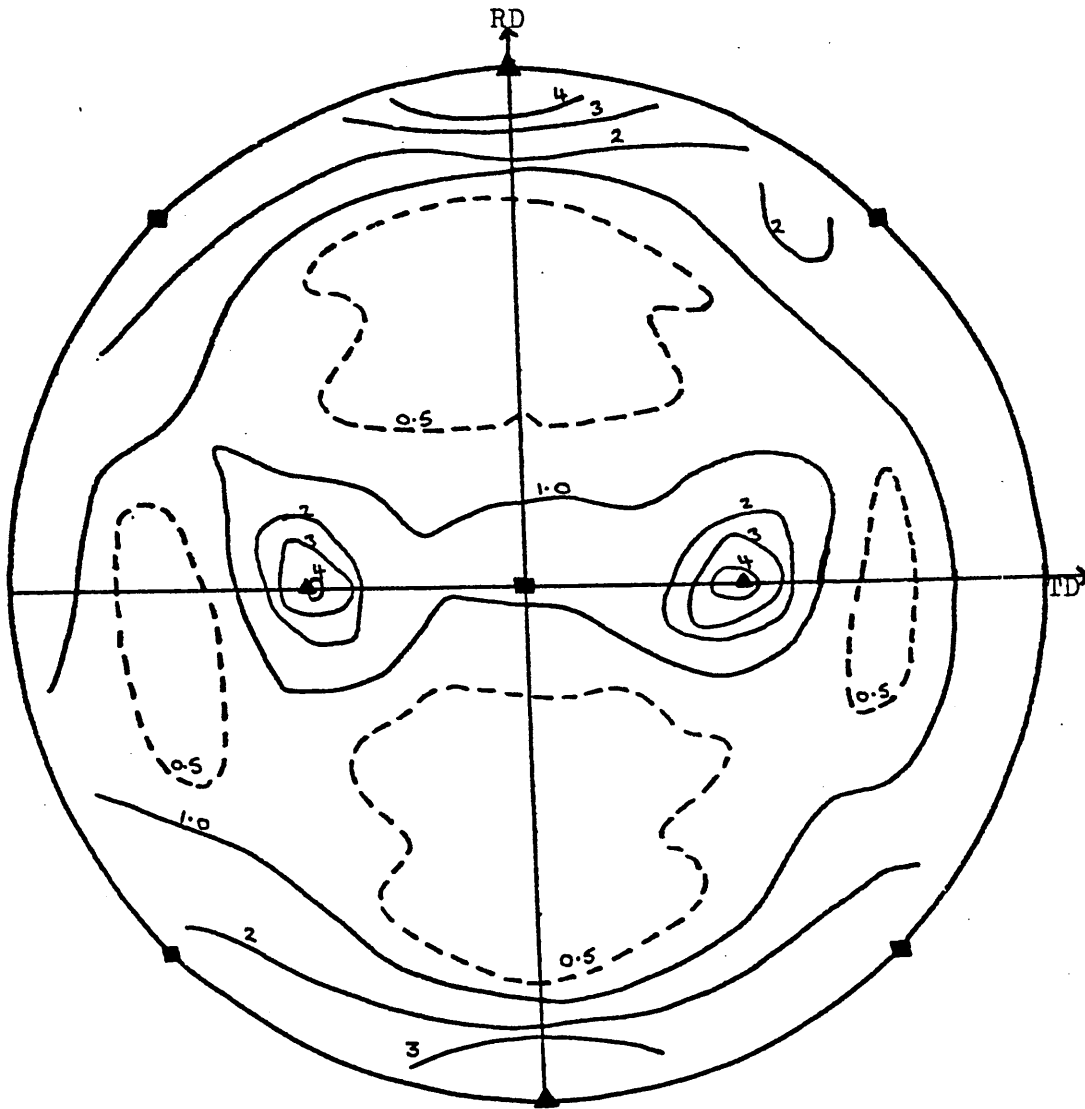


(4935)

← 0.8 μm →

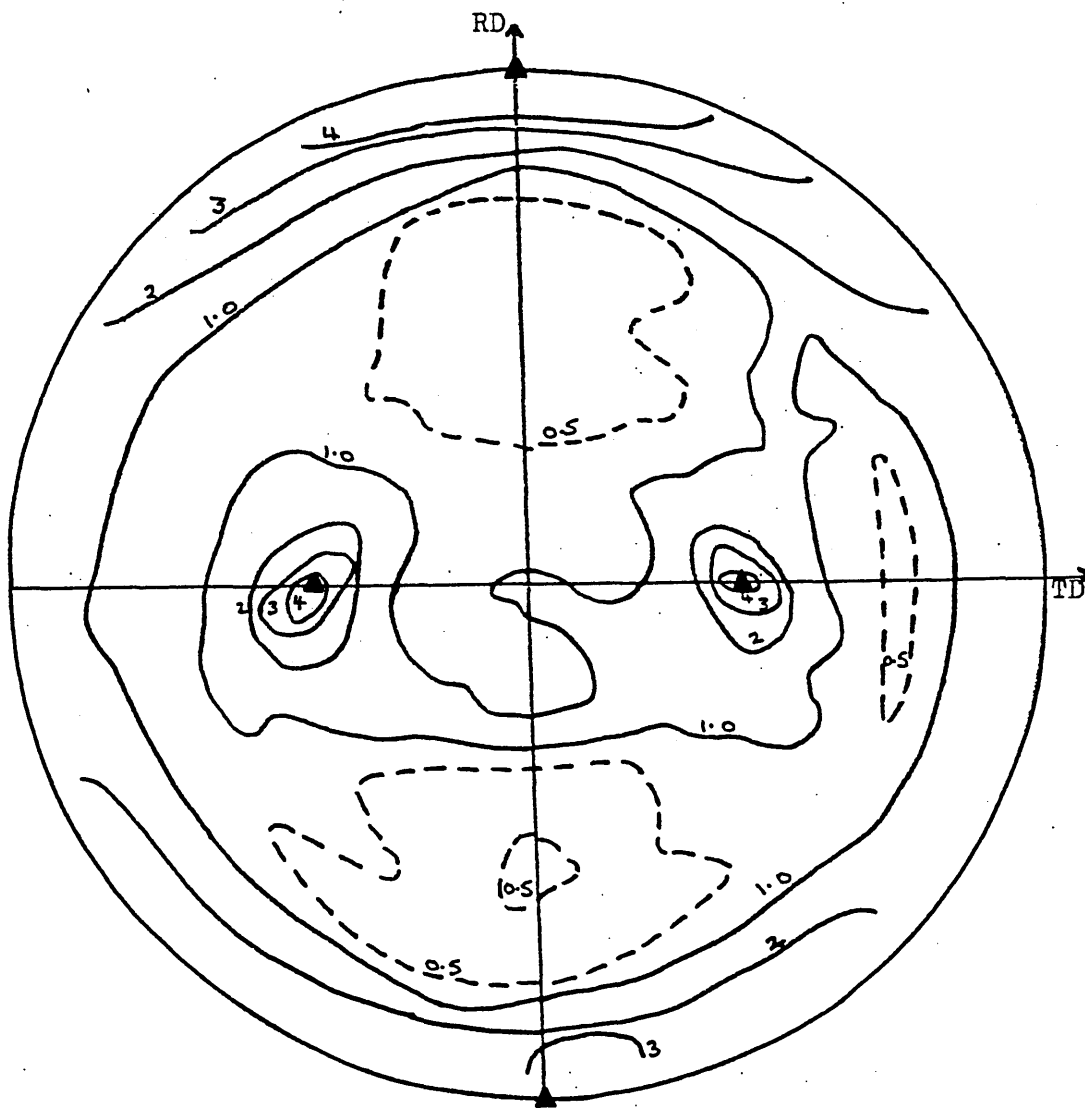
Rapid anneal at 850°C + cold rolled to
90% RA + 5 mins at 650°C

FIG. 36 TEM PHOTOMICROGRAPH SHOWING RECRYSTALLISATION
ADJACENT TO A GRAIN BOUNDARY IN 430 Ti STEEL



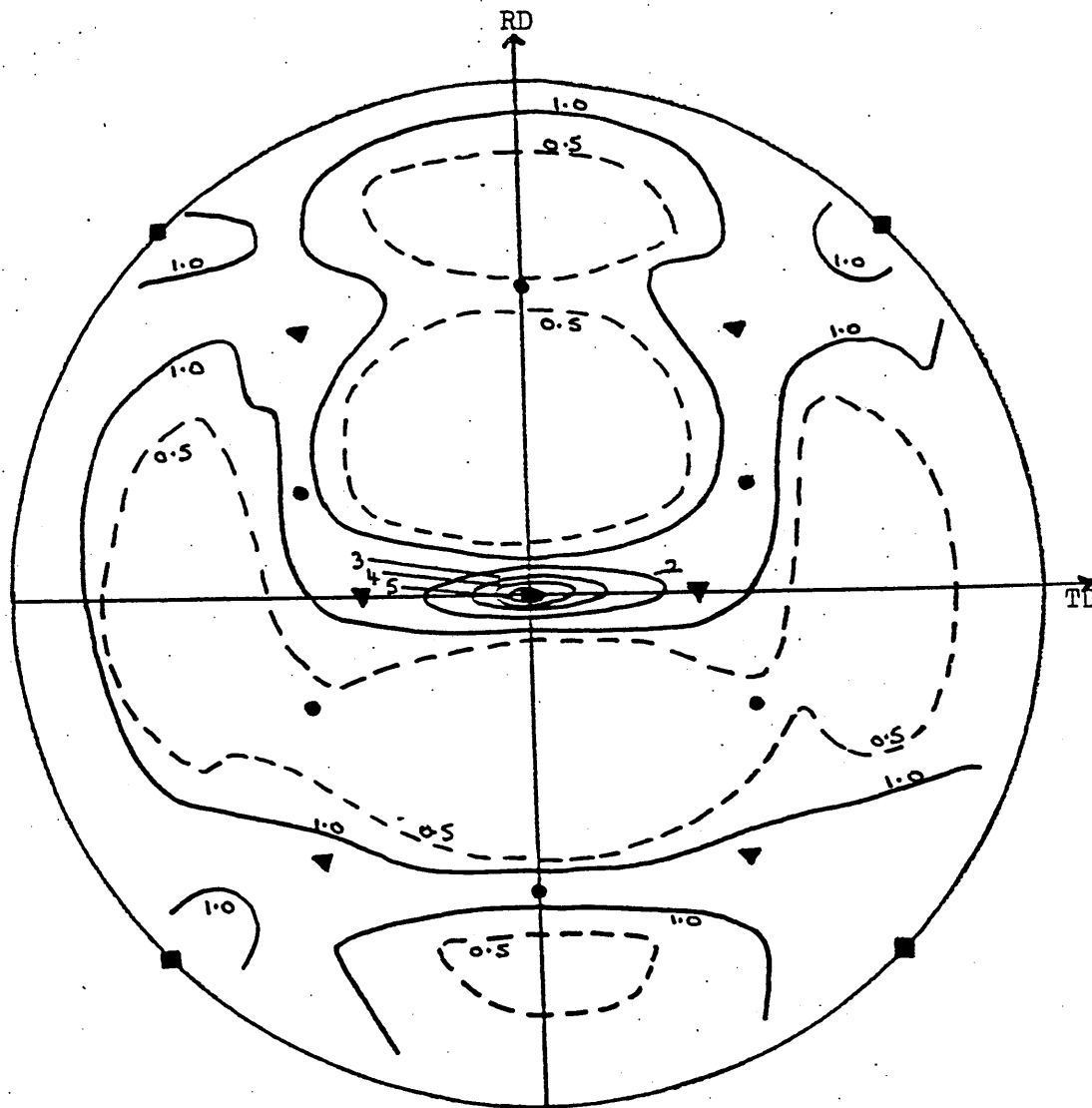
- $\{100\}\langle 011\rangle$
- ▲ $\{110\}\langle 001\rangle$

FIGURE 37 $\{200\}$ Pole Figure for the Surface of Hot Rolled 430 Strip



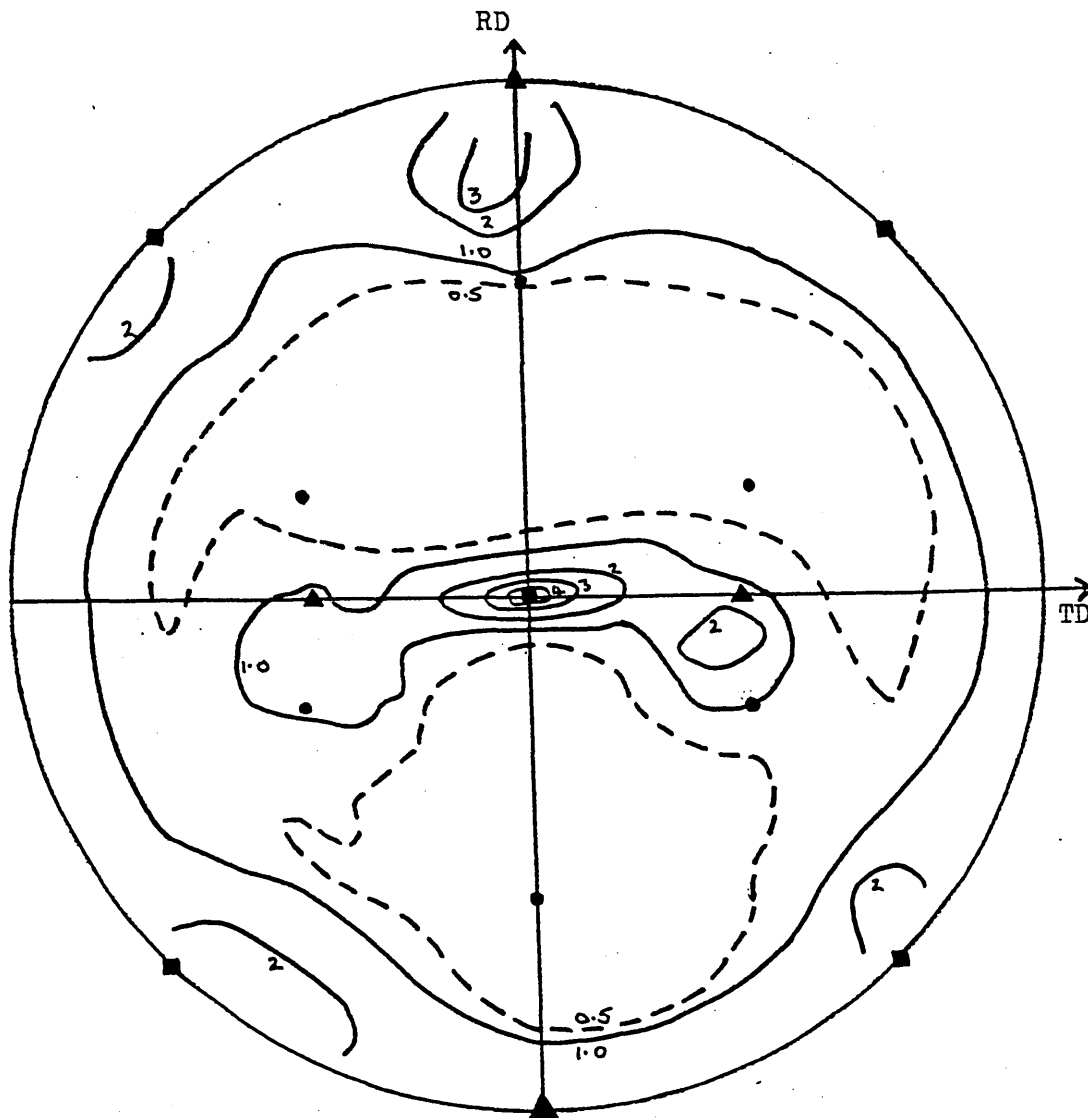
▲ $\{110\}\langle 001\rangle$

FIGURE 38 $\{200\}$ Pole Figure for the Surface of 430 Strip
after Hot Rolling + Rapid Annealing at 850°C.



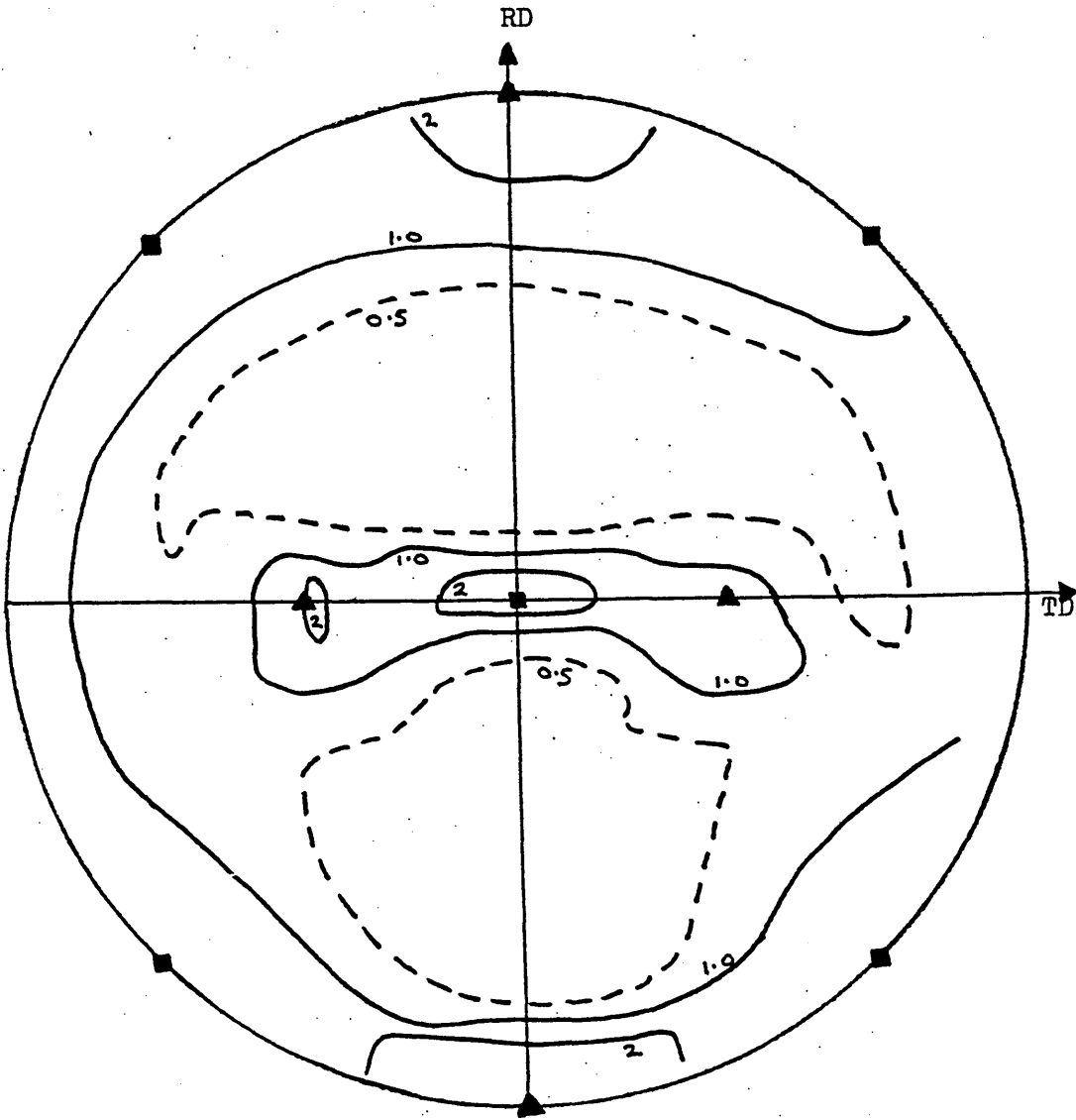
- $\{100\}\langle 011\rangle$
- $\{554\}\langle 225\rangle$
- ▼ $\{112\}\langle 110\rangle$

FIGURE 39 $\{200\}$ Pole Figure for the Quarterplane of Hot Rolled 430 Strip.



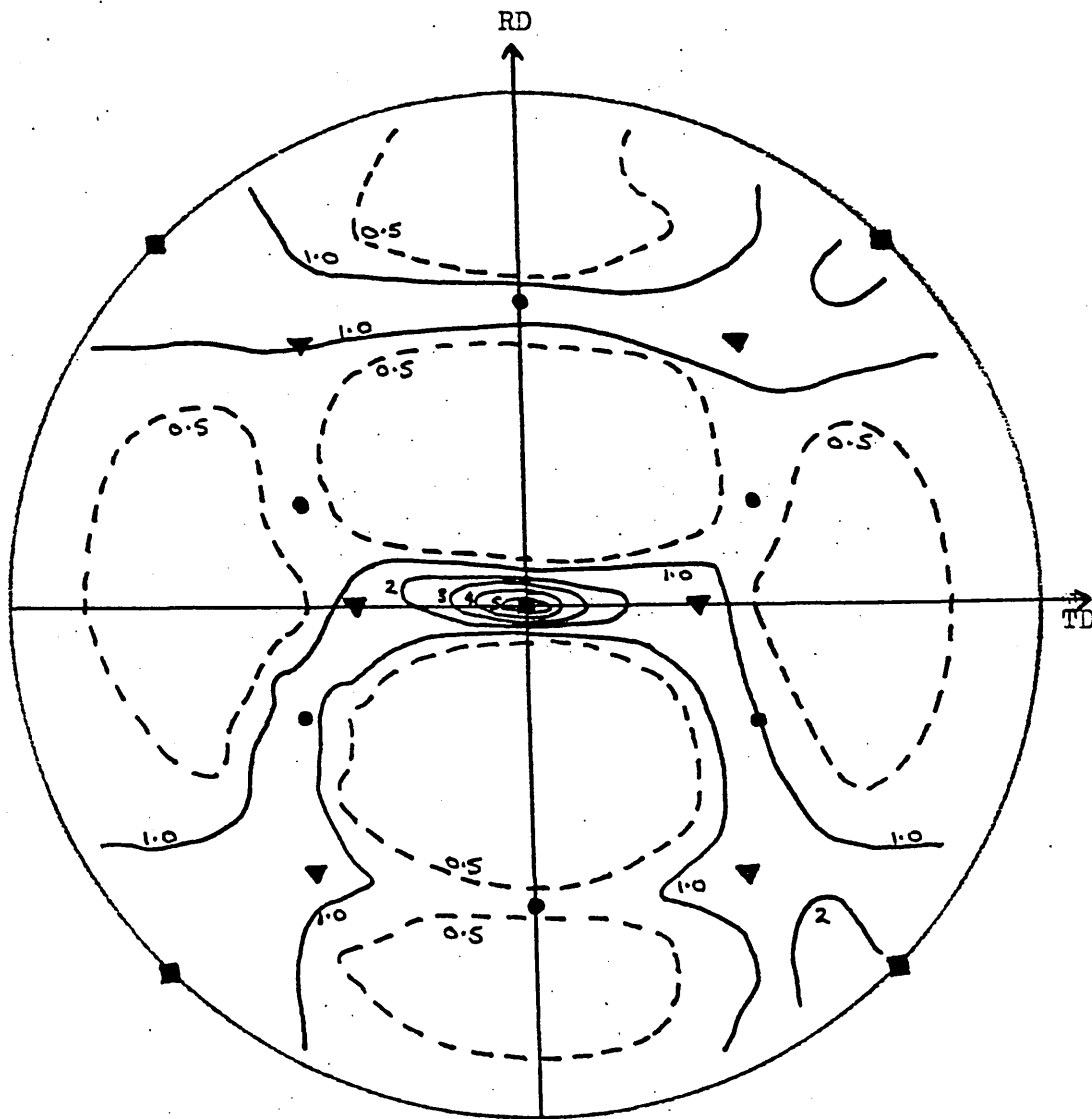
- $\{100\}\langle 011\rangle$
- ▲ $\{110\}\langle 001\rangle$
- $\{554\}\langle 225\rangle$

FIGURE 40 $\{200\}$ Pole Figure for the Quarterplane of 430
Strip after Hot Rolling + Rapid Annealing at 750°C.



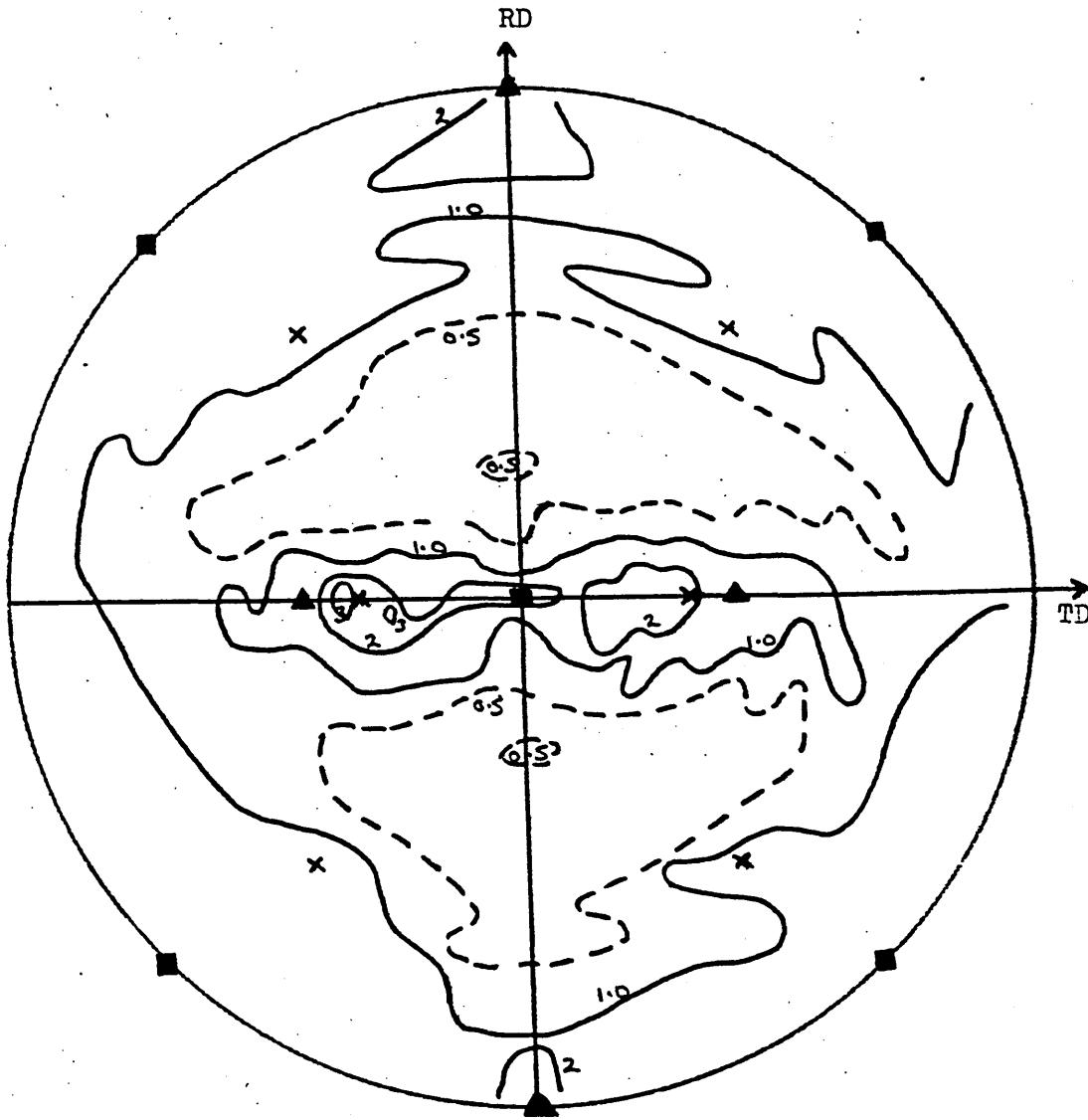
- $\{100\}\langle 011\rangle$
- ▲ $\{110\}\langle 001\rangle$

FIGURE 41 $\{200\}$ Pole Figure for the Quarterplane of 430 Strip
after Hot Rolling and Batch Pre-annealing at 850°C.



- $\{100\} \langle 011 \rangle$
- $\{554\} \langle 225 \rangle$
- ▼ $\{112\} \langle 110 \rangle$

FIGURE 42 $\{200\}$ Pole Figure for the Centre of 430 Strip after Hot Rolling and Rapid Pre-annealing at 850°C.



- $\{100\} \langle 011 \rangle$
- ▲ $\{110\} \langle 001 \rangle$
- × $\{112\} \langle 110 \rangle$

FIGURE 43 $\{200\}$ Pole Figure for the Midplane of 430 Strip
after Hot Rolling and Batch Pre-annealing at 1000°C.

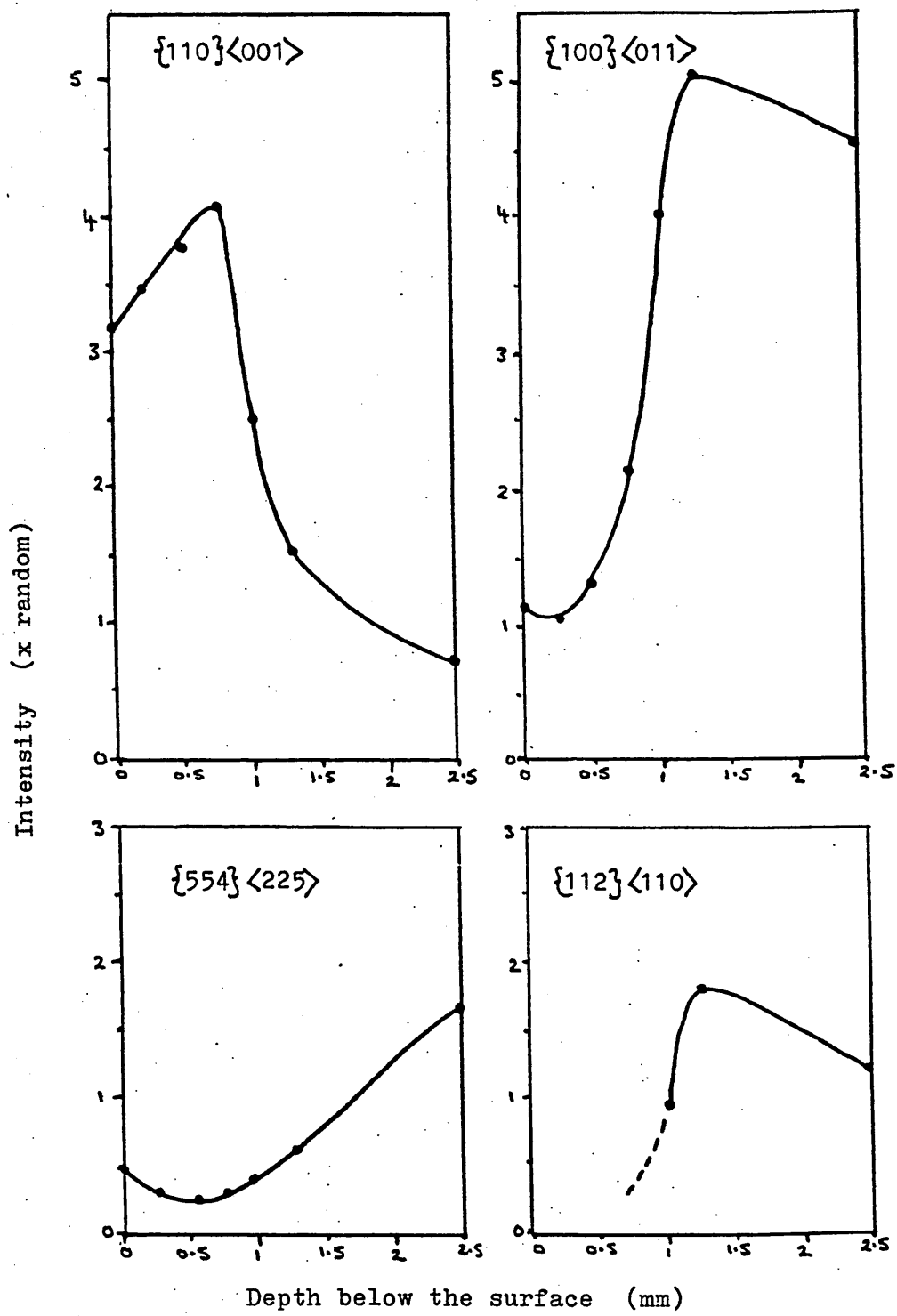


FIGURE 44 Through-Thickness Variation in Intensity of the Main Orientations in 5mm Thick, Hot Rolled 430 Strip.

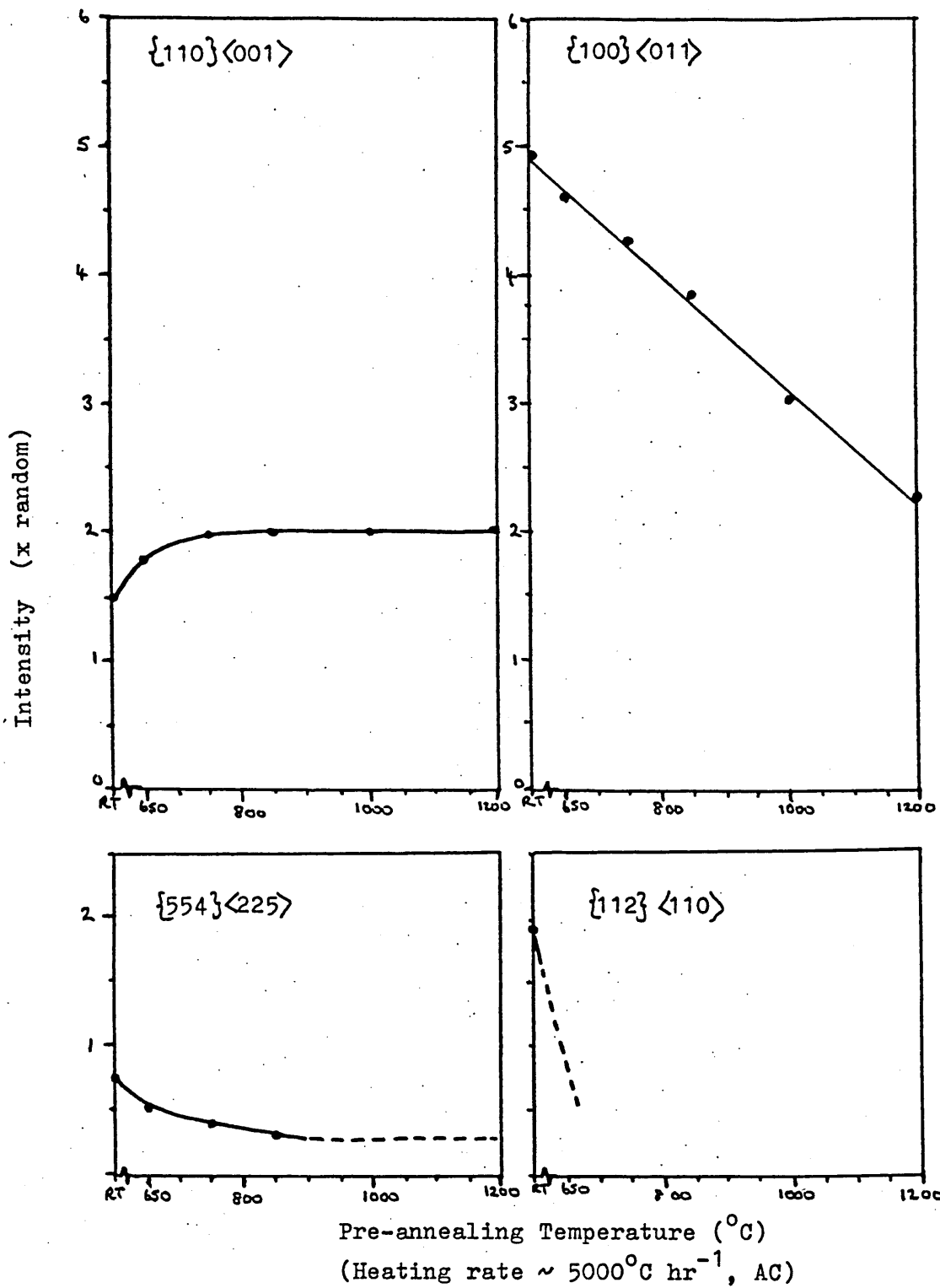


FIGURE 45 Variation in Intensity of the Main Orientations
at the Quarterplane of 430 Strip with Pre-annealing
Temperature.

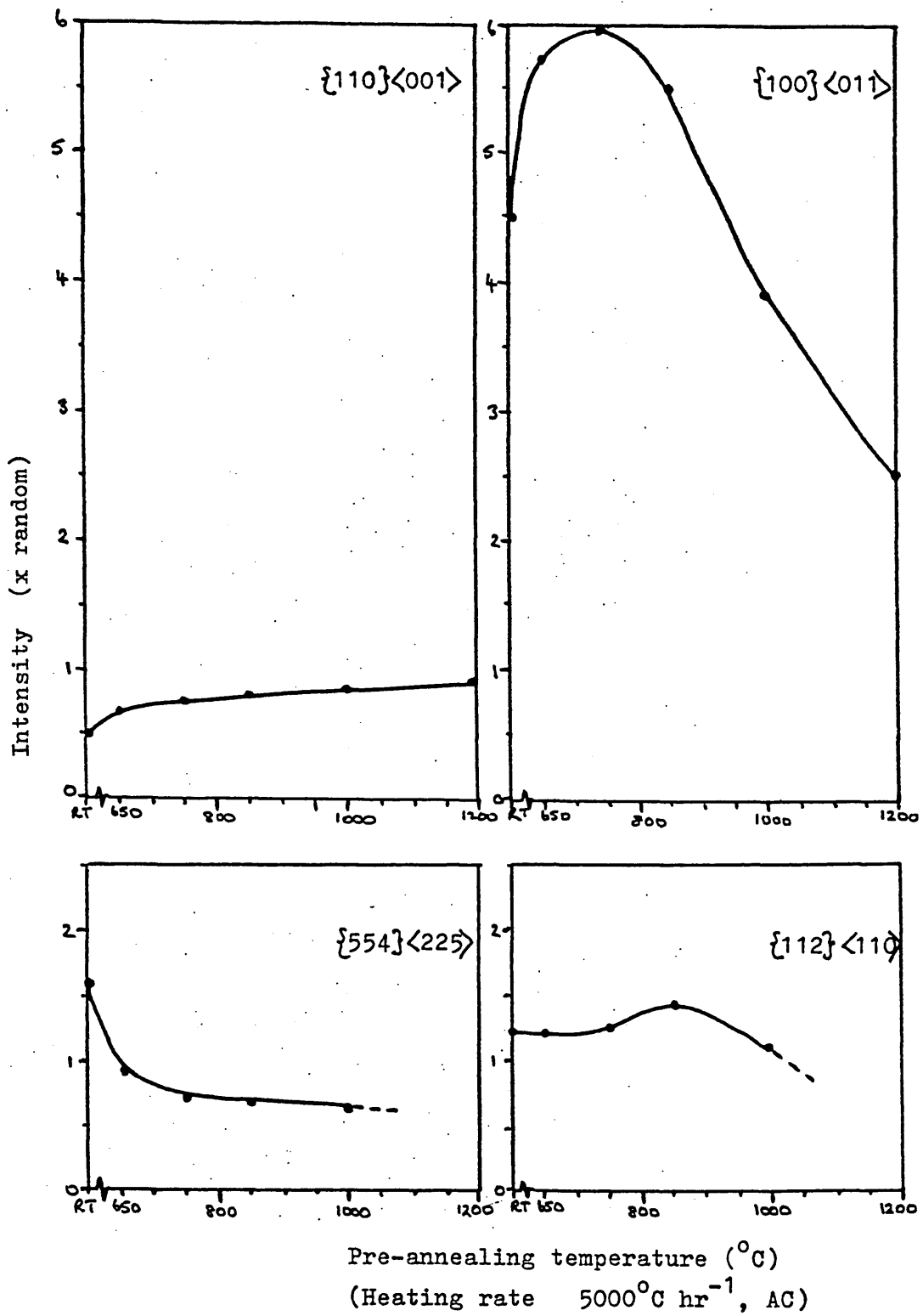


FIGURE 46 Variation of Intensities of the Main Orientations at the Midplane of 430 Strip with Pre-annealing Temperature.

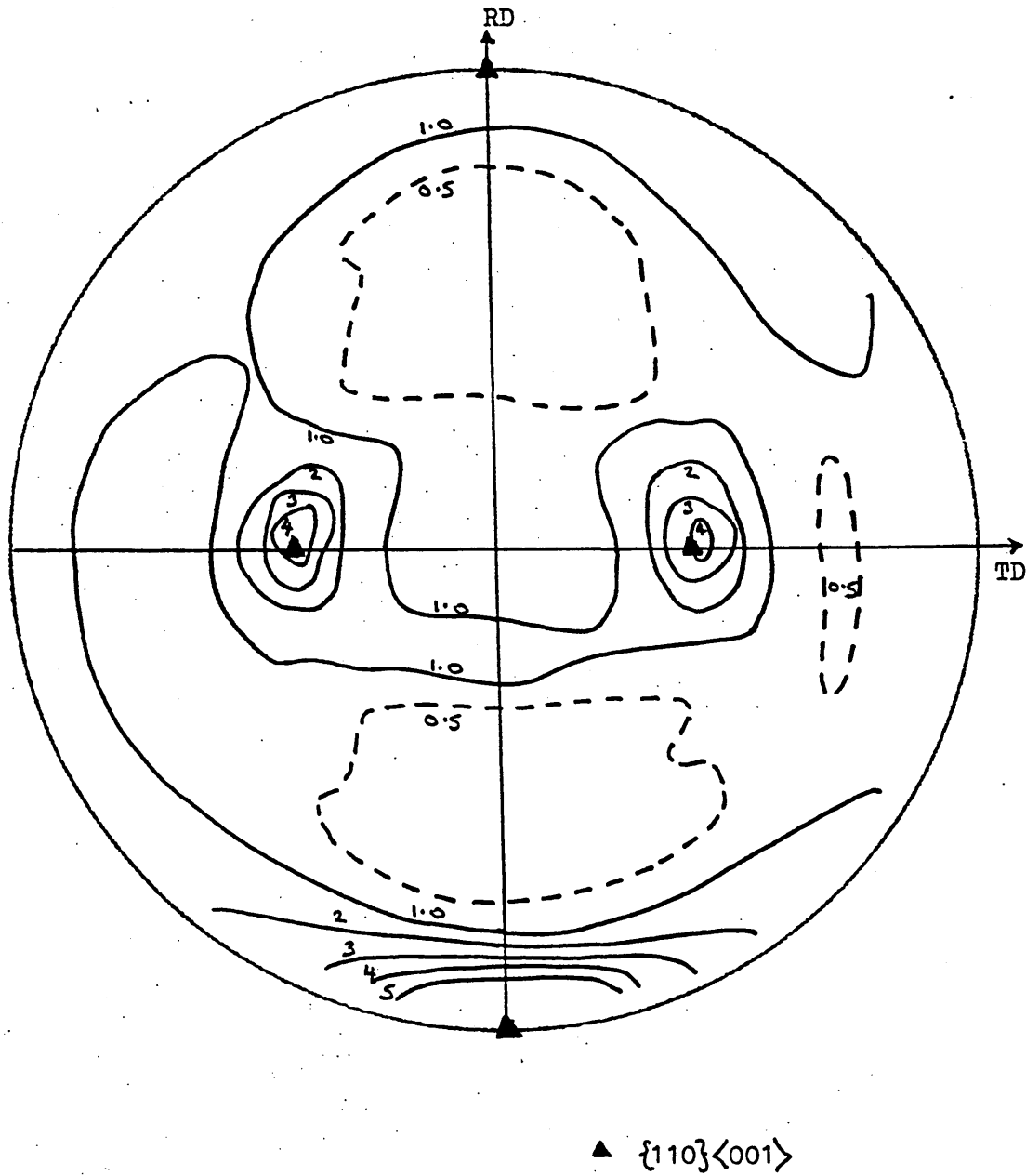
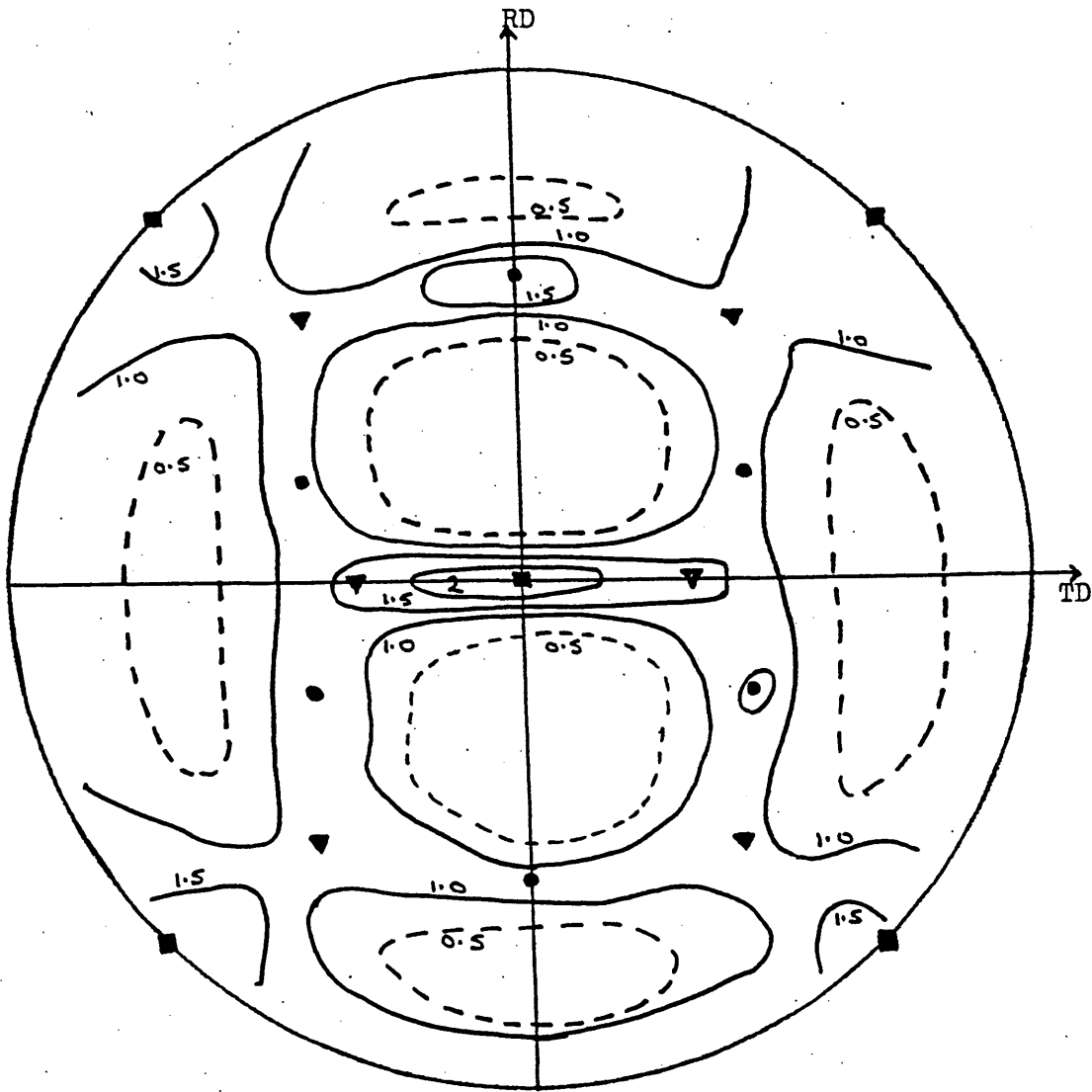
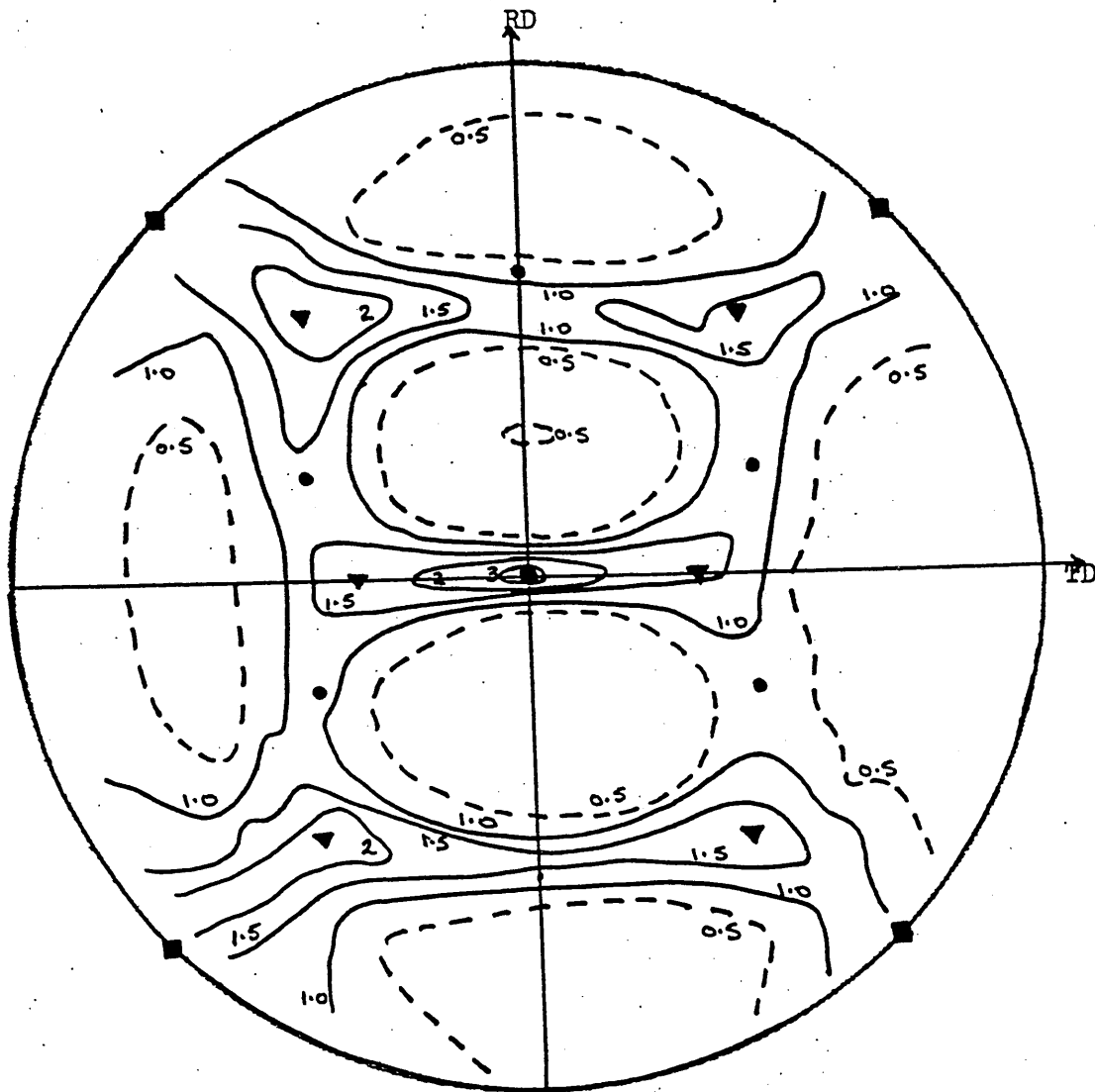


FIGURE 47 $\{200\}$ Pole Figure for the Surface of Hot Rolled 430Ti (0.5Ti) Strip.



- $\{100\} \langle 011 \rangle$
- $\{554\} \langle 225 \rangle$
- ▼ $\{112\} \langle 110 \rangle$

FIGURE 48 $\{200\}$ Pole Figure for the Quarterplane of Hot Rolled 430Ti (0.5Ti) Strip.



- $\{100\}\langle 011\rangle$
- $\{554\}\langle 225\rangle$
- ▼ $\{112\}\langle 110\rangle$

FIGURE 49 $\{200\}$ Pole Figure for the Midplane of Hot Rolled 430Ti (0.5Ti) Strip.

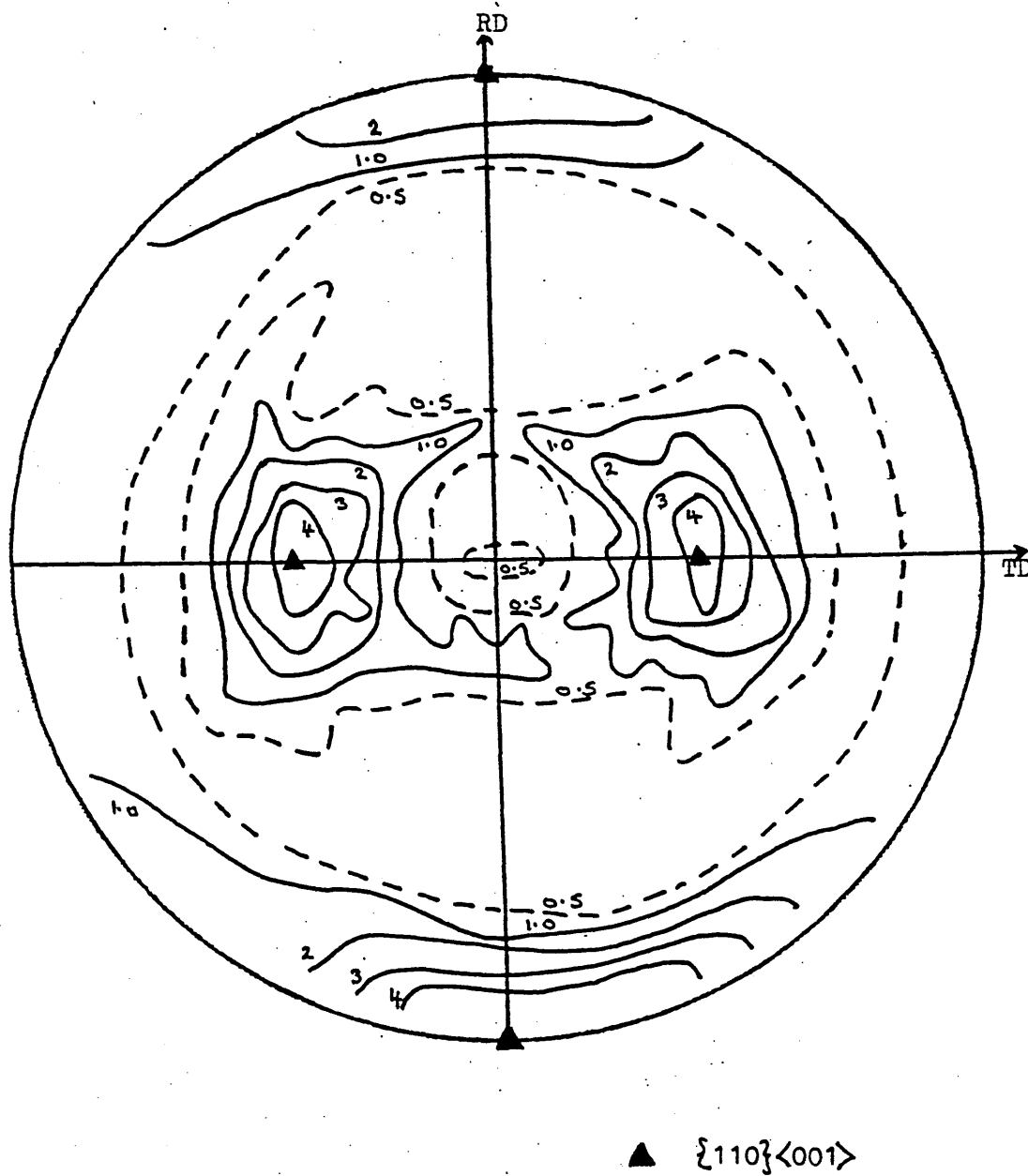


FIGURE 50 $\{200\}$ Pole Figure for the Surface of 430Ti (0.5Ti) Strip after Hot Rolling and Rapid Pre-annealing at 1000°C.

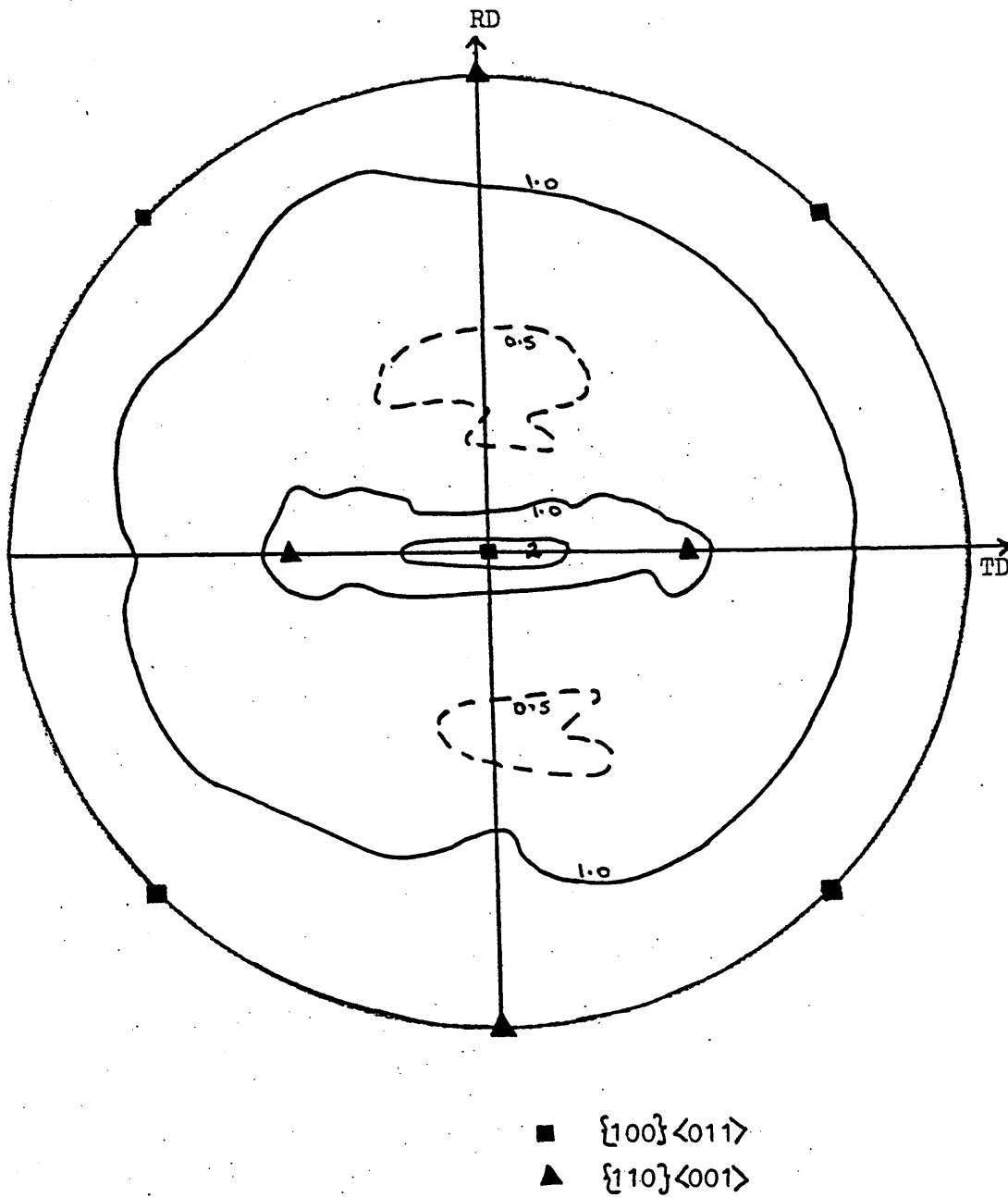
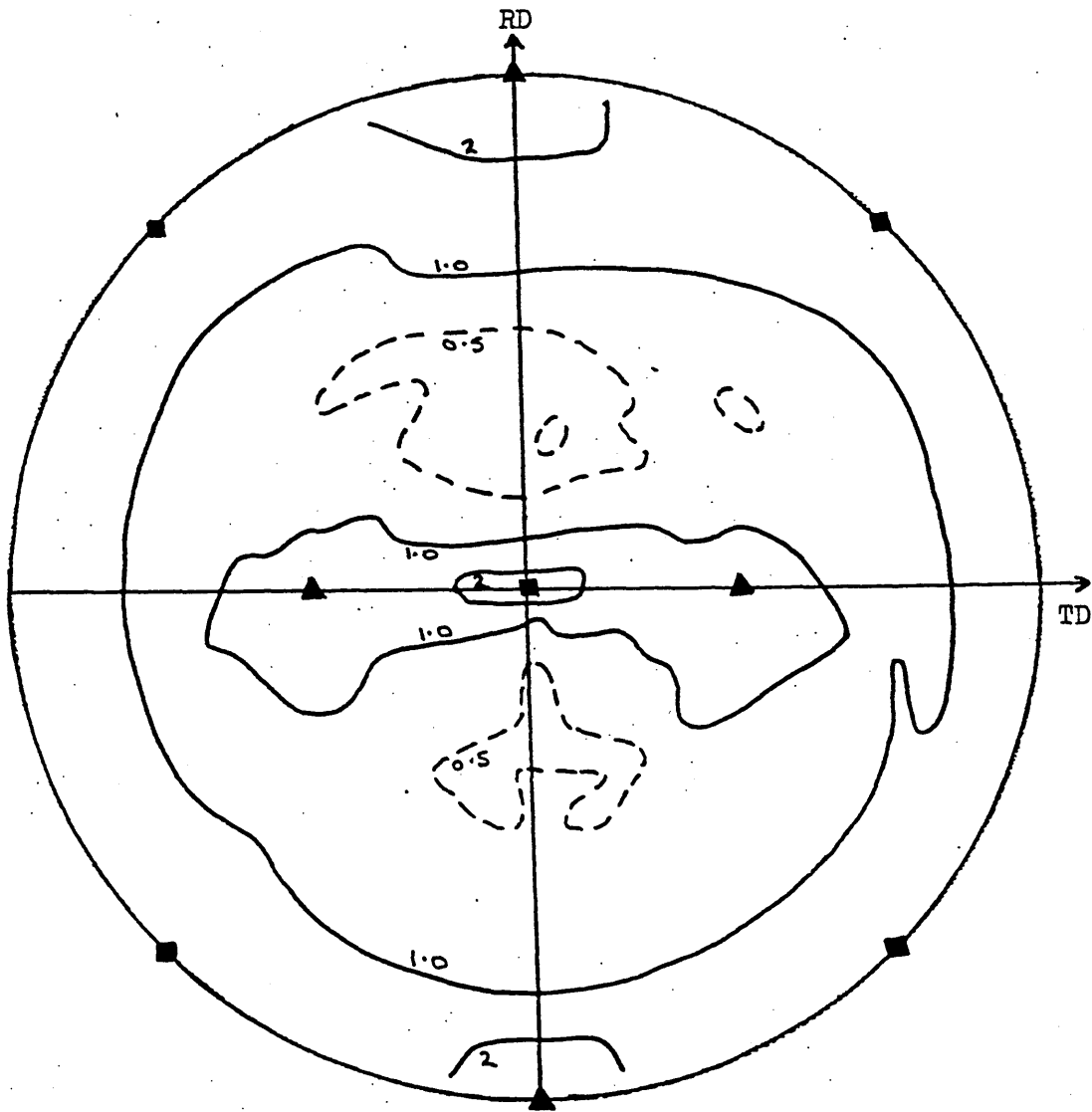
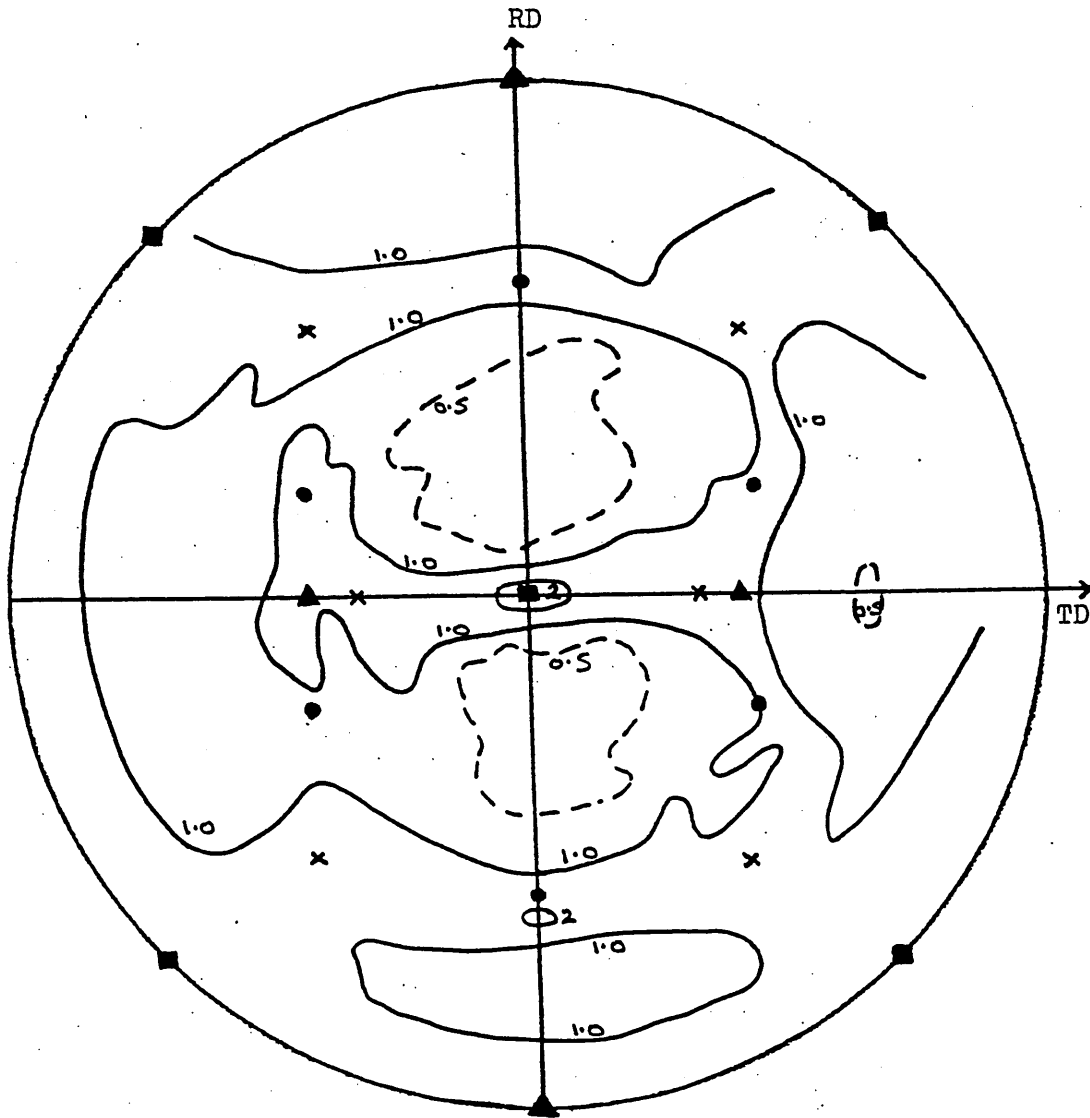


FIGURE 51 $\{200\}$ Pole Figure for the Quarterplane of 430Ti
(0.5Ti) Strip after Hot Rolling and Rapid
Pre-annealing at 850°C.



- $\{100\}\langle 011\rangle$
- ▲ $\{110\}\langle 001\rangle$

FIGURE 52 $\{200\}$ Pole Figure for the Quarterplane of
430Ti (0.5Ti) Steel after Hot Rolling and Batch
Pre-annealing at 850°C.



- $\{100\} \langle 011 \rangle$
- $\{554\} \langle 225 \rangle$
- ▲ $\{110\} \langle 001 \rangle$
- × $\{112\} \langle 110 \rangle$

FIGURE 53 $\{200\}$ Pole Figure for the Midplane of 430Ti (0.5Ti) Steel after Hot Rolling and Batch Pre-annealing at 850°C.

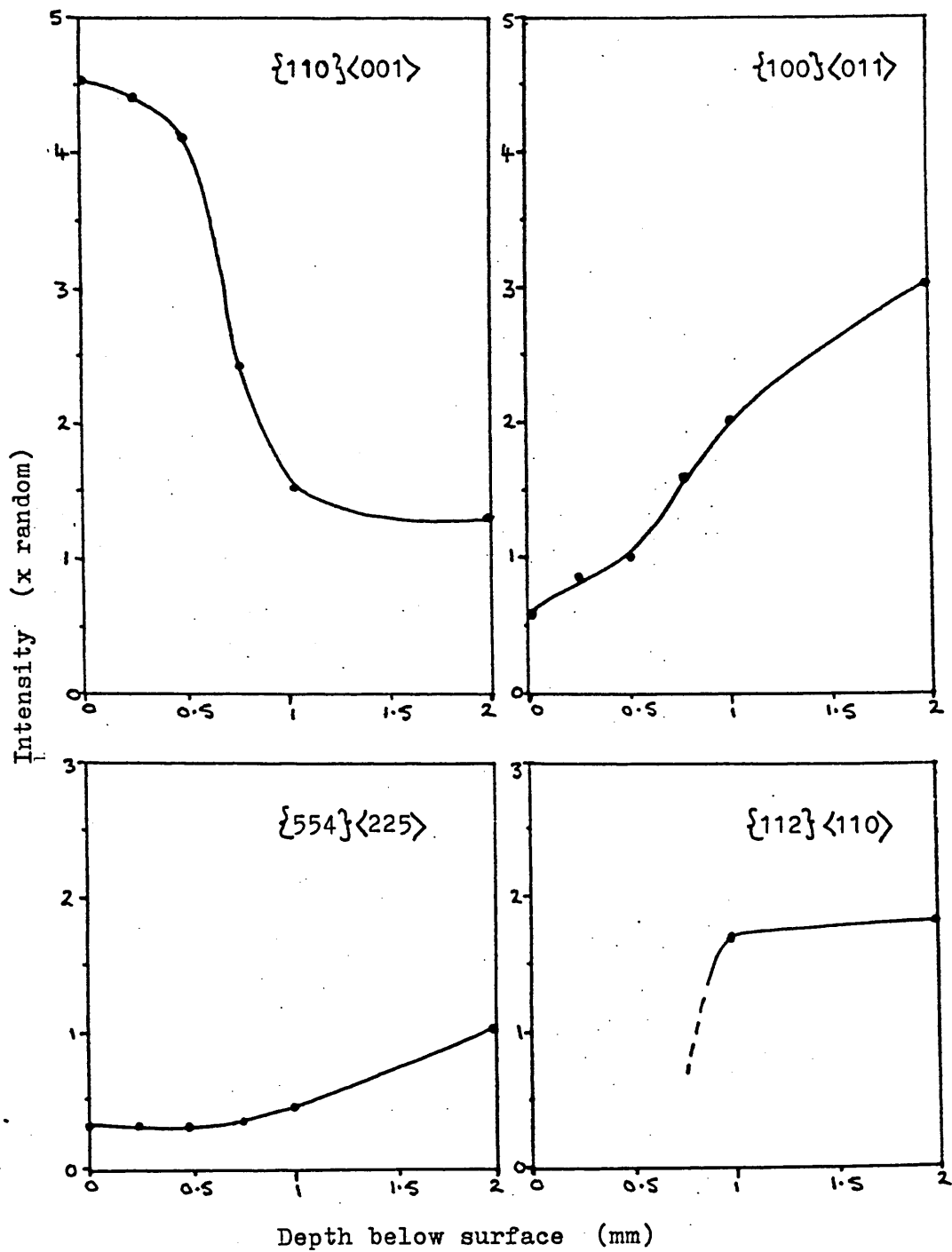


FIGURE 54 Through-Thickness Variation in Intensity of the Main Orientations in 4mm Thick, Hot Rolled 430Ti (0.5Ti) Strip.

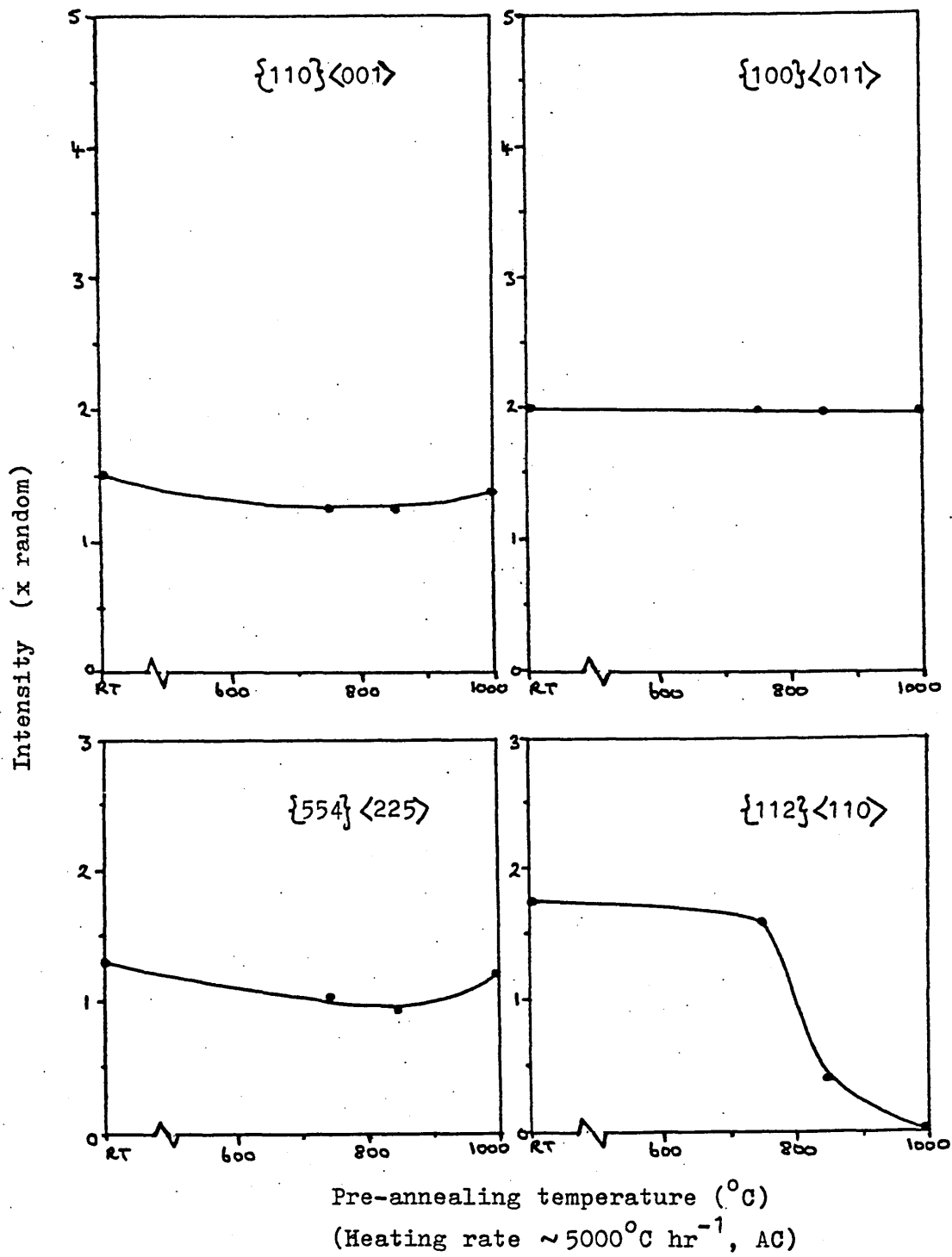


FIGURE 55 Variation of Intensities of the Main Orientations at the Quarterplane of 430Ti (0.5Ti) Strip with Pre-annealing Temperature.

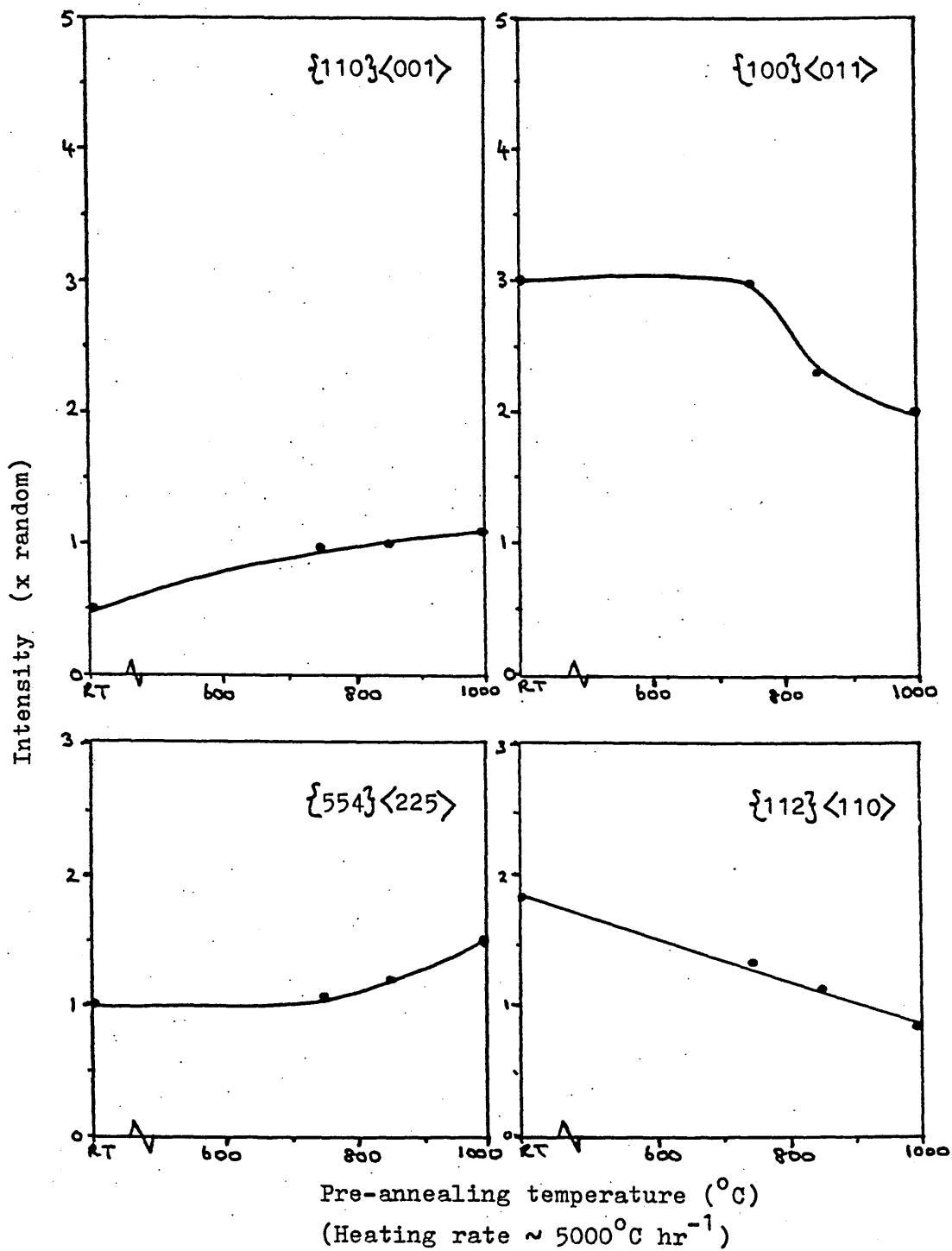
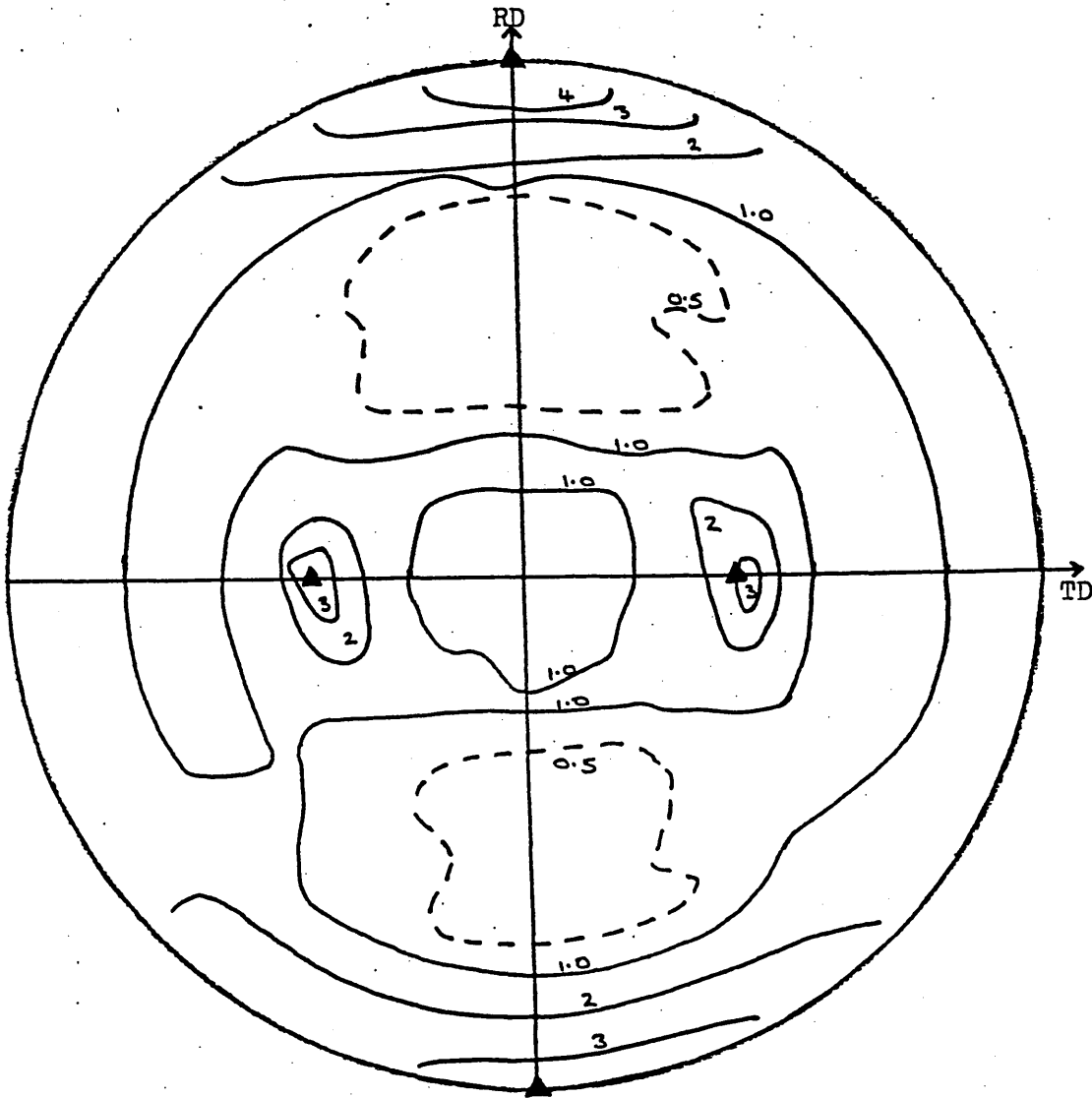
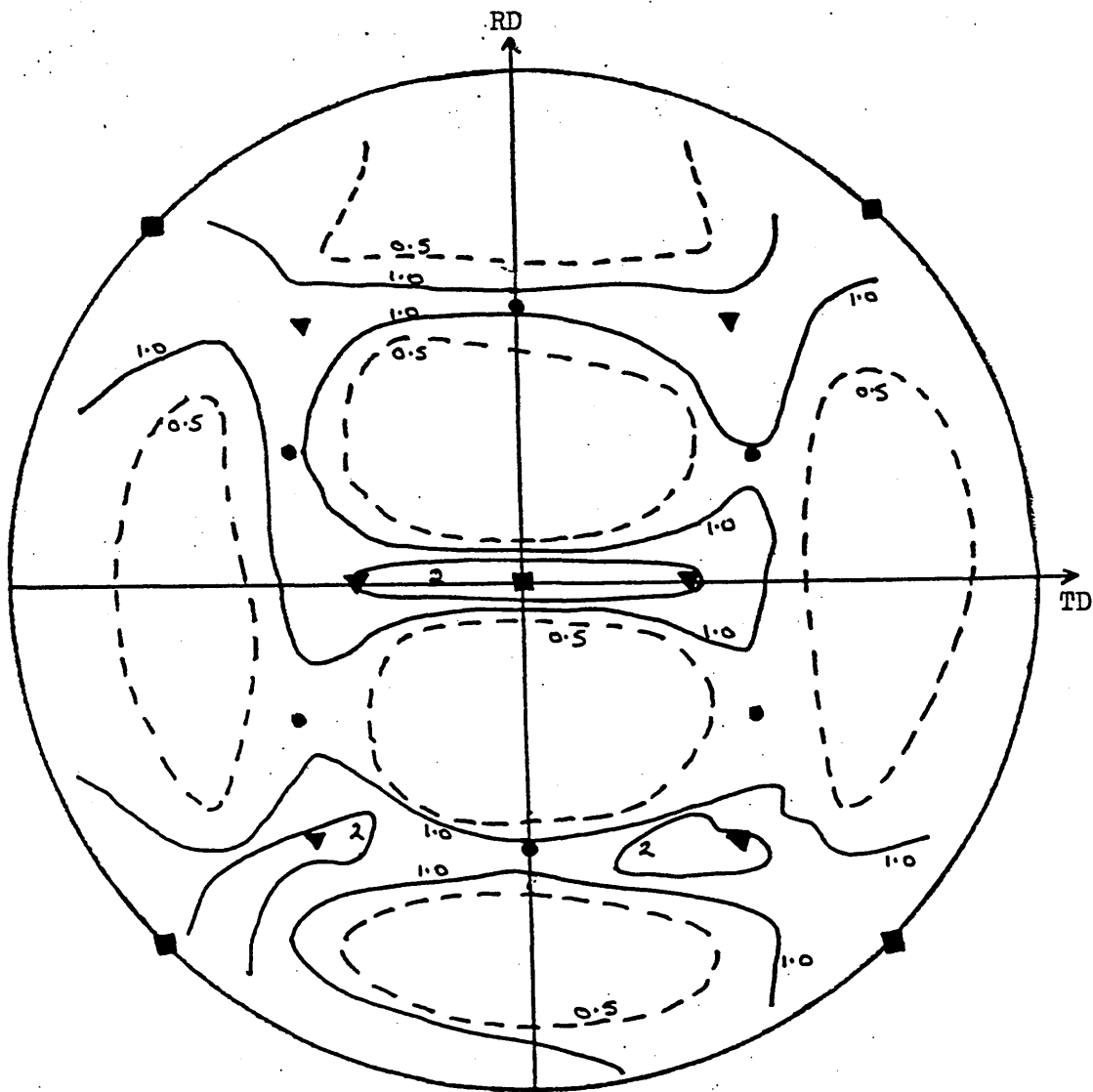


FIGURE 56 Variation of Intensities of the Main Orientations
at the Midplane of 430Ti (0.5Ti) Strip with
Pre-annealing Temperature.



▲ $\{110\}\langle 001 \rangle$

FIGURE 57 $\{200\}$ Pole Figure for the Surface of Hot Rolled 430Ti (0.3Ti) Strip.



- $\{100\}\langle 011\rangle$
- $\{111\}\langle 112\rangle$
- ▼ $\{112\}\langle 110\rangle$

FIGURE 58 $\{200\}$ Pole Figure for the Midplane of Hot Rolled 430Ti (0.3Ti) Strip.

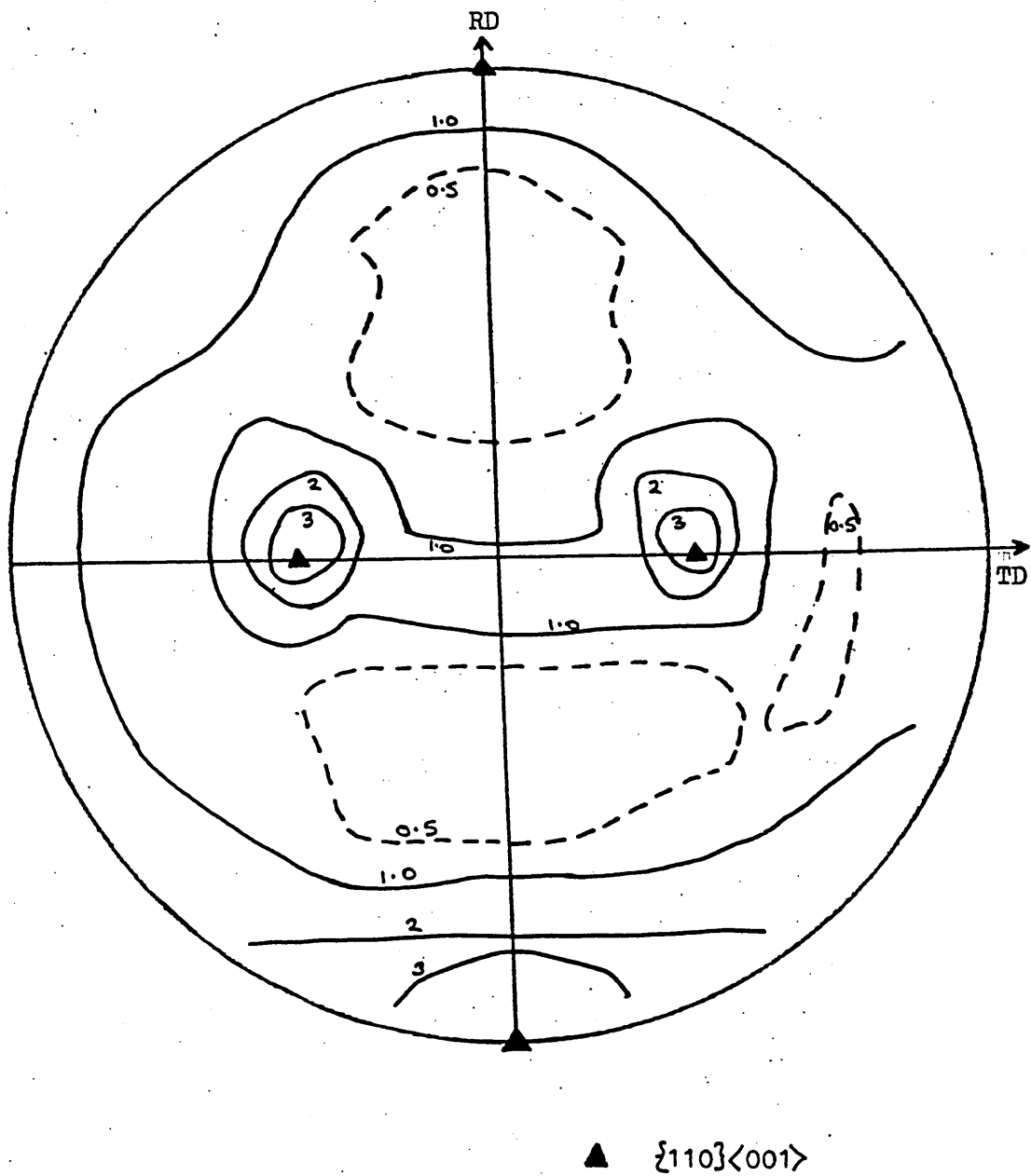
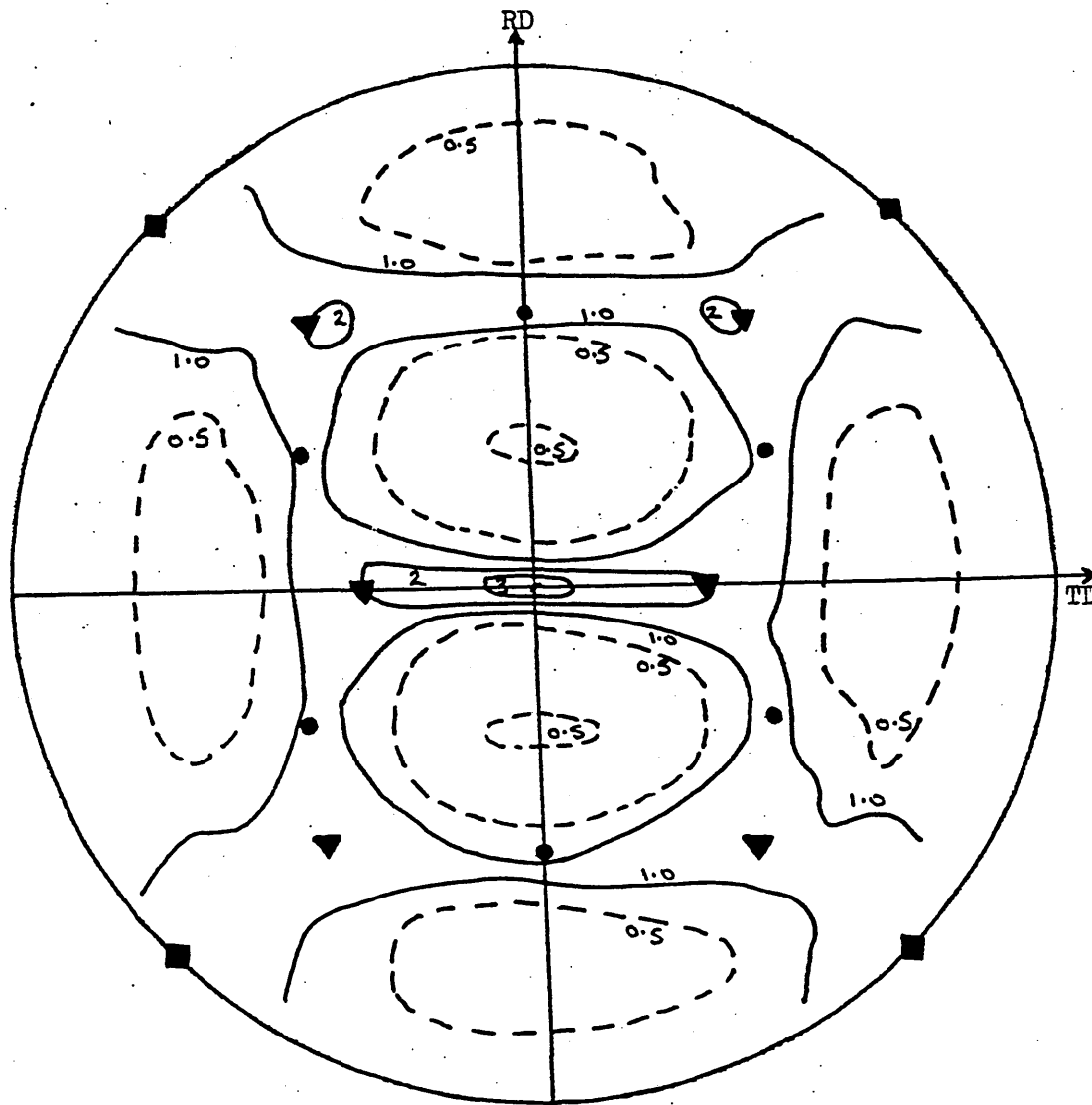
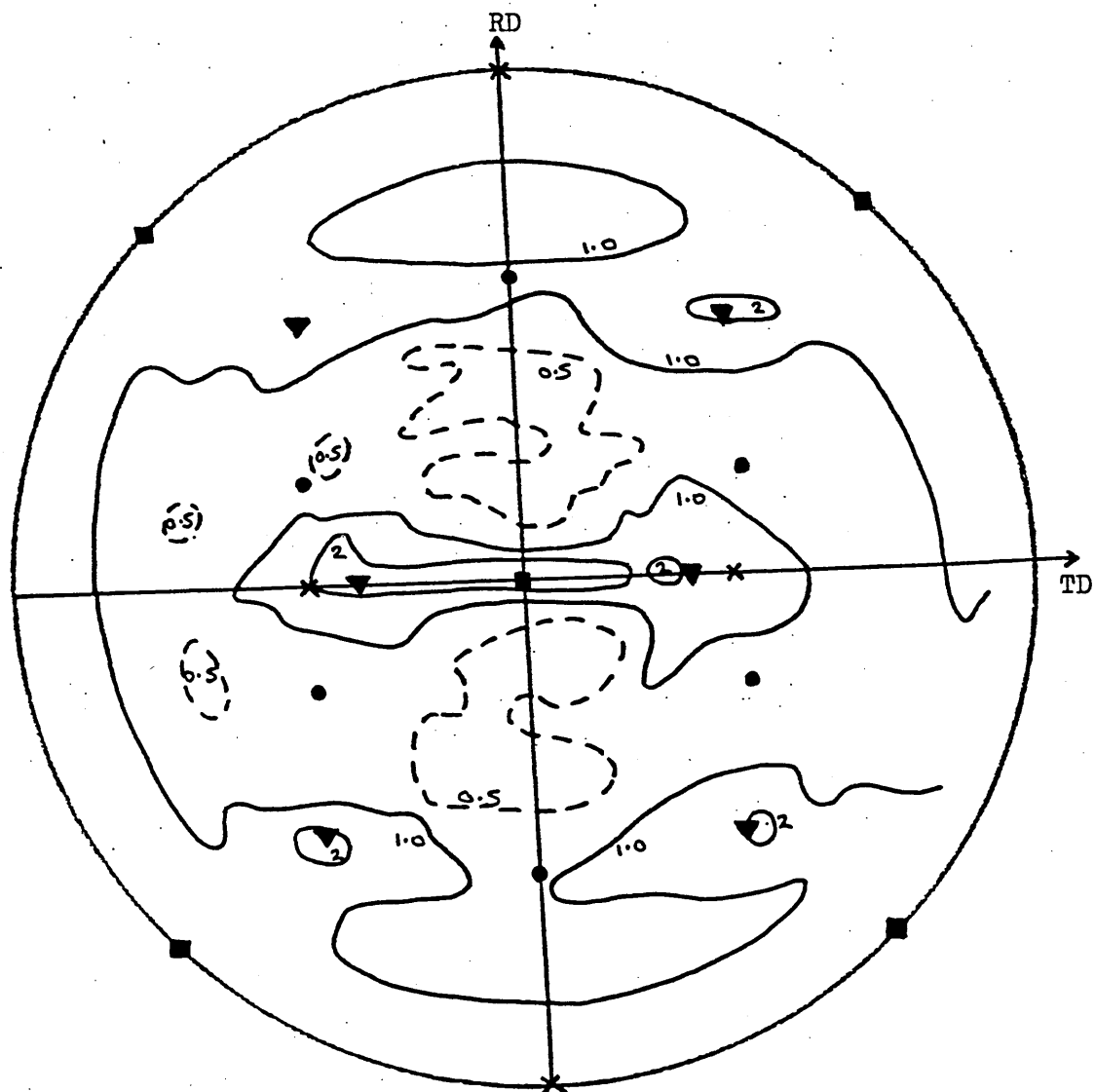


FIGURE 59 $\{200\}$ Pole Figure for the Quarterplane of Hot Rolled 409 Strip.



- $\{100\} \langle 011 \rangle$
- $\{111\} \langle 112 \rangle$
- ▼ $\{112\} \langle 110 \rangle$

FIGURE 60 $\{200\}$ Pole Figure for the Midplane of Hot Rolled 409 Strip.



- $\{100\}\langle 011\rangle$
- $\{554\}\langle 225\rangle$
- ▼ $\{112\}\langle 110\rangle$
- × $\{110\}\langle 001\rangle$

FIGURE 61 $\{200\}$ Pole Figure for the Midplane of 409 Strip
after Hot Rolling and Rapid Pre-annealing at 850°C.

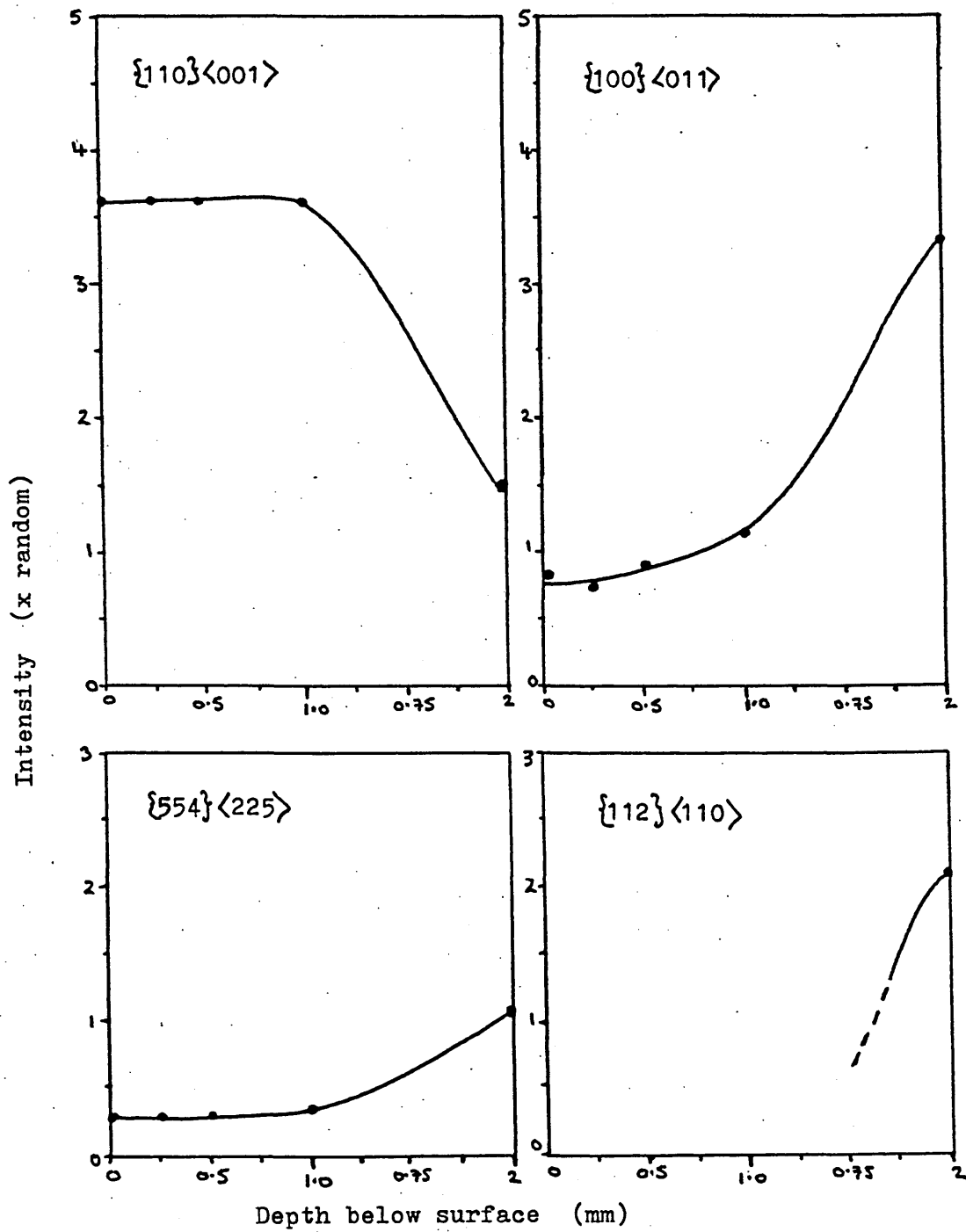
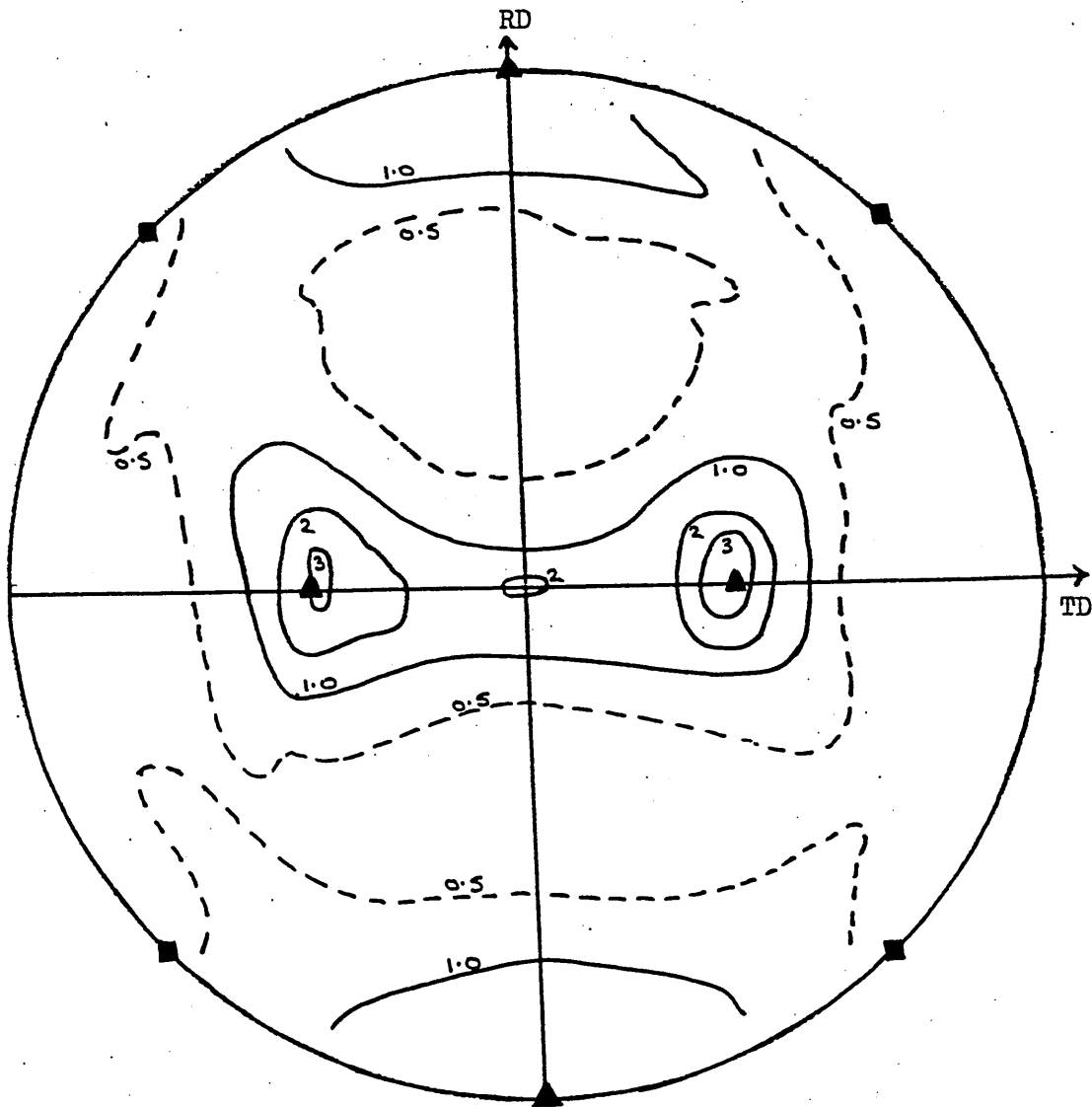
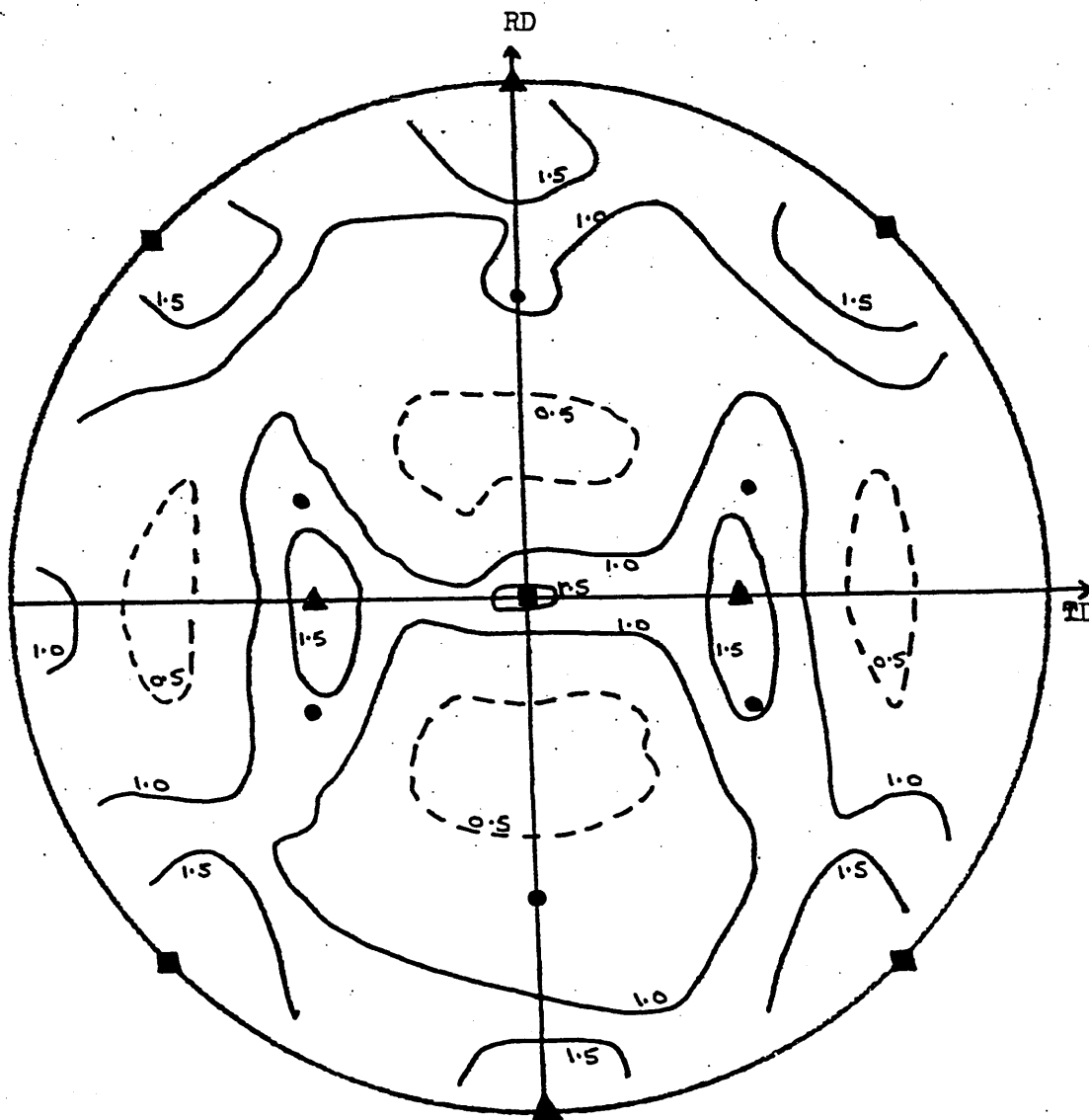


FIGURE 62 Through-Thickness Variation in Intensity of the
Main Orientations in 4mm Thick, Hot Rolled
409 Strip.



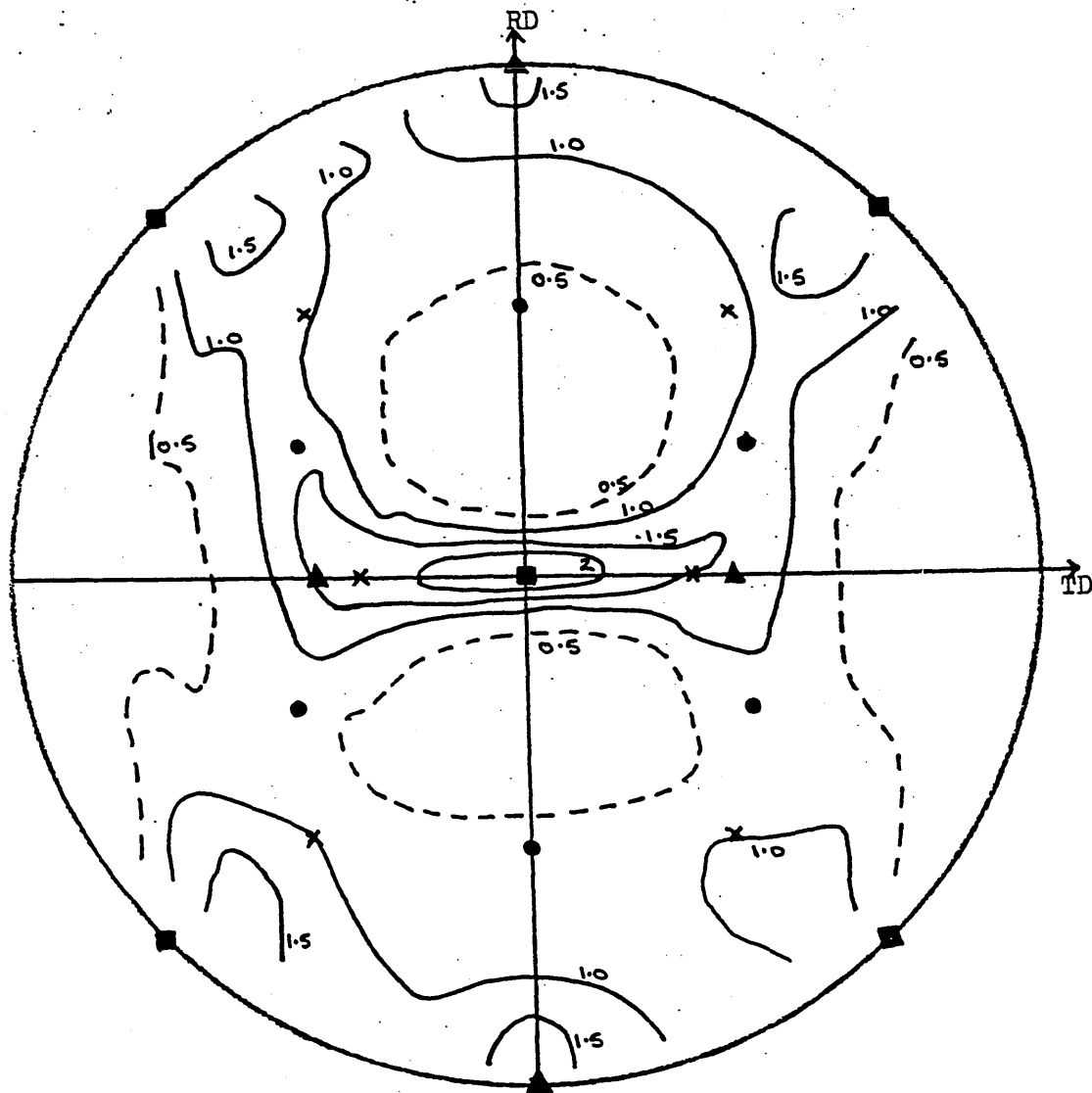
- $\{100\}\langle 011 \rangle$
- ▲ $\{110\}\langle 001 \rangle$

FIGURE 63 $\{200\}$ Pole Figure for 430 Steel after Batch
Pre-annealing at 850°C and Cold Rolling to 50%RA.



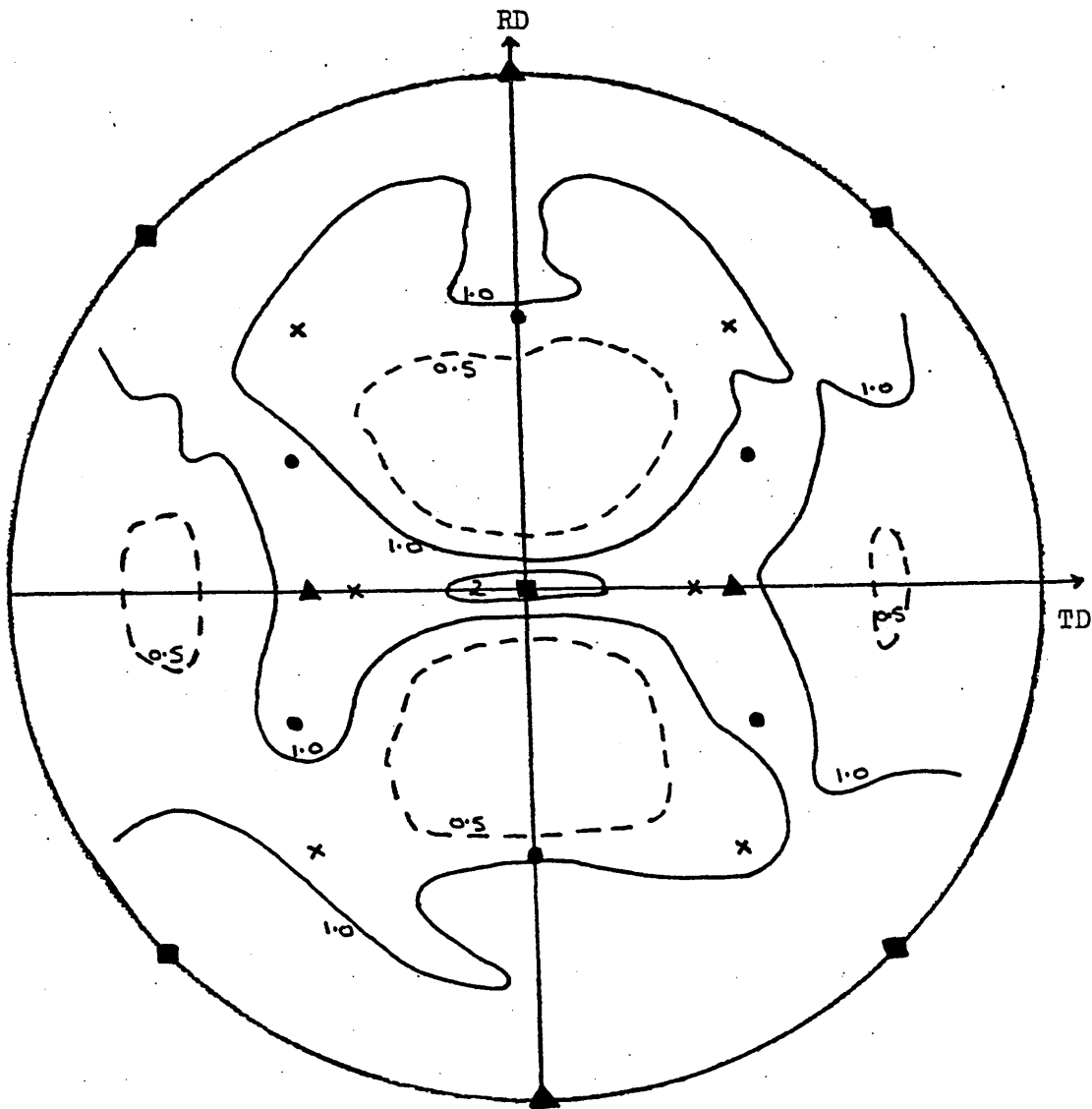
- $\{100\}\langle 011\rangle$
- ▲ $\{110\}\langle 001\rangle$
- $\{554\}\langle 225\rangle$

FIGURE 64 $\{200\}$ Pole Figure for 430 Steel after Hot Rolling and Cold Rolling to 70%RA.



- $\{100\}\langle 011\rangle$
- ▲ $\{110\}\langle 001\rangle$
- $\{111\}\langle 112\rangle$
- × $\{112\}\langle 110\rangle$

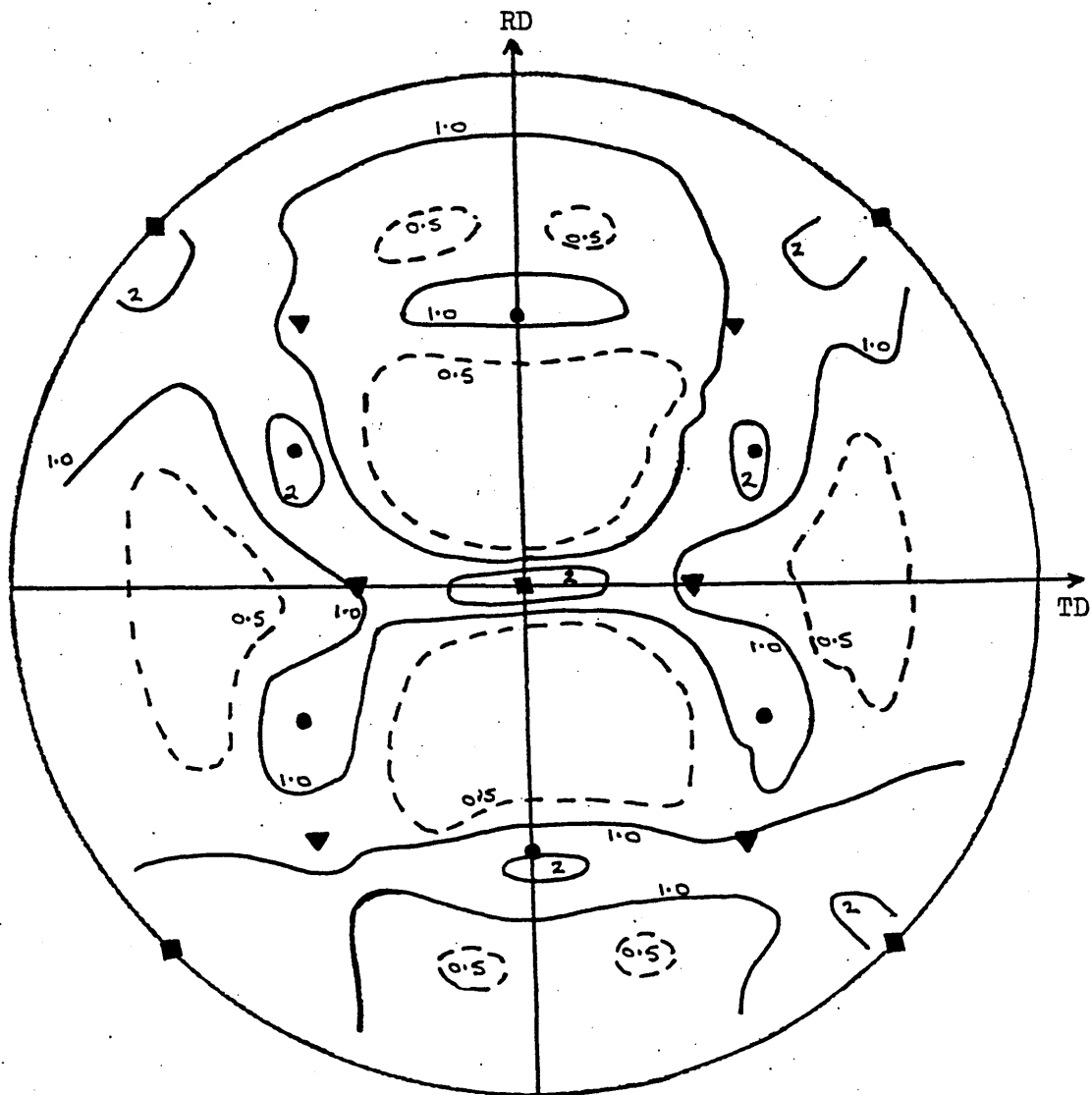
FIGURE 65 $\{200\}$ Pole Figure for 430 Steel after Rapid
Pre-annealing at 850°C and Cold Rolling to 80%RA.



- $\{100\}\langle 011\rangle$
- ▲ $\{110\}\langle 001\rangle$
- $\{111\}\langle 112\rangle$
- × $\{112\}\langle 110\rangle$

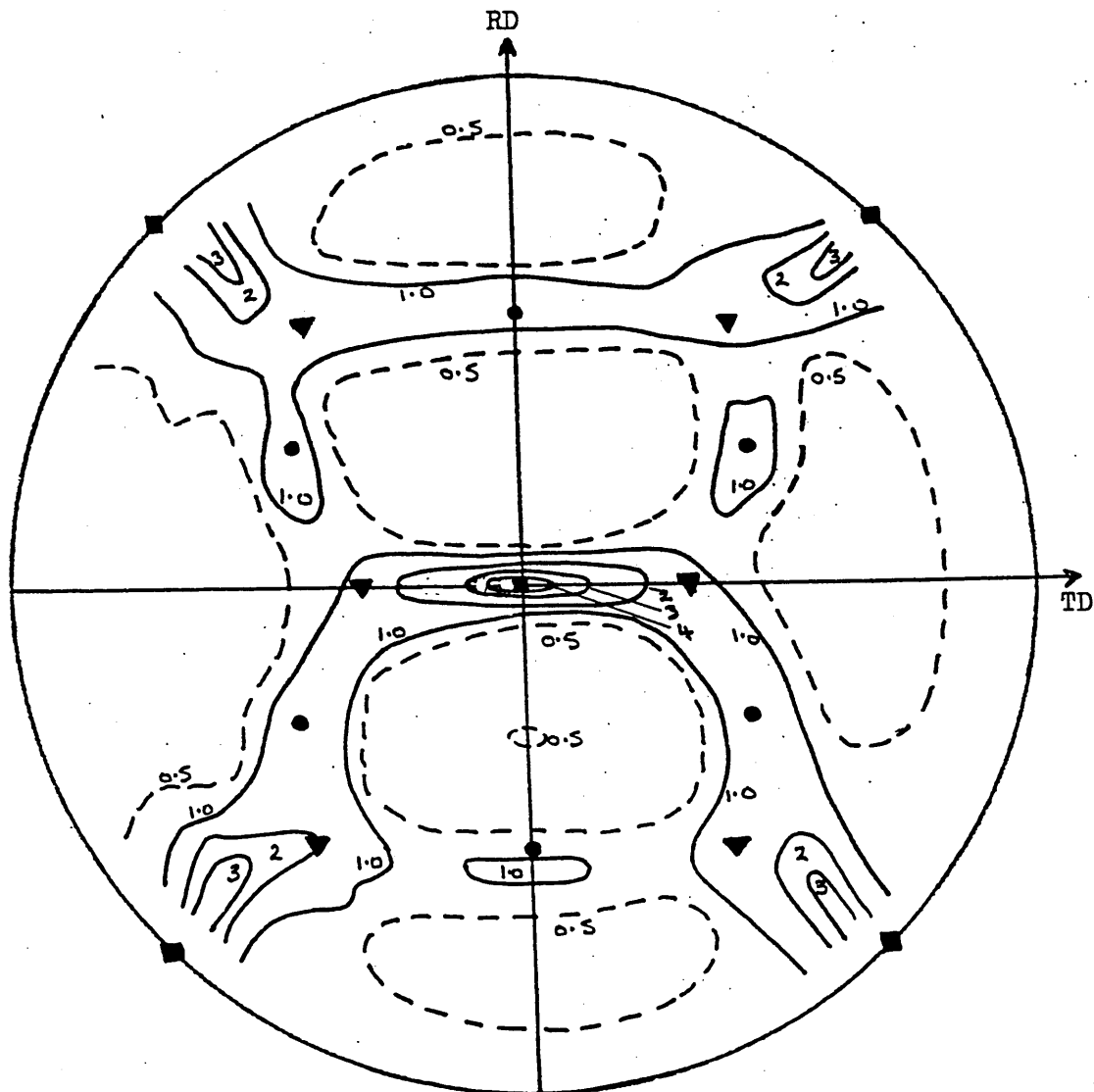
FIGURE 66

$\{200\}$ Pole Figure for 430 Steel after Rapid
Pre-annealing at 1200°C (+ tempering) and Cold
Rolling to 80%RA.



- $\{100\} \langle 011 \rangle$
- $\{111\} \langle 112 \rangle$
- ▼ $\{112\} \langle 110 \rangle$

FIGURE 67 $\{200\}$ Pole Figure for 430 Steel after Rapid Pre-annealing at 1200°C (WQ + temper) and Cold Rolling to 90%RA.



- $\{100\}\langle 011\rangle$
- $\{111\}\langle 112\rangle$
- ▼ $\{112\}\langle 110\rangle$

FIGURE 68 $\{200\}$ Pole Figure for 430 Steel after Rapid
Pre-annealing at 850°C and Cold Rolling to 95%RA.

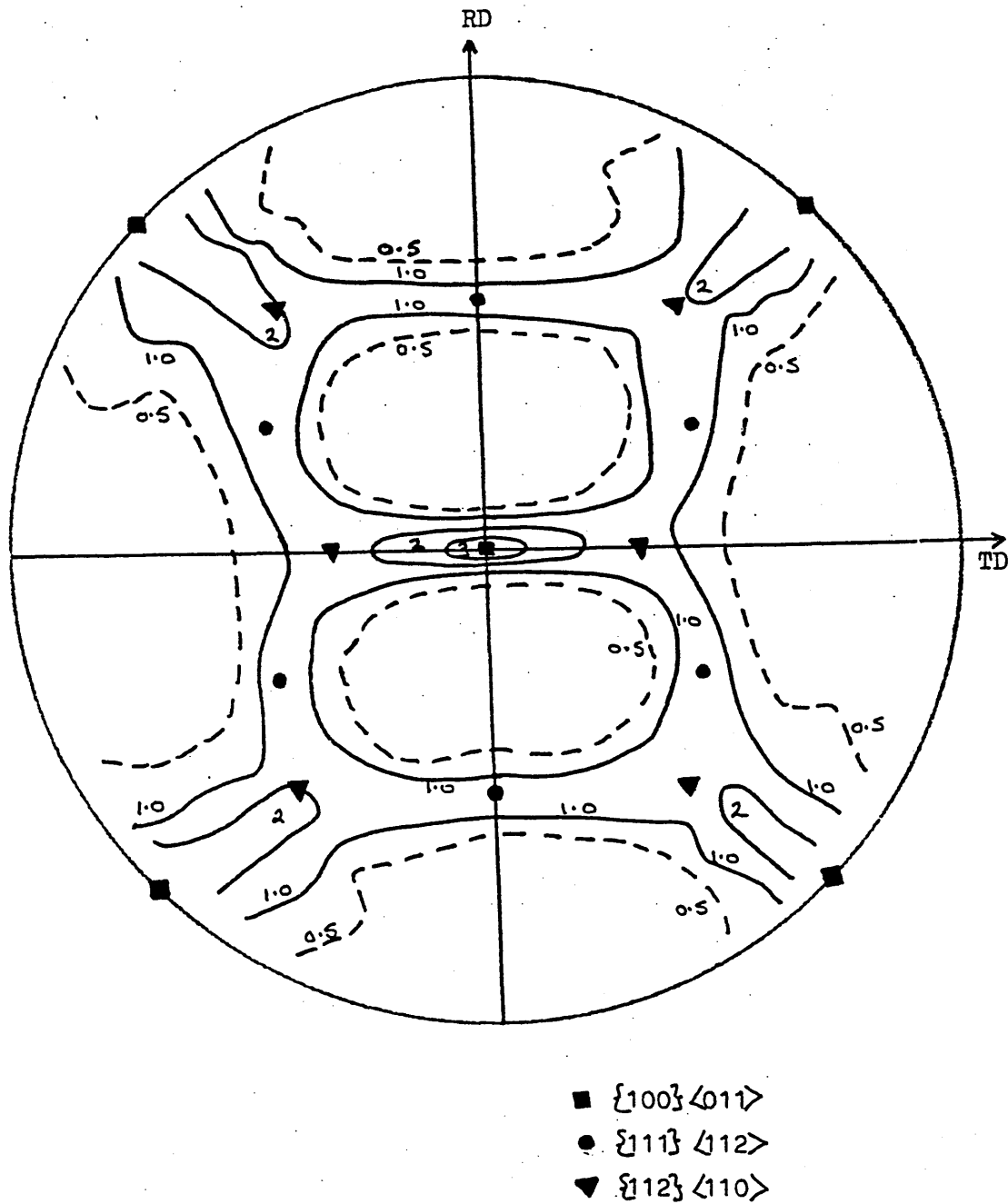


FIGURE 69 $\{200\}$ Pole Figure for 430 Steel after Batch
Pre-annealing at 850°C and Cold Rolling to 95%RA.

Without
Pre-annealing.

Pre-annealed
at 850 C.

Pre-annealed
at 1000 C.

Pre-annealed
at 1200 C.

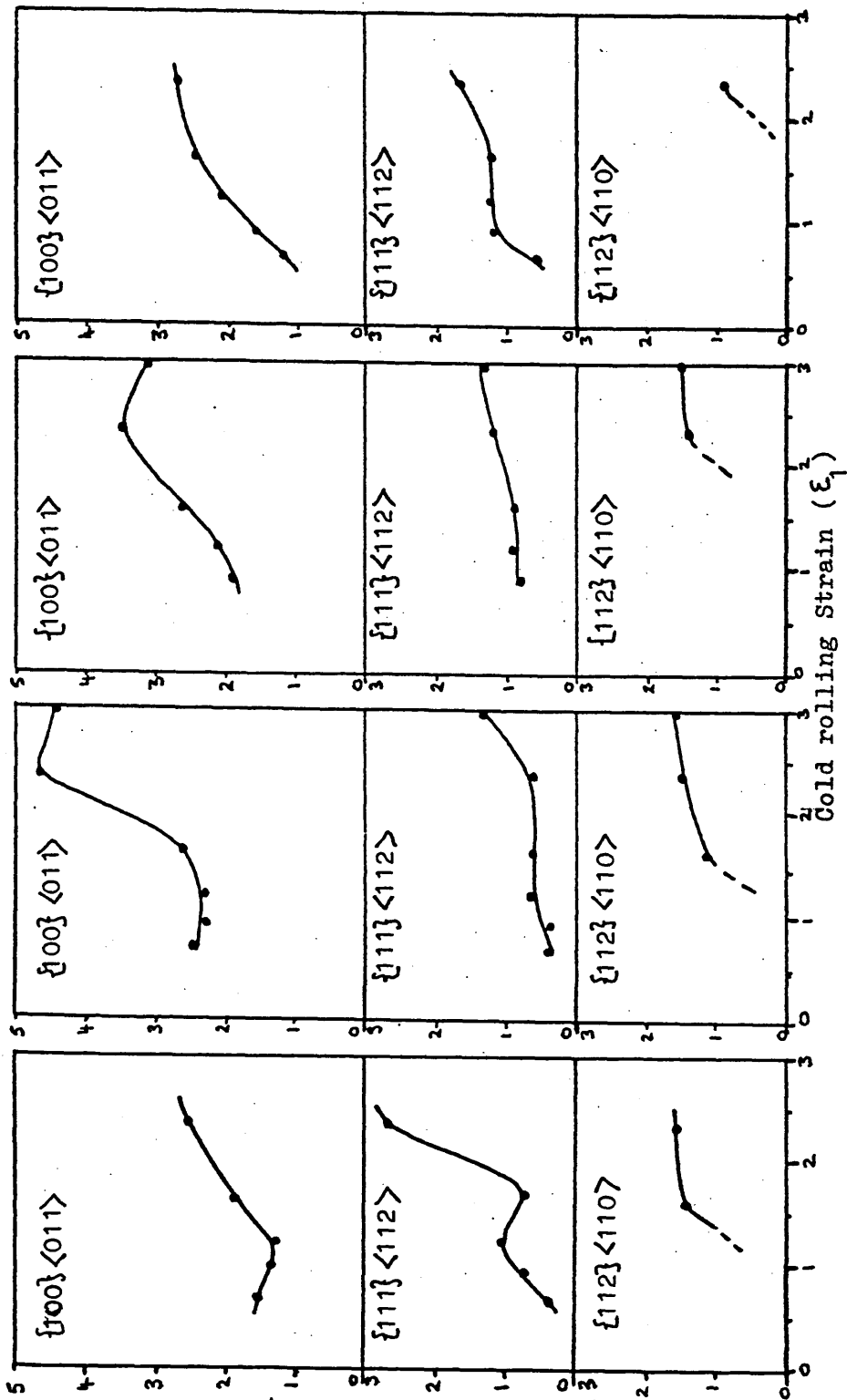


FIGURE 70 Variation of Intensities of the $\{100\}\langle 011\rangle$, $\{111\}\langle 112\rangle$ and $\{112\}\langle 110\rangle$ Orientations with Cold Rolling Strain in Cold Rolled 430 Steel.

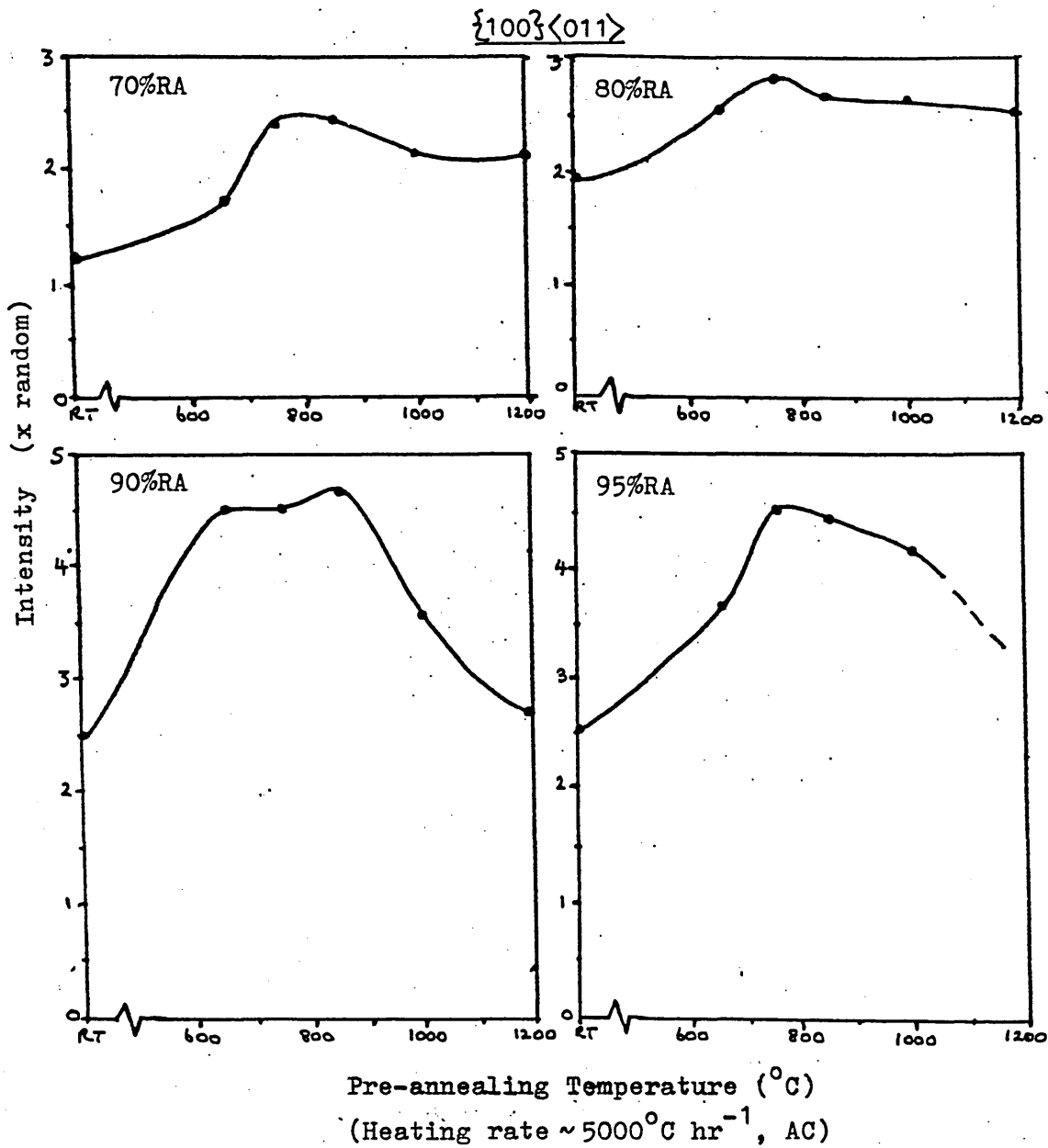


FIGURE 71

Variation of Intensity of the $\{100\}\langle 011\rangle$
Orientation with Pre-Annealing Temperature in
Cold Rolled 430 Steel.

$\{11\bar{1}\} \langle 112 \rangle$

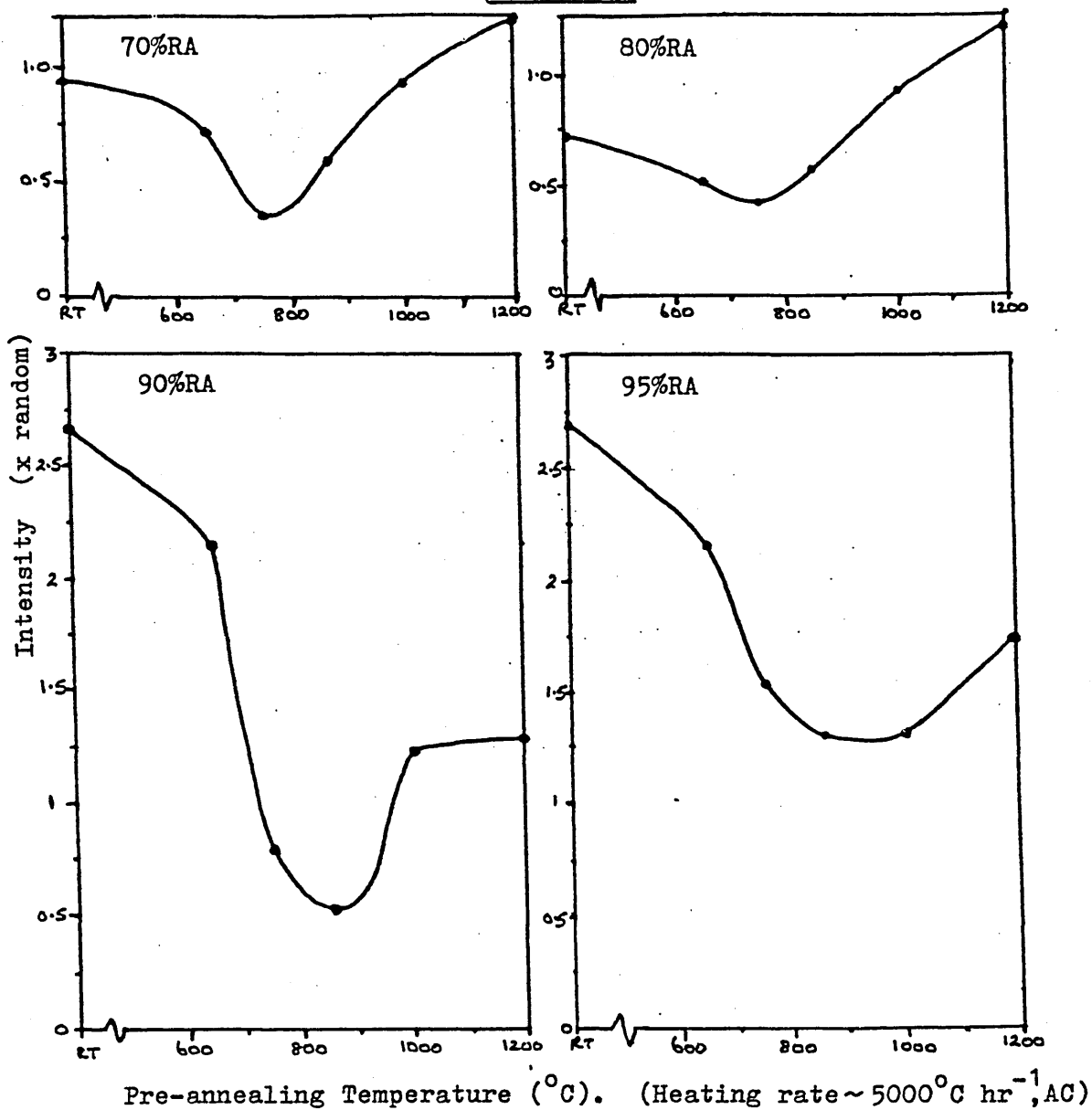


FIGURE 72

Variation of Intensity of the $\{11\bar{1}\} \langle 112 \rangle$
Orientation with Pre-annealing Temperature in
Cold Rolled 430 Steel.

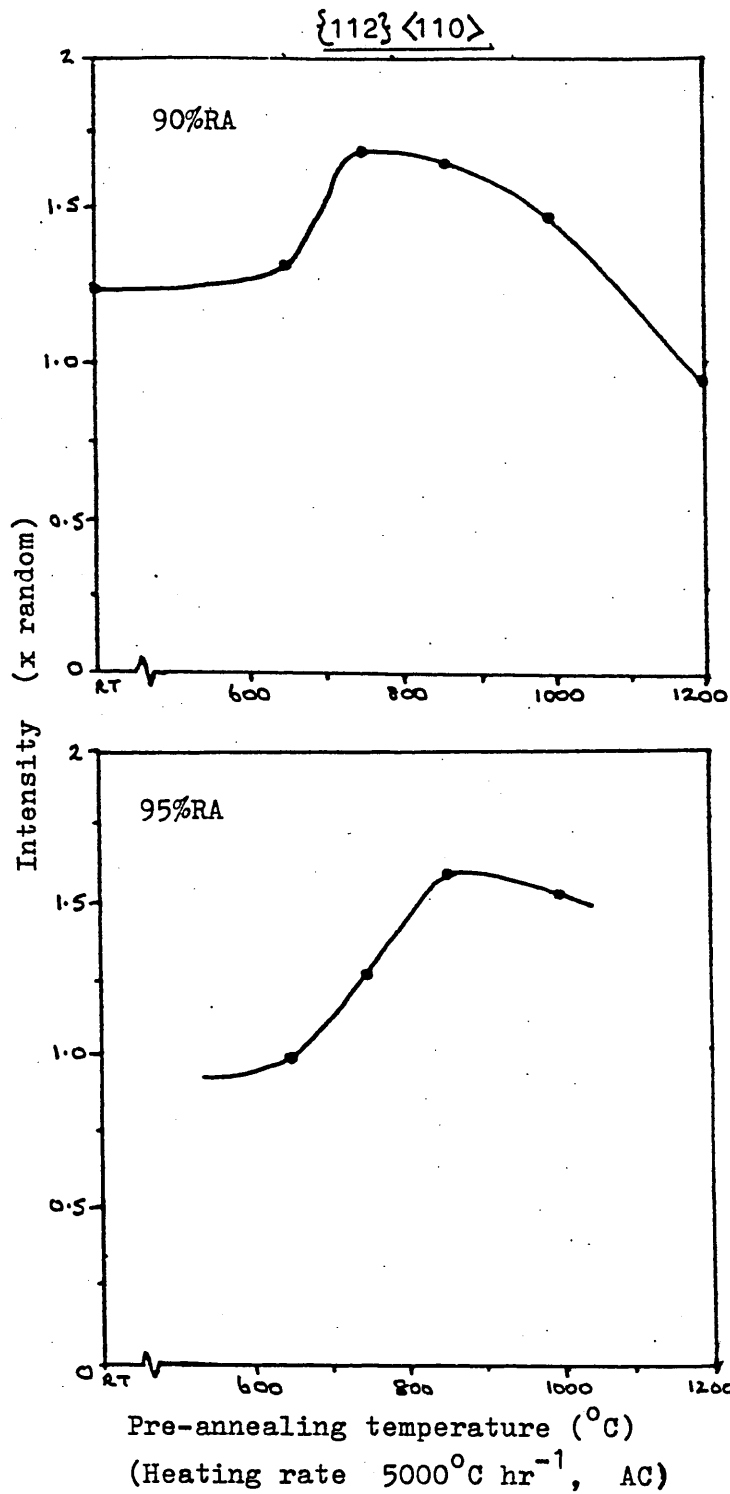


FIGURE 73

Variation of Intensity of the {112} <110>
Orientation with Pre-annealing Temperature
in Cold Rolled 430 Steel.

- ——— Rapid pre-annealing (heating rate $5000^{\circ}\text{C hr}^{-1}$, AC)
- - - - - Batch pre-annealing (heating rate = $50^{\circ}\text{C hr}^{-1}$, FC)

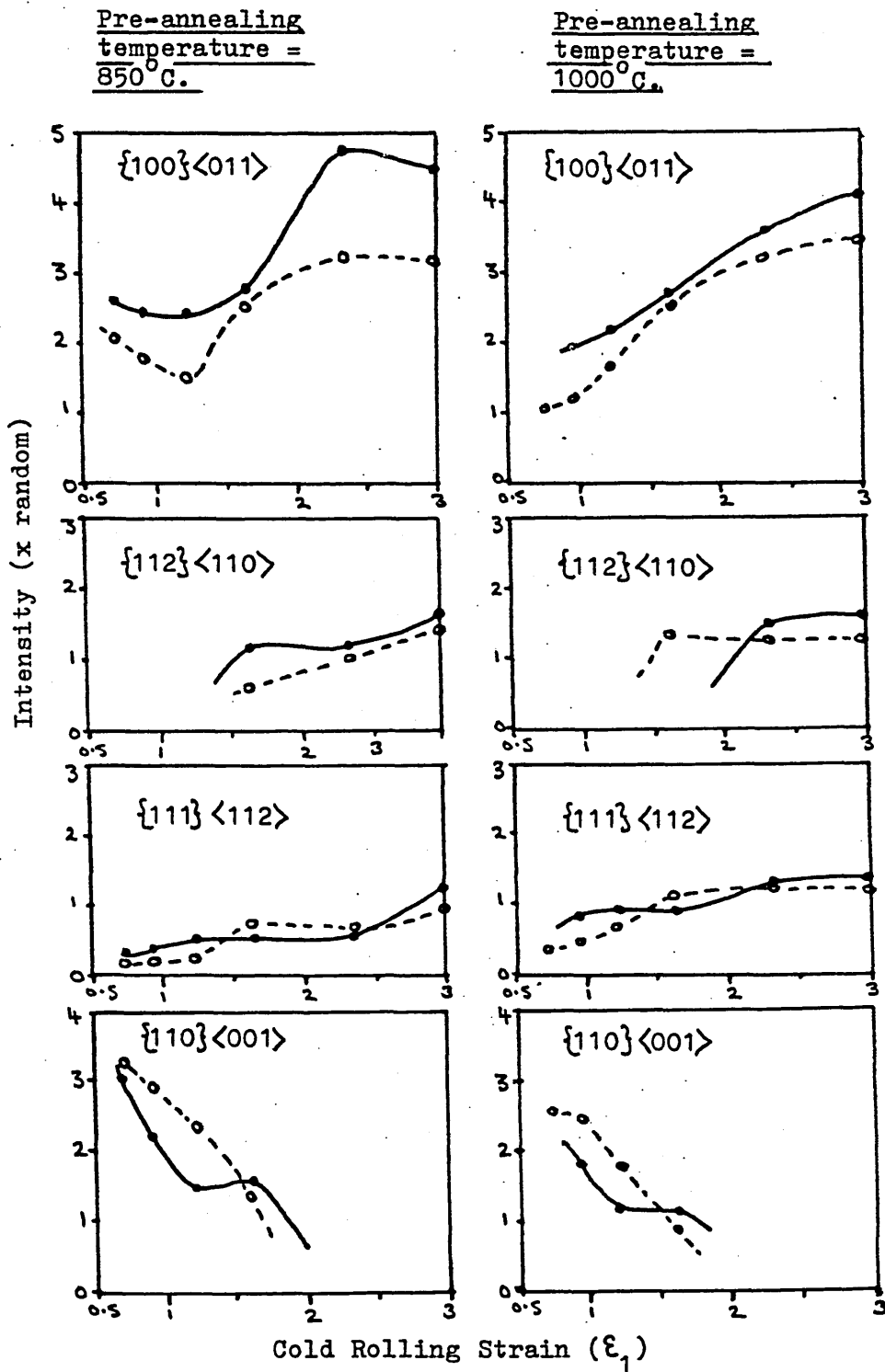
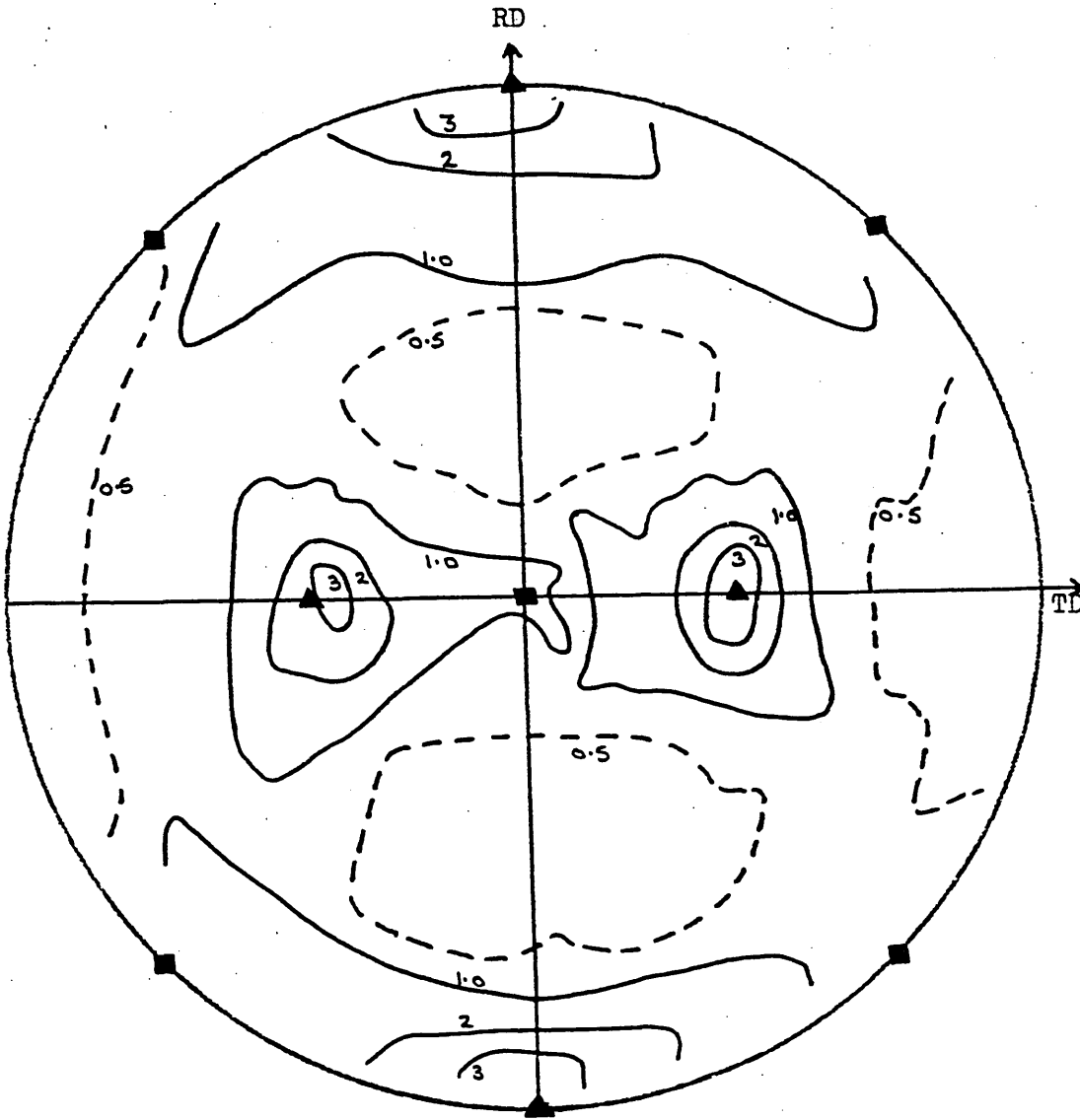
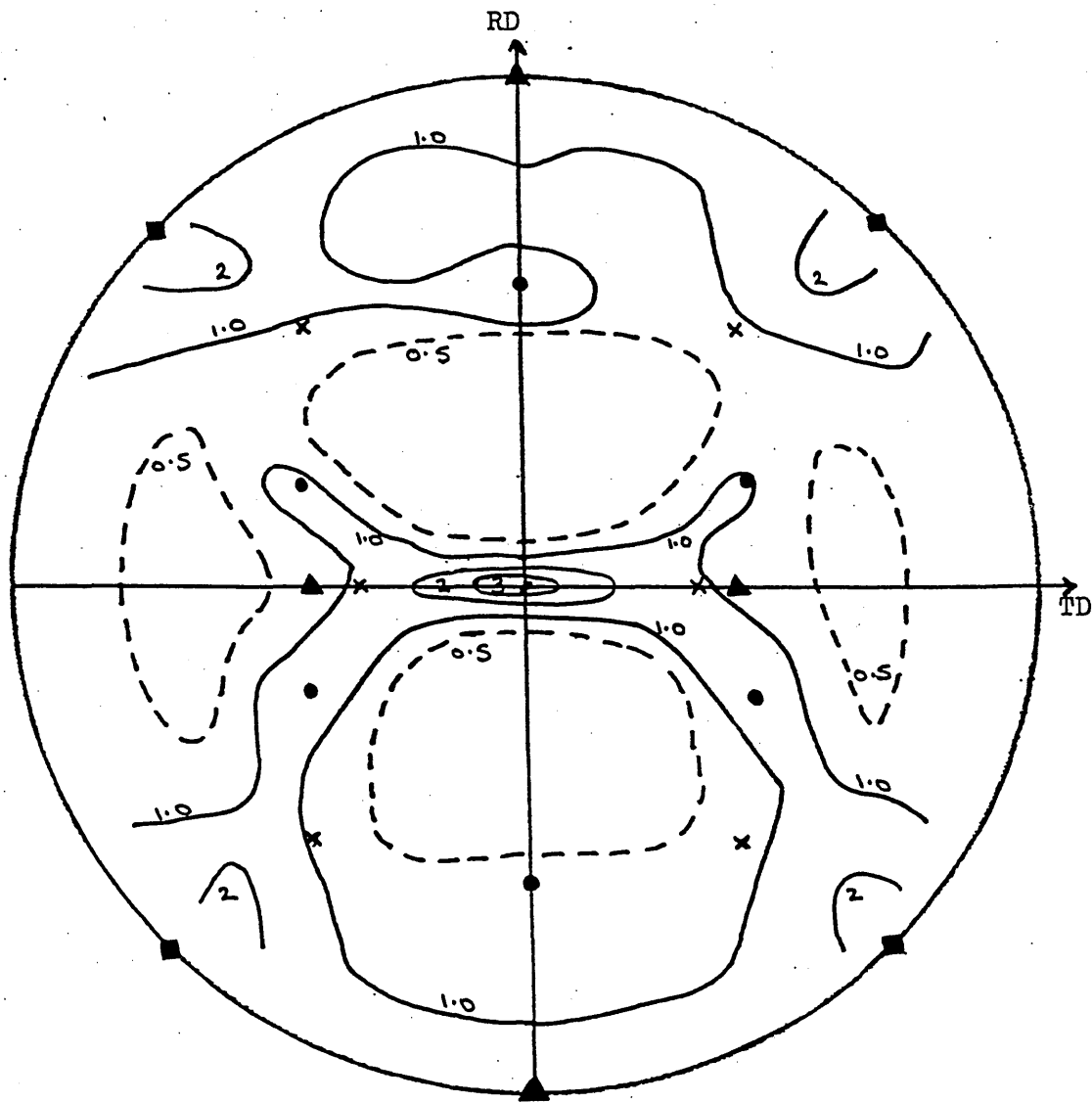


FIGURE 74 COMPARISON BETWEEN RAPID AND BATCH PRE-ANNEALING:-
Variation of Intensities of Orientations with
Cold Rolling Strain in 430 Steel after pre-annealing
and cold rolling.



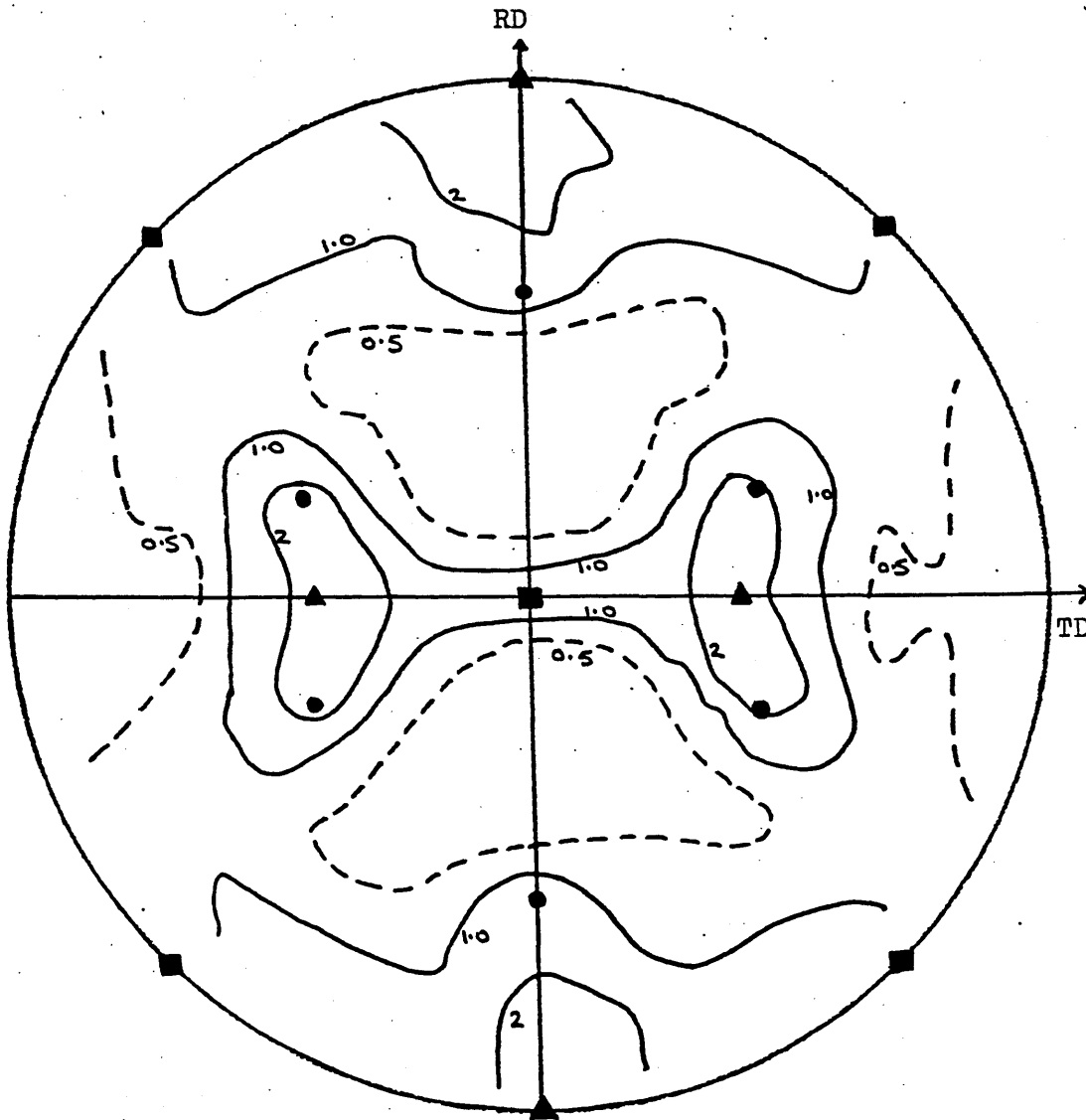
■ $\{100\}\langle 011\rangle$
 ▲ $\{110\}\langle 001\rangle$

FIGURE 75 $\{200\}$ Pole Figure for 430Ti (0.5Ti) Steel after
Batch Annealing at 850°C and Cold Rolling to 50%RA.



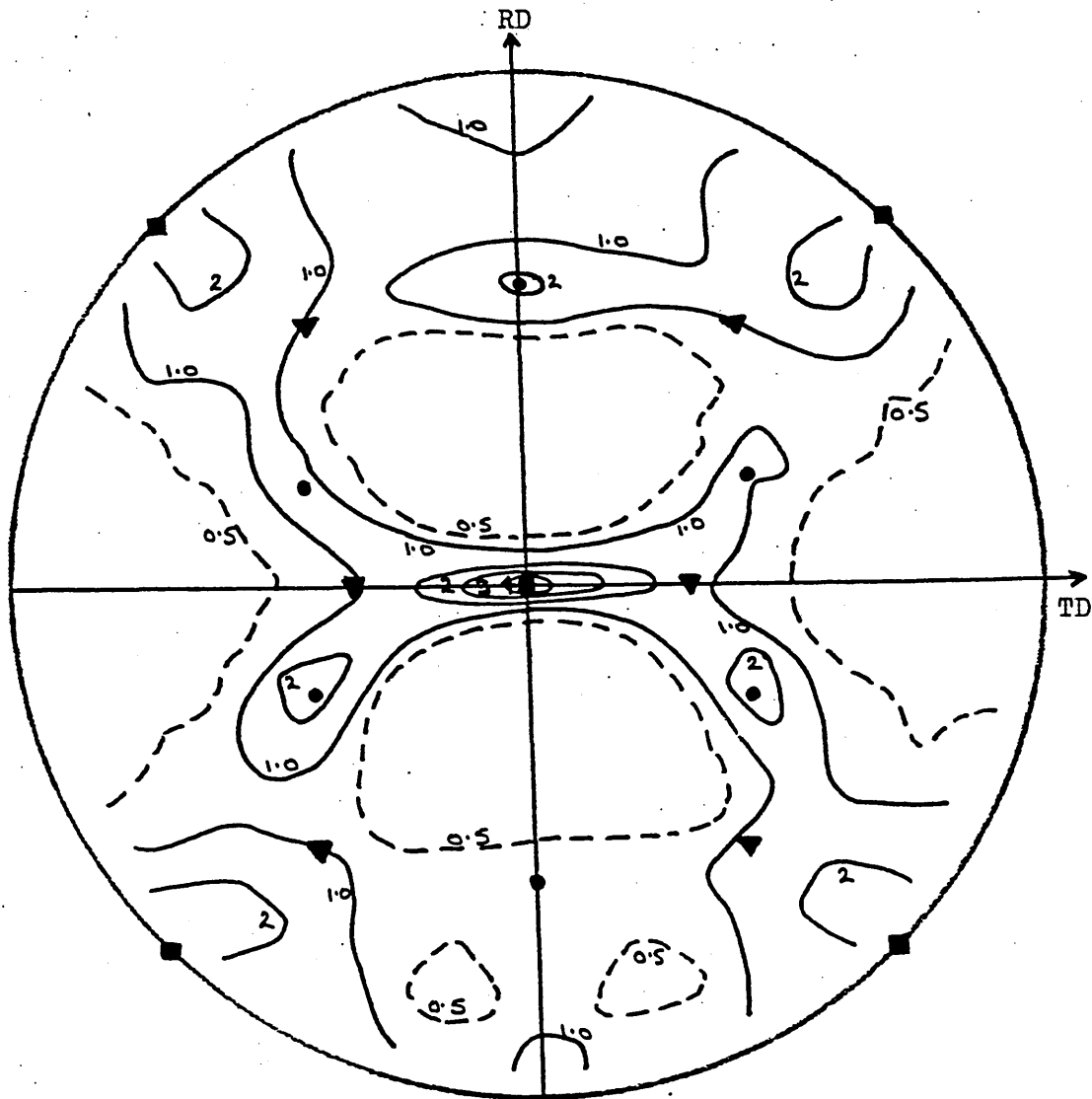
- $\{100\}\langle 011\rangle$
- ▲ $\{110\}\langle 001\rangle$
- $\{554\}\langle 225\rangle$
- × $\{112\}\langle 110\rangle$

FIGURE 76 $\{200\}$ Pole Figure for 430Ti (0.5Ti) Steel after Hot Rolling and Cold Rolling to 70%RA.



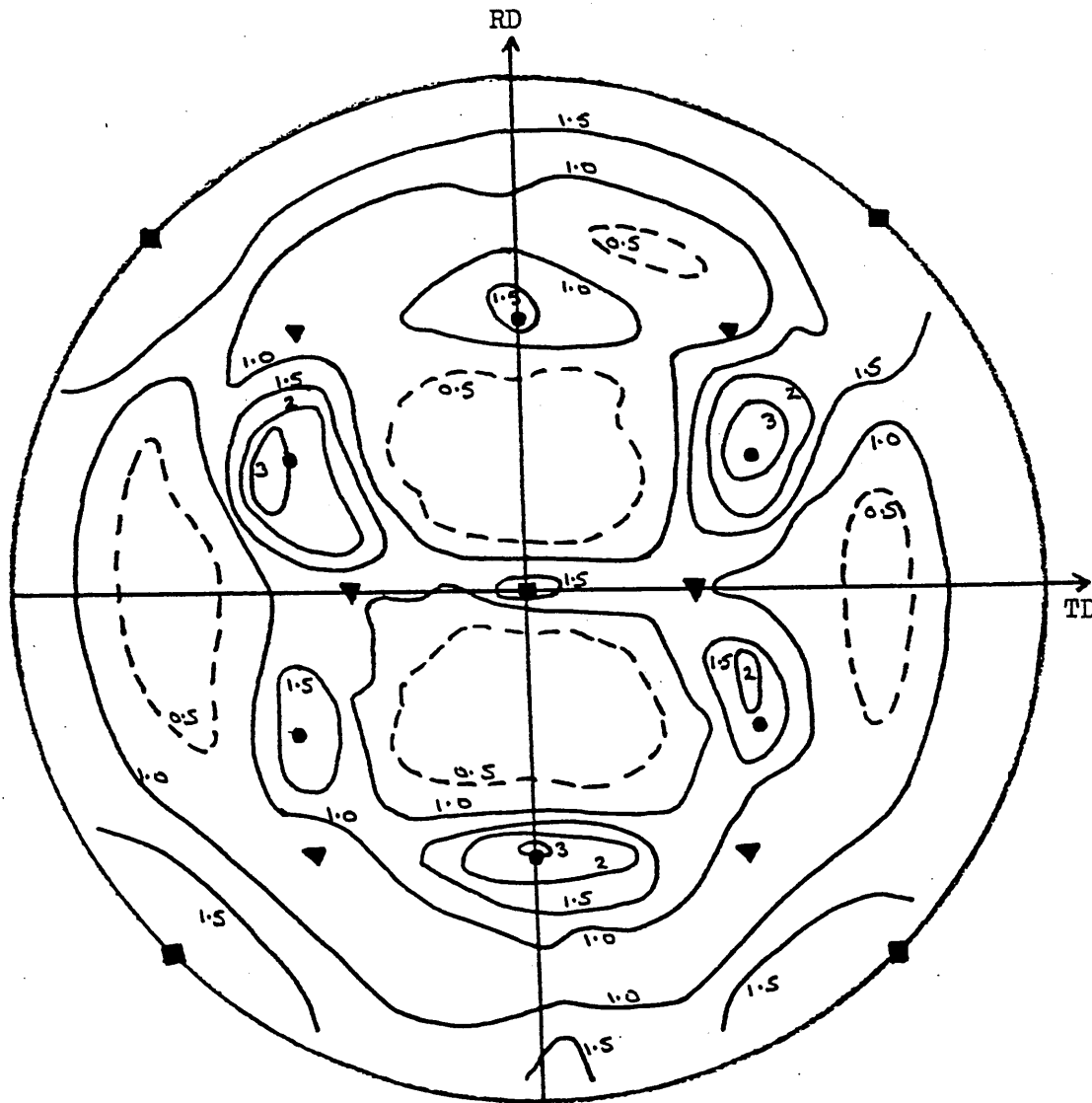
- $\{100\}\langle 011\rangle$
- ▲ $\{110\}\langle 001\rangle$
- $\{554\}\langle 225\rangle$

FIGURE 77 $\{200\}$ Pole Figure for 430Ti (0.5Ti) Steel after
Batch Pre-annealing at 850°C and Cold Rolling
to 70%RA.



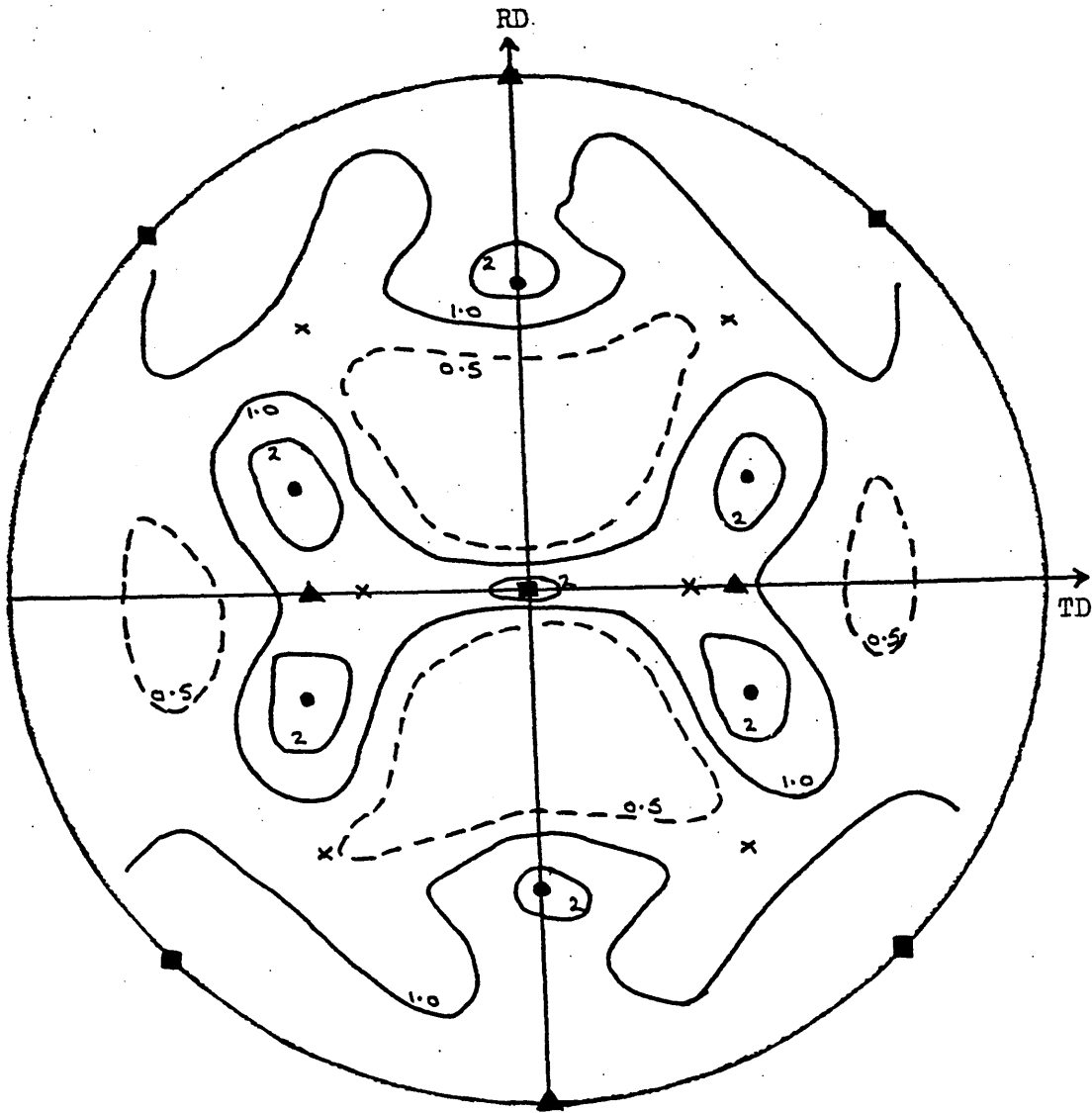
- $\{100\}\langle 011\rangle$
- $\{554\}\langle 225\rangle$
- ▼ $\{112\}\langle 110\rangle$

FIGURE 78 $\{200\}$ Pole Figure for 430Ti (0.5Ti) Steel after Hot Rolling and Cold Rolling to 80%RA.



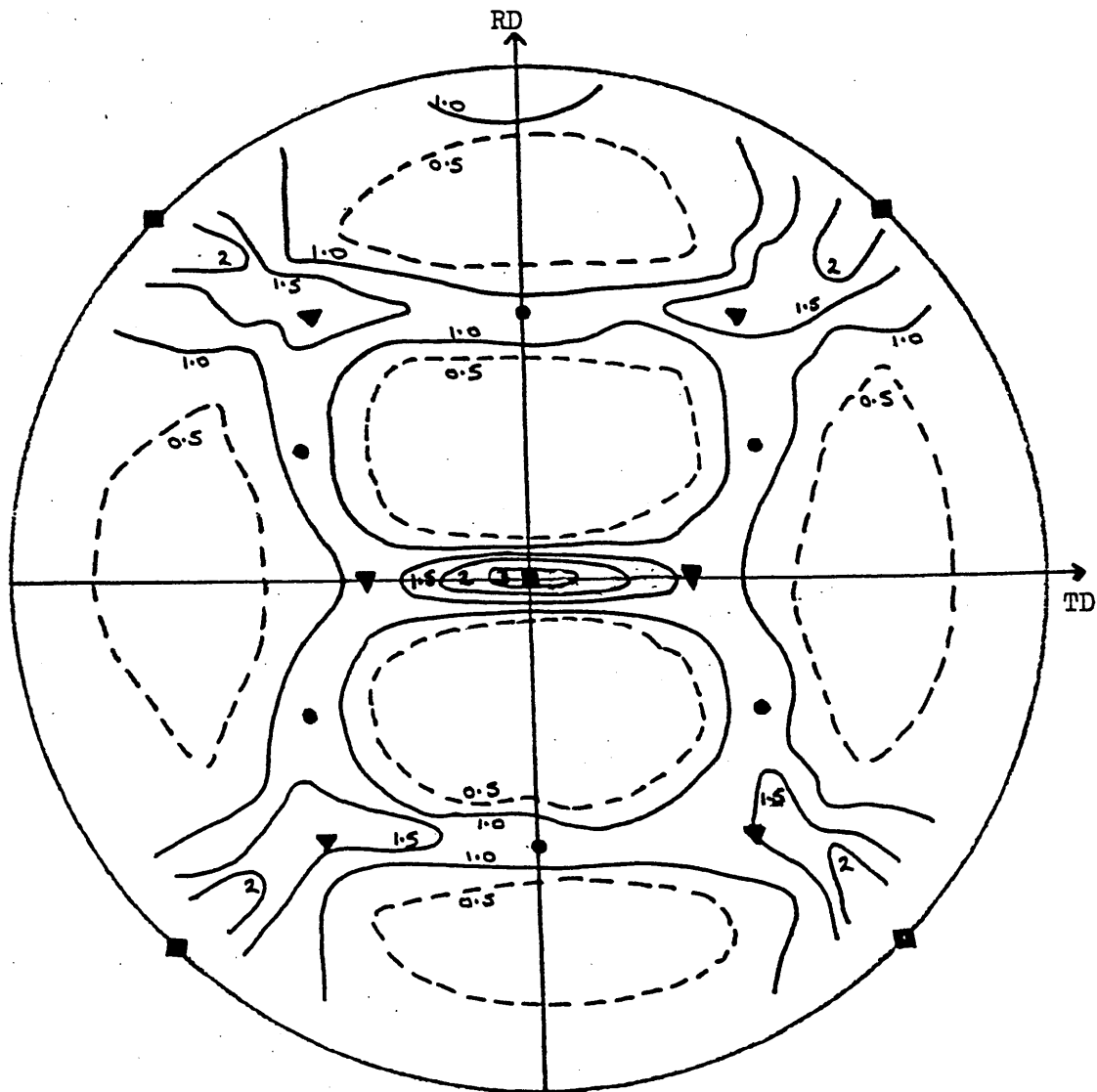
- $\{100\}\langle 011\rangle$
- $\{111\}\langle 112\rangle$
- ▼ $\{112\}\langle 110\rangle$

FIGURE 79 $\{200\}$ Pole Figure for 430Ti (0.5Ti) Steel after Rapid Pre-annealing at 1000°C and Cold Rolling to 80%RA.



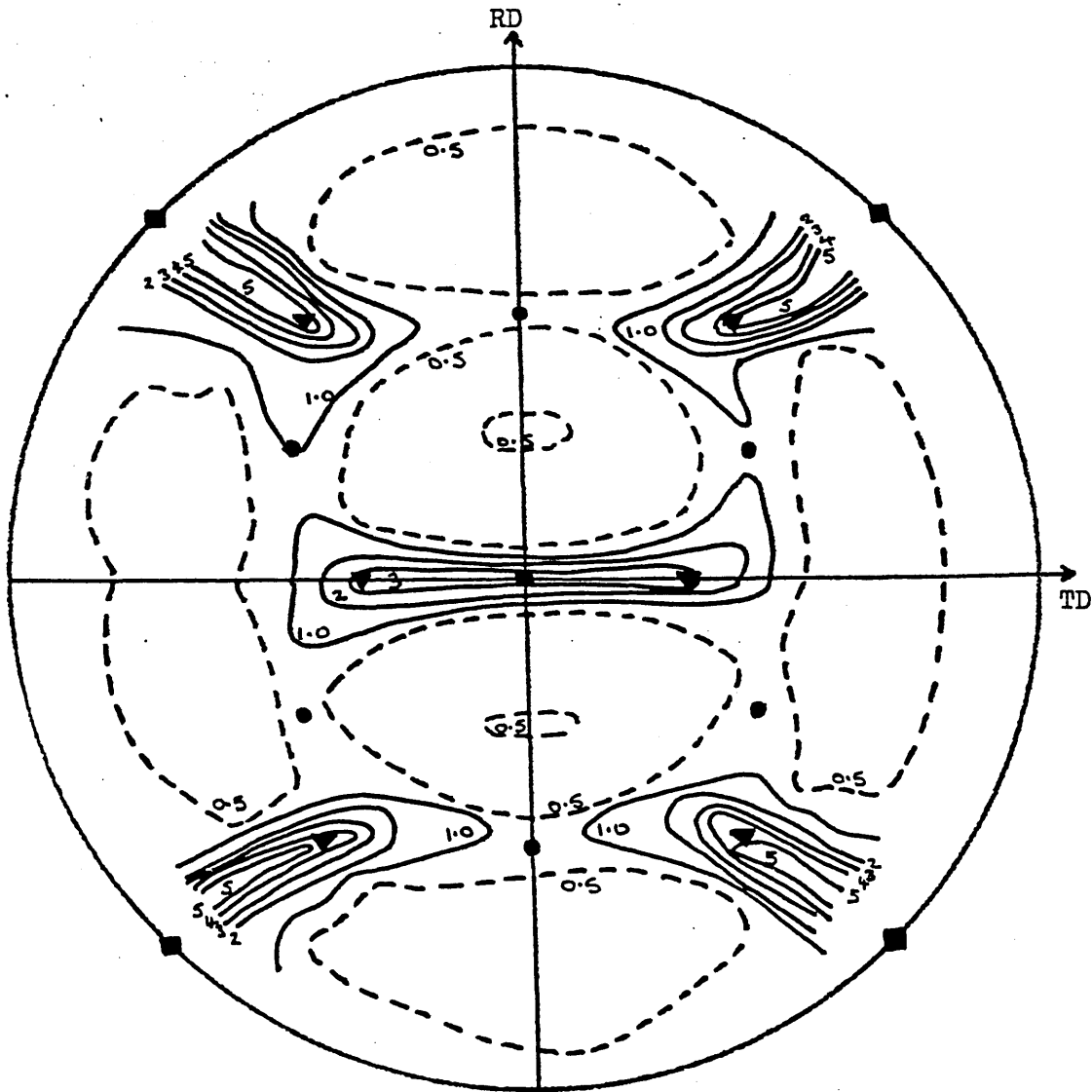
- $\{100\}\langle 011\rangle$
- ▲ $\{110\}\langle 001\rangle$
- $\{554\}\langle 225\rangle$
- × $\{112\}\langle 110\rangle$

FIGURE 80 $\{200\}$ Pole Figure for 430Ti (0.5Ti) Steel after
Batch Pre-annealing at 850°C and Cold Rolling to 80%RA.



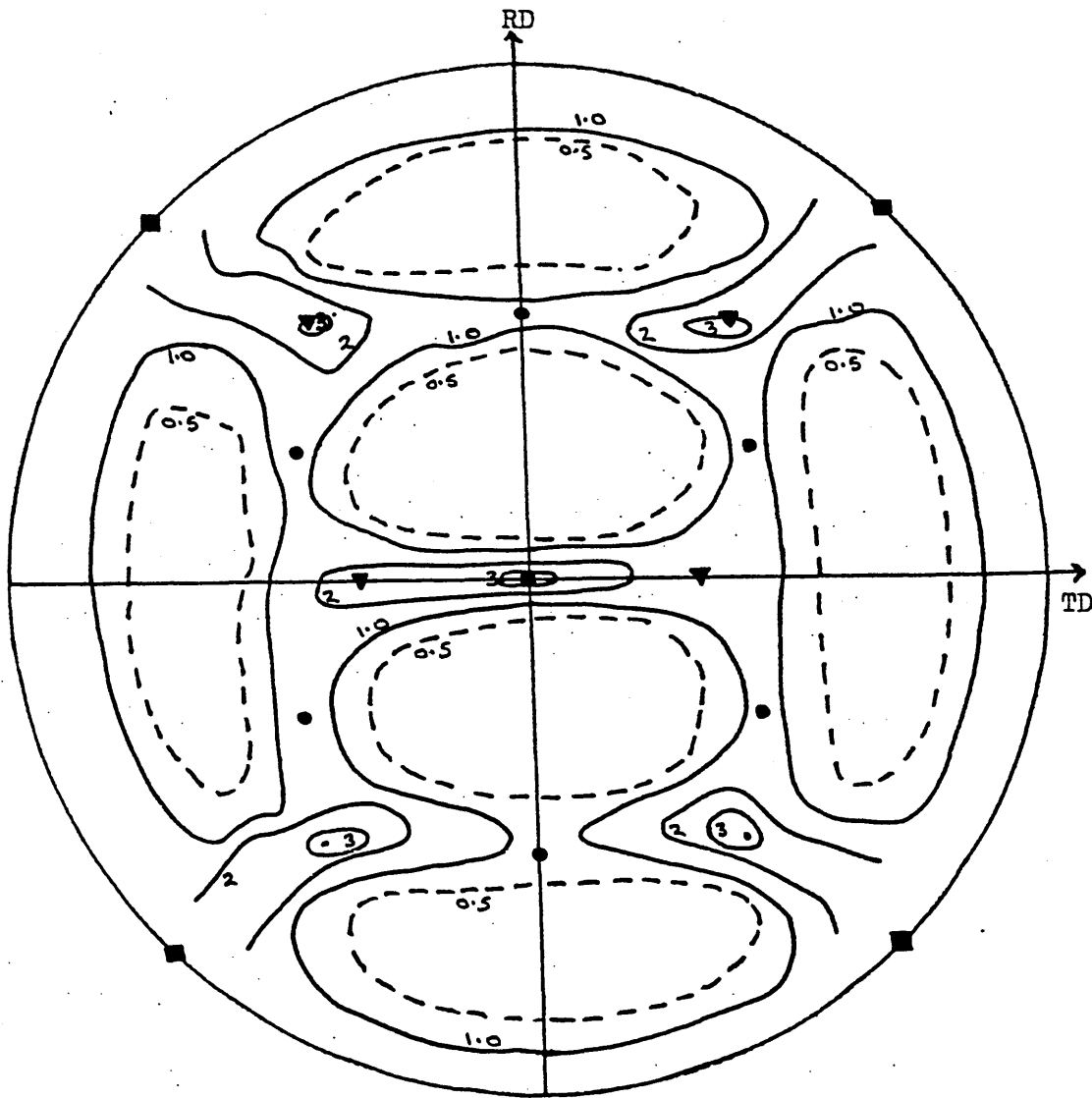
- $\{100\} \langle 011 \rangle$
- $\{111\} \langle 112 \rangle$
- ▼ $\{112\} \langle 110 \rangle$

FIGURE 81 $\{200\}$ Pole Figure for 430Ti (0.5Ti) Steel after Rapid Pre-annealing at 850°C and Cold Rolling to 90%RA.



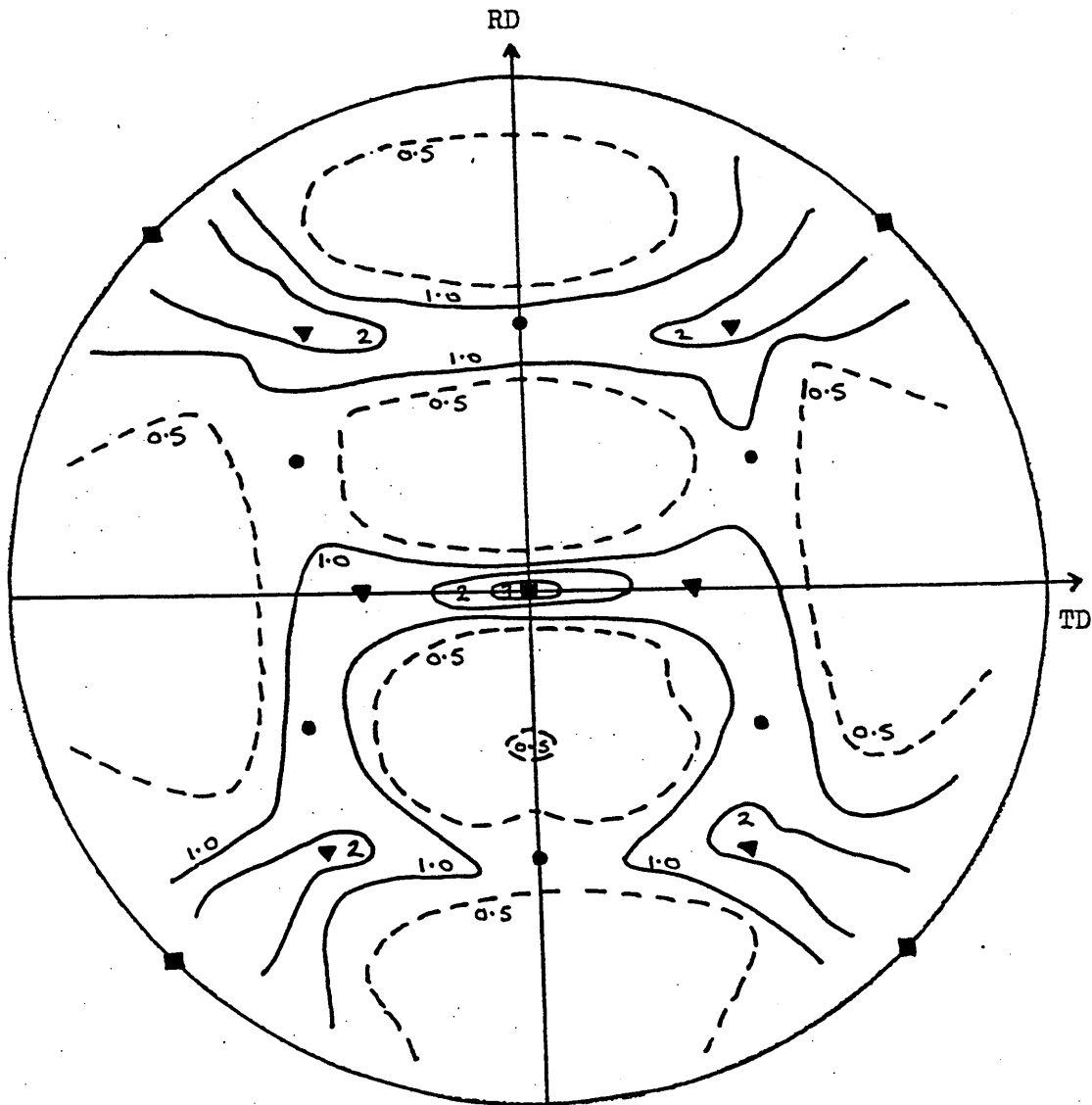
- $\{100\} \langle 011 \rangle$
- $\{111\} \langle 112 \rangle$
- ▼ $\{112\} \langle 110 \rangle$

FIGURE 82 $\{200\}$ Pole Figure for 430Ti (0.5Ti) Steel after
Hot Rolling and Cold Rolling to 95%RA.



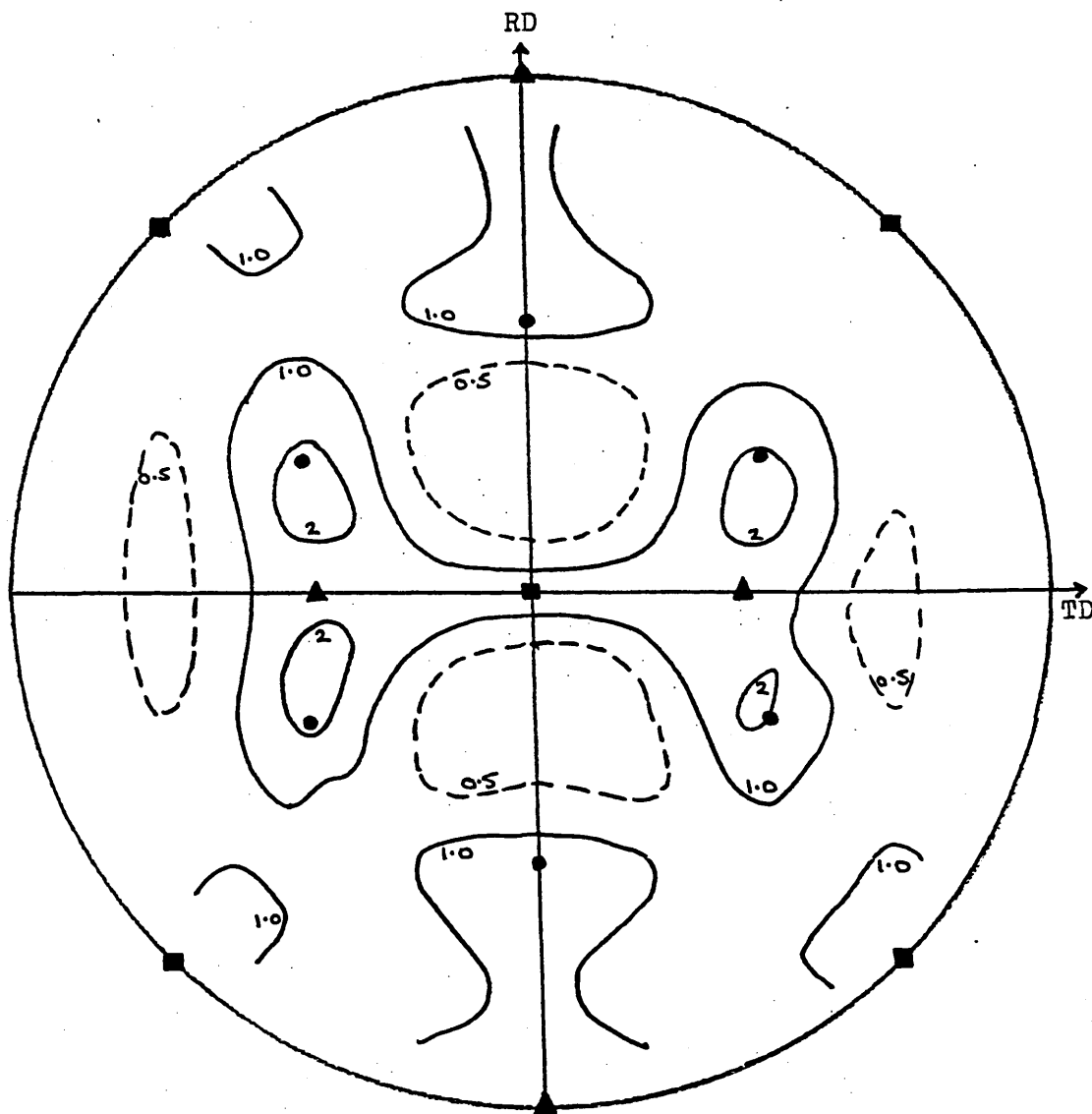
- $\{100\}\langle 011\rangle$
- $\{111\}\langle 112\rangle$
- ▼ $\{112\}\langle 110\rangle$

FIGURE 83 $\{200\}$ Pole Figure for 430Ti (0.5Ti) Steel after Rapid Pre-annealing at 1000°C and Cold Rolling to 95%RA.



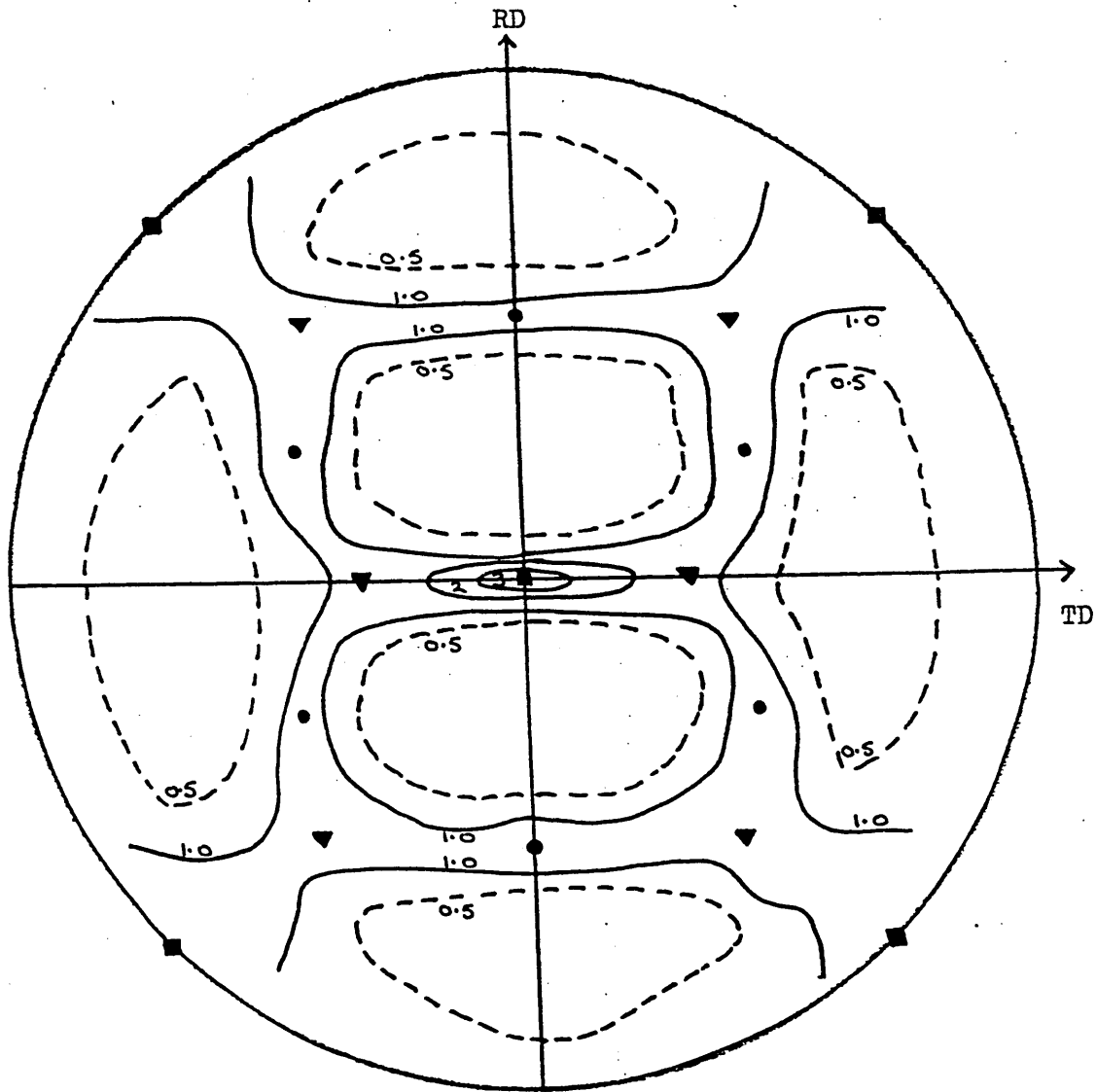
- $\{100\} \langle 011 \rangle$
- $\{111\} \langle 112 \rangle$
- ▼ $\{112\} \langle 110 \rangle$

FIGURE 84 $\{200\}$ Pole Figure for 430Ti (0.5Ti) Steel after
Batch Pre-annealing at 850°C and Cold Rolling
to 95%RA.



- $\{100\} \langle 011 \rangle$
- $\{111\} \langle 112 \rangle$
- ▲ $\{110\} \langle 001 \rangle$

FIGURE 85 $\{200\}$ Pole Figure for 430Ti (0.3Ti) Steel after Rapid Pre-annealing at 850°C and Cold Rolling to 70%RA.



- $\{100\}\langle 011\rangle$
- $\{111\}\langle 112\rangle$
- ▼ $\{112\}\langle 110\rangle$

FIGURE 86 $\{200\}$ Pole Figure for 430Ti (0.3Ti) Steel after
Batch Annealing at 850°C and Cold Rolling to 95%RA.

Without pre-anneal
or with pre-anneal
< 800 °C.

Pre-annealed at
850 °C.

Pre-annealed at
1000 °C.

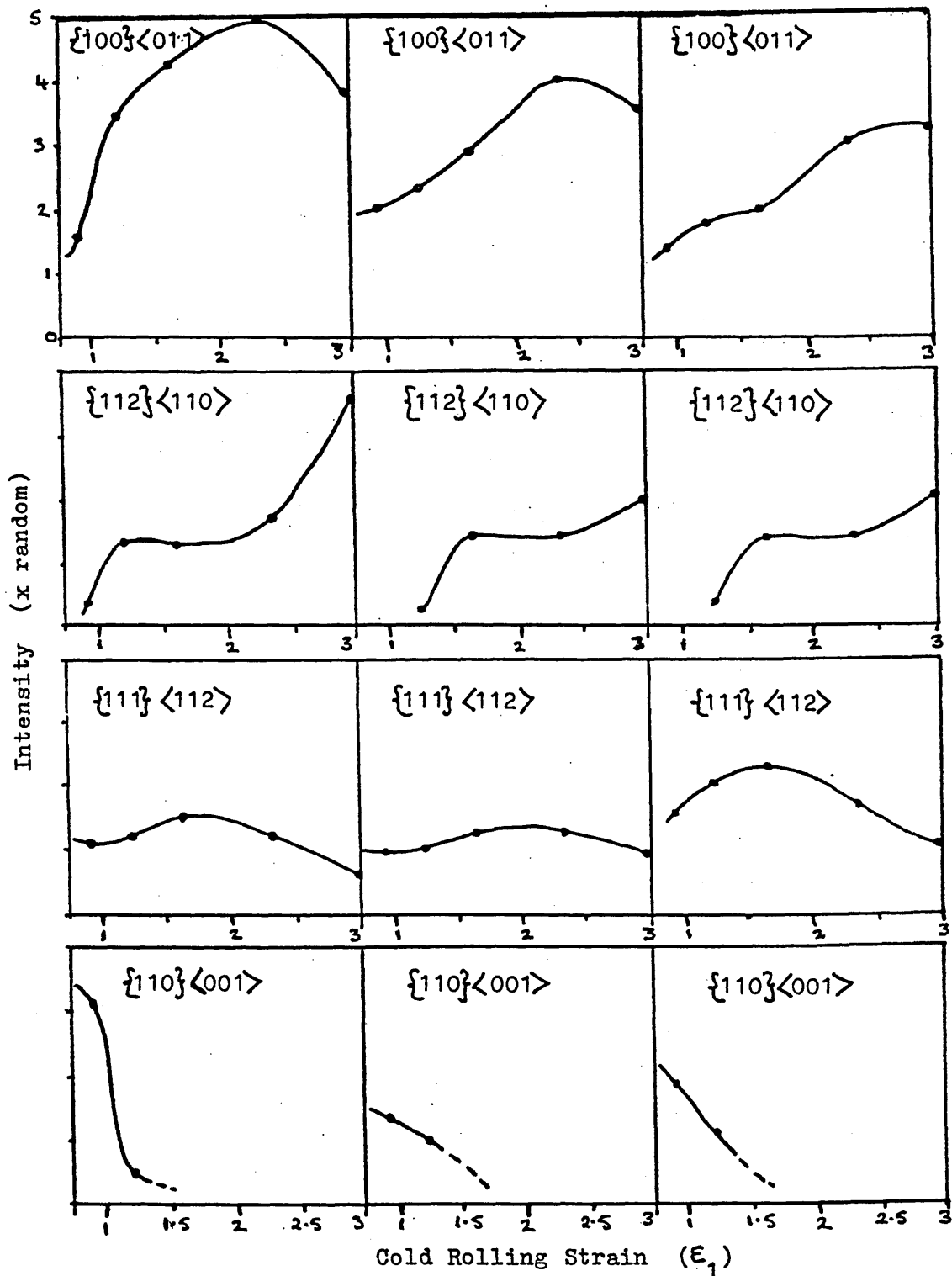
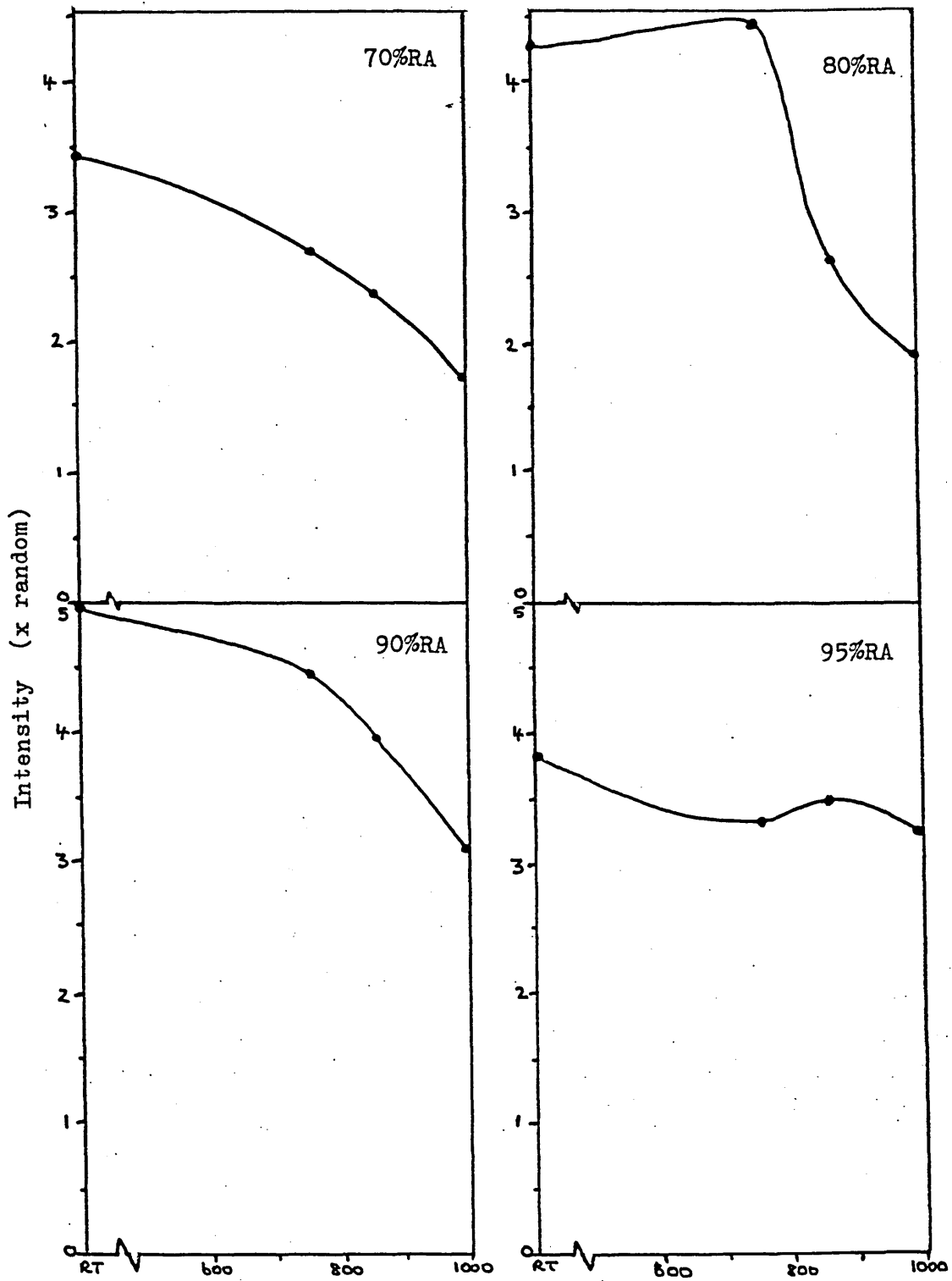


FIGURE 87 Variation of Intensities of Orientations with Cold Rolling Strain for Cold Rolled 430Ti (0.5Ti) Steel.



Temperature of annealing prior to cold rolling ($^{\circ}\text{C}$)
(Heating rate $\sim 5000 \text{ }^{\circ}\text{C hr}^{-1}$, AC)

FIGURE 88 Variation of Intensity of the $\{100\}\langle 011\rangle$ Orientation
with Pre-annealing Temperature in Cold Rolled
430Ti (0.5Ti) Steel.

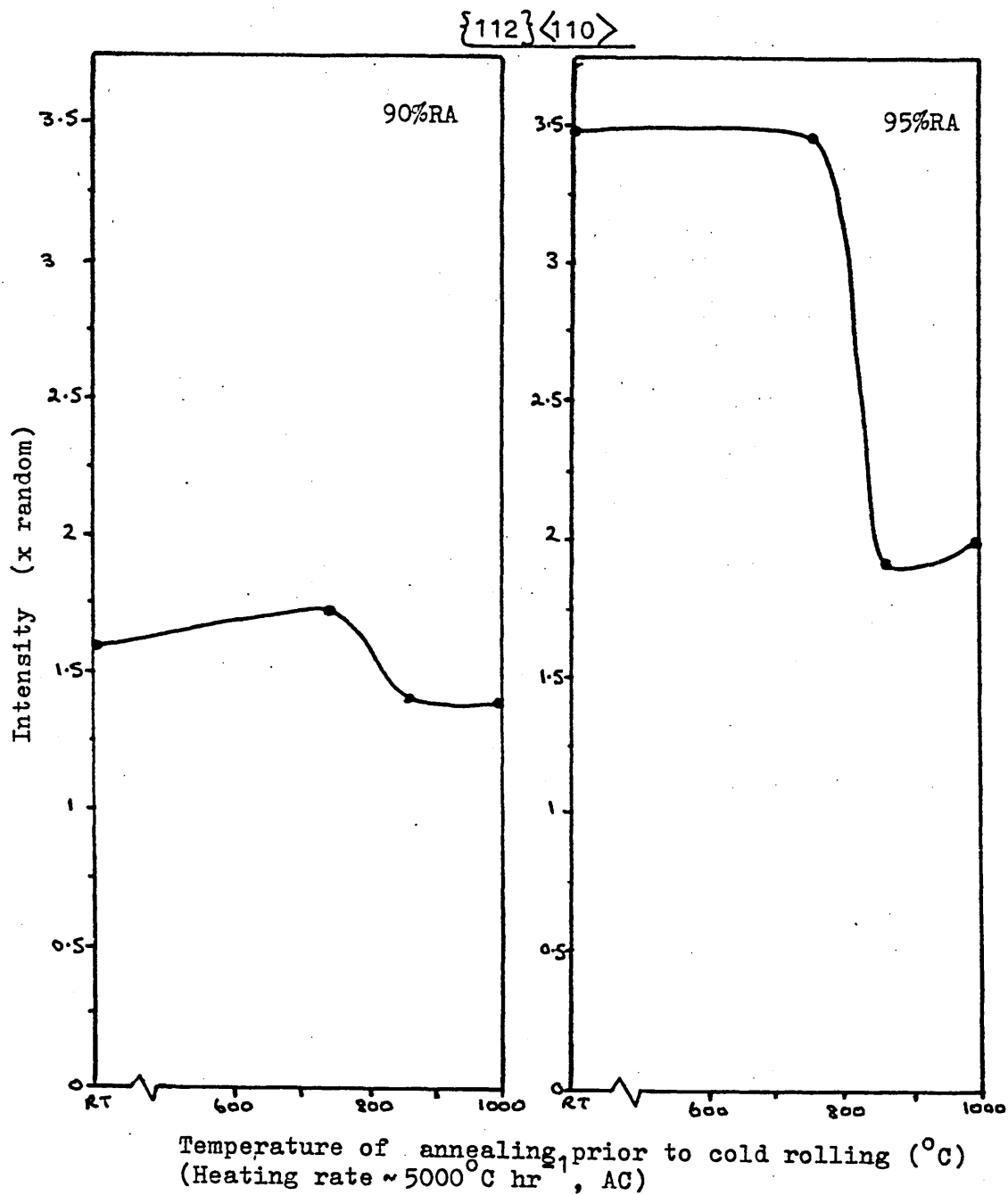


FIGURE 89 Variation of Intensity of the $\{112\}\langle 110 \rangle$ Orientation with Pre-annealing Temperature in Cold Rolled 430Ti(0.5Ti) Steel.

$\{111\}\langle 112\rangle$

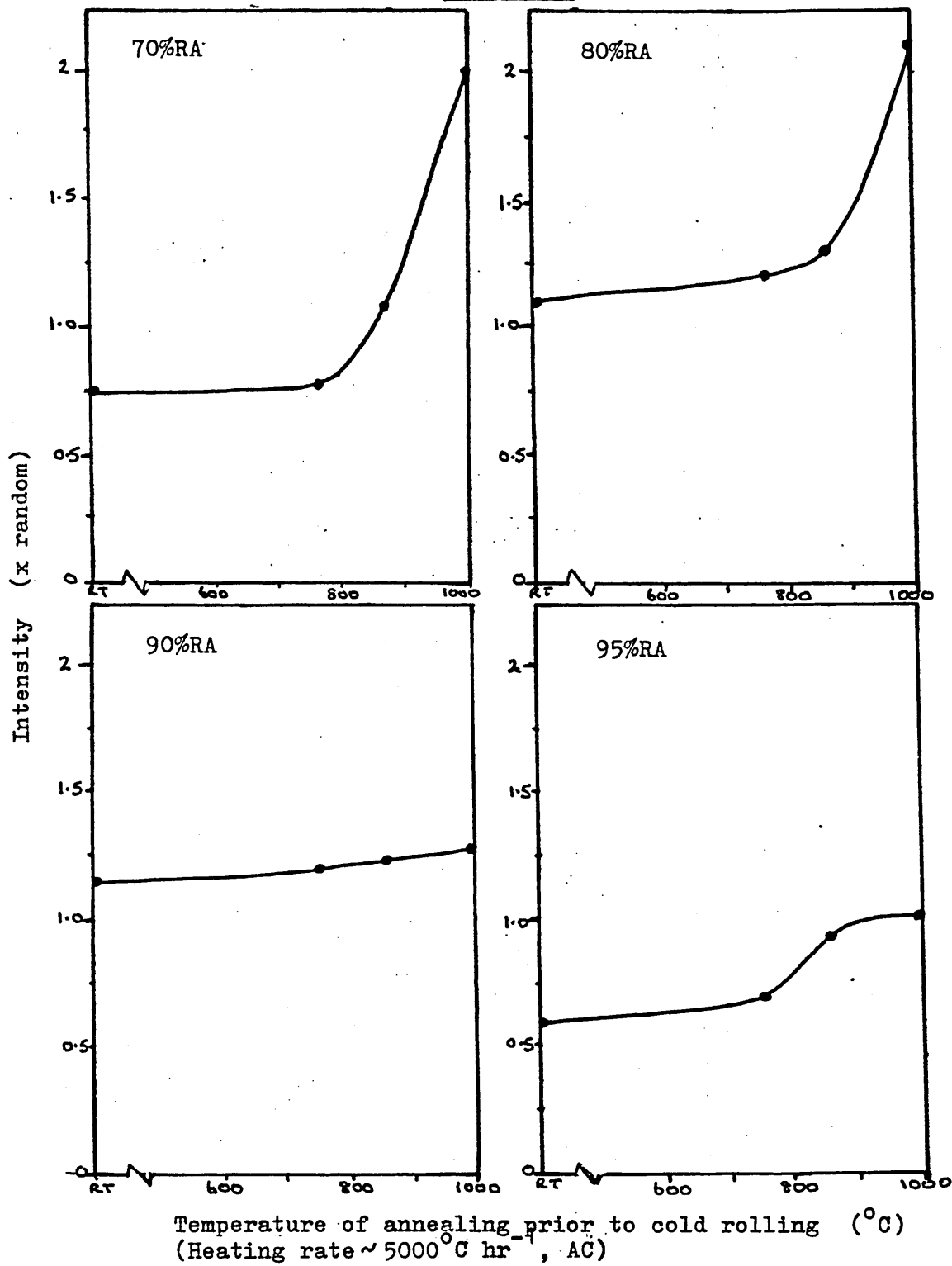


FIGURE 90 Variation of Intensity of the $\{111\}\langle 112\rangle$ Orientation in Cold Rolled 430Ti (0.5Ti) Steel with Pre-annealing Temperature.

Rapid pre-annealing
at 850 °C before
cold rolling.

Batch pre-annealing
at 850 °C before
cold rolling.

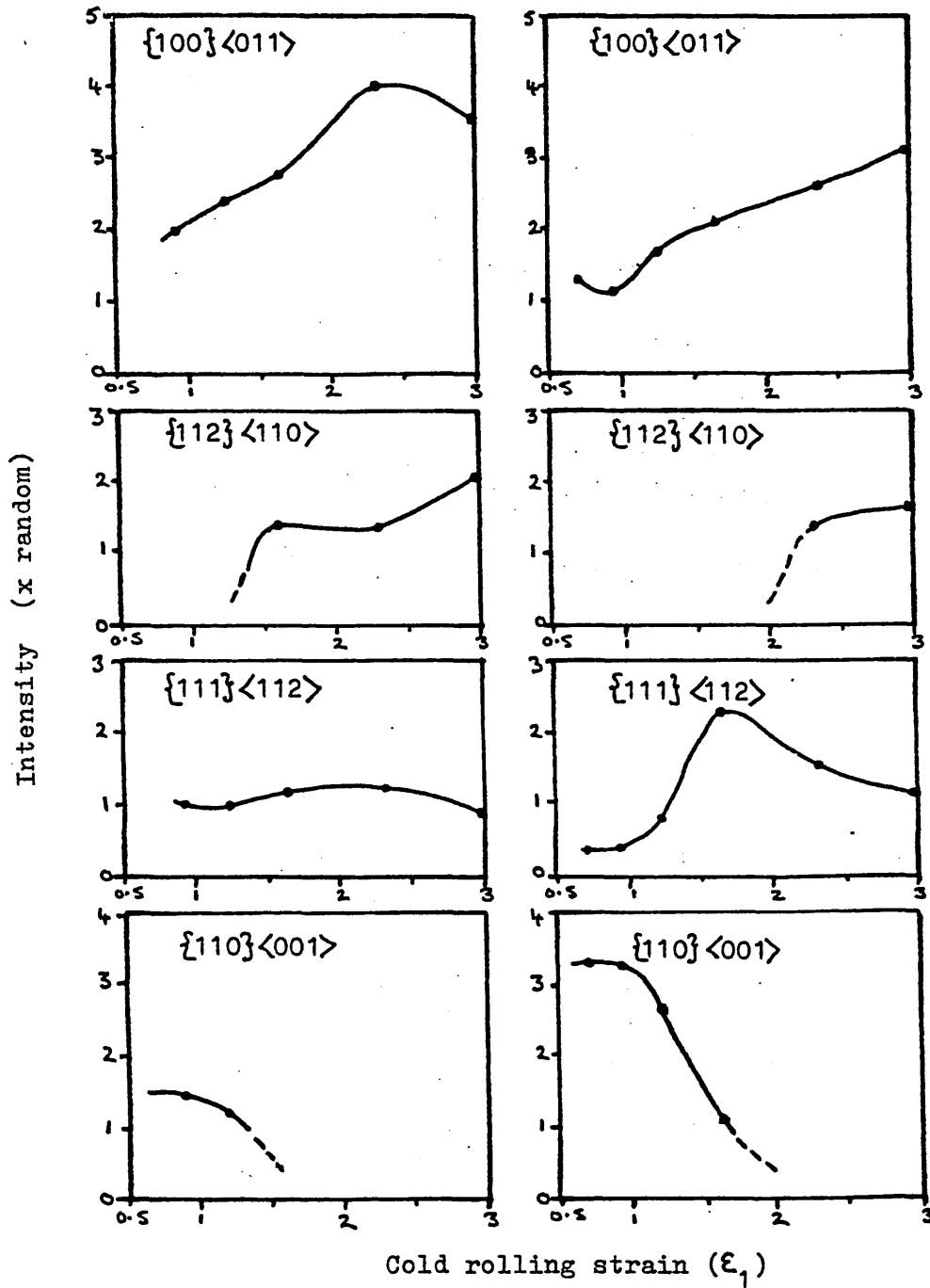
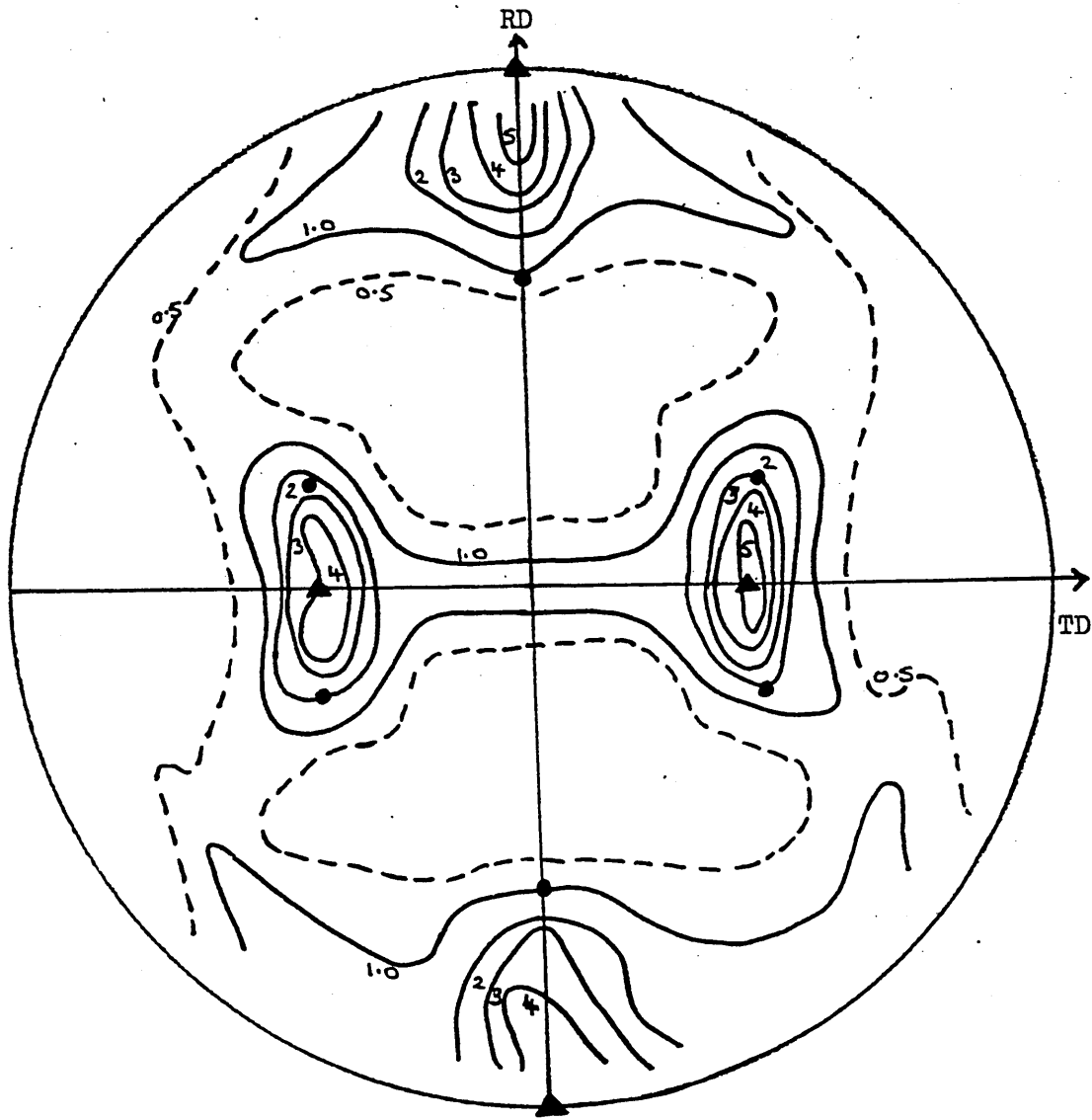
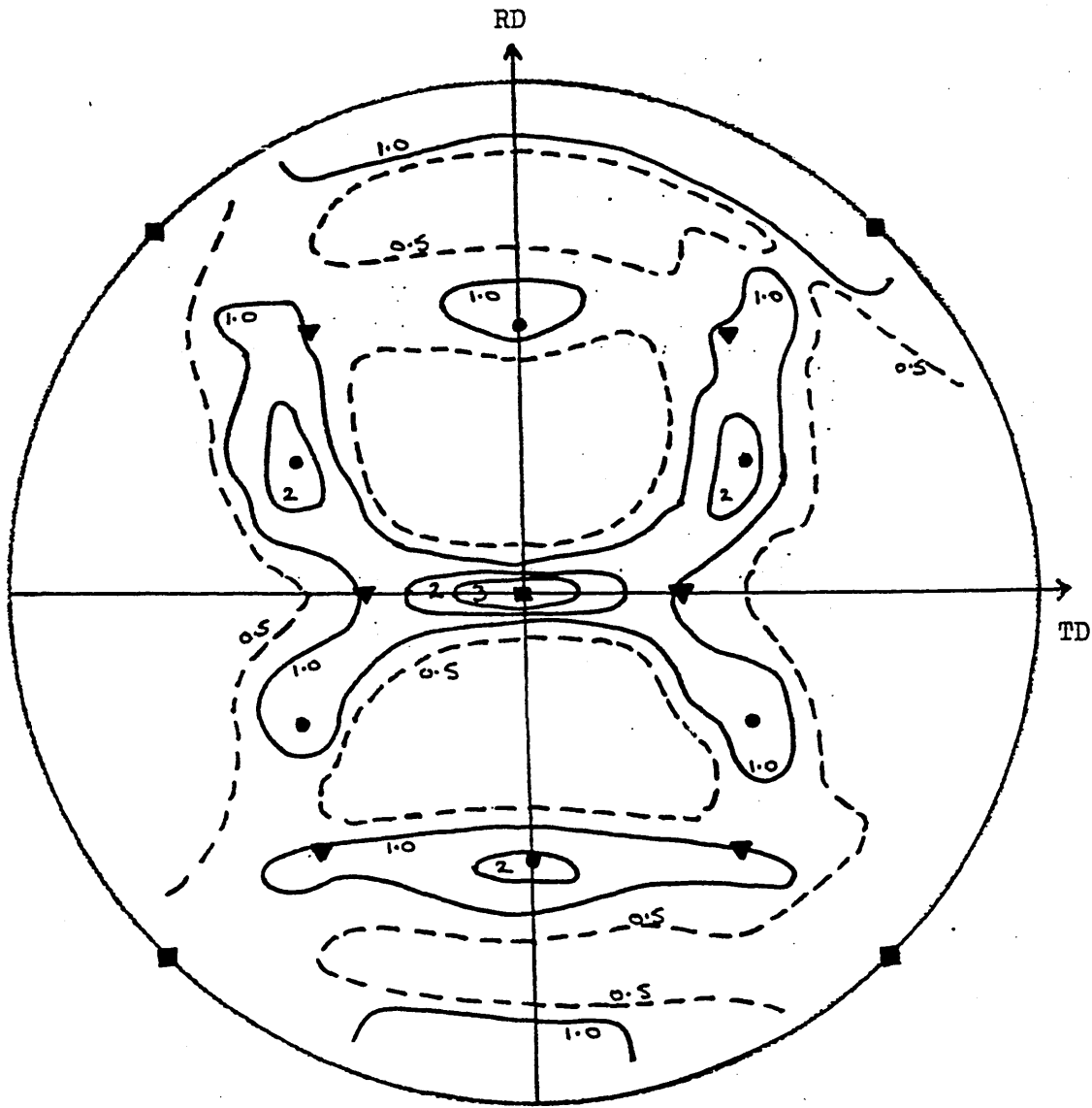


FIGURE 91 COMPARISON BETWEEN RAPID AND BATCH PRE-ANNEALING:-
Variation of Intensities of Orientations with
Cold Rolling Strain for Cold Rolled 430Ti (0.5Ti)
Steel.



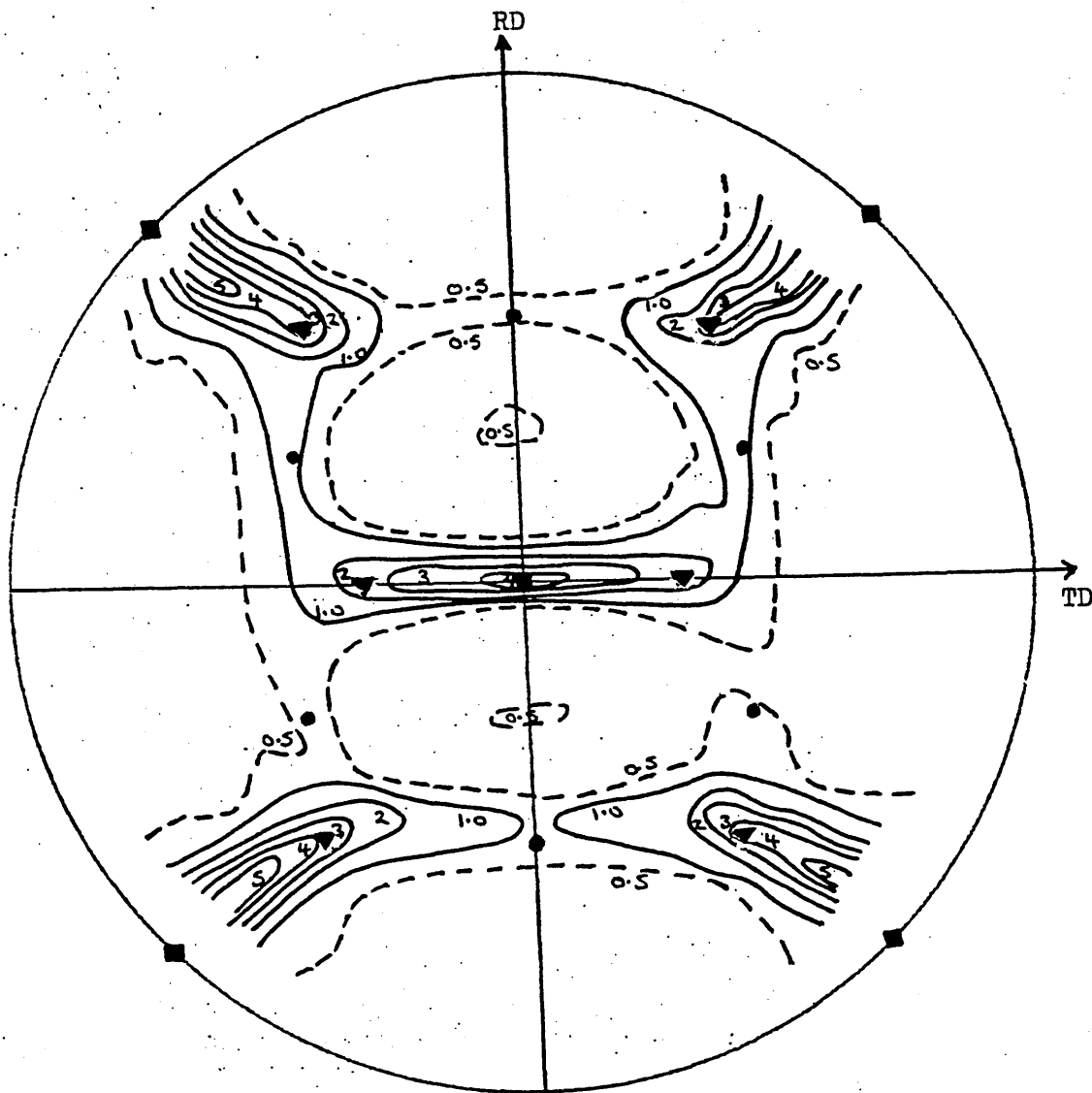
- ▲ $\{110\}\langle 001\rangle$
- $\{554\}\langle 225\rangle$

FIGURE 92 $\{200\}$ Pole Figure for 409 (12Cr,0.5Ti) Steel
after Hot Rolling and Cold Rolling to 70%RA.



- $\{100\}\langle 011\rangle$
- $\{111\}\langle 112\rangle$
- ▼ $\{112\}\langle 110\rangle$

FIGURE 93 $\{200\}$ Pole Figure for 409 (12Cr, 0.5Ti) Steel after Hot Rolling and Cold Rolling to 90%RA.



- $\{100\} \langle 011 \rangle$
- $\{111\} \langle 112 \rangle$
- ▼ $\{112\} \langle 110 \rangle$

FIGURE 94 $\{200\}$ Pole Figure for 409 (12Cr, 0.5Ti) Steel after Hot Rolling and Cold Rolling to 95%RA.

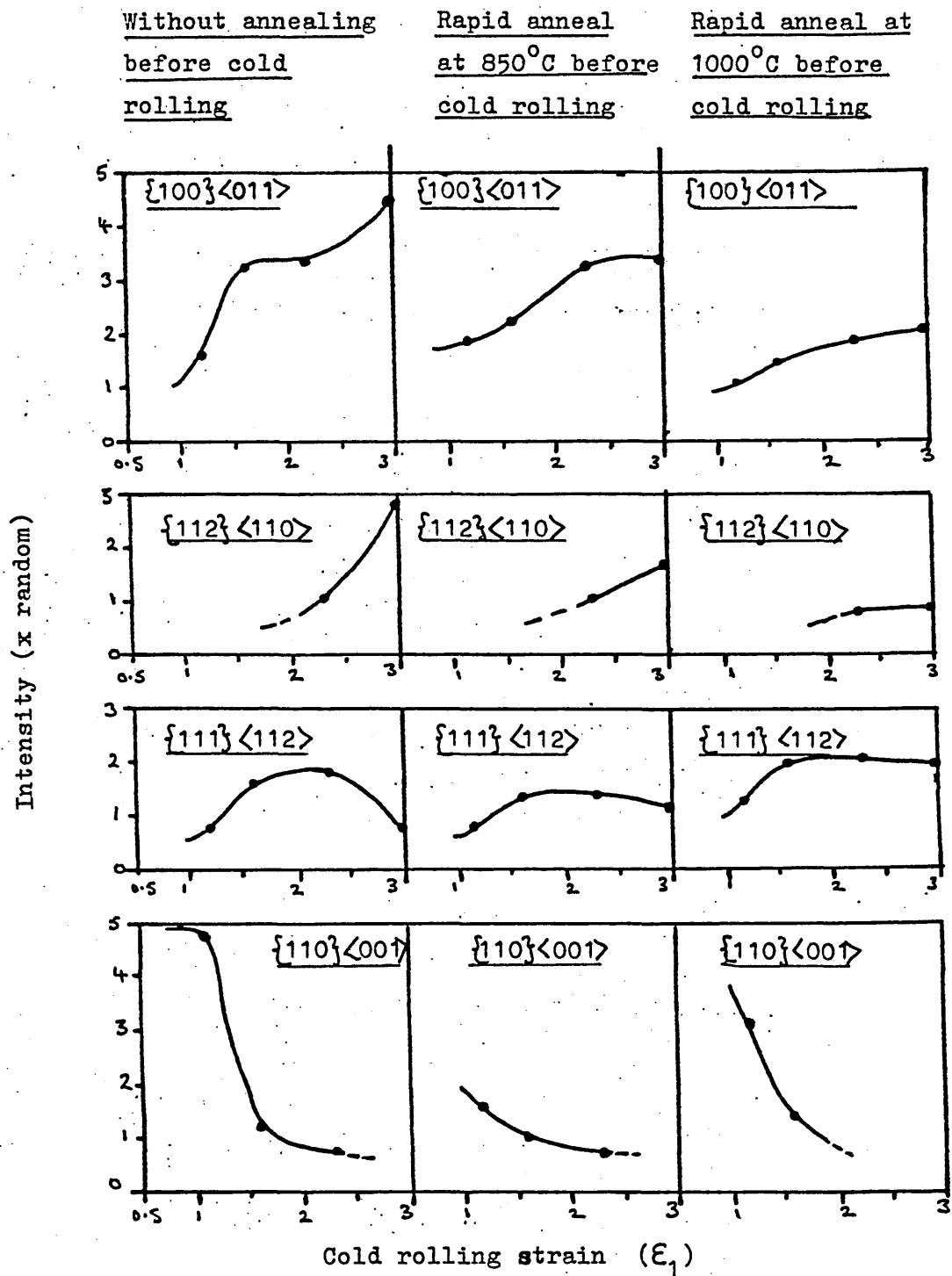
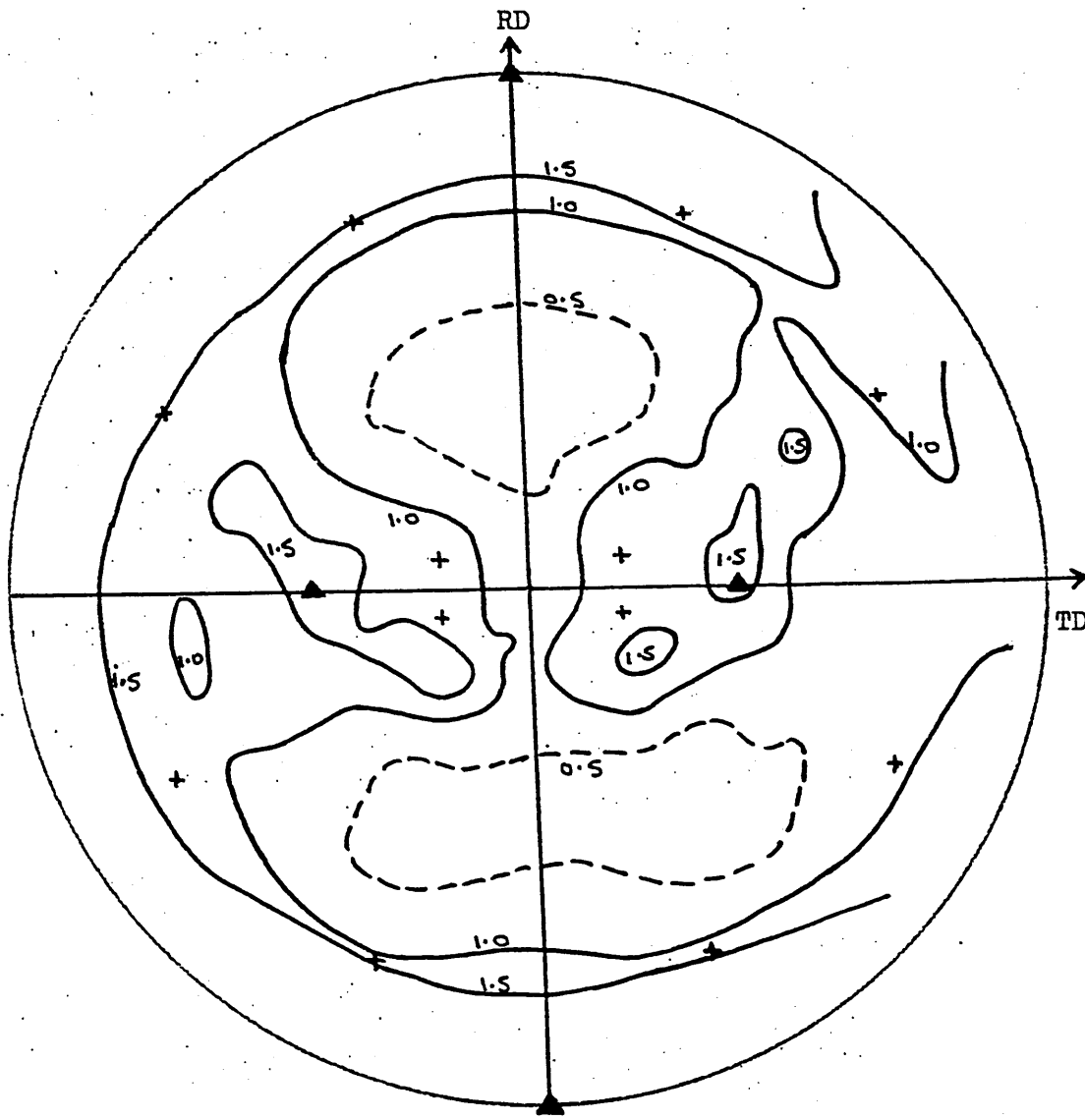


FIGURE 95 Variation in Intensities of Orientations with Strain in Cold Rolled 409 Steel.

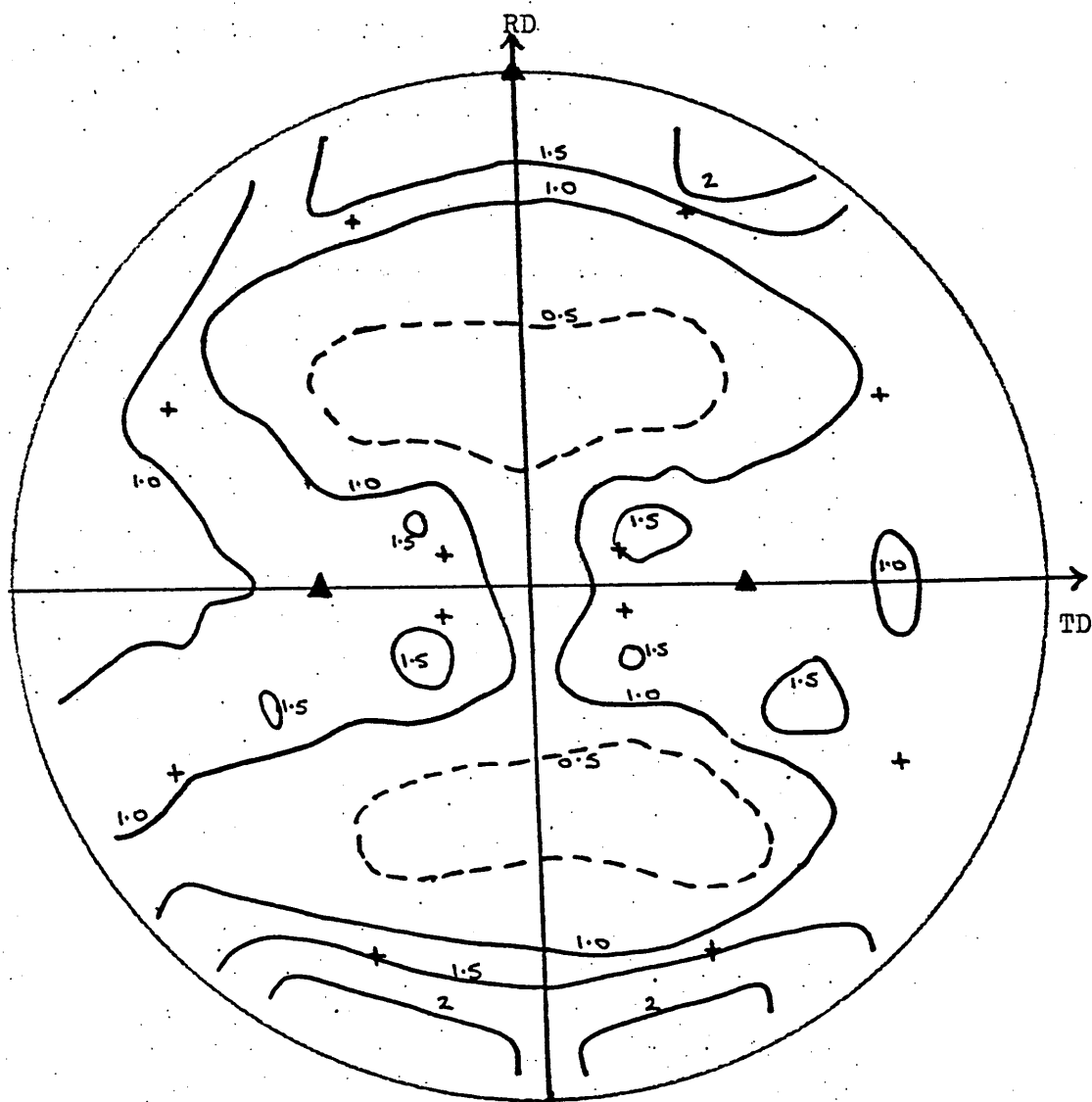


+ $\{114\}\langle 84 \rangle$

▲ $\{110\}\langle 001 \rangle$

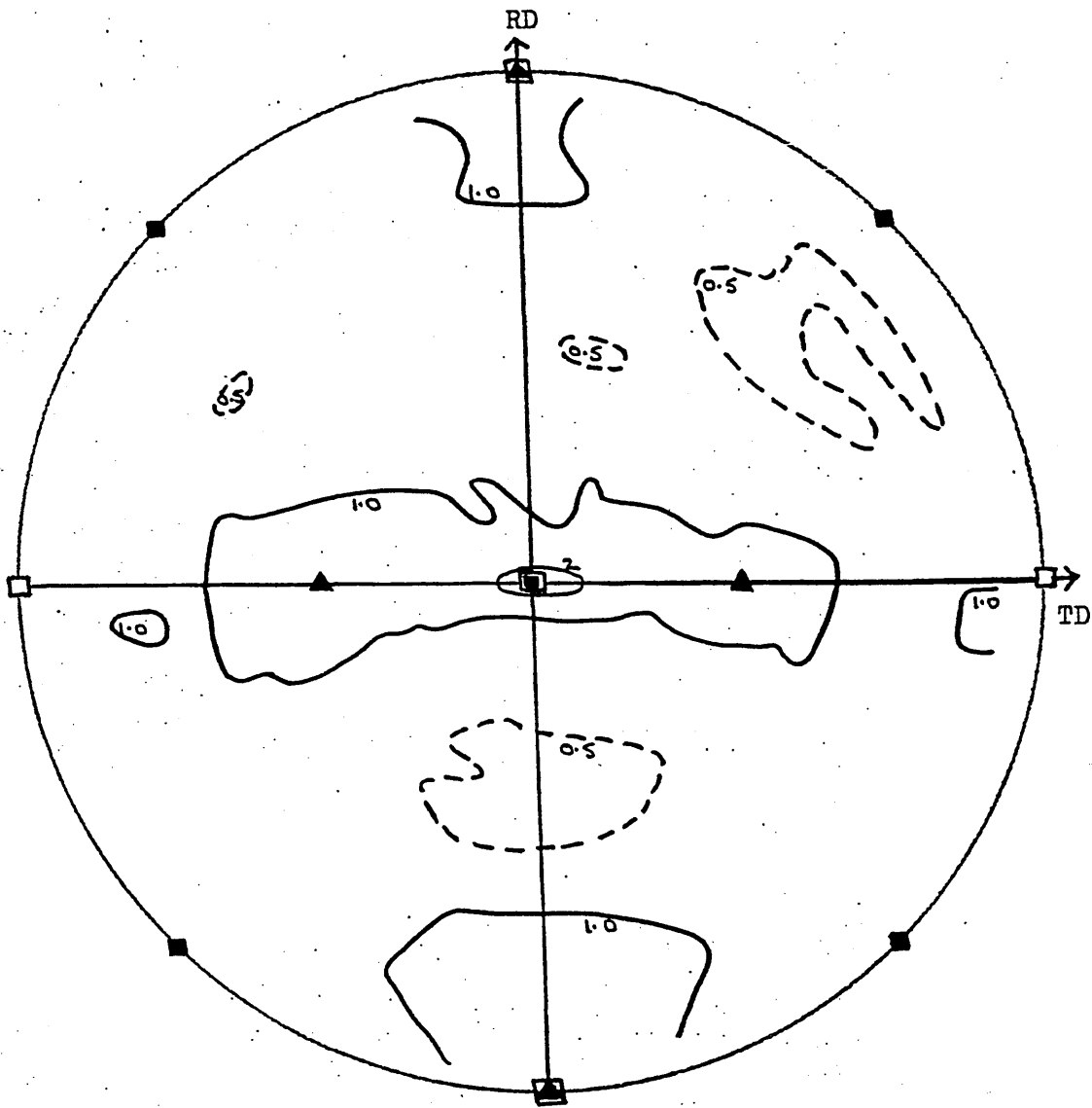
FIGURE 96

$\{200\}$ Pole Figure for 430 Steel after Rapid
Pre-annealing at 850°C , Cold Rolling to 50%RA and
Rapid Final Annealing at 900°C .



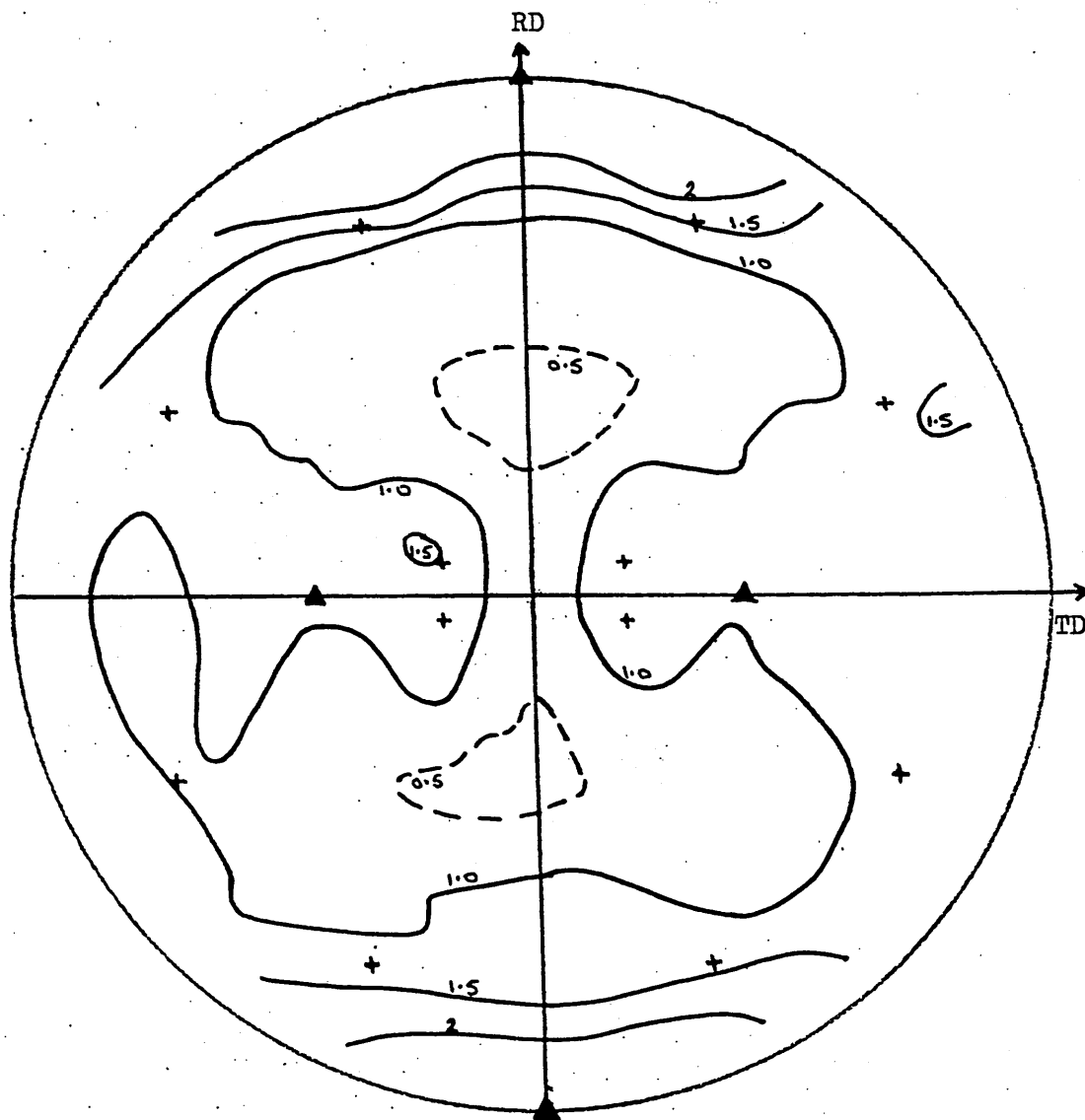
+ $\{114\}\langle 841 \rangle$
 ▲ $\{110\}\langle 001 \rangle$

FIGURE 97 $\{200\}$ Pole Figure for 430 Steel after Rapid
Annealing at 1000°C (+ temper), Cold Rolling to
50%RA and Rapid Final Annealing at 900°C .



- $\{100\}\langle 001 \rangle$
- $\{100\}\langle 011 \rangle$
- ▲ $\{110\}\langle 001 \rangle$

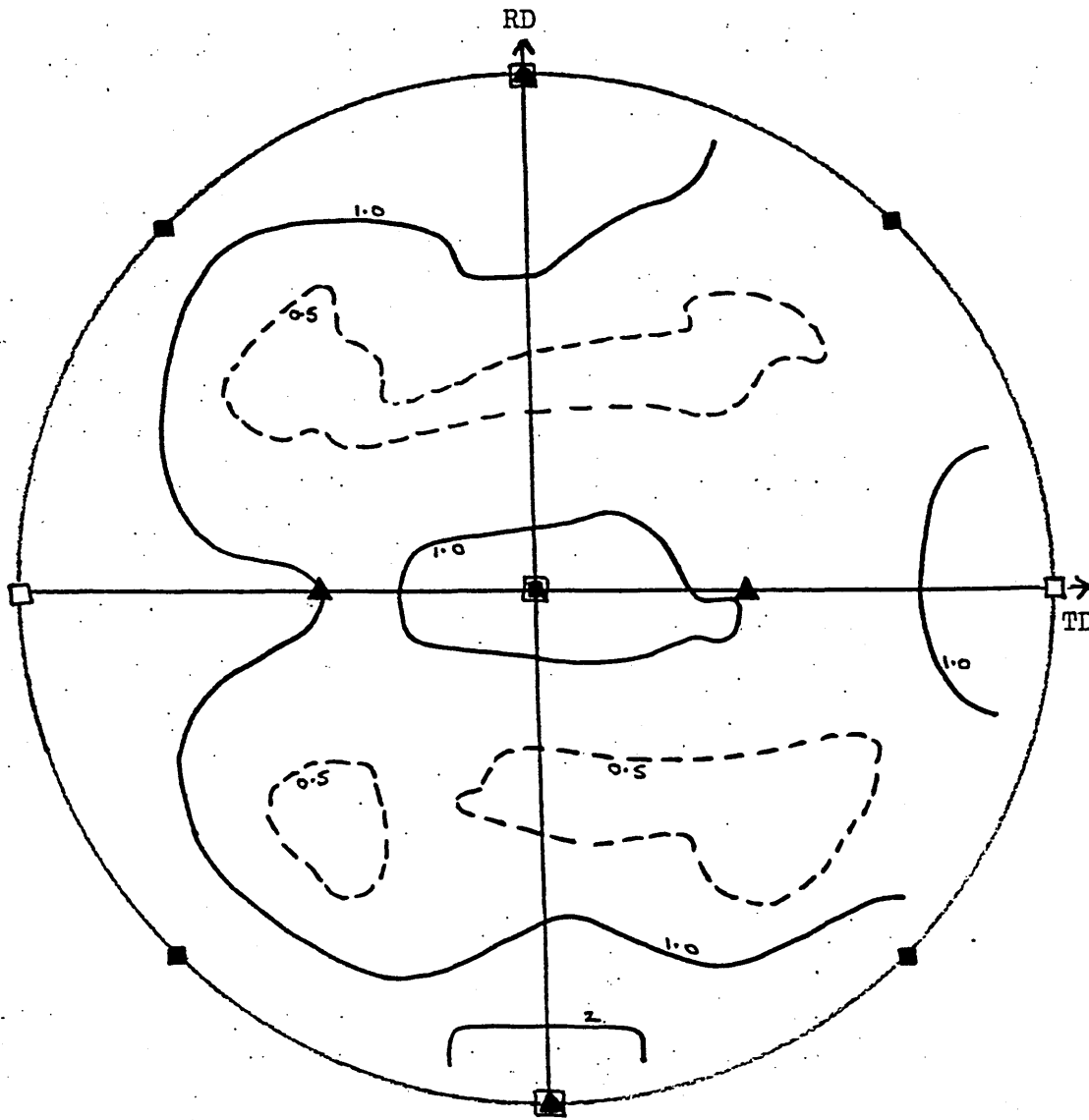
FIGURE 98 $\{200\}$ Pole Figure for 430 Steel after Batch Annealing at 1000°C , Cold Rolling to 50%RA and Rapid Final Annealing at 900°C .



+ $\{114\}\langle 841 \rangle$

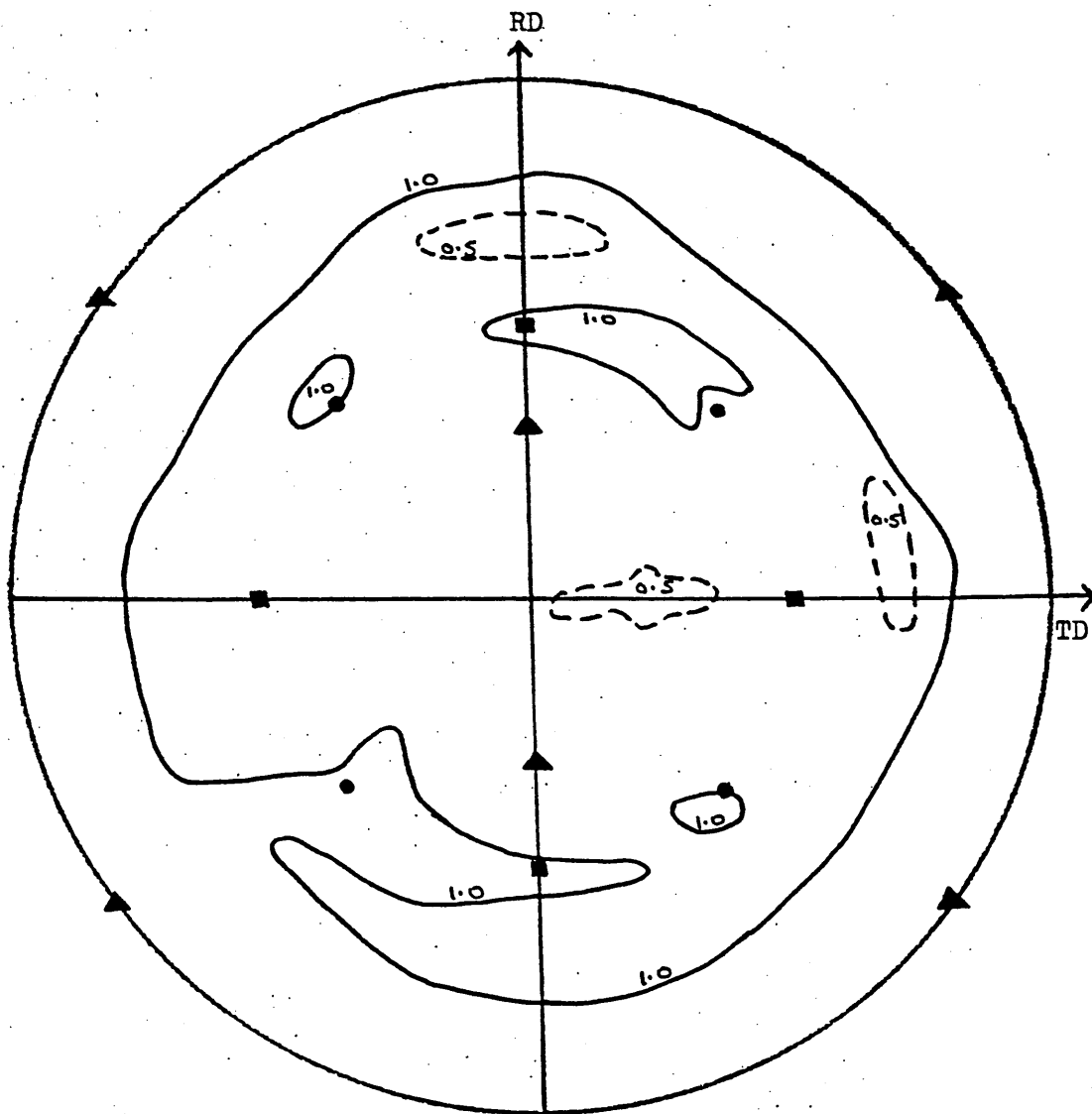
▲ $\{110\}\langle 001 \rangle$

FIGURE 99 $\{200\}$ Pole Figure for 430 Steel after Hot Rolling, Cold Rolling to 70% RA and Rapid Final Annealing at 900°C .



- $\{100\}\langle 001\rangle$
- $\{100\}\langle 011\rangle$
- ▲ $\{110\}\langle 001\rangle$

FIGURE 100 $\{200\}$ Pole Figure for 430 Steel after Annealing at 1000°C, FC, Cold Rolling to 70%RA and Rapid Final Annealing at 900°C.



- $\{100\}\langle 011\rangle$
- $\{100\}\langle 001\rangle$
- ▲ $\{110\}\langle 001\rangle$

FIGURE 101 $\{222\}$ Pole Figure for 430 Steel after Annealing at 1000°C , FC, Cold Rolling to 70%RA and Rapid Final Annealing at 900°C .

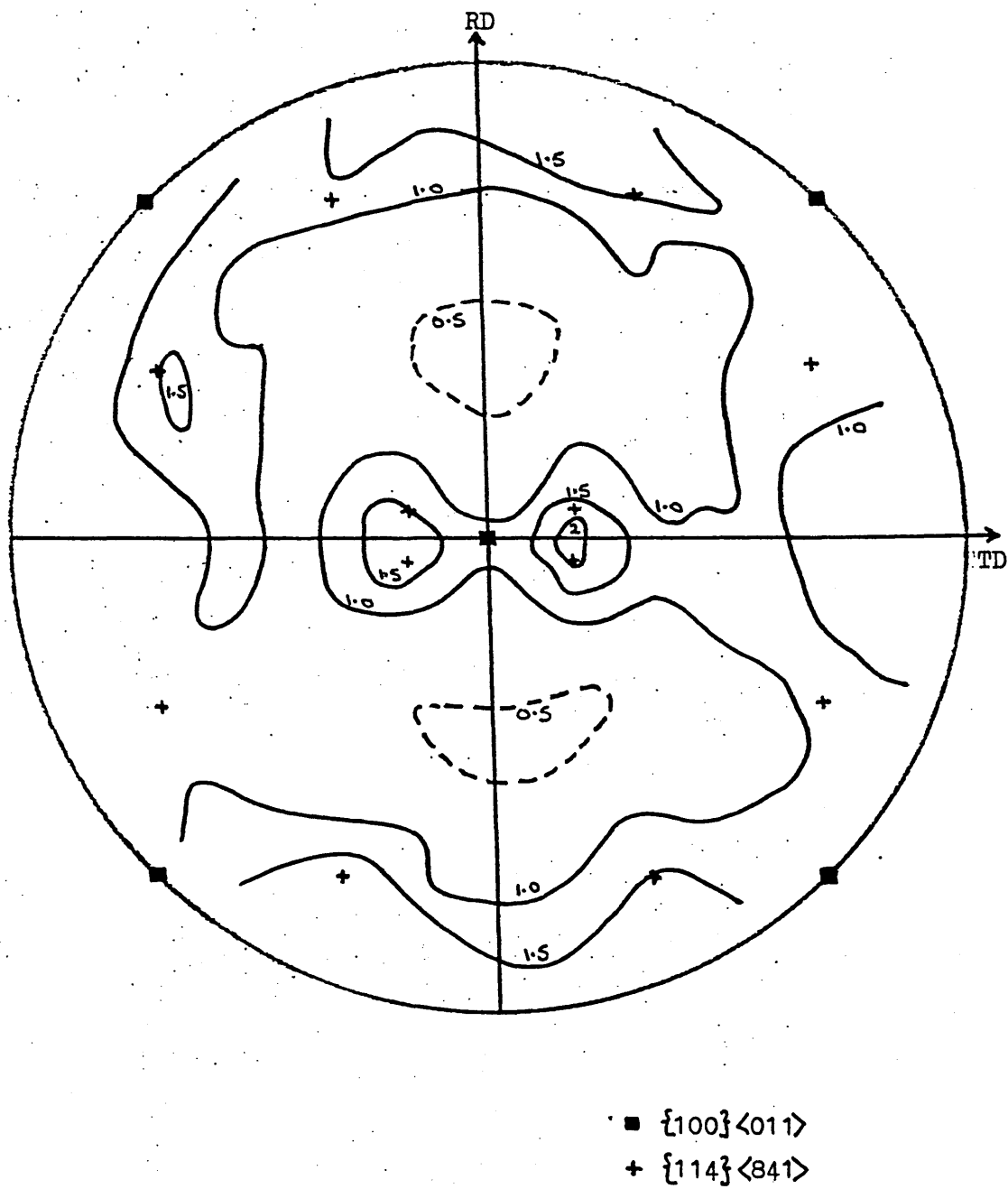
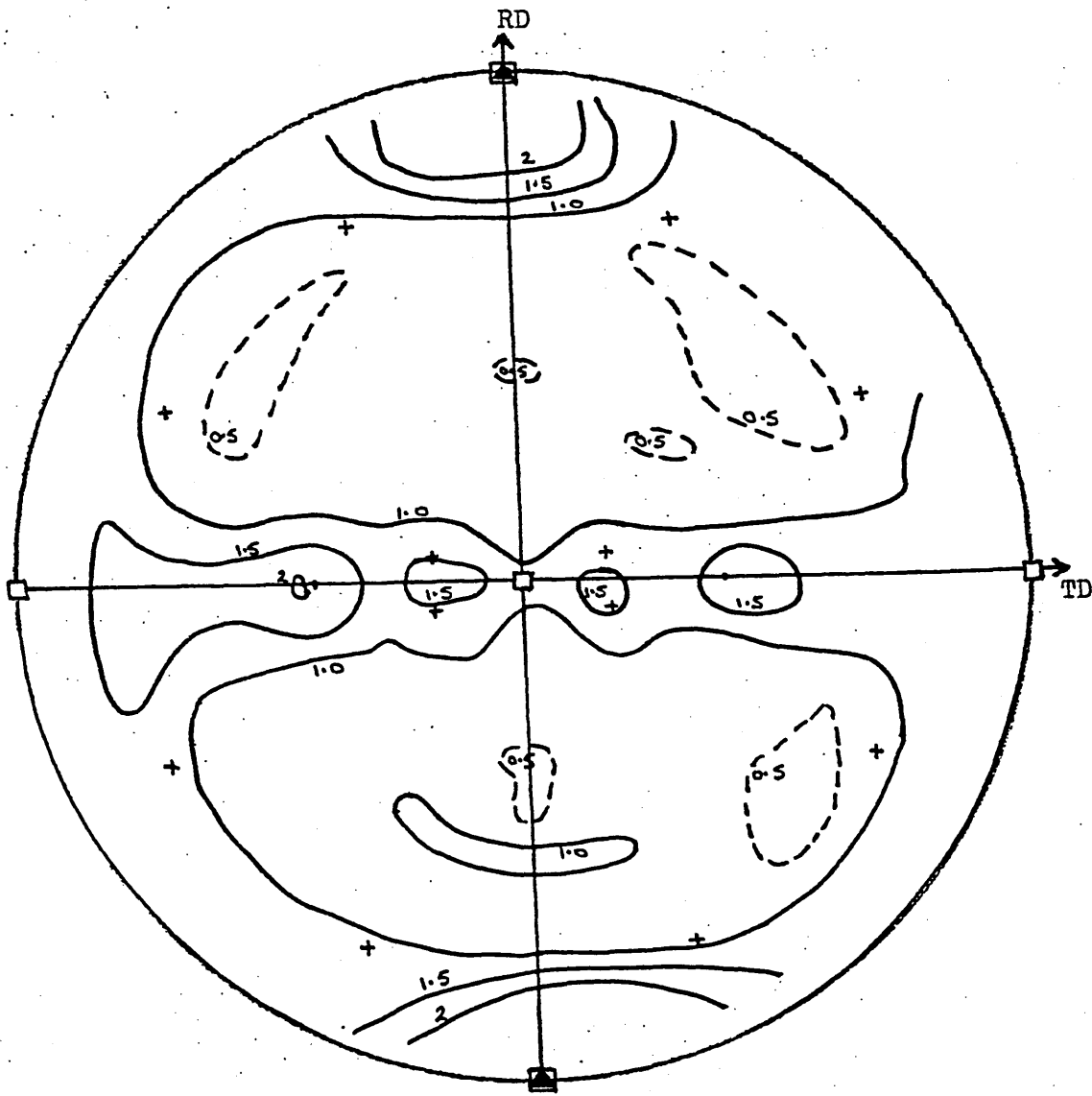
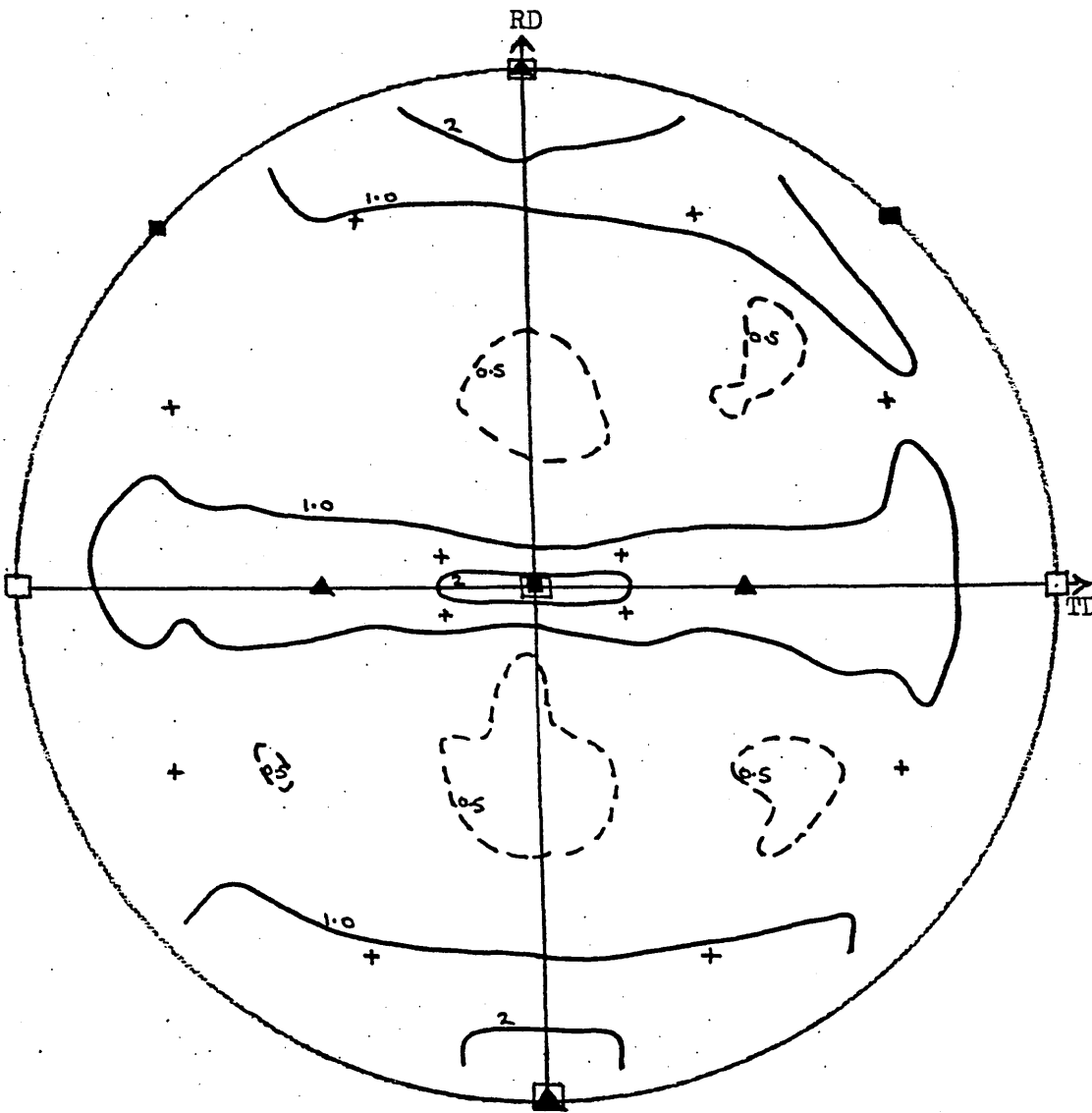


FIGURE 102 $\{200\}$ Pole Figure for 430 Steel after Hot Rolling,
Cold Rolling to 80%RA and Rapid Final Annealing
at 900°C.



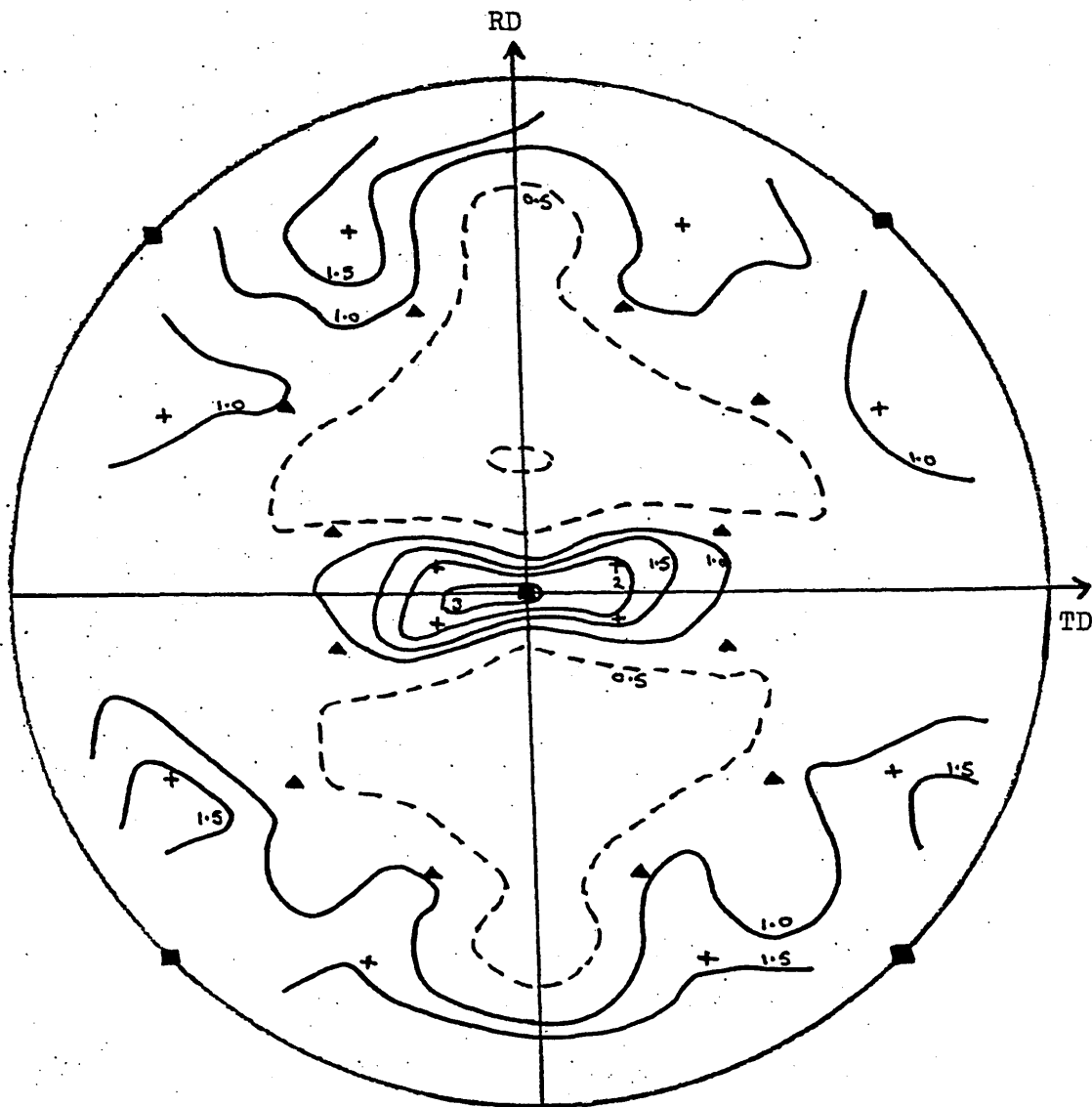
- + $\{114\}\langle 841\rangle$
- ▲ $\{110\}\langle 001\rangle$
- $\{100\}\langle 001\rangle$

FIGURE 103 $\{200\}$ Pole Figure for 430 Steel after Rapid Annealing at 1200°C (+ tempering), Cold Rolling to 80%RA and Rapid Final Annealing at 900°C



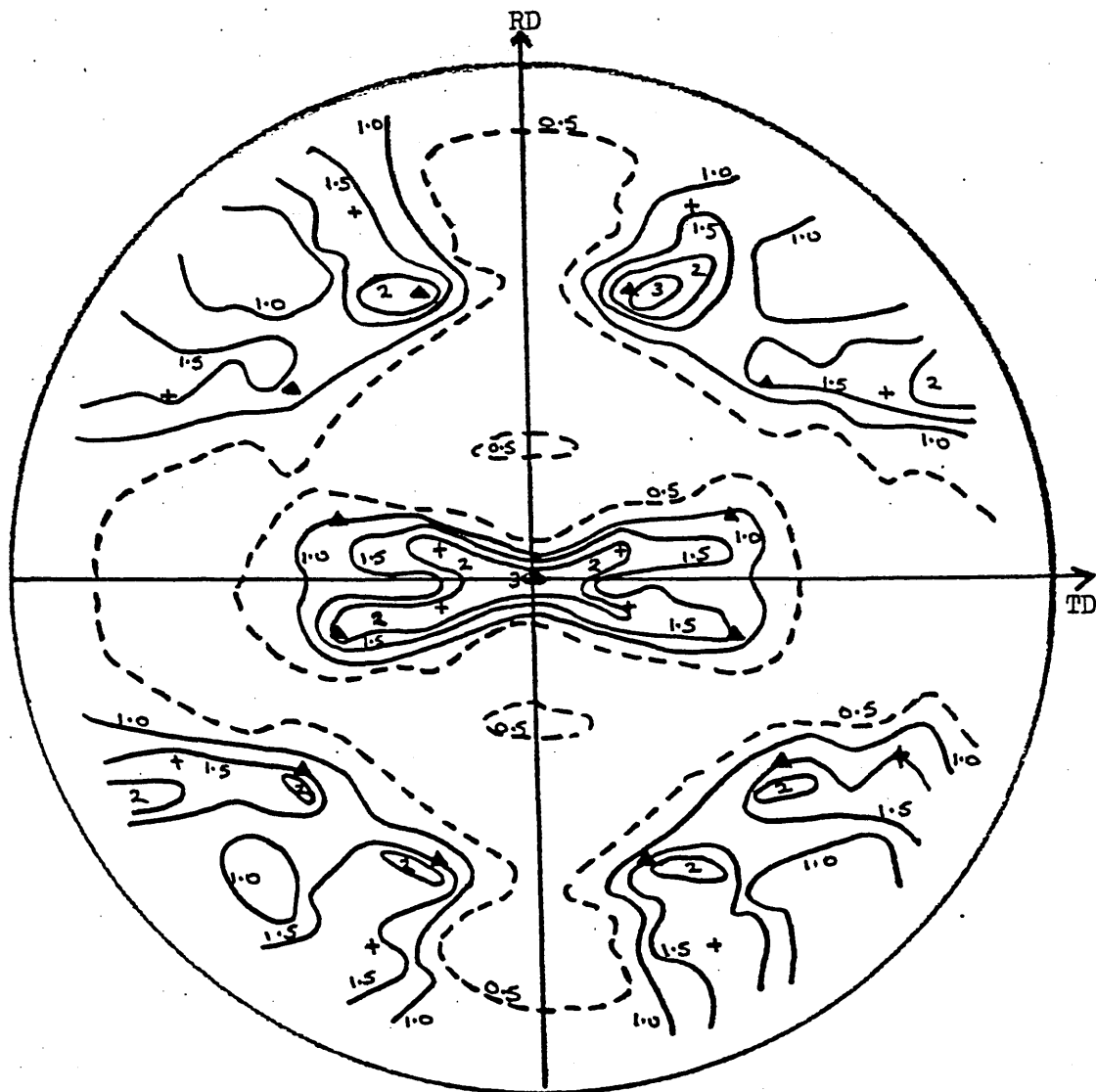
- $\{100\}\langle 001\rangle$
- $\{100\}\langle 011\rangle$
- ▲ $\{110\}\langle 001\rangle$
- + $\{114\}\langle 841\rangle$

FIGURE 104 $\{200\}$ Pole Figure for 430 Steel after Batch
Annealing at 1000°C, Cold Rolling to 80%RA and
Rapid Final Annealing at 900°C.



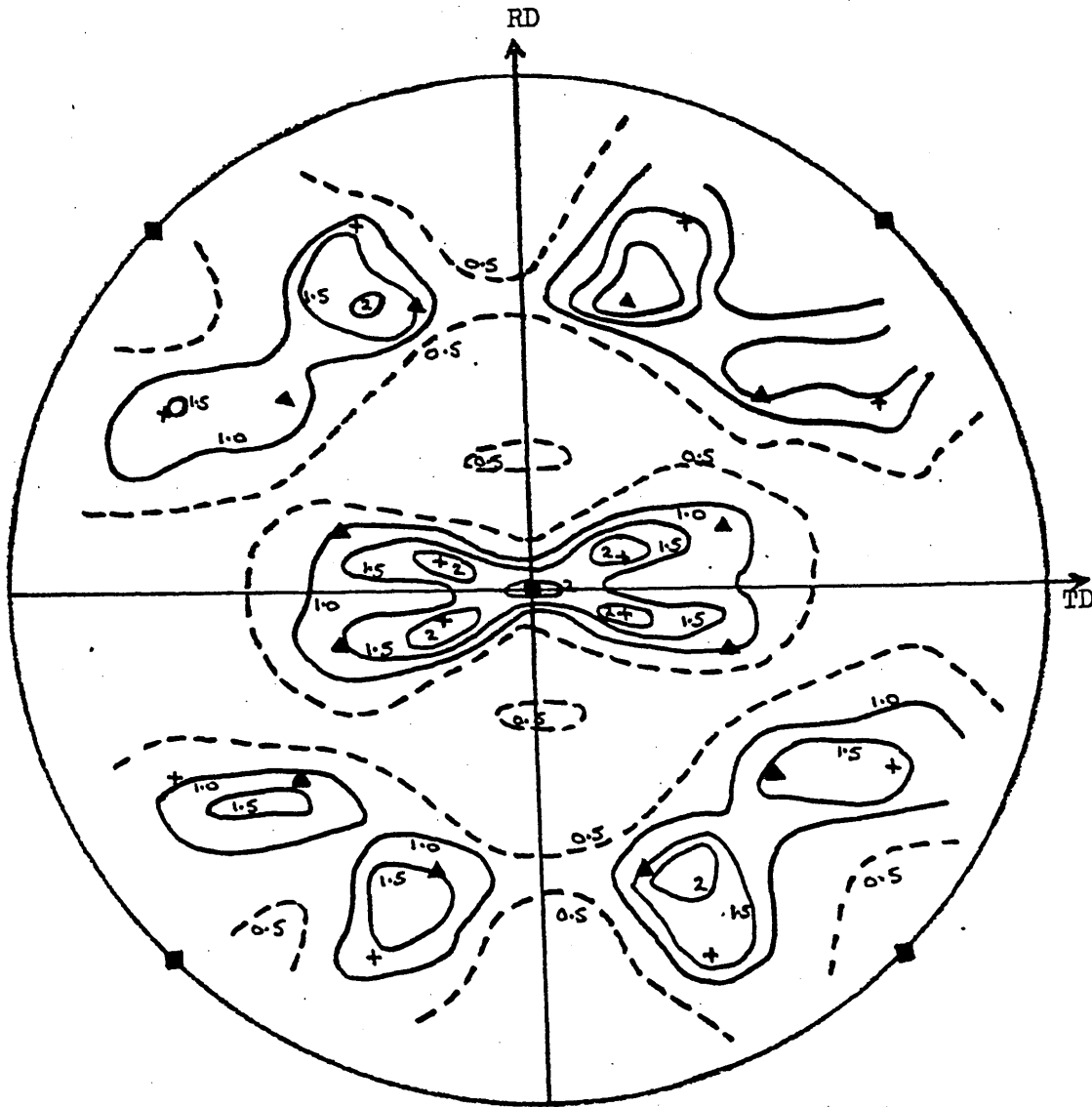
- {100}<011>
- + {114}<841>
- ▲ {223}<962>

FIGURE 105 {200} Pole Figure for 430 Steel after Rapid Annealing at 850°C, Cold Rolling to 90%RA and Rapid Final Annealing at 900°C.



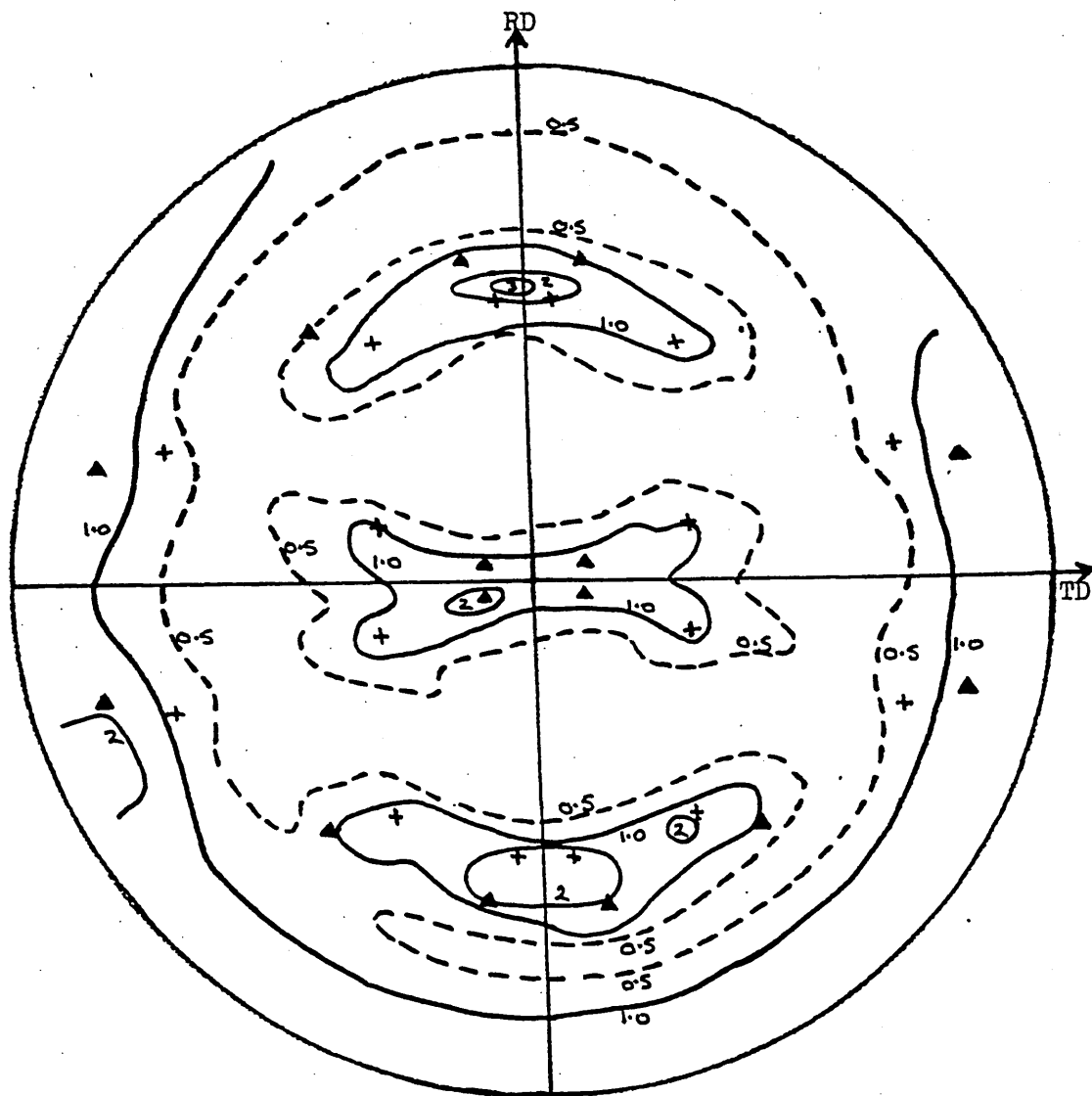
+ {114}<841>
 ▲ {223}<962>

FIGURE 106 {200} Pole Figure for 430 Steel after Hot Rolling,
Cold Rolling to 95%RA and Rapid Final Annealing
at 900°C.



- $\{100\}\langle 011\rangle$
- + $\{114\}\langle 841\rangle$
- ▲ $\{223\}\langle 962\rangle$

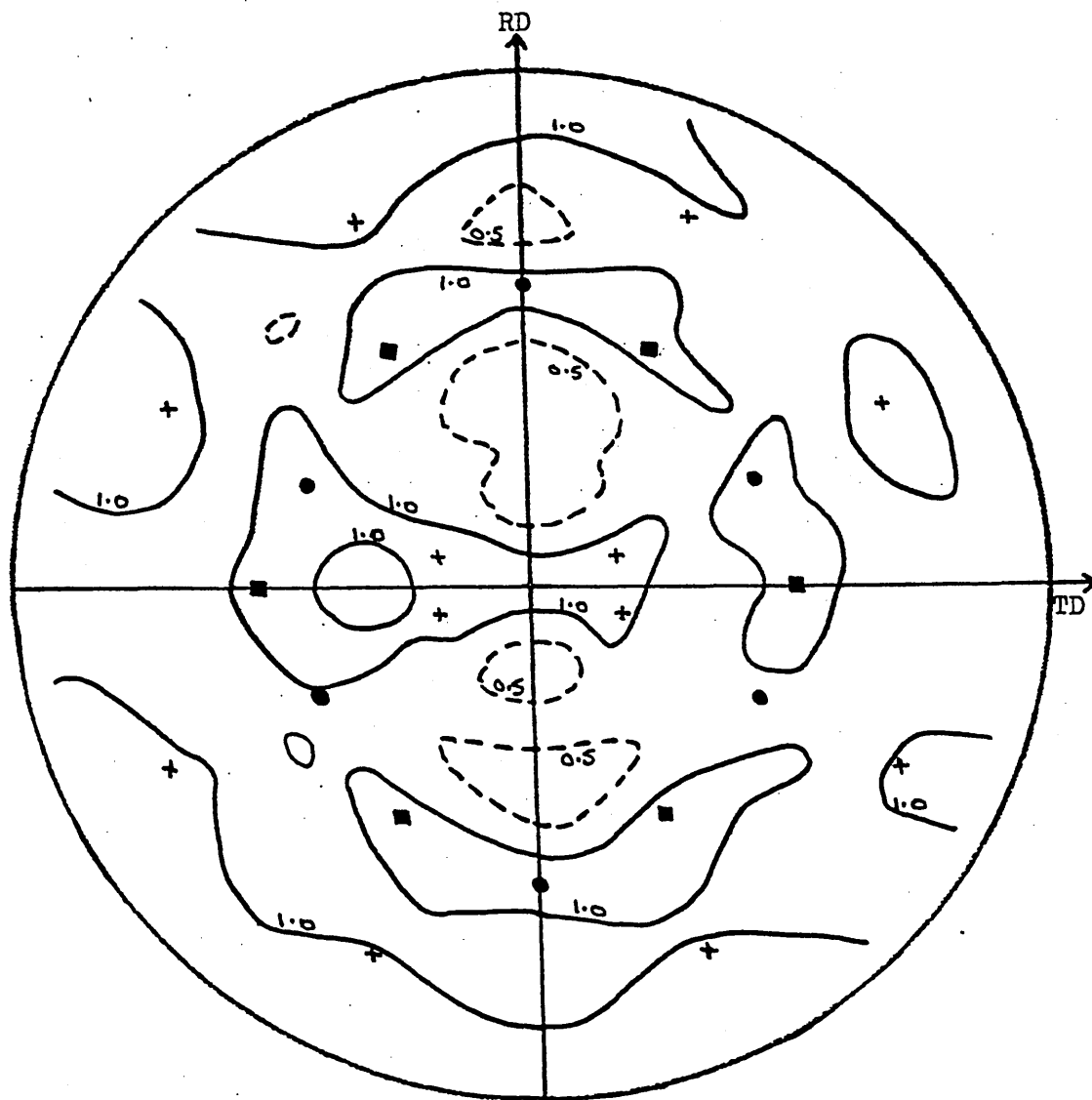
FIGURE 107 $\{200\}$ Pole Figure for 430 Steel after Rapid
Pre-annealing at 850°C, Cold Rolling to 95%RA and
Final Annealing at 1000°C (Heating rate
 $\sim 5000^\circ\text{C hr}^{-1}$, FC)



+ {114}<841>
 ▲ {223}<962>

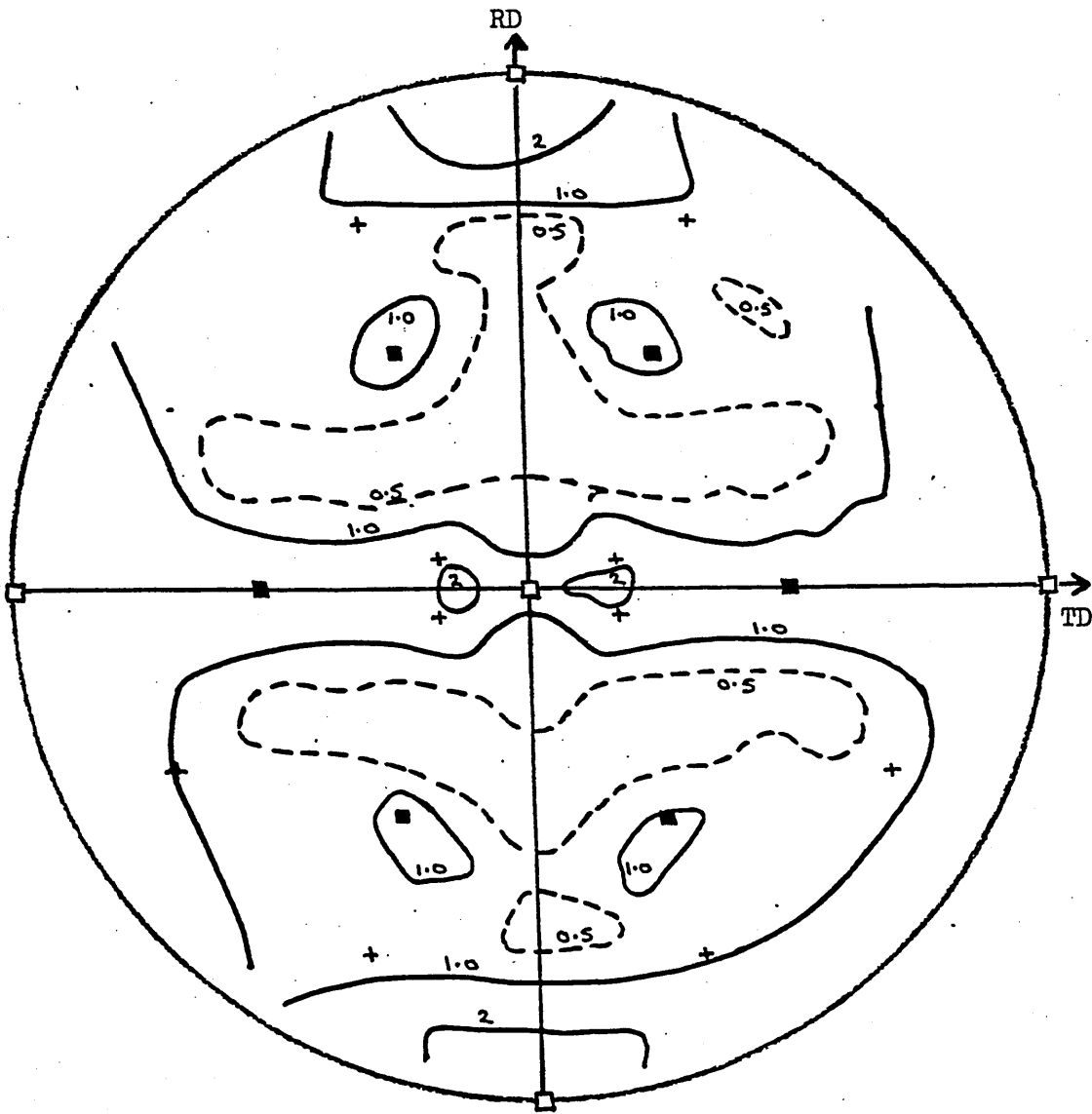
FIGURE 108

{222} Pole Figure for 430 Steel after Rapid Pre-annealing at 850°C, Cold Rolling to 95%RA and Final Annealing at 1000°C (heating rate ~5000°C hr⁻¹, FC).



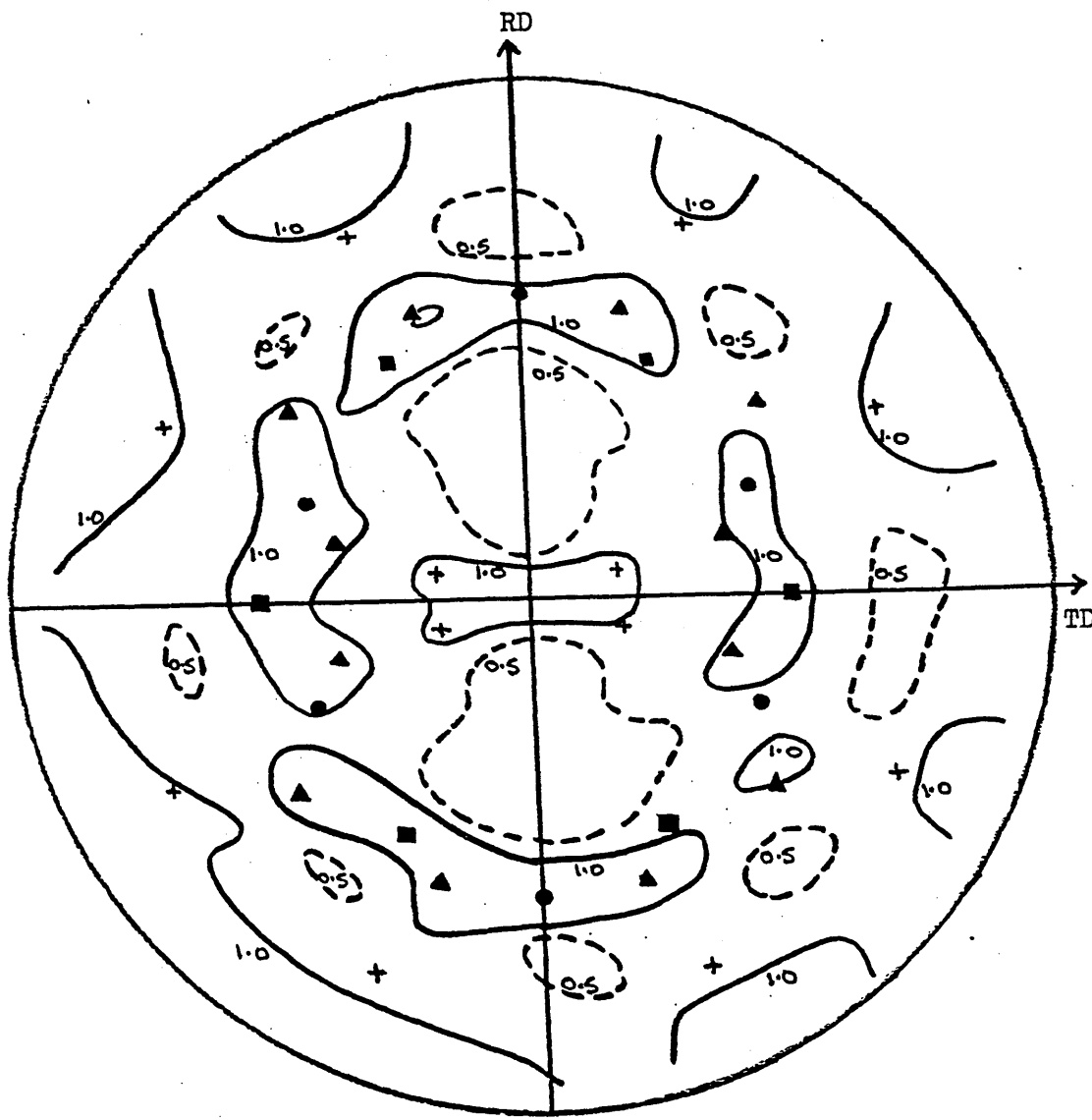
- + {114}<841>
- {554}<225>
- {111}<110>

FIGURE 109 {200} Pole Figure for 430 Steel after Batch
Pre-annealing at 1000°C, Cold Rolling to 90%RA and
Rapid Final Annealing at 900°C.



- {100}<001>
- + {114}<841>
- {111}<110>

FIGURE 110 {200} Pole Figure for 430 Steel after Rapid.
Pre-annealing at 1200°C (+ temper), Cold Rolling
to 90%RA and Rapid Final Annealing at 900°C.



- + {114}<841>
- ▲ {223}<962>
- {554}<225>
- {111}<110>

FIGURE 111 {200} Pole Figure for 430 Steel after Batch
Pre-annealing at 1000°C, Cold Rolling to 95%RA and
Batch Final Annealing at 900°C.

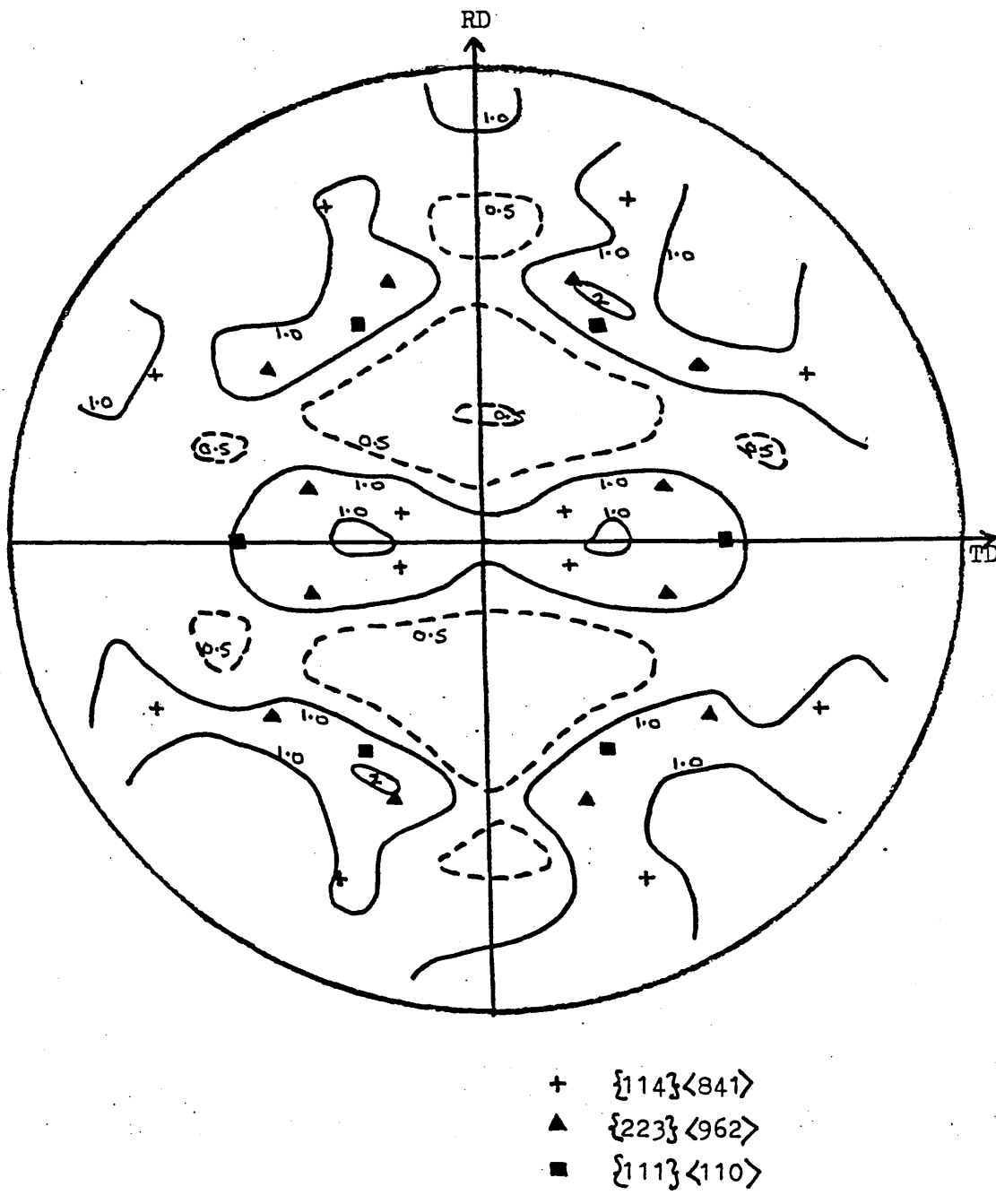
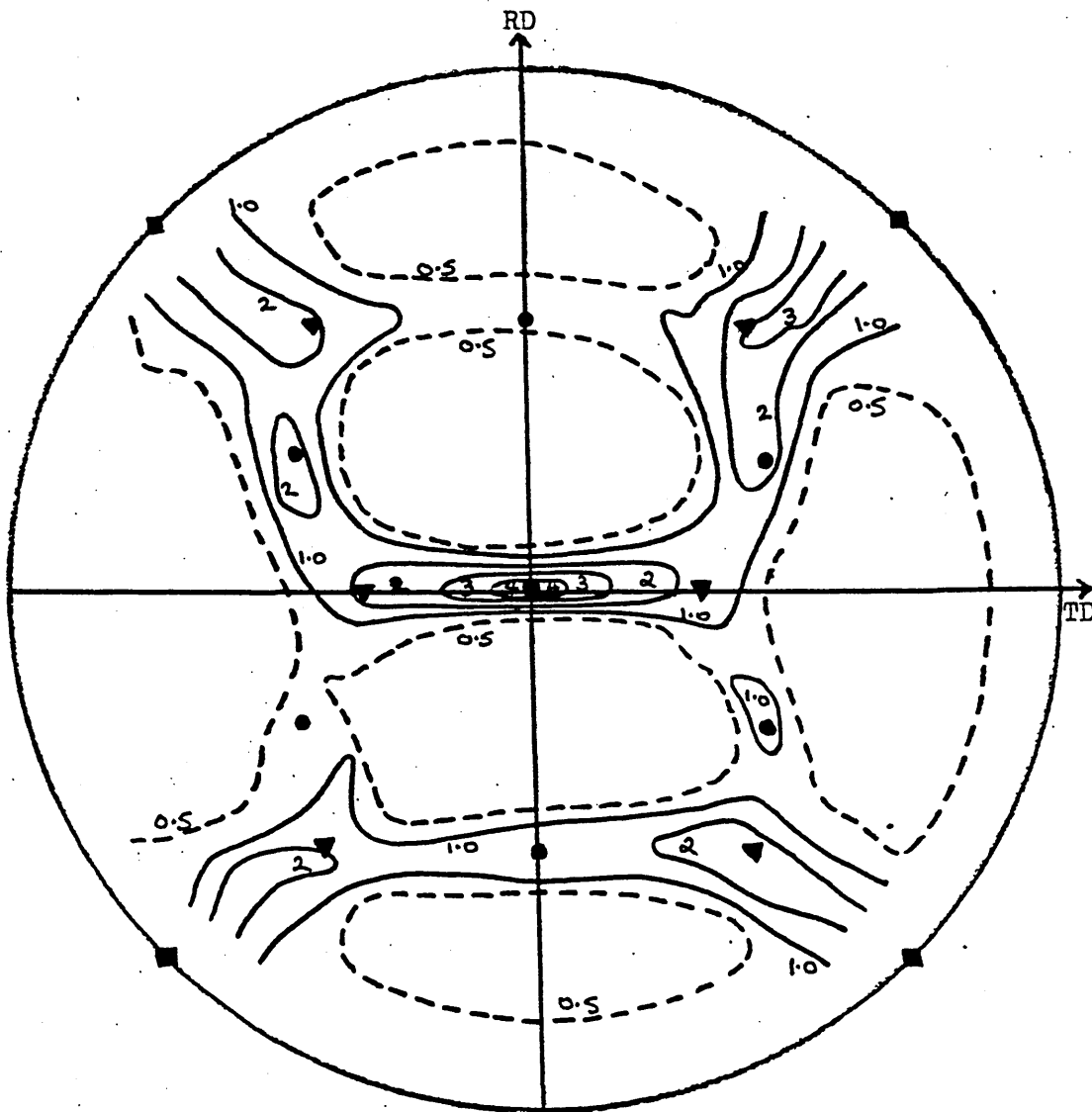
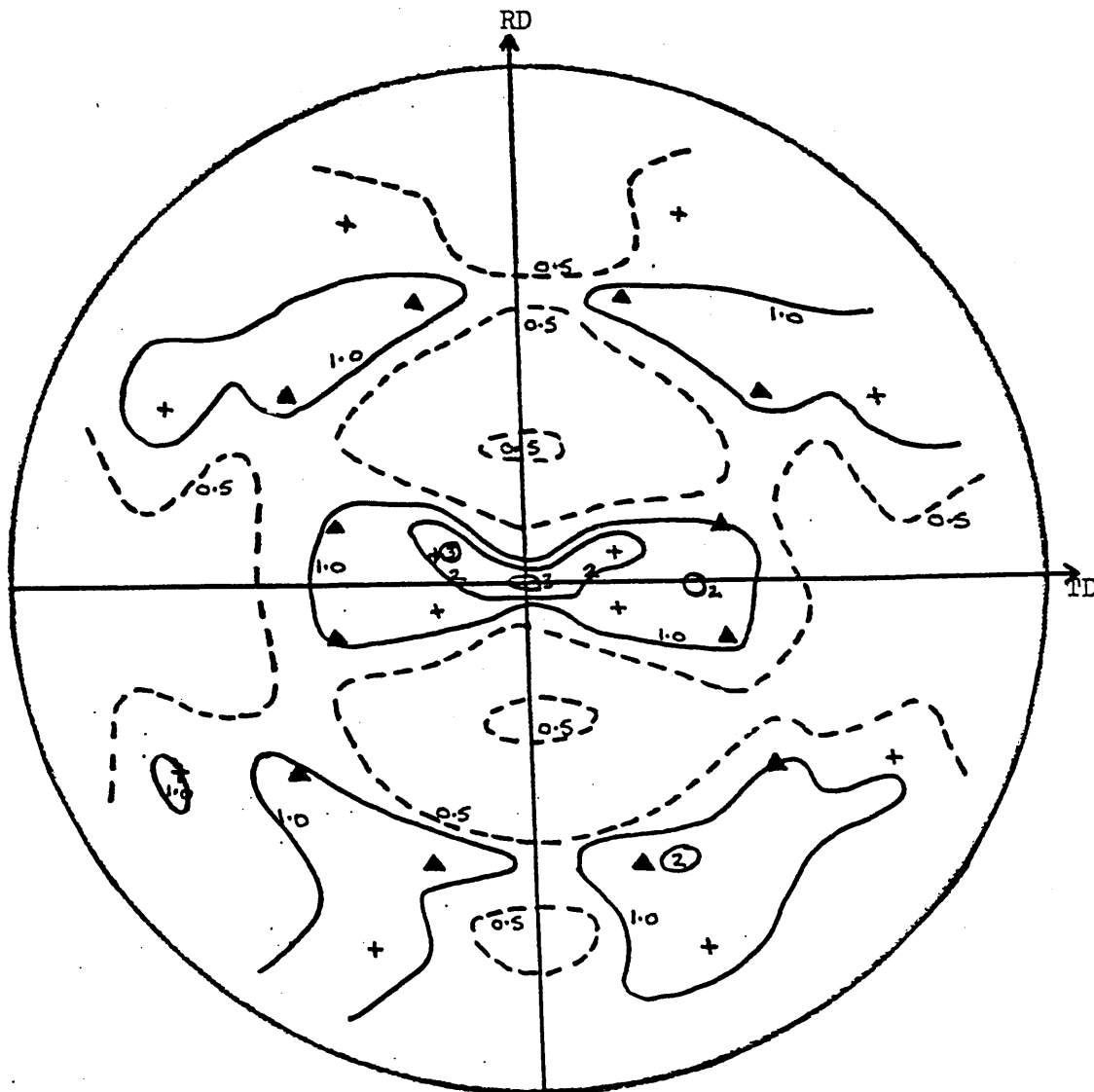


FIGURE 112 {200} Pole Figure for 430 Steel after Rapid Pre-annealing at 1200°C (+ tempering), Cold Rolling to 95%RA and Rapid Final Annealing at 900°C.



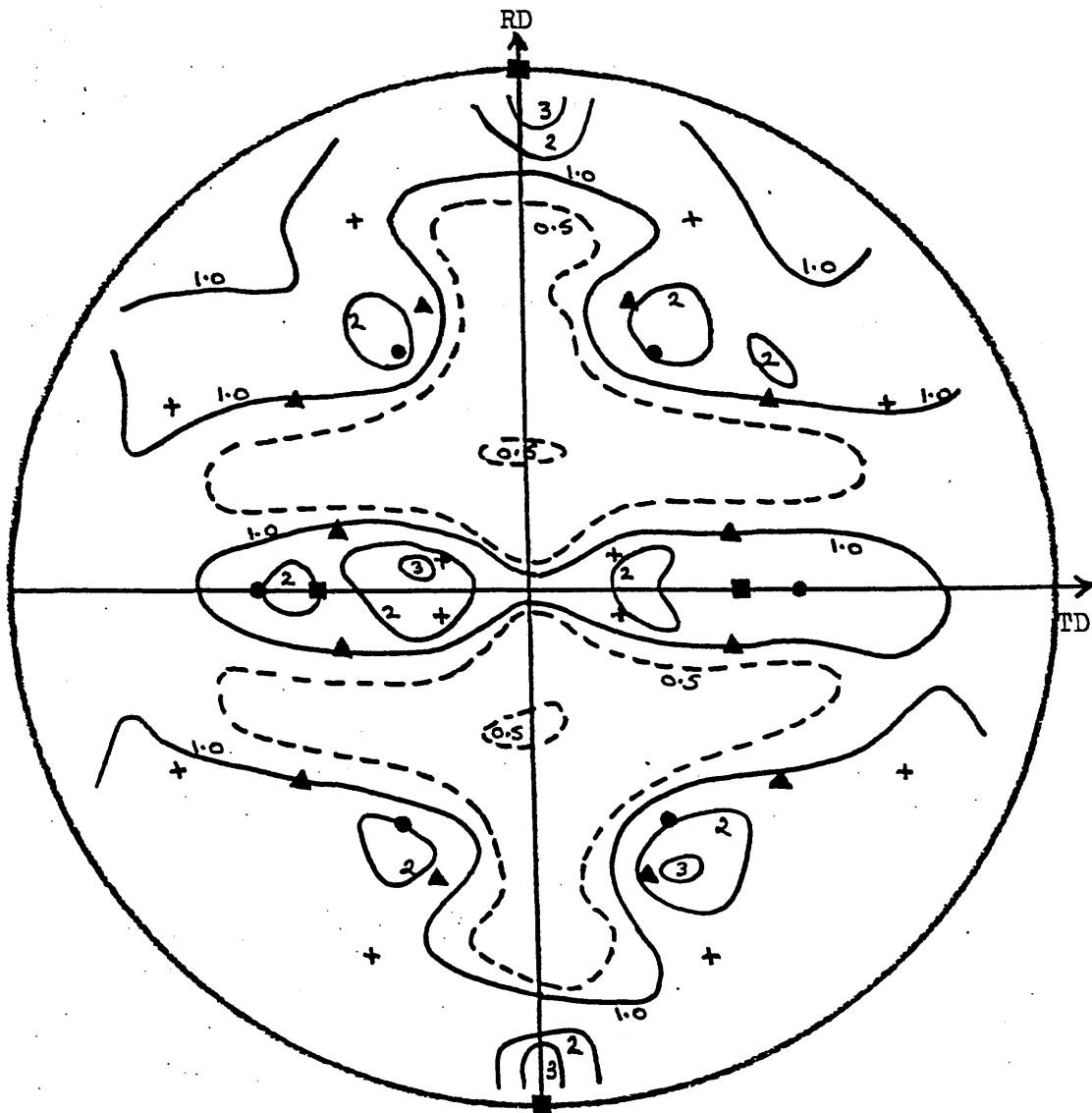
- $\{100\}\langle 011\rangle$
- $\{111\}\langle 112\rangle$
- ▼ $\{112\}\langle 110\rangle$

FIGURE 113 $\{200\}$ Pole Figure for 430 Steel after Hot Rolling,
Cold Rolling to 95%RA and Rapid Final Annealing
at 700°C.



+ {114}<841>
 ▲ {223}<962>

FIGURE 114 {200} Pole Figure for 430 Steel after Hot Rolling,
Cold Rolling to 95%RA and Rapid Final Annealing
at 800°C.



- $\{110\} \langle 001 \rangle$
- + $\{114\} \langle 841 \rangle$
- $\{111\} \langle 110 \rangle$
- ▲ $\{223\} \langle 962 \rangle$

FIGURE 115

$\{200\}$ Pole Figure for 430 Steel after Rapid
Pre-annealing at 850°C , Cold Rolling to 90%RA and
Batch Final Annealing at 900°C .

- ——— Rapid final anneal at 900°C (Heating rate $\sim 5000^\circ\text{C hr}^{-1}$, AC)
- - - - Batch final anneal at 900°C (Heating rate = 50°C hr^{-1} , FC)

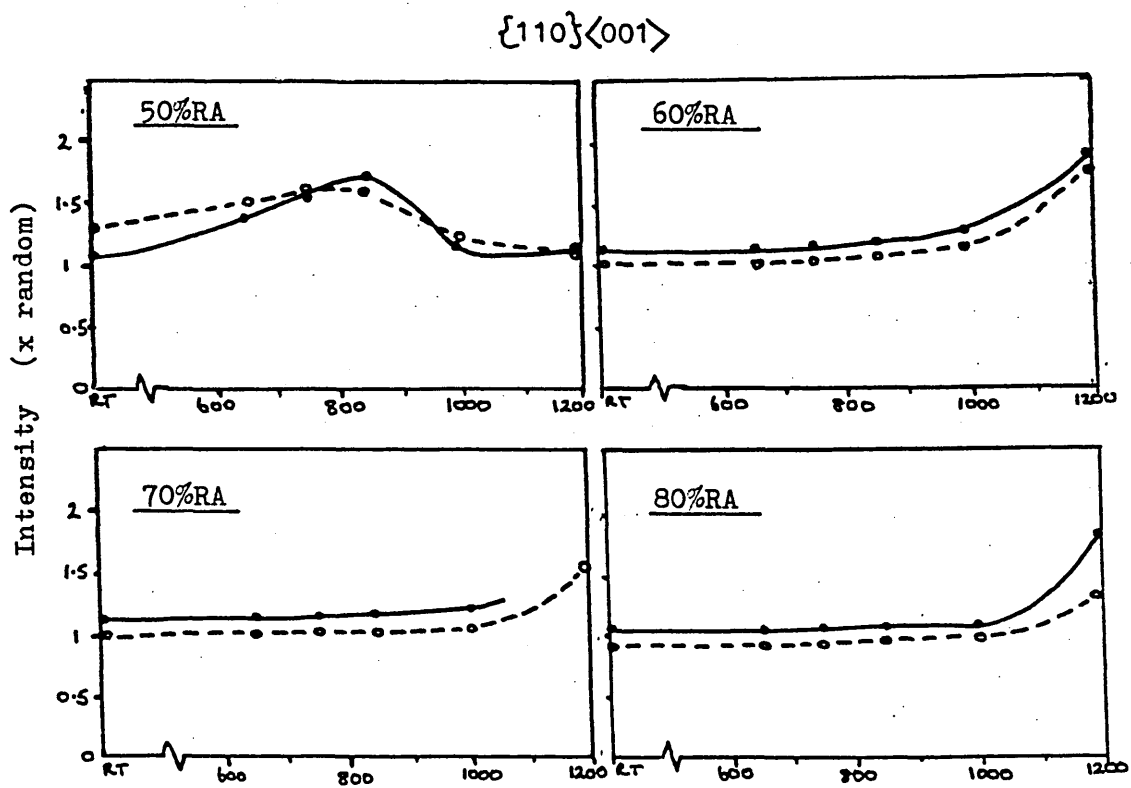
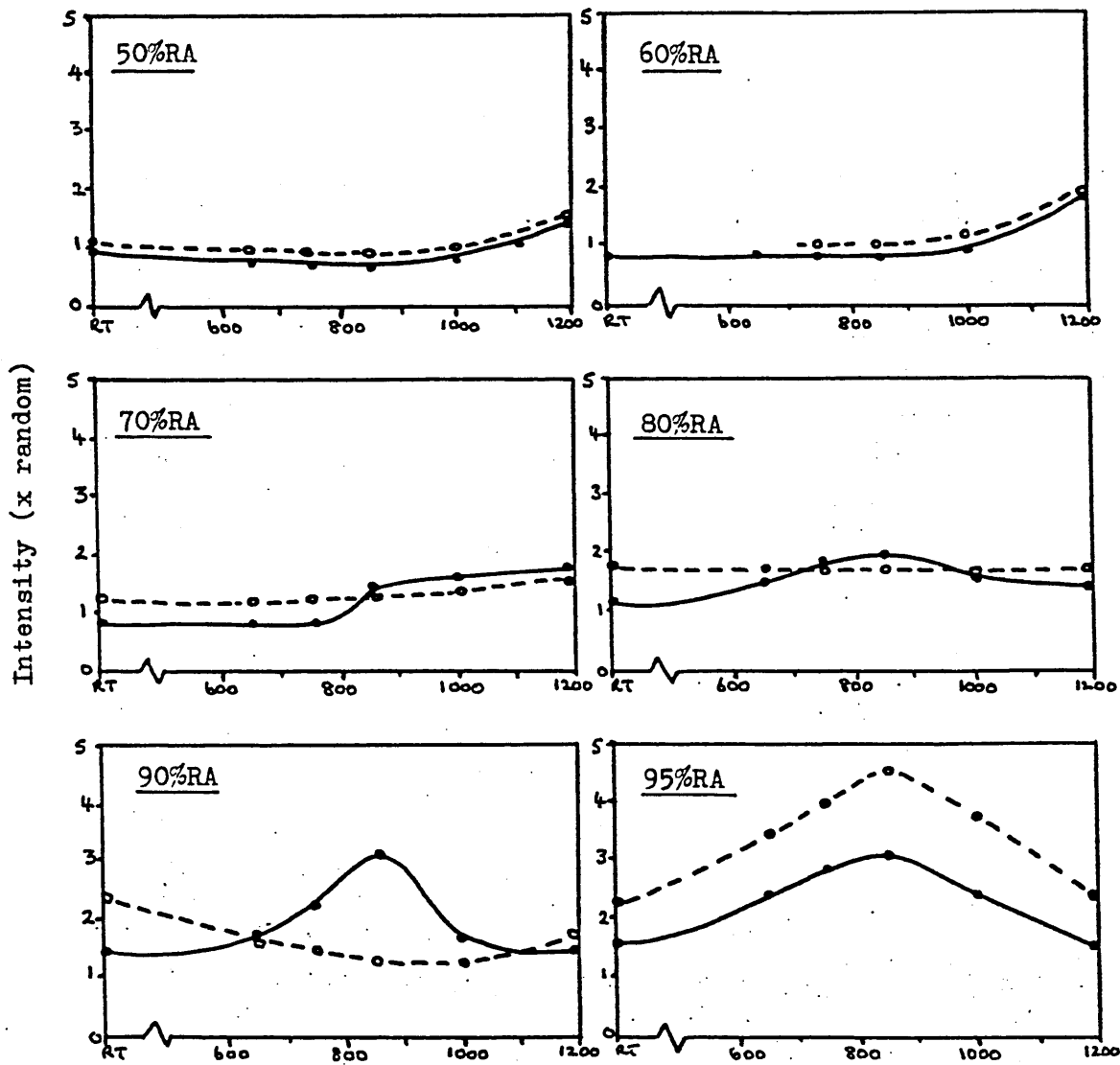


FIGURE 116 Variation of Intensity of the $\{110\}\langle 001 \rangle$ Orientation in Cold Rolled and Annealed 430 Steel with Pre-annealing Temperature.

● ——— Rapid final anneal at 900°C (Heating rate ~5000°C hr⁻¹, AC)

○ - - - - Batch final anneal at 900°C (Heating rate = 50°C hr⁻¹, FC)

$\{100\}\langle uvw \rangle$

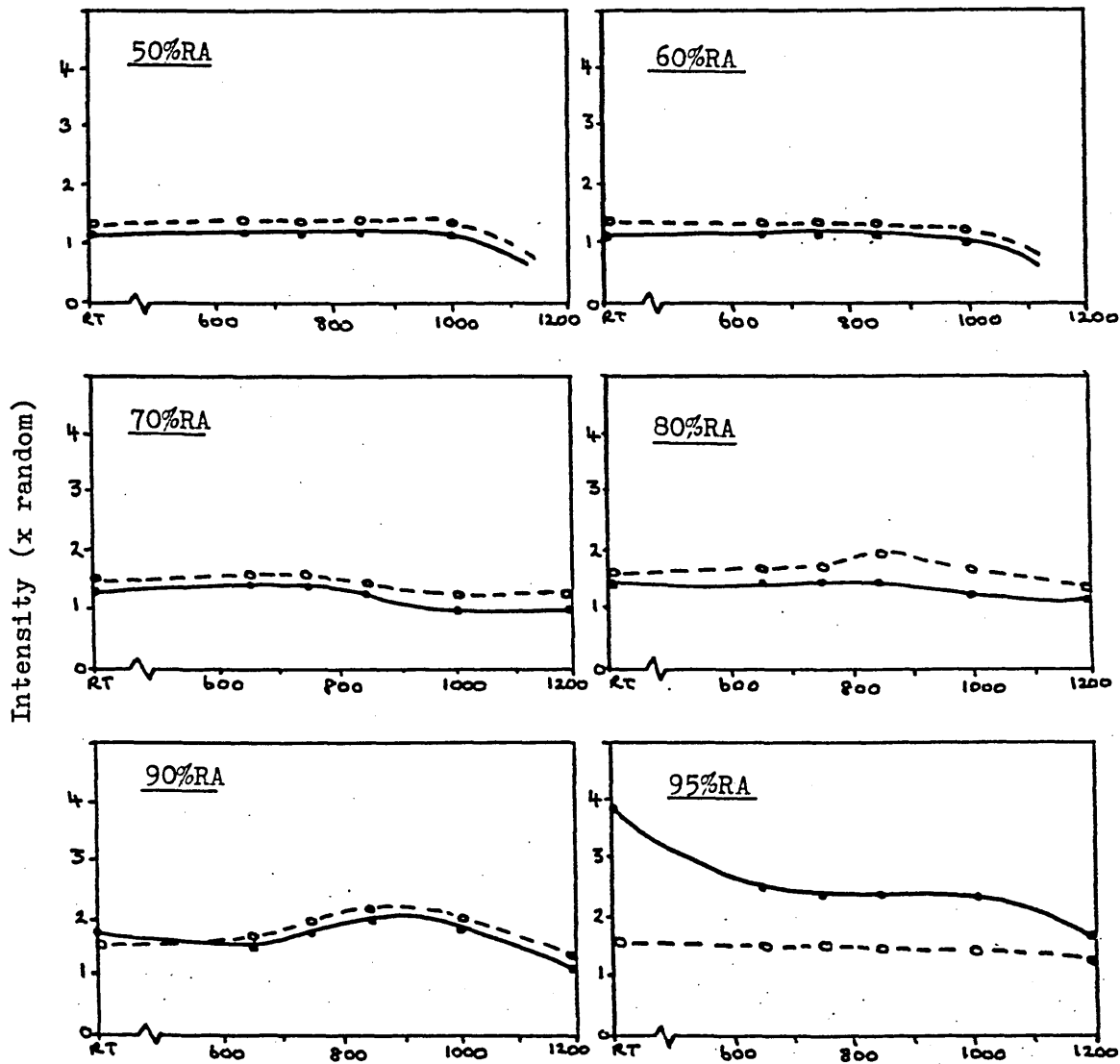


Temperature of annealing prior to cold rolling (Rapid pre-anneal; heating rate ~5000°C hr⁻¹, AC)

FIGURE 117 Variation of Intensity of the $\{100\}\langle uvw \rangle$ Orientation in Cold Rolled and Annealed 430 Steel with Pre-annealing Temperature.

- ——— Rapid final anneal at 900°C (Heating rate ~ 5000°C hr⁻¹, AC)
- - - - - Batch final anneal at 900°C (Heating rate = 50°C hr⁻¹, FC)

{114}<841>



Temperature of annealing prior to cold rolling (°C)
 (Rapid pre-annealing; heating rate ~ 5000°C hr⁻¹, AC)

FIGURE 118 Variation of Intensity of the {114}<841> Orientation
in Cold Rolled and Annealed 430 Steel with
Pre-annealing Temperature

- ——— Rapid final anneal at 900°C (Heating rate ~5000°C hr.⁻¹, AC)
- - - - - Batch final anneal at 900°C, (Heating rate = 50°C hr.⁻¹, FC)

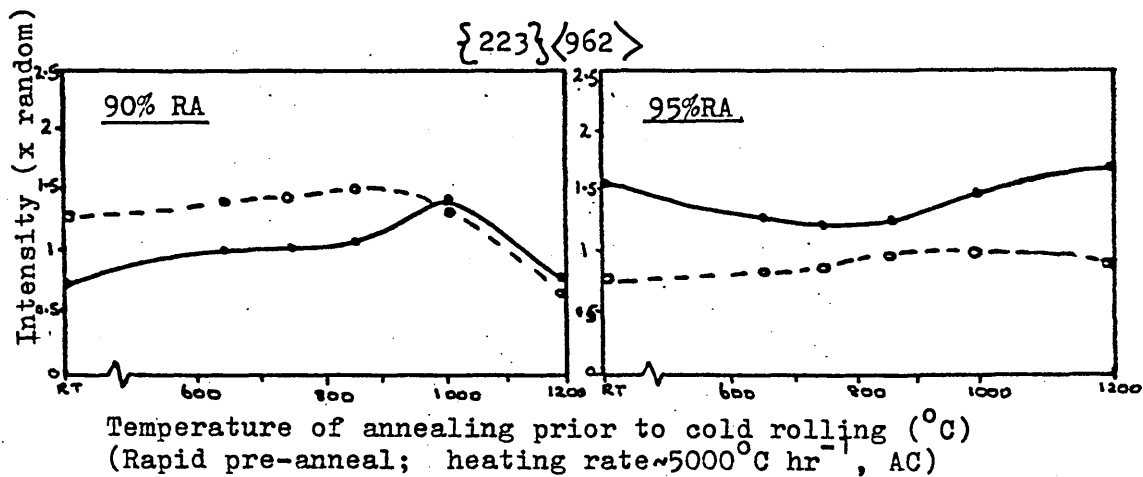


FIGURE 119 Variation of Intensity of the $\{223\}\langle 962 \rangle$ Orientation in Cold Rolled and Annealed 430 Steel with Pre-annealing Temperature

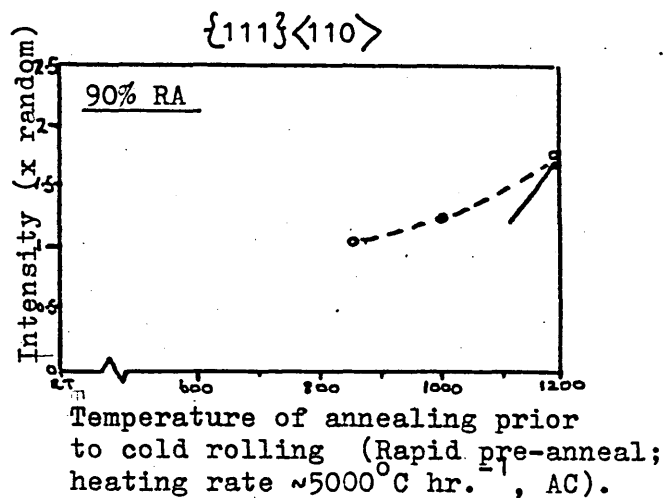
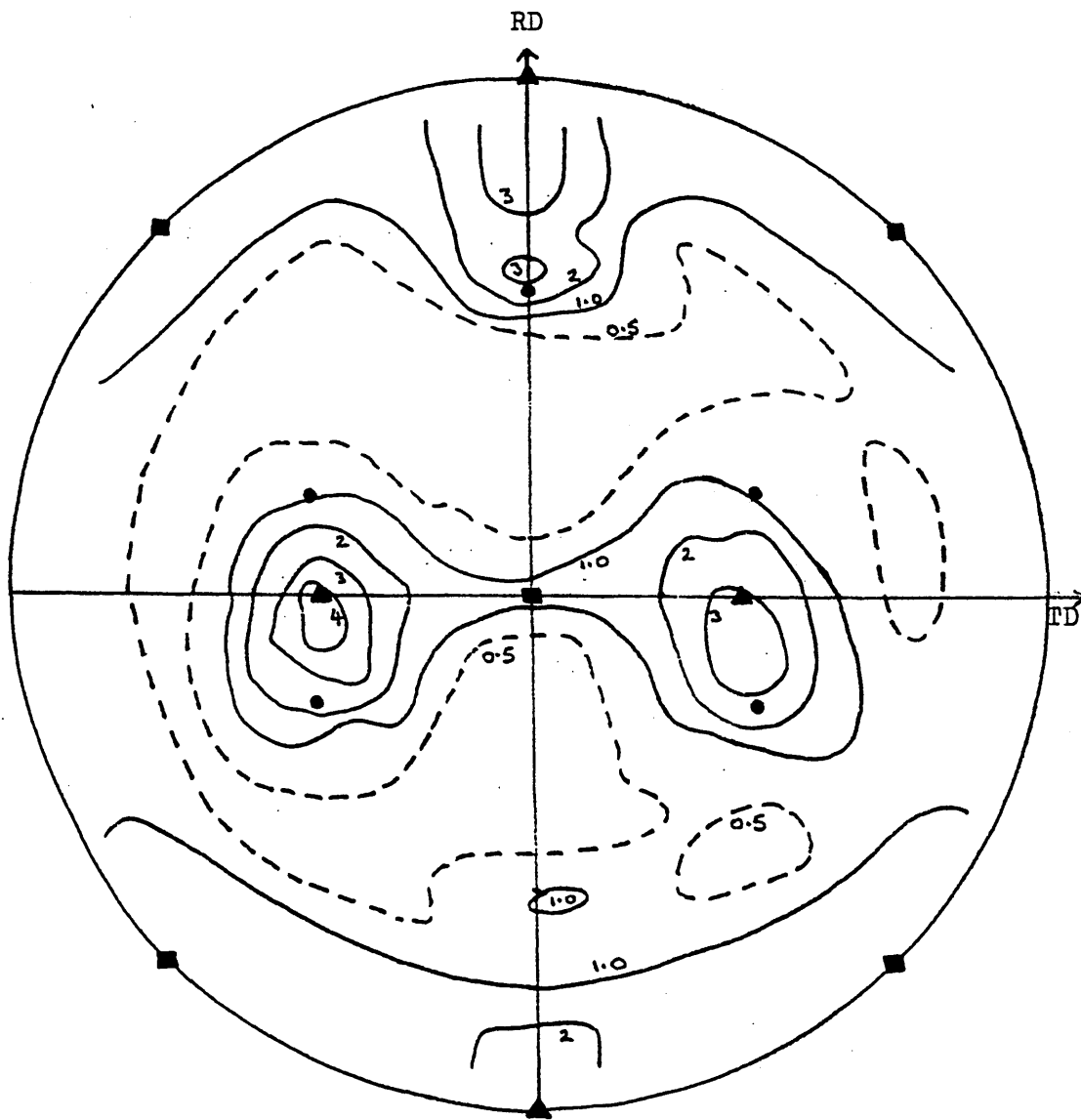


FIGURE 120 Variation in Intensity of the $\{111\}\langle 110 \rangle$ Orientation in Cold Rolled and Annealed 430 Steel with Pre-annealing Temperature



- $\{100\}\langle 011\rangle$
- $\{554\}\langle 225\rangle$
- ▲ $\{110\}\langle 001\rangle$

FIGURE 121 $\{200\}$ Pole Figure for 430Ti (0.5Ti) Steel after Hot Rolling, Cold Rolling to 60% RA and Rapid Final Annealing at 900°C.

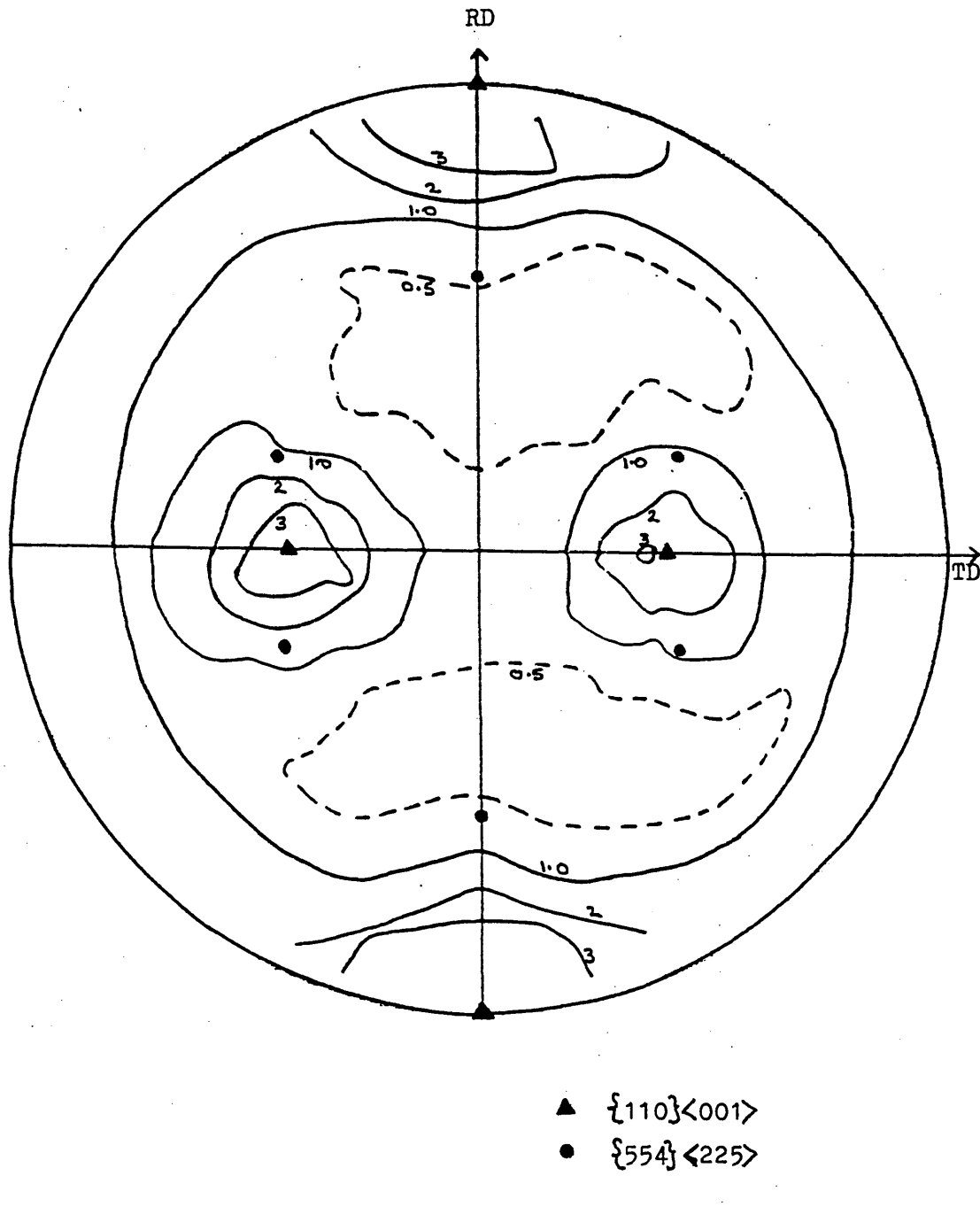
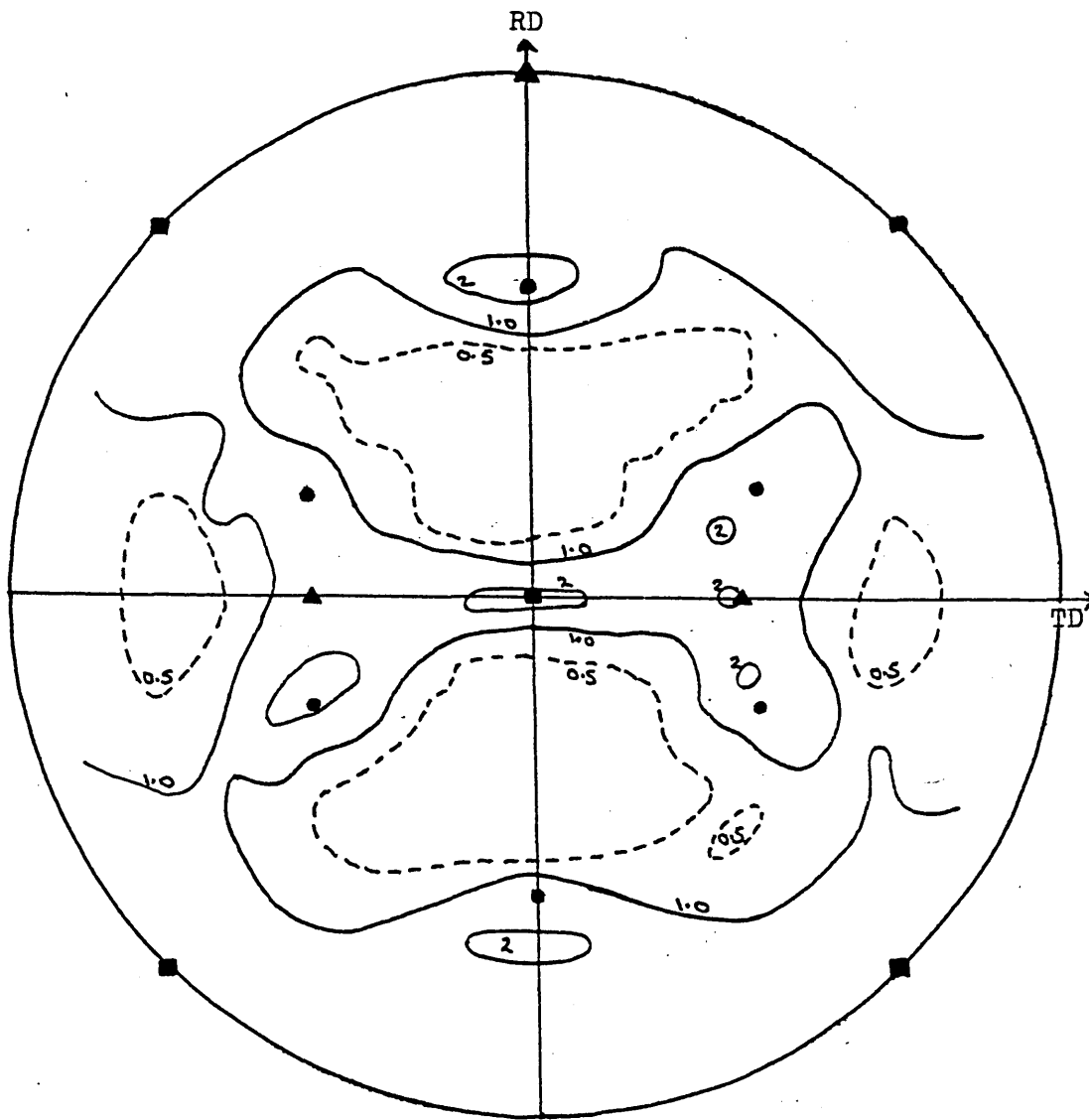
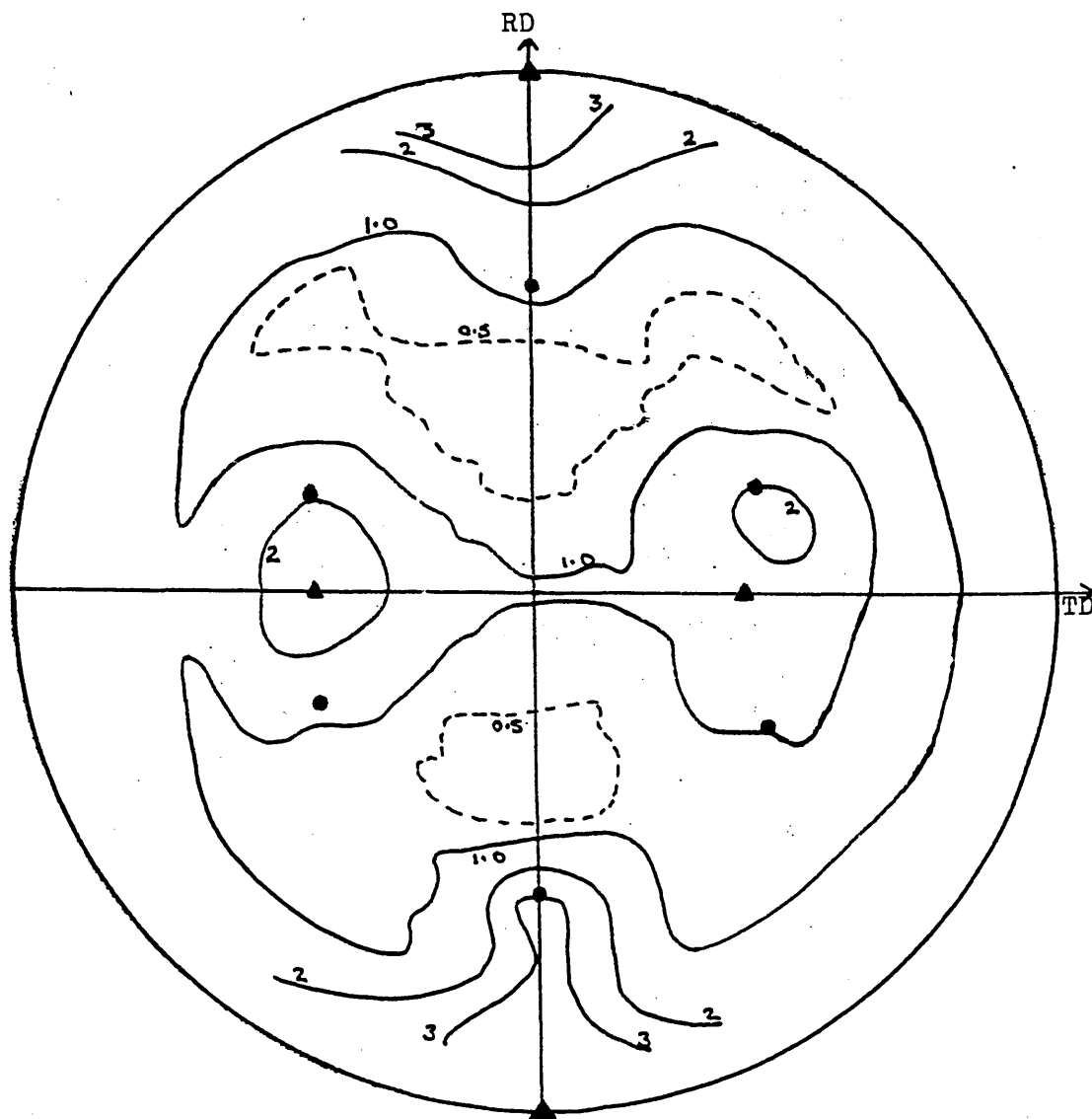


FIGURE 122 $\{200\}$ Pole Figure for 430Ti (0.5Ti) Steel after
Batch Annealing at 850°C, Cold Rolling to 60% RA
and Rapid Final Annealing at 900°C



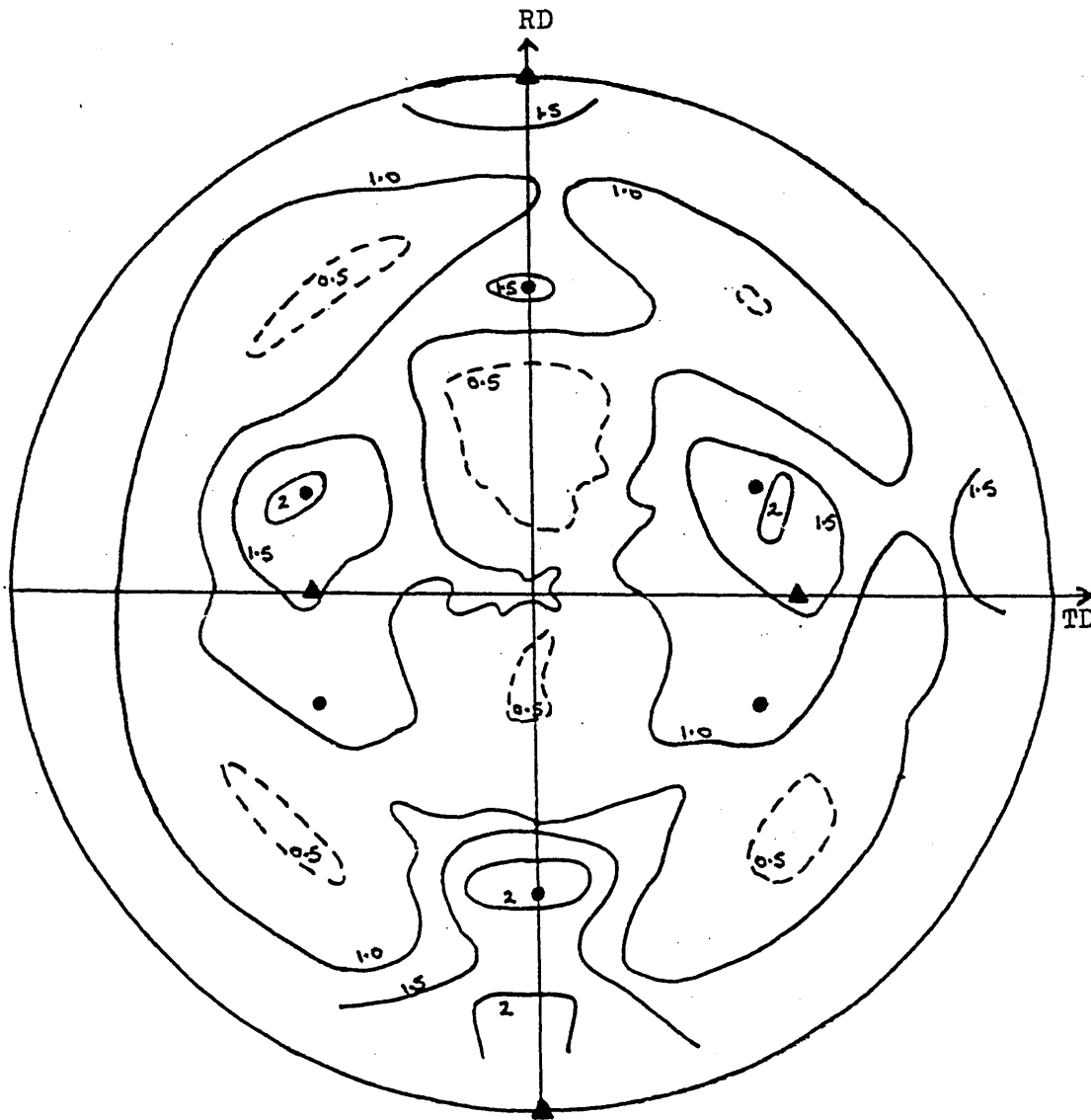
- $\{100\}\langle 011\rangle$
- $\{554\}\langle 225\rangle$
- ▲ $\{110\}\langle 001\rangle$

FIGURE 123 $\{200\}$ Pole Figure for 430Ti (0.5Ti) Steel after Hot Rolling, Cold Rolling to 70% RA and Rapid Annealing at 900°C



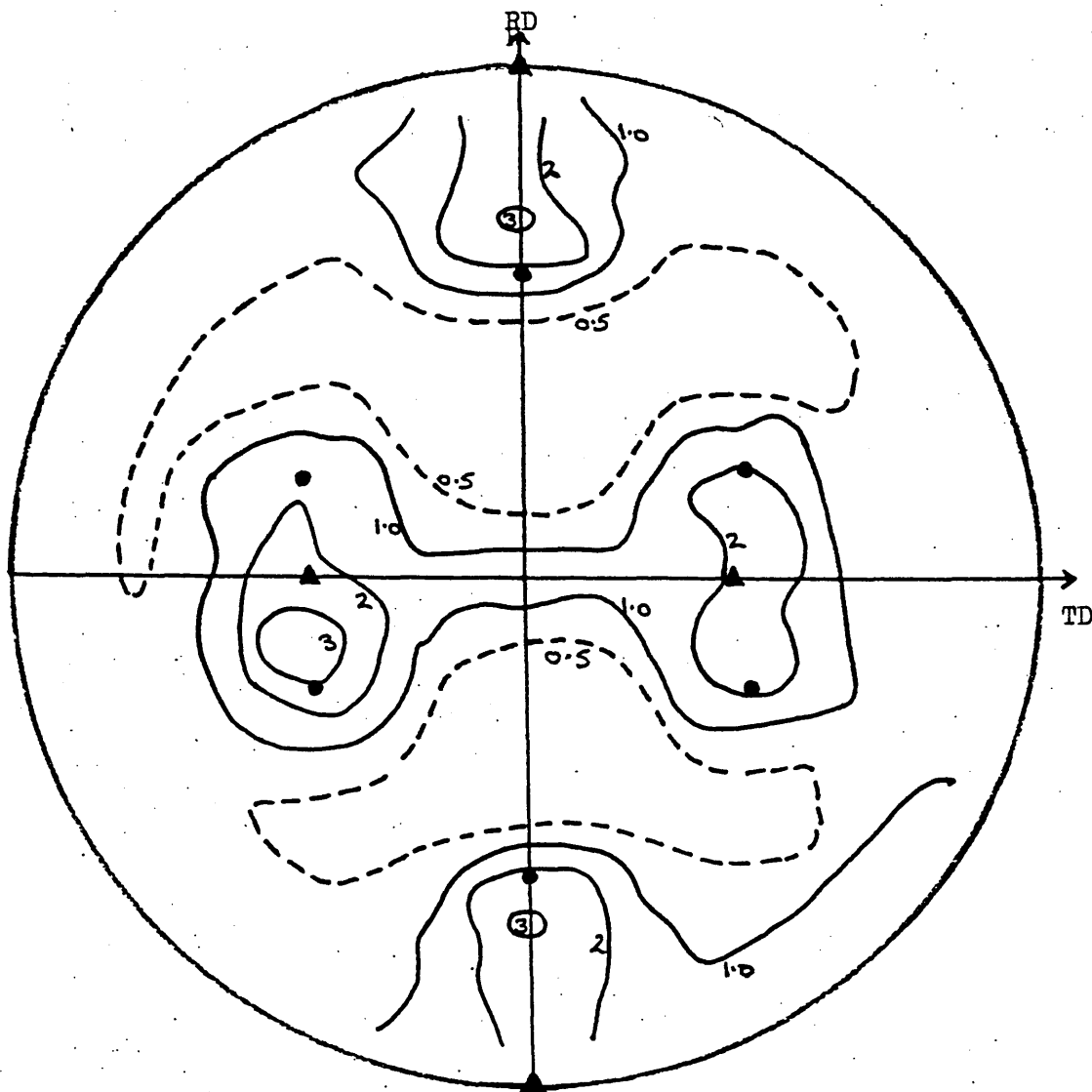
- ▲ $\{110\}\langle 001\rangle$
- $\{554\}\langle 225\rangle$

FIGURE 124 $\{200\}$ Pole Figure for 430Ti (0.5Ti) Steel after Rapid Pre-annealing at 850°C, Cold Rolling to 70% RA and Rapid Annealing at 900°C.



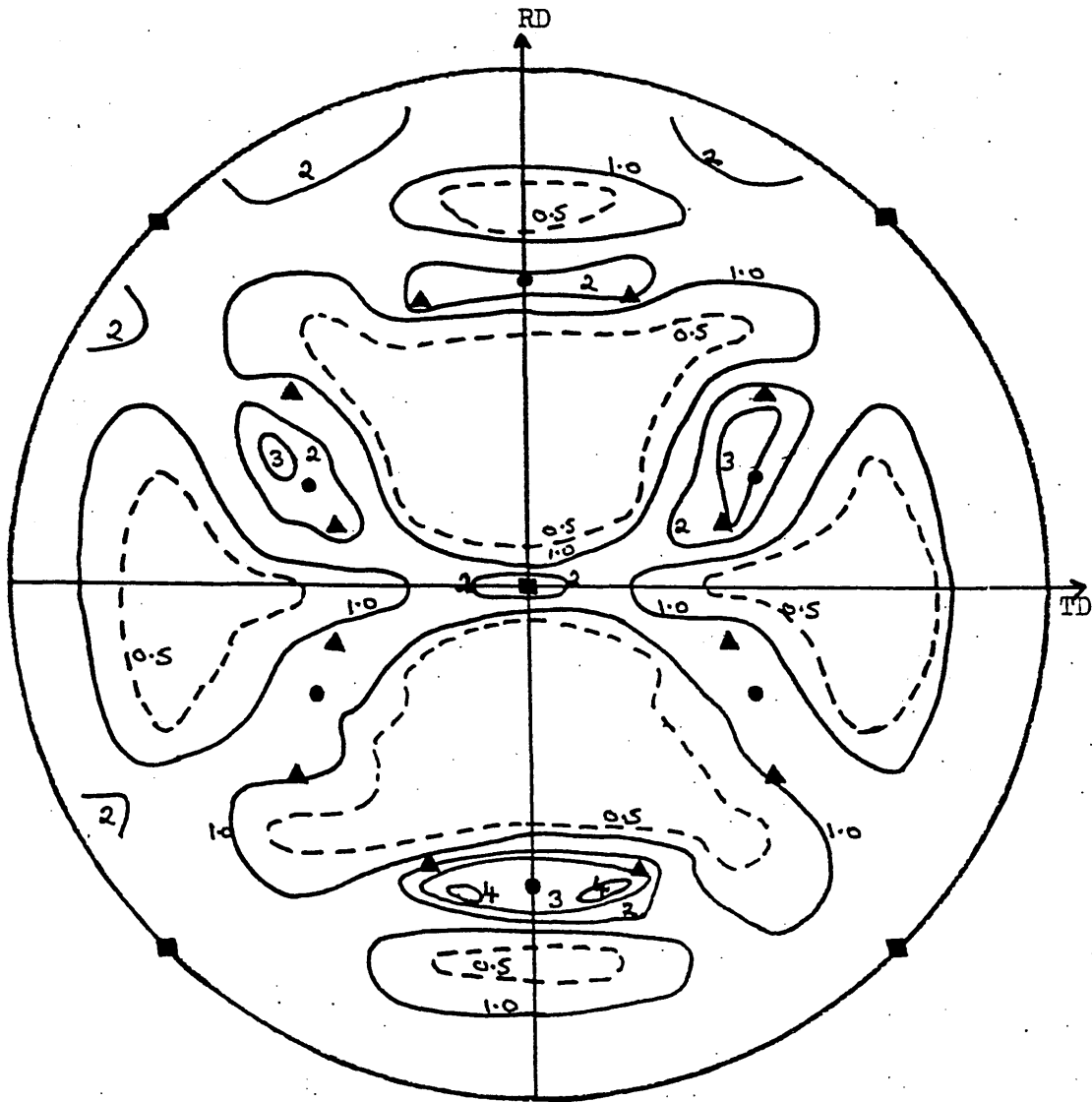
- ▲ $\{110\} \langle 001 \rangle$
- $\{554\} \langle 225 \rangle$

FIGURE 125 $\{200\}$ Pole Figure for 430Ti (0.5Ti) Steel after Rapid Pre-annealing at 1000°C, Cold Rolling to 70% RA and Rapid Annealing at 900°C.



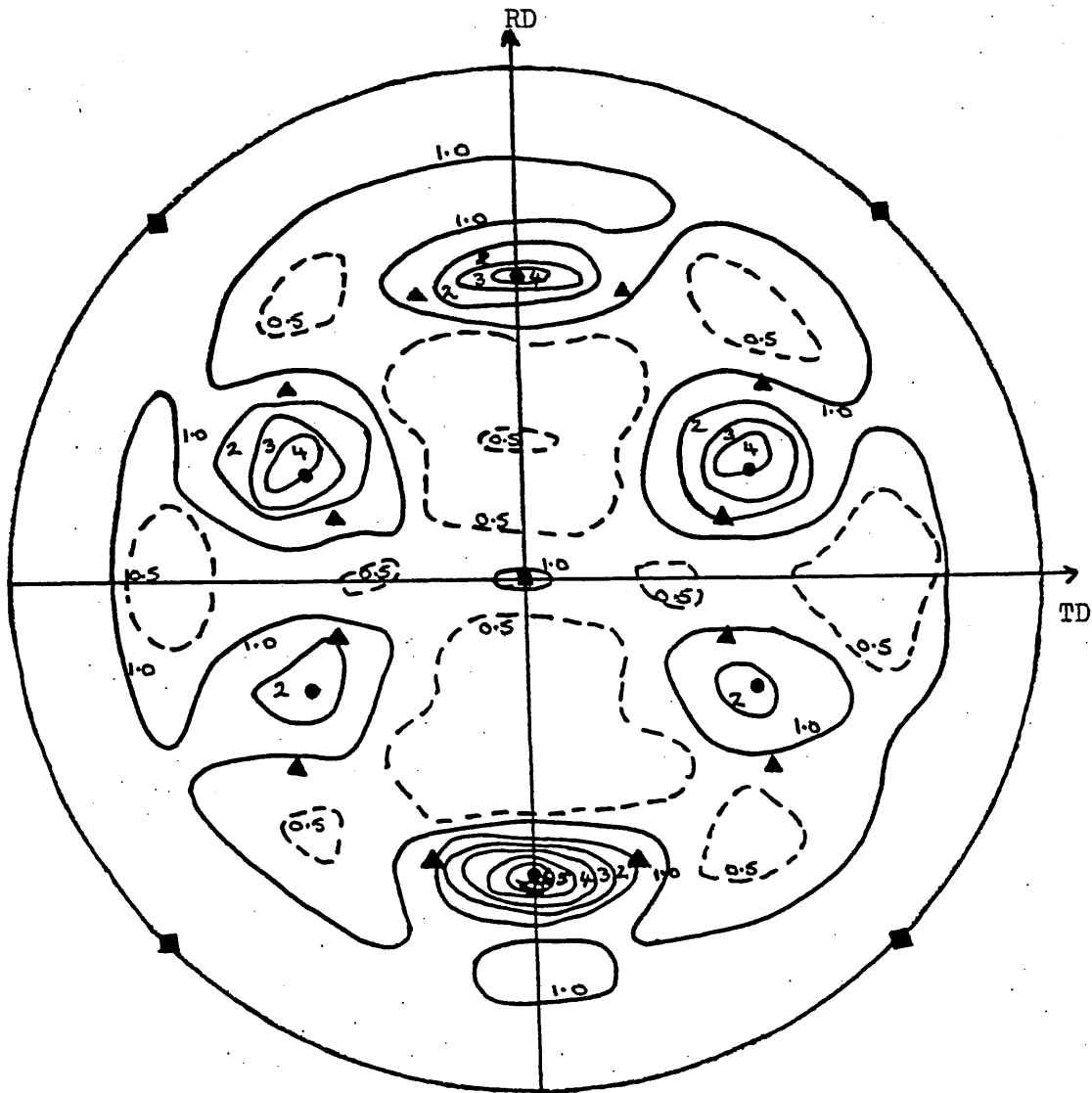
▲ $\{110\}\langle 001\rangle$
 ● $\{554\}\langle 225\rangle$

FIGURE 126 $\{200\}$ Pole Figure for 430Ti (0.5Ti) Steel after
Batch Pre-annealing at 850°C, Cold Rolling to
70%RA and Rapid Final Annealing at 900°C.



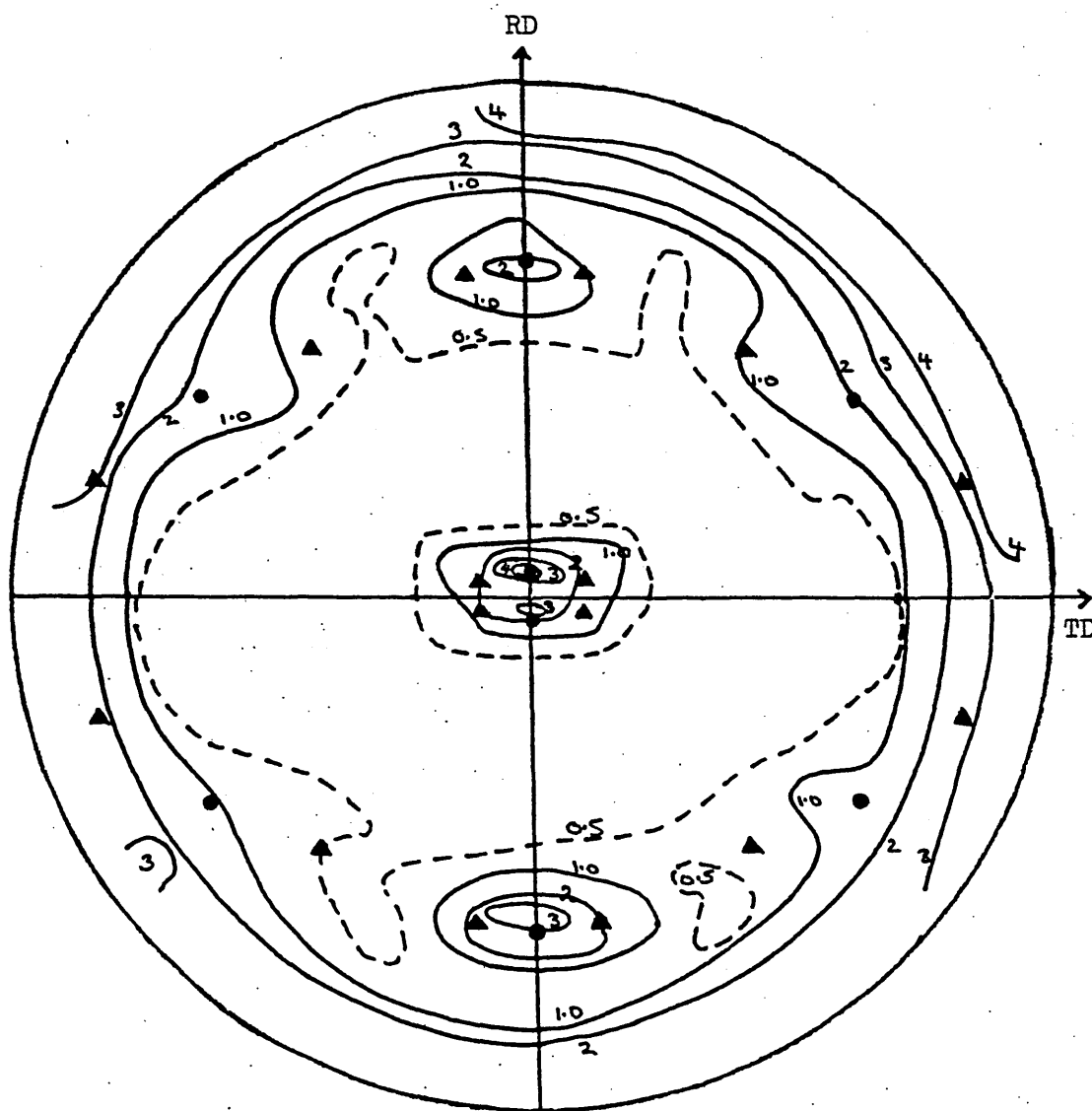
- $\{100\}\langle 011\rangle$
- $\{554\}\langle 225\rangle$
- ▲ $\{223\}\langle 962\rangle$

FIGURE 127 $\{200\}$ Pole Figure for 430Ti (0.5Ti) Steel after Hot Rolling, Cold Rolling to 80%RA and Rapid Final Annealing at 900°C.



- $\{100\} \langle 011 \rangle$
- $\{554\} \langle 225 \rangle$
- ▲ $\{223\} \langle 062 \rangle$

FIGURE 128 $\{200\}$ Pole Figure for 430Ti (0.5Ti) Steel after Rapid Pre-annealing at 850°C, Cold Rolling to 80%RA and Rapid Final Annealing at 900°C.



- $\{554\}\langle 225\rangle$
- ▲ $\{223\}\langle 962\rangle$

FIGURE 129

$\{222\}$ Pole Figure for 430Ti (0.5Ti) Steel after
 Rapid Pre-annealing at 850°C, Cold Rolling to
 80%RA and Rapid Final Annealing at 900°C.

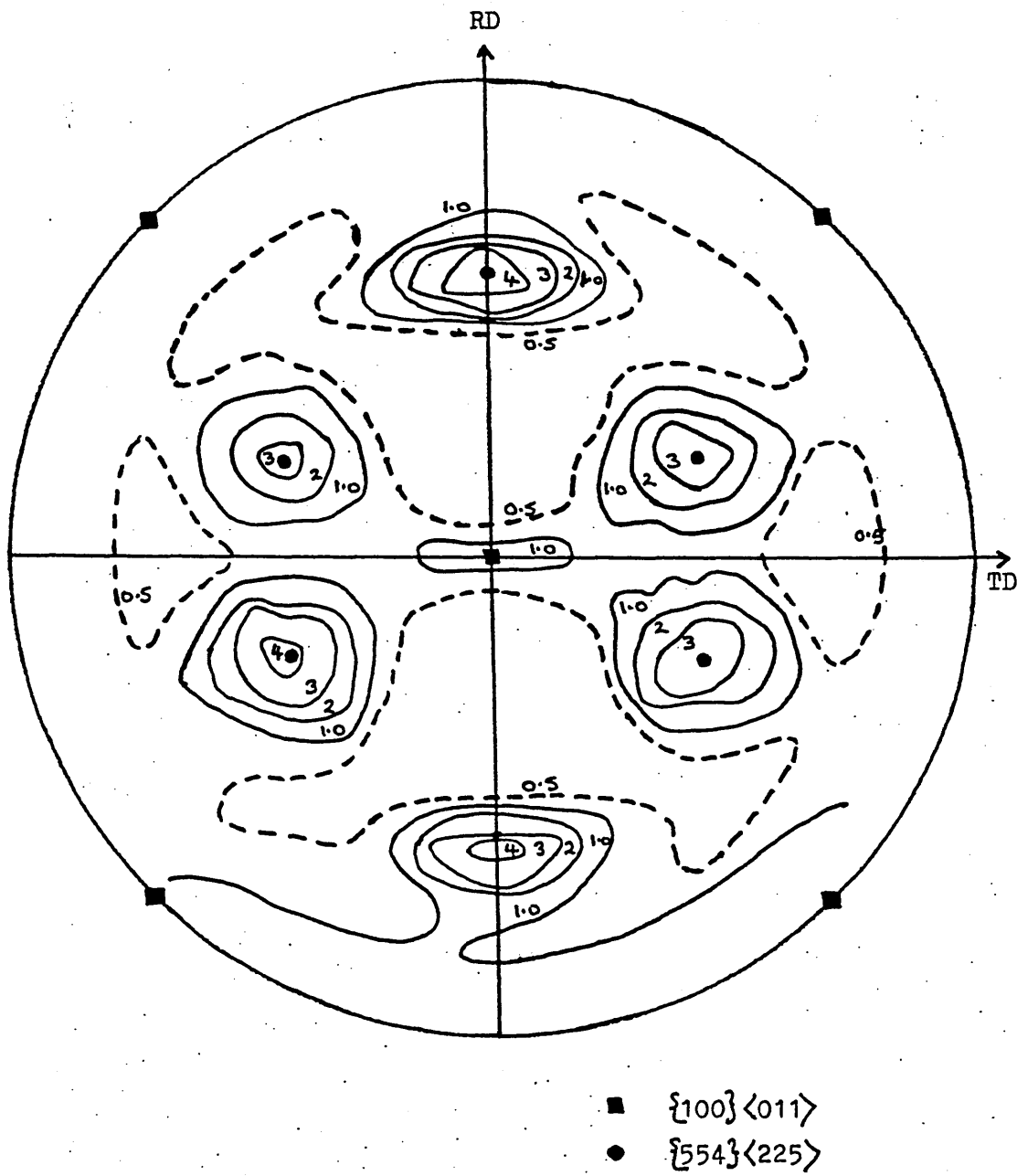


FIGURE 130 {200} Pole Figure for 430Ti (0.5Ti) Steel after
Batch Pre-annealing at 850°C, Cold Rolling to 80%RA
and Rapid Final Annealing at 900°C.

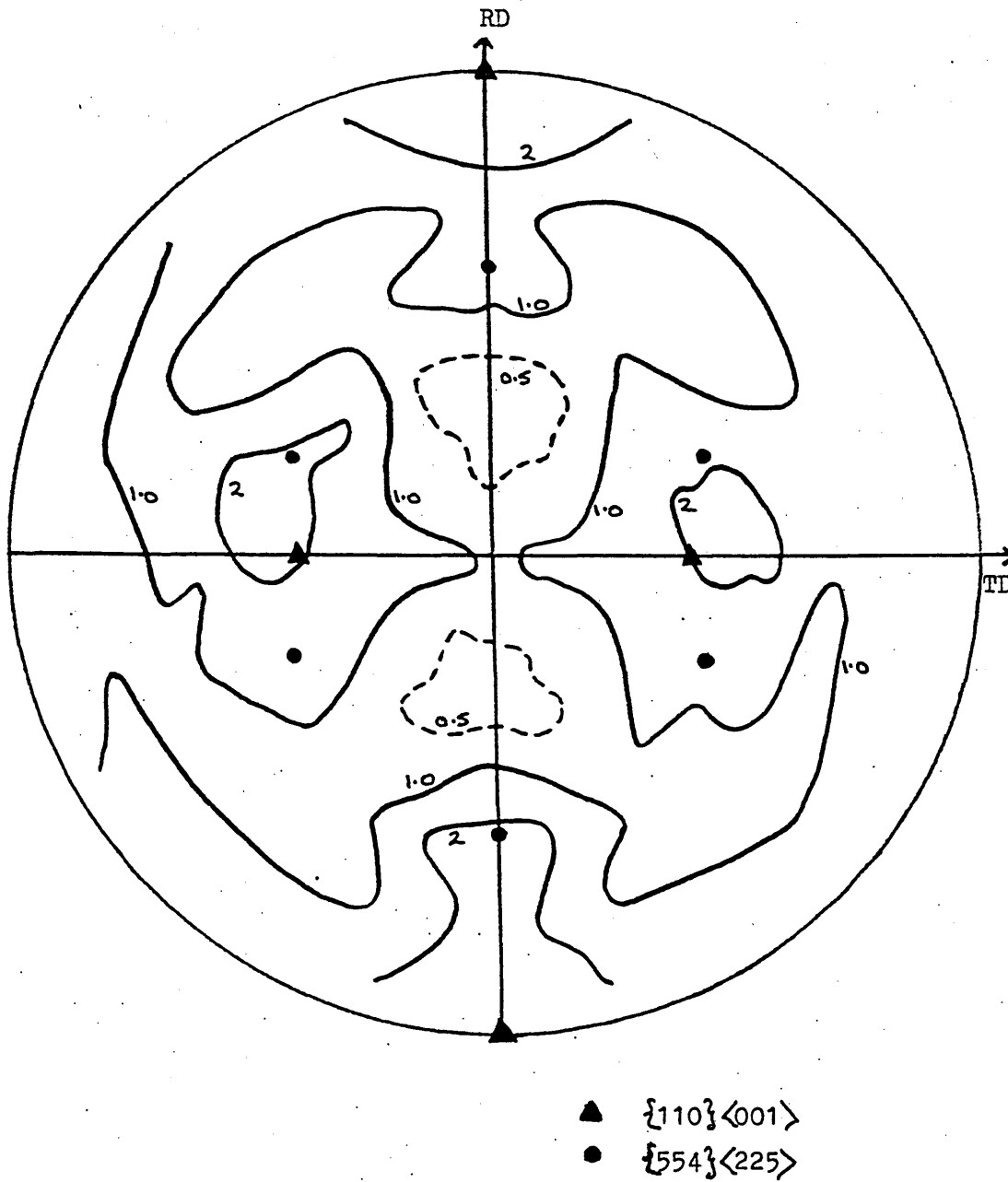
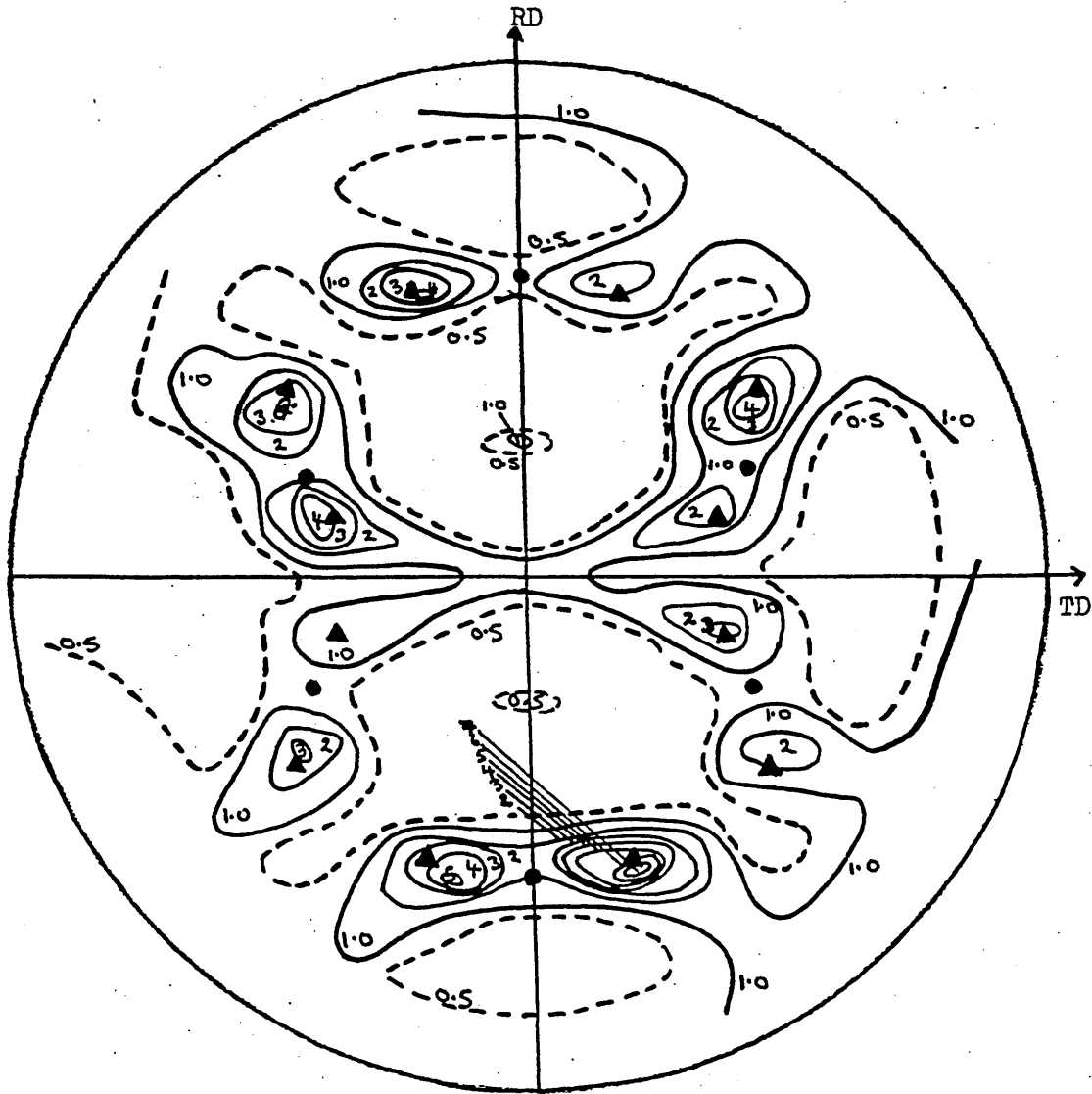


FIGURE 131 $\{200\}$ Pole Figure for 430Ti (0.5Ti) Steel after Rapid Pre-annealing at 1000°C, Cold Rolling to 80%RA and Rapid Final Annealing at 900°C.



- $\{554\}\langle 225 \rangle$
- ▲ $\{223\}\langle 962 \rangle$

FIGURE 132 $\{200\}$ Pole Figure for 430Ti (0.5Ti) Steel after Hot Rolling, Cold Rolling to 90%RA and Rapid Final Annealing at 900°C.

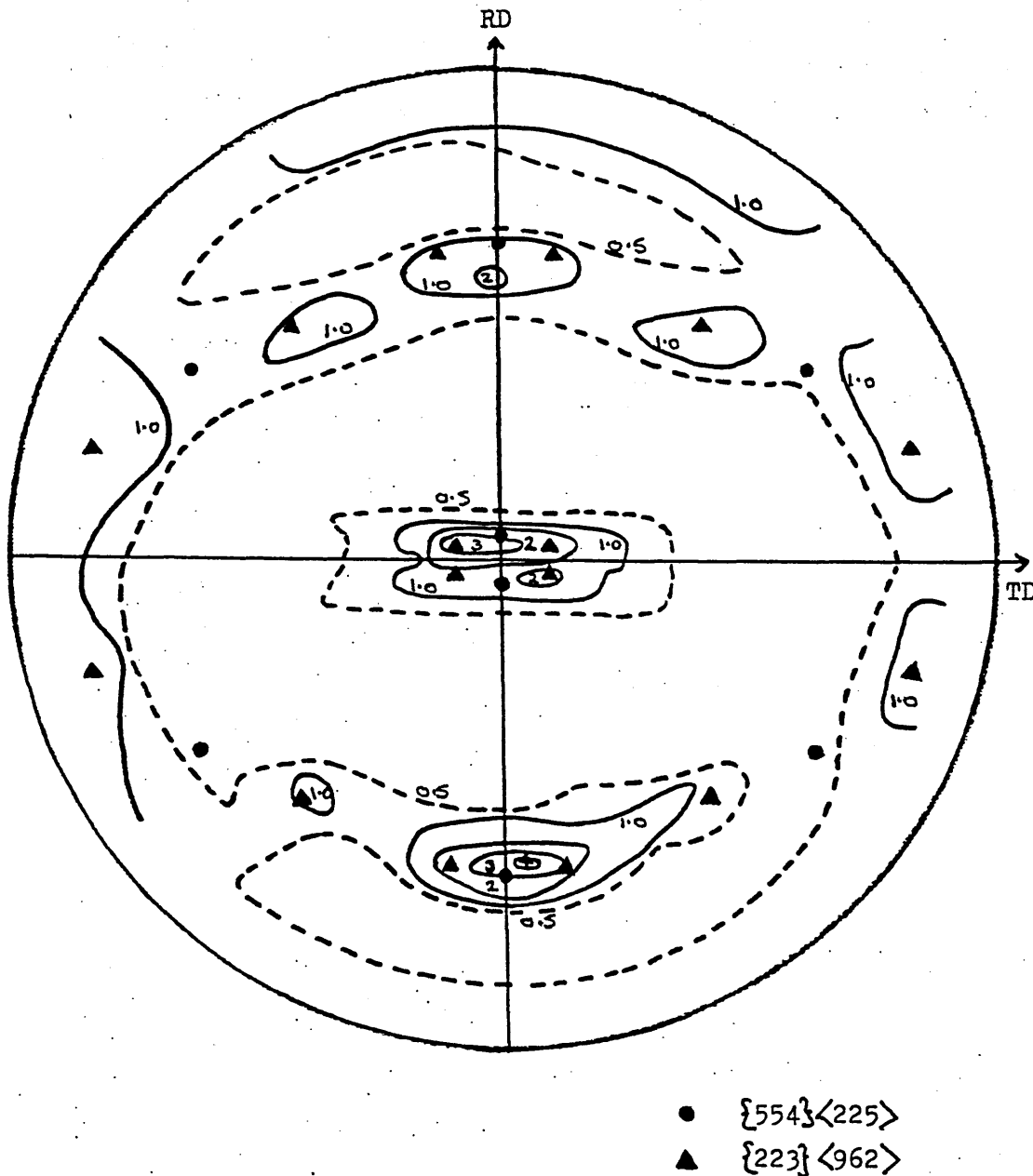
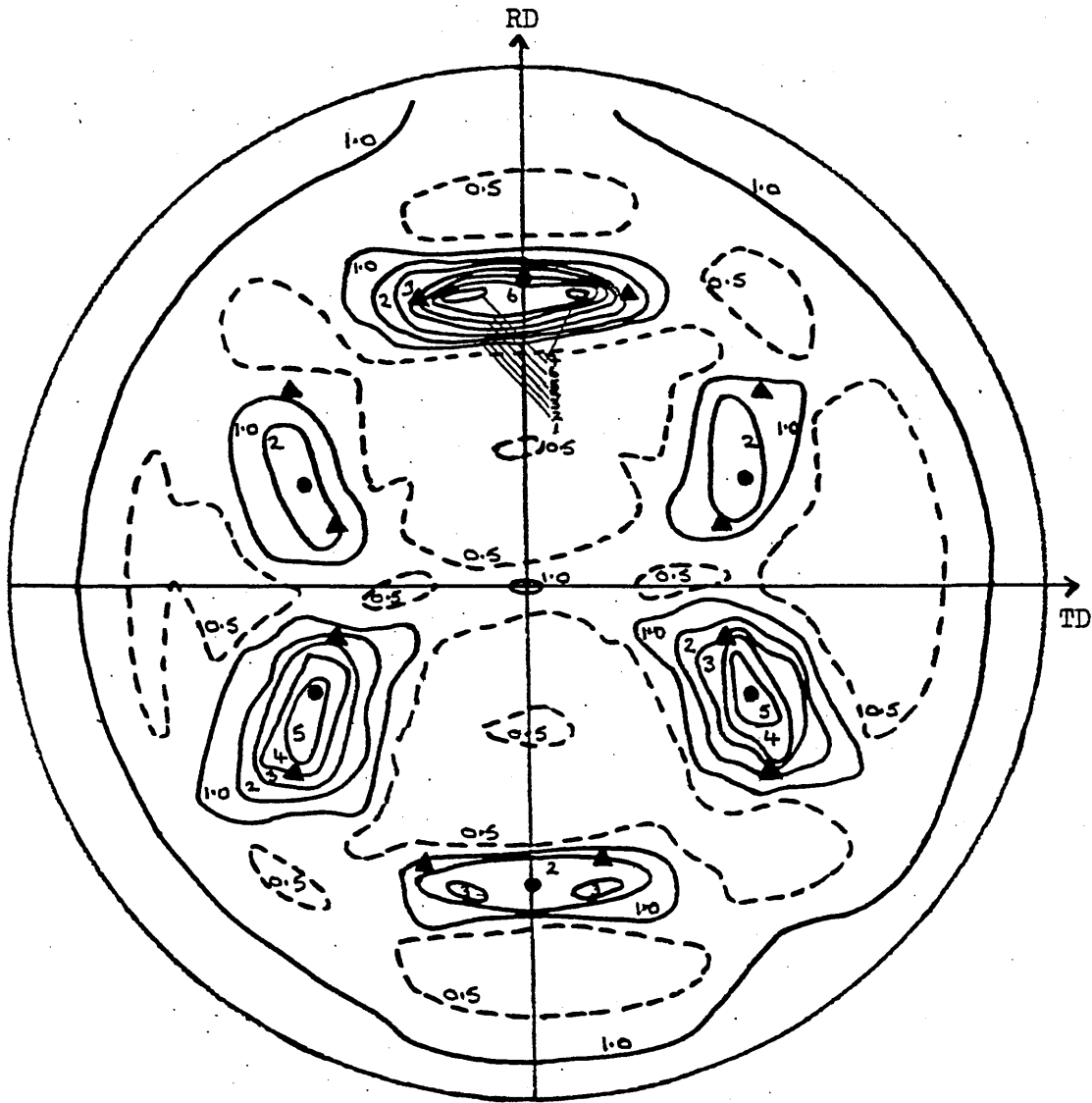


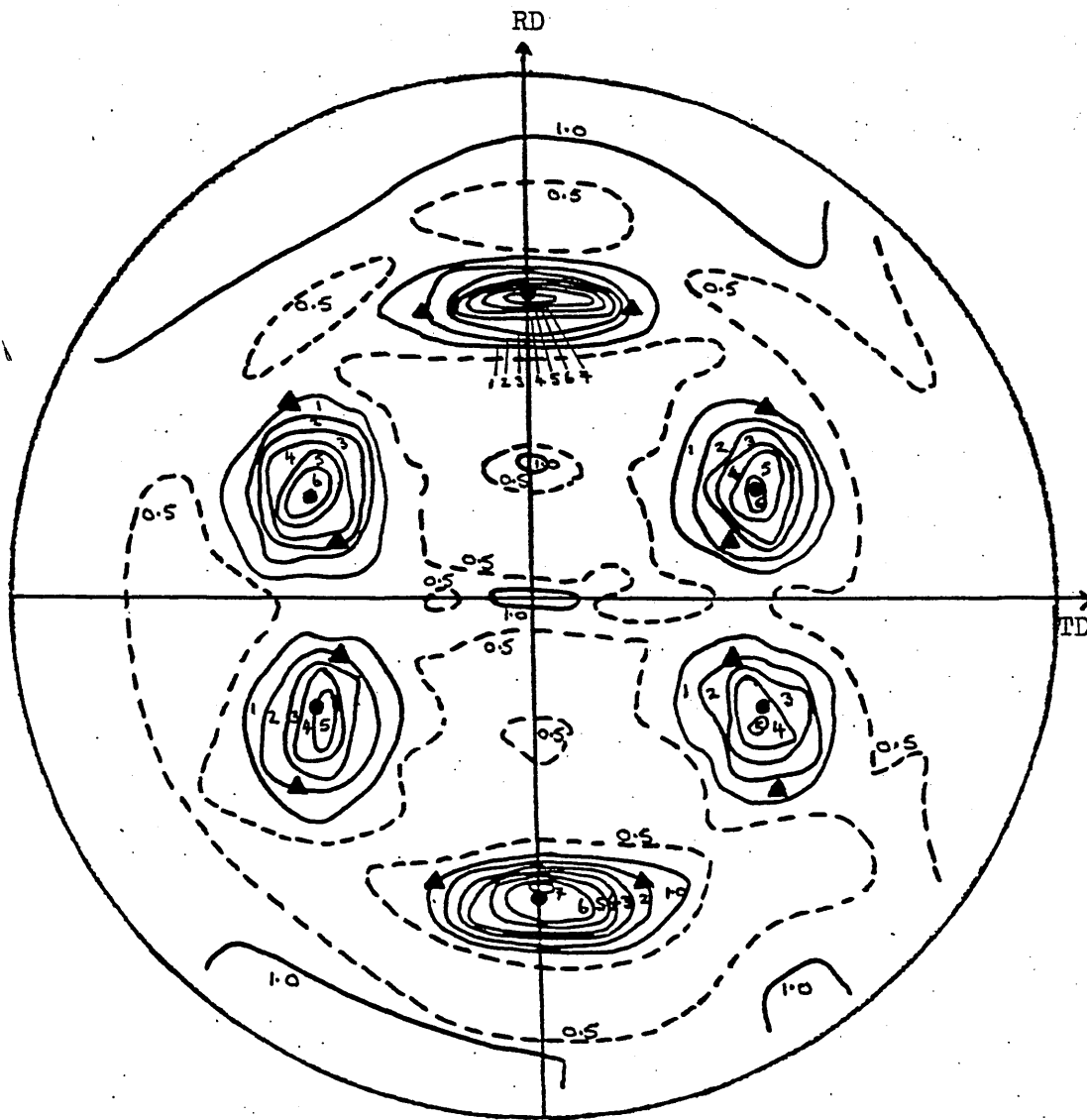
FIGURE 133 $\{222\}$ Pole Figure for 430Ti (0.5Ti) Steel after Hot Rolling, Cold Rolling to 90%RA and Rapid Final Annealing at 900°C.



- $\{554\}\langle 225 \rangle$
- ▲ $\{223\}\langle 962 \rangle$

FIGURE 134

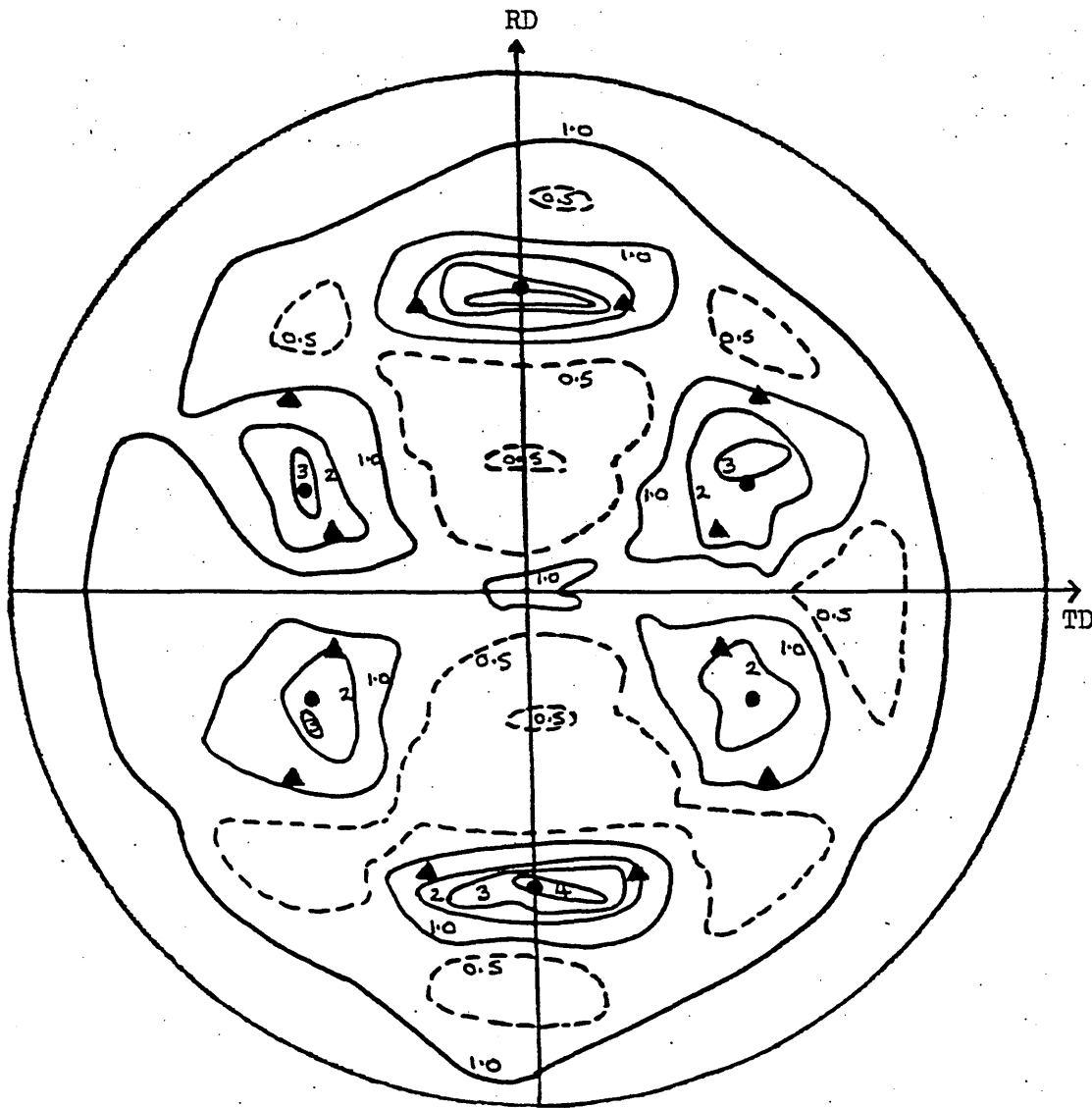
$\{200\}$ Pole Figure for 430Ti (0.5Ti) Steel after Rapid Pre-annealing at 850°C, Cold Rolling to 90%RA and Rapid Final Annealing at 900°C.



- $\{554\}\langle 225 \rangle$
- ▲ $\{223\}\langle 962 \rangle$

FIGURE 135

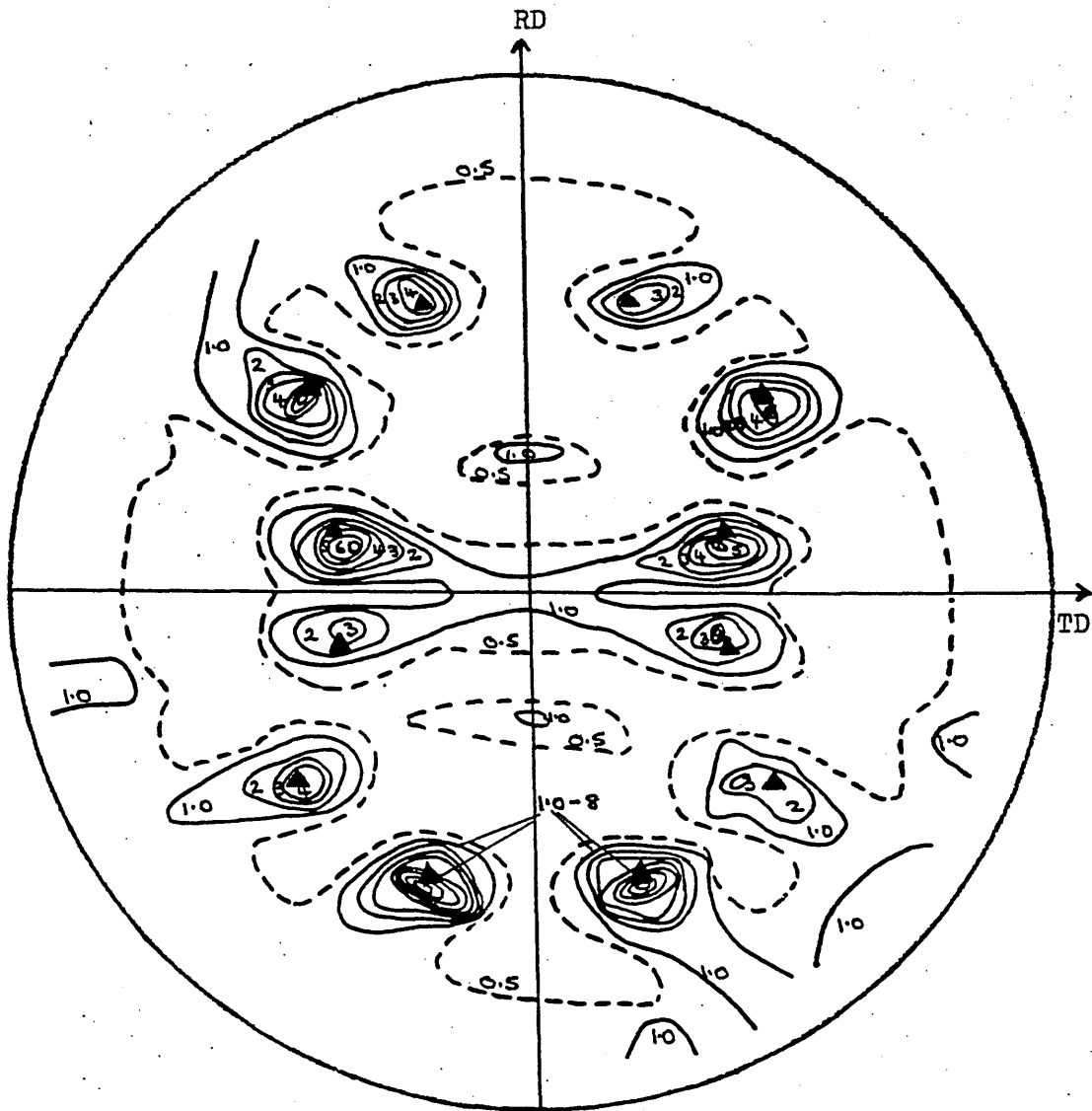
$\{200\}$ Pole Figure for 430Ti (0.5Ti) Steel after
Batch Pre-annealing at 850°C, Cold Rolling to 90%RA
and Rapid Final Annealing at 900°C.



- $\{554\}\langle 225\rangle$
- ▲ $\{223\}\langle 962\rangle$

FIGURE 136

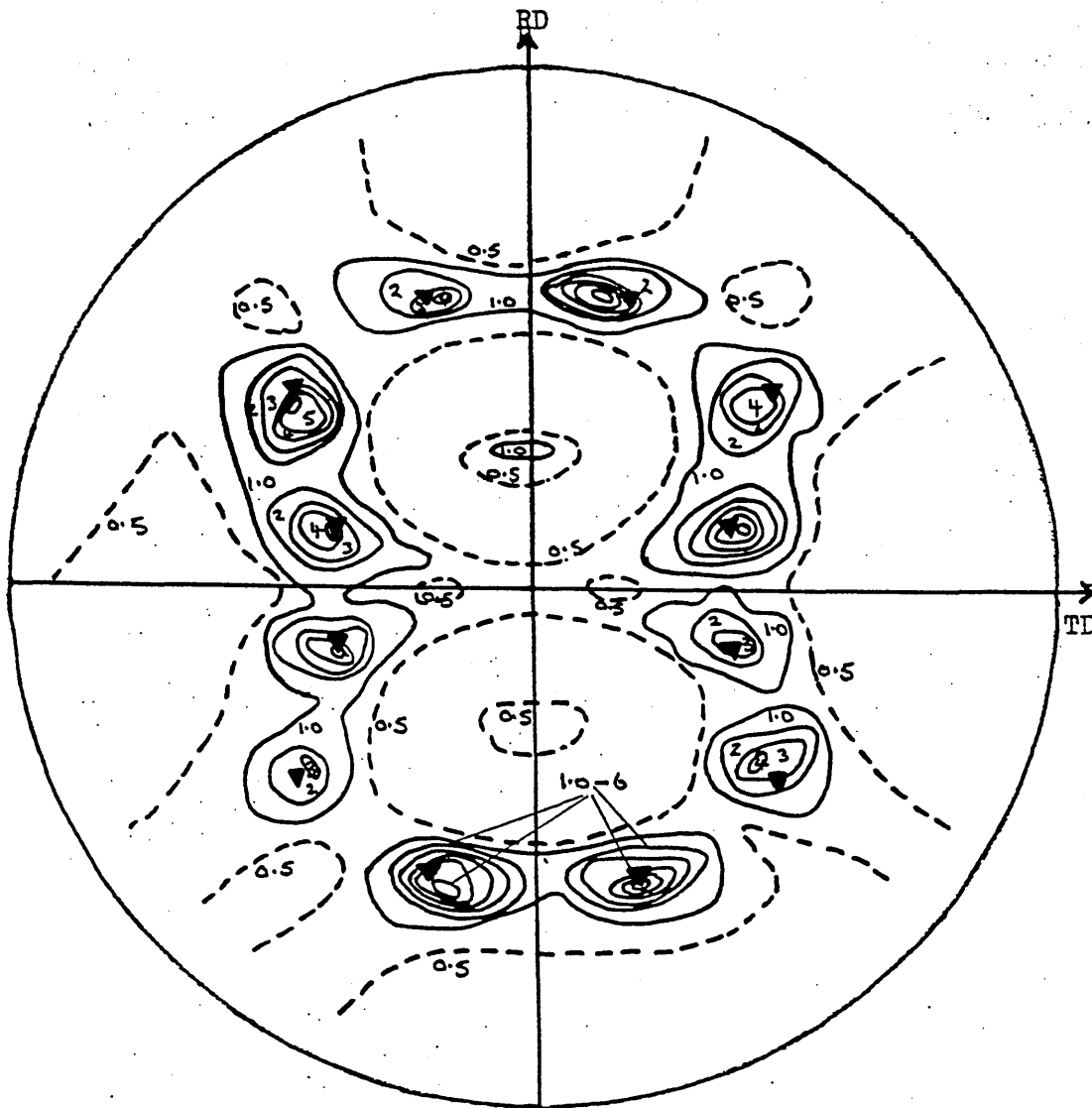
$\{200\}$ Pole Figure for 430Ti (0.5Ti) Steel after Rapid Pre-annealing at 1000°C, Cold Rolling to 90%RA and Rapid Final Annealing at 900°C.



▲ {223} <962>

FIGURE 137

{200} Pole Figure for 430Ti (0.5Ti) Steel after
Hot Rolling, Cold Rolling to 95%RA and Rapid
Final Annealing at 900°C.



▲ $\{223\}\langle 962\rangle$

FIGURE 138

$\{200\}$ Pole Figure for 430Ti (0.5Ti) Steel after
Batch Pre-annealing at 850°C, Cold Rolling to
95%RA and Rapid Final Annealing at 900°C.

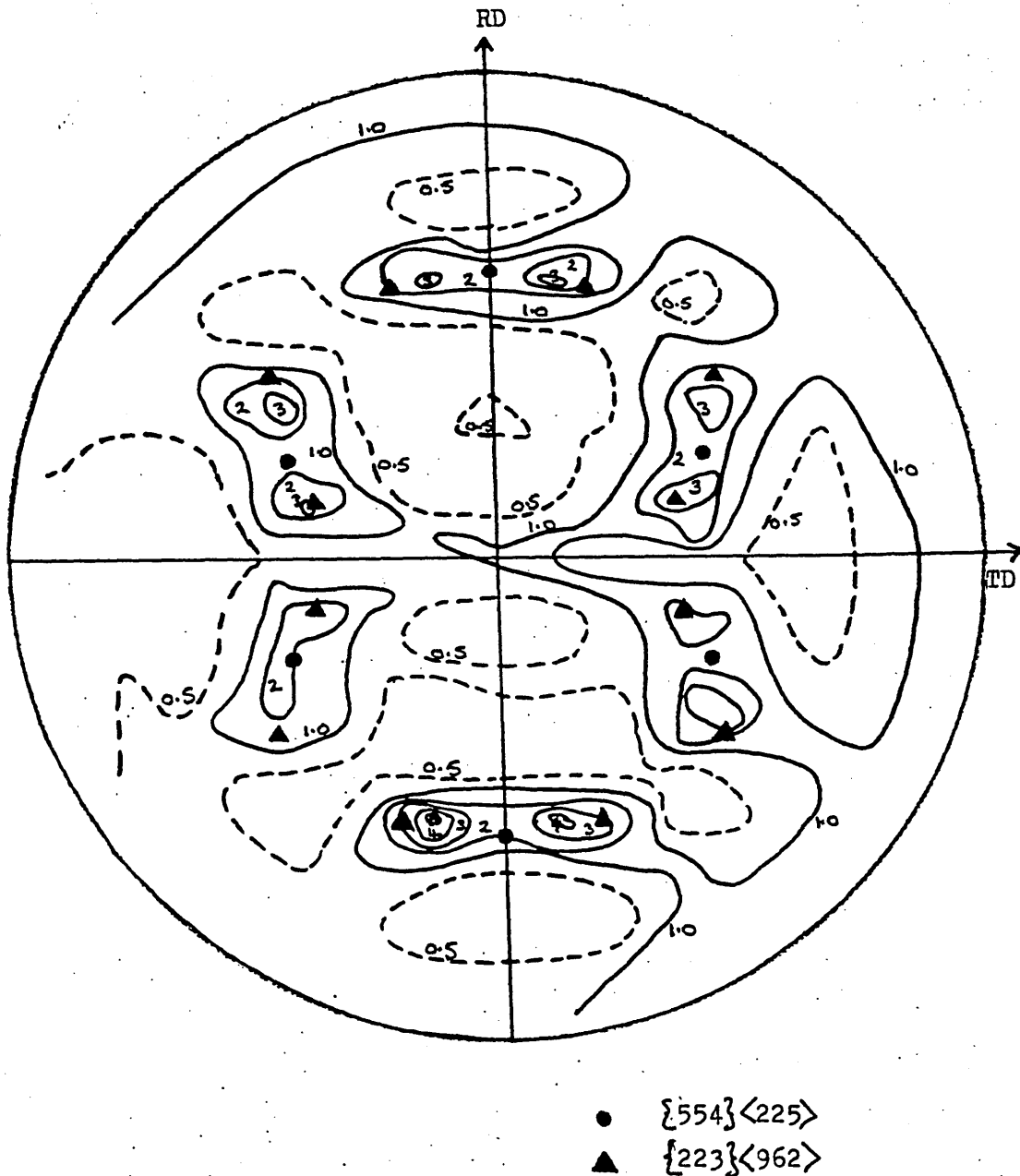
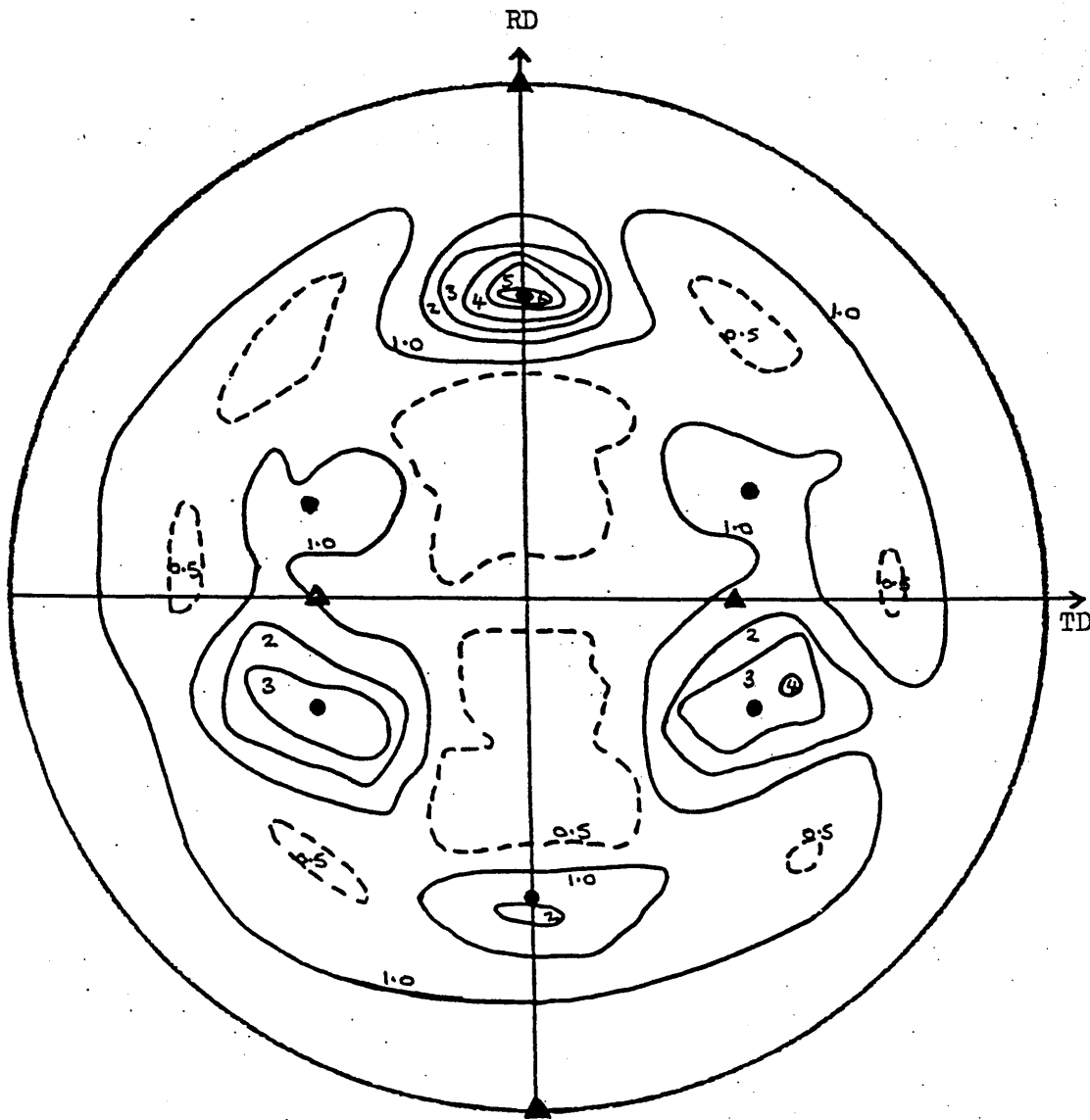


FIGURE 139

{200} Pole Figure for 430Ti (0.5Ti) Steel after
 Rapid Pre-annealing at 1000°C, Cold Rolling to 95%RA
 and Rapid Final Annealing at 900°C.



- ▲ $\{110\}\langle 001\rangle$
- $\{554\}\langle 225\rangle$

FIGURE 140

$\{200\}$ Pole Figure for 430Ti (0.5Ti) Steel after Rapid Pre-annealing at 1000°C, Cold Rolling to 95%RA and Batch Final Annealing at 900°C.

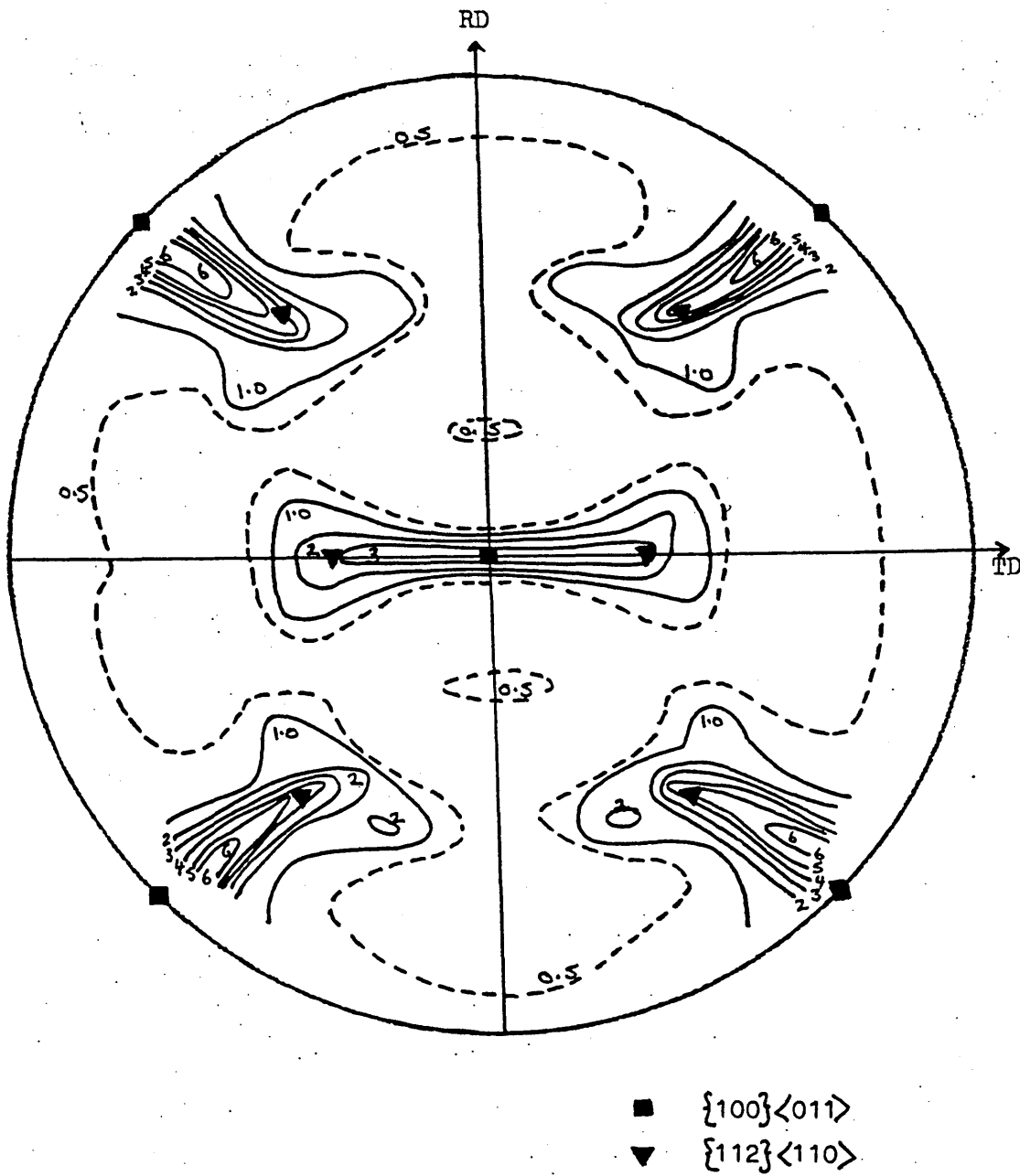
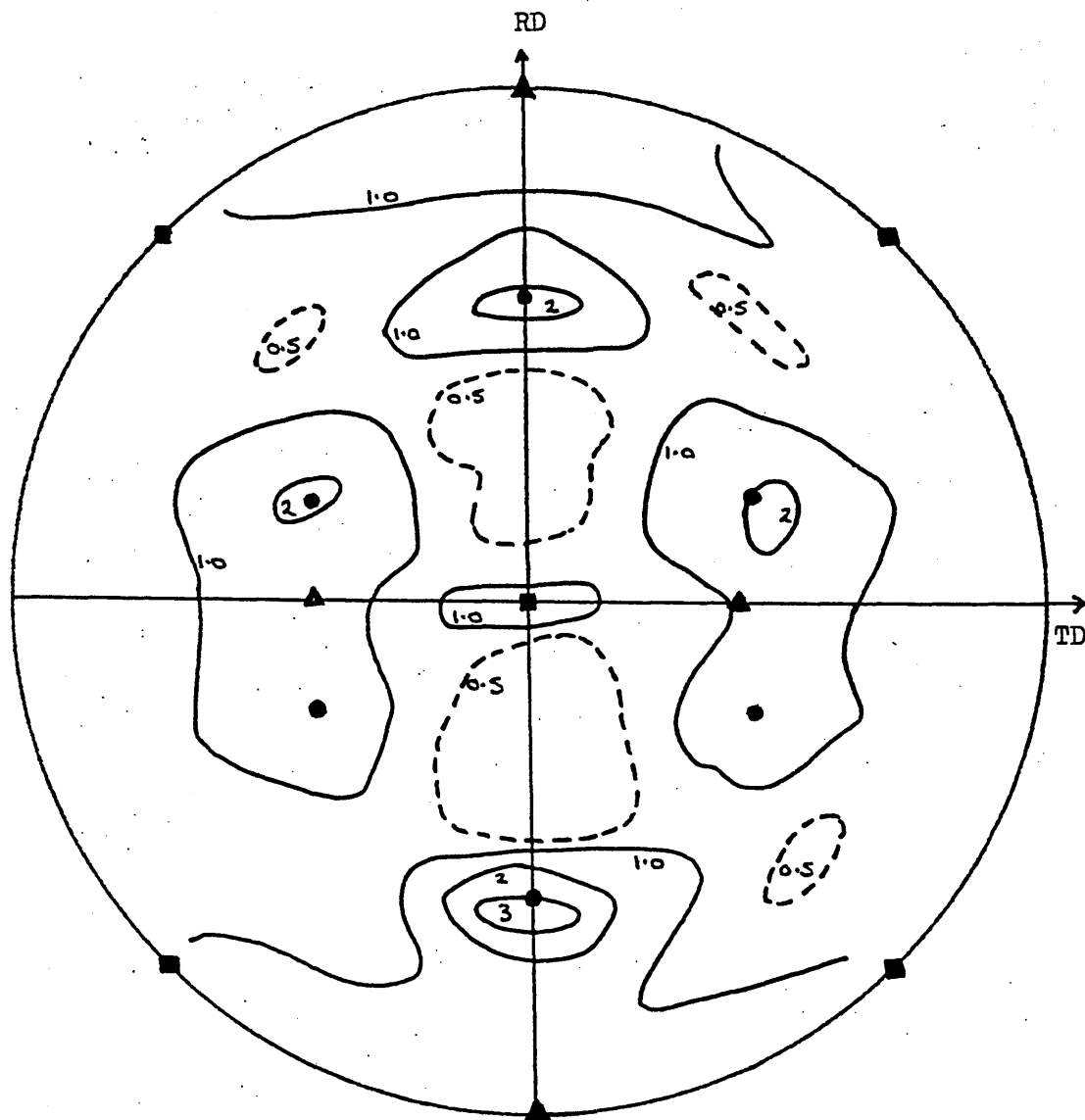


FIGURE 141

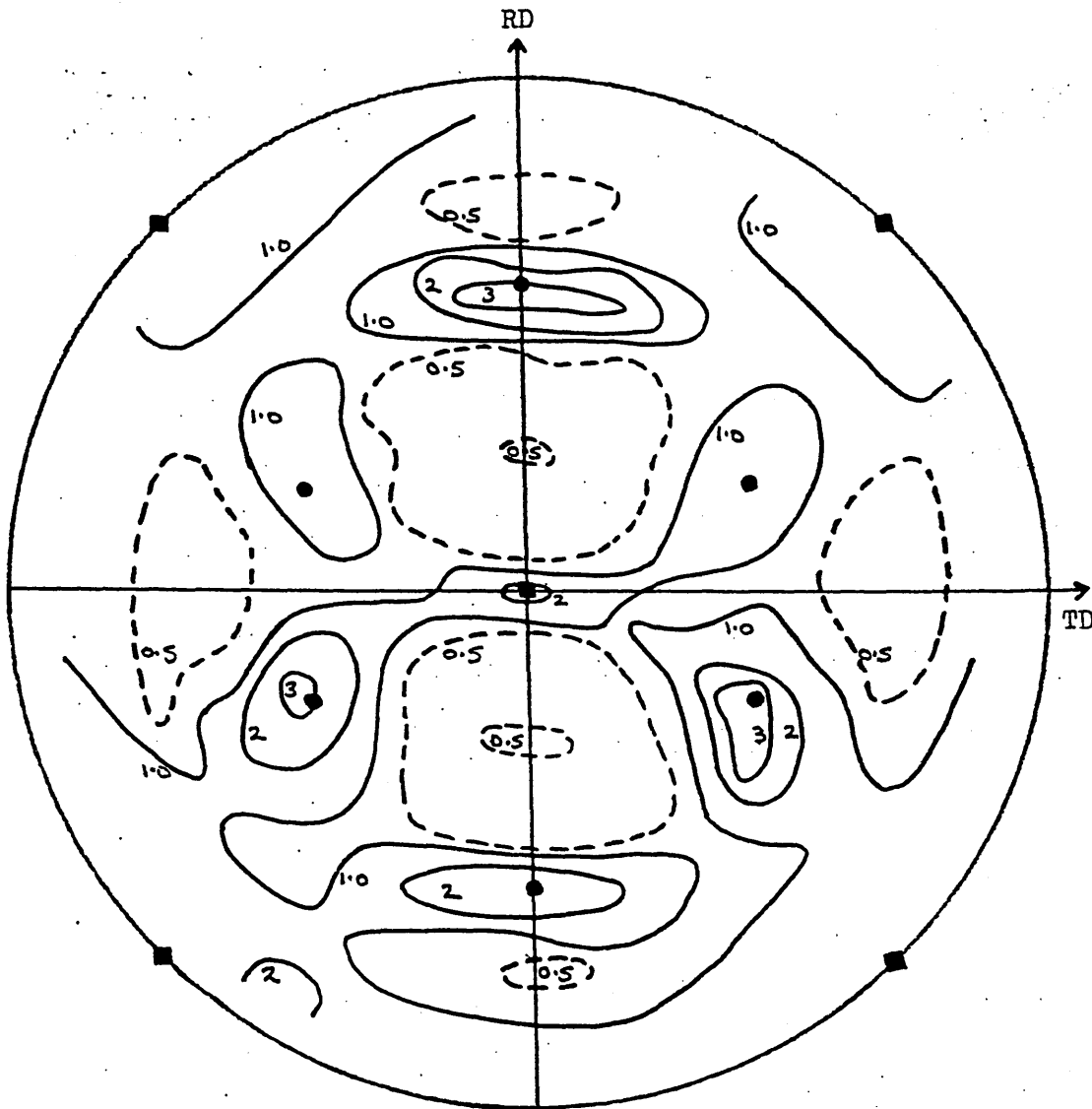
$\{200\}$ Pole Figure for 430Ti (0.5Ti) Steel after
Hot Rolling, Cold Rolling to 95%RA and Rapid
Final Annealing at 700°C.



- ▲ $\{110\} \langle 001 \rangle$
- $\{554\} \langle 225 \rangle$
- $\{100\} \langle 011 \rangle$

FIGURE 142

$\{200\}$ Pole Figure for 430Ti (0.5Ti) Steel after
 Rapid Pre-annealing at 850°C, Cold Rolling to 70%RA
 and Rapid Final Annealing at 800°C.



- $\{100\}\langle 011\rangle$
- $\{554\}\langle 225\rangle$

FIGURE 143 $\{200\}$ Pole Figure for 430Ti (0.5Ti) Steel after Rapid Pre-annealing at 850°C, Cold Rolling to 80%RA and Rapid Final Annealing at 800°C.

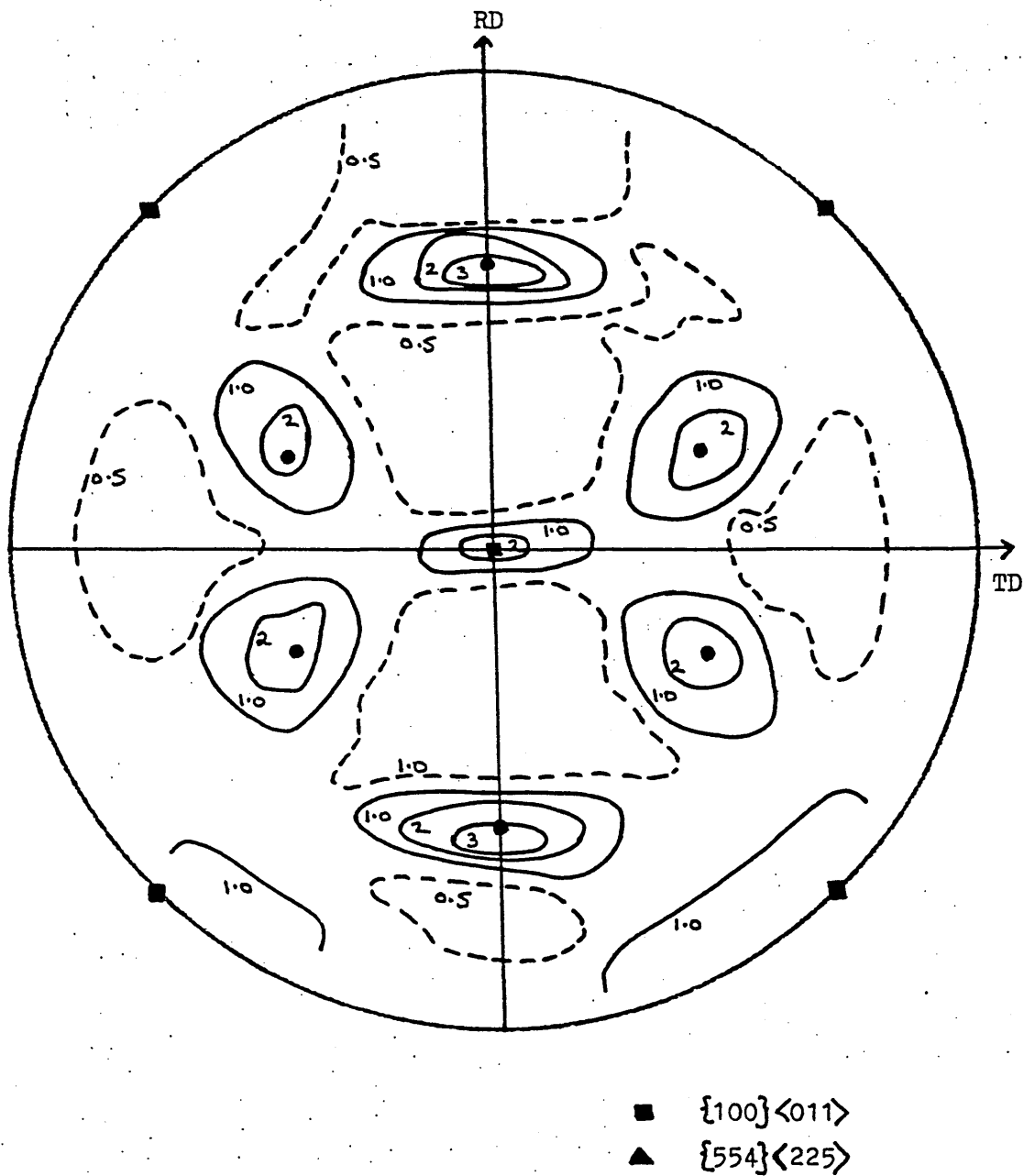
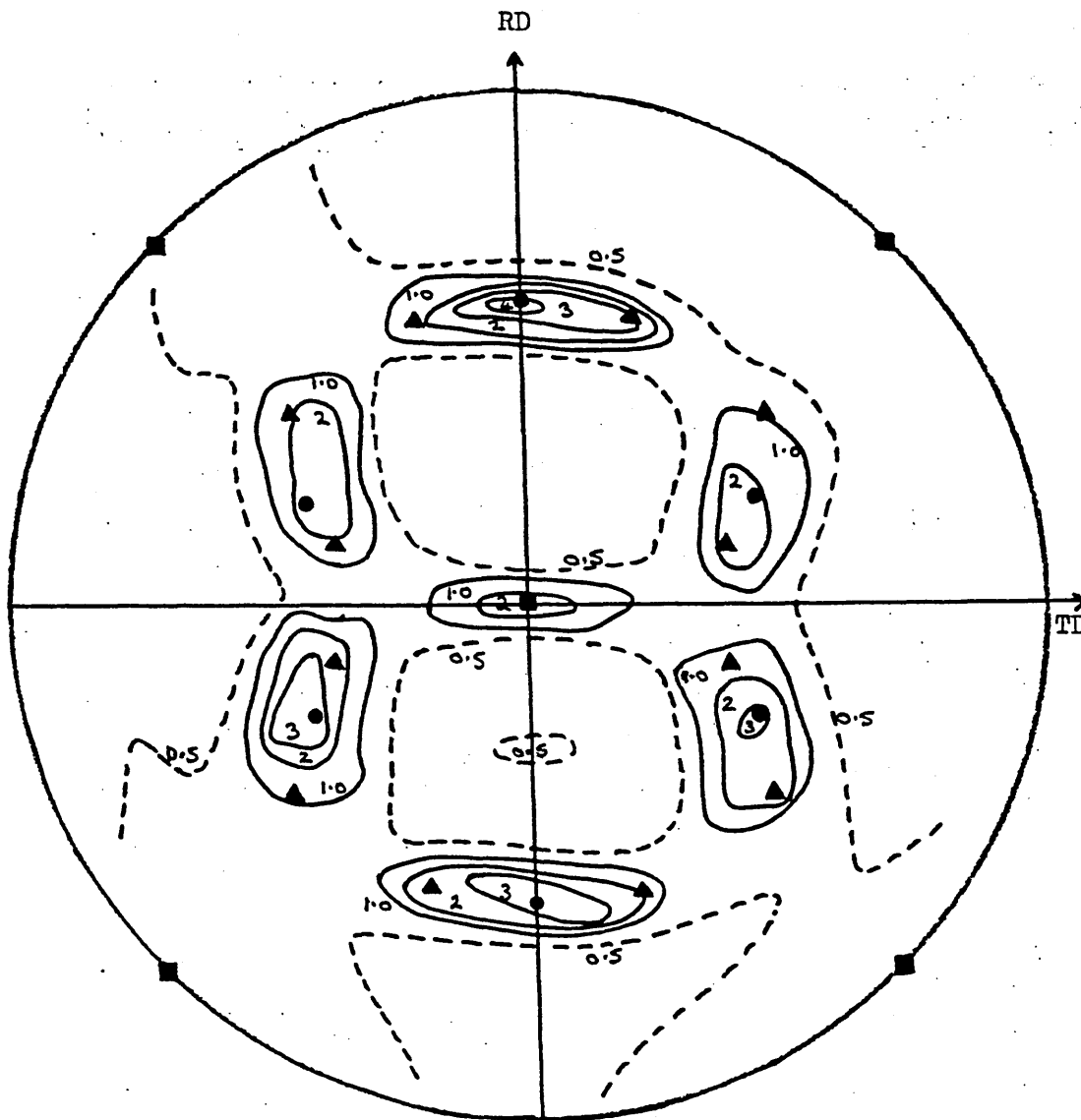
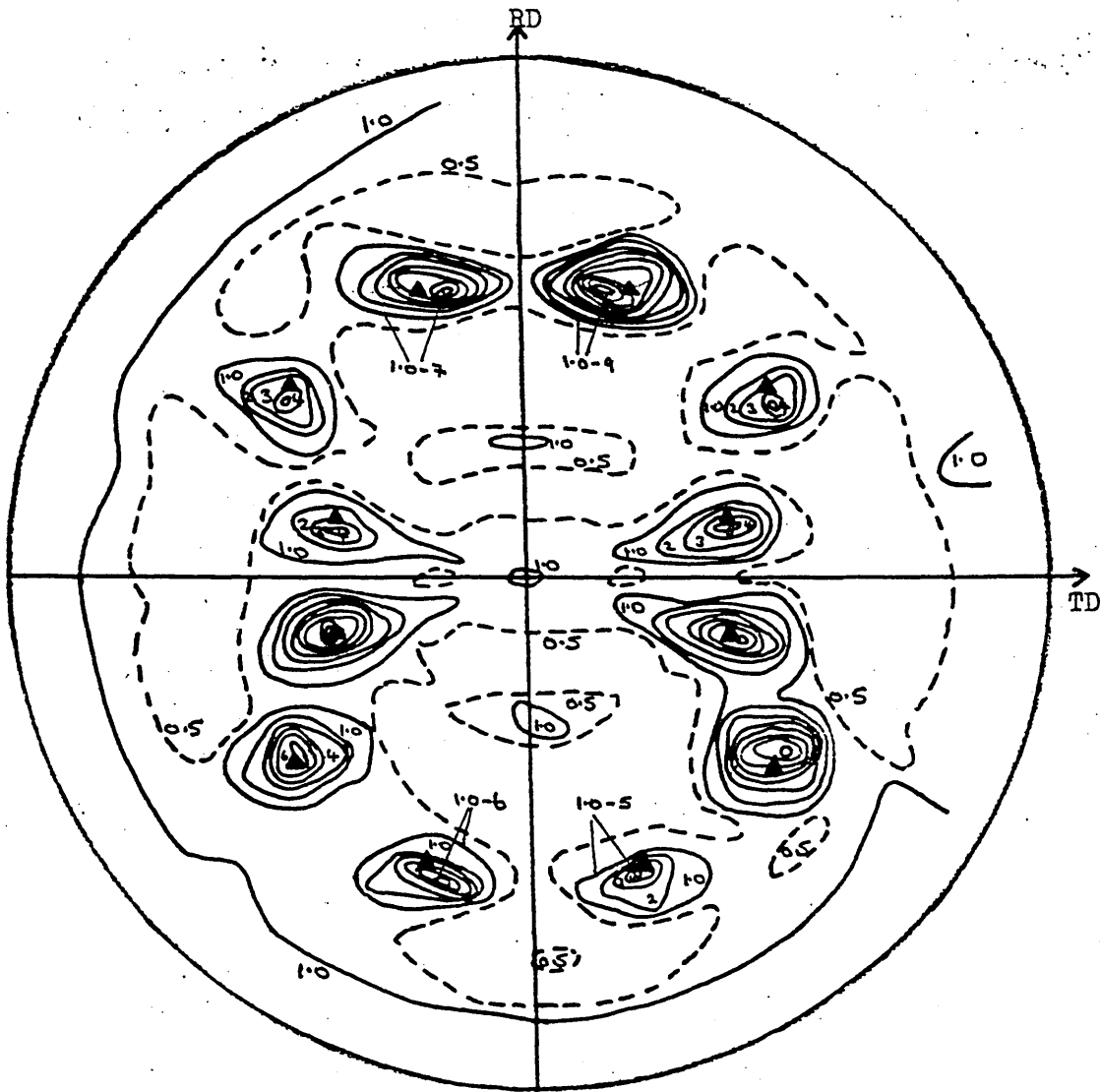


FIGURE 144 $\{200\}$ Pole Figure for 430Ti (0.5Ti) Steel after Rapid Pre-annealing at 850°C, Cold Rolling to 90%RA and Rapid Final Annealing at 800°C.



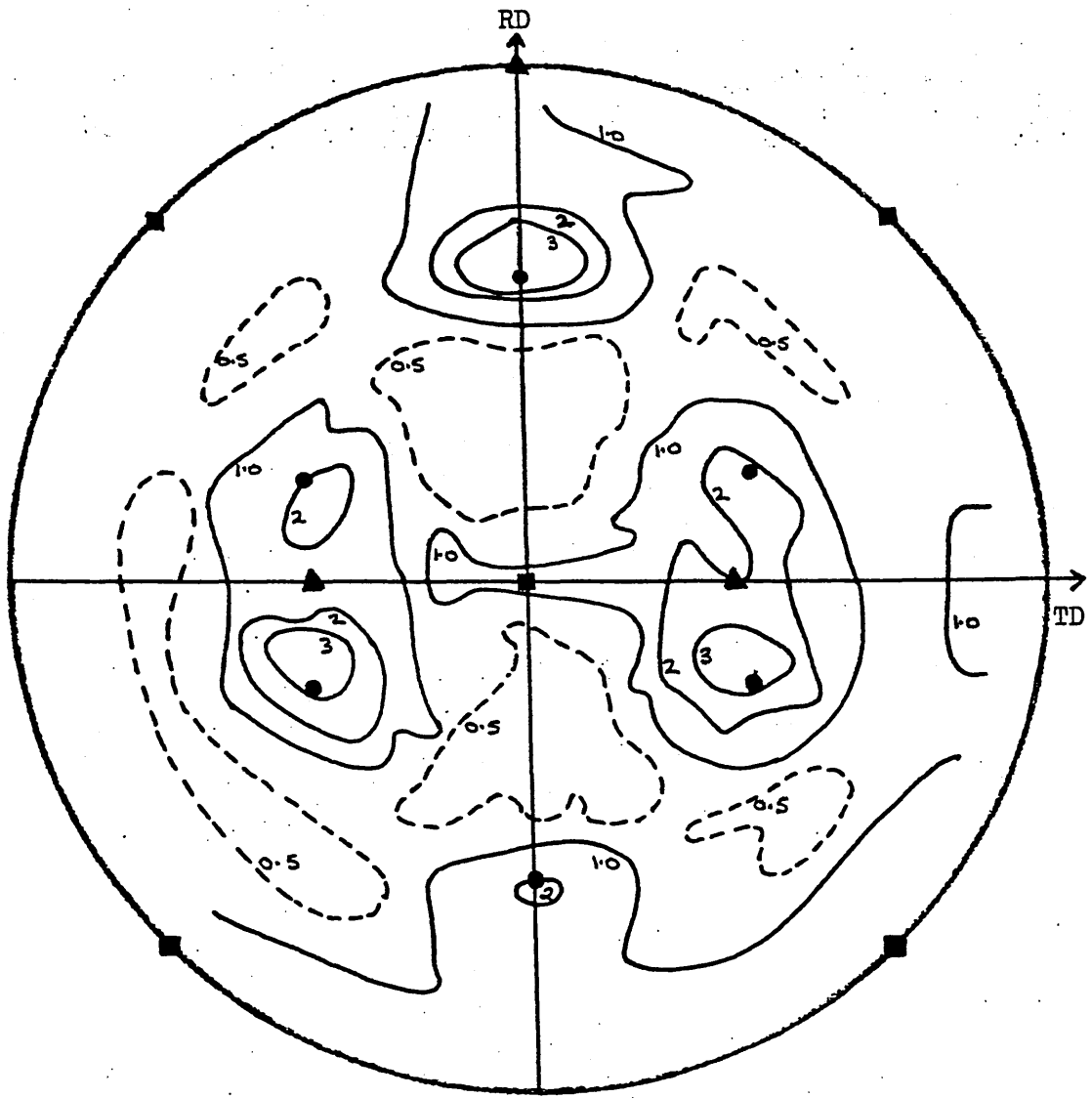
- $\{100\}\langle 011\rangle$
- $\{554\}\langle 225\rangle$
- ▲ $\{223\}\langle 962\rangle$

FIGURE 145 $\{200\}$ Pole Figure for 430Ti (0.5Ti) Steel after
Rapid Pre-annealing at 850°C, Cold Rolling to
95%RA and Rapid Final Annealing at 800°C.



▲ $\{223\}\langle 962\rangle$

FIGURE 147 $\{200\}$ Pole Figure for 430Ti (0.5Ti) Steel after Rapid Pre-annealing at 850°C, Cold Rolling to 95%RA and Rapid Final Annealing at 950°C.



- $\{100\}\langle 011\rangle$
- ▲ $\{110\}\langle 001\rangle$
- $\{554\}\langle 225\rangle$

FIGURE 148 $\{200\}$ Pole Figure for 430Ti (0.3Ti) Steel after
Batch Pre-annealing at 850°C, Cold Rolling to
60%RA and Rapid Final Annealing at 900°C.

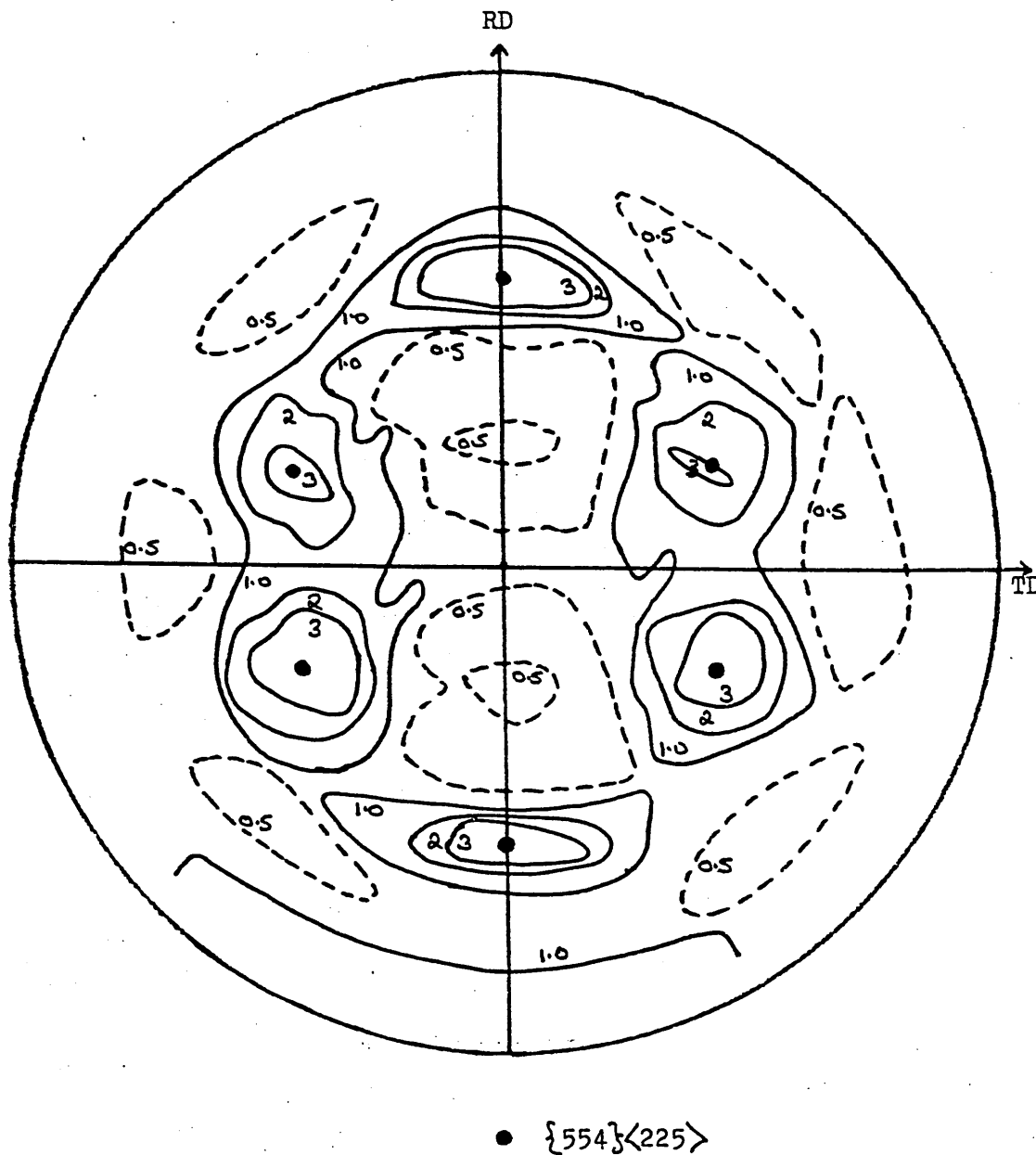
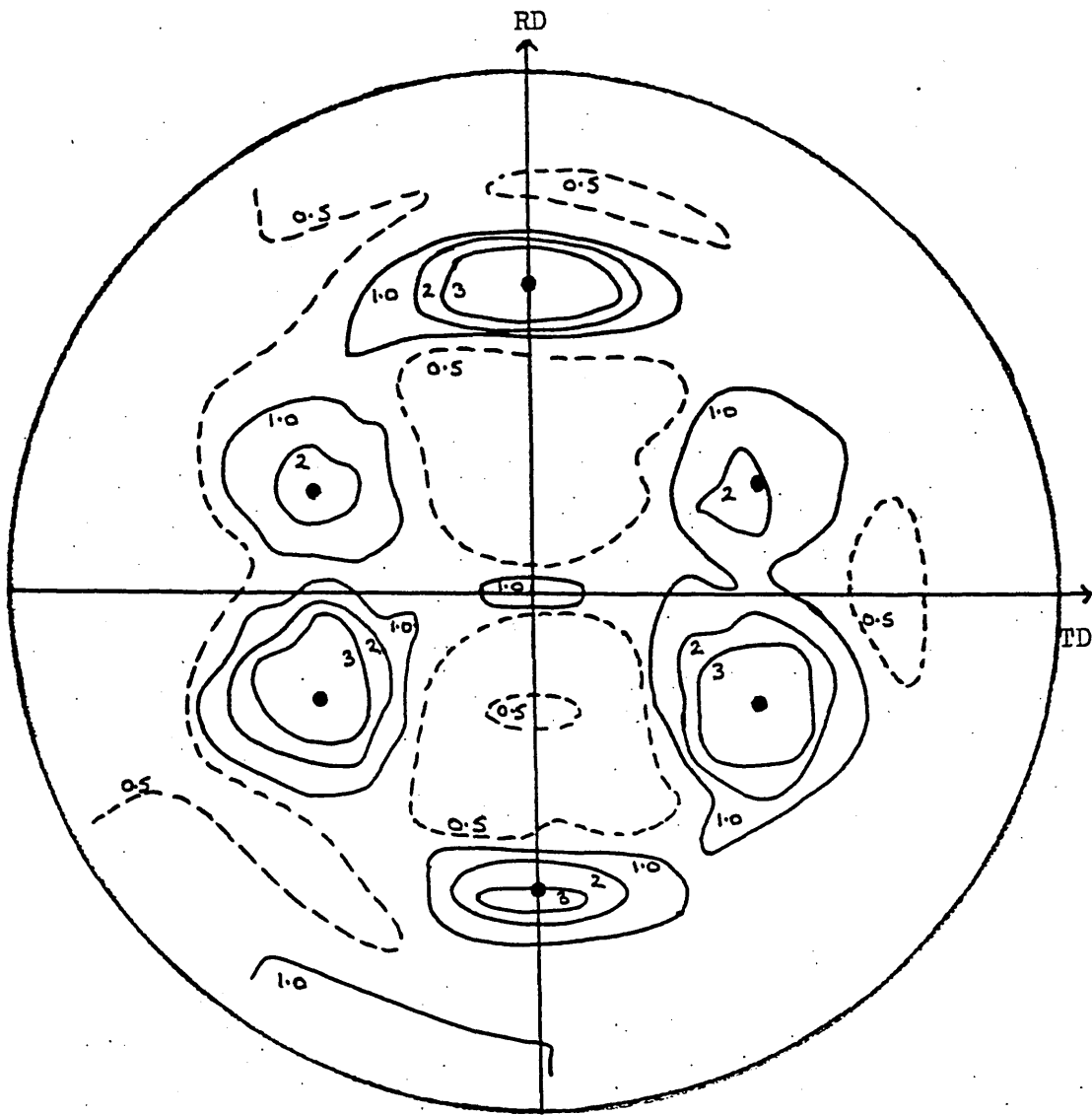


FIGURE 149

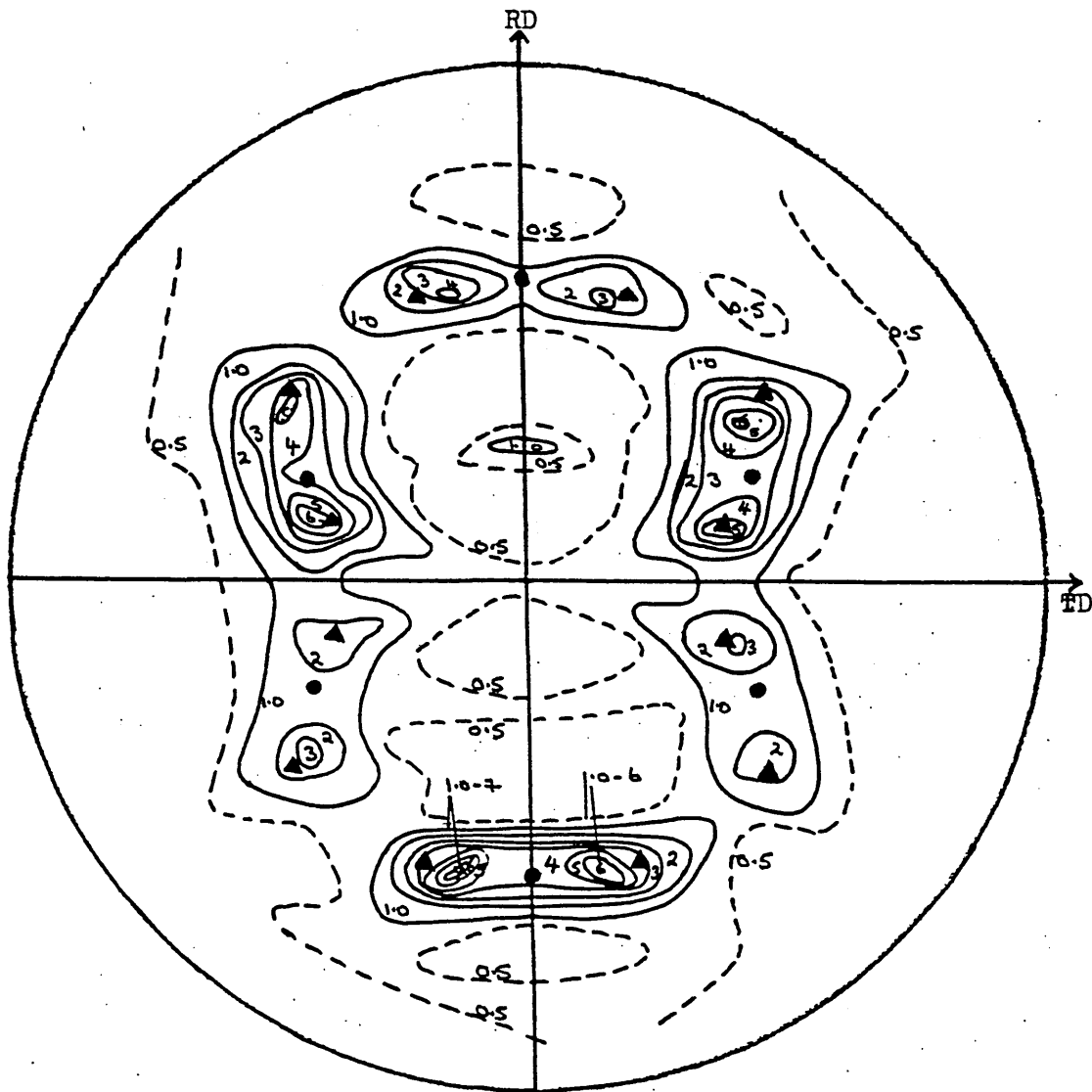
$\{200\}$ Pole Figure for 430Ti (0.3Ti) Steel after
 Rapid Pre-annealing at 850°C, Cold Rolling to
 70%RA and Rapid Final Annealing at 900°C.



● $\{554\}\langle 225 \rangle$

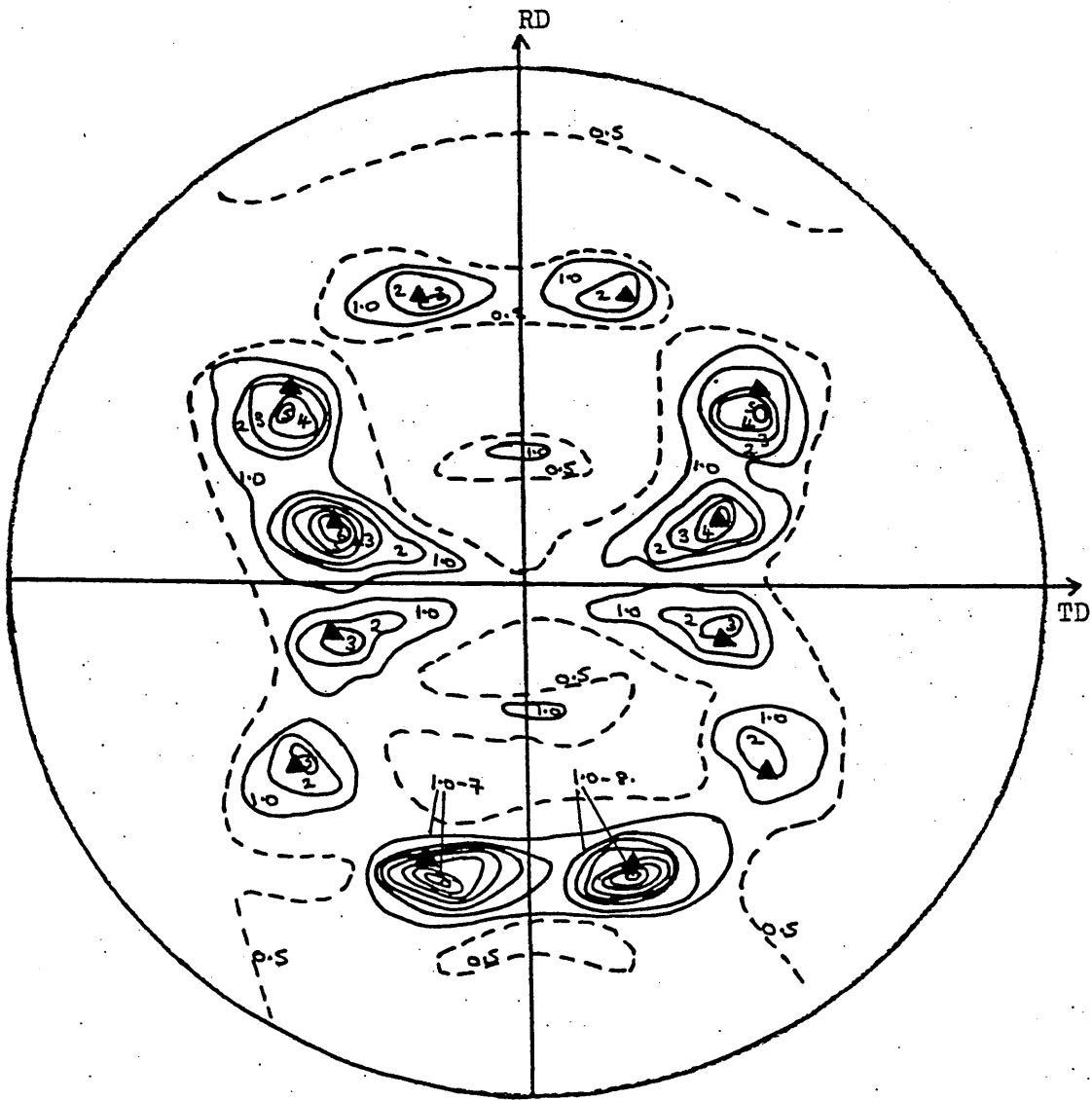
FIGURE 150

$\{200\}$ Pole Figure for 430Ti (0.3Ti) Steel after
Batch Pre-annealing at 850°C, Cold Rolling to
80%RA and Rapid Final Annealing at 900°C.



- {554}<225>
- ▲ {223}<962>

FIGURE 151 {200} Pole Figure for 430Ti (0.3Ti) Steel after
Batch Annealing at 850°C, Cold Rolling to 90%RA
and Rapid Final Annealing at 900°C.



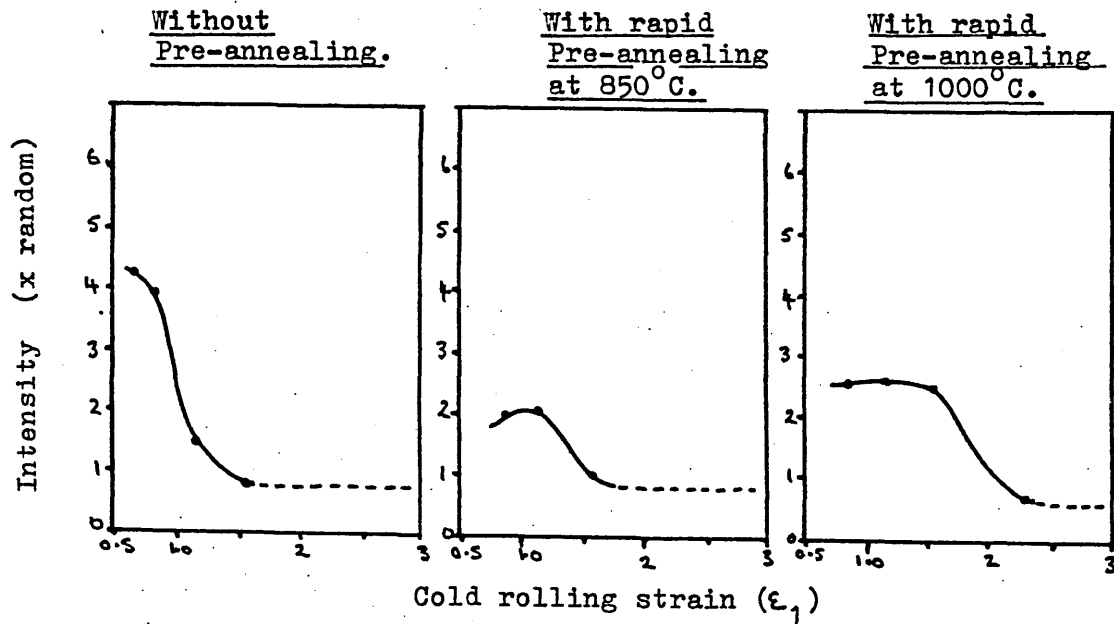
▲ $\{223\}\langle 962\rangle$

FIGURE 152

$\{200\}$ Pole Figure for 430Ti (0.3Ti) Steel after
 Rapid Pre-annealing at 850°C, Cold Rolling to
 95%RA and Rapid Final Annealing at 900°C.

{110}<001>

Rapid Final Annealing at 900°C (Heating rate ~5000°C hr⁻¹, AC)



Batch Final Annealing at 900°C (Heating rate=50°C hr⁻¹, FC)

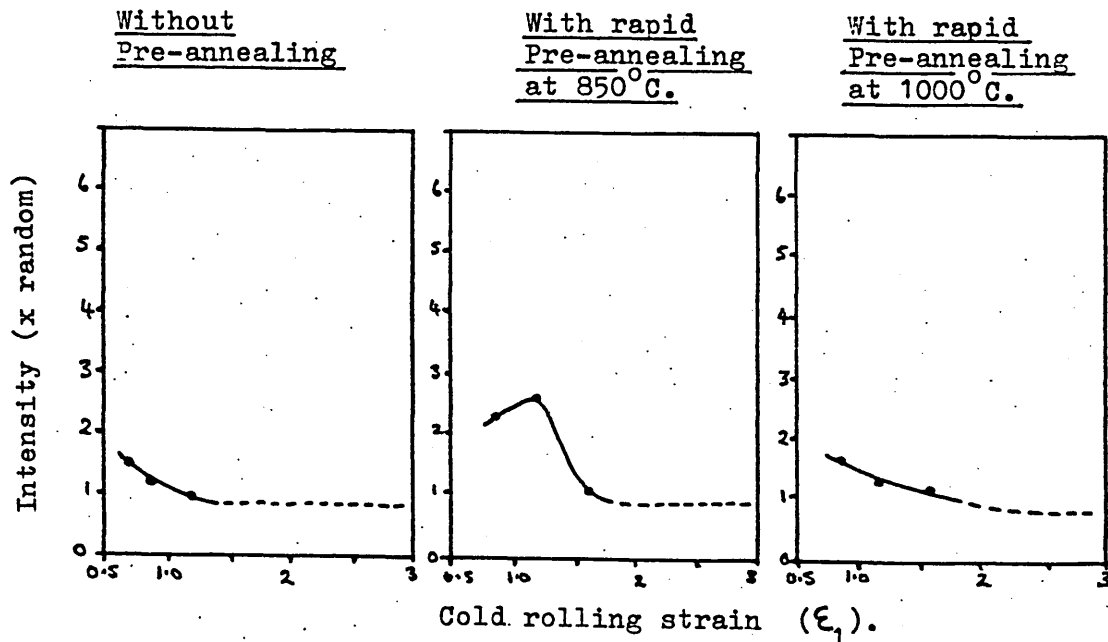
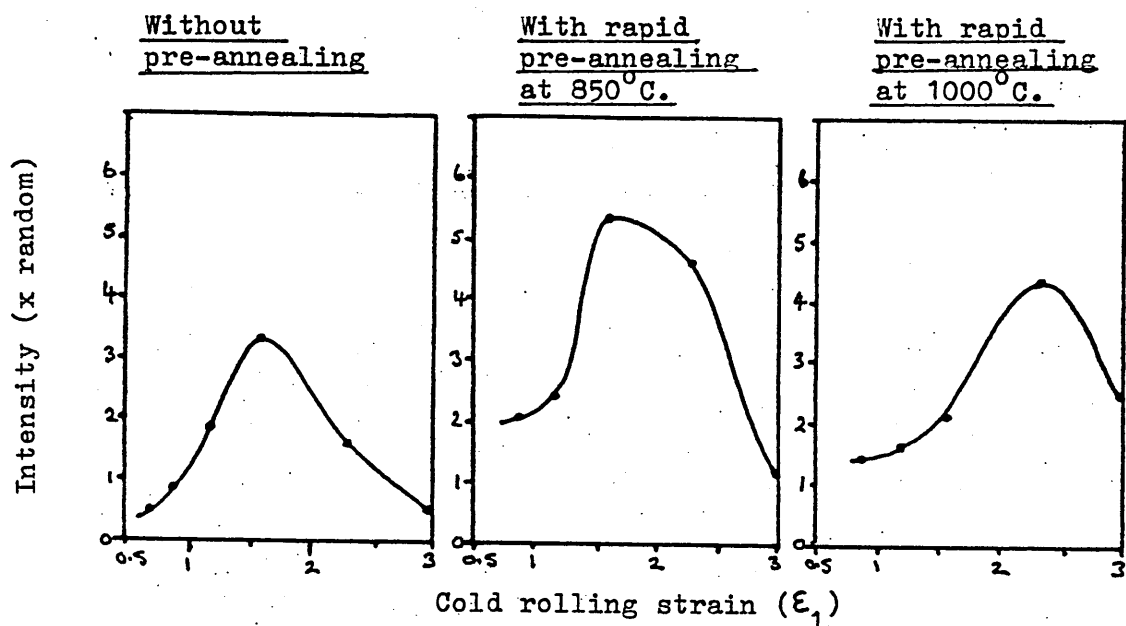


FIGURE 153 Variation of Intensity of the {110}<001> Orientation
with Cold Rolling Strain in Cold Rolled and
Annealed 430Ti (0.5Ti) Steel.

{554} <225>

Rapid Final Annealing at 900°C (Heating rate ~ 5000°C hr⁻¹, AC)



Batch Final Annealing at 900°C (Heating rate = 50°C hr⁻¹, FC)

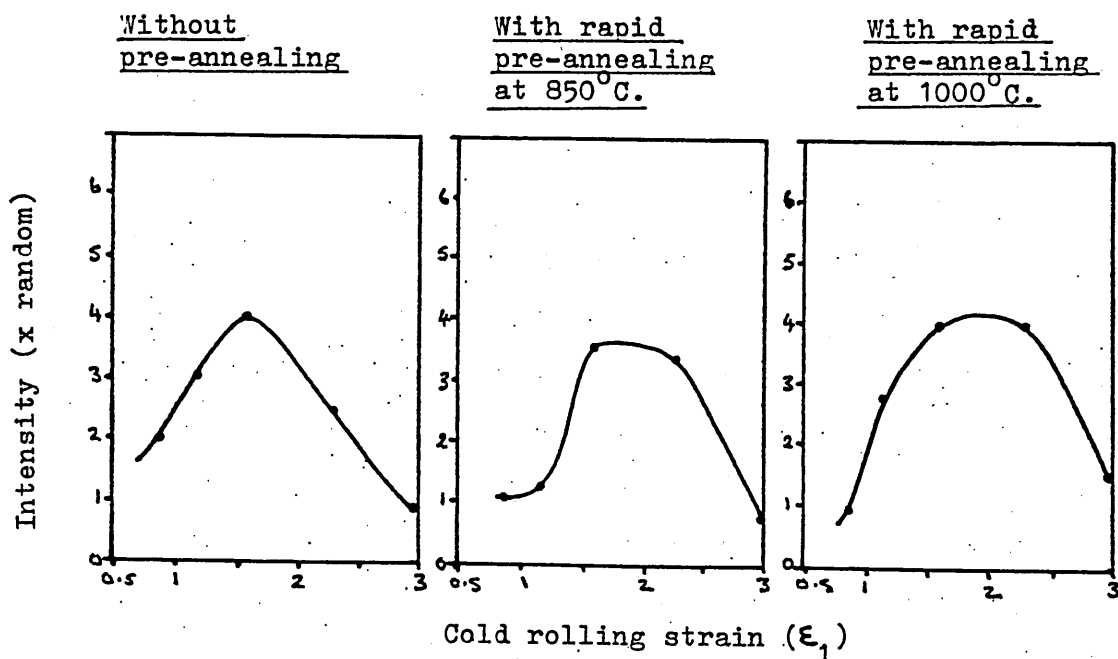
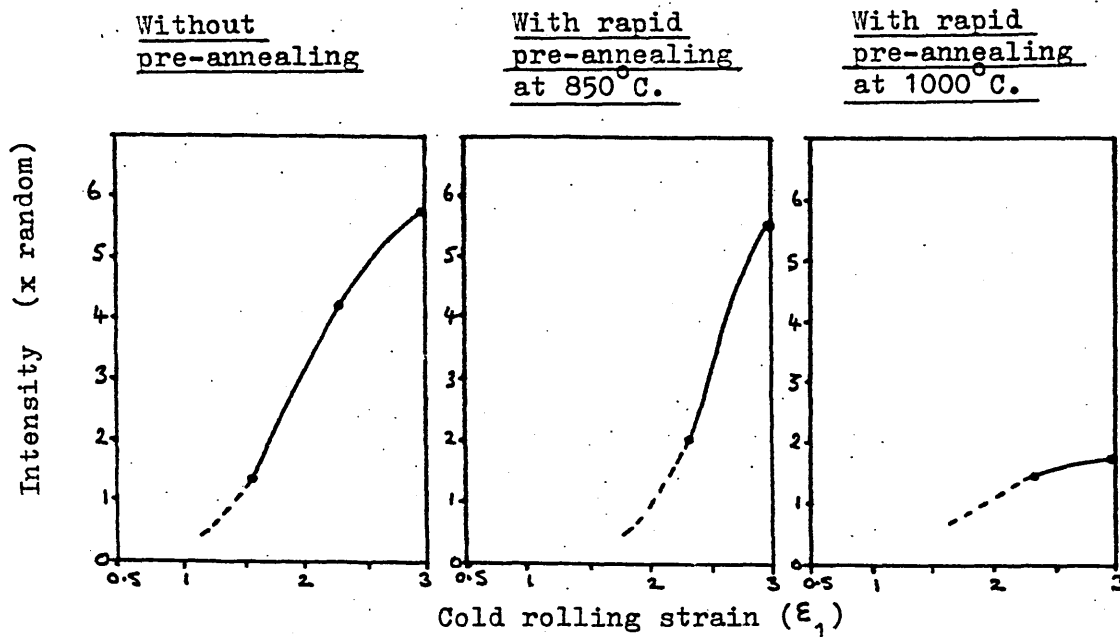


FIGURE 154 Variation of Intensity of the {554} <225> Orientation
with Cold Rolling Strain in Cold Rolled and
Annealed 430Ti (0.5Ti) Steel.

Rapid Final Annealing at 900°C (Heating rate ~ 5000°C hr⁻¹, AC)



Batch Final Annealing at 900°C (Heating rate = 50°C hr⁻¹, FC)

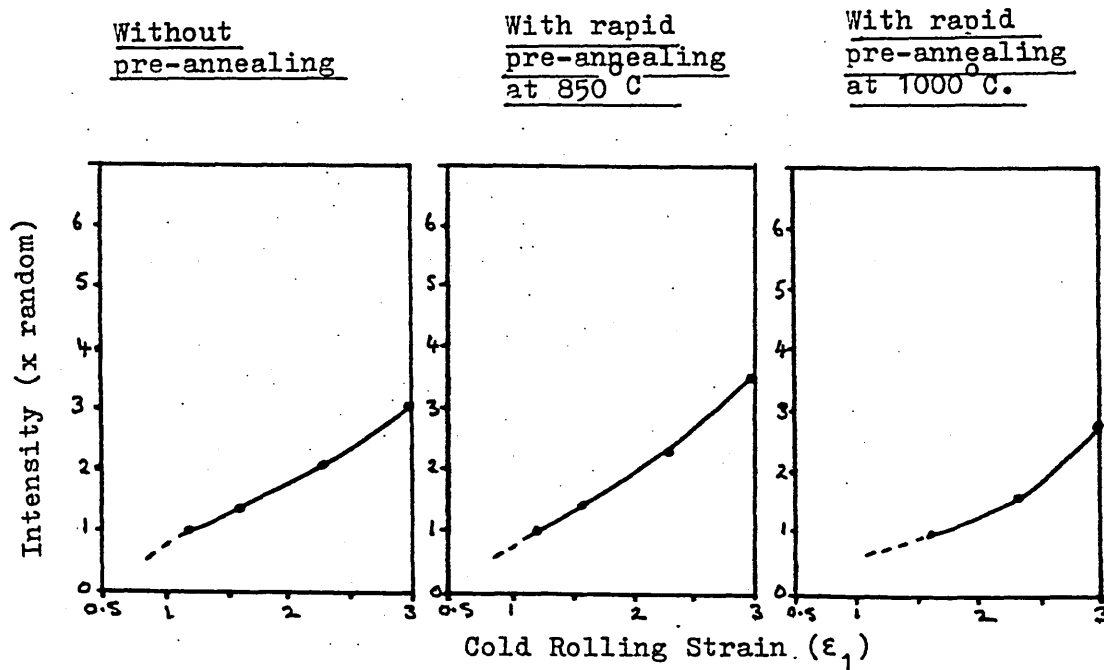
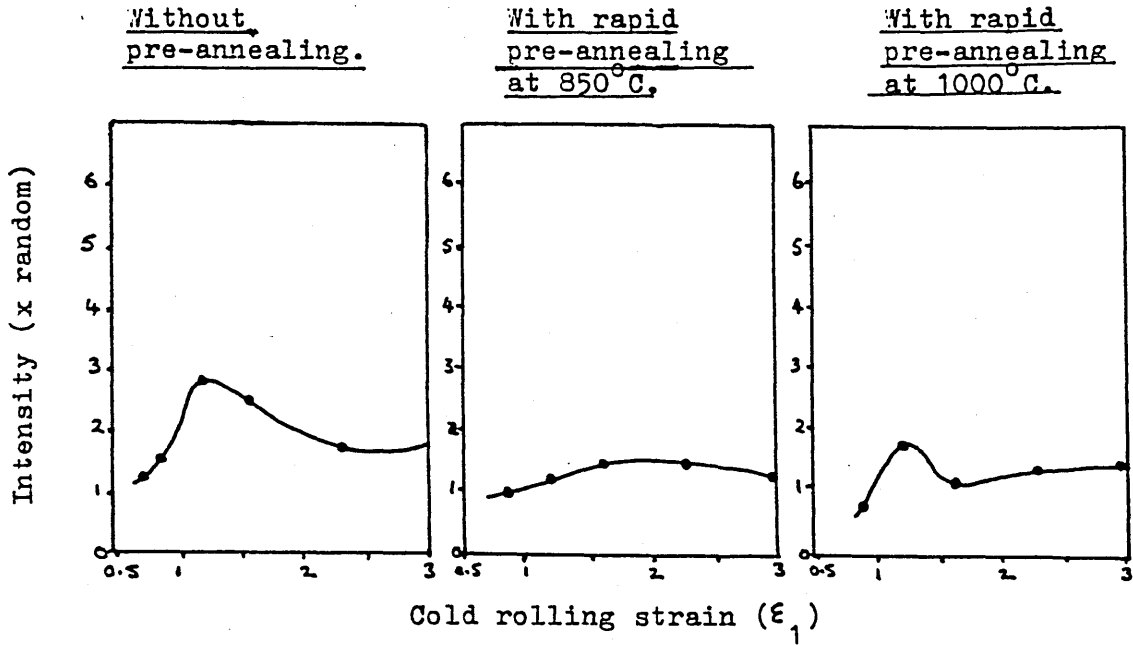


FIGURE 155 Variation of Intensity of the {223}<962> Orientation with Cold Rolling Strain in Cold Rolled and Annealed 430Ti (0.5Ti) Steel.

{100}<uvw>

Rapid Final Annealing at 900°C (Heating rate ~5000°C hr⁻¹, AC)



Batch Final Annealing at 900°C (Heating rate = 50°C hr⁻¹, FC)

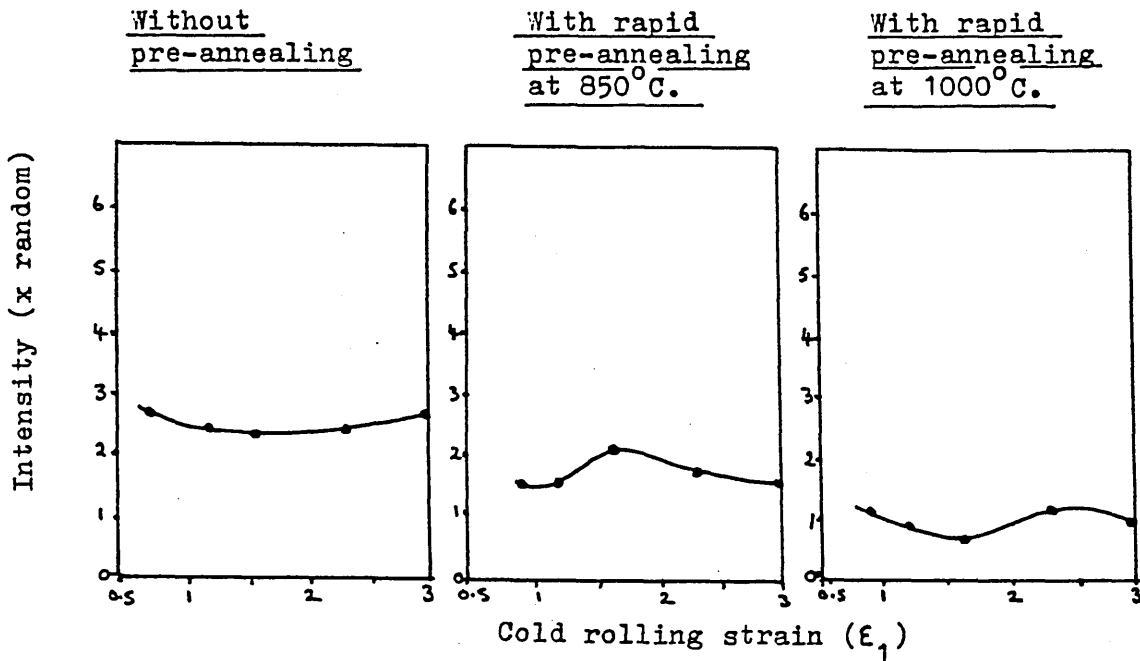


FIGURE 156 Variation of Intensity of the {100}<uvw> Orientation
with Cold Rolling Strain in Cold Rolled and
Annealed 430Ti (0.5Ti) Steel.

{554}<225>

- ——— Rapid final anneal at 900°C (Heating rate ~ 5000°C hr⁻¹, AC)
- - - - - Batch final anneal at 900°C (Heating rate = 50°C hr⁻¹, FC)

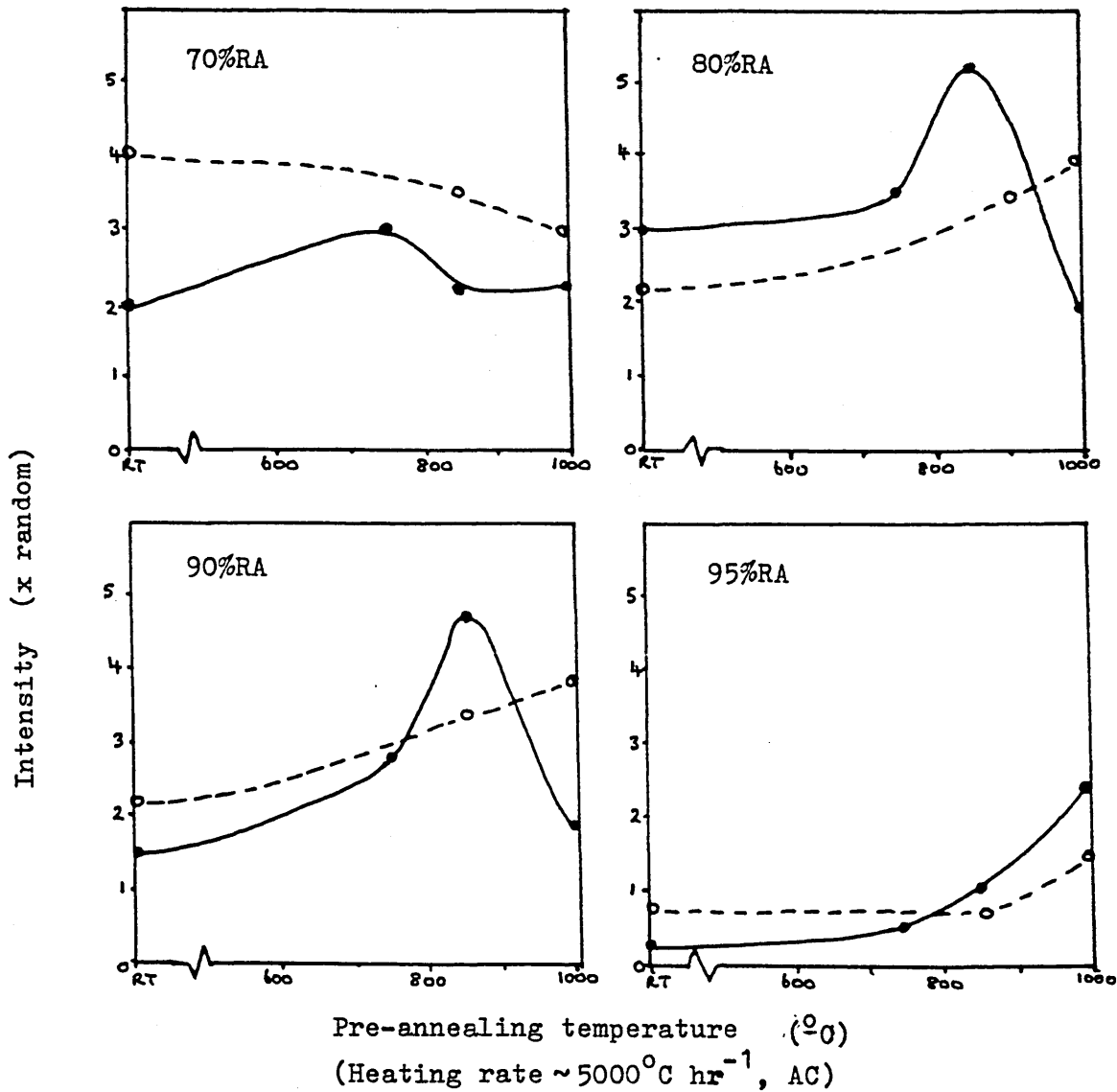


FIGURE 157 Variation of Intensity of the {554}<225> Orientation
with Pre-annealing Temperature in Cold Rolled and
Annealed 430Ti (0.5Ti) Steel.

{100}<uvw>

- ——— Rapid final annealing at 900°C (heating rate ~ 5000°C hr⁻¹, AC)
- - - - Batch final annealing at 900°C (heating rate = 50°C hr⁻¹, FC)

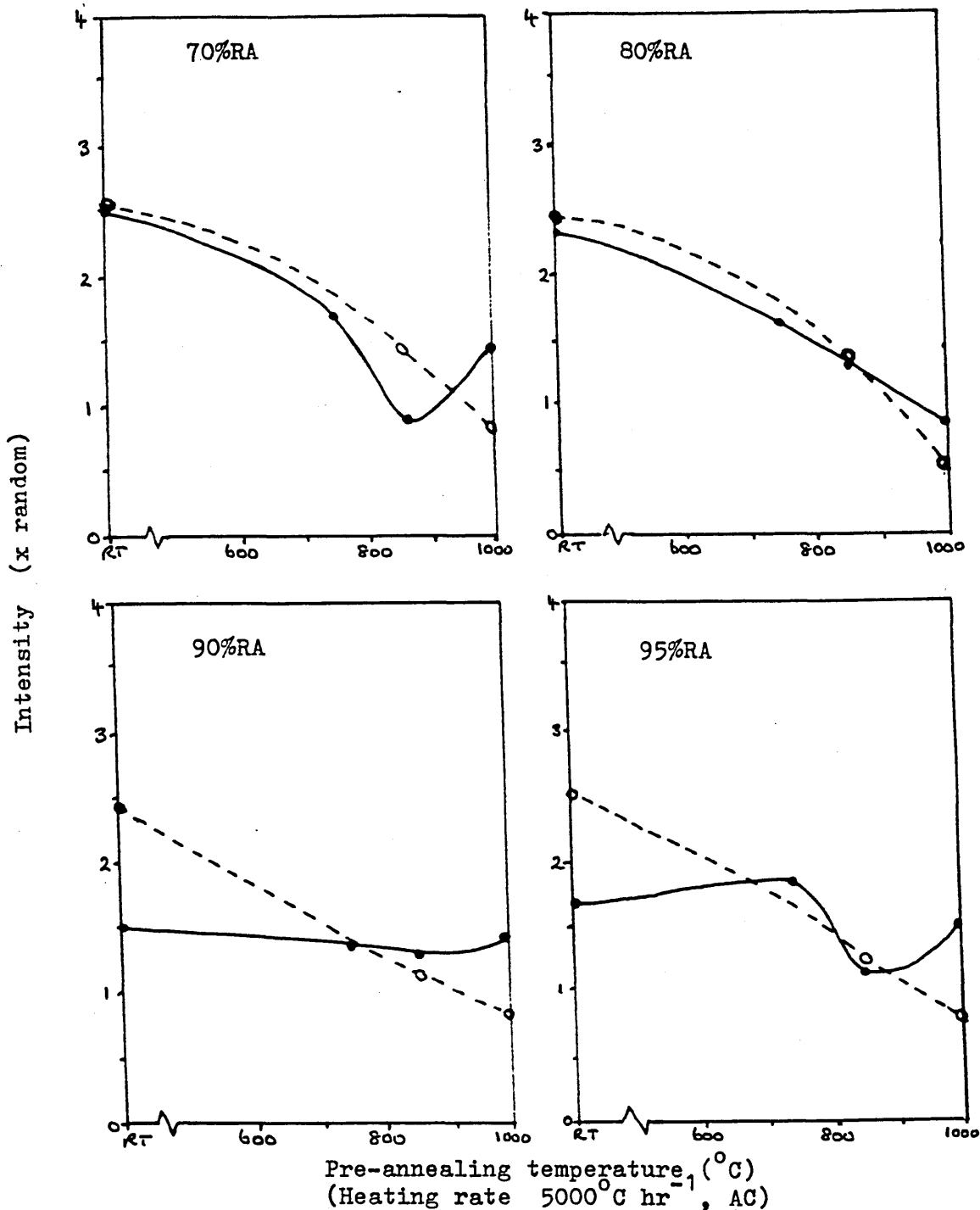


FIGURE 158 Variation of Intensity of the {100}<uvw> Orientation
with Pre-annealing Temperature in Cold Rolled and
Annealed 430Ti (0.5Ti) Steel.

- ——— Rapid pre-anneal at 850°C (heating rate ~5000°C hr⁻¹, AC)
- - - - Batch pre-anneal at 900°C (heating rate = 50°C hr⁻¹, FC)

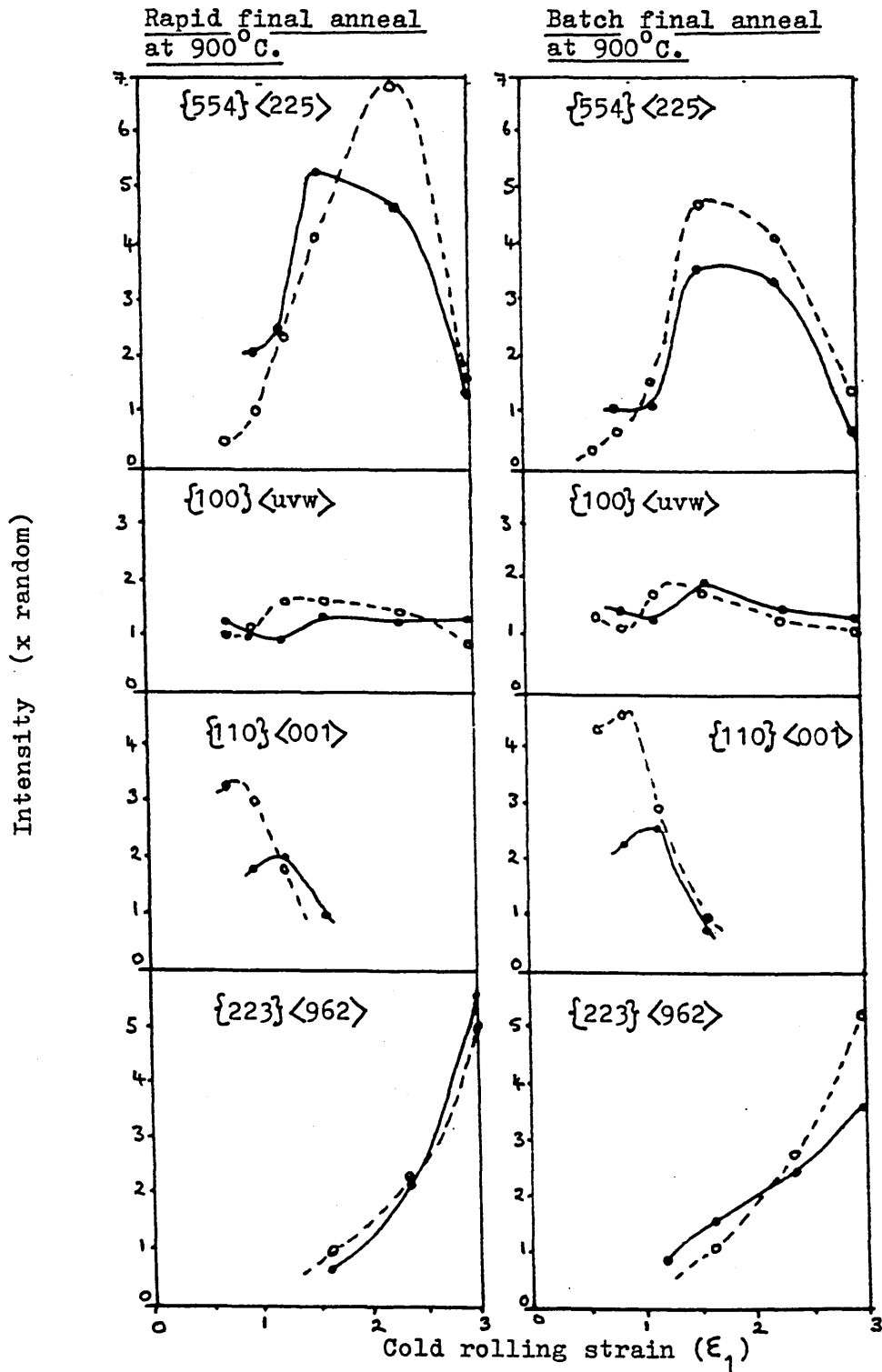


FIGURE 159 Variation of Intensities of the Main Orientations in Cold Rolled and Annealed 430Ti (0.5Ti) Steel with Cold Rolling Strain;- Rapid versus Batch Annealing.

- Commercial Line Pre-anneal (nominal 2mins. at $\sim 900^{\circ}\text{C}$)
- Commercial Batch Pre-anneal ($\sim 5\text{hrs. at } \sim 780^{\circ}\text{C, FC}$)

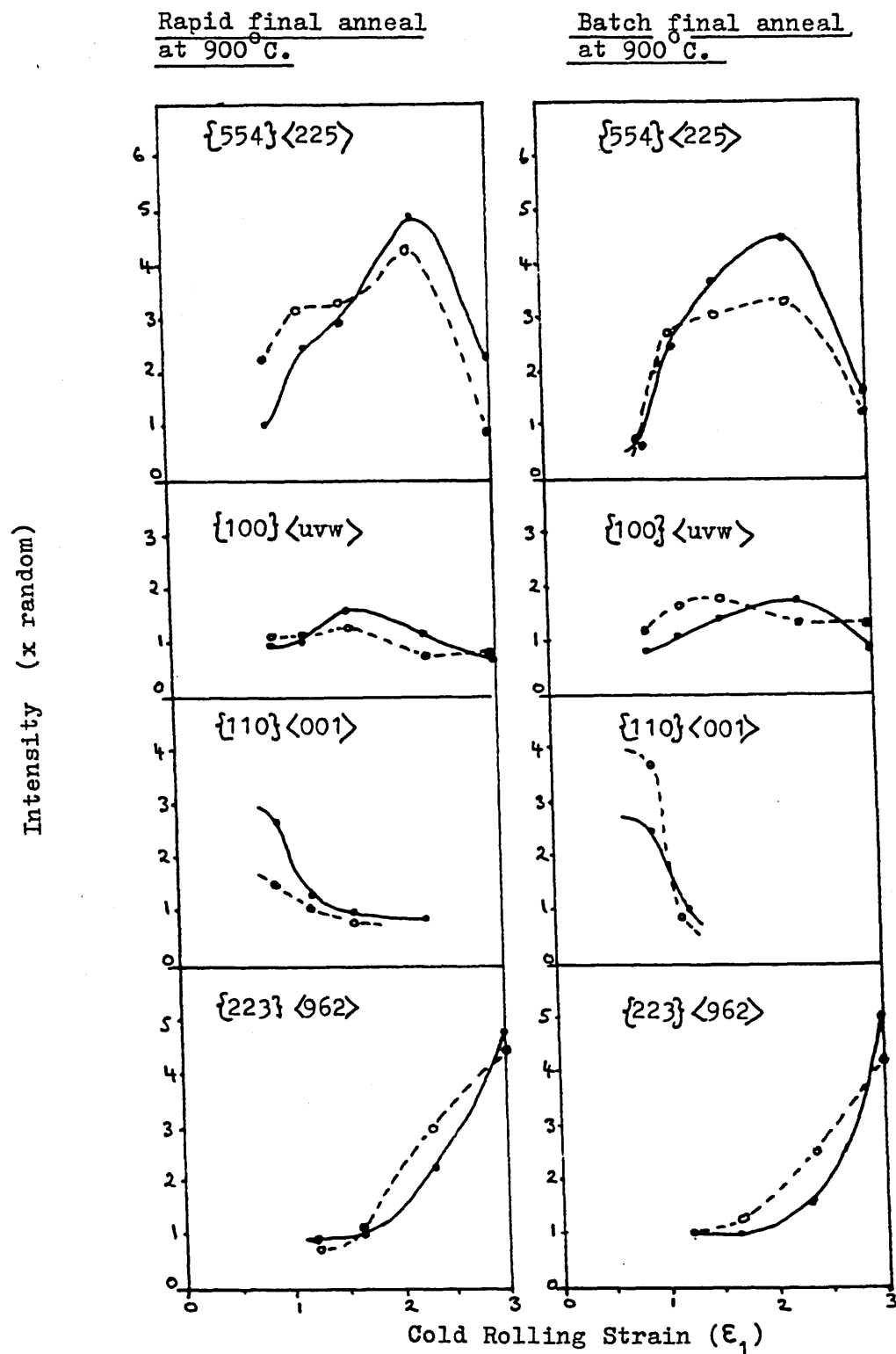


FIGURE 160 Variation of Intensities of the Main Orientations
in Cold Rolled and Annealed 430Ti (0.4Ti) Steel with
Cold Rolling Strain:- Rapid versus Batch Annealing.

- Rapid pre-anneal at 850°C (Heating rate ~5000°C hr⁻¹, AC)
- Batch pre-anneal at 850°C (Heating rate = 50°C hr⁻¹, FC)

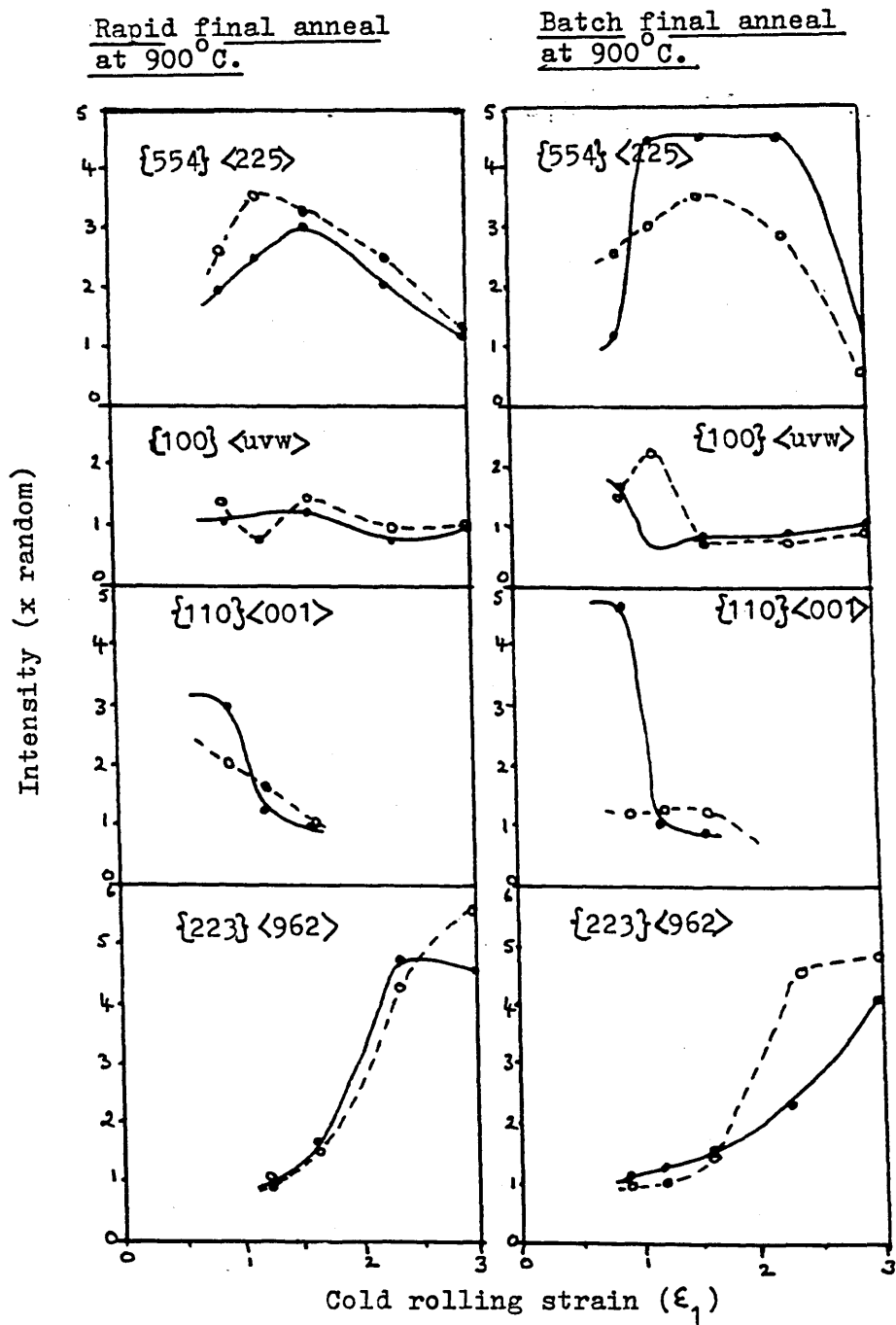


FIGURE 161

Variation in Intensities of the Main Orientations
in Cold Rolled and Annealed 430Ti (0.3Ti) Steel with
Cold Rolling Strain:- Rapid versus Batch Annealing.

$\{100\} \langle uvw \rangle$

- ——— Rapid pre-annealing before cold rolling
- - - - - Batch pre-annealing before cold rolling

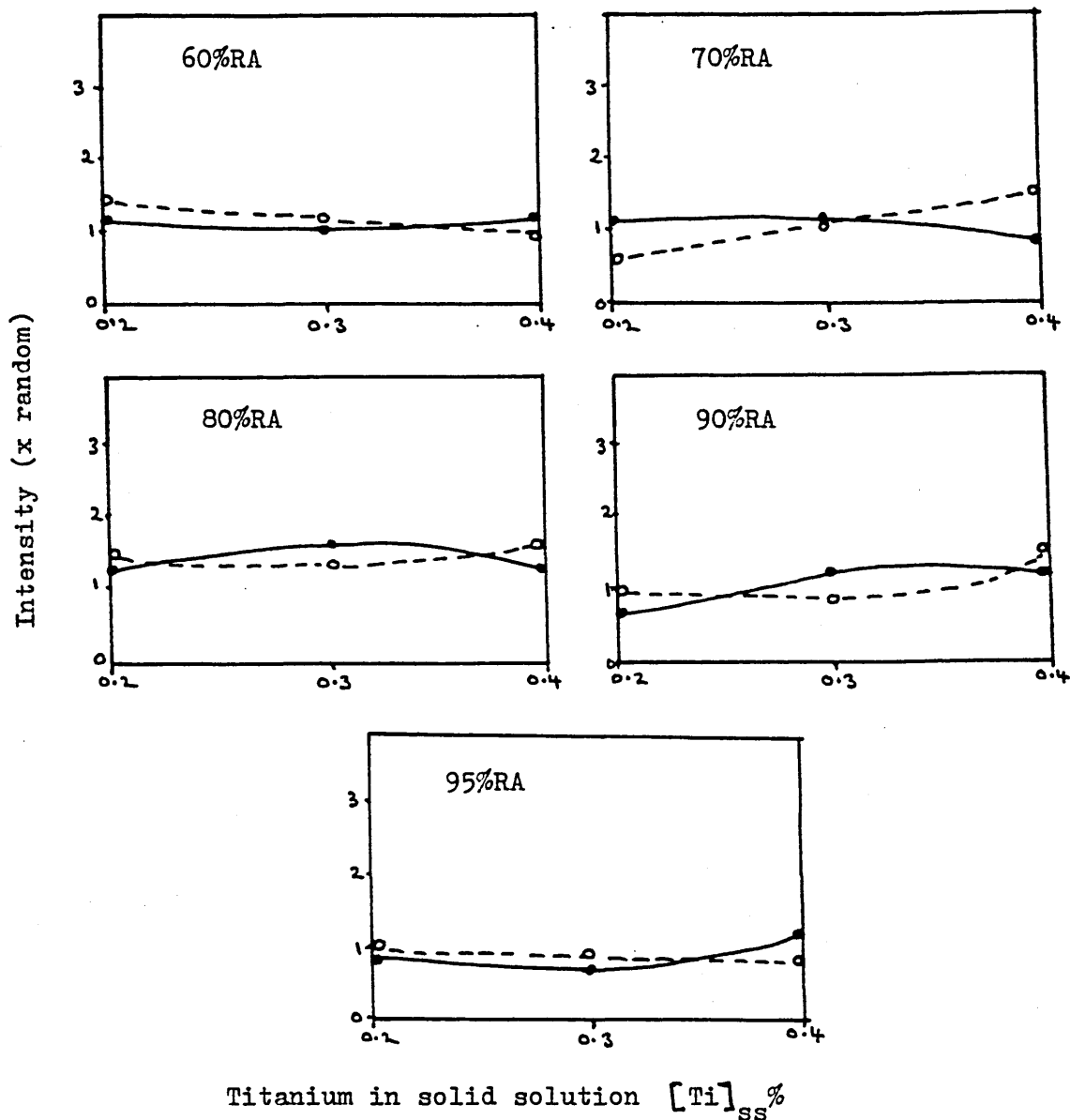


FIGURE 162 Variation of Intensity of the $\{100\} \langle uvw \rangle$ Orientation with $[Ti]_{ss}\%$ for Cold Rolled and Annealed 430Ti Steel after Cold Rolling and Rapid Final Annealing at 900°C.

$\{100\}\langle uvw \rangle$

●——Rapid pre-annealing before cold rolling
○---Batch pre-annealing before cold rolling

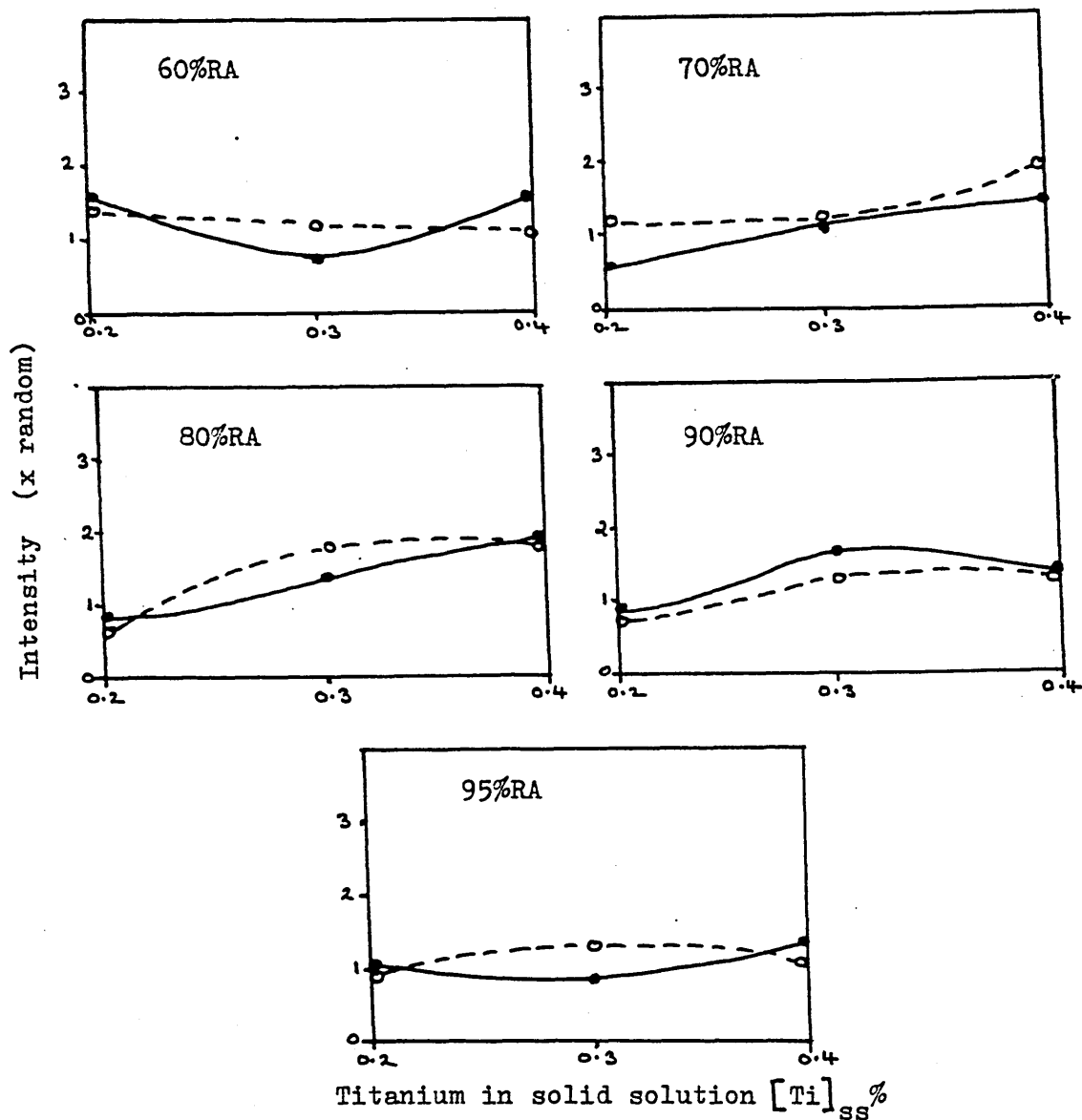


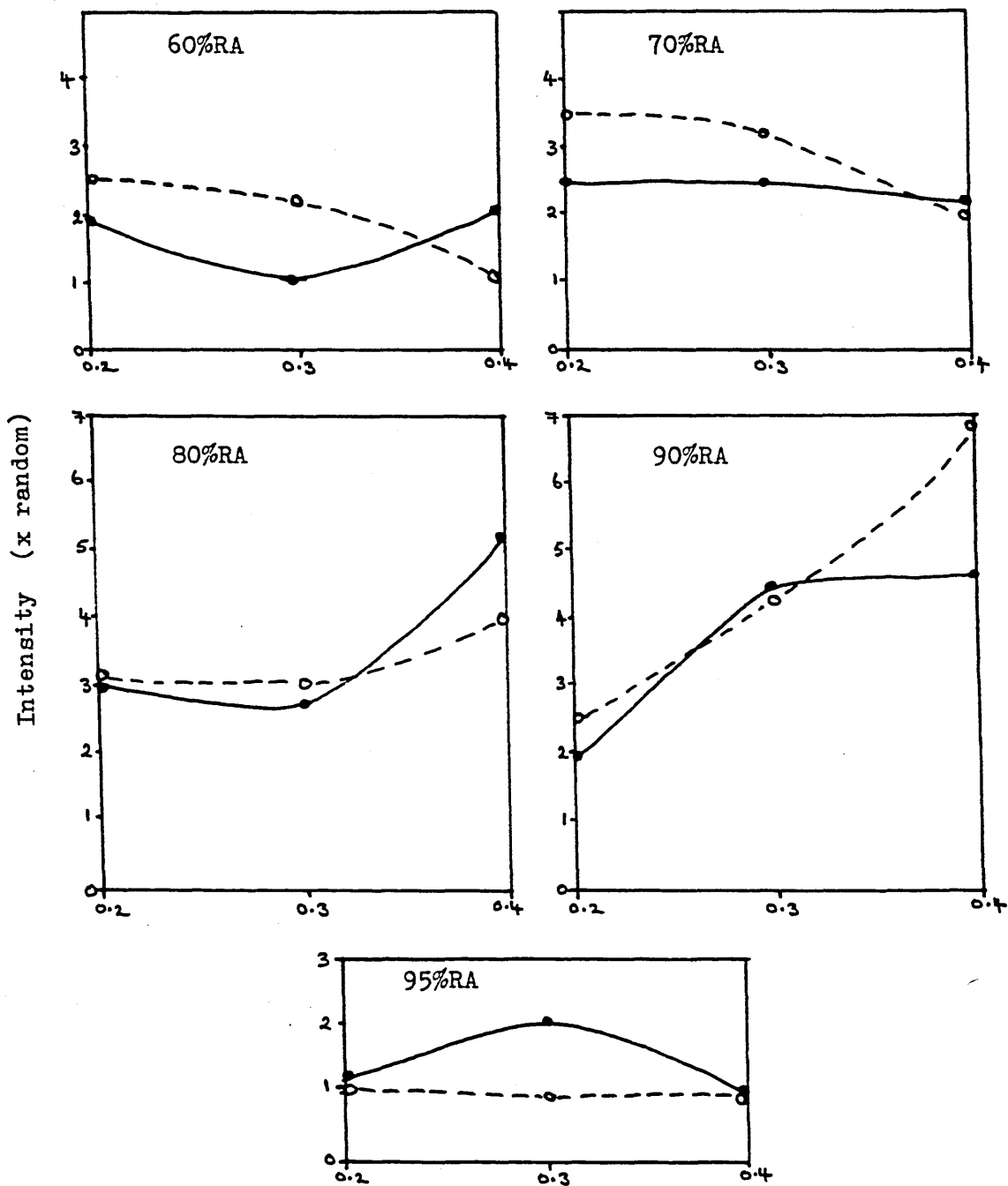
FIGURE 163

Variation of Intensity of the $\{100\}\langle uvw \rangle$ Orientation with $[Ti]_{SS}\%$ for 430Ti Steel after Cold Rolling and Batch Final Annealing at 900°C.

{554}<225>

●—Rapid pre-annealing before cold rolling

○---Batch pre-annealing before cold rolling



Titanium in solid solution [Ti]_{ss}%

FIGURE 164

Variation in Intensity of the {554}<225> Orientation with [Ti]_{ss}% for 430Ti Steel after Cold Rolling and Rapid Final Annealing at 900°C.

{554}<225>

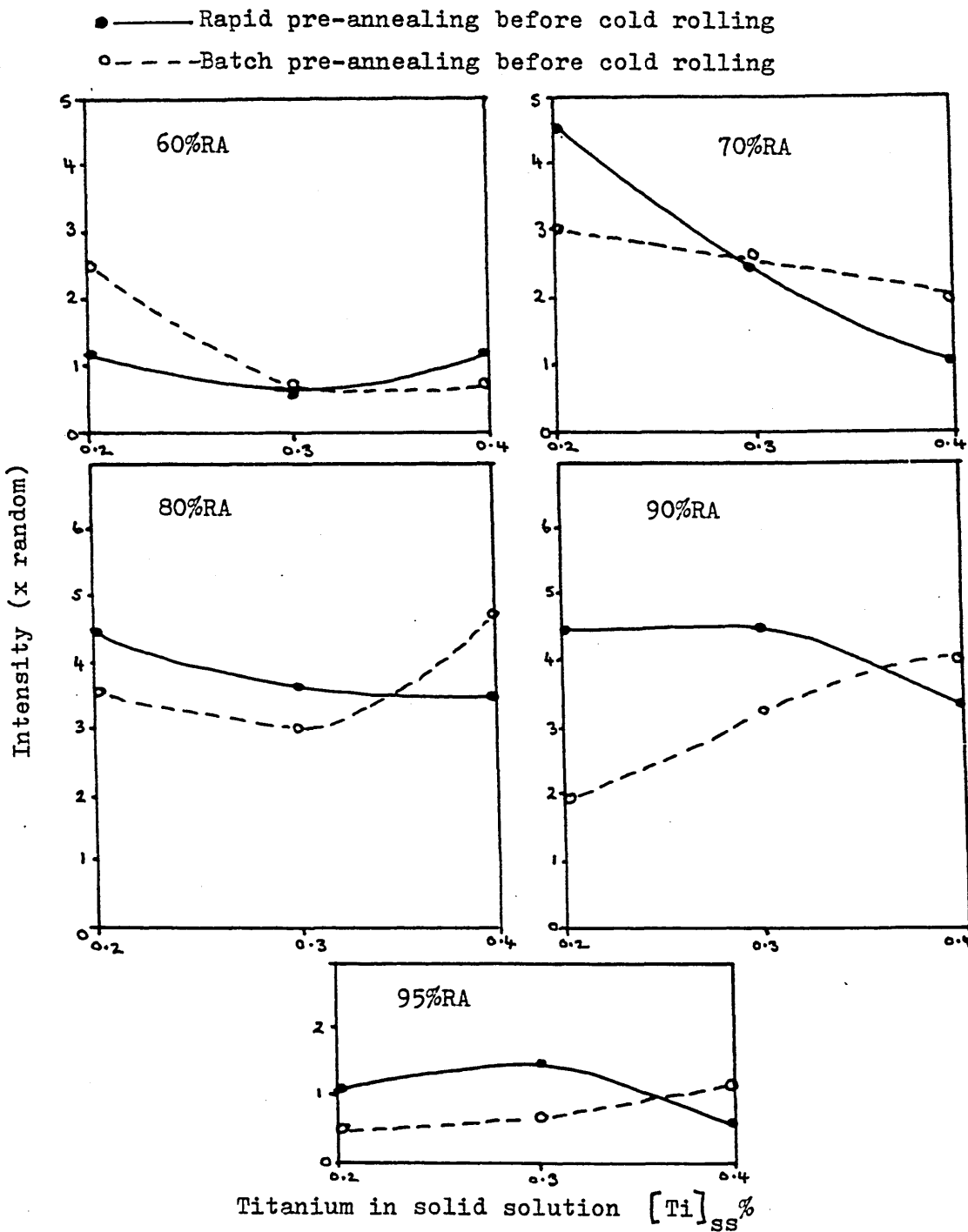
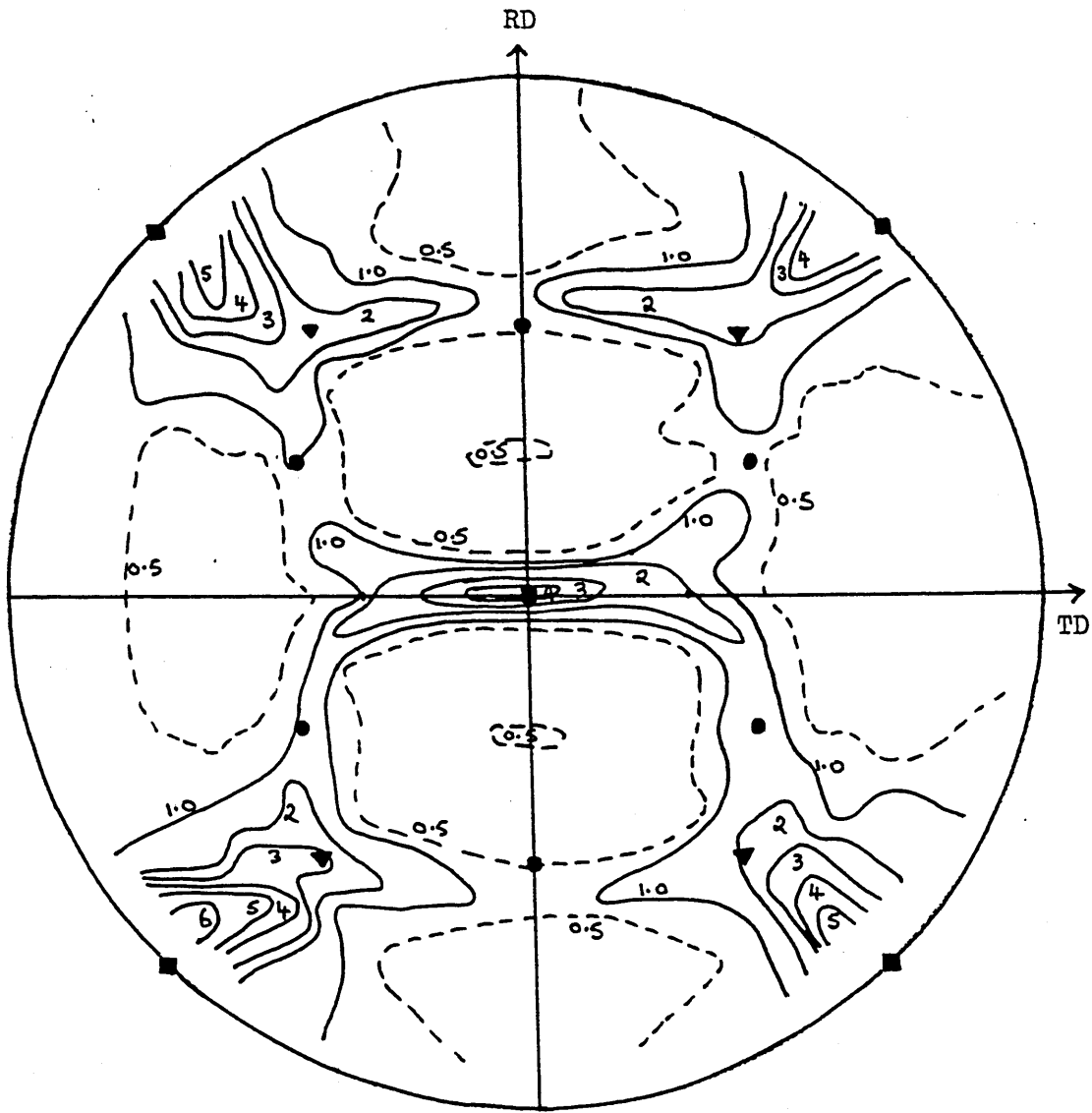


FIGURE 165

Variation of Intensity of the {554}<225> Orientation with $[Ti]_{ss}\%$ for 430Ti Steel after Cold Rolling and Batch Final Annealing at 900°C.



- $\{100\}\langle 011\rangle$
- $\{111\}\langle 112\rangle$
- ▼ $\{112\}\langle 110\rangle$

FIGURE 166 $\{200\}$ Pole Figure for 409 Steel after Hot Rolling, Cold Rolling to 95%RA and Rapid Final Annealing at 750°C.

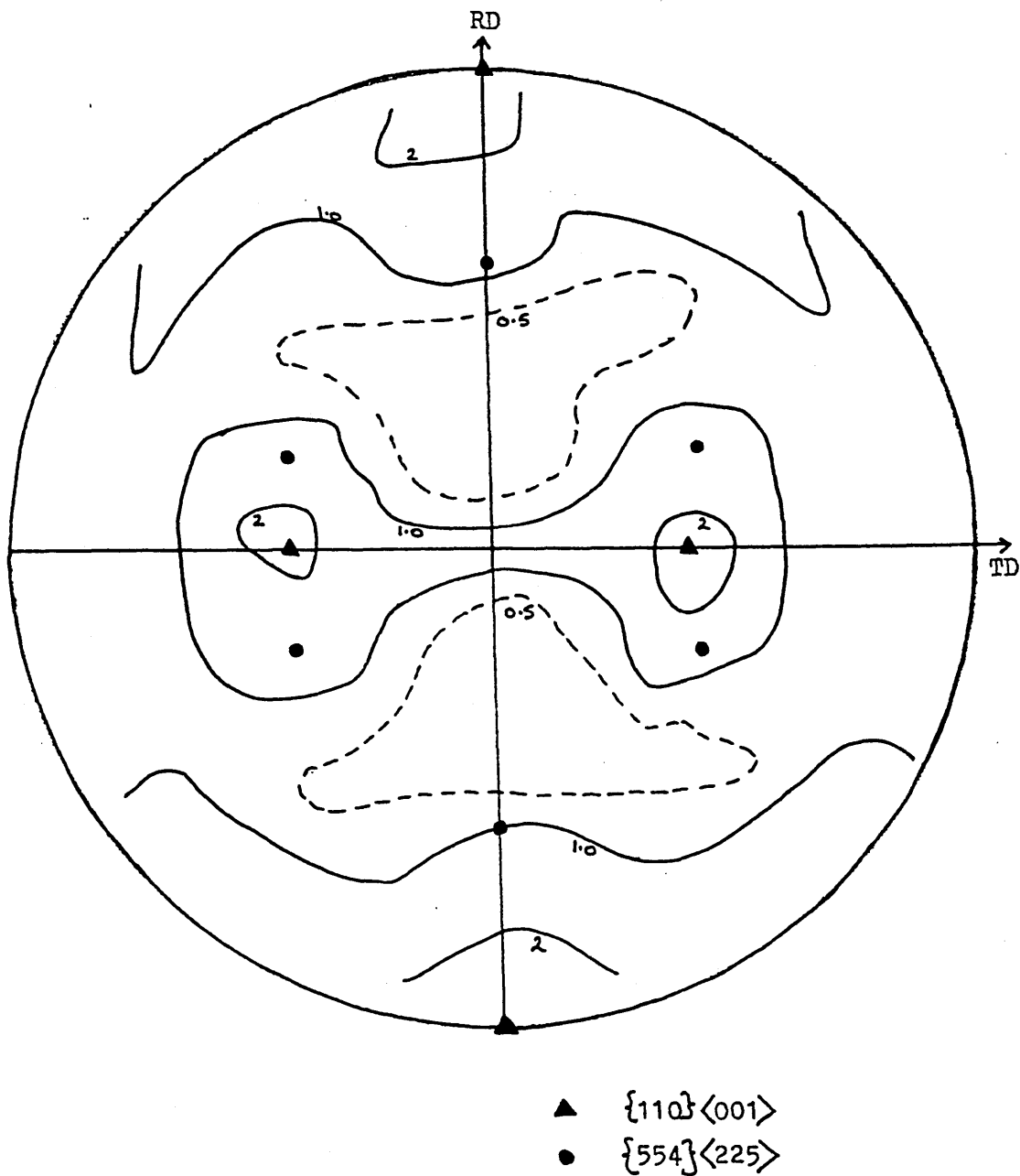


FIGURE 167 $\{200\}$ Pole Figure for 409 Steel after Hot Rolling,
Cold Rolling to 70%RA and Rapid Final Annealing
at 700°C.

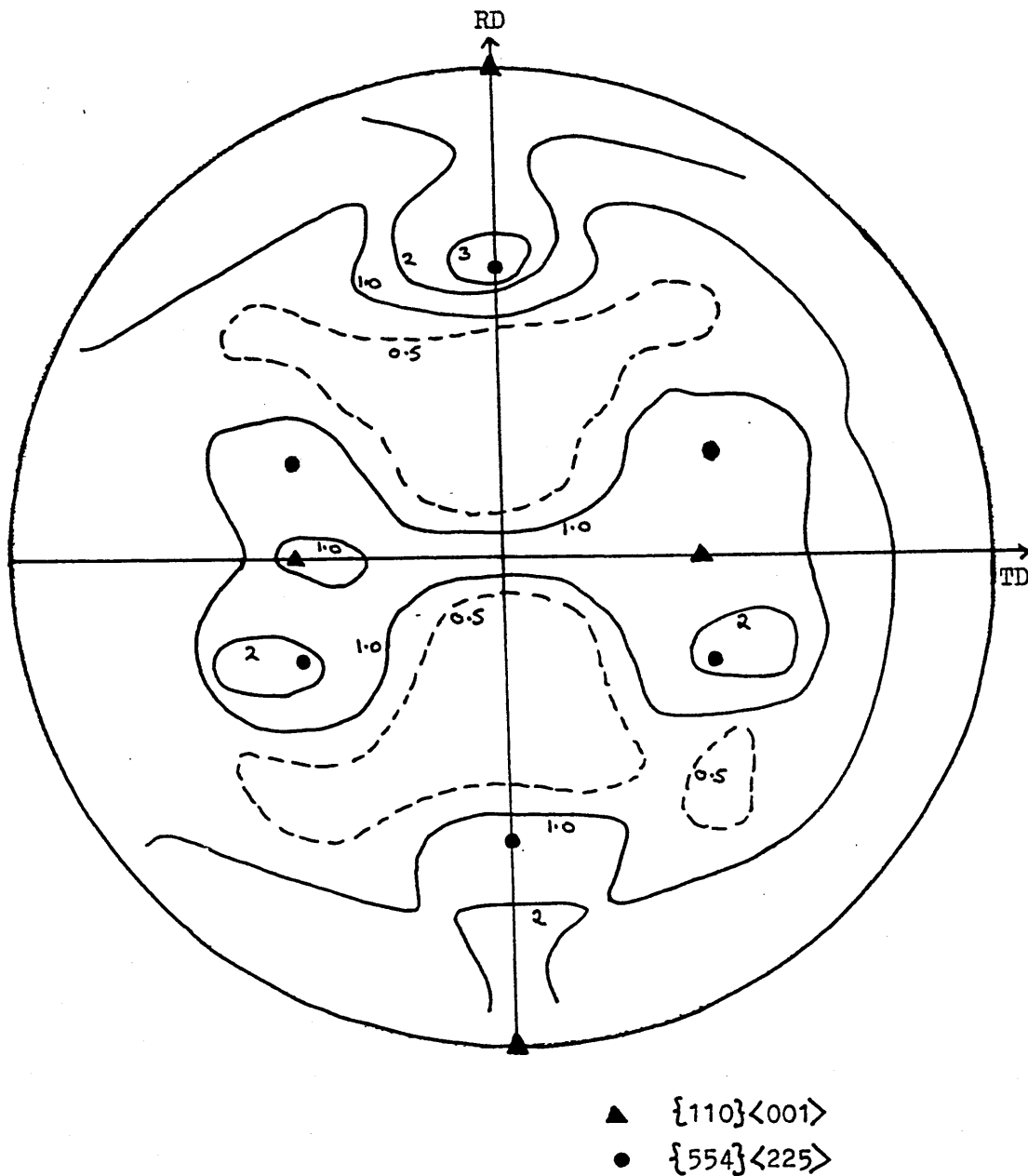


FIGURE 168

{200} Pole Figure for 409 Steel after Rapid
Pre-annealing at 850°C, Cold Rolling to 80%RA,
and Rapid Final Annealing at 900°C.

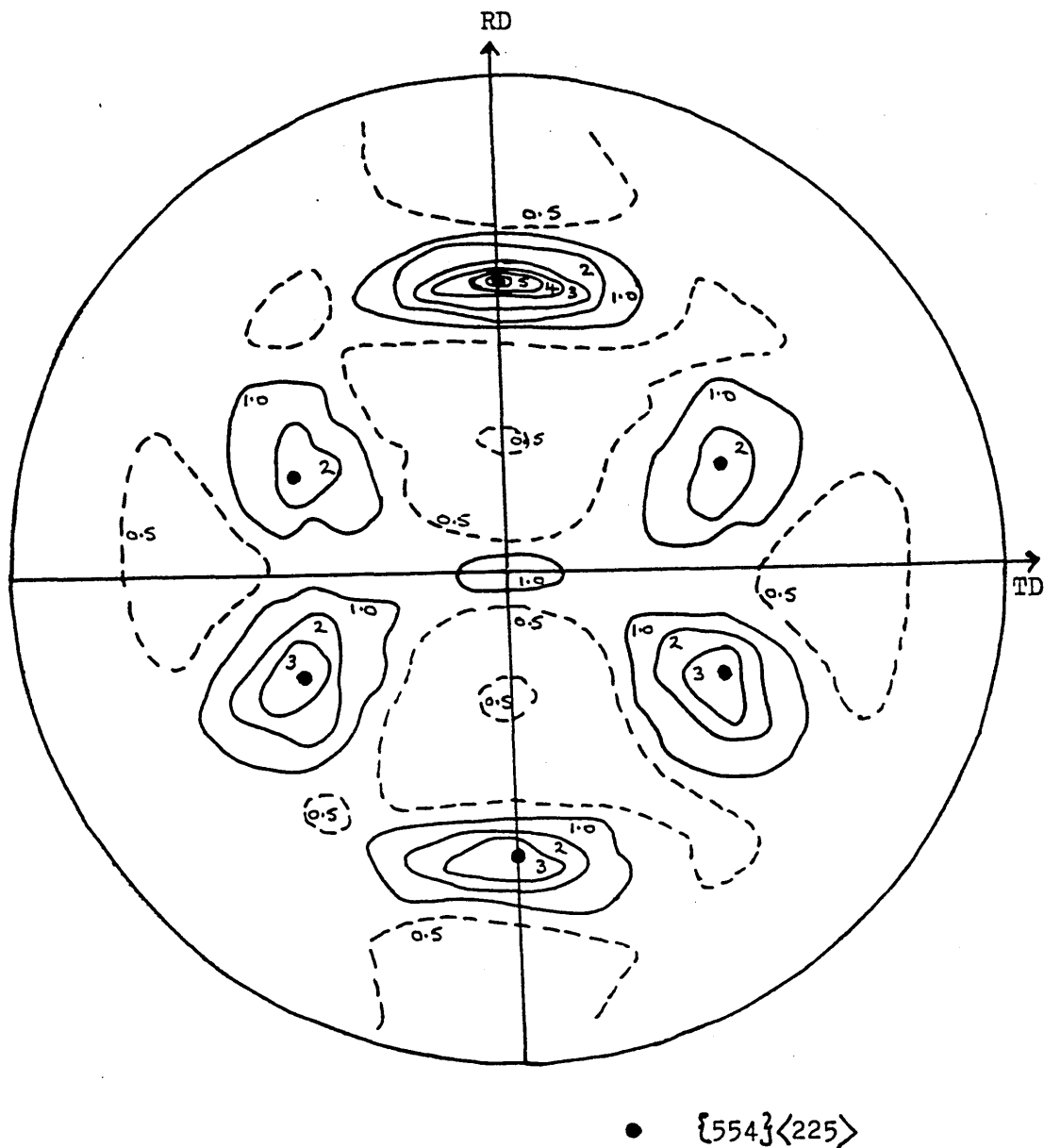
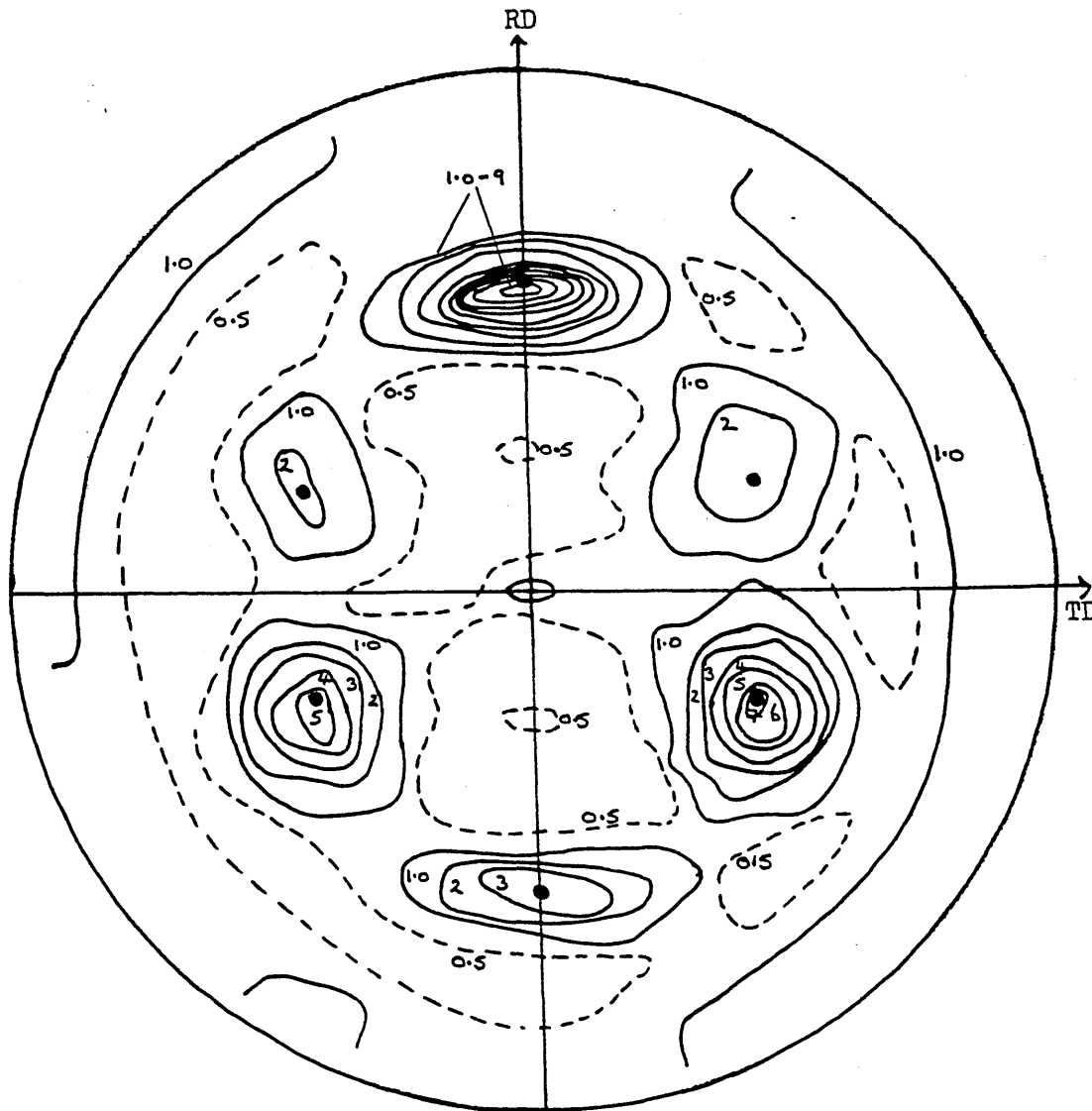


FIGURE 169

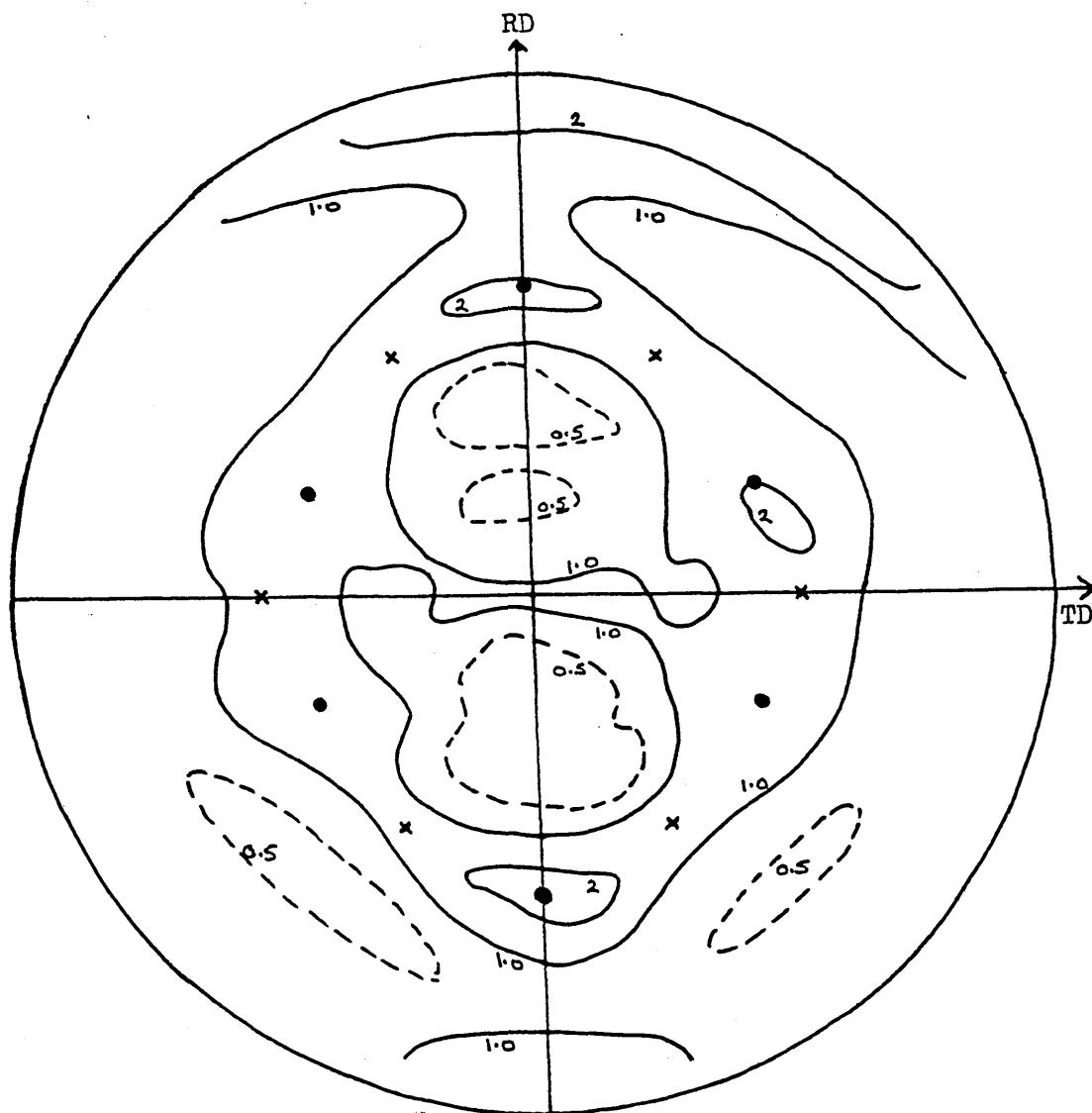
{200} Pole Figure for 409 Steel after Rapid
Pre-annealing at 850°C, Cold Rolling to 90%RA
and Rapid Final Annealing at 900°C.



• $\{554\}\langle 225 \rangle$

FIGURE 170

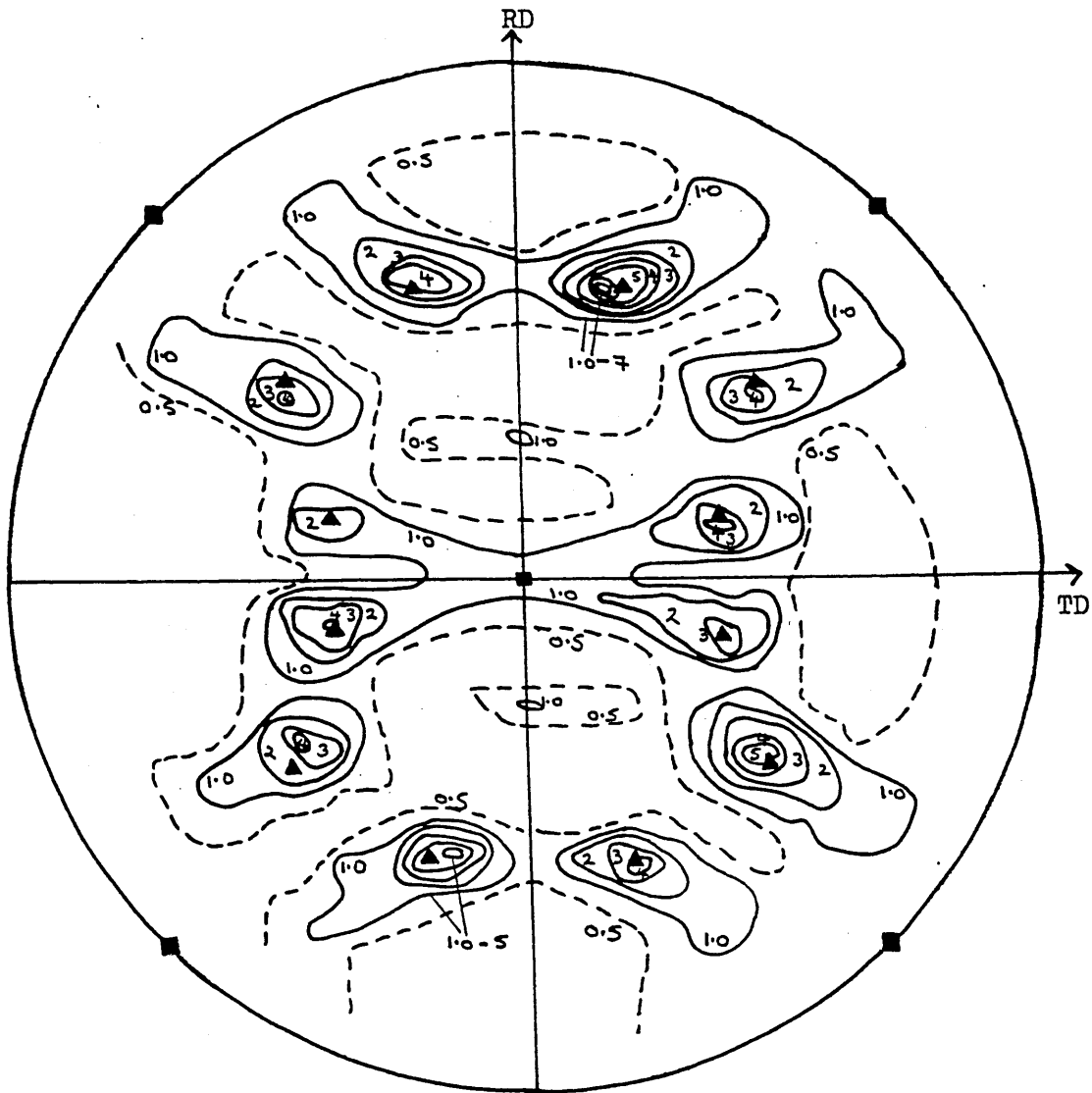
$\{200\}$ Pole Figure for 409 Steel after Batch
Pre-annealing at 850°C , Cold Rolling to 90%RA
and Rapid Final Annealing at 900°C .



- $\{554\}\langle 225 \rangle$
- x $\{111\}\langle 110 \rangle$

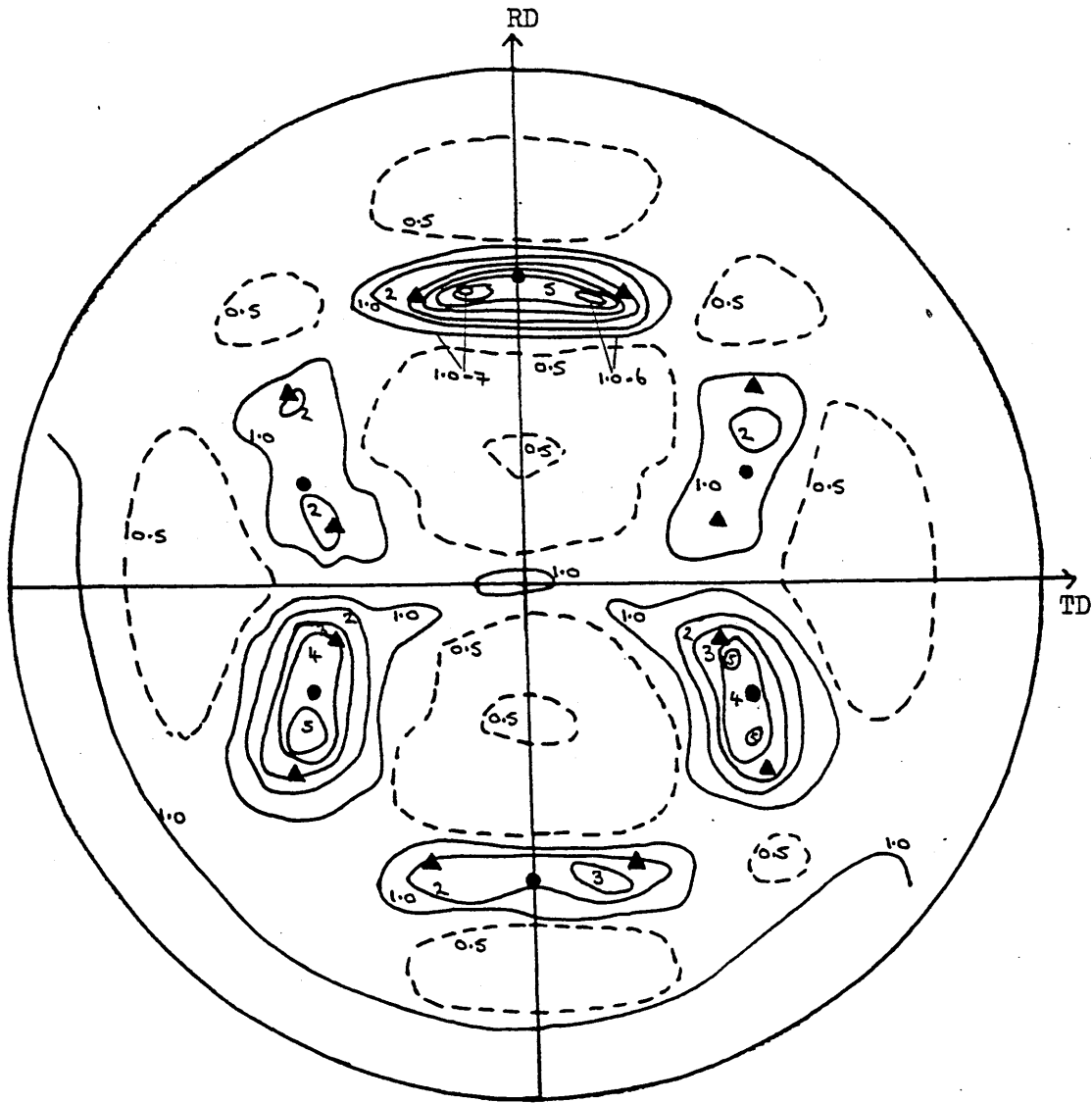
FIGURE 171

$\{200\}$ Pole Figure for 409 Steel after Rapid
Pre-annealing at 1000°C , Cold Rolling to 90%RA
and Rapid Final Annealing at 900°C .



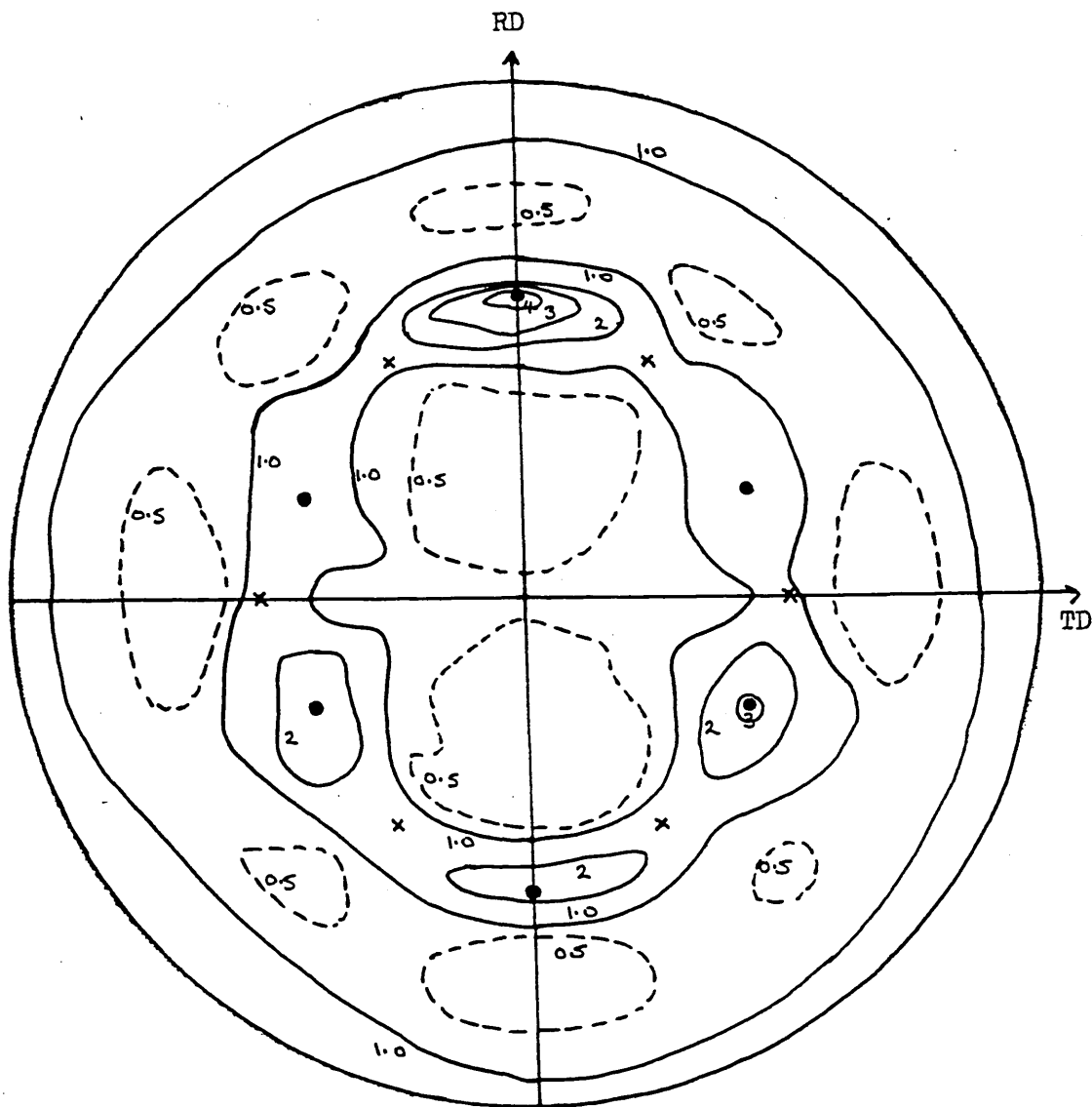
■ $\{100\}\langle 011\rangle$
 ▲ $\{223\}\langle 962\rangle$

FIGURE 172 $\{200\}$ Pole Figure for 409 Steel after Hot Rolling,
Cold Rolling to 95%RA and Rapid Final Annealing
at 900°C.



- {554}<225>
- ▲ {223}<962>

FIGURE 173 {200} Pole Figure for 409 Steel after Rapid
Pre-annealing at 850°C, Cold Rolling to 95%RA
and Rapid Final Annealing at 900°C.



- $\{554\}\langle 225\rangle$
- × $\{111\}\langle 110\rangle$

FIGURE 174 $\{200\}$ Pole Figure for 409 Steel after Rapid Pre-annealing at 1000°C , Cold Rolling to 95%RA and Rapid Final Annealing at 900°C .

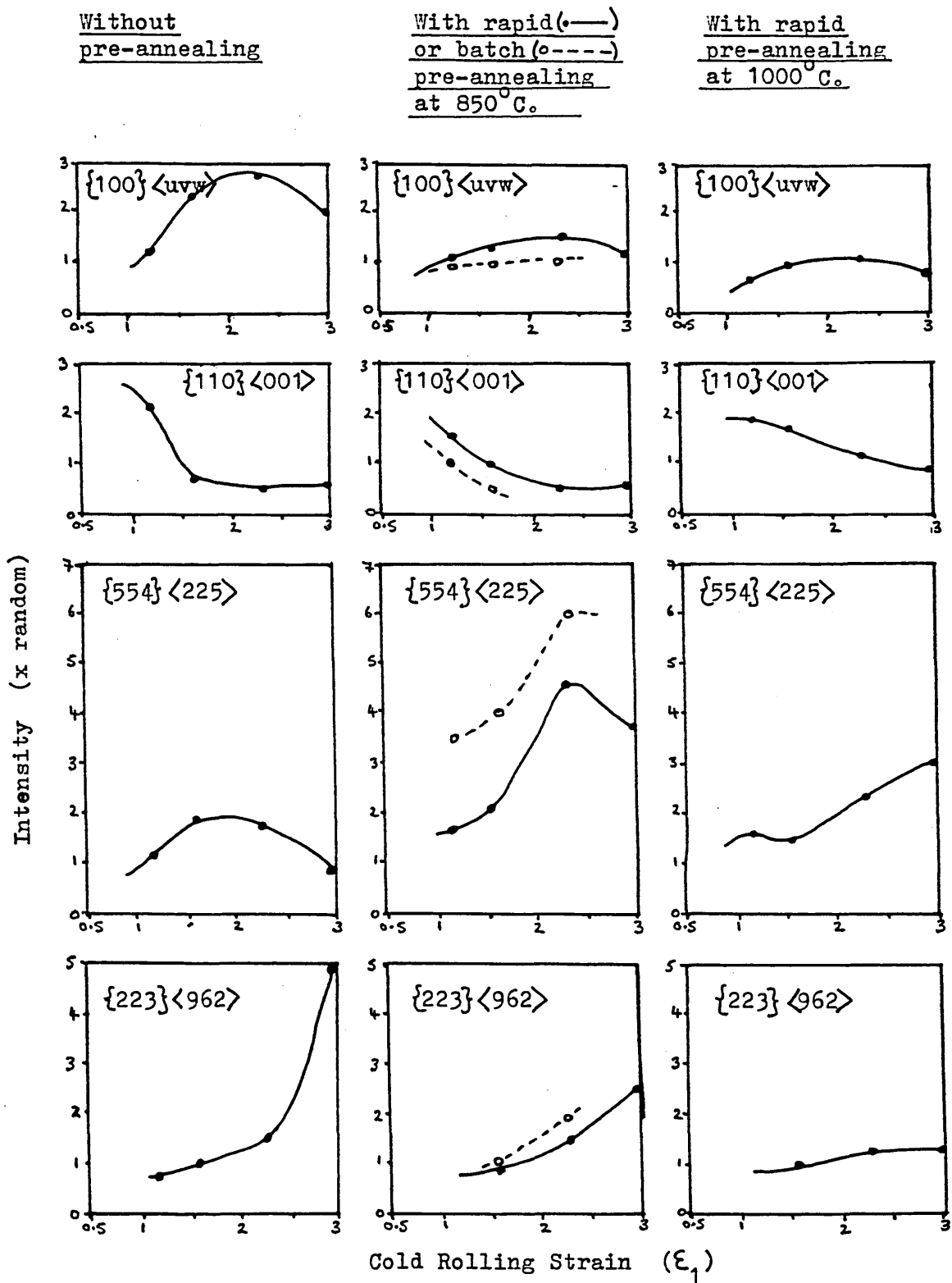


FIGURE 175

Variation of Intensities of the Main Orientations with Cold Rolling Strain for 409 Steel after Cold Rolling and Rapid Final Annealing at 900° C.

- × 430 Steel
- 430Ti Steel
- ▲ 409 Steel

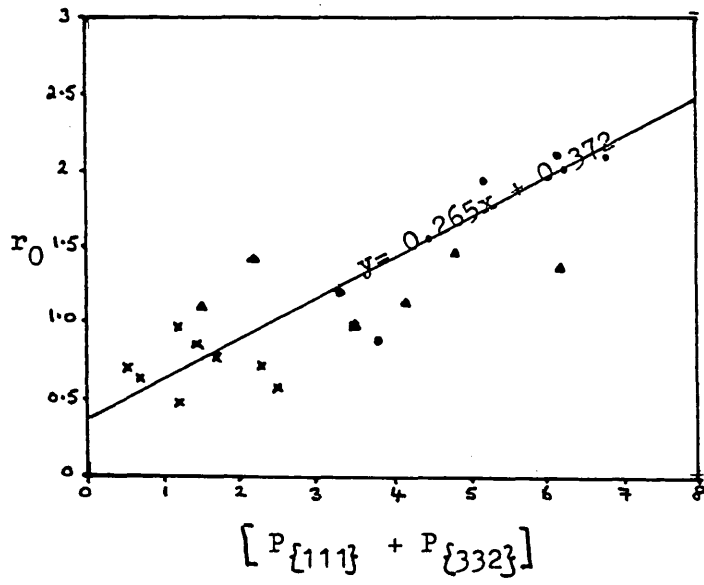
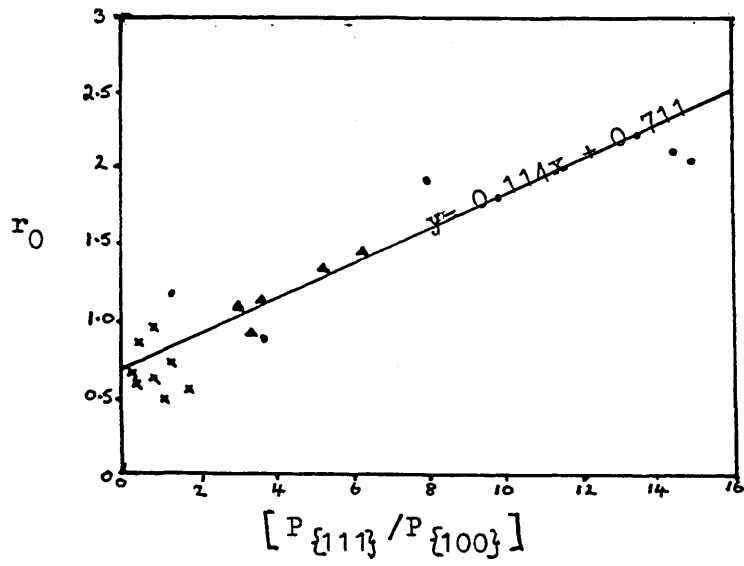


FIGURE 176 Variation of r_0 -Value with Texture Parameters.

- x 430 Steel
- 430T1 Steel
- ▲ 409 Steel

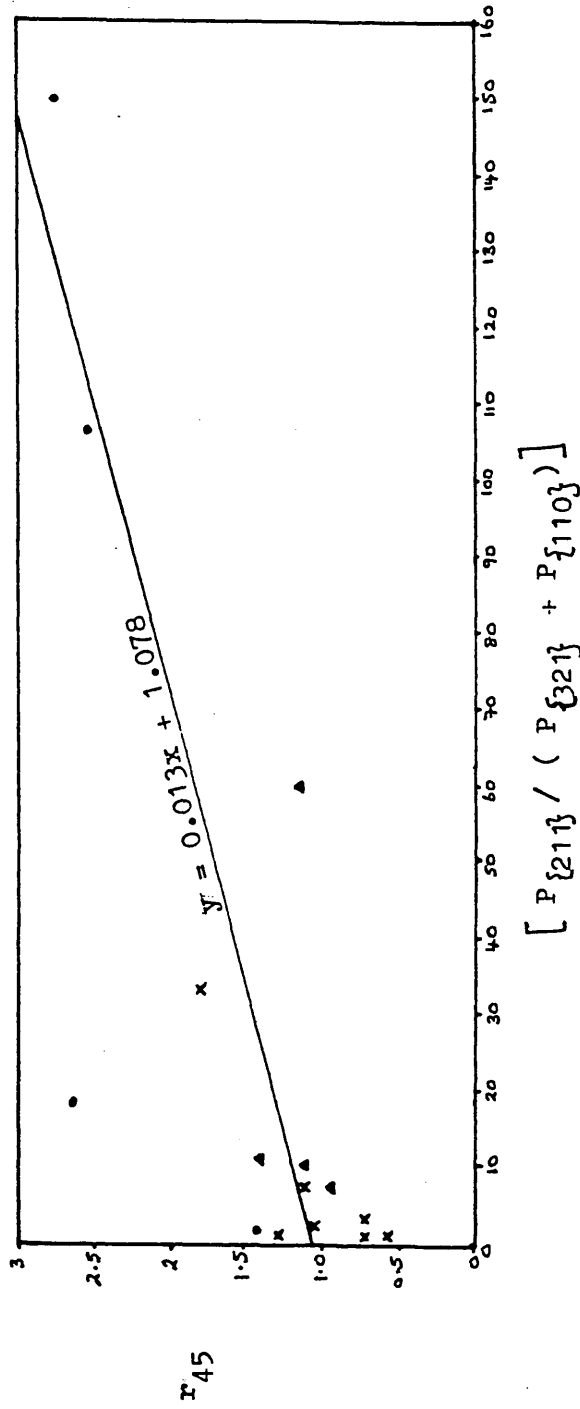


FIGURE 177 Variation of r_{45} -Values with Texture Parameters.

- x 430 Steel
- ▲ 409 Steel
- 430Ti Steel

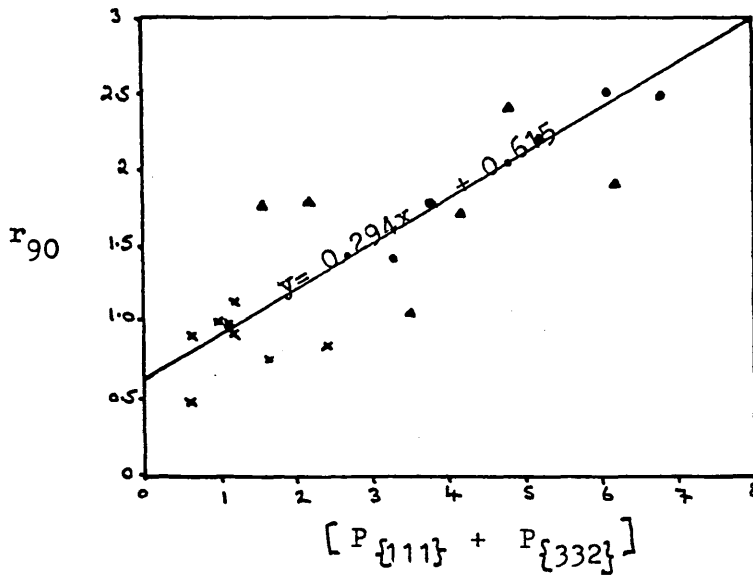
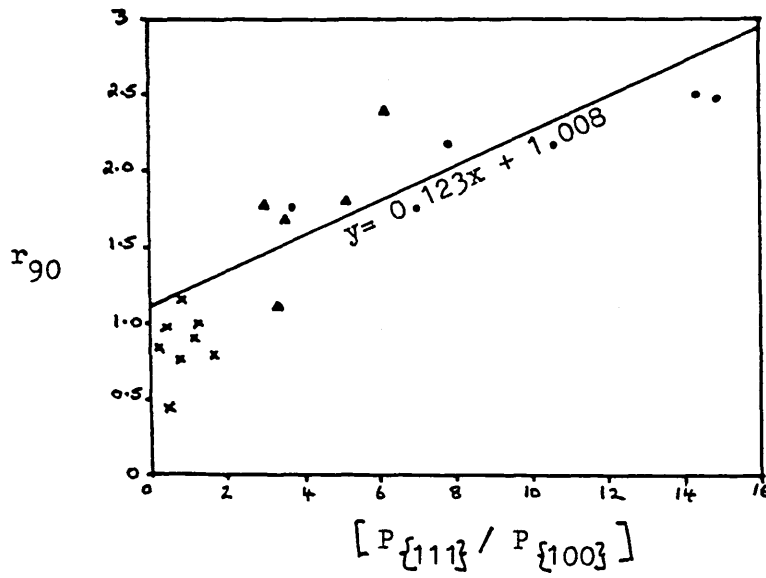


FIGURE 178 Variation of r_{90} -Values with Texture Parameters.

- * 430 Steel
- 430Ti Steel
- ▲ 409 Steel

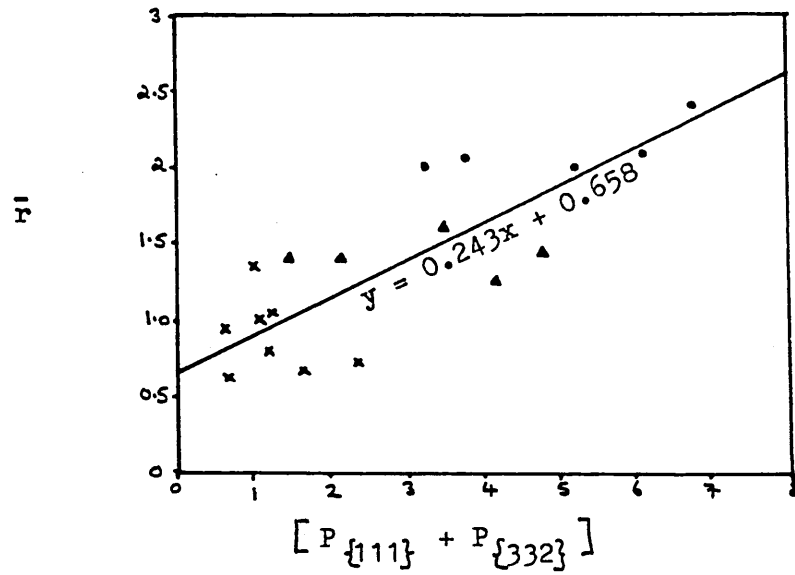
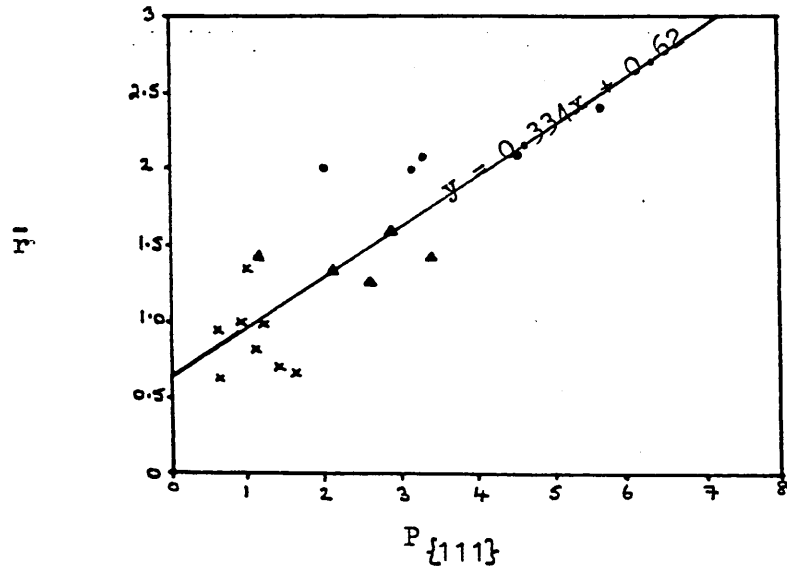


FIGURE 179 Variation of \bar{r} -Value with Texture Parameters.

35/3



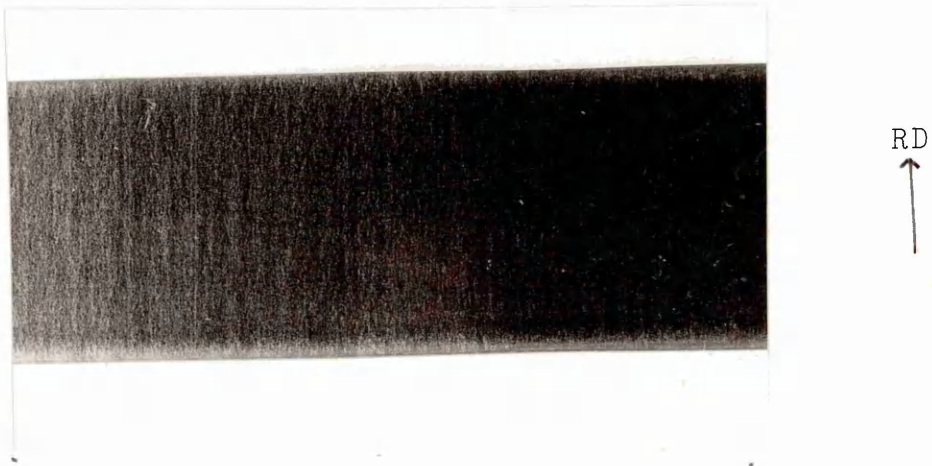
Strained at 0° to RD

35/9



Strained at 45° to RD

35/6



Strained at 90° to RD

FIG.180 SEVERE ROPING IN 1.15mm THICK 430 SHEET

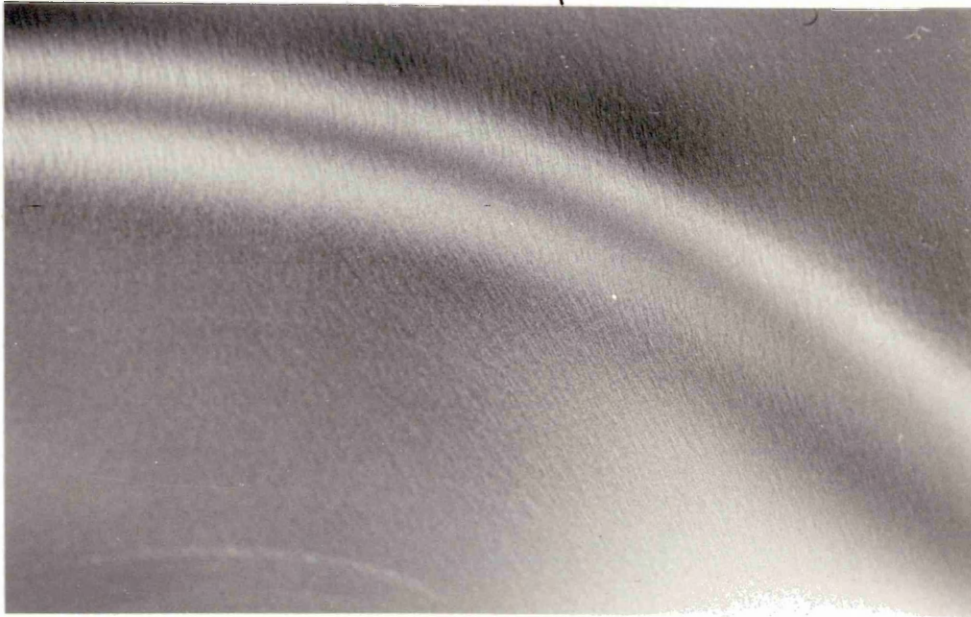
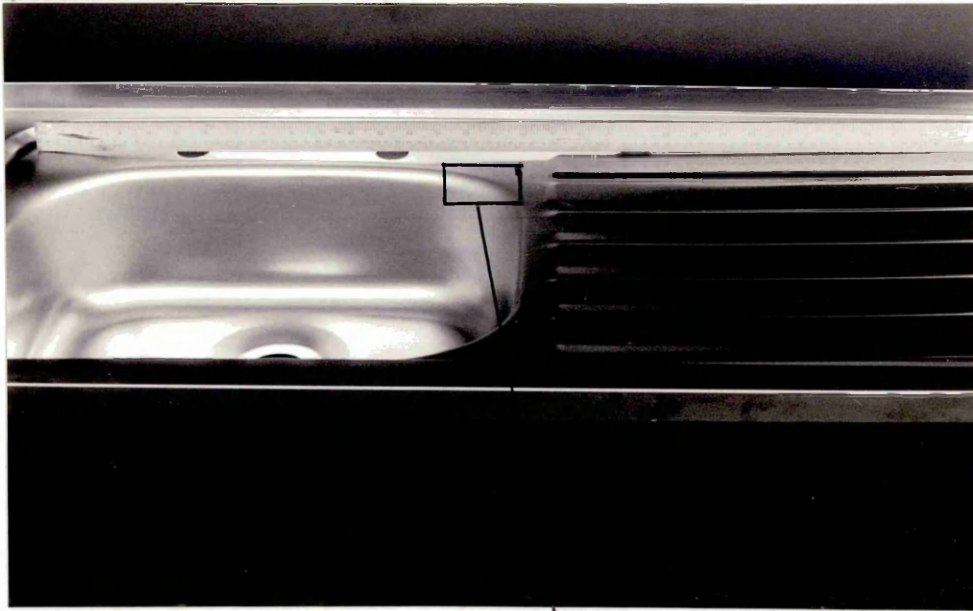


FIG.181 ROPING IN 17% Cr, Ti-STABILISED (430 Ti)
FERRITIC STAINLESS STEEL SINK

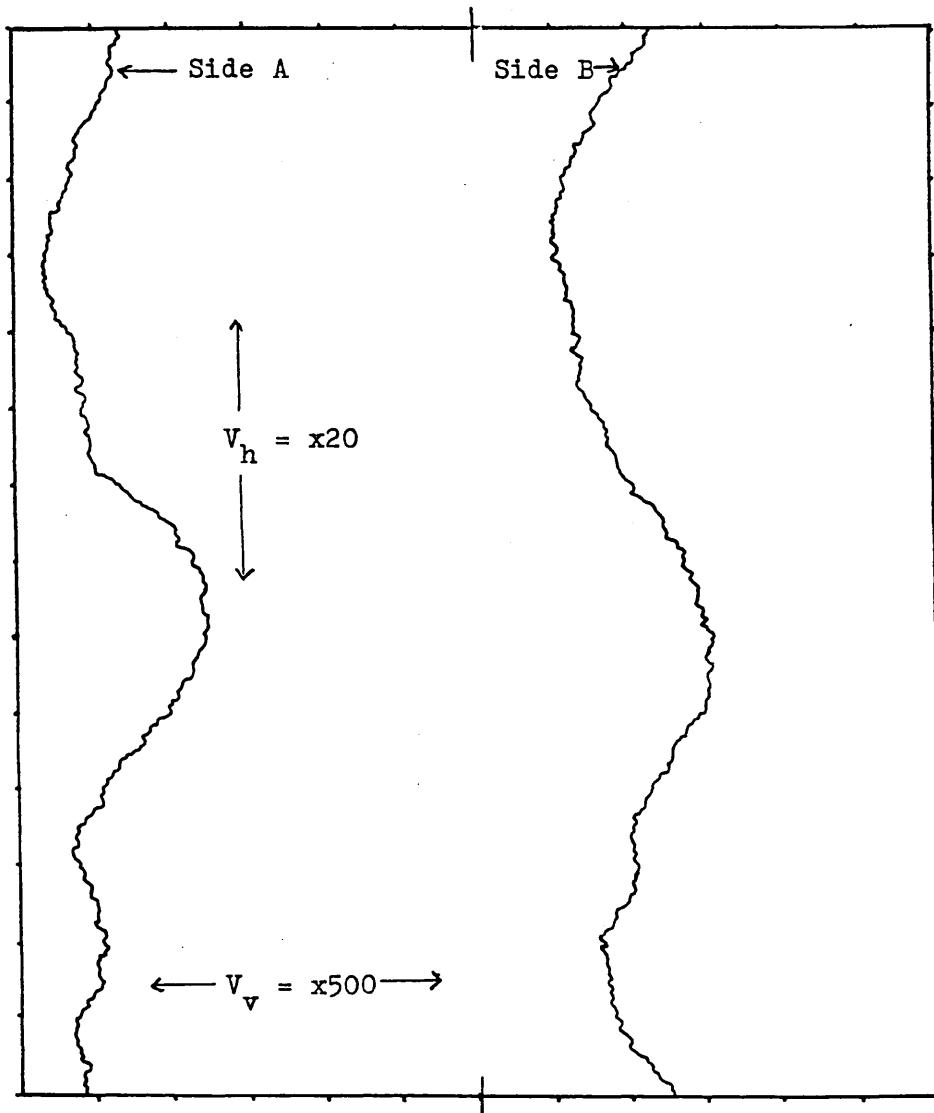


FIGURE 182 Transverse Surface Profile Traces Showing
Severe Roping in 1.15mm Thick 430 Sheet after
Straining to 15% Elongation at 0° to the Rolling
Direction.

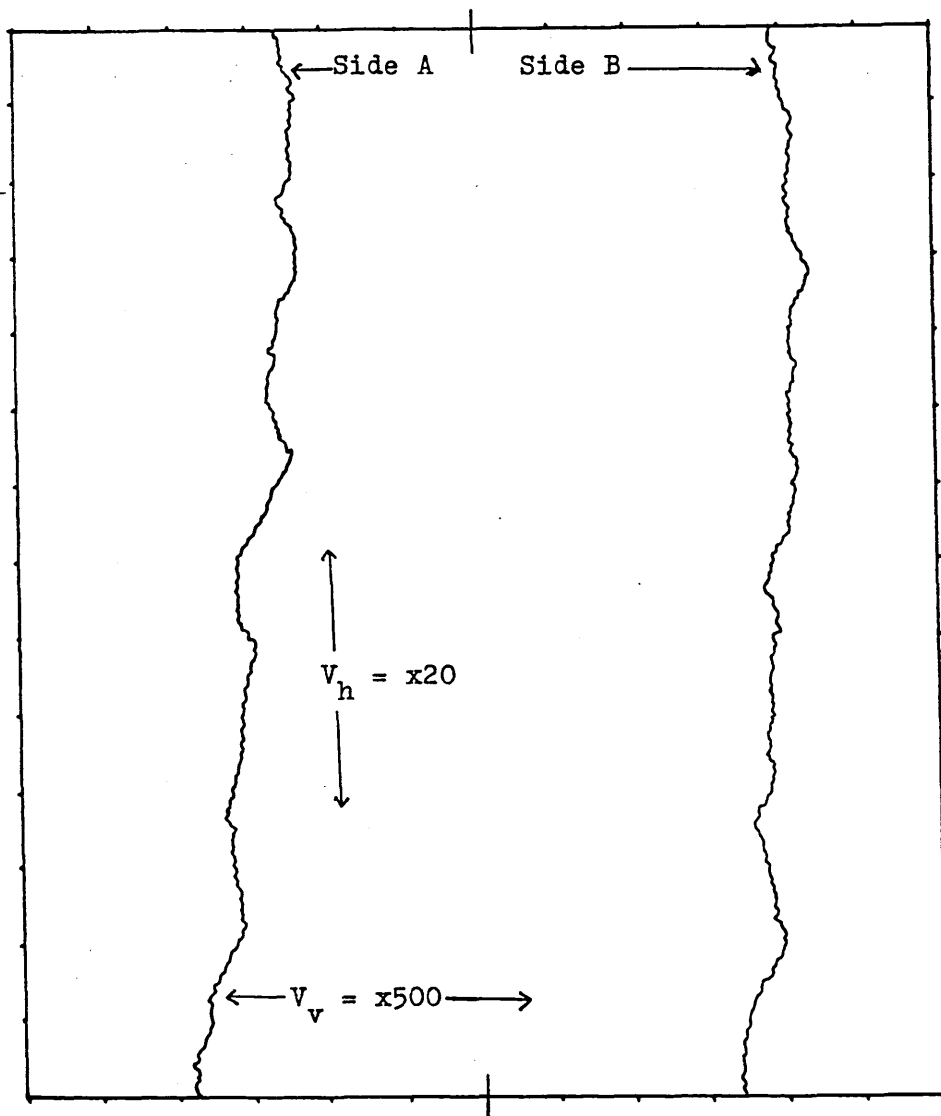
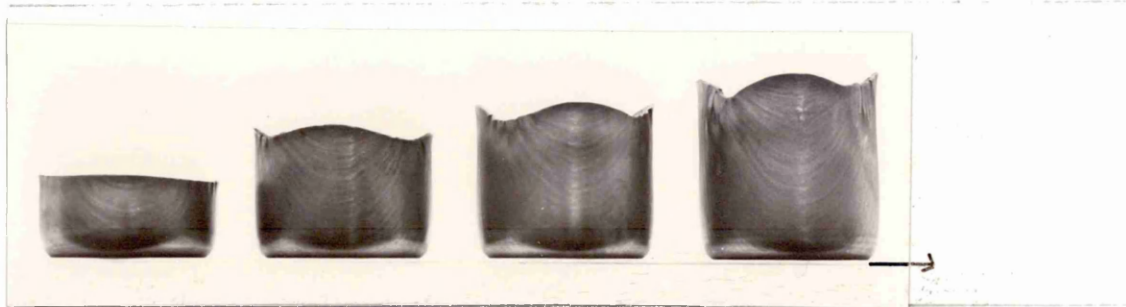
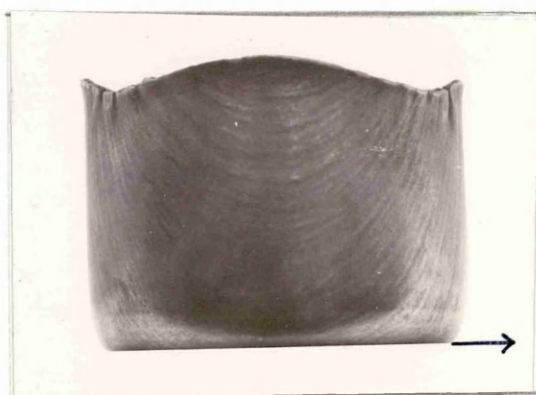


FIGURE 183 Transverse Surface Profile Traces Showing Typical
Roping in 430 Sheet after Straining to 15% Elongation
at 0° to the Rolling Direction.



(a) Cups drawn from blanks of varying diameter
 (Commercially cold rolled to $\sim 77\%$ RA, rapid anneal 900°C)



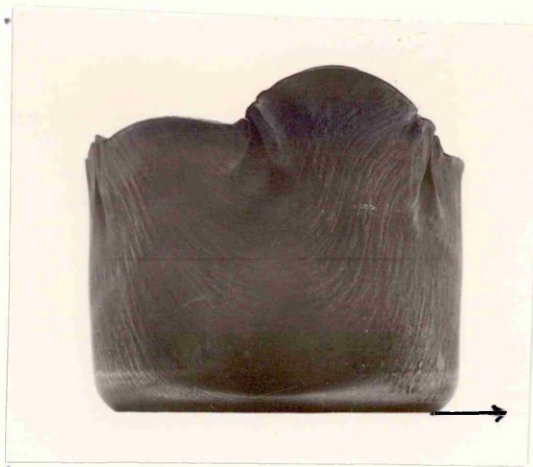
(b) Rapid anneal 850°C
 Cold rolled 80% RA
 Rapid anneal 900°C
 Sheet thickness = 1mm



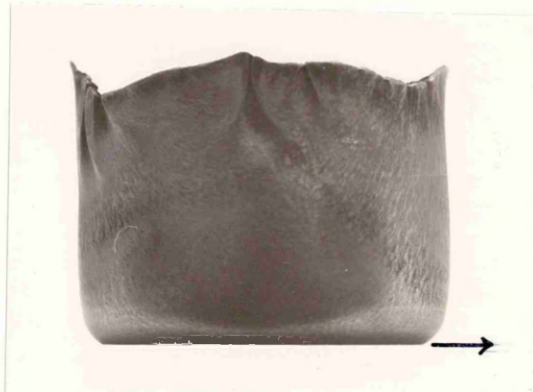
(c) Rapid anneal 1200°C
 + temper
 Cold rolled 80% RA
 Rapid anneal 900°C
 Sheet thickness = 1mm

FIG.184 FULLY DRAWN CUPS IN 430 (17 Cr, 0.077 (C+N)) STEEL (Blank diameter = 100mm unless otherwise stated)

(a) 430 Ti steel
As hot rolled
Cold rolled 80% RA
Rapid anneal 900°C



(b) 430 Ti steel
Rapid anneal 1000°C
Cold rolled 80% RA
Rapid Anneal 900°C



(c) 409 steel
Rapid anneal 850°C
Cold rolled 80% RA
Rapid anneal 900°C

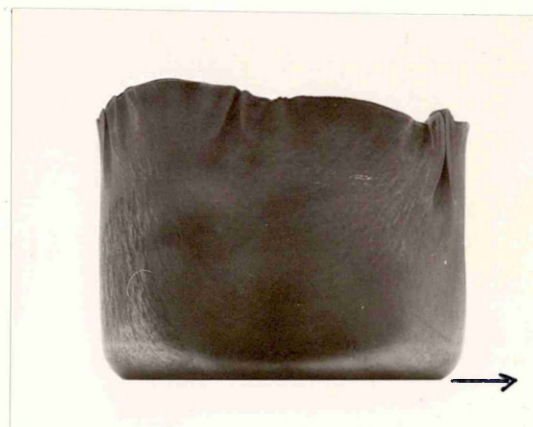


FIG.185 FULLY DRAWN CUPS IN 430 Ti (~17 Cr, 0.029 (C+N), 0.5 Ti)
AND 409 (~12 Cr, 0.039 (C+N), 0.5 Ti) STEELS
(Blank diameter = 100mm, sheet thickness = 0.8mm)

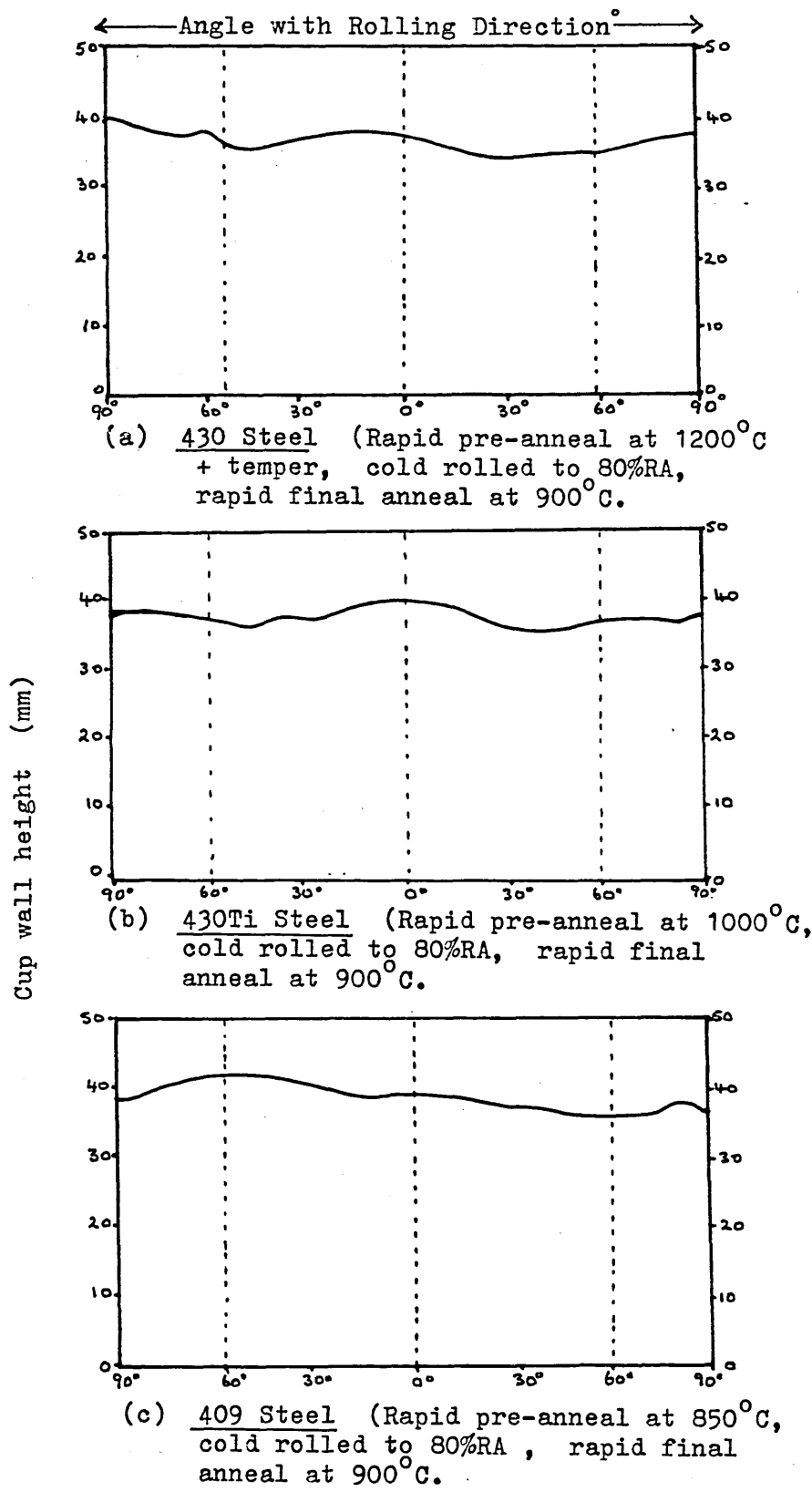


FIGURE 186

Earing Profiles for Typical Flat-Bottomed Cups
Drawn from 100mm Diameter Blanks.

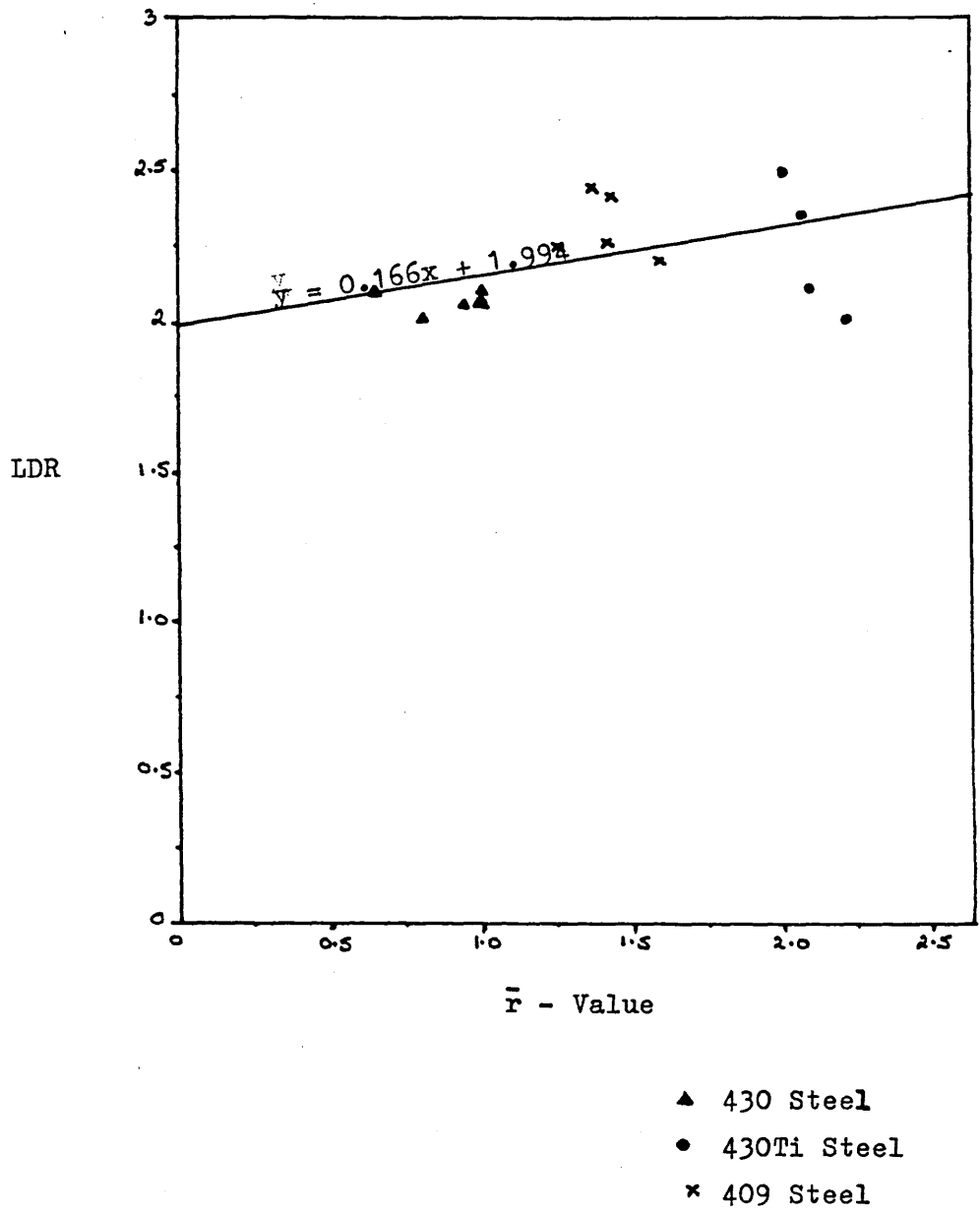
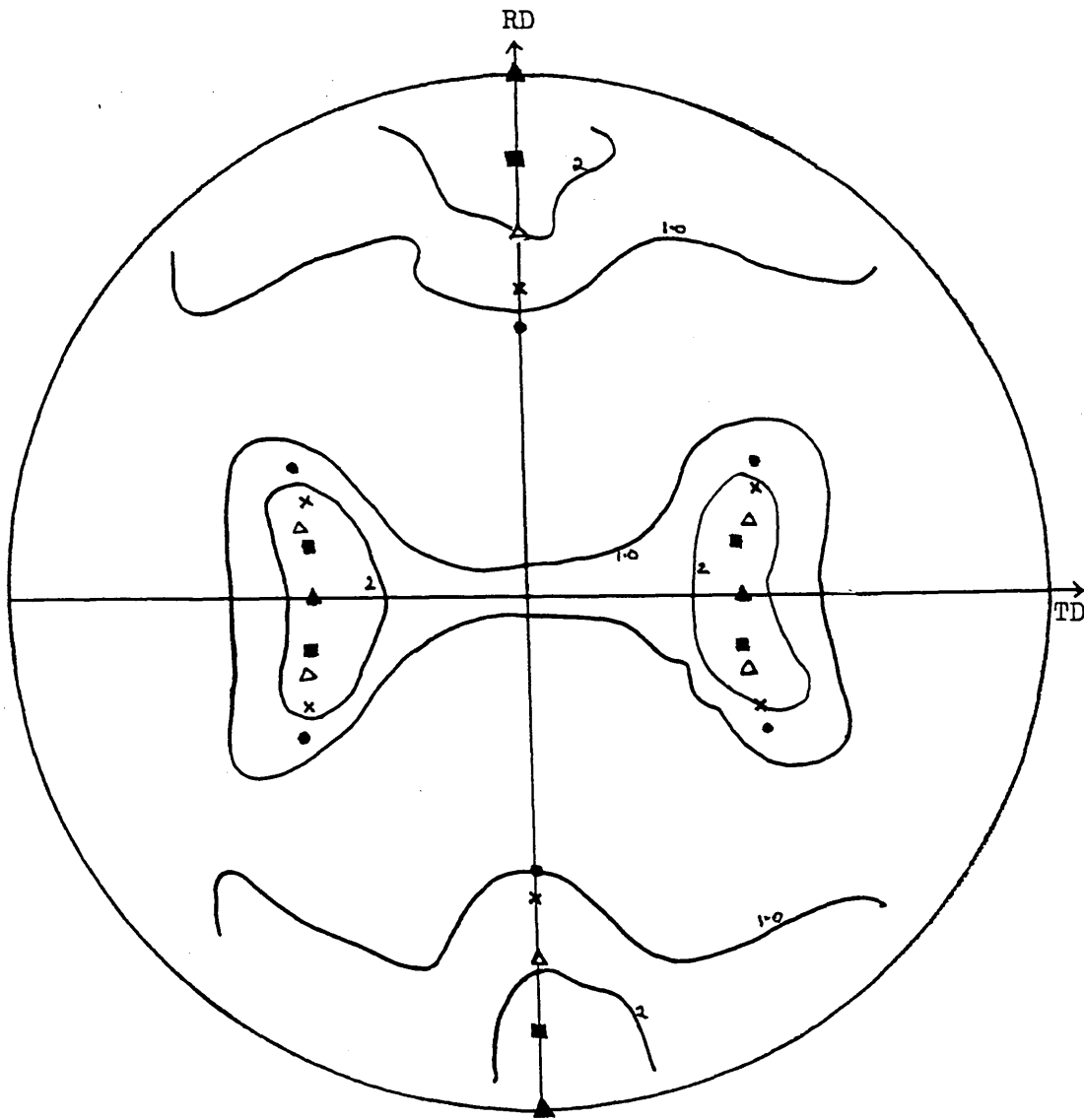


FIGURE 187 Variation of Limiting Drawing Ratio (LDR) with
Average Tensile Strain Ratio (\bar{r} - Value).



- ▲ $\{011\} \langle 100 \rangle$
- $\{144\} \langle 811 \rangle$
- △ $\{122\} \langle 411 \rangle$
- × $\{455\} \langle 522 \rangle$
- $\{111\} \langle 211 \rangle$

FIGURE 191 $\{200\}$ Pole Figure Showing Observed and Predicted Spread of Orientations for 430Ti Steel with a Strong $\{110\} \langle 001 \rangle$ Starting Texture, after Cold Rolling to 70%RA.

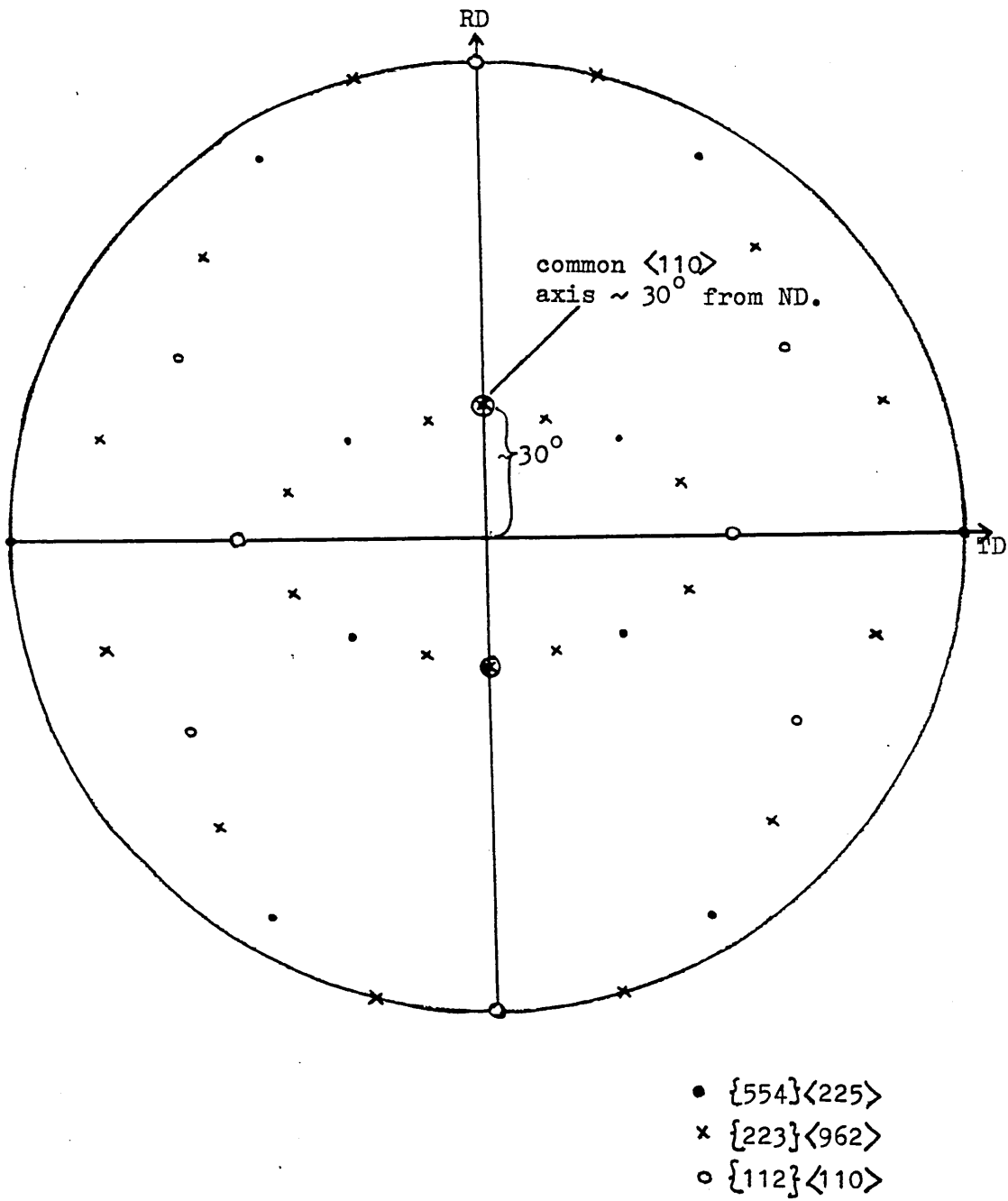
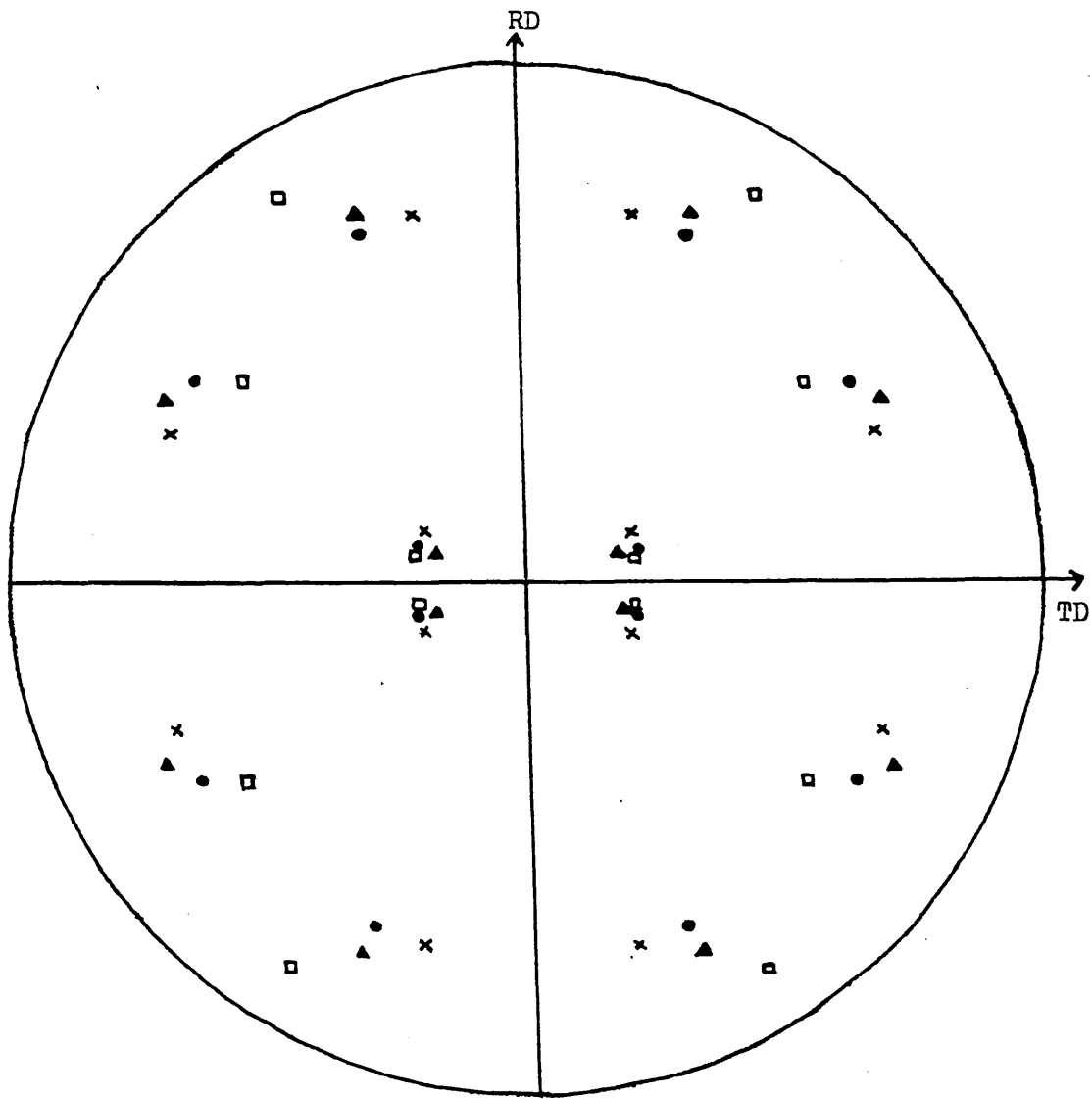
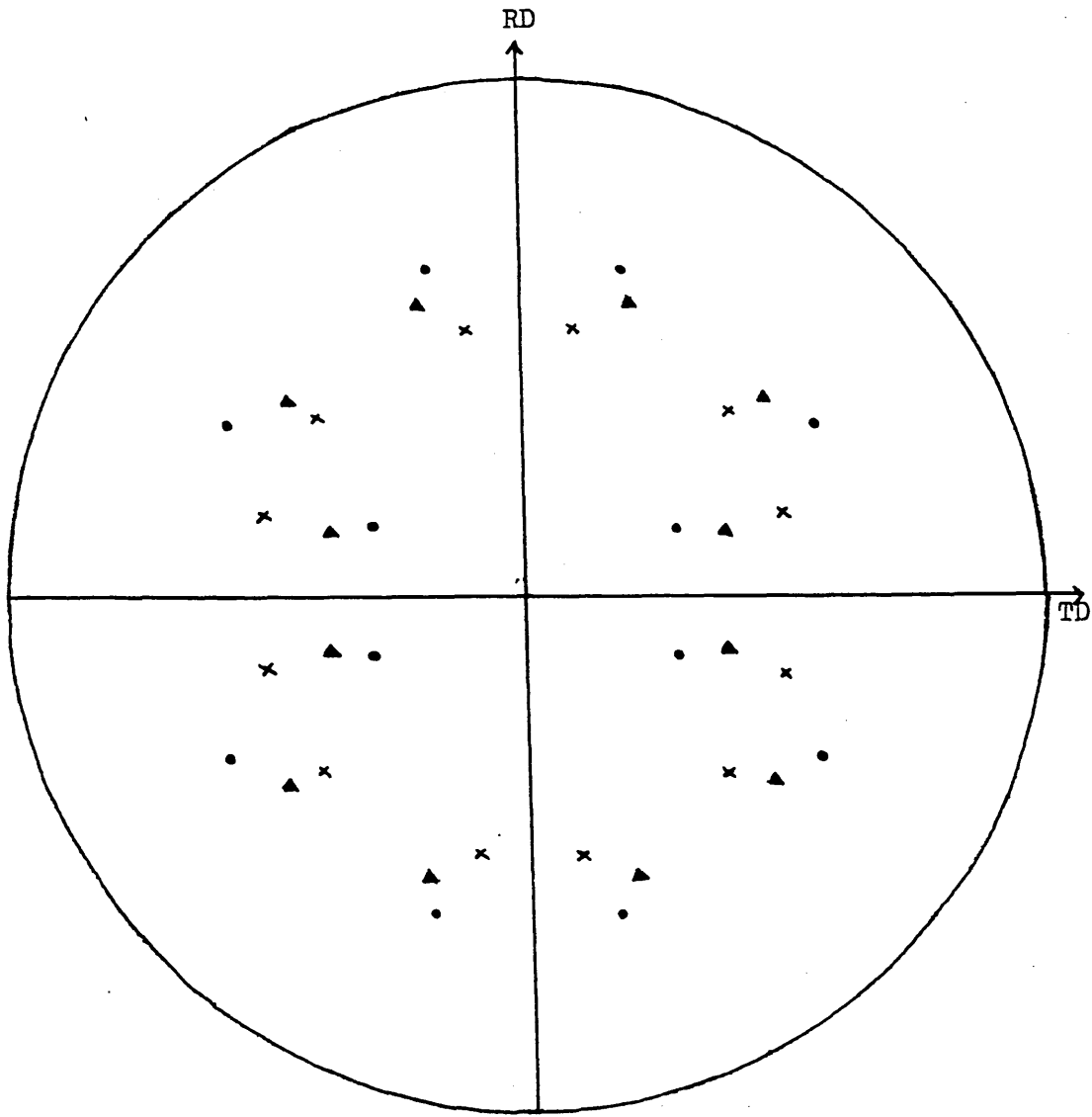


FIGURE 193 $\{110\}$ Pole Figure for the $\{554\}\langle 225 \rangle$, $\{223\}\langle 962 \rangle$ and $\{112\}\langle 110 \rangle$ Ideal Orientations.



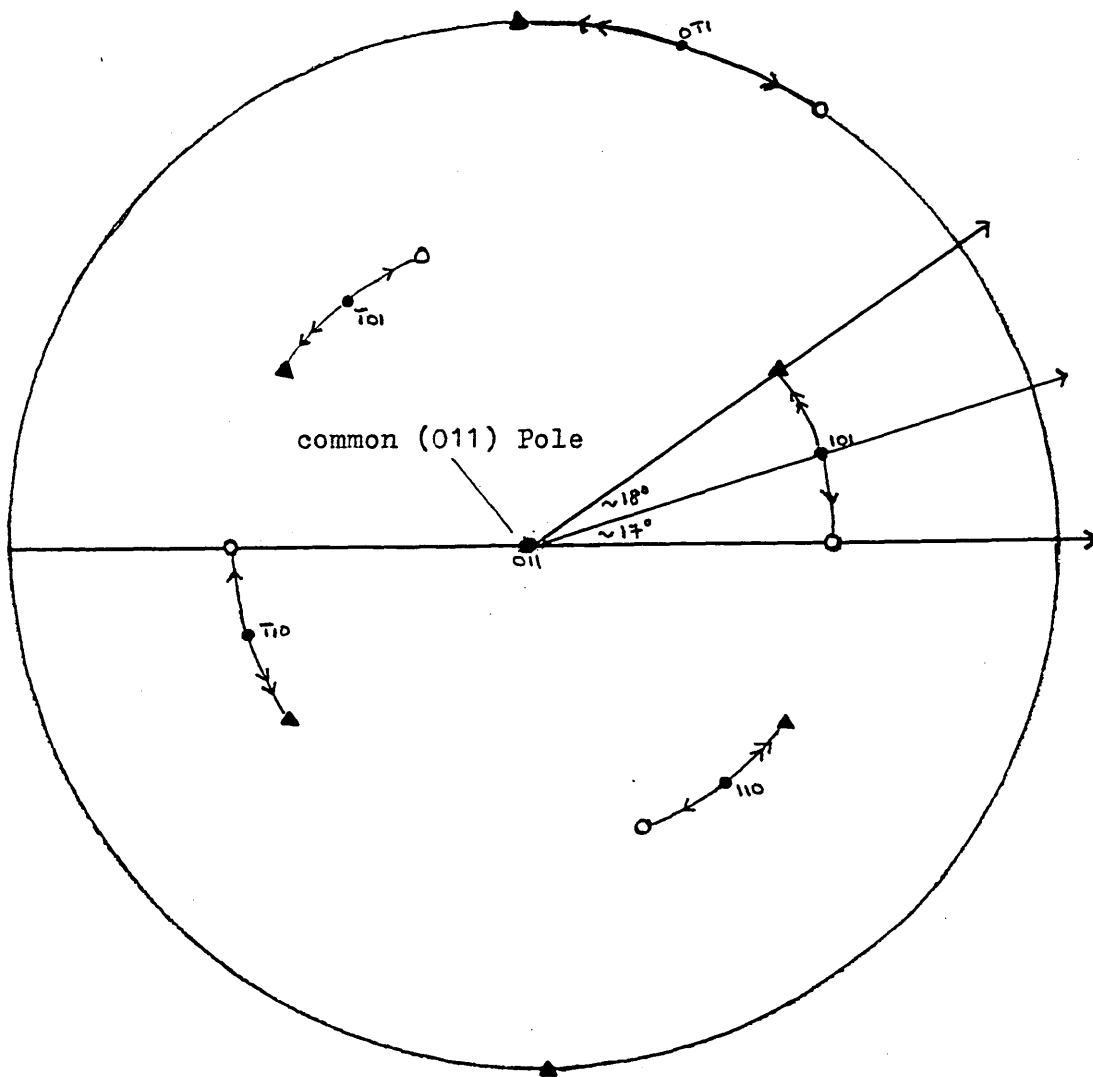
- $\{113\}\langle 741 \rangle$
- × $\{113\}\langle 521 \rangle$
- $\{137\}\langle 851 \rangle$
- ▲ $\{114\}\langle 841 \rangle$

FIGURE 196 $\{200\}$ Pole Figure Showing Orientations of Recrystallisation Nuclei near $\{114\}\langle 841 \rangle$



- x {111} <123>
- {112} <241>
- ▲ {223} <962>

FIGURE 197. {200} Pole Figure Showing Orientations of
Recrystallisation Nuclei near {223} <962>



- (223)[962] poles
- (112)[110] poles
- ▲ (455)[522] poles

FIGURE 198 {110} Poles of the (223)[962], (112)[110] and (455)[522] Orientations, Rotated such that the Common (011) Pole is at the Centre of the Projection.

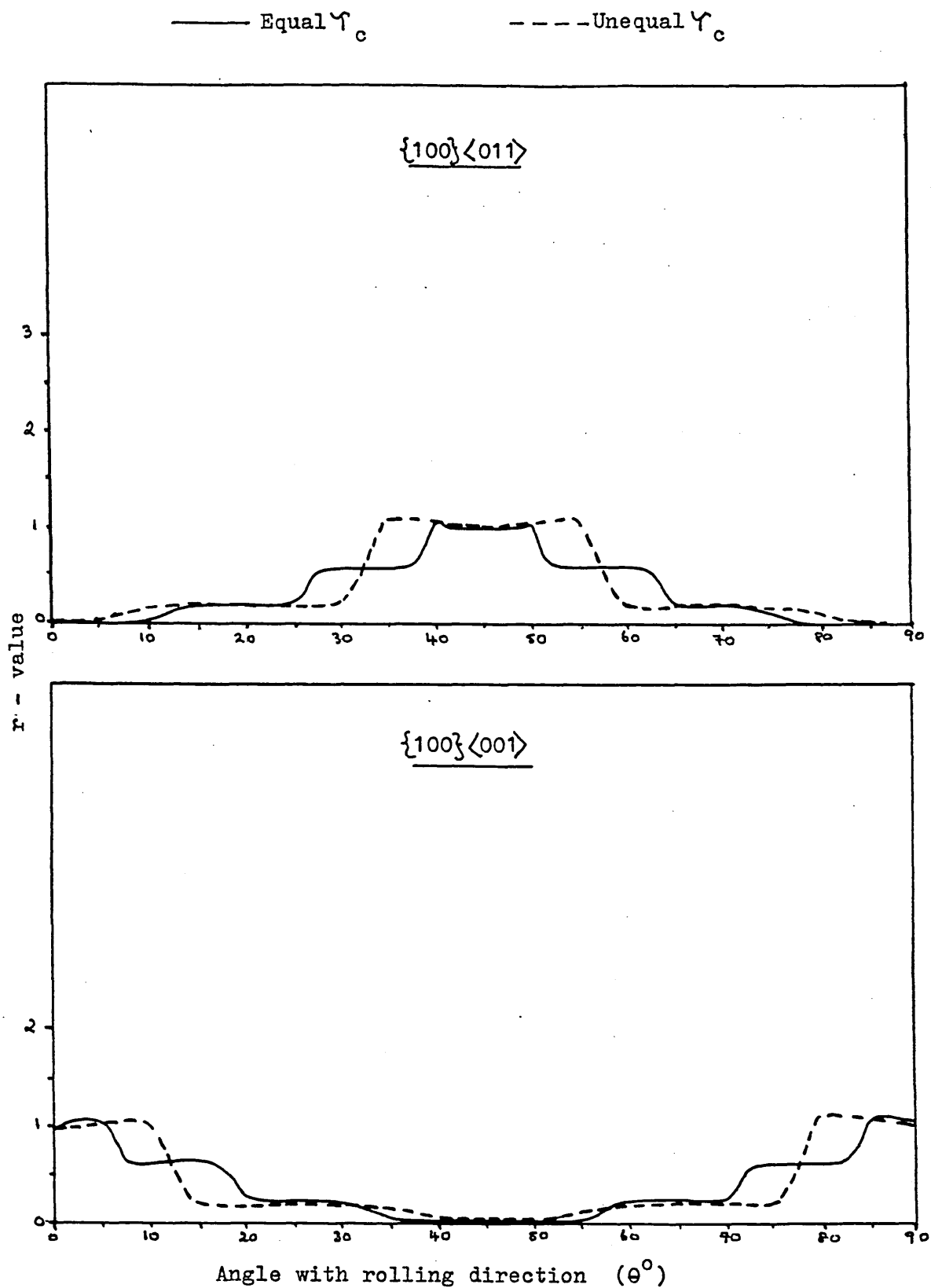


FIGURE 199

Theoretical r-Values for {100}<011> and {100}<001> Textures.

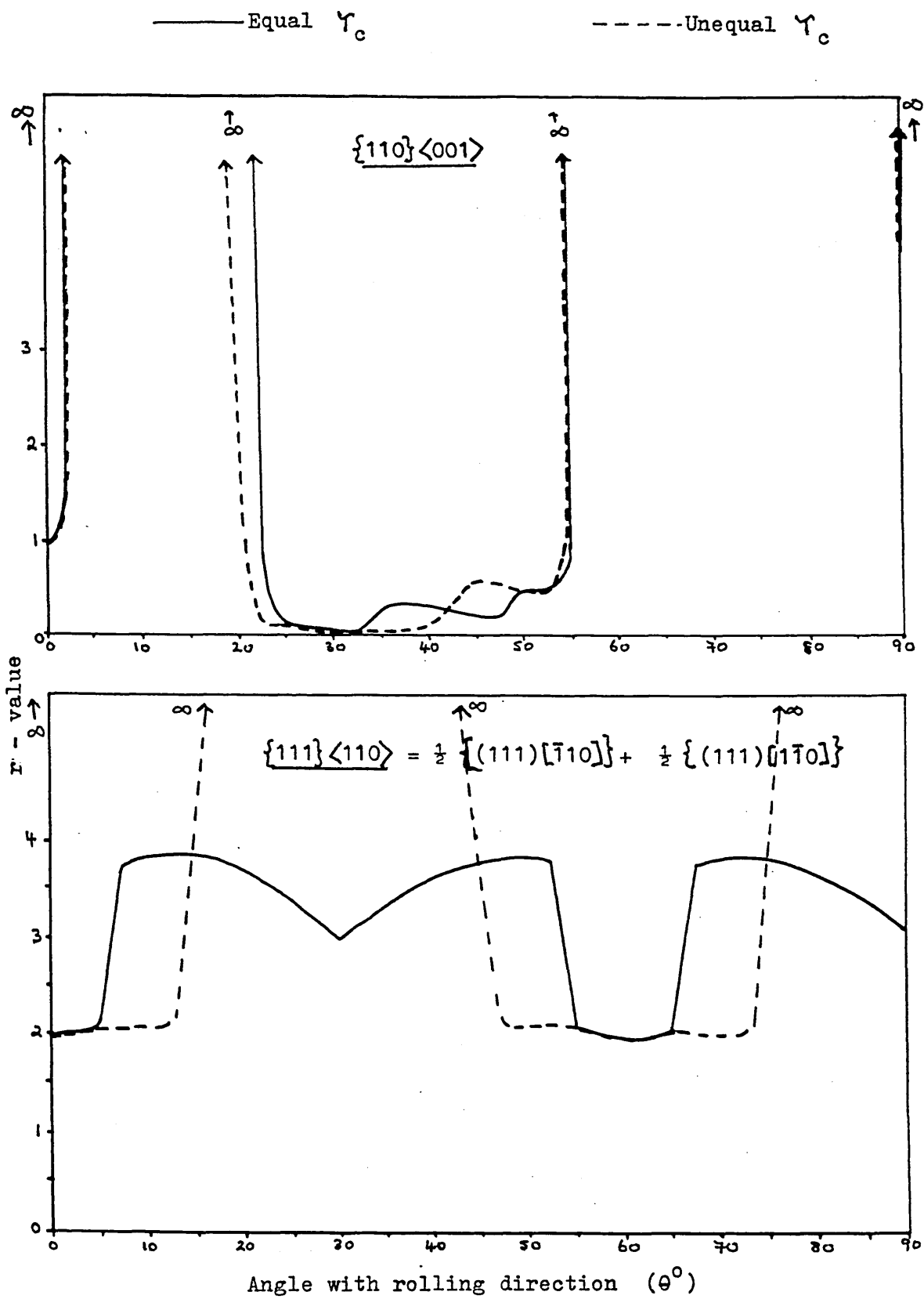


FIGURE 200 Theoretical r - Values for $\{110\}\langle 001\rangle$ and $\{111\}\langle 110\rangle$ Textures.

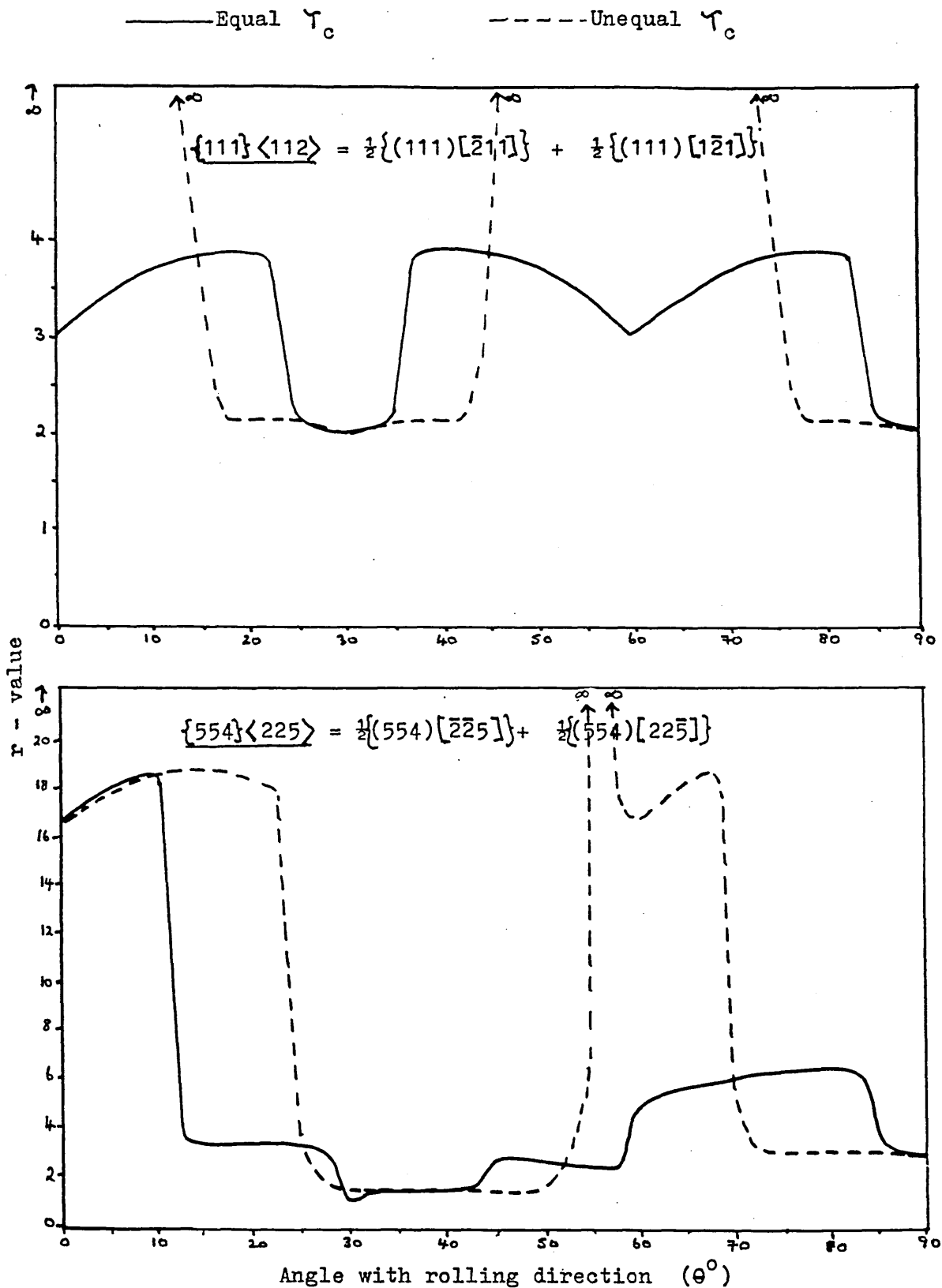


FIGURE 201 Theoretical r - Values for $\{111\}\langle 112\rangle$ and $\{554\}\langle 225\rangle$
Textures.

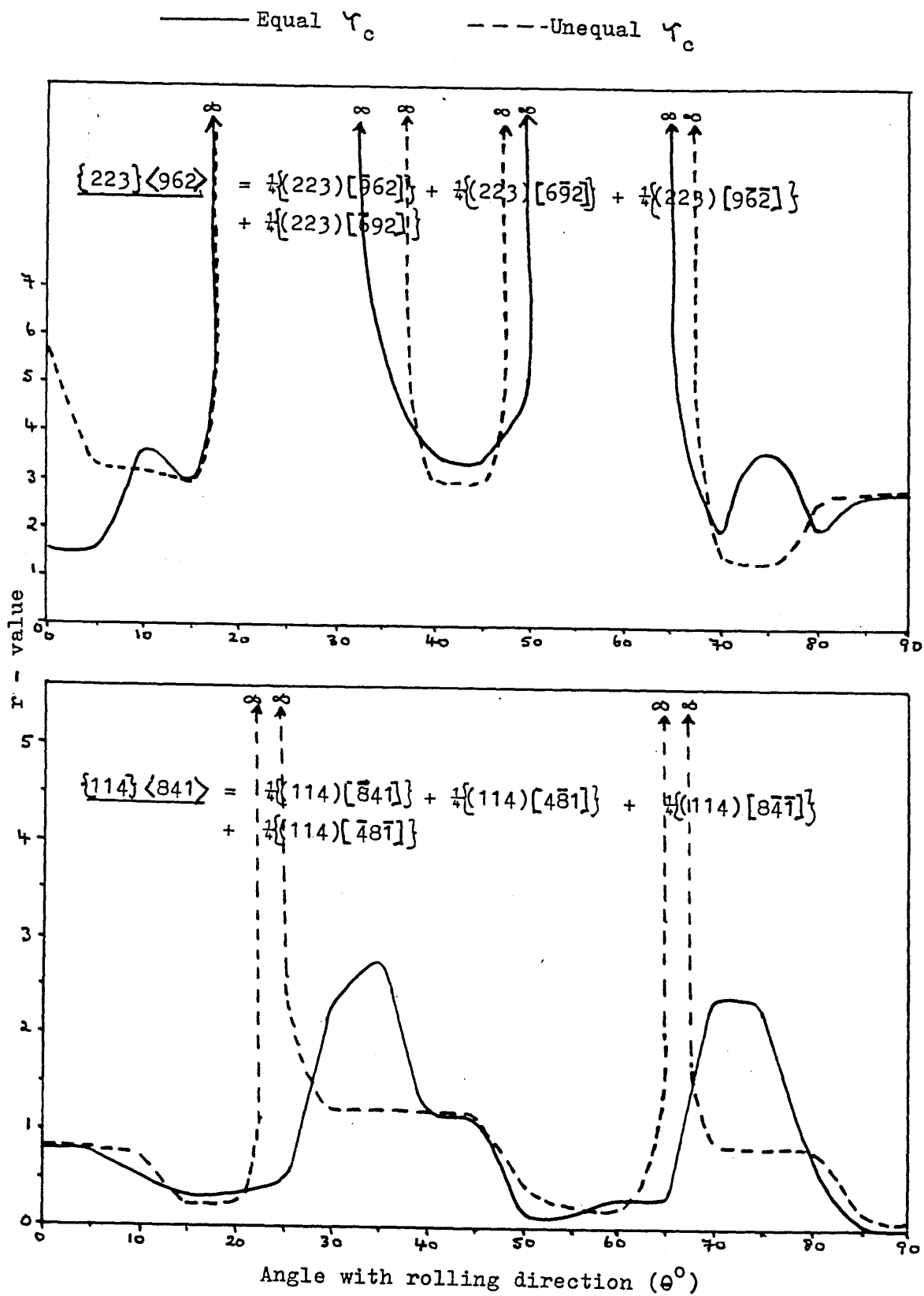


FIGURE 202

Theoretical r - Values for $\{223\}\langle 962\rangle$ and $\{114\}\langle 841\rangle$ Textures

— Equal τ_c - - - Unequal τ_c

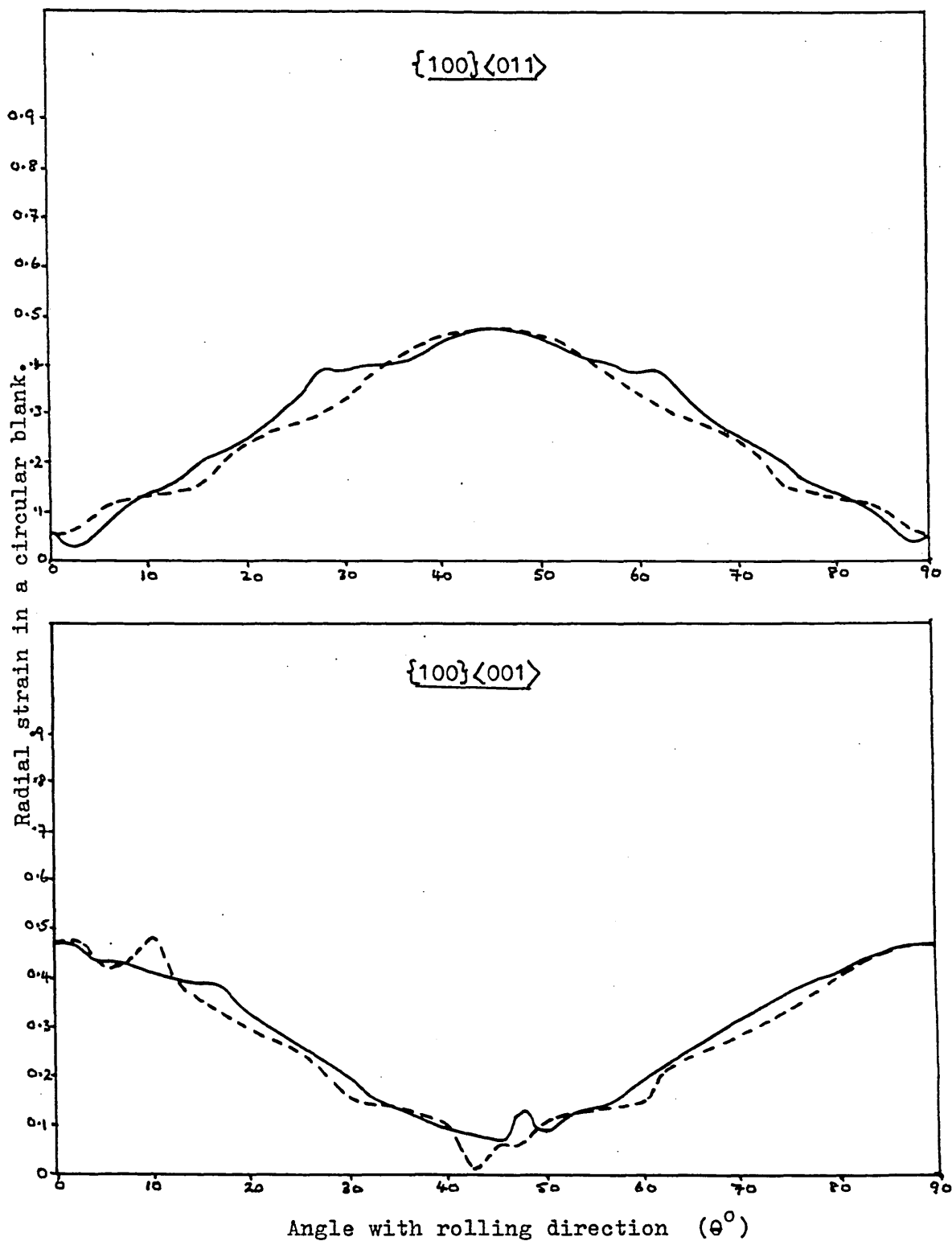


FIGURE 203

Theoretical Earing Profiles for $\{100\}\langle 011\rangle$ and $\{100\}\langle 001\rangle$ Ideal Textures.

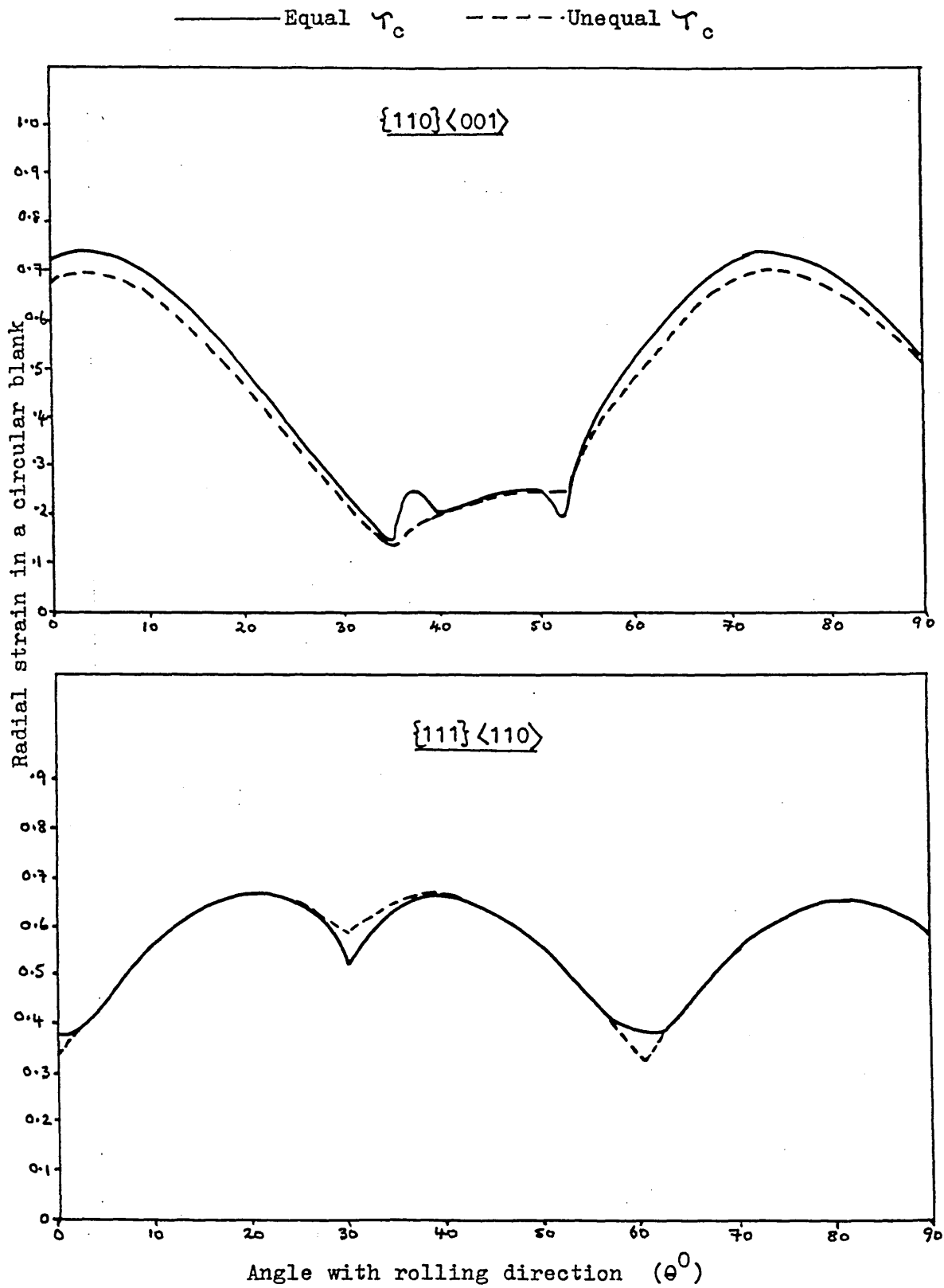


FIGURE 204 Theoretical Earing Profiles for {110}<001> and {111}<110> Textures.

— Equal τ_c - - - - - Unequal τ_c

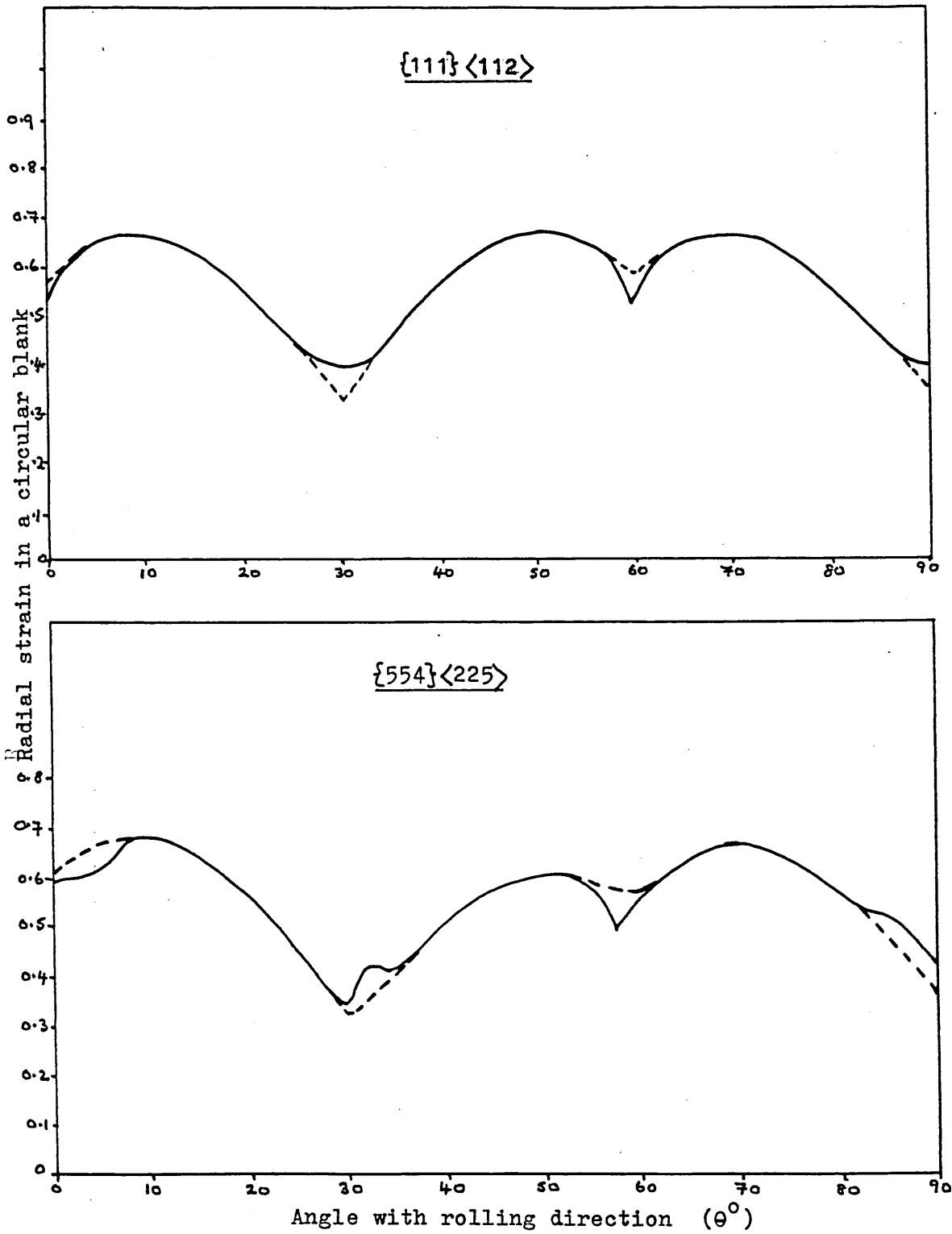


FIGURE 205

Theoretical Earing Profiles for {111}<112> and {554}<225> Ideal Textures.

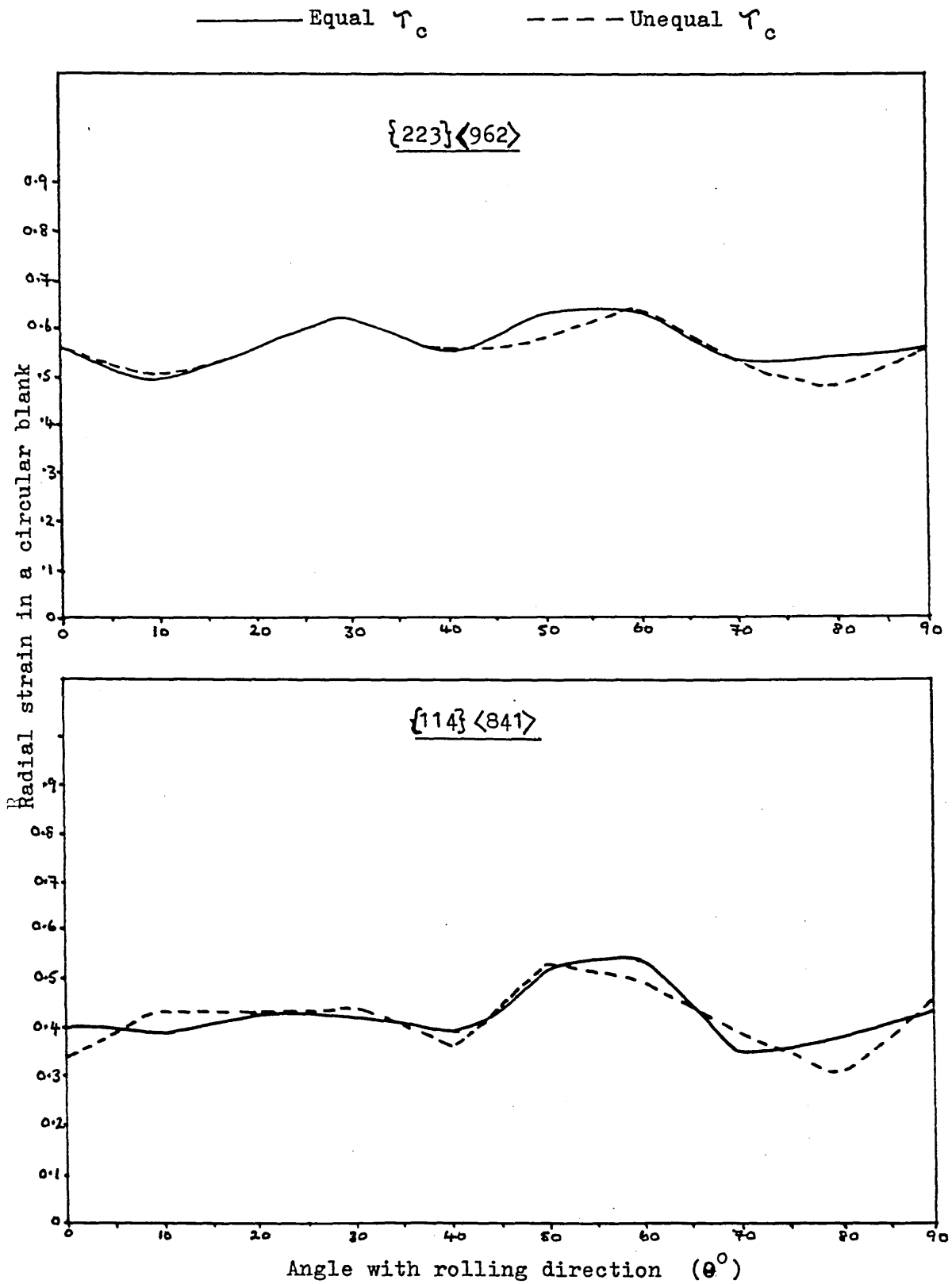
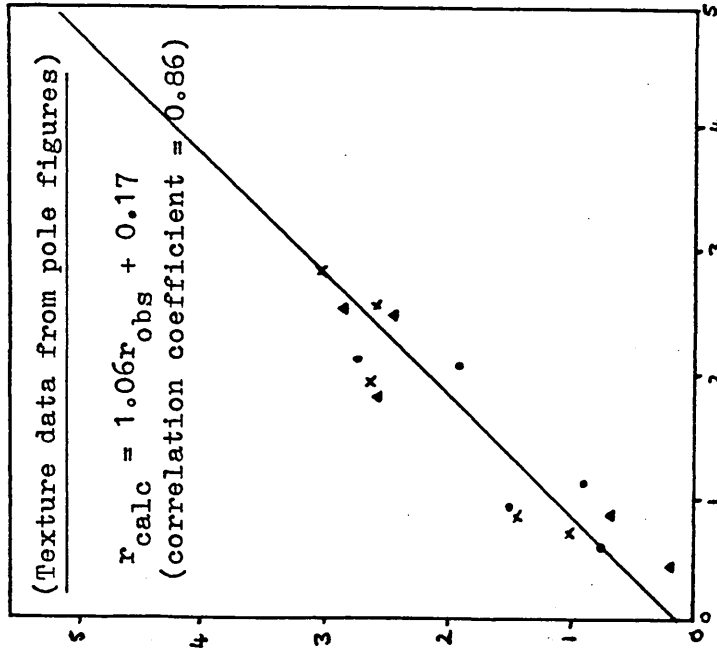


FIGURE 206 Theoretical Earing Profiles for {223}⟨962⟩ and {114}⟨841⟩ Ideal Textures.

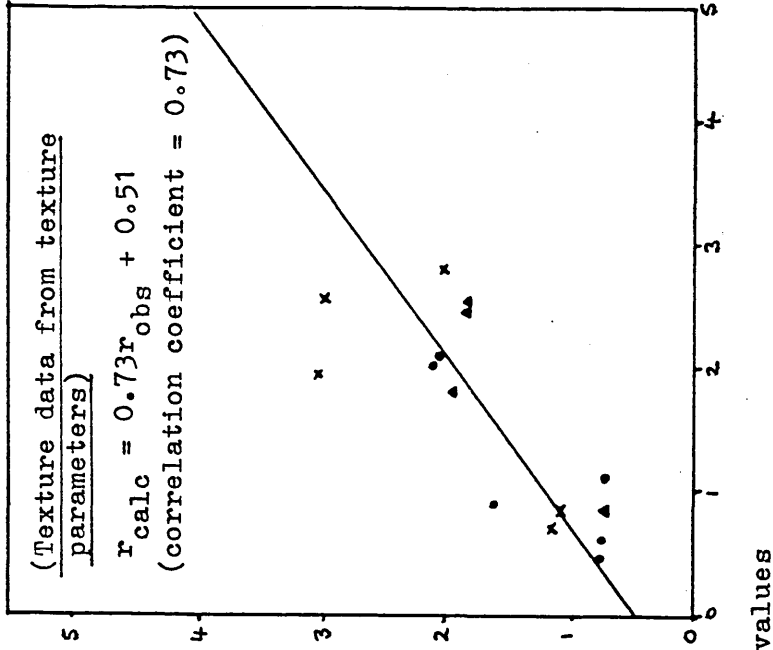
Calculated r-values (Equal ρ assumed)

● = r_0

x = r_{45}



▲ = r_{90}



Observed r - values

FIGURE 207 Calculated versus Observed r-Values for Heavily Cold Rolled and Annealed Material.

CRYSTAL ROTATIONS DUE TO SLIP IN PLANE STRAIN ROLLING

The following assumptions were used as a basis for selecting the operative slip systems in plane strain rolling.

(i) The stress system in rolling consists of a normal compressive stress (σ_3) perpendicular to the rolling plane and an equal tensile stress (σ_1) parallel with the rolling direction. (32)

$$\text{i.e. } \sigma_3 = -\sigma_1; \quad \sigma_2 = 0$$

(ii) Deformation occurs by crystallographic slip on $\{110\} \langle 111 \rangle$, $\{112\} \langle 111 \rangle$ and $\{123\} \langle 111 \rangle$ systems (i.e. there are 48 possible systems).

(iii) Slip will occur when the critical resolved shear stress is reached on one or more systems. The following situations were considered :-

$$\underline{\text{EQUAL } \tau_c} \quad \tau_c \{110\} = \tau_c \{112\} = \tau_c \{123\}$$

or

$$\underline{\text{UNEQUAL } \tau_c} \quad \tau_c \{110\} : \tau_c \{112\} : \tau_c \{123\} = \\ 1:1.03:1.05$$

Re-orientation of the lattice occurs as a result of slip. It is assumed that the tensile axis will rotate towards the operative slip direction, and the compressive axis will move towards the operative slip plane normal. (32)

Once the operative slip system(s) for a given orientation have been selected, small rotations of the stress axes are followed on the stereographic projection. The new

orientation is then determined. The procedure is then repeated, and is subsequently re-iterated for further small re-orientations.

Selection of Operative Slip Systems

For a given orientation (hkl) $[uvw]$, the resolved shear stress (τ) acting on a specific slip system $(h_2 k_2 l_2)$ $[u_2 v_2 w_2]$ is :- (32)

$$\tau = \sigma (D * E - B * C)$$

where σ = applied stress

D = cosine of the angle between ND and slip plane normal

E = " " " " " ND and slip direction

B = " " " " " RD and slip plane normal

C = " " " " " RD and slip direction.

These direction cosines are calculated as follows :-

$$D = \frac{(h h_2 + k k_2 + l l_2)}{[(h^2 + k^2 + l^2) (h_2^2 + k_2^2 + l_2^2)]^{1/2}}$$

$$E = \frac{(h u_2 + k v_2 + l w_2)}{[(h^2 + k^2 + l^2) (u_2^2 + v_2^2 + w_2^2)]^{1/2}}$$

$$B = \frac{(u h_2 + v k_2 + w l_2)}{[(u^2 + v^2 + w^2) (h_2^2 + k_2^2 + l_2^2)]^{1/2}}$$

$$C = \frac{(u u_2 + v v_2 + w w_2)}{[(u^2 + v^2 + w^2) (u_2^2 + v_2^2 + w_2^2)]^{1/2}}$$

For equal τ_c on the various slip planes, the system or systems with highest Schmid factor, T , will operate

$$T = \frac{\tau}{\sigma} = DE - BC$$

For unequal τ_c , the value of T must be modified (T'), and the system(s) with the highest value of T' will operate.

For $\{110\} \langle 111 \rangle$ systems $T' = T = (DE - BC)$

For $\{112\} \langle 111 \rangle$ systems $T' = \frac{T}{1.03}$

For $\{123\} \langle 111 \rangle$ systems $T' = \frac{T}{1.05}$

PROGRAM FOR SELECTING OPERATIVE SLIP SYSTEMS

```

10  REM  RESOLVED SHEAR STRESS FO
    R SLIP IN PLANE STRAIN ROLLI
    NG - 48 SLIP SYSTEMS
20  DIM H2(47),K2(47),L2(47),U2(4
    7),V2(47),W2(47),B(47),C(47)
    ,D(47),E(47),T(47)
30  PRINT "RESOLVED SHEAR STRESS
    FOR SLIP IN PLANE STRAIN ROL
    LING - 48 SLIP SYSTEMS"
40  PRINT "PLEASE INPUT MILLER IN
    DICES OF ORIENTATION"
50  INPUT H,K,L,U,V,W
60  PRINT "THIS COULD TAKE SOME T
    IME - I'LL TELL YOU WHEN I'V
    E FINISHED"
70  REM  FOR EACH SLIP SYSTEM, WD
    RK OUT RESOLVED SHEAR STRESS
    S, ASSUMING PLANE STRAIN CON
    DITIONS AND ZERO TRANSVERSE
    STRESS
80  FOR I = 0 TO 47
90  READ H2(I),K2(I),L2(I),U2(I),
    V2(I),W2(I)
100 D(I) = (H * H2(I) + K * K2(I)
    + L * L2(I)) / ((H ^ 2 + K ^
    2 + L ^ 2) * (H2(I) ^ 2 + K2
    (I) ^ 2 + L2(I) ^ 2)) ^ 0.5
110 E(I) = (H * U2(I) + K * V2(I)
    + L * W2(I)) / ((H ^ 2 + K ^
    2 + L ^ 2) * (U2(I) ^ 2 + V2
    (I) ^ 2 + W2(I) ^ 2)) ^ 0.5
120 B(I) = (U * H2(I) + V * K2(I)
    + W * L2(I)) / ((U ^ 2 + V ^
    2 + W ^ 2) * (H2(I) ^ 2 + K2
    (I) ^ 2 + L2(I) ^ 2)) ^ 0.5
130 C(I) = (U * U2(I) + V * V2(I)
    + W * W2(I)) / ((U ^ 2 + V ^
    2 + W ^ 2) * (U2(I) ^ 2 + V2
    (I) ^ 2 + W2(I) ^ 2)) ^ 0.5
140 T(I) = D(I) * E(I) - B(I) * C
    (I)
150 NEXT I
160 REM  RANK VALUES OF T ETC.
170 FOR J = 0 TO 46
180 FOR I = 0 TO 46
190 IF ABS (T(I)) > = ABS (T(
    I + 1)) THEN GOTO 410
200 TEMP = T(I)
210 T(I) = T(I + 1)
220 T(I + 1) = TEMP
230 TEMP = H2(I)
240 H2(I) = H2(I + 1)
250 H2(I + 1) = TEMP
260 TEMP = K2(I)

```

```

270 K2(I) = K2(I + 1)
280 K2(I + 1) = TEMP
290 TEMP = L2(I)
300 L2(I) = L2(I + 1)
310 L2(I + 1) = TEMP
320 TEMP = U2(I)
330 U2(I) = U2(I + 1)
340 U2(I + 1) = TEMP
350 TEMP = V2(I)
360 V2(I) = V2(I + 1)
370 V2(I + 1) = TEMP
380 TEMP = W2(I)
390 W2(I) = W2(I + 1)
400 W2(I + 1) = TEMP
410 NEXT I
420 NEXT J
430 FOR I = 0 TO 47
440 PRINT T(I)
450 PRINT H2(I),K2(I),L2(I),U2(I)
    ,V2(I),W2(I)
460 IF ABS (T(I)) > ABS (T(I +
    1)) THEN GOTO 480
470 NEXT I
480 PRINT "HOORAH - FINISHED!"
490 DATA 1,1,0,1,-1,1,1,1,0,-1,
    1,1,1,-1,0,-1,-1,1,1,-1,0,1,
    1,1
500 DATA 0,1,1,1,-1,1,0,1,1,-1,
    -1,1,0,-1,1,1,1,1,0,-1,1,-1,
    1,1
510 DATA 1,0,1,-1,1,1,1,0,1,-1,
    -1,1,-1,0,1,1,1,1,-1,0,1,1,-
    1,1
520 DATA 1,1,2,-1,-1,1,-1,1,2,1
    ,-1,1,1,-1,2,-1,1,1,-1,-1,2,
    1,1,1
530 DATA 1,2,1,1,-1,1,-1,2,1,-1
    ,-1,1,1,-2,1,1,1,1,-1,-2,1,-
    1,1,1
540 DATA 2,1,1,-1,1,1,-2,1,1,1,
    1,1,2,-1,1,-1,-1,1,-2,-1,1,1
    ,-1,1
550 DATA 1,2,3,-1,-1,1,-1,2,3,1
    ,-1,1,1,-2,3,-1,1,1,-1,-2,3,
    1,1,1
560 DATA 3,2,1,-1,1,1,-3,2,1,1,
    1,1,3,-2,1,-1,-1,1,-3,-2,1,1
    ,-1,1
570 DATA 3,1,2,-1,1,1,-3,1,2,1,
    1,1,3,-1,2,-1,-1,1,-3,-1,2,1
    ,-1,1
580 DATA 1,3,2,1,-1,1,-1,3,2,-1
    ,-1,1,1,-3,2,1,1,1,-1,-3,2,-
    1,1,1
590 DATA 2,1,3,-1,-1,1,-2,1,3,1
    ,-1,1,2,-1,3,-1,1,1,-2,-1,3,
    1,1,1
600 DATA 2,3,1,1,-1,1,-2,3,1,-1
    ,-1,1,2,-3,1,1,1,1,-2,-3,1,-
    1,1,1
610 END

```

Modifications to Program for Unequal τ_c

Insert the following additional lines :

135 IF ABS (H2 + K2 + L2) > 2 THEN GO TO 142

141 GO TO 150

142 IF ABS (H2 + K2 + L2) > 4 THEN GO TO 145

143 T(I) = (D(I) * E(I) - B(I) * C(I))/1.03

144 GO TO 150

145 T(I) = (D(I) * E(I) - B(I) * C(I))/1.05

APPENDIX B

CALCULATION OF THEORETICAL r-VALUES AND EARING
PROFILES USING THE METHOD OF VIETH AND WHITELEY (89)

Tensile strain ratios (r-values) and radial strains associated with plane-strain drawing of a circular blank (earing profiles) were calculated theoretically using the method of Vieth and Whiteley. (89) Possible rotation of the lattice during straining is ignored, and it is assumed that slip will occur when the critical resolved shear stress is reached on one or more of 48 possible slip systems. The following situations have been considered :-

Equal τ_c $\tau_c \{110\} = \tau_c \{112\} = \tau_c \{123\}$ as
used by Vieth and Whiteley (89)

Unequal τ_c $\tau_c \{110\} : \tau_c \{112\} : \tau_c \{123\} =$
1:1.03:1.05 as suggested by Smoluschowski and
Opinsky. (21)

B.1. Steps in calculation of r-values

(i) For a given orientation $(h_1 \ k_1 \ l_1)$ $[u_1 \ v_1 \ w_1]$ calculate the Miller indices of the tranverse direction $[x_1 \ y_1 \ z_1]$.

(ii) Convert x_1 , y_1 , and z_1 to direction cosines $\frac{x_1}{CD}$, $\frac{y_1}{CD}$, and $\frac{z_1}{CD}$ where

$$CD = (x_1^2 + y_1^2 + z_1^2)^{\frac{1}{2}}$$

Convert u_1 , v_1 and w_1 to direction cosines

$\frac{u_1}{DC}$, $\frac{v_1}{DC}$, $\frac{w_1}{DC}$ where

$$DC = (u_1^2 + v_1^2 + w_1^2)^{\frac{1}{2}}$$

(iii) For each test angle A (angle between test direction and rolling direction), find the indices of the test direction $[UVW]$ and the specimen width direction $[XYZ]$

Test direction $[UVW]$

$$U = \frac{u_1}{DC} \cos A - \frac{x_1}{CD} \sin A$$

$$V = \frac{v_1}{DC} \cos A - \frac{y_1}{CD} \sin A$$

$$W = \frac{w_1}{DC} \cos A - \frac{z_1}{CD} \sin A$$

Specimen width direction [XYZ]

$$X = \frac{x_1}{CD} \cos A + \frac{u_1}{DC} \sin A$$

$$Y = \frac{y_1}{CD} \cos A + \frac{v_1}{DC} \sin A$$

$$Z = \frac{z_1}{CD} \cos A + \frac{w_1}{DC} \sin A$$

(iv) For each slip system $(h_2 k_2 l_2) [u_2 v_2 w_2]$ calculate the following :-

B = cos. angle between test direction and slip plane normal

C = cos. angle between test direction and slip direction.

$$B = \frac{h_2 U + k_2 V + l_2 W}{\left[(h_2^2 + k_2^2 + l_2^2) (U^2 + V^2 + W^2) \right]^{\frac{1}{2}}}$$

$$C = \frac{u_2 U + v_2 V + w_2 W}{\left[(u_2^2 + v_2^2 + w_2^2) (U^2 + V^2 + W^2) \right]^{\frac{1}{2}}}$$

Hence work out the Schmid factor T for each system :

$$T = B * C$$

For equal γ_c , system(s) of maximum Schmid factor will operate. For unequal γ_c , the value of T must be modified to T', and systems of maximum T' will operate.

For $\{110\} \langle 111 \rangle$ systems, $T' = T$

For $\{112\} \langle 111 \rangle$ systems, $T' = \frac{T}{1.03}$

For $\{123\} \langle 111 \rangle$ systems, $T' = \frac{T}{1.05}$

(v) Rank systems in order of decreasing T (T') value, and hence select operative systems.

(vi) Calculate the cosines of the following angles of principal interest, for the operative slip systems.

D = cos. angle between thickness direction and slip plane normal.

E = cos. angle between thickness direction and slip direction.

F = cos. angle between specimen width direction and slip plane normal.

G = cos. angle between specimen width direction and slip direction.

$$D = \frac{h_1 h_2 + k_1 k_2 + l_1 l_2}{[(h_1^2 + k_1^2 + l_1^2)(h_2^2 + k_2^2 + l_2^2)]^{\frac{1}{2}}}$$

$$E = \frac{h_1 u_2 + k_1 v_2 + l_1 w_2}{[(h_1^2 + k_1^2 + l_1^2)(u_2^2 + v_2^2 + w_2^2)]^{\frac{1}{2}}}$$

$$F = \frac{h_2 X + k_2 Y + l_2 Z}{[(h_2^2 + k_2^2 + l_2^2)(X^2 + Y^2 + Z^2)]^{\frac{1}{2}}}$$

$$G = \frac{u_2 X + v_2 Y + w_2 Z}{[(u_2^2 + v_2^2 + w_2^2)(X^2 + Y^2 + Z^2)]^{\frac{1}{2}}}$$

(vii) Hence, calculate r-value (at test angle A).

For slip on one system only

$$r_A = \frac{F.G}{D.E}$$

For slip on many systems

$$r_A = \frac{\sum(F.G)}{\sum(D.E)}$$

(viii) Repeat (iii) to (vii) for each test angle A.

B.2 Steps in Calculation of radial strains associated with plane strain drawing of circular blanks

(i) * For a given orientation $(h_1 \ k_1 \ l_1)$ $[u_1 \ v_1 \ w_1]$, calculate the indices of the transverse direction $[x_1 \ y_1 \ z_1]$.

(ii) * For each angle A, find the indices of the test direction $[UVW]$ and the specimen width direction $[XYZ]$.

(iii) * For each slip system $(h_2 \ k_2 \ l_2)$ $[u_2 \ v_2 \ w_2]$, calculate the values of B, C, F and G.

B = cos. angle between test direction and slip plane normal.

C = cos. angle between test direction and slip direction.

F = cos. angle between specimen width direction and slip plane normal.

G = cos. angle between specimen width direction and slip direction.

(iv) Hence work out the Schmid factor T (and if necessary the modified value T' , for unequal γ_c) for each slip system.

$$T = F.G - B.C.$$

(v) Select operative system(s), with maximum $T(T')$, and work out the radial strain.

For slip on one system

$$\text{Radial strain} = T^2 |B|$$

For many slip systems, determine the average value of radial strain.

(vi) Repeat (ii) - (v) for all required angles (A).

(NOTE * Calculate as for r-value determination (B.1))

B3.1 Program for Calculating r-Values

```

10  REM  R-VALUES FOR CRYSTALLOGR
    APHIC SLIP ASSUMING 48 POSSI
    BLE SLIP SYSTEMS IN BCC SING
    LE CRYSTALS
20  DIM H2(47),K2(47),L2(47),U2(4
    7),V2(47),W2(47),B(47),C(47)
    ,T(47)
30  PRINT "RVALCRYST"
40  PRINT "PLEASE INPUT MILLER IN
    DICES OF ORIENTATION"
50  INPUT H1,K1,L1,U1,V1,W1
60  REM  WORK OUT TRANSVERSE DIRE
    CTION X1,Y1,Z1
70  X1 = L1 * V1 - K1 * W1
80  Y1 = H1 * W1 - L1 * U1
90  Z1 = K1 * U1 - H1 * V1
100 REM  TO WORK OUT R-VALUES FO
    R EACH TEST DIRECTION
110 PRINT "THIS COULD TAKE SOME
    TIME-I'LL TELL YOU WHEN I'VE
    FINISHED"
120 FOR A = 0 TO 90 STEP 2.5
130 AX = A * 2 * 3.141592654 / 36
    0
140 DC = (U1 ^ 2 + V1 ^ 2 + W1 ^
    2) ^ 0.5
150 CD = (X1 ^ 2 + Y1 ^ 2 + Z1 ^
    2) ^ 0.5
160 REM  WORK OUT TEST DIRECTION
    UVW AND SPECIMEN WIDTH DIRE
    CTION XYZ
170 U = U1 / DC * COS (AX) - X1 /
    CD * SIN (AX)
180 V = V1 / DC * COS (AX) - Y1 /
    CD * SIN (AX)
190 W = W1 / DC * COS (AX) - Z1 /
    CD * SIN (AX)
200 X = X1 / CD * COS (AX) + U1 /
    DC * SIN (AX)
210 Y = Y1 / CD * COS (AX) + V1 /
    DC * SIN (AX)
220 Z = Z1 / CD * COS (AX) + W1 /
    DC * SIN (AX)
230 REM  FOR EACH SLIP SYSTEM H2
    ,K2,L2,U2,V2,W2 WORK OUT RES
    OLVED SHEAR STRESS T
240 FOR I = 0 TO 47
250 READ H2(I),K2(I),L2(I),U2(I)
    ,V2(I),W2(I)

```

```

260 B(I) = (H2(I) * U + K2(I) * V
      + L2(I) * W) / ((H2(I) ^ 2 +
      K2(I) ^ 2 + L2(I) ^ 2) * (U ^
      2 + V ^ 2 + W ^ 2)) ^ 0.5
270 C(I) = (U2(I) * U + V2(I) * V
      + W2(I) * W) / ((U2(I) ^ 2 +
      V2(I) ^ 2 + W2(I) ^ 2) * (U ^
      2 + V ^ 2 + W ^ 2)) ^ 0.5
280 T(I) = ABS (B(I)) * ABS (C(
      I))
290 NEXT I
300 REM RANK VALUES OF T AND CO
      RRESPONDING SLIP SYSTEMS ETC

310 FOR J = 0 TO 46
320 FOR I = 0 TO 46
330 IF T(I) > = T(I + 1) THEN GOTO
      610
340 TEMP = T(I)
350 T(I) = T(I + 1)
360 T(I + 1) = TEMP
370 TEMP = H2(I)
380 H2(I) = H2(I + 1)
390 H2(I + 1) = TEMP
400 TEMP = K2(I)
410 K2(I) = K2(I + 1)
420 K2(I + 1) = TEMP
430 TEMP = L2(I)
440 L2(I) = L2(I + 1)
450 L2(I + 1) = TEMP
460 TEMP = U2(I)
470 U2(I) = U2(I + 1)
480 U2(I + 1) = TEMP
490 TEMP = V2(I)
500 V2(I) = V2(I + 1)
510 V2(I + 1) = TEMP
520 TEMP = W2(I)
530 W2(I) = W2(I + 1)
540 W2(I + 1) = TEMP
550 TEMP = B(I)
560 B(I) = B(I + 1)
570 B(I + 1) = TEMP
580 TEMP = C(I)
590 C(I) = C(I + 1)
600 C(I + 1) = TEMP
610 NEXT I
620 NEXT J
630 REM WORK OUT DATA NEEDED FO
      R R-VALUES ASSUMING SLIP SYS
      TEMS WITH MAX. T ONLY OPERAT
      E
640 QQ = 0
650 SS = 0
660 FOR I = 0 TO 47
670 D = (H1 * H2(I) + K1 * K2(I) +
      L1 * L2(I)) / ((H1 ^ 2 + K1 ^
      2 + L1 ^ 2) * (H2(I) ^ 2 + K
      2(I) ^ 2 + L2(I) ^ 2)) ^ 0.5

```

```

680 E = (H1 * U2(I) + K1 * V2(I) +
      L1 * W2(I)) / ((H1 ^ 2 + K1 ^
      2 + L1 ^ 2) * (U2(I) ^ 2 + V
      2(I) ^ 2 + W2(I) ^ 2)) ^ 0.5

690 F = (H2(I) * X + K2(I) * Y +
      L2(I) * Z) / ((H2(I) ^ 2 + K
      2(I) ^ 2 + L2(I) ^ 2) * (X ^
      2 + Y ^ 2 + Z ^ 2)) ^ 0.5
700 G = (U2(I) * X + V2(I) * Y +
      W2(I) * Z) / ((U2(I) ^ 2 + V
      2(I) ^ 2 + W2(I) ^ 2) * (X ^
      2 + Y ^ 2 + Z ^ 2)) ^ 0.5
710 Q = F * G
720 S = D * E
730 QQ = QQ + ABS (Q)
740 SS = SS + ABS (S)
750 IF T(I) > T(I + 1) THEN GOTO
      770
760 NEXT I
770 IF QQ = 0 THEN GOTO 830
780 IF SS = 0 THEN GOTO 810
790 R = QQ / SS
800 GOTO 840
810 R = 1000
820 GOTO 840
830 R = 0
840 PRINT "A=";A;"      R=";R
850 RESTORE
860 NEXT A
870 PRINT "HOORAH, FINISHED!"
880 DATA  1,1,0,1,-1,1,1,1,0,-1,
      1,1,1,-1,0,-1,-1,1,1,-1,0,1,
      1,1
890 DATA  0,1,1,1,-1,1,0,1,1,-1,
      -1,1,0,-1,1,1,1,1,0,-1,1,-1,
      1,1
900 DATA  1,0,1,-1,1,1,1,0,1,-1,
      -1,1,-1,0,1,1,1,1,-1,0,1,1,-
      1,1
910 DATA  1,1,2,-1,-1,1,-1,1,2,1
      ,-1,1,1,-1,2,-1,1,1,-1,-1,2,
      1,1,1
920 DATA  1,2,1,1,-1,1,-1,2,1,-1
      ,-1,1,1,-2,1,1,1,1,-1,-2,1,-
      1,1,1
930 DATA  2,1,1,-1,1,1,-2,1,1,1,
      1,1,2,-1,1,-1,-1,1,-2,-1,1,1
      ,-1,1
940 DATA  1,2,3,-1,-1,1,-1,2,3,1
      ,-1,1,1,-2,3,-1,1,1,-1,-2,3,
      1,1,1
950 DATA  3,2,1,-1,1,1,-3,2,1,1,
      1,1,3,-2,1,-1,-1,1,-3,-2,1,1
      ,-1,1
960 DATA  3,1,2,-1,1,1,-3,1,2,1,
      1,1,3,-1,2,-1,-1,1,-3,-1,2,1
      ,-1,1

```

970 DATA 1,3,2,1,-1,1,-1,3,2,-1
 ,-1,1,1,-3,2,1,1,1,-1,-3,2,-
 1,1,1
 980 DATA 2,1,3,-1,-1,1,-2,1,3,1
 ,-1,1,2,-1,3,-1,1,1,-2,-1,3,
 1,1,1
 990 DATA 2,3,1,1,-1,1,-2,3,1,-1
 ,-1,1,2,-3,1,1,1,1,-2,-3,1,-
 1,1,1
 1000 REM H1,K1,L1,U1,V1,W1 = OR
 IENTATION
 1010 REM H2,K2,L2,U2,V2,W2 = SL
 IP SYSTEM
 1020 REM RO = R-VALUE, NO ROTAT
 ION
 1030 REM RL = R-VALUE, LARGE RO
 TATION
 1040 REM A=ANGLE BETWEEN ROLLIN
 G AND TEST DIRECTIONS
 1050 REM T=RESOLVED SHEAR STRES
 S ON SLIP SYSTEM
 1060 REM X1,Y1,Z1 = TRANSVERSE
 DIRECTION
 1070 REM U,V,W = TEST DIRECTION

 1080 REM X,Y,Z = SPECIMEN WIDTH
 DIRECTION
 1090 REM B=COS ANGLE BETWEEN TE
 ST DIRECTION AND SLIP PLANE
 NORMAL
 1100 REM C=COS ANGLE BETWEEN TE
 ST DIRECTION AND SLIP DIRECT
 ION
 1110 REM D=COS ANGLE BETWEEN TH
 ICKNESS DIRECTION AND SLIP P
 LANE NORMAL
 1120 REM E=COS ANGLE BETWEEN TH
 ICKNESS DIRECTION AND SLIP D
 IRECTION
 1130 REM F=COS ANGLE BETWEEN SP
 ECIMEN WIDTH DIRECTION AND S
 LIP PLANE NORMAL
 1140 REM G=COS ANGLE BETWEEN SP
 ECIMEN WIDTH AND SLIP DIRECT
 IONS
 1150 END

B3.2 Earing Profiles

```
10  REM  EARING CALCULATIONS FOR
    BCC SINGLE CRYSTALS ASSUMING
    CRYSTALLOGRAPHIC SLIP WITH
    48 POSSIBLE SLIP SYSTEMS
20  DIM H2(47),K2(47),L2(47),U2(4
    7),V2(47),W2(47),B(47),C(47)
    ,F(47),G(47),T(47)
30  PRINT "EARCRYST"
40  PRINT "PLEASE INPUT MILLER IN
    DICES OF ORIENTATION"
50  INPUT H1,K1,L1,U1,V1,W1
60  REM  WORK OUT TRANSVERSE DIRE
    CTION X1,Y1,Z1
70  X1 = L1 * V1 - K1 * W1
80  Y1 = H1 * W1 - L1 * U1
90  Z1 = K1 * U1 - H1 * V1
100 REM  WORK OUT RADIAL STRAIN
    FOR EACH TEST ANGLE
110 PRINT "THIS COULD TAKE SOME
    TIME-I'LL TELL YOU WHEN I'VE
    FINISHED"
120 FOR A = 0 TO 90 STEP 2.5
130 AX = A * 2 * 3.141592654 / 36
    0
140 DC = (U1 ^ 2 + V1 ^ 2 + W1 ^
    2) ^ 0.5
150 CD = (X1 ^ 2 + Y1 ^ 2 + Z1 ^
    2) ^ 0.5
160 REM  WORK OUT TEST DIRECTION
    UVW AND SPECIMEN WIDTH DIRE
    CTION XYZ
170 U = U1 / DC * COS (AX) - X1 /
    CD * SIN (AX)
180 V = V1 / DC * COS (AX) - Y1 /
    CD * SIN (AX)
190 W = W1 / DC * COS (AX) - Z1 /
    CD * SIN (AX)
200 X = X1 / CD * COS (AX) + U1 /
    DC * SIN (AX)
210 Y = Y1 / CD * COS (AX) + V1 /
    DC * SIN (AX)
220 Z = Z1 / CD * COS (AX) + W1 /
    DC * SIN (AX)
230 REM  FOR EACH SLIP SYSTEM H2
    ,K2,L2,U2,V2,W2 WORK OUT RES
    OLVED SHEAR STRESS T
240 FOR I = 0 TO 47
250 READ H2(I),K2(I),L2(I),U2(I)
    ,V2(I),W2(I)
```

```

260 B(I) = (H2(I) * U + K2(I) * V
      + L2(I) * W) / ((H2(I) ^ 2 +
      K2(I) ^ 2 + L2(I) ^ 2) * (U ^
      2 + V ^ 2 + W ^ 2)) ^ 0.5
270 C(I) = (U2(I) * U + V2(I) * V
      + W2(I) * W) / ((U2(I) ^ 2 +
      V2(I) ^ 2 + W2(I) ^ 2) * (U ^
      2 + V ^ 2 + W ^ 2)) ^ 0.5
280 F(I) = (H2(I) * X + K2(I) * Y
      + L2(I) * Z) / ((H2(I) ^ 2 +
      K2(I) ^ 2 + L2(I) ^ 2) * (X ^
      2 + Y ^ 2 + Z ^ 2)) ^ 0.5
290 G(I) = (U2(I) * X + V2(I) * Y
      + W2(I) * Z) / ((U2(I) ^ 2 +
      V2(I) ^ 2 + W2(I) ^ 2) * (X ^
      2 + Y ^ 2 + Z ^ 2)) ^ 0.5
300 T(I) = ABS (F(I) * G(I) - B(
      I) * C(I))
310 NEXT I
320 REM RANK VALUES OF T AND CO
      RRESPONDING SLIP SYSTEMS ETC

330 FOR J = 0 TO 46
340 FOR I = 0 TO 46
350 IF T(I) > = T(I + 1) THEN GOTO
      420
360 TEMP = T(I)
370 T(I) = T(I + 1)
380 T(I + 1) = TEMP
390 TEMP = B(I)
400 B(I) = B(I + 1)
410 B(I + 1) = TEMP
420 NEXT I
430 NEXT J
440 EK = 0
450 FOR I = 0 TO 47
460 N = I + 1
470 ER = ABS (B(I)) * T(I) ^ 2
480 EK = EK + ER
490 RS = EK / N
500 IF T(I) > T(I + 1) THEN GOTO
      520
510 NEXT I
520 REM RS=AVE. RADIAL STRAIN
530 PRINT "A=";A;" RADIAL ST
      RAIN=";RS
540 RESTORE
550 NEXT A
560 PRINT "HOORAH, FINISHED"
570 DATA 1,1,0,1,-1,1,1,1,0,-1,
      1,1,1,-1,0,-1,-1,1,1,-1,0,1,
      1,1
580 DATA 0,1,1,1,-1,1,0,1,1,-1,
      -1,1,0,-1,1,1,1,1,0,-1,1,-1,
      1,1
590 DATA 1,0,1,-1,1,1,1,0,1,-1,
      -1,1,-1,0,1,1,1,1,-1,0,1,1,-
      1,1

```

```

600 DATA 1,1,2,-1,-1,1,-1,1,2,1
      ,-1,1,1,-1,2,-1,1,1,-1,-1,2,
      1,1,1
610 DATA 1,2,1,1,-1,1,-1,2,1,-1
      ,-1,1,1,-2,1,1,1,1,-1,-2,1,-
      1,1,1
620 DATA 2,1,1,-1,1,1,-2,1,1,1,
      1,1,2,-1,1,-1,-1,1,-2,-1,1,1
      ,-1,1
630 DATA 1,2,3,-1,-1,1,-1,2,3,1
      ,-1,1,1,-2,3,-1,1,1,-1,-2,3,
      1,1,1
640 DATA 3,2,1,-1,1,1,-3,2,1,1,
      1,1,3,-2,1,-1,-1,1,-3,-2,1,1
      ,-1,1
650 DATA 3,1,2,-1,1,1,-3,1,2,1,
      1,1,3,-1,2,-1,-1,1,-3,-1,2,1
      ,-1,1
660 DATA 1,3,2,1,-1,1,-1,3,2,-1
      ,-1,1,1,-3,2,1,1,1,-1,-3,2,-
      1,1,1
670 DATA 2,1,3,-1,-1,1,-2,1,3,1
      ,-1,1,2,-1,3,-1,1,1,-2,-1,3,
      1,1,1
680 DATA 2,3,1,1,-1,1,-2,3,1,-1
      ,-1,1,2,-3,1,1,1,1,-2,-3,1,-
      1,1,1
690 REM H1,K1,L1,U1,V1,W1 = ORI
      ENTATION
700 REM H2,K2,L2,U2,V2,W2 = SLI
      P SYSTEM
710 REM A=ANGLE BETWEEN ROLLING
      AND TEST DIRECTIONS
720 REM T=RESOLVED SHEAR STRESS
      ON SLIP SYSTEM
730 REM X1,Y1,Z1 = TRANSVERSE D
      IRECTION
740 REM U,V,W = TEST DIRECTION
750 REM X,Y,Z = SPECIMEN WIDTH
      DIRECTION
760 REM B=COS ANGLE BETWEEN TES
      T DIRECTION AND SLIP PLANE N
      ORMAL
770 REM C=COS ANGLE BETWEEN TES
      T DIRECTION AND SLIP DIRECTI
      ON
780 REM D=COS ANGLE BETWEEN THI
      CKNESS DIRECTION AND SLIP PL
      ANE NORMAL
790 REM E=COS ANGLE BETWEEN THI
      CKNESS DIRECTION AND SLIP DI
      RECTION
800 REM F=COS ANGLE BETWEEN SPE
      CIMEN WIDTH DIRECTION AND SL
      IP PLANE NORMAL
810 REM G=COS ANGLE BETWEEN SPE
      CIMEN WIDTH AND SLIP DIRECTI
      ONS
820 END

```

PROPERTIES, APPLICATIONS AND PROCESSING OF FERRITIC
STAINLESS STEELS - A CASE STUDY *

C1. INTRODUCTION

Currently, in the United Kingdom, ferritic grades of stainless steel account for only ~10% of the total stainless steel market, ^(C1) although this proportion is considerably higher elsewhere. ^(C2,C3) For example, in 1981 the 17-18% Cr steels represented more than 40% of French stainless steel tonnage. ^(C2) A potential market for increasing usage of ferritic stainless steels is evident, as cost-effective replacement materials either for the more highly alloyed steels or for lower grades of steel having inferior corrosion resistance and hence shorter average life.

It is in this context that the properties and applications of 430 (17 Cr, 0.05C), 430 Ti (17 Cr, 0.03C, 0.5 Ti) and 409 (12 Cr, 0.03C, 0.5 Ti) steels have been reviewed. The maximum benefit (in terms of cost reductions) from the use of ferritic stainless steels can be derived only if production costs are kept to a minimum. Processing schedules for economic production of the steels under consideration have, therefore, been examined, within the limitations of property requirements and commercial practicability.

* A case study submitted as part of Module IV of the
MSc course in Metallurgical Process Management.

C2.1 Cost

Although cost is not a material property, it is an important factor in material selection, so that its consideration in this section is not wholly inappropriate. Relative cost factors (from the literature) for ferritic stainless steel strip compared with mild steel and austenitic stainless steels are shown in Table C1. The relative cost of alloying elements in the stainless steels, calculated from world alloy prices during the same period, (C4) are also shown in the table. Differences between 'finished' costs and alloy costs may reflect, to some extent, differences in processing costs. However, it must be remembered that these world alloy costs do not necessarily represent the true cost of raw materials, because they do not take into account the contribution to alloy content from stainless steel scrap.

Although ferritic stainless steels are considerably more expensive than mild steel, their use is often more cost-effective in applications where mild steel has traditionally been used, due to increased service life. Car exhaust systems are such an example. (C5) Ferritic stainless steels are less expensive than austenitic steels of equivalent chromium content because they do not contain nickel, which is approximately three times the price of chromium. (Ni ~ £3000/tonne, Cr ~ £1000/tonne). (C4)

Ferritic stainless steels exhibit a ductile-brittle transition. The ductile-brittle transition temperature (DBTT) increases with section thickness, and at thin gauges all ferritic stainless steels are ductile at room temperature. (C6) However, for thick sections the DBTT is above room temperature, (C6) unless the interstitial (C+N) content is very low (< 100 ppm or < 400 ppm for Ti-stabilised steel). (C7) In general, ferritic stainless steels are not used for thick plates. Limiting sheet thicknesses in 430 Ti and 409 grades are normally ~ 3.2 mm and ~ 3.8 mm respectively, to ensure that the DBTT is below room temperature. (C6)

Increasing the chromium content of the steel raises the DBTT, whereas reducing carbon and nitrogen contents improves toughness. (C6) Excess titanium in solid solution also increases the DBTT. However, stabilisation with titanium removes harmful carbon and nitrogen from solid solution, thereby improving toughness, (C6) so that stabilised ferritic stainless steels may have a room temperature impact energy higher than that of 430 steel, and approaching that of the austenitic grades. (C8) Titanium-bearing grades have higher impact energies than the extra-low-interstitial (< 0.03 (C+N)) non-stabilised steels, partly because all (C+N) is removed from solid solution but also due to the effect of Ti (CN) particles in restricting grain growth. (C9) Coarse grain sizes are a problem in the extra-low-interstitial steels, and increasing grain size raises the impact transition temperature of 17% Cr

steels as follows :- (C9)

Increasing grain size	<u>ASTM grain size</u>	<u>Impact Transition</u>
		<u>Temperature °C</u>
↓	ASTM 8	~ 0°C
	ASTM 6	~ R.T.
	ASTM 4	~ 40°C
	ASTM 2	~ 80°C

C2.3 Weldability

Standard type 430 steel (17 Cr, 0.05C) is susceptible to hot cracking during welding (C10) and intergranular corrosion after welding, (C7, C10, C11) although susceptibility to intergranular attack may be removed by a post-weld heat treatment in the range 600-800°C. Very low interstitial ($< 0.03 (C+N)$) 430 steel has acceptable resistance to hot cracking, (C10) but coarse grain sizes in the weld zone and Heat Affected Zone (HAZ) reduce weld ductility. (C1) It is also very difficult to ensure that carbon and nitrogen are not picked up during welding (nitrogen from the air; carbon from organic fluxes and grease). The welding procedures used for austenitic stainless steels are generally not sufficiently protective for high purity ferritic stainless steels. (C12) Gas-tungsten arc or gas-metal arc (TIG/MIG) techniques should be used, and a low heat input is required to avoid grain growth and the associated fall in impact resistance. (C7) The low work-hardening rate of ferritic stainless steels also makes them more sensitive than austenitic steels to

defective welds containing notches. (C13)

Stabilisation with titanium, tantalum, titanium + niobium or titanium + tantalum, imparts acceptable resistance to hot cracking for interstitial contents up to 0.04%. (C10) However, niobium stabilisation alone will not prevent hot-cracking. (C10) Titanium is considered the best stabilising element for improved ductility after welding. (C10,C14) This is thought to be due to its effect in restricting grain size, either as excess titanium in solid solution ($[Ti]_{ss}$) or as Ti (CN) particles. (C14) In general, stabilisation with $Ti \geq 12.5 (C+N)$ or with $(Ti + Nb) \geq 9 (C+N)$ is considered sufficient to prevent susceptibility to intergranular attack after welding. (C10) However, if the titanium content is too high, this is detrimental to ductility, since excess $[Ti]_{ss}$ raises the impact transition temperature. For optimum ductility and corrosion resistance after welding, $[Ti]_{ss}$ should be in the range 0-0.4%. (C13)

Devine and Ritter (C15) found that a 12 Cr, Ti-stabilised steel was not susceptible to intergranular corrosion after water quenching from $1200^{\circ}C$, but subsequent aging at temperatures $< 600^{\circ}C$ (which might be encountered in service), caused sensitisation. They proposed that some titanium carbides decompose and go into solution at high temperatures, but do not re-precipitate during rapid cooling. Low temperature aging was believed to cause precipitation of grain boundary chromium-carbides, whereas high temperature aging $> 600^{\circ}C$ results in precipitation of chromium-free,

titanium-carbides. Devine and Ritter (C15) found that a very high Ti:C ratio, ≥ 57.5 , prevented sensitisation altogether. However, the excess titanium in solid solution would be too high for good weld ductility. (e.g., For a 0.03C, 0.01N steel, a titanium content of 1.63% would be required. Excess $[Ti]_{ss}$ would be $> 1.0\%$, since $12.5 (C+N) = 0.5\%$). Post-weld annealing at $\sim 850^{\circ}C$ would be more beneficial, since this would restore intergranular corrosion resistance and also improve weld ductility by coarsening fine precipitates. (C13)

C2.4 Formability

Ferritic stainless steels have low work-hardening rates, comparable with other low-carbon steels. (C16) This is an advantage for deep-drawing, but a disadvantage for stretch-forming. (C13) Ferritic stainless steels are, therefore, suitable for forming by deep-drawing, or a combination of stretching and drawing, but not by pure stretch-forming. (C16) The work-hardening coefficient (\bar{n}) is not highly process sensitive, (C17) and the potential for increasing \bar{n} seems low. (C1, C17) Miyakuso, Uematsu and Hoshino (C18) reported the following relationship between work-hardening exponent and composition :-

$$n = 0.3274 - \left\{ 0.015 \text{ Si} + 0.003 \text{ Mn} + 0.560 \text{ P} + 0.004 \text{ Cr} + 0.050 [Al]_{ss} + 0.069 [Ti]_{ss} + 0.094 [C+N]_{ss}^{\frac{1}{2}} \right\}$$

The authors (C18) also claimed to have developed a high purity ferritic stainless steel with good stretch formability, suitable for producing sinks previously made in 304 type austenitic stainless steel. The new steel was based on a low (carbon + nitrogen), low phosphorous, titanium-stabilised, 13% chromium steel. (C18) The work hardening coefficient reported was ~ 0.27 , which is only slightly higher than recorded for commercial 430, 409 and 430 Ti types, (C17) and still much lower than for austenitic stainless steels ($n \simeq 0.4-0.5$). (C16) The sink illustrated (C18) appeared to have a shallow bowl depth, more typical of a ferritic product (C17) than a modern austenitic stainless steel sink.

Average strain ratios (\bar{r} -values) are often used as a measure of deep drawability, and austenitic stainless steels generally have \bar{r} -values close to unity. (C19) Standard 430 steel also has \bar{r} -values ~ 1.0 , although it has been shown that this can be increased to $\sim 1.2-1.3$ by high temperature pre-annealing at 1000°C and heavily cold rolling reductions $\sim 80-90\%$ RA. (C17) However, with such high pre-annealing temperatures, either very slow cooling or re-heating in the range $600-800^{\circ}\text{C}$ are required to avoid brittleness and sensitisation. Sawatani et al (C20) reported similar \bar{r} -values of $1.2-1.3$ for 430 steel containing $0.1-0.2\%$ Al which had been subjected to a rapid annealing treatment at $\sim 1000^{\circ}\text{C}$ before cold rolling. The authors (C20) found that the addition of aluminium effectively raised the AC_1 temperature, by removing nitrogen from solid solution as AlN precipitates,

so that annealing could be carried out in the 900-1000°C range without sensitisation or partial transformation to austenite.

Low-interstitial, titanium-stabilised steels can be produced with \bar{r} -values ≥ 1.5 . (C19) Experimental work with commercial Ti-stabilised steels has shown that r -values (which are closely related to crystallographic texture), are very process-sensitive and \bar{r} -values up to 2.4 can be achieved with high cold rolling reductions and suitable heat treatments before and after cold rolling. (C17) Composition is also important, and the deep drawability of 409 steel is reputedly enhanced by low carbon and low silicon contents. (C21)

As a result of their improved drawability and low work hardening coefficients, low-interstitial, Ti-stabilised ferritic stainless steels have replaced austenitic stainless steels in some applications, e.g., deep-drawn automotive parts, because they can be drawn and re-drawn without intermediate annealing. (C13) Ferritic stainless steels may also be used to replace mild steel and other low carbon steels to give products of improved corrosion resistance and hence prolonged service life without the need for new capital investment, since the same equipment can still be used for their manufacture.

C2.5 Elevated Temperature Properties

Ferritic stainless steels have higher thermal conductivities and lower coefficients of thermal expansion than austenitic grades, (C22) and this

combination of properties makes them more useful for applications such as heat exchangers. The oxidation resistance of ferritic stainless steels is also high compared with austenitic types. The "scaling temperature" (defined as the temperature at which weight loss through scaling is a maximum of 0.3mm/year (C13)) of 430 Ti steel is $\sim 1000^{\circ}\text{C}$, compared with $\sim 860^{\circ}\text{C}$ for 304 and 316 grades of austenitic stainless steels. (C13) Additions of silicon and aluminium are reputed to enhance oxidation resistance still further. (C6) Ferritic stainless steels also have good resistance to attack by sulphur-containing gases. (C13)

Steels containing $>13\%$ Cr suffer embrittlement as a result of prolonged exposure to temperatures in the range $\sim 340-540^{\circ}\text{C}$, the maximum loss of ductility and toughness occurring $\sim 450-540^{\circ}\text{C}$. (C6, C23) However, since steels containing $\leq 13\%$ Cr do not undergo this 475°C embrittlement, type 409 steel (12 Cr, 0.5 Ti) can be used within this range. (C24, C25) Hot strength of ferritic stainless steels decreases at $\sim 540^{\circ}\text{C}$, although oxidation resistance is still good and the strength is adequate for applications involving low applied stresses. (C6) For dynamic loading, however, the service temperature of $\sim 17\%$ Cr steels should not exceed $\sim 375^{\circ}\text{C}$. (C13)

C2.6 Corrosion Resistance

The corrosion resistance of ferritic stainless steels is far superior to that of mild steel and, for some applications can even offer competition with

austenitic stainless steels. In general, the corrosion resistance is adequate when in contact with 'common' media, such as moisture and the atmosphere (Table C2^(C26)), and ordinary food products. (C8) Ferritic stainless steels can perform better than 304 type austenitic steel in oxidising media, but not in reducing acids such as H_2SO_4 . (C6) The extra-low-interstitial Ti-stabilised steels have good corrosion resistance in organic acids,^(C13) but cannot be used for service in nitric-acid because HNO_3 attacks Ti(CN) particles. (C27)

The resistance of ferritic stainless steels to pitting corrosion is comparable to that of austenitic steels of the same chromium content, and is improved by stabilisation with titanium. (C2) Additions of molybdenum increase pitting resistance still further, though at increased cost. (C2) Åslund (C13) found that low manganese contents (0.1-0.2% Mn) also enhanced pitting resistance, and suggested that the chromium content of sulphide inclusions (where pits are usually initiated) was higher for low-manganese steels, so that the sulphides were more resistant to attack. Good surface condition has also been found to be important for pitting resistance. A ground surface gives lowest pitting resistance whereas a ground + electrolytically polished + passivated surface has high resistance to pitting corrosion. (C13)

An important advantage of the ferritic stainless steels is that, unlike austenitic stainless steels containing $< \sim 30/40\%$ Ni, they are immune to stress-corrosion-cracking in chloride environments,

except perhaps when very heavily cold worked. (C2)

C2.7 Surface Quality

Standard 430 type steel is often used as flat products, for which the main customer requirements are good surface quality and brightness. (C1) Two surface phenomena which can impair the surface of ferritic stainless steels are "ridging" and "roping". Ridging is a slight rippled effect seen on the surface before straining, and it impairs the reflectance of the surface and also its clarity of image. (C1) Most of this effect can be removed by careful cold planishing after annealing.

In contrast, roping is characterised by corrugations parallel to the rolling direction, which appear after straining $\sim 10\%$. (C28) If roping is severe, extensive polishing of a formed product may be necessary for applications requiring good cosmetic appearance. Roping is minimised by control of processing conditions, especially the finishing temperature after hot rolling. (C28) Steels containing $< 13\%$ Cr do not exhibit roping, and it also tends to be less severe in Ti-stabilised steels. However, Ti-stabilised steels cannot be polished without spoiling the surface, and so any effect due to roping remains permanent.

Low interstitial steels, especially those without stabilising additions which restrict grain growth, also suffer from the 'orange peel' defect after forming. Grain sizes coarser than \sim ASTM 7 are undesirable for

good surface finish in formed products.

Stringers of coarse Ti(CN) particles can impair surface quality in titanium-stabilised steels. This effect is a greater problem in ingot products than in continuously cast steels, since titanium may segregate to the surface and combine with carbon in mould wall compounds. (C1)

Table C3 gives examples of applications (either in the United Kingdom or elsewhere) for the steels under consideration. These may be conveniently subdivided into 'normal' (R.T. or $\leq 100^{\circ}\text{C}$) temperature and elevated temperature applications, and also heat transfer applications which may be for 'normal' or elevated temperatures.

C3.1 Normal ($\leq 100^{\circ}\text{C}$) Temperature Applications

The properties exploited are mainly corrosion resistance, formability and sometimes weldability. In many of these applications, (e.g., vehicle parts, mining equipment, catwalks), ferritic stainless steels have been used to replace mild steel. Although mild steel is cheaper, and may be protected by painting or coating with zinc or aluminium, the protection is lost if a painted or aluminised coating is damaged (e.g., in vehicle undersides, by stones thrown up or the action of ice and salt in winter). Although galvanising protects the underlying metal even when scratched, zinc embrittlement can be a problem. (C5) An advantage of using ferritic stainless steels (instead of austenitic stainless steels) to replace mild steel is that their properties are similar so that, in general, the same manufacturing techniques and equipment can be used, although more care is needed for welding.

For applications such as food handling equipment, sinks, dishwashers, hot-water tanks, etc.,

general corrosion resistance and also pitting and crevice corrosion are important. Provided that the corrosion conditions are not too severe, ferritic stainless steels can compete with austenitic stainless steels in many of these applications. (C2) Steels used in food handling equipment must be capable of resisting corrosion not only by the food itself, but also by the cleaning solutions used. (C2)

Hot water tanks may have quite a high chloride ion content, and the immunity to stress corrosion cracking of ferritic stainless steels is therefore an advantage in this application. Pitting corrosion resistance is also important if leaks are to be avoided, so that surface quality must be good.

Ferritic stainless steel sinks have been produced in this country, as a cheaper product to satisfy some foreign markets. (C29) However, there is no demand for them in this country at present, nor is any home market envisaged unless nickel prices rise dramatically and the cost of austenitic stainless steels becomes prohibitive. (C29) The comparatively poor stretch formability of ferritic stainless steels prevents their use for the modern, deep (often double-bowl), "luxury" sinks currently in demand. The surface appearance of ferritic stainless steel sinks also tends to be variable, since the phenomenon of roping causes the more heavily formed bowl to have a duller appearance than the draining-board section.

C3.2 Heat Transfer Applications. (e.g., radiators heat-exchangers)

Corrosion resistance, low thermal expansion coefficients and high thermal conductivity are all exploited in heat transfer applications. Resistance to stress-corrosion cracking and pitting corrosion may be important, for example in cooling fins and condenser tubing. Some heat transfer applications involve high temperatures where the oxidisation resistance of ferritic stainless steels is a great advantage, e.g., internal heat exchangers for accelerated cooling in batch furnaces.

C3.3 Elevated Temperature Applications

For high temperature applications, oxidation resistance and adequate hot strength are required in addition to corrosion resistance, and sometimes good formability and weldability.

e.g. (i) Vehicle Exhaust Systems

The average life of a mild steel exhaust system is only ~ 18 months. (C30) Failure is usually a combination of fatigue and corrosion. (C31) Fatigue failures can be minimised by improved design and corrosion damage can be minimised by materials selection. Corrosion is suffered both internally and externally in exhaust systems. External corrosion is due to water and solids thrown up from the surface of the road, and is accelerated by grit impact and salt spray. (C30) Protective coatings may be used (e.g., aluminised steel), but these are easily damaged. (C31) Internal damage is of two types, depending upon the temperature inside the

system. For short journeys, and especially on cold days, low-temperature condensate corrosion is the main form of attack. With longer journeys, the damage is caused by high temperature oxidation and erosion by exhaust fumes. (C30)

The properties required in a stainless steel for manufacture of exhaust systems are corrosion resistance, oxidation resistance, weldability and formability (deep drawability rather than stretch-formability). (C31)

Type 409 ferritic stainless steel is generally regarded as the preferred material for economic mass production of stainless steel exhaust systems. (C5)

Rolls Royce have been using austenitic stainless steel exhausts since 1963 but, for the average car, austenitic stainless steels are not necessarily cost effective. (C31)

Typical average life and cost/life ratios for mild steel and stainless steel exhausts are as follows :- (C31)

<u>Material</u>	<u>Ave.life (years)</u>	<u>Cost/life ratio</u>
Mild steel	1.5	1.0
Aluminised mild steel	2.25	0.9
409 stainless	5.0	0.53
304 stainless	5 - 10	0.65 - 0.32

e.g. (ii) Catalytic Converter Casings

Casings for catalytic converters represent a large, potential market for ferritic stainless steels when new emission-control regulations come into force in the United Kingdom. Japan and the USA already have strict

controls, and most companies solve the problem of cleaning up vehicle exhaust fumes by using catalytic converters. (C3) In ~ 1975, this new use increased stainless steel consumption in the USA by ~100/180 thousand tonnes per year (~ 20%). (C3)

The function of catalytic converters is to convert carbon monoxide, oxides of nitrogen and hydrocarbons into their harmless derivatives :- carbon dioxide, nitrogen and water. Ceramic or metal honeycombs, or aluminium pellets, are coated with a platinum or rhodium catalyst, which catalyses the reactions that produce these derivatives at elevated temperatures. Use of catalytic converters requires lead-free petrol, since lead 'poisons' the platinum-group catalysts. (C32)

The casings for catalytic converters require oxidation resistance and high-temperature strength. Operating temperatures depend on the catalyst used, since different catalysts are activated at different temperatures. Some converters operate at ~ 450°C and others at ~ 600°C. Legal speed restrictions must also be considered since these can affect the anticipated working temperature.

Type 409 steel performs satisfactorily at ~ 450°C (C30) and is widely used in the USA. (C5)

Some USA companies promoted alternative 12 Cr ferritic steels with additions of silicon and aluminium for increased oxidation resistance, but the majority opted for 409 steel. (C3) Problems of 'sagging', which lead

to restricted gas flow, were encountered initially, due to limited hot strength. (C3) However, most US manufacturers chose to overcome the problem by using extra supports rather than higher alloyed steels such as 321 (18 Cr, 11 Ni + Ti) austenitic stainless steel, which has similar oxidation resistance but greater hot-strength at $\sim 450^{\circ}\text{C}$. (C32) For operating temperatures $\sim 600^{\circ}\text{C}$ 409 does not perform satisfactorily, and 430 Ti (17 Cr + Ti) steel is recommended. (C30)

C4.1 Melting and Casting

Ferritic and austenitic stainless steels are made by electric arc furnace melting followed by AOD (Argon-oxygen decarburisation) secondary steelmaking. The introduction of the AOD process has made possible the commercial production of high tonnages of low interstitial steel with good production economy. (C13) With AOD secondary refining the chromium additions can be made before blowing, in the form of stainless steel scrap and high-carbon charge-chrome. Previously, low carbon, high-chromium steel could only be made by adding chromium in a very expensive, low-carbon form after decarburisation by oxygen blowing.

Ferritic stainless steels may either be cast into ingots, or continuously cast and cut into slabs. Continuous casting is preferred because it is a cheaper route, (C1) and also enables a more uniform product to be made. (C33) Nonmetallic inclusions are generally finer and more evenly distributed, and are, therefore, less detrimental to ductility and formability. (C33) Peripheral segregation is less of a problem with concast Ti-stabilised steels than with ingot products, in which titanium tends to combine with mould wall compounds. (C1) Some segregation does occur even in concast steels, but this may be minimised by electromagnetic stirring.

Due to the tendency for hot cracking to occur in ferritic stainless steels, they must be cooled more slowly than austenitic steels after casting. Slabs are

usually stacked, and any dressing is done while the steel is warm (200-400°C), to prevent clinking. (C1)

C4.2. Hot Rolling

Similar hot rolling conditions are applicable to 409, 430 and 430 Ti steels. For optimum hot ductility, the working range for ferritic stainless steels is ~ 850/900°C to 1200°C. (C8) The soaking temperature is usually ~ 1200°C, although Sawatani et al (C20) found that, for a 17 Cr + Al steel, decreasing the slab-heating temperature to ~ 1000/1050°C allowed recrystallisation of the hot-rolled strip to be accomplished with lower annealing temperatures. Too high a soaking temperature causes sagging of the billets. (C1)

The duplex α/γ structure present during hot-rolling of 430 steel has an adverse effect on hot workability. Cracking may be initiated at α/γ or carbide/ α interfaces. (C22) The hot ductility of 17 Cr steels is improved dramatically by additions of titanium, aluminium or molybdenum, especially titanium, due to restriction or elimination of the two-phase field. (C22)

The hot-rolling finishing temperature is normally ~ 900°C. (C1) Decreasing the finishing temperature to ~ 720°C has been claimed to improve \bar{r} -values, \bar{n} -values and roping severity significantly. (C23, C28) However, in practice, lower finishing temperatures have been found to have an adverse effect on the surface quality of 430 steel. During the early stages of hot rolling, simultaneous bending

and transformation of the columnar grains at the surface results in a 'blocky' structure, in which planes of weakness correspond with α/δ interfaces. (C1) Entire grains may be extracted due to roll surface friction if the rolling temperature is too low, resulting in pitting and poor surface quality. (C1) The severity of this problem varies from mill to mill, but the optimum temperature for finishing the 'roughing' passes is $\sim 1050^{\circ}\text{C}$. (C1) Some hot rolling below the dynamic recrystallisation temperature is desirable, particularly for heavier sections, since this promotes a fine grain size after annealing, which is beneficial to ductility and impact toughness. (C13)

The hot-rolled gauge depends on the final thickness required and the cold rolling schedule. The minimum hot-band gauge is $\sim 2.5\text{mm}$, and the most usual thicknesses are in the range $\sim 3\text{-}6\text{mm}$. (C1)

Coiling after hot-rolling may be carried out while the strip is still hot, in which case the coiling temperature is $\sim 200^{\circ}\text{C}$ lower than the finishing temperature, (C1) or the strip may be spray-quenched before coiling. The main problem with hot-coiling is that the ends of the coil cool faster than the centre, and therefore uniform properties throughout the length of the coil are not generally achieved. However, the slower cooling rate associated with hot rolling would allow more recovery to occur, which might be important if the material was to be cold-rolled without pre-annealing. With 430 steel, it would also have the effect of tempering any martensite formed, which might otherwise

cause brittleness. Spray quenching before coiling might be beneficial to Ti-stabilised steels, depending on the softening treatment to be applied before cold rolling.

C4.3 Softening and Descaling

The hot rolled strip must be descaled before cold rolling, and this is usually carried out using a nitric acid/HF solution. If the material is to be softened, this is done before descaling. A choice between batch annealing and continuous line annealing must be made.

C4.3.1. Batch (Tight Coil) Annealing

Tightly wound coils are arranged in stacks, separated from each other by convector plates, in single or multiple stack configurations. (C34) A steel cover is placed over each stack to retain the circulating protective atmosphere, which also increases heat-transfer to the coils. The covered stacks are heated by a bell-type furnace. (C34)

Modern batch-annealing furnaces are usually direct fired, and make use of high-momentum burners and fan-assisted circulation to ensure more rapid, uniform heating and conserve energy. (C35,C36) Use of ceramic fibre furnace linings and internal recuperators (which preheat the air used for combustion and hence save fuel) also conserve energy. (C35-C37)

Accelerated cooling is also widely used, to increase production and prevent batch annealing becoming a bottleneck. (C35) For ferritic stainless steels,

accelerated cooling also avoids prolonged exposure to temperatures in the range 350-550°C, reducing the risk of 475°C embrittlement. Both internal and external heat exchangers are used for accelerated cooling (C36) (internal heat exchangers are positioned in the base of the furnace). Water flowing through the fins during the cooling cycle (but not during the heating cycle) causes rapid cooling of the atmosphere gas recirculating within the inner cover. This in turn cools the load by forced convection from the base fan. (C35) It is claimed that such a system can halve the cooling time for a 240 tonne charge, giving increased capacity and reduced costs. (C35)

Computer control of batch processing gives improved repeatability and reliability. (C35,C36) In addition, energy savings can be made due to reductions in excess heating, since coil conditions are known and heating times can be minimised. (C35,C36)

C4.3.2. "Semicontinuous-Batch Annealing"

Nippon Kokan have developed a semi-continuous batch annealing process ("Uniflow"). (C38) This consists of a two-chamber, stationary furnace (i.e., no removable bell), with sophisticated door seals which eliminate the need for an inner cover. Coils are loaded, one deep (not stacked), onto a tray which is then transferred into the heating chamber on friction rollers. Heating is by radiation from radiant tubes in the roof and walls, and by convection of the protective furnace gas. More uniform heating than conventional batch annealing is claimed because the coils are not stacked. (C38)

Once heating is complete, the tray moves through to the cooling chamber, which is sealed off from the furnace section by a partition door during the heating cycle. The next tray of coils then enters the heating chamber, which is still hot. The cooling cycle must be quicker than the heating cycle to keep the process running smoothly, i.e., one tray of coils must be discharged from the cooling chamber before the next tray is ready to enter it. Cooling is assisted by circulating fans and heat exchangers. (C38)

Nippon Kokan reported that installation of this system (~1983) halved the processing time and allowed savings in fuel and manpower, for a capital cost only ~ 10% higher than a conventional batch furnace system. (C38)

G4.3.3 Continuous Annealing

With continuous ('line') annealing, the strip is uncoiled at the entry to the line and re-coiled at the exit. A continuous band of strip, therefore, passes through the furnace and cooling chambers, and annealing is rapid (~ 2-3 minutes residence in the furnace). Line speeds and furnace temperature settings are adjusted to give the correct annealing conditions for the gauge and composition of steel passing through the furnace. The furnace section is generally divided into several heating zones, whose temperature settings may be adjusted independently. The zone settings are generally higher than the temperature of the strip, since movement through the furnace is rapid.

The entry and exit sections of the line have to be stopped periodically for successive coils to be joined (welded on), or cut off after processing. The entry and exit sections are, therefore, separated from the annealing section by strip-storage towers ('accumulators'), which provide strip reservoirs to keep the annealing section running continuously. (C39)

During prolonged line stoppages (e.g., breakdowns) furnace zone settings have to be reduced to prevent the strip from achieving too high a temperature. Even so, the microstructure and properties of the section of coil residing in the furnace during such a line stoppage can be different from the rest of the coil, and that section may eventually have to be cut out.

Benefits of continuous annealing generally include greater consistency of properties throughout a coil, (C33) reduced production time, (C38) and reduced equipment and manpower costs. (C38) With line annealing, pickling and cleaning tanks can be included in the same line, whereas batch-annealed material must be uncoiled and sent down a separate pickling line after heat-treatment.

C4.3.4 Pre-annealing Treatments for Ferritic Stainless Steels

(a) 430 Steel

Hot-rolled 430 steel is sensitised and therefore susceptible to intergranular corrosion. Softening is therefore essential, to allow back-diffusion of chromium to denuded regions, and prevent

severe intergranular attack during pickling. (C1)

Failure to soften causes surface problems or cracking during later stages of processing. (C1) Transformation to austenite and re-solution of the carbides during heat treatment must be prevented, to avoid introducing martensite into the structure and re-sensitising.

Hot-rolled 430 steel is not line-annealed because, at the permissible temperatures, the times required for back-diffusion of chromium are too long, so that sensitisation is not eliminated. Lula (C40) suggested that a very slow line anneal might be sufficient to restore immunity to intercrystalline corrosion, but this would be very expensive and could cause delays in production. Batch annealing is, therefore, used for 430 steel. (C1) During batch annealing, the temperature is limited to $< \sim 810^{\circ}\text{C}$, but sufficient time above the recrystallisation temperature must be allowed. A typical batch annealing cycle would aim for ~ 5 hours $> 750^{\circ}\text{C}$.

Experimental work (C17) has shown that \bar{r} -values of cold rolled and annealed 430 strip can be improved by heat-treating the as hot-rolled material at 1000°C before cold rolling. However, a subsequent softening treatment, or slow cooling and holding in the range $600-800^{\circ}\text{C}$, would be required for softening and restoration of corrosion resistance. However, this two-stage, prolonged heat treatment would be too expensive and would cause a bottleneck in production. Additions of aluminium to 430 steel are reputed to make continuous annealing at high temperatures ($\sim 900-1000^{\circ}\text{C}$)

viable and to improve \bar{r} -values. (C20) The effect of aluminium is to raise the A_c temperature, by removing nitrogen from solid solution, so that annealing can be carried out at the higher temperature without transformation to austenite occurring, and without the steel being sensitised. (C20)

However, aluminium additions, like titanium additions, reduce the polishability of the steel. The benefits to be gained from aluminium additions, in terms of increased \bar{r} -values, are not as great as with titanium stabilisation.

(b) 409 and 430 Ti Steels

The low-interstitial, titanium-stabilised steels do not suffer from the sensitisation problems associated with 430 steel, and they can, therefore, be descaled without prior softening. Cold rolling without pre-annealing is also possible because no martensite is formed, and the work-hardening rate is low. It is usual to process 409 steel without softening. (C1)

Experimental work (C17) on 430 Ti steel has shown that \bar{r} -values up to ~ 2.0 can be achieved without pre-annealing, but that higher \bar{r} -values coupled with lower planar anisotropy (Δr) can be realised if the hot-rolled strip is heat-treated. Laboratory 'batch-annealing' (heating rate = 50°C hr^{-1} , FC at 50°C hr^{-1}) generally promoted higher \bar{r} -values than 'rapid' annealing (heating rate $\sim 5000^\circ\text{C hr}^{-1}$, AC). (C17) Commercial trials also indicated that batch annealing of 430 Ti steel promoted higher \bar{r} -values than line annealing, although line annealing promoted more uniform properties

throughout the coil. (C1) Spray quenching after hot-rolling might help to promote more uniform properties by ensuring uniform cooling, provided that the thickness is less than ~ 4 mm (to avoid problems with toughness and ductility). However, differences in the heating and cooling rates experienced by opposite ends of a coil are inevitable in a tight-coil batch annealing process.

Commercial batch annealing of 430 Ti steel has been found to be more cost effective than line annealing. For 4mm thick hot-rolled strip, the estimated total cost of line annealing and descaling was 1.4 times the cost of batch-annealing (calculations based on the speed of the line needed to achieve the required properties). (C1) Line softening and descaling is more cost effective for austenitic stainless steels because the line can be operated approximately twice as fast. (C1) Spray quenching after hot rolling might improve the response to line annealing, by restricting recovery and thereby providing a greater driving force for recrystallisation, but this has not been studied.

Cold rolling of 430 Ti steel without prior annealing may be viable for some applications, particularly those for which 409 steel is sometimes used (e.g., catalytic converter casings), since similar textures are developed as a result of equivalent processing conditions in the two steels. However, increased roping severity (a problem not encountered in 409 steel) might be a problem with 430 Ti steel. (C41) Conversely, batch annealing of 409 steel would be

beneficial for applications requiring better deep drawability than is normally achieved.

C4.4 Cold Rolling

Stainless steel strip is cold rolled using Sendzimir mills (Z-mills), which can accept hot-band gauges up to a maximum of 8mm. (C37) Cold rolling is very expensive compared with hot rolling, and therefore the aim is to achieve the maximum feasible reduction by hot rolling, using the minimum amount of cold rolling necessary for the properties required. Two-cycle cold rolling schedules, incorporating intermediate annealing, are even more expensive and undesirable. However, there is a limit to the amount of cold reduction that can be accomplished in a single cycle without impairing strip shape and surface condition. (C1) For a commercial, wide-strip operation, the limit is ~ 70-80% RA.

Some authors (C27,C42) claim that \bar{r} -values are enhanced by a two-stage cold rolling process with a high second cold reduction, but others (C43,C44) have found that single-stage cold rolling promoted higher \bar{r} -values in stabilised ferritic stainless steels. Two-stage cold rolling is also reputed to have the disadvantage of increasing planar anisotropy in both stabilised and non-stabilised ferritic stainless steels. (C42,C45)

Commercial trials on 430 Ti steel indicated that marginally higher \bar{r} -values were achieved using a two-stage reduction, but that differences in formability

resulting from single and double cycle processing were not sufficiently large to be noticeable to the customer. (C1)

Laboratory heat-treatment and cold rolling of commercial hot-rolled 430 Ti strip indicated that \bar{r} -values up to 2.4 can be achieved using single stage cold rolling, coupled with suitable annealing treatments before and after rolling. (C17) Highest \bar{r} -values were generally achieved with high cold reductions ($\sim 90\%$) in both 409 and 430 Ti steels, but \bar{r} -values were only slightly lower after 80% RA, especially with batch pre-annealing. Even without pre-annealing, the maximum \bar{r} -value for 430 Ti steel was 1.98. (C17)

Average strain ratios for 430 steel only exceeded unity with a high pre-annealing temperature ($\geq 1000^\circ\text{C}$), and then the optimum cold rolling reduction was $\sim 80\text{-}90\%$ RA. (C17) For commercially viable pre-annealing treatments, there was little difference in \bar{r} -values achieved after 70% RA and 90% RA, and the lower cold rolling reduction could be used.

The most common final gauges of ferritic stainless steels are in the range 0.5-1.0mm (especially 0.7 and 0.8mm), and also 2mm. (C1) Hot-rolled gauges are usually between 3mm and 6mm, but the range of possible gauges is $\sim 2.5\text{-}8\text{mm}$. (C1,C37) Table C4 shows suggested hot-rolled gauges for different final thicknesses, assuming single cycle cold rolling to 70-80% RA (430 steel) and 75-80% RA (430 Ti/409 steels).

Final annealing of stainless steel strip is always carried out on a continuous annealing line. Batch annealing is not applicable because, at this stage, paper interleaving is required to protect the surface of the coil, and this would be destroyed in a batch furnace. (C1) The coils must, therefore, be uncoiled, the paper removed, passed down a continuous annealing line, and re-coiled with fresh paper interleaving. (C1) There are two types of annealing process, depending upon the surface finish required. Bright annealing is used to give a 2A finish, (C46) whilst line softening and descaling gives a duller, 2D finish, (C46) which becomes a 2B finish after cold planishing. (C46) Grade 409 steel is usually supplied with a 2B finish, and is, therefore, processed on a soften + descale line of the type used for line annealing of hot-rolled strip. (C1) The demand for 430 steel is usually in a bright-annealed condition. (C1)

Bright Annealing

Bright annealing is carried out in high purity atmospheres of hydrogen and nitrogen, with low dew-points ($\sim -50^{\circ}\text{C}$). (C47) Rapid, uniform final cooling to the discharge temperature ($\sim 90^{\circ}\text{C}$) is used, to enhance steel quality without dimensional distortion. An example of the plant demanded by the special steel industry is the "U-type" vertical tower furnace, in which heating and cooling are accomplished in the downward pass. (C47)

A continuous band of strip is guided through the inlet seals and up the atmosphere tunnel to a terminal

drum at the top of the tower, and into the furnace section. Heating is by heavy-duty molybdenum rod electric heaters, suspended from the high purity alumina refractory lining. (C47) The furnace is divided into four temperature setting zones, and both sides of the coil are heated simultaneously. (C47) As the coil passes out of the heating section and into the cooler section, it is cooled by jets of cold atmosphere. Each jet cooler is fitted with an independent heat exchanger and fan, and the protective atmosphere is recirculated in a definite path, designed to achieve rapid and uniform cooling. (C47) The protective atmosphere is generally provided by electrically heated ammonia dissociators. Continuous atmosphere seals must be fitted to the entry and exit vestibules. (C47)

Austenitic and ferritic stainless steels can be heat-treated with maximum outputs of ~ 12 tonne hr^{-1} and ~ 8 tonne hr^{-1} respectively. (C47) Temperature settings for 430 steel are usually $\sim 920-940^{\circ}\text{C}$, although the strip temperature never exceeds $\sim 900^{\circ}\text{C}$, (C1) or re-hardening could occur. Re-hardening is not a problem with titanium stabilised steels, but grain coarsening occurs at $\sim 950^{\circ}\text{C}$. (C17) Commercial trials have been carried out on 430 Ti steel using the temperature settings used for 430 steel, but the line had to be operated at a slower speed, due to the more sluggish recrystallisation of the titanium-stabilised steel. (C1) This means that 430 Ti steel is more expensive to anneal than 430 steel. Increased

temperature settings might allow normal line speeds to be used for 430 Ti steel to increase production rate, but costs would still be higher (higher energy costs), and care would be needed to avoid grain coarsening.

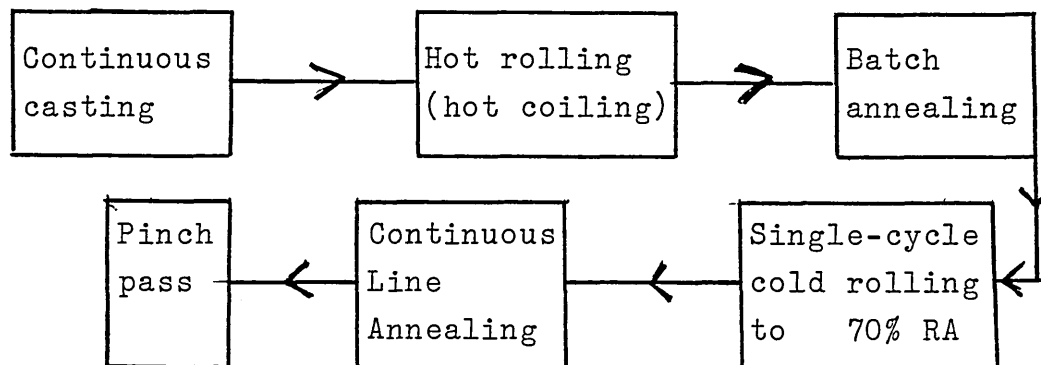
C4.6 Pinch Pass Cold Rolling

After final annealing, stainless steel strip is subjected to a cold-rolling pinch pass. The amount of cold rolling reduction is negligible, and the deformation is usually described in terms of $\sim 1\%$ elongation of the surface. This improves surface quality, and eliminates the yield point in 430 steel so that stretcher-strains are not observed during forming. (Titanium stabilised steels do not exhibit a definite upper and lower yield point).

At present, ferritic stainless steels represent only ~ 10% of the United Kingdom market. However, potential for increased use of high-formability ferritic stainless steels is foreseen, especially in the automotive and food industries. There seems to be little scope for improving formability of 430 steel within commercial processing limitations. Titanium-stabilised steels offer excellent deep-drawability together with weldability and improved ductility, toughness and corrosion resistance.

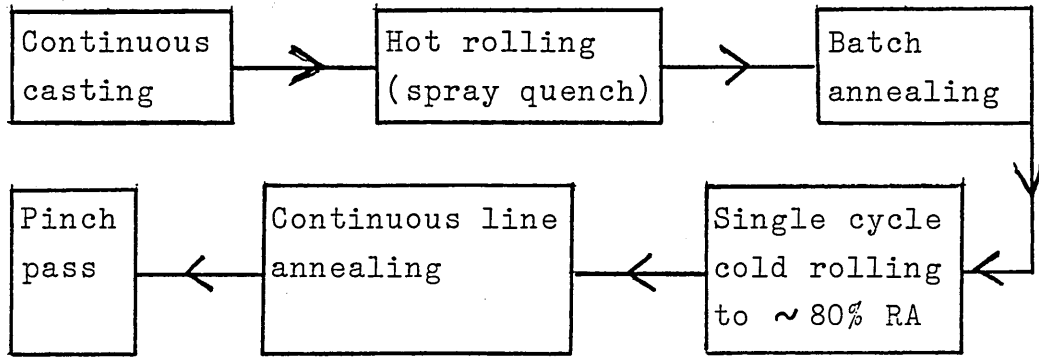
Processing schedules considered suitable for cost-effective production of the steels under review are as follows :-

(a) 430 steel (17 Cr, 0.05C)

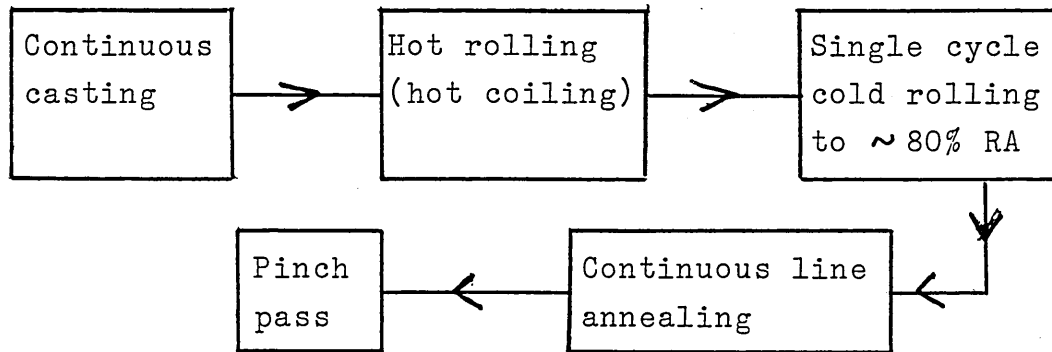


(b) 409 (12 Cr, 0.03C, 0.5Ti) and 430 Ti
(17 Cr, 0.03C 0.5Ti) Steels

(i) For 'high' formability (very high \bar{r} -values)



(ii) For good \bar{r} -values at reduced cost



- C 1 J. WILKINSON & B. HARKNESS :- Private
Communication.
- C 2 G. DAUFIN et al :- Mem. Étud. Sci. Rev. Metall.,
1981, (12), p.647-662 (BISIT 20786).
- C 3 R. JACKSON :- Metals Australia, April, 1975,
p.57-61.
- C 4 P. ROBINS & J. EDWARDS :- "Guide to Nonferrous
Metals and their Markets" (Kogan Page).
- C 5 J.R. FLETCHER :- Stainless Steels Ind., May 1977,
5, (25), p.8-9.
- C 6 R.A. LULA :- Metal Progress, July 1976,
p.24-29.
- C 7 H. SPÄHN :- Metal Progress, Feb. 1979, p.32-37.
- C 8 M GUTU et al :- Wiad.Hutn., 1982, (6),
p.183-188. (BISIT 22519).
- C 9 F.B. PICKERING :- Int. Metals Review,
Dec. 1976, p.227.
- C10 D.H. KAH & D.W. DICKINSON :- Supplement to
the Welding Journal, Aug. 1981, 135.S-142.S.
- C11 M. TAKEDA et al :- Tetsu-to-Hagane, 1977, 63,
(5), p.622-630 (BISIT 17032).
- C12 A.J. SEDRIKS :- "Corrosion of Stainless Steels",
(Wiley Interscience, 1979).
- C13 C. ÅSLUND :- Scand. J. Metallurgy, 1976,
(5), p.200-207.
- C14 R.N. WRIGHT :- Welding J. Research Supplement,
Oct. 1971.

- C15 T.M. DEVINE & A.M. RITTER :- Met. Trans.,
Aug. 1983, (14A), p.1721-1728.
- C16 PECKNER & BERNSTEIN :- "Handbook of Stainless
Steels". (McGraw-Hill).
- C17 C. BOULTON :- Experimental work.
- C18 K. MIYAKUSU, Y. UEMATSU, K. HOSHINO :-
IDDRG 13th Biennial Congress, Melbourne,
Australia, 20-24th Feb. 1984.
- C19 K.J. BLOM :- Sheet Metal Ind, Jan. 1980,
p.25-29, 80.
- C20 T. SAWATANI, T. ASHIURA, M. WAKAMATSU,
H.YOSHIMURA, M. ISHII, A. YAMAMOTO :- Nippon
Steel Tech. Report, June, 1983, (21),
p.275-290.
- C21 B. POLLARD & A.H. ARONSON :- Metals Eng.
Quarterly, Aug. 1973, p.28-31.
- C22 S.K. SEN, S.R. MEDIRATTA, V. RAMASWAMY :-
Tool Alloy Steel, March, 1981, 15, (3)
p.95-98.
- C23 S.R. MEDIRATTA, V. RAMASWAMY :- Tool Alloy
Steel, Dec. 1976, 10, (12), 451-461.
- C24 R. TRICOT & R. CASTRO :- Metal Treatment,
Oct. 1966, p.401-405.
- C25 T.J. NICHOL, A. DATTA, G. AGGEN :- Met. Trans,
April 1980, (11A), p.573-585.
- C26 METAL PROGRESS, Feb. 1980, p.46.
- C27 R.F. STEIGERWALD, H.J. DUNDAS, D. REDMOND,
R.M. DAVISON :- The Metallurgist & Materials
Technologist, April 1978, p.181-189.

- C28 K. WETZLAK & M. MOZEK :- DEW Technishe
Berichte, 1970, 10, (2), p.188-196.
- C29 I. MOSS :- Private Communication.
- C30 B.S.C STEEL RESEARCH, 1975, p.43-45.
- C31 R.A.E. HOOPER :- Sheet Metal Ind., Jan. 1978,
p.15-22.
- C32 J. STANSELL :- New Scientist, 24th Nov. 1983,
p.564-567.
- C33 R.M. HOBBS :- IDDRG 13th Biennial Congress,
Melbourne, Australia, 20-24th Feb. 1984.
- C34 R.M. LEWIS :- BHP Technical Bulletin, No. 2,
Nov. 1981.
- C35 IRON & STEEL ENGINEER, July 1980, p.25-28.
- C36 INDUSTRIAL HEATING, Oct. 1980, p.8-12.
- C37 SHEET METAL INDUSTRIES, Jan. 1981, p.27-33.
- C38 E. TOHMATA, M. KURATA, M. WATANABE, T. TANAKA,
K. SEKIGUCHI :- Iron & Steel Engineer,
Nov. 1983, p.43-49.
- C39 J. LONSDALE & P. DEACON-SMITH :- Steel Times,
May 1980, p.358-367.
- C40 R.A. LULA :- Trans. ASM, 1954, (46), p.197.
- C41 Y. NAKAGAWA, T. SAKAMOTO, I.YAMAUCHI,
T. YAMAZAKI, M. UENO :- Tetsu-to-Hagane, 1980,
(6), p.657-666.
- C42 S. KADO, T. YAMAZAKI, T. SAKAMOTO, Y. NAKAGAWA,
S. INOUE, S. IZUMI, T.ASHIURA, & S. UCHIDA :-
Trans. ISI Japan, 1979, (19), p.315-323.
- C43 T. SAWATANI, K. SHIMIZU, T. NAKAYAMA &
M. MIYOSHI :- Trans. ISI Japan, 1978, 18,
(11), p.676-685.

- C44 T. SAWATANI, K. SHIMIZU, T. NAKAYAMA, T. HIRAI:-
Trans. ISI Japan,, 1978, 18, (11), P.686-695.
- C45 R.M. DAVISON :- Met. Trans. Nov. 1974, (5),
p.2287-2294.
- C46 BRITISH STANDARD B.S. 1449 Part 2 (1983).
- C47 J.W. FRANCIS :- Steel Times, April 1979,
p.254-268.

C7 TABLES

TABLE C1

RELATIVE COST FACTORS FOR FERRITIC STAINLESS STEELS

(a) Relative cost factors for 0.8-mm thick sheet in 1981, compared with 304 austenitic stainless steel (C2)

<u>Grade</u>	<u>Relative cost factor (finished sheet) (C2)</u>	<u>Relative Alloy cost factor (C4)</u>
304 (18 Cr, 10 Ni)	1.0	1.0
430 (17 Cr)	0.75	0.48
430 Ti (17 Cr, 0.5 Ti)	0.90	0.79
316 (18 Cr, 11 Ni, 2.5 Mo)	1.37 - 1.71	1.88

(b) Relative cost factors for 1.2mm thick sheet (1978) (C31)

<u>Grade</u>	<u>Relative cost factor (C31)</u>	<u>Relative Alloy cost (C4)</u>
304	1.0	1.0
409	0.77	0.57
Mild Steel	0.32	-

(c) Relative cost factors for 1.5mm thick strip (1977) (C5)

<u>Grade</u>	<u>Relative cost factor (C5)</u>	<u>Relative Alloy cost (C4)</u>
304	1.0	1.0
430	0.68	0.61
409	0.62	0.57
Mild Steel	0.15	-

RELATIVE CORROSION RESISTANCE OF STAINLESS STEELS (C26)

GRADE	CORROSIVE ENVIRONMENT *						
	Mild Atmospheric and Fresh water	Atmospheric		SALT WATER	Chemical		
		Industrial	Marine		Mild	Oxidising	Reducing
<u>304</u>	x	x	x	-	x	x	-
<u>409</u>	x	-	-	-	x	-	-
<u>430</u>	x	x	-	-	x	x	-
<u>316</u>	x	x	x	x	x	x	x

* An "x" indicates that the stainless steel may be considered resistant to the corrosive environment.

APPLICATIONS OF FERRITIC STAINLESS STEELS(a) Normal temperature applications

Application	Steel Grade(s)	Reference Source
Decoration and architecture	430, 430Ti	C2, C22
Hot water tanks, radiator tanks	409, 430, 430Ti	C5, C6, C21
Sinks, dishwashers	430, 430Ti	C2, C22
Food handling, including dairy, brewing and sugar industries	430Ti	C2, C6
Kitchen utensils	430	C2, C22
Steam irons	430, 430Ti	C22
Condenser tubing	430Ti	C6
Containers, culverts, dry fertilizer tanks	409	C6
Hospital and medical equipment	430, 430Ti	C22
Chemical plant accessories including catwalks, stairways, handrails	409	C5
Mining equipment :- chutes, sizing screens, hoppers, bunkers	409	C5
Petrochemical plant :- bubble caps, filters, trays, vessels	409	C5
Motor vehicle parts :- petrol tanks and caps, underbody frames. Wheel-arch liners	409	C5

(b) Elevated temperature applications

Application	Steel grade(s)	Reference Source
Heat-transfer applications (heat exchangers, etc.)	430Ti	C2, C6
Furnace parts	409	C5, C21
Exhaust systems	409	C6, C30, C31
Catalytic converter casings	409, 430Ti	C3, C6, C30

TABLE C4

FINAL GAUGES AND SUGGESTED HOT-ROLLED GAUGES FOR
430, 409, and 430 Ti STRIP

Final Gauge (mm)	430 steel (17 Cr)		409 (12 Cr,0.5Ti)/430Ti (17 Cr,0.5Ti) steels	
	Hot-band gauge(mm)	RA %	Hot-band gauge(mm)	RA %
0.5	2.5	80	2.5	80
0.6	2.5	76	3.0	80
0.7	2.5	72	3.0	77
0.8	3.0	73	4.0	80
0.9	3.0	70	4.0	78
1.0	3.5	71	4.0	75
1.5	5.0	70	6.0	75
2.0	7.0	71	8.0	75